STUDY OF THREE-DIMENSIONAL HETEROGENEITY BENEATH SEISMIC ARRAYS IN CENTRAL CALIFORNIA AND YELLOWSTONE, WYOMING

by

George Zandt

B.S., University of Wisconsin, Milwaukee

(1973)

SUBMITTED IN PARTIAL FULFILLMENT

OF THE REQUIREMENTS FOR THE DEGREE OF

DOCTOR OF PHILOSOPHY

at the

July, 1978

Signature of Author.....
Department of Earth and Planetary Sciences
14 July 1978

Certified by.....
Thesis Supervisor

Accepted by.....
Chairman, Departmental Committee on Graduate Students

STUDY OF THREE-DIMENSIONAL HETEROGENEITY BENEATH SEISMIC ARRAYS IN CENTRAL CALIFORNIA AND YELLOWSTONE, WYOMING

by

George Zandt

Submitted to the Department of Earth and Planetary Sciences
on 14 July 1978 in partial fulfillment of the requirements for the
degree of Doctor of Philosophy.

ABSTRACT

Teleseismic P-wave travel time residuals for two separate, dense seismic arrays in the western United States are inverted for three-dimensional structure beneath the arrays. Both arrays are situated in areas of active tectonics and provide an opportunity to study the deep structure of important tectonic elements of the western United States.

The U.S.G.S. Central California network is in an area dominated by strike-slip motion on the San Andreas fault thought by many to separate the Pacific and North American plates. Our results provide many valuable clues on the nature of this boundary. Lateral velocity anomalies in the uppermost mantle (30-60 km) generally follow the regional NW-SE tectonic trend; however, north of Hollister, positive and negative anomalies are separated along a line parallel to the Calaveras-Hayward faults, suggesting that they are more fundamental and deep-seated than the San Andreas. The regional trend disappears at 60-90 km which might indicate the asthenosphere has been reached.

Another U.S.G.S. array, located in and around Yellowstone National Park is used to study the subsurface expression of the Quaternary volcanic field and test the idea of mantle plumes. The inversion delineates a very pronounced low-velocity anomaly beneath the Yellowstone caldera extending into the upper mantle as deep as 250 km. The anomaly is as low as -12% in the upper crust but is reduced to around -5% at greater depths. The cross-sectional area of the anomaly increases with depth and at its deepest point is greatly elongated in a direction parallel to the trend of the Snake River Plain. This and other evidence seem to favor an interpretation of a propagating fracture through which a thermal plume is rising. The deep expression of the anomaly can be interpreted as either an indication that the lithosphere is nearly 250 km thick or that the upwelling of magma has created a downward growing root.

Name and Title of Thesis Supervisor: Keiiti Aki
Professor of Geophysics

ACKNOWLEDGEMENTS

This study was initiated and completed under the able guidance of my thesis advisor, Keiiti Aki. I seriously appreciate his allowance in " giving me enough rope " at my request, and his tireless efforts at the end to prevent the usually inevitable result. I have learned much from this experience.

Many people have contributed directly to this work. Primary among them are Bill Ellsworth whose experience and insight into seismological problems were invaluable, and Ken Anderson who initiated and nurtured me on the IBM 370-168 but whom I still consider a friend. Members of the U.S. Geological Survey in Menlo Park were generous hosts during summer visits in 1975 and 1976. Among them, W.H.K. Lee contributed greatly to the material of Chapter II. Chapter IV was possible only with the generous aid of H.M. Iyer and A.M. Pitt. Data, preprints, and discussions provided by R.B. Smith of the University of Utah were most helpful in learning about recent tectonics of Yellowstone.

Fellow inmates...uh, students are ultimately responsible for the " total experience " of graduate school. Although it is difficult (and dangerous?) to single out individuals the following deserve special blame. The original Four in the Hole in the Wall Gang: Arthur Cheng, Neal Goins, and Tony Shakal. Tony and I go a long way back, I hope we go a long ways ahead. Arthur, my official biographer,

and I have shared one office or another for five years, and we are still friends. The Night Owl Club regulars included Mike Fehler, Randy Richardson (honorary captain), and Steve Taylor. Mike and I have fished together, Randy and I have howled at the moon together, and Steve stinks. Seriously, Steve Taylor was an active participant in the Yellowstone refraction work (all his fault) and provided critical comments on much of this work; of course, any shortcomings of this thesis and errors of omission or commission are entirely his responsibility. There are many others, to them all... thanks.

Heidi had the herculean task of getting me going, keeping me on track, and winding me down. I enjoyed the last the most but appreciate the former two. She also drafted most of the figures and in many other ways made life easier for me in order that I could concentrate on this work.

Ellen Loiselle typed much of the manuscript and otherwise put it together. Sheila Parker also put in long hours typing the manuscript and the numerous tables. I sincerely appreciate the aid of both.

This work was possible with the support of the U.S.G.S. Geothermal Energy grant 14-08-0001-G-339.

Finally I would like to thank my parents who made it all possible.

TABLE OF CONTENTS

LIST OF FIGURES

LIST OF TABLES

CHAPTER I. Introduction

The purpose of this thesis is to document the development and application of a new seismological tool to the study of regional tectonics. The new method fills a crucial gap in the resolving power of seismic probing techniques. On one end of the spectrum of techniques, seismic reflection profiling provides high resolution images of the earth but is limited to relatively shallow depths (<50 km). On the other end, seismic refraction and surface wave studies can provide information on deep structure but only at the price of poor lateral resolution. The new technique provides spatial resolution on the scale of tens of kilometers to depths of hundreds of kilometers. Such images of the crust and upper mantle could provide many clues and insights into tectonic processes which operate in the outer layers of the earth. The only major requirement of the method is the location of a network of seismometers above the area of interest.

The western United States is a region of present day active tectonism. Active faulting, high heat flow, and young volcanic provinces all indicate a mobile and dynamic upper mantle. Yet, at present lateral heterogeneity is mapped only on a scale of hundreds of kilometers. In this thesis we provide images of selected areas in the western U.S. with an order of magnitude improvement in resolution. The major physiographic provinces of the western United

States are shown in Figure 1.1. The study areas of this thesis are located in two of the most active provinces: the central California Coast Ranges, and the focal point of several provinces at Yellowstone in the northwestern corner of Wyoming. Let us start with a review of the current ideas on the Cenozoic tectonics of the western U.S. Most tectonic models fall into one of four categories (Stewart, 1977; Christiansen and McKee, 1977):

(1) The western U.S., especially the Great Basin, is a broad shear zone accommodating right-lateral motion between the Pacific and North American plates (Atwater, 1970).

(2) Subduction of the East Pacific Rise and its persistence beneath the Great Basin is responsible for the active extensional tectonics (Menard, 1960; Cook, 1969).

(3) Back-arc convection initiated during the subduction of the Farallon plate, combined with the relaxation of compressive forces after cessation of subduction is responsible for active extensional tectonics (Scholtz et al., 1971).

(4) Movement of the North American plate over one or more upwelling mantle plumes causes breakup of the western U.S. (Mathews and Anderson, 1973; Smith and Sbar, 1974; Suppe et al., 1975).

Some combination of the above could possibly act together. We shall consider and develop some of these ideas during

the course of this thesis.

While admittedly the study areas were chosen on the basis of the presence of seismic arrays and availability of data, perhaps better choices could not have been made. Both localities are areas with important tectonic elements. In the California Coast Ranges the San Andreas Fault system supposedly is the surface trace of the Pacific - North American plate boundary. Yellowstone is supposedly atop an active mantle plume. By studying the deep structure of these two areas we hope to learn something about the mechanism responsible for their development. From there perhaps we will be able to generalize and comment on the validity of some or all of the hypotheses listed above.

The bulk of this thesis is divided into three major chapters. Chapter II is devoted to describing the formulation, numerical aspects, and the empirical aspects of the method. For those not interested in the numerical details, the second section can be skipped without loss in continuity.

Chapter III and Chapter IV are on California and Yellowstone, respectively. Both chapters are organized similarly; first a geologic and geophysical setting is provided, then the results of application of method are discussed in context of the setting. The California chapter describes the data in greater detail because it is new. Finally, in Chapter V a summary of the major conclusions is presented.

Figure Captions

Figure 1.1 Physiographic provinces of the western United States; from Stewart (1977).

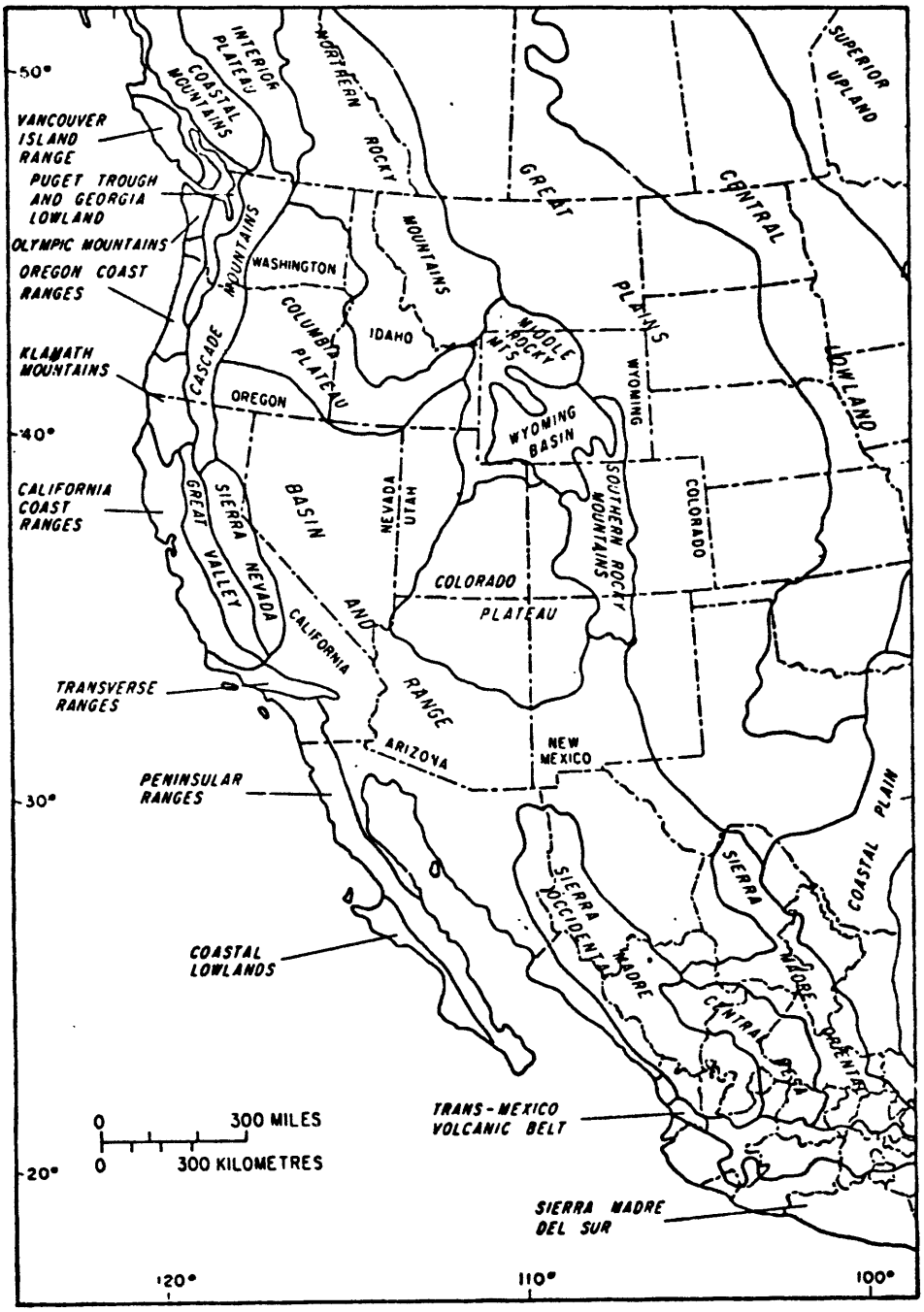
50°
40°
30°
20°
120°
110°
100°
VANCOUVER ISLAND RANGE
PUGET TROUGH AND GEORGIA LOWLAND
OLYMPIC MOUNTAINS
OREGON COAST RANGES
KLAMATH MOUNTAINS
CALIFORNIA COAST RANGES
TRANSVERSE RANGES
PENINSULAR RANGES
COASTAL LOWLANDS
TRANS-MEXICO VOLCANIC BELT
SIERRA MADRE DEL SUR
COASTAL MOUNTAINS
INTERIOR PLATEAU
NORTHERN ROCKY MOUNTAINS
GREAT PLAINS
CENTRAL LOWLAND
SUPERIOR UPLAND
CASCADE MOUNTAINS
WASHINGTON
IDAHO
OREGON
COLUMBIA PLATEAU
MIDDLE ROCKY MTS
WYOMING
WYOMING BASIN
SOUTHERN ROCKY MOUNTAINS
COLORADO
COLORADO PLATEAU
NEVADA
UTAH
BASIN AND RANGE
CALIFORNIA
GREAT VALLEY
SIERRA NEVADA
ARIZONA
NEW MEXICO
SIERRA MADRE OCCIDENTAL
SIERRA MADRE CENTRAL
MESA CENTRAL
SIERRA MADRE ORIENTAL
COASTAL PLAIN
0 300 MILES
0 300 KILOMETRES

Figure 1.1

CHAPTER II. Formulation of Three-Dimensional Inversion and Numerical Problems

The method used in this thesis for investigating deep structure is three-dimensional inversion of travel time residuals of P-waves from the teleseismic events observed by a network of seismographs. Originally, the method is due to Aki, Christofferson and Husebye (1977) hence it will be referred to as the ACH method. This chapter is divided into three sections: The first is an account of the formulation with emphasis on the major assumptions; the second delves into the numerical problems; and the third is a qualitative discussion of the effects on the solution of different initial models and inversion parameters. The section on the numerical problems is the longest because the material is not generally covered in the papers so far published on the subject.

2.1 FORMULATION OF THREE-DIMENSIONAL INVERSION SCHEME

A detailed account of the ACH method is available in the original paper by Aki, Christoffersson, and Husebye (1977) and also in Ellsworth (1978). The purpose of this section is to review the formulation in enough detail to provide the reader with the basic tenets of the method. A few more details are found in Appendix A. First we present a heuristic description of the method followed by a more detailed formulation showing how the major assumptions enter into the method.

2.1.1 Heuristic Description

Consider a seismic array covering an area of the earth of L^2 km^2 with an average station spacing of about ℓ km (typical values of L and ℓ are 100 km and 10 km respectively). A teleseismic event is recorded by the array as the arrival of a plane wave sweeping across the array with given azimuth and ray parameter (dt/dx). Given the location of the event the wavefront's step-out time between stations is predictable from some standard earth model. Any deviation from the predicted step-out time (a travel time residual) could be due to a number of causes; for now assume it is due to lateral variation in velocity beneath the array. If the array records many teleseismic events from various azimuths and distances the resulting suite of residuals contains information on the lateral distribution of velocity beneath the array. To

quantize the contribution of various portions of a raypath approaching a station, the earth under the array is modeled by a small number of initially homogeneous, flat layers. Assuming we can, at best, resolve lateral inhomogeneity on the scale of ℓ kilometers, each layer is divided into a number of homogeneous "blocks" with horizontal dimensions of this scale (figure 2.1). Each "block" is characterized by a fractional velocity perturbation, $x = (\Delta v/v)$, where v is the velocity of the layer in which the block is located. Let $\underline{x}$ be a vector with elements x_k, $k = 1,\ldots,NB$ where NB = total number of blocks in the model. The vector, $\underline{x}$, contains the unknowns which define the lateral variations of velocity in each layer that produces the observed residuals. Let the vector, $\underline{b}$, contain elements R_{ij} which are the residuals recorded at station j for event i. The length of $\underline{b}$ is NB, the total number of residuals. Then, making several assumptions to be specified later, the vectors $\underline{x}$ and $\underline{b}$ are linearly related by the following matrix equation:

$$\underline{b} = A\underline{x} \tag{2.1}$$

where A is the coefficient matrix of size ND x NB. The elements of matrix A turn out to be simply related to the travel time of a ray through a layer. Let t'_{ijk} denote the travel time of a ray from the i^{th} event to the j^{th} station spent in the k^{th} block. Note that t'_{ijk} is zero if the ray does not penetrate the k^{th} block. The elements of a_{ijk} of A are,

$$a_{ijk} = t'_{ijk} - \frac{1}{n_i} \sum_{j=1}^{n_i} t'_{ijk} \qquad (2.2)$$

In words, the elements a_{ijk} are the travel time spent by the ij^{th} ray in the block k minus its average over j. n_i is the total number of stations supplying data for event i. Solution of the matrix equation for $\underline{x}$ provides the desired information.

Like any mathematical model of the earth this method requires a number of simplifying assumptions in order to make the solution tractable. These assumptions usually place rigid constraints on the realism of a model and therefore are of critical importance in the evaluation of any modelling technique. The major assumptions in the ACH method are: (1) the residuals are due solely to lateral velocity heterogeneity that persists beneath the array to some datum depth D; (2) the earth beneath the array to the depth D can be initially modelled as a small number ($\leqslant 6$) of constant velocity horizontal layers; (3) lateral heterogeneity within each layer occurs as discrete jumps; and (4) the magnitude and scale of heterogeneity justifies the use of geometrical ray theory.

We have just presented the basic concepts of the method. Next we examine the nature of teleseismic travel time residuals and seismic ray travel times in order to illustrate how the major assumptions listed above enter

into the method.

2.1.2 Teleseismic Travel Time Residuals

A seismic travel time residual is simply the observed arrival time at a station of a seismic wave from an event minus the corresponding theoretical time based on some standard earth model and known or assumed hypocenter and origin time of the event. For the larger (m_b > 5) earthquakes and underground nuclear explosions the hypocenter and origin time is known or calculated from world-wide seismic network data. A residual is the net effect of a number of factors affecting both the observed and calculated travel times. The observed travel time might be in error due to timing problems and picking errors. These errors can be kept small (0.1 sec standard error) by good instrumentation, careful analysis, and picking only well-recorded events. Calculated travel times are affected by the origin time accuracy, and by the necessarily simple earth model used in the calculation. The standard earth models most often used are either the Jeffreys-Bullen (JB) Earth model (Jeffreys and Bullen, 1958) or the Herrin (HERR) Earth model (Herrin et al., 1968) both of which are radially varying average velocity models. Any systematic error in the standard model will introduce errors into the residual. Also lateral velocity variations along any portion of the ray path will affect the residual. Our model, however, can explain only the component of the residual due to lateral velocity varia-

tions beneath the array. There are two methods of isolating that component; the use of a reference station or the average event residual. Before explaining these, we introduce the following notation:

Tm_{ij} is the arrival time of a wavelet measured at station j for event i.

Tc_{ij} is the predicted travel time of the P-wave between event and station as given by a specified earth model.

OT_i is the event origin time.

The travel time residual T_{ij} is then given by,

$$T_{ij} = Tm_{ij} - Tc_{ij} - OT_i \tag{2.3}$$

Notice that for a given event i, the quantity OT_i is common to all stations. This fact forms the basis for eliminating source effects from the data. Commonly, a reference station is chosen and for each event the travel time for the reference station, T_{io}, is subtracted from all the other travel times forming relative residuals, $R_{ij} = T_{ij} - T_{io}$. Using equation 2.3,

$$T_{io} = Tm_{io} - Tc_{io} - OT_i \tag{2.4}$$

and

$$R_{ij} = Tm_{ij} - Tc_{ij} - Tm_{io} + Tc_{io} \tag{2.5}$$

This procedure eliminates any error in origin time OT_i. In fact any error common to all the stations, such as a syste-

matic error in the standard earth, source mislocation, and lateral velocity variations in the source region are all eliminated. The major drawback is that relative residuals contain information on "relative" lateral velocity variations and the information on the absolute velocity is lost. The use of a reference station contains an implicit assumption that the earth beneath it is relatively free of anomalous structure. Sometimes it is possible to choose a reference station that satisfies that criterion, more often it is not.

Another 'referencing' method which circumvents the latter problem is in the use of the average event residual,

$$\overline{T}_i = \frac{1}{n_i} \sum_{j=1}^{n_i} T_{ij} \qquad (2.6)$$

where n_i is the number of stations supplying data for event i. Subtracting (2.6) from each residual, the relative residuals, $R_{ij} = T_{ij} - \overline{T}_i$, are

$$R_{ij} = Tm_{ij} - Tc_{ij} - \overline{Tm}_i + \overline{Tc}_i \qquad (2.7)$$

where $\overline{Tm}_i = \frac{1}{n_i} \sum_{j=1}^{n_i} Tm_{ij}$ and $\overline{Tc}_i = \frac{1}{n_i} \sum_{j=1}^{n_i} Tc_{ij}$.

This method has all the advantages of using a reference station without the implicit assumption of no anomaly beneath the reference station. The assumption of this method is that the earth below the datum D beneath the array has <u>on the average</u> no lateral velocity gradient that might "tilt"

the incoming plane wave. Such an assumption is at least self consistent with other assumptions of the method and is likelier to be satisfied in nature.

The datum depth D is usually chosen to be approximately equal to the array's aperture L. If the datum is pushed much deeper the resolution of the deeper layers degrade appreciably as the seismic rays diverge away from the array. The depth D is usually on the order of 100 km and heterogeneity undoubtedly persists to greater depths. However, with the possible exception of subduction zones the degree of heterogeneity is greater by an order of magnitude in the crust and upper mantle compared to the middle and lower mantle (Sengupta, 1975). Thus we are confident that the relative residuals are controlled principally by lateral velocity variations below the array and above depth D.

2.1.3 Seismic Ray Travel Time

The travel time of a seismic ray from point A to point B is given by

$$t = \int_A^B v^{-1}(s)\,ds \qquad (2.8)$$

where v(s) is the velocity along the travel path s and ds is an incremental length along the path. Now consider a ray arriving at a station from a teleseismic event. Near

the station we can use a rectangular coordinate system (see figure 2.2) and write the travel time from depth z = D to the surface as,

$$t = \int_D^0 \eta^2 \left(\eta^2 - p^2\right)^{-1/2} dz \qquad (2.9)$$

where $\eta \equiv v^{-1}$ and the ray parameter p is a constant along the ray by Snell's law which states, in terms of the angle γ between the vertical unit vector $-\hat{z}$ and a vector $\vec{ds}$ parallel to the ray path,

$$p = dt/d\ell = \sin\gamma/V = \text{constant} \qquad (2.10)$$

where $d\ell^2 = dx^2 + dy^2$.

For an array with a small aperture (<200 km) the ray parameters of rays from a teleseismic event ($\Delta > 30°$) are nearly a constant across the array, that is, the rays arrive as a plane wave. Thus the travel time of the wavefront from datum D with respect to the origin of the coordinate system is,

$$t_{ij} = \int_D^0 \eta^2 \left(\eta^2 - p_i^2\right)^{-1/2} + \vec{p}_i \cdot \vec{\ell}_j \qquad (2.11)$$

where $\vec{p}_i = p_i \vec{ds}$ and $\vec{\ell}_j = x_j\hat{x} + y_j\hat{y}$.

The plane wave assumption is good if $dp/d\ell$ is small compared to p.

Fermat's principle states that the travel time integral, equation (2.8), has an extremum value along the actual ray path and thus the ray path is a path of stationary time. Therefore, for a small perturbation in velocity, δv, the first order change in travel time, δt, is given by

$$\delta t = -\int_A^B v^{-2} \delta v \, ds \tag{2.12}$$

Note that this step gives us a linear equation in the unknown δv which can also be shown by expanding (2.8) in a Taylor's series and keeping only the first order terms although we still need Fermat's principle to ignore terms involving δs. In a rectangular coordinate system and using equation (2.9) to represent the travel time ds/v, (2.12) becomes,

$$\delta t = -\int_D^0 \eta^2 \left(\eta^2 - p^2\right)^{-1/2} \frac{\delta v}{v} \, dz \tag{2.13}$$

The velocity distribution in the crust is often modelled as a small number of constant velocity layers. Although the velocity distribution in the upper 300 km of the mantle varies continuously with depth, several constant velocity layers can adequately represent the velocity distribution. By using a discrete velocity model, the integral in equation (2.13) can be replaced by a summation over the NL layers between the surface and z = D,

$$\delta t = -\sum_{k=1}^{NL} \eta_k^2 \left(\eta_k^2 - p^2\right)^{-1/2} \frac{\delta V_k}{V_k} \Delta z_k \qquad (2.14)$$

This last equation provides a simple means of calculating the elements of the coefficient or partial derivative matrix of our inverse problem.

The remaining step in the formulation of the problem is the representation of the lateral velocity perturbations. The ACH method uses the simplest yet most flexible method of specifying a rectangular grid in each layer which specifies somewhat arbitrary boundaries at which the velocity can change discontinuously and thus breaking up the volume between the surface and depth D into a three-dimensional configuration of blocks. The discontinuous and arbitrary nature of the lateral boundaries is weakened somewhat by using only the midlayer location of the ray path to assign the ray path coefficient to a specific unknown. Thus the procedure for computing the coefficients in equation (2.1) is the following: For a particular event, the ray parameter and azimuth is used to trace the ray paths up through the layered model to each of the recording stations. The travel time through a layer is constant for all stations because of the plane wave assumption. This time is assigned to the element of the coefficient matrix corresponding to the block containing the ray's midlayer position. The elements corresponding to unsampled blocks are set to zero.

The computations are repeated for each event-station pair and the coefficient matrix is thus filled. The resulting matrix is very sparse with many zero elements. At this point we have the following equation,

$$T_{ij} = \sum_{k=1}^{K} \eta_k^2 \left(\eta_k^2 - P_i^2\right)^{-1/2} \Delta z_k \, \delta_{ijk} \left(-\frac{\delta V}{V}\right)_k \qquad (2.15)$$

where we defined that $\delta_{ijk} = 1$ if the k^{th} block contains the mid-point of the ij^{th} ray in the layer to which the k^{th} block belongs and otherwise $\delta_{ijk} = 0$. K is the total number of blocks. Earlier we noted that in order to remove the errors common to a source we need to subtract from T_{ij} the average of Tij over all the stations

$$\overline{T}_i = \sum_{k=1}^{K} \eta_k^2 \left(\eta_k^2 - P_i^2\right)^{-1/2} \Delta z_k \frac{1}{NS} \sum_{j=1}^{NS} \delta_{ijk} \left(-\frac{\delta V}{V}\right)_k \qquad (2.16)$$

Thus,

$$R_{ij} = \sum_{k=1}^{K} -\eta_k^2 \left(\eta_k^2 - P_i^2\right)^{-1/2} \Delta z_k \left(\delta_{ijk} - \frac{1}{NS} \sum_{j=1}^{NS} \delta_{ijk}\right)\left(\frac{\delta V}{V}\right)_k \qquad (2.17)$$

The above equation can be written in matrix form (2.1)

$$\underline{b} = A\underline{x}$$

where the components of $\underline{b}$ are Rij and

$$x_k = \left(\frac{\delta V}{V}\right)_k \qquad (2.18)$$

Now the critical importance of the initial layer model to the solution is clearer. The initial model determines the elements of the coefficient matrix A which couples the solution vector $\underline{x}$ to the data vector $\underline{b}$. An accurate model of velocity with depth is also important in attributing the observed anomalies to the correct location beneath the array. This involves tracing rays through the medium. Simple geometrical ray theory is used for this purpose. The condition for the validity of geometrical optics is (Officer, 1958):

$$\lambda_o \frac{\delta V'}{V} \ll 1 \qquad (2.19)$$

where $\delta v'$ is the change in velocity gradient v' over a distance λ_o, the characteristic wavelength of the seismic wave. For a one hertz teleseismic arrival $\lambda_o \sim$ v km, thus,

$$\delta V' \ll 1 \text{ km/sec per km} \qquad (2.20)$$

Except in areas of exceptional heterogeneity, this condition is usually satisfied.

Now that the formulation of the problem is completed, the following section deals with solving equation (2.1) for the unknown vector $\vec{x}$. Since the number of unknowns are usually less than the number of observations in our problem, it is reduced to a least squares problem.

2.2 NUMERICAL METHODS FOR SOLVING LEAST SQUARES PROBLEMS

We are now ready to treat different approaches for solving the least squares problem. Due to the immense scope of the subject we neither attempt to cover all the techniques nor all the different cases in least squares problems. We restrict the discussion to the case with real numbers and more equations than unknowns. Further we consider only the normal equations, Householder reduction, and singular value analysis approaches. None of the various iterative techniques such as the conjugate gradient method recently applied to earthquake data by Crosson (1976) are considered.

The techniques we did investigate are described in the following three subsections. In each subsection a brief summary of the motivation of the method is followed by a description of how the method is applied to find not only the solution vector but also the resolution and covariance matrices. Computational advantages and disadvantages are stressed throughout. The last subsection is an important one dealing with the modifications necessary in the case of rank deficiency in the matrix A.

2.2.1 Normal Equations Approach

The normal equations arise directly from the definitions of least squares. In least squares, the solution vector to a set of simultaneous linear equations is defined to

be the one which has the minimum squared residual. That is, given our matrix equation (2.1)

$$A x = b \tag{2.21}$$

the least squares solution, $\hat{x}$, is the vector which minimizes,

$$r^2 = \| b - A\hat{x} \|^2 \tag{2.22}$$

where $\| \cdot \|$ denotes euclidean length

or

$$\begin{aligned} \tilde{r}r &= \widetilde{(b - A\hat{x})}(b - A\hat{x}) \qquad \text{where } \sim \text{ denotes transpose} \\ &= (\tilde{b} - \tilde{\hat{x}}\tilde{A})(b - A\hat{x}) \end{aligned}$$

$$\tilde{r}r = \tilde{b}b - 2\tilde{\hat{x}}\tilde{A}b + \tilde{\hat{x}}\tilde{A}A\hat{x} \tag{2.23}$$

To minimize (2.23), we take the usual procedure of computing the derivation of the expression with respect to $\hat{x}$ and setting the derivative expression equal to zero.

$$\frac{d}{d\hat{x}}(\tilde{r}r) = -2\tilde{A}b + 2\tilde{A}A\hat{x} = 0 \tag{2.24}$$

or

$$\tilde{A}A\hat{x} = \tilde{A}b \tag{2.25}$$

Equation (2.25) is the normal equation form of (2.21) and is readily recognized as simply equation (2.21) premultiplied by $\tilde{A}$. However, the above derivation better expresses the minimization aspect of the normal equations. Thus, the least squares solution is

$$\hat{x} = (\tilde{A}A)^{-1}\tilde{A}b \tag{2.26}$$

if the inverse $(\tilde{A}A)^{-1}$ exists. For the present, we assume the existence of $(\tilde{A}A)^{-1}$ and consider how to numerically compute the solution vector $\hat{x}$.

The expression for the solution vector (2.26) immediately suggests the computation of the inverse matrix $(\tilde{A}A)^{-1}$ and postmultiplying by $\tilde{A}b$. Although this method is straightforward, it is computationally inefficient. The computations are faster and more accurate if some Gaussian elimination scheme is applied to the set of linear equations (2.25).

The fact that the coefficient matrix $(\tilde{A}A)$ in equation (2.25) is symmetric and nonnegative definite, permits the use of a very economical and stable Gaussian elimination scheme known as Cholesky's method. The method is based on the existence of the following decomposition. If G is a symmetric, nonnegative definite matrix, then it can be decomposed uniquely into $\tilde{L}L$, where L is a lower triangular matrix with positive diagonal elements (see, e.g., Forsythe and Moles, 1967, p. 29).

In equation (2.25) let

$$G = \tilde{A}A \tag{2.27}$$

$$d = \tilde{A}b \tag{2.28}$$

so we have,

$$G\hat{x} = d \tag{2.29}$$

Applying the decomposition,

$$G = L\tilde{L} \tag{2.30}$$

equation (2.29) becomes,

$$L\tilde{L}\hat{x} = d \tag{2.31}$$

Equation (2.31) can be separated into the following two simple equations,

$$Ly = d \tag{2.32}$$

and

$$\tilde{L}\hat{x} = y \tag{2.33}$$

The solution of equations (2.32) and (2.33) are simple because both have triangular systems of coefficients which allows direct forward and back substitution for the unknowns y and $\hat{x}$.

Once a solution vector $\hat{x}$ is computed we might want to estimate the bounds on the errors of the elements of that solution. The covariance matrix provides a means of making such an estimation. If we let $\Delta\hat{x}$ represent the errors in the solution then the proper quantity to examine is

$$E\left\{\Delta\hat{x}\,\widetilde{\Delta\hat{x}}\right\} \tag{2.34}$$

where, $E\{\cdot\}$ is the expectation operator (Draper and Smith,

1966). From equation (2.26) we can write,

$$\Delta\hat{x} = (\tilde{A}A)^{-1}\tilde{A}\,\Delta b \tag{2.35}$$

therefore,

$$\Delta\hat{x}\,\widetilde{\Delta\hat{x}} = (\tilde{A}A)^{-1}\tilde{A}\,\Delta b\,\widetilde{\Delta b}\,A\,(\tilde{A}A)^{-1} \tag{2.36}$$

Assuming the errors in the data, Δb are normally distributed and statistically independent so that,

$$E\{\Delta b\,\widetilde{\Delta b}\} = \sigma_b I \tag{2.37}$$

then,

$$E\{\Delta\hat{x}\,\widetilde{\Delta\hat{x}}\} = \sigma_b (\tilde{A}A)^{-1} \tag{2.38}$$

The number σ_b which is an estimate of the standard errors of the errors in the data must be obtained from independent sources (or an educated guess). The covariance matrix,

$$C = (\tilde{A}A)^{-1} \tag{2.39}$$

is, in this case, simply the inverse of the coefficient matrix of the normal equations (2.25).

As we mentioned earlier the Gaussian elimination method has the distinct advantage of being the fastest known technique for solving a set of linear equations. For example, Forsythe and Moler point out that once the decomposition of the A matrix to $L\tilde{L}$ is accomplished, the solution of $L\tilde{L}\,\hat{x}$

= d requires n^2 multiplicative operations, and once G^{-1} has been computed, the formation of $G^{-1}d$ requires n^2 multiplications. However, the calculations of $L\tilde{L}$ and G^{-1} require about 1/3 n^3 and n^3 operations, respectively. Thus the Gaussian elimination scheme is faster than calculating G^{-1}, even in the case of many data vectors.

The one disadvantage of the elimination schemes (as well as finding G^{-1}) occurs when the original A matrix (or the $G = \tilde{A}A$ matrix) is ill-conditioned, that is singular or near-singular. Although diagonal pivoting schemes can stabilize matrices with mild cases of ill-conditioning the schemes cannot handle a real singularity. Perhaps even worse, in the case of near-singularity the algorithm will converge to a solution; however, that solution, even though it may have a small residual vector, is highly suspect. Later we given an example of such a case and illustrate how to detect the presence of the near-singularity and several methods of circumventing the ill-conditioning (Appendix B).

2.2.2 Householder Reduction Approach

We wish to motivate the discussion on the Householder reduction approach to solving equation (2.21) by considering some aspects of error analysis. Forsythe and Moler (1968, Chapter 8) present a lucid summary of estimating the effect of errors in either the partial derivative matrix A or the data vector b. They showed that for a nonsingular matrix A, there are expressions that set upper bounds on the error in

the solution. These expressions are known for the case where A is known exactly but the vector b contains errors, and the case where b is known exactly but the matrix A is uncertain.

In the former case let b + δb be another data vector which is within the "noise" of the original data. Then we can write

$$A(x + \delta x) = b + \delta b \tag{2.40}$$

where δx represents the resulting error in the solution. The question now is, for a given δb, how large can δx become? The answer is (Forsythe and Moler, 1967, p. 20),

$$\frac{\|\delta x\|}{\|x\|} \leq \|A\| \cdot \|A^{-1}\| \frac{\|\delta b\|}{\|b\|} \tag{2.41}$$

or

$$\frac{\|\delta x\|}{\|x\|} \leq \text{cond}(A) \cdot \frac{\|\delta b\|}{\|b\|} \tag{2.42}$$

where cond (A) $\equiv \|A\| \cdot \|A^{-1}\| = \frac{S_1}{S_n}$ (2.43)

where S_1 and S_n are the largest and smallest singular values of A, respectively. Thus large condition numbers place large upper bounds on the induced error in the solution.

For the latter case where b is known exactly and a matrix A + δA is within the "noise" of the original matrix A, we have,

$$x + \delta x = (A + \delta A)^{-1} b \tag{2.44}$$

and after some manipulation (Forsythe and Moler, 1967, p. 23),

$$\frac{\|\delta x\|}{\|x + \delta x\|} \leq \text{cond}(A) \frac{\|\delta A\|}{\|A\|} \tag{2.45}$$

Thus, the importance of the condition number is again apparent. The larger the condition number is the larger is the possible magnification effect on any errors in b or A.

Recall that the condition number of a nonsingular matrix is the ratio of the largest to smallest singular value. Therefore, the normal equation approach of the previous subsection which forms and works on the matrix product $\tilde{A}A$ will require γ^2 precision to obtain comparable results working with γ precision directly on the matrix A. The reason is simply because the singular values of a matrix A are the square root of the eigenvalues of the square matrix $\tilde{A}A$. Note that the term "singular value" is usually reserved for nonsquare matrices and "eigenvalues" for squared matrices, however, it is consistent to equate the eigenvalues of $\tilde{A}A$ to the singular values of $\tilde{A}A$. Thus, if

$$\text{cond}(A) = S_1 / S_2 \tag{2.46}$$

then

$$\text{cond}(\tilde{A}A) = (S_1 / S_2)^2 \tag{2.47}$$

and the upper bounds defined by equations (2.44) and (2.45) are a power of two greater when working on the matrix $\tilde{A}A$ compared to matrix A.

The Householder reduction approach to solving equation (2.21) has the advantage of working directly on the non-square m by n matrix A, where m > n, thereby reducing the precision γ required to obtain similar results using the normal equations approach.

In practice, the Householder reduction is just an orthogonal decomposition of the matrix A (For a proof of existence of such a decomposition, see Lawson and Hanson, 1974, p. 11.). The Householder decomposition is achieved by pre-multiplying the matrix A with a sequence of Householder transformation matrices, Q_i, i = 1,2,...,n, such that

$$\{Q_n Q_{n-1} \cdots Q_2 Q_1\} A \equiv QA = R \tag{2.48}$$

The matrix R has the following form:

$$R = \begin{bmatrix} \hat{R} \\ O \end{bmatrix} \tag{2.49}$$

where $\hat{R}$ is a n by n upper triangular matrix. The matrix Q_1 is constructed to zero the first column of matrix A in elements 2 through m, Q_2 is constructed to zero the second column of matrix Q_1A in elements 3 through m, and so on. In this way a product of, at most, n orthogonal matrices will

transform matrix A to an upper triangular form R. Once this is accomplished, the problem of Ax = b is changed to

$$QA\,x = Q\,b \tag{2.50}$$

or

$$R\,x = Q\,b \tag{2.51}$$

where R is an m by n matrix, x is an n-vector, and Qb is an m-vector. Equation (2.51) can be partitioned as:

$$\begin{bmatrix} \hat{R} \\ 0 \end{bmatrix} x = \begin{bmatrix} g_1 \\ g_2 \end{bmatrix} \tag{2.52}$$

where $\hat{R}$ is the n by n upper triangular matrix, and

$$\begin{bmatrix} g_1 \\ g_2 \end{bmatrix} \equiv g \equiv Q\,b \tag{2.53}$$

where g_1 is an n-vector, and g_2 is an (m-n)-vector. From equation (2.53), the solution vector must satisfy,

$$\hat{R}\,x = g_1 \tag{2.54}$$

which can be solved rapidly by back substitution since $\hat{R}$ is an upper triangular. Obviously the solution $\hat{x}$ to (2.54) cannot satisfy (2.52) exactly unless $g_2 = 0$. The computation of the residual vector,

$$r \equiv b - A\hat{x} \tag{2.55}$$

is simplified by taking advantage of the decomposed form of

A. From equation (2.48),

$$b - A\hat{x} = b - QR\hat{x} \tag{2.56}$$

or

$$r = Q(Qb - R\hat{x}) \tag{2.57}$$

using the unusual property of Q, which due to symmetry and orthogonality, is its own inverse ($Q = Q^{-1}$). Using the notation (2.53)

$$r = Q(g - R\hat{x}) \tag{2.58}$$

or in partitioned form (equation (2.52)):

$$g - Rx = \begin{bmatrix} g_1 \\ g_2 \end{bmatrix} - \begin{bmatrix} \hat{R} \\ 0 \end{bmatrix} \hat{x} \tag{2.59}$$

or

$$g - Rx = \begin{bmatrix} 0 \\ g_2 \end{bmatrix} \tag{2.60}$$

since $\hat{R}\hat{x} = g_1$. Finally,

$$r = Q \begin{bmatrix} 0 \\ g_2 \end{bmatrix} \tag{2.61}$$

and the r.m.s. error is simply the length of the vector r,

$$\rho \equiv \|r\| = \|g_2\| \tag{2.62}$$

since by definition of orthogonality,

$$\| Q \| = 1$$

Similarly the decomposed form of A can be utilized to simplify the computation of the covariance matrix (equation 2.39). Again using equation (2.48),

$$C \equiv (\tilde{A}A)^{-1} = (\tilde{R}\tilde{Q}\,QR)^{-1} = (\tilde{R}R)^{-1} \tag{2.63}$$

Then using the identity,

$$(\tilde{R}R)^{-1} = R^{-1}(\widetilde{R^{-1}}) \tag{2.64}$$

we have,

$$C = (R^{-1})(\widetilde{R^{-1}}) \tag{2.65}$$

This form of the covariance matrix allows us, by taking advantage of the fact that the inverse of a triangular matrix is also triangular, to formulate a direct recursive formula for R^{-1}. Let the elements of matrix R be represented by r_{ij}, and the elements of matrix R^{-1} by p_{ij}, then

$$P_{ij} = \begin{cases} r_{ij}^{-1} & \text{if } j = i \\ -r_{ij}^{-1} \sum_{k=i}^{j-1} P_{ik}\, r_{kj} & \text{if } j > i \end{cases} \tag{2.66}$$

(Lawson and Hanson, 1974, p. 69). Of course, once R^{-1} is computed, it is a simple matter to compute the covariance

matrix by equation (2.65).

2.2.3 Singular Value Analysis Approach

The solution of problem (2.21) by the Householder approach discussed in the previous section leads to another computational scheme developed recently by Golub and others (e.g., Golub and Businger, 1965, Golub and Kahan, 1965, and Golub and Reinsch, 1971). Known as singular value analysis (SVA), the method requires more computations but provides more information on various aspects of the solution. This latter aspect is especially important in cases where the A matrix is ill-conditioned, that is, singular or nearly singular. The next subsection deals with this aspect of SVA among other methods of handling ill-conditioned matrices. The following paragraphs deal with constructing a solution and other quantities assuming we can decompose any m by n matrix A of rank k into a product of the following three matrices:

(1) U, an m by m orthogonal matrix,

(2) V, an n by n orthogonal matrix, and

(3) S, an m by n matrix in the following form:

$$S = \begin{bmatrix} \hat{S} \\ O \end{bmatrix} \tag{2.66}$$

where $\hat{S}$ is an n by n diagonal matrix. That is,

$$A = US\tilde{V} \tag{2.67}$$

Lawson and Hanson (1974, p. 18) proved the above decomposition theorem.

The motivation behind the decomposition (2.67) is clarified by the following derivation from Aki (1975) due originally to Lanczos (1961). Given the m by n matrix A, where m > n, form the square (m+n) by (m+n) matrix G as follows:

$$G = \begin{pmatrix} O & A \\ \tilde{A} & O \end{pmatrix} \begin{matrix} \} m \\ \} n \end{matrix} \qquad (2.68)$$

Note that $\tilde{G} = G$, which assures the existence of an orthogonal set of eigenvectors, w_i, $i = 1,2,\ldots,m+n$, with real eigenvalues λ_i which satisfy the characteristic equation of the eigenvalue problem:

$$Gw_i = \lambda_i w_i \quad ; \quad i = 1,2,\ldots,m+n \qquad (2.69)$$

The eigenvectors w_i have m+n components so it is natural to divide the components into two groups as follows

$$w_i = \begin{bmatrix} u_i \\ v_i \end{bmatrix} \begin{matrix} \} m \\ \} n \end{matrix} \qquad (2.70)$$

Then equations (2.69) can be written as,

$$\begin{pmatrix} 0 & A \\ \tilde{A} & 0 \end{pmatrix} \begin{pmatrix} u_i \\ v_i \end{pmatrix} = \lambda_i \begin{pmatrix} u_i \\ v_i \end{pmatrix} \begin{matrix} \} m \\ \} n \end{matrix} \qquad (2.71)$$

for $i = 1,2,\ldots,m+n$

We should note here that the two groups u_i and v_i in equations (2.70) and (2.71) are often referred to as being in the data (or m) space and the solution (or n) space, respectively. This refers to the fact that in the equation $Ax = b$, the data vector has m-components and the solution vector has n-components. Notice also that the A matrix has its columns in the solution space and its rows in the data space. Returning to equation (2.71), for non-zero eigenvalues λ_i, $i = 1,2,\ldots,k$, $k \leq n$, we have two coupled equations which span both data and solution space.

$$Av_i = \lambda_i u_i \qquad (2.72)$$

and

$$\tilde{A} u_i = \lambda_i v_i \qquad (2.73)$$

for $i = 1,2,\ldots,k$

In order to decouple the equations multiply (2.72) by λ_i then substitute equation (2.73) into (2.72). This yields,

$$A\tilde{A} u_i = \lambda_i^2 u_i \qquad i = 1, 2, \ldots, K \qquad (2.74)$$

Similarly,

$$\tilde{A} A v_i = \lambda_i^2 v_i \qquad i = 1, 2, \ldots, k \qquad (2.75)$$

Equations (2.74) and (2.75) define the standard eigenvalue problem of $A\tilde{A}$ and $\tilde{A}A$, respectively. Therefore u_i and v_i are the eigenvectors of the matrices $A\tilde{A}$ and $\tilde{A}A$, respectively.

Define the m by m matrix U with columns consisting of the normalized eigenvectors u_i and the n by n matrix V with columns of the normalized eigenvectors v_i. Due to the orthogonality of eigenvectors,

$$\tilde{U}U = U\tilde{U} = I \qquad (2.76)$$

and

$$\tilde{V}V = V\tilde{V} = I \qquad (2.77)$$

Also define a diagonal matrix, S, with a k by k submatrix $\hat{S}$ whose elements are the nonzero eigenvalues λ_i, i = 1,2,...,k. Now equations (2.72) and (2.73) can be written in matrix notation as,

$$AV = U \begin{bmatrix} \hat{S} \\ O \end{bmatrix} \qquad (2.78)$$

and

$$\tilde{A}U = V \begin{bmatrix} \hat{S} & O \end{bmatrix} \qquad (2.79)$$

Postmultiplying equation (2.78) and premultiplying equation (2.79) by $\tilde{V}$ yields the desired results,

$$A = U\begin{bmatrix}\hat{S}\\ O\end{bmatrix}\tilde{V} \tag{2.80}$$

and

$$\tilde{V}\tilde{A}U = [\hat{S}\ O] \tag{2.81}$$

With this background we can return to equations (2.66) and (2.67) and interpret the components of the decomposition. The m by m matrix U contains the eigenvectors of the matrix $\tilde{A}A$ and is therefore in the data space of problem Ax = b. The n by n matrix V contains the eigenvectors of the matrix $\tilde{A}A$ and is therefore in the model space of problem Ax = b. The diagonal matrix S contains the eigenvalues of the matrix $A\tilde{A}$ or equivalently of $\tilde{A}A$ and is responsible for the coupling between the data space and the model space.

Now we deal with the task of solving Ax = b using the singular value decomposition of matrix A. Equation Ax = b can be rewritten using equation (2.80) as follows,

$$U\begin{bmatrix}\hat{S}\\ O\end{bmatrix}\tilde{V}x = b \tag{2.82}$$

Premultiplying by $\tilde{U}$ produces,

$$\begin{bmatrix}\hat{S}\\ O\end{bmatrix}\tilde{V}x = \tilde{U}b \tag{2.83}$$

Reparameterize x and b as

$$y = \tilde{V}x \tag{2.84}$$

and

$$g = \tilde{U}b \tag{2.85}$$

Then equation (2.83) becomes

$$\begin{bmatrix} \hat{S} \\ 0 \end{bmatrix} y = g \tag{2.86}$$

In the new parameters equation (2.86) is similar to equation (2.52) of the Householder reduction approach. Again it is a simple matter to solve for y because $\hat{S}$ is diagonal. If we let y_i and g_i represent the components of the vectors y and g respectively, and let s_i represent the singular values then the solution components $\hat{y}_i$ are simply,

$$\hat{y}_i = g_i / s_i \quad , i = 1,2,\ldots k, \quad k \leq n \tag{2.87}$$

The unparameterized solution, $\hat{x}$, using equation (2.84) becomes,

$$\hat{x} = Vy \tag{2.88}$$

It is instructive to rewrite the solution vector as a sum of component vectors. Let v_j represent the j^{th} eigenvector (column) in the matrix V, then

$$\hat{x} = \sum_{j=1}^{k} \hat{y}_j v_j \tag{2.89}$$

Thus the solution vector is seen to be composed of a sum of weighted eigenvectors of the matrix $\tilde{A}A$ in the model space. The weights are, in turn, composed of the data vector b transformed by the eigenvectors of the matrix $A\tilde{A}$ in the data space and multiplied by the inverse of the singular values of the A matrix. The solution x to the problem Ax = b in the form of equation (2.89) provides important insights into the case of ill-conditioned matrices to be discussed in the next subsection.

As in the case of the Householder reduction appraoch, the decomposed form of A can be used to simplify the computations of the residual and covariance matrix. Using a similar procedure as in equations (2.55) to (2.62), the residual vector is given by:

$$r = U\begin{bmatrix} 0 \\ g_2 \end{bmatrix} \tag{2.90}$$

where g_2 is the unexplained part of the transformed data vector. Likewise, the r.m.s. error is given by:

$$\rho = \| g_2 \| \tag{2.91}$$

The covariance matrix is this time given by:

$$C = (\tilde{A}A)^{-1} = VS^{-2}\tilde{V} \tag{2.92}$$

or in terms of the elements, c_{ij}, of the C matrix,

$$c_{ij} = \sum_{k=1}^{n} V_{ik} V_{jk} / s_k^2 \qquad (2.93)$$

The significance of equation (2.92) or (2.93) is discussed in the next section.

2.2.4 Treating the Rank-Deficient Case

Previously we have often mentioned the possibility of an ill-conditioned matrix A in problem Ax = b, but have delayed consideration of that case. We are now ready to consider how to recognize and to circumvent the effects of an ill-conditioned matrix. All three of the methods of solving the least squares problem which we have so far considered can be modified to handle this possibility. However, the singular value analysis method of the previous subsection is especially well suited for detecting and handling singularity problems. Therefore, we first present the modifications required in SVA before discussing those required for the Householder and normal equations approaches.

Ill-conditioning manifests itself as small or zero singular values of the matrix. Let us first consider the effects of small singular values in the solution. From equation (2.87) we see that small singular values will produce large components in the reparameterized solution vector $\hat{y}$. These, in turn, produce large oscillations in the

solution vector $\hat{x}$ as evident from equation (2.89). This condition is also detectable in the covariance matrix formula (2.92). Equation (2.93) shows that the elements of the covariance matrix become inflated. Since the diagonal element is porportional to the square of the standard error of the corresponding element of the solution vector, large standard errors are an indicator of an ill-conditioned matrix. Notice that the expressions for the residual vector and its norm (equations (2.90) and (2.91)) do not include any singular values, therefore, a small residual alone is not a reliable indicator of a good solution.

In the event one or more of the singular values are zero the equations for the solutions (2.87) and (2.89) and for the covariance matrix (2.93) are still valid because the upper limit of the summation is k, the rank of the matrix. We are assuming for these formulas that the singular values in $\hat{s}$ are arranged in descending order and thereby summing components up to k will automatically leave out the zero singular values. Wiggins (1971) suggested choosing a "cutoff" limit $k' \leq k$ to exclude the effects of small singular values. Such a procedure has the desired effect of damping large oscillations of the solution and reducing the standard errors. However, it also has negative effects. Here we need to introduce the concept of the resolution matrix. The problem Ax = b in decomposed form is,

$$U S \tilde{V} x = b \qquad (2.94)$$

and the solution, $\hat{x}$, is given by

$$\hat{x} = (V S^{-1} \tilde{U}) b \tag{2.95}$$

Substituting the expression for b in (2.94) into (2.95) yields,

$$\hat{x} = V\tilde{V} x \equiv R x \tag{2.96}$$

where

$$R \equiv V\tilde{V} \tag{2.97}$$

R is called the resolution matrix in model space. It can be thought of as a "filter" that relates the computed solution $\hat{x}$ to the real solution x. Thus the ideal situation occurs when R = I. Recall that we had earlier stated in equation (2.77) that $V\tilde{V} = I$. This statement is true only if the eigenvectors are complete. The meaning of this is better understood by writing equation (2.77) in component form,

$$r_{ij} = \sum_{\ell=1}^{k} v_{i\ell} v_{j\ell} \tag{2.97}$$

Then,

$$r_{ij} \begin{cases} = 1 & \text{if } k = n,\ i = j \\ < 1 & \text{if } k < n,\ i = j \\ = 0 & \text{if } k = n,\ i \neq j \\ > 0 & \text{if } k < n,\ i \neq j \end{cases} \tag{2.99}$$

When k = n, we say the eigenvectors are complete and condi-

tion (2.77) is satisfied and R = I; otherwise, the diagonal elements of R are less than unity, and the off-diagonal elements become nonzero. This degradation of the resolution is the negative effect which we mentioned earlier. Thus there is a tradeoff between resolution and covariance whenever the "cutoff" criterion is used. The resolution is also a measure of the uniqueness of a solution. If R = I then k = n and the matrix is of full rank. This implies that the problem has a unique solution.

In the case of zero singular values, the theory of linear algebra states that there is no unique solution. This raises the question of how to choose one particular solution from an infinity of solutions. One series of solutions is suggested by Wiggins' cutoff criterion. That is,

$$\hat{x}^{(k')} = \sum_{j=1}^{k'} y_j v_j \qquad k' \geq k < n \tag{2.100}$$

where $\hat{x}^{(k')}$ is a solution obtained by retaining k' singular values in the solution. Each solution (2.100) has a corresponding resolution and covariance matrix.

$$r_{ij}^{(k')} = \sum_{\ell=1}^{k'} v_{i\ell} v_{j\ell} \tag{2.101}$$

$$c_{ij}^{(k')} = \sum_{\ell=1}^{k'} v_{i\ell} v_{j\ell} / s_\ell^2 \tag{2.102}$$

By comparing the tradeoff between the resolution and covar-

iance of each solution, the investigator could choose an "optimal" solution. An alternative measure of this tradeoff lies in comparing the lengths of the solution vector and the residual vector. By examining equations (2.100) and (2.90) one can see that as more singular values are excluded from the solution the solution norm will decrease as the residual norm increases. Again it is up to the investigator to choose an optimal point on the tradeoff curve. Both of these techniques are demonstrated on a simple example in Appendix B.

As we mentioned in the beginning of this subsection the other two methods are also capable of modification to handle zero singular values. The Householder reduction approach can be altered to include a column interchanging sheme to make matrix R (see equations (2.50) and (2.51)) non-increasing in magnitude. Then when a diagonal element r_{kk} drops below some tolerance level, the rest of the rows in R are set to zero. This procedure is equivalent to the singular value cutoff scheme discussed earlier and produces similar consequences to the solution, resolutions, and covariance.

Modification of the normal equation approach requires a different scheme because the matrix A is never decomposed (as in SVD) or in a reduced form (as in Householder). Thus to stabilize an ill-conditioned normal equations matrix we make the following modification to problem $Ax = b$.

$$(\tilde{A}A + \theta^2 I)x = \tilde{A}b \tag{2.103}$$

This procedure of adding a small positive number, θ^2, to the diagonal elements of matrix $\tilde{A}A$ is known variously as damped least squares, Marquardt-Levenberg method, ridge regression, or stochastic inverse. The method was first proposed by Levenberg (1944) and has since been used extensively in many fields. We will use the term "damped least squares" for this procedure in the rest of this thesis.

The solution to equation (2.103) is given by:

$$\hat{x} = (\tilde{A}A + \theta^2 I)^{-1}\tilde{A}b \tag{2.104}$$

The inverse in equation (2.104) is guaranteed to exist if a large enough θ^2 is chosen. Substitution of equation (2.21) for b in equation (2.104) yields the expression for the resolution matrix:

$$\hat{x} = (\tilde{A}A + \theta^2 I)^{-1}\tilde{A}Ax \tag{2.105}$$

or

$$\hat{x} = Rx \tag{2.106}$$

where

$$R \equiv (\tilde{A}A + \theta^2 I)^{-1}\tilde{A}A \tag{2.107}$$

From equation (2.107) we see that the price we pay for a stabilized inverse in equation (2.104) is a deterioration

in the resolution matrix. On the other hand, the expression for the covariance matrix C becomes:

$$C \equiv E\left\{\Delta\hat{x}\,\widetilde{\Delta\hat{x}}\right\}$$

$$= E\left\{(\tilde{A}A+\theta^2 I)^{-1}\tilde{A}\,\Delta b\,\widetilde{\Delta b}\,A\,(\tilde{A}A+\theta^2 I)^{-1}\right\} \tag{2.108}$$

$$= \sigma^2(\tilde{A}A+\theta^2 I)^{-1}\tilde{A}A(\tilde{A}A+\theta^2 I)^{-1} \tag{2.109}$$

or

$$C = \sigma^2(\tilde{A}A+\theta^2 I)^{-1}R \tag{2.110}$$

Because

$$E\left\{\Delta b\,\widetilde{\Delta b}\right\} \equiv \sigma^2 I \tag{2.111}$$

where σ^2 is the variance of the data, and matrices $(\tilde{A}A + \theta^2 I)^{-1}$ and R are symmetric. Equation (2.110) illustrates again, the tradeoff between resolution and covariance. As the resolution is degraded it acts to dampen the inverse matrix $(\tilde{A}A + \theta^2 I)^{-1}$ and thus improve the covariance matrix.

Although it is possible to compute all the quantities required to characterize a solution with equations (2.104) through (2.111), it is nevertheless, instructive to look at the singular value decomposition of equation (2.103). Writing matrix A, in its decomposed form (equation (2.67)), equation (2.103) becomes,

$$V(S^2+\theta^2 I)\tilde{V}x = VS\tilde{U}b \tag{2.112}$$

or

$$(S^2 + \theta^2 I)\tilde{V}x = S\tilde{U}b \qquad (2.113)$$

In this form we can see that the damping of the ill-conditioning is accomplished by adding the scalar θ^2 to all the singular values. In this light the following formulas for the resolution covariance are informative in comparison with the respective formulas (equations (2.97) and (2.92)) for the SVD solutions:

$$R = V\left[S^2/(S^2+\theta^2)\right]\tilde{V} \qquad (2.114)$$

and

$$C = V\left[S^2/(S^2+\theta^2)^2\right]\tilde{V} \qquad (2.115)$$

2.2.5 Comparisons and Conclusions

Three programs were written and tested: Damped least squares is used in the first program based on the original program of ACH and further developed by Bill Ellsworth and myself; and the other two use the singular value decomposition technique. Because of the similarity of the Householder approach and SVD, the former technique was not programmed. Of the two SVD programs, one decomposed the $\tilde{A}A$ matrix instead of A. This admittedly negated one of the major assets of SVD, its higher precision; but it did provide us with all the information on eigenvalues and eigen-

vectors that is not available from damped least squares. The other SVD program employed a sequential accumulation technique and decomposed the nonsquare A matrix directly.

For comparison purposes, several computational runs were performed with all three programs both on artificial data and real data. We were especially interested in comparing computational cost, numerical precision, and value of output. The details of the comparison are in Appendix B. Here we briefly summarize our conclusions.

Cost was an overwhelming factor. It is much more costly to perform the SVD, especially on the larger nonsquare A matrix. The higher cost is due both to the large array size requirements and long computation time. The SVD programs were written and the examples in the appendix were computed while the author was employed for the summer at the Menlo Park Office of the U.S.G.S. There we had access to the computational facilities of the Stanford Linear Accelerator Center (SLAC) where computational costs were very low. Attempts at running the same programs at M.I.T.'s Information Processing Center were prohibitively expensive except for the simplest models. The tests at SLAC, however, demonstrated that the three programs yielded essentially the same results. Individual solutions might differ by as much as 10% but the patterns remained the same. There is no doubt that the SVD approach provides much more information on the numeric aspects of the technique and also more flexibility in forming several different solutions (different

thresholds for eliminating small eigenvalues) during one run. However, unless the prime interest of the user is the numerical analysis of the method the additional information supplied by the SVD is not essential. My experiences with all the programs have convinced me that for the purposes of the tectonic interpretation of the results, the damped least squares program is quite adequate. For these reasons the models presented in the following chapters were computed using the damped least squares technique.

All the models to be presented are one-step, noniterative solutions. Ellsworth (1977) extended the method to allow iteration including ray tracing through 3-dimensionally inhomogeneous body and demonstrated that the major variance reduction occurs in the first step. The iteration quickly converged and the final solution showed the same general features obtained in the first iteration.

2.3 QUALITATIVE ASPECTS OF QUANTITATIVE INVERSION

As in most numerical modelling techniques there are several aspects which require some intuition or experience in choosing the correct parameters. Thus qualitative aspects such as starting models, inversion parameters, and interpretation of results are discussed in this section. Much of this material is based on my own experience with the method but also takes into account the experiences of Aki et al. (1977) and Ellsworth (1977).

2.3.1 Initial Models

The first step in the application of the ACH method to a set of data is the selection of the parameters of the initial model. These parameters include: (a) the number, thickness, and velocities of the horizontal layers; and (b) the number and dimension of the blocks in each layer.

Ideally, the best procedures would be to choose the number of layers and their velocity to correspond with crustal structure derived from a seismic refraction experiment. In reality there are overriding considerations such as resolvability and computer cost.

The former constrains the minimum layer thickness to about the average station spacing. With incidence angles of teleseismic rays ranging from 15° to 30°, any thinner layers would lack adequate "cross-fire" and thus be coupled to its neighbors. Because the method involves the inversion

of a large matrix there is a practical cost limitation on the maximum number of blocks (unknowns). For M.I.T.'s IBM/168 this maximum is about 400 blocks. Because each layer usually contains from 80 to 150 blocks, the maximum number of layers is 6. Normally one or two layers are used to model the crust and two or three to model the upper mantle. The crustal layers are chosen to fit crustal refraction data as best as possible within the constraints given above. The mantle layers are chosen to provide good resolvability but otherwise arbitrarily. Mantle layer velocities are chosen to reflect average velocities within the interval. This is not a bad representation because mantle velocity increases slowly in the first hundred kilometers. If information is available on an upper mantle low-velocity zone, this can be included in a layered model.

Choosing the block dimensions for the crustal layer is controlled primarily by the array's station spacing. Smaller blocks will be unresolved and larger blocks degrade resolution. The program allows different spacing in the x and y coordinates to take advantage of different spacing patterns. If the station distribution is irregular, the best procedure is to choose a small enough block size to separate the closest spaced stations. Because the program does not take into account unsampled blocks, this procedure does not necessarily accumulate too many blocks; however, a disadvantage is that in the results a number of unsampled holes makes interpretation difficult. Of course, the blocks

must be larger than the wavelength of a teleseismic P-wave; otherwise the condition for the use of geometrical optics would be violated. However, station spacing is seldom dense enough to make this a problem.

For the mantle layers the block size is often larger. This in part reflects the larger scale of heterogeneity expected in the mantle compared to the crust, but also reflects the necessity to keep the total number of blocks below a definite maximum.

2.3.2 Damping Parameter

To understand the significance of the damping parameter we briefly introduce the stochastic inverse (Franklin, 1970). In the following we follow the presentation of Aki (1975). Consider the data d to consist of signal m and noise n, both being stochastic processes. Then,

$$d = Gm + n \qquad (2.116)$$

Assume,

$$\langle m \rangle = 0$$

$$\langle n \rangle = 0$$

where $\langle \cdot \rangle$ denotes averaging

and

$$\langle m \tilde{m} \rangle = R_{mm}$$

$$\langle n \tilde{n} \rangle = R_{nn}$$

The stochastic inverse operator L is obtained by minimizing

the statistical average of $|m - Ld|^2$ in the model space. This procedure leads to the following expression for the stochastic inverse operator,

$$L = R_{mm}\,\tilde{G}\left(G\,R_{mm}\,\tilde{G} + R_{nn}\right)^{-1} \qquad (2.117)$$

assuming that m and n are uncorrelated, $\langle m\tilde{n}\rangle = 0$. The damped least squares inverse is a special case of the stochastic inverse. Consider the case where the components of the solution and noise vectors are statistically independent and have constant variance,

$$R_{mm} = \sigma_m^2 I$$

$$R_{nn} = \sigma_n^2 I$$

Substituting into equation (2.117) yields,

$$L_o = \tilde{G}\left(G\tilde{G} + \frac{\sigma_n^2}{\sigma_m^2} I\right)^{-1} \qquad (2.118)$$

which can be shown to be

$$L_o = \left(\tilde{G}G + \frac{\sigma_n^2}{\sigma_m^2} I\right)^{-1}\tilde{G} \qquad (2.119)$$

Comparison with equation (2.104) provides the desired result,

$$\theta^2 = \frac{\sigma_n^2}{\sigma_m^2} \qquad (2.120)$$

With this definition of the damping parameter we can estimate an approximate value for use in the inversion. The noise variance is estimated to be .01 sec^2. The model variance is somewhat more variable; however, if we take it to be 2%, equation (2.120) yields

$$\theta^2 = .01/2 = .005 \ (sec/\%)^2$$

Practically, however, several inversion computations were made with various values of the damping parameter to test its effects on the solution. From these experiments the following conclusions were made: (a) Only order of magnitude changes in the damping parameter significantly changed the solution; (b) Elements of the solution with poor resolution change erratically with different damping; whereas elements with good resolution are much more stable independent of the choice of the damping parameter; and (c) the value of $\theta^2 \cong .005 \ (sec/\%)^2$ provided a good trade-off between solution resolution and variance.

2.3.3 Interpretation Scheme

All the formulations and computations described so far result in a set of numbers; namely, percent velocity perturbations for each layer in the model. The next step in the interpretive process is to contour the velocity variations for each layer. This is a very subjective procedure but aids in bringing out patterns and trends which are diffi-

cult to pick out from just a set of numbers. The contouring also is a smoothing operator albeit a very biased one. An important point is that we are not too much concerned with each individual block but rather groups or patterns of several "blocks". Patterns and trends which are stable for several runs with different initial models are the significant features.

Compressional wave velocities in the crust and upper mantle are affected by stress, temperature, chemistry and mineralogy, fabric, crack and pore properties, and the presence of fluid or partial melt (Iyer et al., 1977). Thus a unique interpretation of P-wave velocity perturbations in terms of physical conditions and material is clearly impossible. Each final model must be considered in the context of the region's geology and tectonic history. Other geophysical data such as gravity, magnetics, and heat flow provide additional constraints on our interpretation. Fortunately the regions studied in this thesis, central California and Yellowstone, Wyoming are past sites of extensive geological and geophysical studies.

In the following two chapters the interpretive scheme outlined above is used to investigate the deep structure of two regions which are of crucial importance in understanding the tectonics of the western United States.

Figure Captions

Figure 2.1 Hypothetical cross section beneath a seismic array showing division of the earth beneath the array into layers and blocks. P-wave path from arriving plane wave indicated by dashed line. Blocks sampled by this particular event are shaded. L is the array aperture. ℓ is the average station spacing. D isthe maximum model depth.

Figure 2.2 Rectangular coordinate system used in formulation of the method. $\hat{x}$, $\hat{y}$, $\hat{z}$ are unit vectors for respective coordinates. $\vec{ds}$ is a vector that is tangent to the ray paths. The angle γ is the incidence angle.

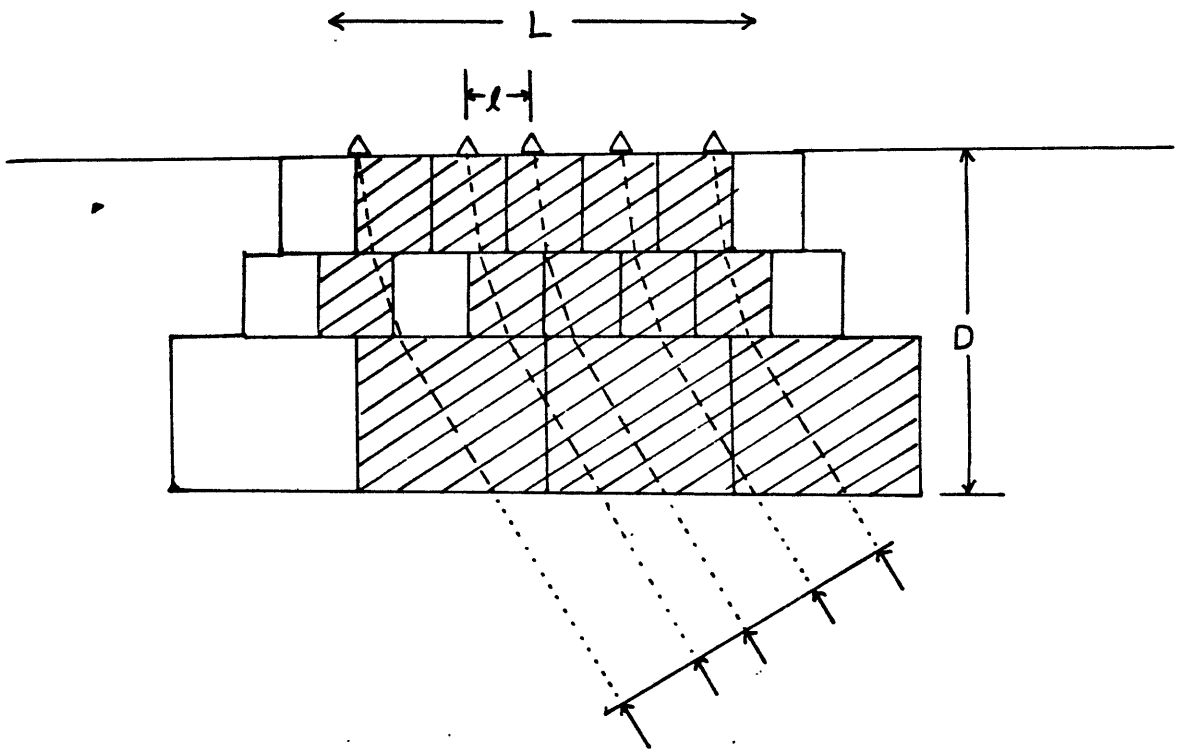

Figure 2.1

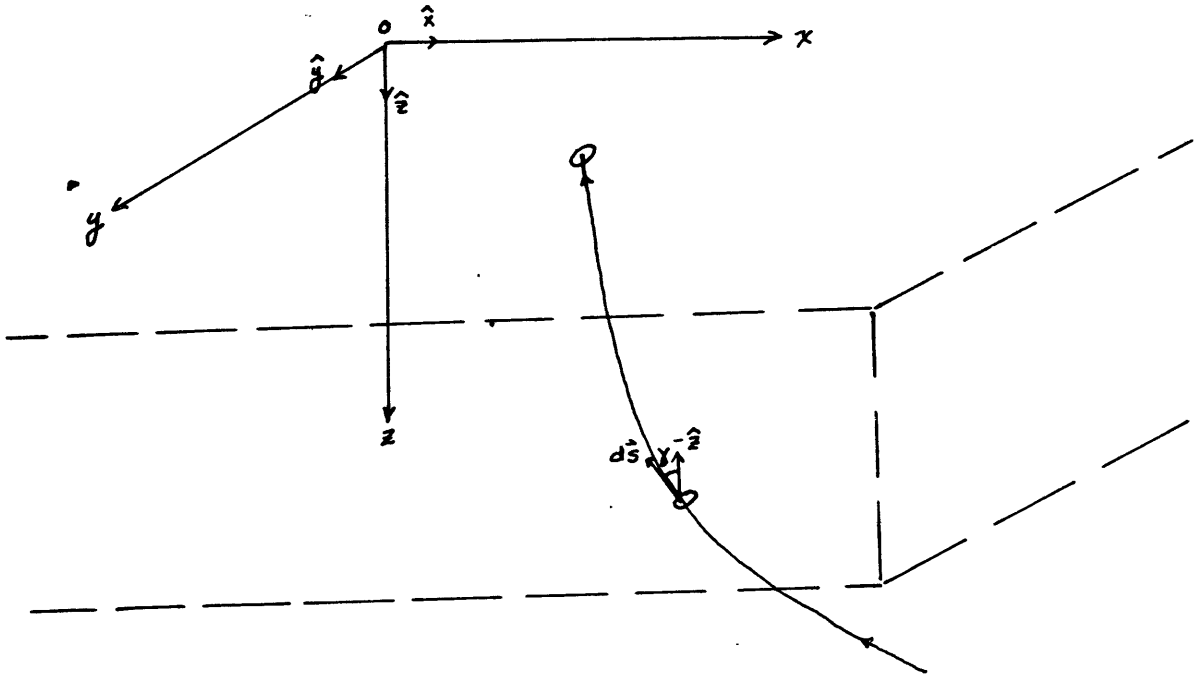

Figure 2.2

CHAPTER III. Central Coast Ranges, California: Deep Structure Beneath an Active Continental Margin

With the advent of sea-floor spreading and plate tectonic concepts in the late 1960's a broad framework for the late Cenozoic geologic evolution in coastal California was firmly established (Atwater, 1970). Yet, a more detailed account of the tectonic history and of even present day tectonic processes are proving to be elusive. Thus, for example, we know that sometime later than 30 million years ago (mya) the East Pacific Rise migrated into a trench located off the west coast of North America; however, we do not know what happened when the oceanic ridge collided with the trench. Was the ridge subducted or did the ridge and trench mutually annihilate each other? Also, geologists cannot agree (see e.g., Hill, 1974 and ensuing discussion in Geology, 1975, p. 155-159) whether the San Andreas fault system is a deep-seated ridge-fault transform plate boundary (Silver, 1975), or whether it is a shallow crustal feature decoupled from the deeper lithospheric boundary.

A very real possibility in such a complicated region is that due to the complex geometry of the interacting plates, tectonic effects will vary as a function of latitude of the interaction. For instance, as the East Pacific Rise

migrated towards the North American plate, subduction beneath the leading edge of North America ceased progressively during the last 30 million years from about latitude 20°N to 40°N and was replaced by transform motion. South of about 30°N a component of tension produced the opening of the Gulf of California, whereas the northern segment underwent "pure" transform movement on the San Andreas fault; perhaps with a small component of compression. Nevertheless, the entire Gulf of California-San Andreas system can be considered a transform fault although the southern half is very "leaky" (Elders and Biehler, 1975). Another possibility is that the northern part of the San Andreas fault is deep seated, that is, corresponds with the plate boundary, whereas the southern part is shallow and decoupled from a deeper system of faults (Anderson, 1971; Hadley and Kanamori, 1977).

In this chapter, results of an application of three-dimensional inversion of teleseismic travel time residuals are presented and discussed in context of some of the tectonic questions raised in prior paragraphs. Insight into the deep structure beneath central California provides critical data for the understanding of complex tectonic mechanisms. We begin with reviews of the present state of knowledge of the tectonic history (section 3.1) and the geophysical data (section 3.2) pertinent to our study. New teleseismic residual data from the U.S.G.S Central California seismic network is presented and examined in section 3.3.

In the following section, 3.4, a detailed three-dimensional model of the crust of central coastal California is analyzed and compared with surface geology and the implication of heterogeneity on the mode of earthquake occurrence on the San Andreas fault system is considered. Finally, in section 3.5 the upper mantle anomaly patterns are described with emphasis on their interpretation in terms of the late Cenozoic interaction of the Pacific, Farralon, and North American plates.

3.1 TECTONIC EVOLUTION AND GEOLOGIC SETTING

The present day configuration of tectonic units in California is illustrated in Figure 3.2 (place names are given in Figure 3.1). The major geologic units from oldest to youngest are:

(1) Precambrian shield rocks of all kinds exposed intermittently in southern California;

(2) Paleozoic metamorphosed sedimentary and volcanic rocks: remnants of Paleozoic island arcs accreted to the continental margin which are now exposed principally in the Klamath Mountains and western north Sierras;

(3) Pre-Late Jurassic meta-sedimentary and meta-volcanic rocks and granitic intrusive rocks which represent Early Mesozoic volcanic arc complexes are also exposed in the Klamath Mountains and northern Sierras;

(4) A Late Jurassic-Cretaceous Andean-type continental arc complex is delineated by the deep ocean-trench melenge of the Franciscan assemblege, the shelf and slope sedimentary rocks of the Great Valley sequence, and the granitic plutons of the Sierra Nevada and Salinian Block; and finally

(5) Cenozoic marine and continental sedimentary and volcanic rocks, the latter exposed predominantly in the southern Cascades-Modoc Plateau and western Nevada and Owens Valley.

How these units were juxtaposed into their present distribution is still incompletely understood. The Late Mesozoic and Cenozoic history is now known with some confidence but the Early Mesozoic and, especially, the Paleozoic history is still very speculative. Nevertheless, a brief

summary of the sequence of events through the Phanerozoic is presented next as a guide to evaluate interpretations to be offered in later sections. The younger events are discussed in greater detail, not only because they are better understood, but also because they are more crucial to the present study.

The tectonic evolution of California is due principally to interactions between the North American plate and the Pacific and proto-Pacific plates since at least early Mesozoic time (Hamilton, 1969) and possibly early Paleozoic time (Burchfiel and Davis, 1972). Within this general framework the major tectonic elements of California and neighboring regions represent exhumed remnants of Phanerozoic arc systems which collided with and were welded onto the older, stable continental margin of western North America. Specifically the tectonic development of California and neighboring Nevada can be divided into four periods:

(1) Paleozoic development of a Klamath-Sierran island arc-marginal basin which finally collapsed in Permian time, Figure 3.3a-e;

(2) Early Mesozoic development of an east-dipping Andean-type arc on a newly truncated Paleozoic margin which collided with an eastward migrating island arc-interarc basin-remnant arc complex during the Late Jurassic, Figure 3.4a-c;

(3) Redevelopment in the Late Mesozoic of the east-dipping Franciscan-Great Valley-Sierran continental margin formed by accretion of the early Andean type on the new Mesozoic complex, Figure 3.4d-f; and

(4) A Cenozoic (two-stage ?) mutual annihilation of the Pacific oceanic ridge and the North American

continental arc system and the subsequent transition to the San Andrean transform boundary, Figure 3.5a,b.

Each of these periods will be examined in more detail in the following paragraphs. Most of the following interpretations are condensed from review papers by Burchfiel and Davis (1972, 1975) and Schweickert and Cowan (1974).

3.1.1 Paleozoic Island Arcs and Marginal Basins

The Paleozoic terranes of the Klamath Mountains and northwestern Sierra Nevada are believed to be the remnants of a Ordivician-Silurian island arc and back arc marginal basin complex lying offshore of the Paleozoic continental margin as pictured in Figure 3.3b (Burchfiel and Davis, 1972). Closing of the marginal basin and accretion of the Klamath-Sierran arc complex occurred in two stages during the Late Devonian-Early Mississippian Antler orogeny (Figure 3.3c) and the Late Permian-Early Triassic Sonoma orogeny (Figure 3.3e); however, the actual mechanism involved is still in dispute (Burchfiel and Davis, 1972; Moores, 1970). What is more definite is that the final collapse of the marginal basin produced an abrupt westward shifting of the continental margin which was further modified by oblique truncation of Paleozoic structural and stratigraphic trends during a Late Permian or Early Triassic period of continental rifting (?) and drift (Burchfiel and Davis, 1975). Schweichert (1976) postulated a complicated sequence of

rifting and northward lateral transport of the missing southwestern part of the Cordilleran. He identified the western Paleozoic and Triassic belt of the Klamath terrain as part of the missing marginal basin sequence that was shifted some 500-600 km northwest from its original position, and the corresponding arc segment was postulated to have been transported to its present position in southeastern Alaska (Jones et al., 1972). Regardless of the actual mechanism, the new margin was then parallel to the present northwestward trend instead of the northeastward Paleozoic trends.

3.1.2 Early Mesozoic Arc-Continent Collisions

The Early Mesozoic (pre-latest Jurassic) history is also recorded in the rocks of the Klamath Mountains and northern Sierras. Schweichert and Cowan (1974) postulated another complicated sequence of events to explain the present juxtaposition of several arc-type rock assemblages. Their admittedly tentative model initiates after the continental rifting (?) episode with the presence of an Andean-type east-dipping subduction complex of Late Triassic-Early Jurassic (210-180 mybp) time along the newly created continental margin (Figure 3.4a). This period of plate consumption, recorded in the arc-rock assemblage of the eastern belt of the western Sierra foothills and eastern Sierran granitic plutons of the Lee Vining (210-195 mya) and Inyo Mountains (180-160 mya) intrusive epochs (Evernden and

Kistler, 1970) ceased in Middle or Late Jurassic time. During the Middle Jurassic time, a separate west-dipping island arc developed at some distance westward of the continental margin (Figure 3.4b). This eastward-migrating island arc system itself had a complex history with the formation of a back-arc basin (Figure 3.4c). As the "western" island arc and "eastern" continental arc approached one another by consuming the intervening oceanic plate, the former complex developed a remnant arc (Karig, 1972) beyond which new oceanic crust was generated that would form the ophiolitic floor for the basal beds of the Great Valley sequence exposed today in the Coast Ranges. In the Late Jurassic, some 150 million years before present (mybp), the two arc-trench systems collided, extinguishing both subduction systems, "plastering" the island arc-marginal basin-remnant arc complex to the North American continental margin, and causing deformation eastward that is generally termed the "Nevadan orogeny" (Figure 3.4d). After the collision, subduction again stepped westward of the accreted arc complex and reinstated another Andean-type continental margin with an eastward dipping Benioff zone (148-132 mya) marked today by the granitic rocks of the Yosemite intrusion epoch (Evernden and Kistler, 1970). It was in this continental arc system that deposition of the Great Valley sequence began on the arc-trench gap and the contemporary deposition and deformation of the Franciscan assemblage occurred within the trench. The new continental arc system was stable

throughout Cretaceous (130-65 mya) time with continued evolution of the Great Valley-Franciscan complex and concomittant Sierran plutonism occurring in two more distinct intrusive epochs: the Huntington Lake (121-104 my) and Cathedral Range (90-80 my) (Evernden and Kistler, 1970).

3.1.3 Late Mesozoic Andean-Type Continental Margin

The scenario of the tectonic evolution presented so far is very conjectural and will undoubtedly change in its details as further studies are completed. The Late Cretaceous and Cenozoic tectonic reconstruction, although still speculative, is based not only on geologic data but also on marine magnetic data and is consequently more reliable. The following scenario of events is based primarily on summaries of:

(1) marine magnetic data by Atwater (1970) and Atwater and Molnar (1973);

(2) geochemistry and geochronology of igneous rocks (Lipman et al., 1972; Christiansen and Lipman, 1972; and Synder et al., 1976);

(3) the displacement history of the San Andreas fault system (Crowell, 1973); and

(4) California geology (Hamilton, 1969; Dickinson, 1970).

As mentioned earlier the period 130-80 mybp (Early and Middle Cretaceous) was characterized by an Andean-type subduction system along the western continental margin. The

last two major epochs of Sierran batholithic intrusion occurred while the Franciscan-Great Valley sedimentary rock assemblages were deposited respectively in a deep ocean-trench environment and continental slope-shelf or sedimentary trough environment offshore from the Mesozoic volcanic arc (Hamilton, 1969; Dickinson, 1970). Interpretations on the exact modern analogues of the Franciscan-Great Valley assemblages are numerous and varied, however, for the sake of continuity, its discussion will be delayed until a later section. Dickinson (1970) using trends in K_{60} and K_{65} variations transverse to the Sierra Nevada batholith, reconstructed the position of Late Mesozoic paleoseismic zone beneath the Sierra Nevada region and obtained an apparent dip of about 50° for the inclined paleo-seismic zone which projected to the present ground surface near the western edge of the Great Valley of California. If the reconstruction is valid, it implies that the paleoseismic zone occupied the same general position for at least 100 my because of the range of ages of the individual plutons which compose the Sierra Nevada batholith.

The period 80-70 mya appears to have been a time of several regionally and perhaps globally important tectonic transitions (Coney, 1971). In California it marked the end of major plutonic intrusion in the Sierra Nevada, the termination of Franciscan deposition (Bailey et al., 1964), and possibly the initiation of an ancestral San Andreas fault (Garfunkel, 1973; Crowell, 1973). Coney (1971, 1972)

attributes the 80 my transition to an increase of the spreading rate between North America and Eurasia.

If an ancestral San Andreas fault did initiate in Late Cretaceous or Paleocene time it would infer cessation of subduction off the coast of central California at that time. Snyder et al. (1976) proposed such an occurrence to explain an absence of early Cenozoic (65-40 mya) igneous rocks in the Great Basin between the Snake River Plain and southern Arizona. Volcanism was fully re-established in this area by 40 mya suggesting that subduction was also re-initiated. Coney (1971) also proposed the 40 my age as a period of widespread tectonic transitions related to near cessation of spreading between North America and Eurasia. Lipman et al. (1972) reconstructed a Middle Cenozoic paleoseismic zone for the western United States using the variation of K_2O in igneous rocks of the appropriate ages. Their data show two separate trends of eastward-increasing depths to the Benioff zone, implying the existence of two separate but parallel shallow-dipping subduction zones. The dip after correcting for late Cenozoic extensional deformation was estimated to be 20°-25°. The apparent imbricate subduction zones which have no known presentday counterpart may be a consequence of the short-lived transform movement postulated on the basis of the Middle Cenozoic hiatus of igneous activity (Snyder et al., 1976).

3.1.4 Cenozoic Ridge-Trench Collision

Atwater (1970) and Atwater and Molnar (1973) have reconstructed the relative plate motions of the last 40 million years based on marine magnetic data, thereby providing a relatively detailed framework of plate geometries during this period (Figure 3.5a). The shallow dipping subduction zone inferred from the Middle Cenozoic igneous rocks seems at least consistent with the approaching oceanic ridge inferred from the magnetic data. As the ridge neared the continental margin, younger and consequently hotter and more bouyant lithosphere was forced beneath the continental margin, accounting for the shallow dip. According to the latest effort to reconstruct the relative positions of the Pacific and North American plates using the sea-floor spreading history of the North Atlantic, Indian, and South Pacific Oceans, the Pacific and North American plates were in contact by 29 mya (Atwater and Molnar, 1973). The ridge and subduction zones were "annihilated" between the Mendocino and Murray fracture zones between 29 and 21 mya. The Mendocino triple junction made contact first with the North American continent somewhere near 30° N lattitude. Initially, the Pacific lithosphere was very young and weak and thus probably took up most of the strike-slip deformation offshore. As the lithosphere continued to cool, however, it thickened and grew stronger and the deformation moved inland, initiating again the San Andreas fault and breaking off a piece of California from the North American

plate (Atwater, 1970). Such a sequence of events is in general agreement with evidence of movement on the San Andreas fault where the segment north of the "big bend" reinitiated movement about 23 mya after a 25 my hiatus and the southern segment first initiated movement on the San Gabriel fault between 26-16 mya (Crowell, 1973). Others, however, place the date of coupling between the North American and Pacific plates at 26 my which coincides with a circum-Pacific wide orogenic event (Handschumacher, 1976; Dott, 1976). Whenever the collision occurred it is widely agreed that it happened somewhere off the northern coast of Mexico and migrated north-westward due to the geometry and relative motion of the two plates. Concomitant with the migration of the triple junction was a change in the stress pattern; as the ridge and subduction zones were mutually annihilated, the relative displacement was accommodated by transform faulting thereby relieving a major component of compressive stress. Christiansen and Lipman (1972) were the first to document a correlation between the northwestward migration of the Mendocino triple junction with a parallel migration in the western United States of the transition from predominantly andesitic to fundamentally basaltic volcanism as depicted in Figure 3.5b. If the figure is accurate, it implies that an actively subducting slab was present beneath California and western Nevada north of about latitute 35°N as recently as 10 mya. The data also document an approximately 5 my time lag between the passage

of the triple junction and cessation of andesitic volcanism.

About 4.5 mya the Pacific plate was about 250 km southeast of its present position relative to the North American plate and increased its rate of motion to its present 5.5 cm/yr. Comparison of the relative plate motions and geologically inferred displacements on the San Andreas fault follow parallel paths although the former show about twice that inferred from the latter. The similarity implies that motion on the San Andreas has been tightly coupled to the relative plate motions for the last 30 my. The discrepancy in absolute displacements could be explained by sympathetic movement on other faults parallel to the San Andreas, by deformation and stretching of the Salinian block (Johnson and Normark, 1974), or right-lateral shearing within the Basin and Range (Atwater, 1970).

3.1.5 Coast Ranges Geology and the San Andreas Fault

Although the tectonic evolution on the regional scale presented above is relevant to the present study, we are, in particular, interested in the Coast Ranges because the USGS array is located within its geographic province. Hence, we now examine in greater detail the geology of the Coast Ranges, California (see Page, 1966, for an overview of the geology). Referring to Figures 3.2 and 3.6 there are two major "basement" types in the central Coast Ranges. The Franciscan assemblage outcrops in a wedge between the San Andreas fault and the Great Valley and also along the coast

southwest of the Salinian block. The latter terrain is floored by the second major bedrock type: granitic plutons of the Sierran arc which have been displaced to its present position by about 500 km of left lateral movement on the San Andreas and proto-San Andreas faults as discussed earlier.

Franciscan rocks are described in detail by Bailey et al. (1964). Briefly the Franciscan is an assemblage of predominantly clastic, first-cycle sediments deposited near and in an oceanic trench; also deep ocean cherts, pillow lavas, and ultramafic rocks. Some units are coherent while others are incoherent and often termed a melenge (Hsui, 1971). A metamorphic zonation parallel to the coastline shows evidence of increasingly higher pressure paleo-environments within the Franciscan in a direction towards the continent (Ernst, 1974). Closely associated with the Franciscan group is a thick (aggregate thickness of 40,000 feet or more) sequence of well-bedded sedimentary rocks characteristic of shallow marine environments and is relatively undeformed and unmetamorphosed. Structurally the Great Valley sequence overlies the Franciscan along a steep and locally overturned fault contact which is marked along most of its length by mafic and ultramafic rocks.

The tectonic interpretation of the Franciscan-Great Valley assemblages has been debated in the literature for many years. Bailey et al. (1964) referred to the coexisting assemblages as eugeosynclinal and miogeosynclinal,

respectively, referring to the now outmoded concept of paired sedimentary geosynclines, the former a narrow and deep subsiding trough alongside the shallow shelf and slope environment of a miogeosyncline. Hamilton (1969) adopted the newly developing concepts of sea floor spreading to present modern interpretations of the Franciscan as abyssal and trench deposits which were underthrust beneath the Great Valley continental slope and shelf deposits along a fossil Benioff zone. Ernst (1970) also interpreted the metamorphic zonation within the Franciscan assemblage as evidence that it is an exhumed subducted complex. Further, in 1970, Bailey and others identified the mafic and ultramafic rocks separating the Franciscan and overlying Great Valley rocks as a Mesozoic ophiolite (oceanic crust and upper mantle) sequence on which the Great Valley sediments were deposited; and the great thrust fault separating the coeval assemblages was recognized to be at the base of the ophiolite and was coined the Coast Range Thrust. Dickinson (1970) further modified this model by proposing the Great Valley sequence was deposited on an arc-trench gap between the Franciscan trench deposits and the Sierran volcano-plutonic arc. Objections to these later models were summaried by Blake et al. (1976) who proposed instead that a remnant arc must have been located between the Franciscan and Great Valley sequence, no evidence of which remains because it was subsequently eroded away and its roots subducted. This latest model was proposed in order to

explain details of the sedimentary facies within the two units which cannot be satisfactorily explained by a simple trench-shelf-arc configuration. However, since there is no other evidence of a remnant arc in Late Jurassic to Early Tertiary time the existence and significance of such an arc remains in doubt.

Also in some doubt is what underlies the Franciscan-Great Valley rocks. There is general agreement that the Franciscan is floored by oceanic crust though it might be highly sheared and deformed. Also if one accepts the identification of the ophiolite in the Coast Ranges by Bailey et al. (1970), the westernmost basal members of the Great Valley sequence must also rest on Mesozoic oceanic crust which in turn lies structurally atop the Franciscan via the Coast Range thrust along the western edge of the Great Valley. On the valley's eastern side, the Great Valley sequence rests unconformably atop the Sierra granitic batholith. The contact between the Franciscan and Sierran rocks is exposed as a low-angle, east-dipping thrust in northwestern California. Some investigators (Page, 1970; Ernst, 1974) believe that this contact extends beneath the Great Valley strata coincident with a medial gravity and magnetic high; while others (Bailey et al., 1970; Cady, 1977) believe the Sierran basement underlies the eastern third of the valley whereas the western two-thirds is floored by the western oceanic crust of the leading edge of the North American plate and therefore the Franciscan and Sierran

are nowhere in direct contact.

As mentioned earlier, the Sierran plutonic rocks are predominantly Late Jurassic to Late Cretaceous quartz diorites and granodiorites. The Salinian Block which is bounded by the San Andreas fault on the east and the Sur-Nacimiento fault on the west constitutes the southern portion of the Coast Ranges. Petrologically similar to the Sierran plutonic rocks, the Coast Range plutons have isotopic age determinations that fall within the Huntington Lake Intrusive Epoch of Early Cretaceous age (121-104 mya) (Evernden and Kistler, 1970). These similarities have been frequently cited as evidence that the Salinian Block was once (during Early Cretaceous time) contiguous with the Sierran magmatic arc and that its present position is due to nearly 600 km of left-lateral displacement on the northern segment of the San Andreas fault. Both the northern and southern parts of the San Andreas are documented to have about 300 km of displacement since the Miocene (Crowell, 1970), however, there is no evidence of earlier movement on the southern part of the San Andreas. This paradox prompted Crowell (1973) and Garfunkel (1973) to postulate a two-stage history of movement involving an ancestral San Andreas which was identical to the present northern portion of the fault but was distinct and as yet unrecognized in the southern region. An alternate model by Johnson and Normark (1974) denies the existence of a proto-San Andreas fault and instead postulates that the nearly 600 km of offset is only an apparent effect due to extensive

shearing and slivering of the Salinian block which was nearly doubled in length during the process. Their hypothesis suggests that the San Andreas is not a clear boundary between the Franciscan and granitic terrains and therefore slivers of the former should exist within the Salinian block. They claim that such slivers occur in the Gualala area off the coast of northern California and in the Santa Cruz mountains. The western boundary of the Salinian block is marked by the Sur-Nacimiento fault which separates the granitic terrain from the Franciscan terrain along the coast. Page (1970a, 1970b) identified the Sur-Nacimiento as part of a subduction zone which ceased activity before the end of the Oligocene (<25 mya).

In summary, the complicated surface geology exposed in the Coast Ranges of central California have been interpreted in terms of complex three-dimensional plate tectonics processes. Just as these processes have left their imprint on the exposed portions of the crust, the subsurface, the deeper crust, as well as the upper mantle, are also affected. By studying the third dimension, further insights are obtained on the relevent tectonic mechanism. With these thoughts we now consider geophysical data from central California.

3.2 GEOPHYSICAL SETTING

Geophysical data from past studies are summarized in this section. Seismic refraction data is useful in choosing initial models for the inversion scheme which is incapable of estimating a mean layer velocity. Station time terms from P_g and P_n studies are useful in estimating near-surface effects on teleseismic delays. Previous teleseismic studies in central California provide a basis for comparison. Finally, gravity and aeromagnetic data are especially helpful for interpretation of crustal anomalies.

3.2.1 Explosion Seismic Refraction Profiles

Much of the seismic refraction work in California has been performed by the U.S. Geological Survey (USGS) as part of a regional study of the western United States (Pakiser, 1963, and most recently reviewed by Prodehl, 1970). The results from refraction lines pertinent to our area are summarized as perspective fence diagrams in Figure 3.7 which is modified from a compilation by Warren (1968) that was based on work by Eaton (1963, 1966) and Healy (1963). One additional line was added from Stewart (1968) and modified according to Cady (1977, p. 21). All the profiles shown are reversed and interpreted using standard assumptions: (1) sharp boundaries between layers; (2) layers of constant velocity; and (3) increasing velocity with depth (Warren, 1968). Estimates of the precision of the velocity

measurements is ±0.1 km/sec and depths to 10 percent assuming, of course, the validity of the above assumptions.

The two profiles parallel to and on opposite sides of the San Andreas fault are the most direct data on the extent of the crustal discontinuity across the fault. It appears the discontinuity is restricted to the upper 12 km of the crust where there is a 5 to 8 percent contrast in P-wave velocity, the higher velocity on the southwest side. Velocities in the lower crust of 6.8 km/sec on the southwest profile and 6.9 km/sec on the northeast profile are not significantly different and P_n velocity is 8.0 km/sec on both sides. Depth to the Mohorovicic (Moho) discontinuity is less on the southwest side, but the magnitude of the effect is uncertain. Along the southwestern profile the depth to Moho varies from 22 km near San Francisco to 25 km near Camp Roberts whereas on the Diablo Range profile, the Moho is at a depth of 29 km. This apparent step or dip of the Moho is uncertain, however, because of the uncertainty of the interpretation of arrivals along the southwestern profile. Healy (1963) states that the calculated depth to the Moho can vary from 22 km to 30 km within the constraints of the data.

Stewart's (1968) interpretation of the profile through the Diablo Range provides more detailed velocity information on the Franciscan rocks. He estimates the Franciscan rocks to be characterized by northwest-dipping layers, with velocities of 3.3 km/sec, 5.0 km/sec, and 5.7 km/sec at successively greater depth, and the bottom at a depth of 10

to 16 km.

More detailed refraction profiles on the southwest side of the San Andreas fault include the work of Hamilton et al. (1964) and Stewart (1968). The former study used quarry blasts near Salinas as sources to record unreversed profiles to the northwest and southeast. They found the following apparent velocities: direct P, 4.2 km/sec; P_g, 6.3 km/sec; and P_n, 8.0 km/sec. Using data from the USGS San Francisco to Camp Roberts profile (Healy, 1963) to reverse their refraction line, Hamilton et al. computed a crustal model with P_g = 6.2 km/sec, P_n = 8.0 km/sec, and a nearly horizontal Moho at a depth of about 22 km. In an alternate model the crust is 2 km thicker.

Stewart's (1968) preliminary analysis of a profile along the Gabilan Range showed velocities in the granite increase from about 4.8 km/sec to 6.1 km/sec. However, he noted that the arrival times were not well behaved, which was attributed to strong lateral velocity heterogeneity. An unexpected result of his study was the extreme attenuation of first arrivals at a distance range of 40 to 80 km. A possible explanation for the observation is the presence of a crustal low velocity zone starting at a depth of about 10 km. Two possible explanations for the cause of such a low velocity zone are high temperature at depth within the granitic pluton, or that the Gabilan Range is underlain by the lower velocity Franciscan rocks. An important consequence of the possible existence of a crustal low velocity

zone is that crustal thickness calculated without knowledge of the low velocity zone will be overestimated. For example, Stewart (1968) states that a crust calculated to be 23 km thick by the standard interpretation techniques will be about 20 km thick if the crustal low velocity zone is present. Thus the crustal thickness of the Salinian block is constrained by presently available seismic-refraction data to be anywhere from 20 to 26 km thick.

3.2.2 Local and Regional Earthquake and Blast Studies

An array-wide study of local and regional earthquake (and blast) travel time data also provide information on crustal velocities. Two such studies are available for the California network: Wesson et al. (1973) analyzed P_g travel times to investigate upper crustal structure, and Kind (1972) used P_n arrivals to delineate crustal and Moho structure.

Wesson et al. (1973) collected all available blast travel time data from the Coast Ranges and made a time term analysis of the P_g phase. Time terms of the P_g phase are related to the depth to "basement" which is granite and metamorphic rocks southwest of the San Andreas fault and the Franciscan Formation northeast of the fault. Their results indicate large thicknesses of Cretaceous and younger sedimentary rocks (as much as 6 km) in the northern Santa Cruz Mountains, in the northern part of the Diablo Range, and in graben structures bounded by the Sargent and San Andreas faults and in the Hollister Trough. These time

terms help to bound the maximum effect of near-surface low-velocity deposits on teleseismic travel time delays.

Kind (1972) made a similar study of the P_n phase from four Nevada nuclear blasts and 10 regional earthquakes. A P_n velocity of 8.0 km/sec was derived from the time term analysis and the stations residuals closely reflected the crustal geology and structure. Stations southwest of the San Andreas and Calaveras-Hayward faults were dominately negative whereas to the northeast the station residuals were dominantly positive - another indicator of the basic crustal difference of the Salinian block and the Franciscan complex. Kind's results are referred to again in a later section.

Several other smaller scale seismic experiments have been performed in our study area. These are described in the appropriate context.

3.2.3 Teleseismic P-Wave Studies

The earliest studies of the Coast Ranges area using teleseismic sources are the works of Otsuka (1966a,b), Bolt and Nuttli (1966), and Nuttli and Bolt (1969). These investigators used data from the University of California array which encompassed the area presently covered by the USGS array although with far fewer instruments. Because of this limitation, their interpretations could not be very detailed, however, their studies did produce important evidence of strong lateral heterogeneity in the upper mantle

beneath central California.

Otsuka studied azimuth and slowness anomalies of teleseismic waves measured by the array. The anomalies were consistent and regular: waves propagating parallel to the California coastline were deflected toward the continent and waves arriving perpendicular to the coast were either deflected into a steeper angle of incidence or a shallower angle of incidence depending of whether they arrived from either a westerly or easterly direction. We also see this effect in our array diagram (Figure 3.17). Otsuka interpreted his data as due to a moderately dipping (to the NE) Moho below which a second interface with lower velocities below it dips steeply towards the ocean. He gave the depth beneath the Coast Ranges of the second interface as about 80 km.

Nuttli and Bolt (1969) studied P-wave residuals. Their interpretation basically involved eastward thinning of the low velocity zone.

More recent teleseismic studies are by Peake and Healy (1976) and Husebye et al. (1976). Results from the former study show crustal thinning to the west with a sharp gradient along the San Andreas fault. The latter study which presented the preliminary results on which this chapter builds was hampered by poor resolution. The reason for this was that only 26 stations contributed data and these stations were distributed in a linear pattern, thus producing a large proportion of peripheral blocks.

3.2.4 Gravity and Magnetic Studies

A large number of gravity studies of central California are available in the literature. As a summary we present Figure 3.8. The map is based primarily on the Transcontinental Geophysical Investigation Maps. Figure 3.9 is an aeromagnetic map at the same scale. Features of these maps will be mentioned in later sections.

3.3 TELESEISMIC P-WAVE RESIDUALS

A major portion of the work for this thesis involved the collection, reduction, and interpretation of suites of teleseismic P-wave residuals. Described in this section is the procedure for the collection and reduction of the data set from the USGS Central California Seismograph Network. Because the residuals form the fundamental data set in this study, it is displayed in two complementary formats and preliminary interpretations are presented prior to rigorous inversion.

The central California array consists of 118 stations in a corridor about 450 km long by 100 km wide stretching from Parkfield to Point Arena (Figure 3.10). The network was established to monitor and study the earthquake activity along the San Andreas fault and, therefore, the stations are concentrated near the fault and its major branches. Thus although the average station spacing is about 20 km, much higher densities occur locally and some outlying regions are sparsely sampled. For the purposes of studying tectonic structures a more equidimensional array or even an elongate array situated perpendicular to the regional structure would be preferable, but such is not the case and we must make do with what is available.

3.3.1 Collection and Reduction

A total of 122 events (earthquakes or large underground

nuclear explosions) located on Figure 3.11, were sources for seismograms recorded at the California array. Seismograms from 51 events, listed in Table 3.1, were "picked" by myself. Of the remainder, data from 23 events were obtained from a thesis by C.A. Powell (1976) and data from 48 other events recorded by fewer stations were provided by C.A. Powell and used in a preliminary interpretation by Husebye et al. (1976).

The instrumentation of the USGS central California network is described fully by Wesson et al. (1974). Briefly, each station includes a vertical component, 1 Hz seismometer. The signal is telemetered to the USGS office in Menlo Park, California, and recorded on 16 mm film using a Develocorder. Seismograms from up to 16 neighboring stations are recorded on each Develocorder film and also recorded simultaneously are two timing signals (WWVB and a chronometer). The overall response of the system is peaked at 10 Hz (magnification about 10^6 with attenuation set at 42 db), and drops off an order of magnitude at 1 Hz which is the predominant frequency of teleseisms. Although the system is tuned to record local earthquakes, the response was found to be quite adequate for recording most teleseisms with $M_b \geq 5.5$.

Relative arrival times of the P-wave were read directly from the Develocorder films after magnification. Due to the emergent nature of the first arrival, no attempt was made to pick it except in some instances of impulsive arrivals. Normally a characteristic peak, trough, or zero crossing was

chosen from the first several cycles of the P-wave and used as a datum to pick relative arrival times across the array. In difficult cases tracings of several representative waveforms were made and used to correlate between traces. This technique was especially useful in finding traces with erroneously reversed polarity.

The time "picks" were digitized and processed with a program available in Menlo Park which corrects for optical distortion due to the recording system. The final product of the collection procedure is a deck of IBM cards with station code, weighting factor, arrival time, and any relevant comments. This procedure is standard for reading teleseismic relative arrival times and is accurate to at least .1 second.

The next step of the data analysis is the reduction of the arrival times to relative residuals. First, we review some notation and definitions. In this regard we follow the notation used by Ellsworth (1977). The arrival time of a wavelet measured at station j for event i is denoted by Tm_{ij}. This is related to an <u>absolute travel time residual</u>, T_{ij}, by

$$T_{ij} = Tm_{ij} - \Delta T_i - Tc_{ij} - OT_i$$

where ΔT_i is the interval between the initial P-wave arrival and the arrival time of the measured wavelet. Tc_{ij} is the predicted travel time of the P-wave between event and station as given by a specified earth model, and OT_i is the event

origin time. The absolute event residual, $\bar{T}_i$, is the mean of the absolute travel time residuals calculated for event i,

$$T_i = \sum_j \frac{T_{ij}}{n_i}$$

where n_i is the number of stations with usable records for event i. Relative travel time residuals, R_{ij}, are then calculated by subtracting the absolute event residual, $\bar{T}_i$, from T_{ij}.

$$R_{ij} = T_{ij} - \bar{T}_i$$

Note from the above definitions that R_{ij} is not dependent on ΔT_i, the interval between the initial P-wave arrival and the arrival time of the measured wavelet, nor on OT_i, the origin time of the event. One other definition we need is the average station residual,

$$\bar{R}_j = \frac{\Sigma R_{ij}}{n_j}$$

where n_j is the number of observations for station j.

Relative residuals, R_{ij}, then are dependent on Tm_{ij} which is measured and on Tc_{ij} which is a theoretical travel time based on some earth model. In practice, Tc_{ij} was obtained by interpolating the Herrin (HERR) or Jeffreys-Bullen (JB)

travel time tables (Herris et al., 1968; Jeffreys and Bullen, 1958). Ellipticity corrections for the above tables were used (Dziewonski and Gilbert, 1976) although the corrections are insignificant ($\leq$ .05 sec) for the relative residuals even over the full extent (350 km) of the array. Also, the differences between the HERR and JB tables, although significant on absolute travel time residuals, is again insignificant over the aperture of the array. However, for consistency, all the following relative residuals were computed using the HERR table unless otherwise noted.

3.3.2 Qualitative Analysis of Teleseismic Delays

Prior to any interpretation, the combined data set are presented in two complementary displays. First, the delays are "mapped" by event, that is, for each event the spatial variation (SV) of the delays over the array is displayed on a map (Figure 3.12). Secondly, the delays are plotted on a "station focal sphere" (SFS) projection plot. This is a polar graph with the station-to-event azimuth measured on the azimuthal coordinate and the incidence angle measured on the radial coordinate (Figure 3.13-3.15). To utilize the plots it is helpful to imagine a hemisphere projecting downward at the base of the crust beneath the station; the point of intersection of the dome by a seismic ray from a teleseism is projected up onto the horizontal plane of the base of the dome. In both types of displays the sign and magnitude of the delay is represented by an appropriate symbol.

The maps and plots are especially useful in trying to visualize an approximate shape or location of an anomalous body. For example, the SV maps examined for events with varying azimuths and distances, are used to constrain the cause of a particular anomaly as shallow (little variation of delays with different events) or deep (moving shadow effect). Similarly, the SFS plots are used to estimate the proximity of an anomalous body by checking if the delays change position on plots of neighboring stations. Also the mean value of the delays of the SFS plots are a good estimate of the relative upper crustal velocity. Examples of both types of displays for the California data are discussed next.

Figure 3.12 has eleven maps illustrating the changing patterns of anomalies depending on the event azimuth. All the events except one have incidence angles between 19° and 33°; the exception is an NTS nuclear explosion which was not used in the inversion but is presented here as an example of an event with a steep angle of incidence. It is instructive to divide the seismic array into three sections and study the residual patterns separately for each section.

The northernmost section extends northwestward of a line passing through San Pablo Bay and is centered near Santa Rosa. Stations on the eastern edge of the area are consistently slow; indicating a shallow anomaly which is undoubtedly a thick section of sedimentary rocks. For the

NTS shot a changing pattern of negative to positive residuals extends from the coast to the Great Valley. The cause is probably a combination of northeastward crustal thickening and the thickening of sedimentary strata into the Great Valley. The remaining data show that for most stations the delays are predominantly negative for all azimuths except for event 118 (AZM=32) for which large positive delays are indicated. The reason for the latter effect is not immediately obvious.

The middle section of the array extends from San Pablo Bay on a line through Monterey Bay and is centered near San Jose. The complexity of the geology of this area is reflected in the complex patterns of delays. Positive delays are azimuthally independent for the northeastern area of the section (except for stations atop Mt. Diablo) and for stations along the Calaveras fault. Stations west of the San Andreas have generally negative delays except for eastern and southeastern azimuths for which the delays are large and positive. In fact, all stations in this section have positive delays for azimuths ranging from at least 72° to 138°. The exception is the NTS shot with an angle of incidence of 81° which shows a neat dichotomy of negative residuals west of the Calaveras-Hayward fault system and positive residuals on the other side. These patterns suggest the existence of a deep low-velocity anomaly in the upper mantle east-southeast of the array.

The third section encompasses the rest of the array

from Monterey Bay to Parkfield. An interesting effect for this area is the wedge of negative residuals between the San Andreas and Calaveras faults near Hollister denoting a shallow high-velocity feature. Stations located in the Gabilan Range are also 'fast' which is consistent with their location atop a granitic batholith. Stations near the San Andreas fault are consistently 'slow' in the northern part of the area but in the southern half the residuals are highly azimuthally dependent. This pattern change must be indicative of a profound structural change in this area.

The data are also displayed in polar plots for representative stations in each of the three sections mentioned previously (Figures 3.13-3.15). Plots for eight stations from the Santa Rosa region are in Figure 3.13. All the stations have negative average station residuals ($\overline{R}_j$) except those near the Great Valley (BRP, MIX, GVR). All stations have 'fast' directions to the west and southwest. Stations south of a line through GVR, TMN, WHW also have negative delays in the northwest quadrant whereas stations on the line and north of it have positive delays which become larger with shallower incidence angles. A possible explanation for this effect is an upper mantle low-velocity anomaly associated with the recent volcanics in the Clear Lake area.

Station focal sphere plots for eleven stations in the San Jose region are in Figure 3.14. Unlike the Santa Rosa region, the plots display a variety of delay patterns. The average station residuals vary from +0.3 for station

DOO near the Great Valley to -0.3 for station EGR in the granitic Ben Lomond Mountains of the Salinian block.

Stations west of the Calaveras-Hayward faults (ANG, LTW, SAW, EGR, CYH, CBO, EUC) generally show early arrivals in the two western quadrants. For these stations the only other quadrant with sufficient data, the southeast, displays generally smaller delays but with a more complicated pattern. For instance, the plots for stations ANG, LTW, and SAW show positive delays becoming smaller or even changing sign near an azimuth of 120°, whereas the plots for stations CBO and EUC have an opposite polarity reversal near the same azimuth. The significance of these patterns will be clearer after examining the plots of stations in the Bear Valley region to the south, therefore the discussion of it will be delayed until then.

Stations east of the Calaveras-Hayward faults (DOO, PAL, COE, RUS) generally have plots with predominantly positive delays for all azimuths although smaller positive delays or even negative delays are present for western azimuths. The exception which has predominantly early arrivals is station RUS located on the eastern flank of Mt. Diablo, a piercement structure discussed previously. An interesting feature of the plot is visible in the southeast quadrant where an abrupt change from negative to positive residuals occurs at an incidence angle of about 25°. This indicates that there exists a relatively sharp contact between the high velocity core of the body and the lower velocity

country rock and that this contact, at least locally, dips downward at an angle of approximately 25°.

The third and final section, Bear Valley, is represented by plots of eleven stations (Figure 3.15). Again, the near-surface geology is reflected in the stations' average residuals. Stations FRP and PNC, located on outcrops of granitic rocks, have average residuals of -0.3 and -0.2, respectively; whereas stations BEN and HER, situated in areas of thick sedimentary cover have average residuals of 0.3 and 0.2, respectively. An anomalous station in this respect is CHR which is located on the edge of a wedge of Franciscan between the Sargeant and Calaveras faults which is normally characterized by slightly negative average station residuals. Station CHR has an average residual of -0.3 and has a plot which looks remarkably similar to those for stations in the granitic Gabilan Range (e.g., FRP) on the opposite side of the San Andreas fault. However, it is unlikely that granitic basement occurs in the area, therefore a plausible explanation for the unexpectedly large negative average residual is that the Franciscan beneath CHR is locally rich in higher velocity rocks, perhaps unaltered ultrabasic rocks of the ophiolite thought to underlie the Franciscan.

Large variations with azimuth and incidence angle are also noticeable in the plots. An example of the latter effect occurs for an azimuth of about -40° on plots for stations JOL, MOP, BVL, PCL, and LTR. For the first three

stations a narrow band of negative residuals, sandwiched between positive residuals, occur for incidence angles roughly between 25° to 35°; for the last two stations negative residuals occur for incidence angles greater than about 30°. Such a pattern is difficult to explain qualitatively and points out the necessity of a quantitative inversion of the data.

An abrupt change in sign of delays as a function of azimuth is displayed in the southeast quadrants of the plots. The negative to positive (or at least to less negative) change in a clockwise direction on the plots is similar to that described for stations CBO and EUC in the San Jose region. Thus this pattern appears to characterize a majority of stations southeast of a line passing just northwest of CBO and EUC. This agains points out a fundamental difference in the deep structure beneath the northwestern and southeastern parts of the array. A discussion of the structure causing this effect will be deferred until the section on the three-dimensional inversion models.

Finally, the average station residuals ($\bar{R}_i$) corrected for elevation (minus elevation/5.6 km/sec) are plotted in hundredths of seconds at the station locations and contoured in Figure 3.16. Station residuals with fewer than 10 readings are less reliable and are denoted on the map by parenthesis. The averages and other pertinent station data are tabulated in Table 3.2. The range of 1.3 seconds is very similar to the Pg time term range and also to the

range of average station residuals in the Pn study. The contours show a close correspondence to surface geology except north of San Pablo Bay where the averages are more negative than expected for Franciscan terrain covered in parts by sedimentary rocks. Perhaps it is due to the projection of a deeper mantle effect into the average station residuals.

3.3.3 Preliminary Models

Although we were able to make some qualitative inferences about crustal structure from examination of the spatial variation maps and station focal sphere plots, a quantitative inversion is necessary to take advantage of the vast amount of information in the data. In this section we describe a preliminary three-dimensional velocity model of the crust and upper mantle beneath the U.S.G.S. Central California Seismic Array using the method of inversion described in Chapter 2.

The model was obtained at an early stage of this study and although it has since been replaced by more detailed models, the results are important in demonstrating the appropriateness of one of the basic assumptions of the inversion method: that the main source of the delays are within the volume being modeled.

The mislocation diagram in Figure 3.17 indicates substantial and consistent error in the observed direction of arrival of a plane wave from the theoretical direction

expected from the JB model. If the source of the deviation is below our maximum modeling depth we should invert the data set which does not contain the error, that is the plane wave residuals; on the other hand, if the source is within our modeling volume, we should invert the data set which contains the effects of the source, namely the JB (or Herrin) residuals. The same reasoning applies in choosing between the theoretical or observed plane wave parameters (azimuth and incidence angle) in tracing the ray back through the model in calculating the partial derivatives for the inversion.

Zandt and Aki (1976) resolved the ambiguity of which data set to invert by inverting both and choosing the model which was most consistent with independent geophysical data. The results of the inversion of the JB residuals and the plane wave residuals are tabulated in Tables 3.3 and 3.4, respectively. In Figure 3.18 the crustal layer velocity perturbations from each inversion are compared with a similar model obtained from a P_n time term study (Kind, 1972). In the California array P_n study, Kind computed station time terms which are presumably independent of the event and reflect a mean crustal structure beneath the station. In order to facilitate comparison with the velocity perturbation maps, the time terms given in seconds were converted to percent velocity perturbation using the following assumption: the time terms are due entirely to a velocity perturbation within a 25 km thick crust with average

V_p = 8.0 km/sec.

Comparison of the crustal layers shows some similarity among all three models; in fact, the smaller scale features in the maps are very similar. Nevertheless the JB and plane wave models are dissimilar on a larger scale, the former having northwest-southeast trends which the latter lacks. Thus the JB model is consistent with the known geologic structure and with Kind's P_n time term analysis and implies that the systematic deflection of the plane waves is due to a systematic velocity structure within our model volume. In the case of central California, therefore, the inversion of the JB (or Herrin) residuals is appropriate and henceforth only such results will be considered.

3.4 THREE-DIMENSIONAL INVERSION RESULTS - CRUSTAL LAYERS

After the preliminary inversion efforts discussed previously, additional data was collected. The new data included residuals from new stations along the periphery of the array as well as within the array thus providing the possibility of inverting for finer details using smaller block sizes. As explained in Chapter 2 the computer cost limitation placed a definite ceiling on the maximum number of blocks or unknowns allowed in a model. Therefore, we chose to divide the array into three segments and invert the data from each segment separately. The same division used in the discussion of the data was retained for the inversion, namely from north to south: Santa Rosa, San Jose, and Bear Valley (Figure 3.19).

The initial model parameters for each region were chosen on the basis of an average crustal model from the seismic refraction profiles described in 3.2.1. The block size in the upper crustal layer is 10 km x 10 km x 10 km, small enough to allow the expression of strong heterogeneity where it is expected. The second layer was made 20 km thick thus definitely encompassing the Moho throughout the region. Any structure on the Moho is expected to contribute to the velocity perturbations in the second layer. An increase in block size in the second layer to 20 km x 20 km was necessary to improve resolution (more hits per block) and keep the total number of blocks within the ceiling. Two upper

mantle layers were used: both layers 30 km thick with 25 km x 25 km block size. The larger block size partly reflects the effort to keep the total number of unknowns down and also anticipates smoother (larger scale) heterogeneity in the mantle.

A damping value of .005 $(sec/\%)^2$ was found to provide the best trade-off of resolution vs. standard error during the preliminary inversions and thus was used in all the succeeding inversion runs. Experience from the preliminary runs also indicated that the variance reduction showed little improvement beyond a 4-layered model. However, to assess the influence of an added layer on the previous layers, a 5-layer model was run for the San Jose region and is compared to its otherwise identical 4-layer model.

Details of the initial model's parameters, and solutions for each region, are provided in tables: Santa Rosa, 3.5; San Jose, 3.6; and Bear Valley, 3.7. The velocity perturbations are mapped in Figures 3.20 to 3.23 and the contours of the velocity perturbations for each layer are illustrated in Figures 3.24-3.27. In these figures the separate segments have been synthesized to provide a regional picture. In the following discussion, however, the crustal layers are interpreted separately for each area. In the next section the mantle layers are discussed on a regional scale in the context of questions brought up at the beginning of this chapter.

3.4.1 Santa Rosa Region

The northernmost region is a rectangular area centered near Santa Rosa. The area is bounded by the San Andreas fault and the western edge of the Great Valley and extends from Clear Lake southeastward to San Pablo Bay. Geologically, exposed Franciscan rocks predominate but thick sequences of Tertiary sedimentary rocks occur in structural depressions. As in most of the Coast Ranges, the structural grain is northwestward and major northwest-trending faults have produced a series of parallel horst and graben structures (Chapman, 1975). Volcanic activity in this region is attested to by two volcanic fields: the Sonoma volcanics in the southern part of the area and the Clear Lake volcanics which cover an area of about 85 square miles immediately south of Clear Lake (Chapman, 1975). Both fields are predominantly andesitic in composition, the former being of Pliocene age (12-5 my) and the latter of Pleistocene age (<3 my) (Christianson and Lipman, 1972). Christiansen and Lipman (1972) attribute these fields and the Sutter Buttes volcanics, another young (about 1.5 my) andesitic field in the Great Valley 60 km to the northeast, to oblique subduction of a constricted but still active part of the Juan de Fuca plate between the Mendocino and Blanco fracture zones.

The youthfullness of the Clear Lake volcanic field is demonstrated by abundant thermal features at the Geysers geothermal field and active microearthquake activity.

Analysis of a 25 mgal gravity low with an areal extent of about 250 square miles and centered south of Clear Lake has lead Chapman (1975) to conclude that a hot intrusive mass, such as a magma chamber underlies the volcanic field. Observation of teleseismic delays by a dense network of seismometers deployed around the anomaly has apparently confirmed the presence of a very low velocity anomaly in the crust (Iyer, 1978, pers. comm.).

In the present study, twenty-four stations occupied the Santa Rosa region (Figure 3.19). At least five of these stations recorded data from 90 events for a total set of 845 P-wave residuals. The layer-block configuration and other inversion parameters are listed in Table 3.5. Data variance before inversion was .08 sec^2 and the residual variance was .02 sec^2 for a variance reduction of 75%. The solution parameters are listed in Table 3.5 and contour maps of the solution for the crustal layers are presented in Figures 3.24 and 3.25, the discussion of which follows. Due to the relative sparsity of stations in this region there are a number of "holes" or unsampled blocks within Layer 1, nevertheless, a consistent interpretation is possible. Consideration of the geology of the seismometer sites suggests that lateral velocity variations are due primarily to the thickness of Tertiary sedimentary cover atop the Franciscan basement. In fact, a good correlation is observed with exposed Franciscan basement associated with high velocities and Tertiary sedimentary cover

corresponding to low velocities. The lowest relative velocities (-3 to -5%) occur along the western edge of the Great Valley where the Tertiary sedimentary beds are thickest, whereas areas of exposed Franciscan rocks have consistently higher velocities (.5 to 3%). An interesting exception to the above correlation is a low-velocity anomaly near station SGM located at the southern edge of the Clear Lake volcanics. The anomaly is probably associated with the hot intrusive mass inferred to lie below the volcanic field.

In Layer 2 (10-30 km) the observed velocity anomalies could be due to variations in crustal thickness, lateral compositional differences, or a combination of both effects. The pattern of high velocities near the coast giving way to low velocities inland is consistent with crustal thickening. Simple calculations considering a homogeneous crust (V_p = 6.9 km/sec) over a homogeneous mantle (V_p = 8.0 km/sec) indicate that an 8° dip is required to explain the approximately 10% velocity decrease in a span of 100 km. In other terms, the crust thickens from 20 km near the coast to 34 km at the western edge of the Great Valley. These numbers are not unreasonable and are consistent with the large gravity gradient observed in this region (Figure 3.8).

3.4.2 San Jose Region

Extending from San Pablo Bay to a line through Monterey Bay the San Jose region has the highest density of

stations of the entire central California array. Three major faults splay around San Francisco Bay: the San Andreas bisects the San Francisco peninsula and across the bay the Calaveras and Hayward faults form a major offshoot branch from the San Andreas system. Southwest of the San Andreas fault granitic plutons outcrop within the Salinian block. The wedge between the San Andreas and Calaveras-Hayward faults is a complex series of exposed Franciscan basement and deep troughs of Tertiary sedimentary rocks. On the east side of the Calaveras fault the Franciscan again outcrops in the core of the Diablo antiform. A unique feature located in the northern corner of the region is Mount Diablo, a circular piercement structure poking through the thick Tertiary sedimentary cover located in that area.

Fifty-six stations are located within the San Jose region. Using 118 events, a total of 2126 residuals were used in the inversion. With an initial data variance of .11 sec^2 and a final variance of .07 sec^2 the variance improvement was only 39%. Again, consider the contoured solution maps (see Table 3.6 for detailed input and solution parameters).

The complicated pattern of anomalies in the crust reflects, quite accurately, the complex geology of this region. As in the Santa Rosa region, the lowest velocities correlate with areas of thick Tertiary sedimentary deposits. For example, the broad low-velocity area east of San Pablo Bay forms a continuation of a similar feature in the Santa

Rosa region. Within the former area are two large amplitude anomalies. One is a prominent high-velocity block associated with Mount Diablo which exhibits a 20% velocity contrast with neighboring blocks. The feature, also marked by a +50 mgal gravity anomaly and a 250γ positive magnetic anomaly has been attributed to an intrusive diabase laccolith with a 1 km thick head nearly 13 km in diameter and a 1.5 km wide stem extending downward about 13 km (Griscom, 1966). However, the significant effect the feature has on teleseismic delays indicates that the "stem" must be larger than 1.5 km in diameter; a cylindrical body with an average velocity of 6.4 km/sec about 10 km diameter extending down at least 10 km would better explain the seismic anomaly. The other large amplitude anomaly is a low-velocity trough defined by two blocks immediately south of Mount Diablo. Comparison with the geology map (Figure 3.6) suggests that the feature is a fault-bounded trough of Tertiary sedimentary rocks. A hidden northward extension of the Calaveras fault bounds it on the west side and an inferred fault brings the Tertiary beds in contact with Cretaceous sedimentary beds on the east side. We can estimate the thickness of the low-velocity material by noticing the similarity of the anomaly to another two-block low-velocity anomaly located between the Calaveras and Silver Creek faults. This latter seismic anomaly corresponds exactly with the Evergreen gravity low studied in detail by Robbins (1971) who ascribed the gravity effect to a combination of 6 km of

sedimentary rocks in the upper crust and a lower crustal graben that may extend into the upper mantle. Mayer-Rosa (1972) studied the same feature using local earthquake delays and concluded that a 7-8 km wide zone between the faults extending down at least 6 km has a velocity decrease of about 1.2 km/sec. This estimate is inconsistent with the teleseismic delays, probably due to the smoothing effect of the longer wavelength teleseismic waves.

One other low-velocity anomaly west of San Jose is coincident with the Cupertino gravity anomaly studied by Robbins (1971) and is probably due to about 4 km of sedimentary deposits in a graben causing a fault contact with Franciscan basement to the west. The latter terrain forms a narrow outcrop east of the San Andreas fault and is bound by the +2% contour in our solution. Three minor higher velocity anomalies lie within the Franciscan tract and probably indicate areas containing a higher proportion of high-velocity material in the heterogeneous Franciscan assemblage.

The Salinian block west of the San Andreas fault is characterized by four anomalies: high velocities associated with the granitic Ben Lomond Mountain; and three low velocity areas associated with narrow but deep sediment-filled graben structures between the Vergeles and San Andreas faults, between the Ben Lomond and Zayante faults, and in a broader area between the San Gregorio and San Andreas faults. All these anomalies are also well defined by P_g

time terms (Wesson et al., 1973).

3.4.3 Bear Valley Region

Bounded by a line through Monterey Bay on the north and a line through Peach Tree Valley on the south, the Bear Valley region is structurally much simpler than the neighboring San Jose region to the north. The San Andreas fault splits the area in two; to the west, Salinian granitic rocks are exposed in the Gabilan Mountains and to the east Franciscan rocks outcrop in the southern half of the Diablo Mountains and in a narrow strip along the San Andreas fault south of station BTW. Twenty kilometers to the east lies a 5 by 13 kilometer elliptical mass of serpentinized ultramafic rock, lesser amounts of which outcrop to the southeast near, or adjacent to, the San Andreas fault. Within this region, the San Andreas fault is paralleled 5 km to the east by the Paicines-San Benito fault forming a structural depression, referred to as the Hollister trough, in which slivers of various rock types are found.

There are 43 stations in this region, the majority of which are within a narrow strip astride the San Andreas fault. With 118 events recorded at some or all of these stations, a total of 2043 residuals were used in the inversion. The data variance was .06 sec^2 and the residual variance was .02 sec^2 for an improvement of 68%. The solution parameters are listed in Table 3.7 and the contoured solution map for the crustal layers are discussed now.

The upper crustal heterogeneity reflects the simpler structure in this region and is dominated by two long, narrow anomalies of opposite polarity on opposite sides of the San Andreas fault. The positive anomaly coincides with the outcrop of granitic rock in the Gabilan Mountains and reaches peak values of +7% at station FRP and between stations JHC and SHG. On the other side of the San Andreas fault a low-velocity trough parallels the positive anomaly from Hollister to station LRV with the lowest value of -13% centered around San Benito.

Several previous seismic investigations in the Bear Valley area are relevant to the present study. Wesson (1971) using three-dimensional ray tracing to locate local earthquakes first showed that a low-velocity trough existed between the San Andreas and San Benito faults. The P_g term analysis of Wesson et al. (1973) indicated more than 3 km of Tertiary sediments in the Hollister trough. A detailed two-dimensional velocity model perpendicular to Bear Valley was derived by Healy and Peak (1975) from local earthquake data. Their model has a 12 km deep low-velocity zone between the San Andreas and San Benito faults which is about 30% lower than the crustal section to the northeast. These magnitudes are about twice those obtained in the present study and (similar to the comparison of 'local' vs. 'teleseismic' models for the Silver Creek-Calaveras low-velocity wedge) are due to the smoothing effect of longer wavelength teleseismic P-waves. A recent study by Aki and Lee (1976)

has the most direct bearing on our model because they used an inversion technique very similar to the method described in Chapter 2; the main difference being the use of local earthquake data which requires the addition of the hypocenter parameters as variables in the inversion. They used a block size of 3 x 4 x 5 km in applying their technique to Bear Valley data and obtained two similar models for the lateral velocity structure of the upper crust. Their models have a 'low' of about -15% sandwiched between 'highs' of about 6%, very similar to our model. The transitions from 'high' to 'low' in Aki and Lee's maps are sharper, however, this is to be expected because our larger block size will tend to smooth out transitions. The correlation between the 'local' and 'teleseismic' models is revealed by comparing Aki and Lee's Figure 11 with the corresponding area in Figure 3.24. The similarity is emphasized if a constant +2% is added to the contour lines of the 'teleseismic' case, a reasonable change because we are investigating relative velocity anomalies. Then the 'teleseismic' model also has a 'low' of -8% to -12% sandwiched between 'highs' of about 4% to 6%. Again, the magnitudes of the anomalies are somewhat less than the 'local' models, but the overall agreement is quite striking.

Sediments in the Hollister trough are prime candidates as the primary source for the seismic low-velocity anomaly. Both the gravity map (Figure 3.8) and the magnetic map (Figure 3.9) have anomalies marking the Hollister trough, and whereas the gravity anomaly is a 'low' as expected,

the magnetic anomaly is a 'high'. Hanna et al. (1972) concluded that of all the rock types in the region only serpentine had the required properties to produce the appropriate gravity and magnetic anomalies. Their conclusion was that a large ridge of serpentine must underlie the Hollister trough despite the fact that large outcrops of serpentine occur only south of San Benito.

Serpentinized ultramafic rocks have been documented to have velocities inversely proportional to the degree of serpentinization by hydration of the original rock mass (Christensen, 1966). Thus the low velocities associated with the Hollister trough reinforce the conclusion that a significant serpentine ridge underlies the depression. The low velocities also indicate that the original ultramafic rock mass must be over 80% serpentine (see Figure 2, Coleman, 1971). A possible explanation for the presence of the serpentine ridge is that the San Andreas fault system acted as a weak zone through which massive shearing and hydration of the original rock mass could take place.

3.4.4 Crustal Heterogeneity and Mode of Earthquake Occurrence

The purpose of this section is to consider whether seismic mapping methods such as teleseismic delay inversion might be useful aids to geologists in evaluating earthquake hazards. We do this by checking correlations between anomaly patterns and areas of fault creep, microseismicity,

and rupture lengths of large earthquakes.

Within our study area segments of the San Andreas, Calaveras, and Hayward faults are characterized by different mechanical behavior. The San Andreas fault from Cholame to San Juan Bautista, and the Calaveras and Hayward faults are characterized by a high rate of microseismicity and fault creep. The segment of the San Andreas fault north of San Juan Bautista, on the other hand, ruptured along its entire length during the San Francisco earthquake of 1906, but currently has a low rate of microseismicity and no fault creep (Allen, 1968). Examining the velocity anomalies in layer one we find no consistent pattern associated with faults having different mechanical behavior. For example, the San Andreas south of Hollister is marked by a very strong velocity contrast across the fault with an adjacent low-velocity trough, but a similar pattern is found on the fault north of Hollister near San Jose.

One feature in the velocity pattern, however, does appear related to a mechanical aspect of the fault system. Almost the entire length of the major faults are marked by a velocity contrast, or at least does not cross-cut any major anomaly; the one exception, near San Juan Bautista, occurs where the San Andreas has a major splay into the Calaveras fault. There, a high-velocity anomaly associated with the Gabilan Range traverses the San Andreas and terminates within the Y-shaped wedge formed by the branching

Calaveras fault. This feature may be a major asperity which locks the northern portion of the San Andreas until a sufficient level of stress builds up and breaks through the asperity. If so, the identification of other major asperities could help define areas of high earthquake hazards.

3.5 INTERPRETATION OF UPPER MANTLE HETEROGENEITY

Although a number of factors could produce the crustal and mantle heterogeneity mapped beneath the Central California Seismic Array, the most plausible sources of the anomalies, considering the recent active tectonism of the region, are compositional inhomogeneity and thermal perturbations. The crustal layers are probably dominated by compositional differences as indicated by the close correlation between surface geology and anomaly patterns. Deeper inhomogeneities are probably due to both compositional and thermal variations. A unique interpretation is clearly not possible, the best we can do is examine the anomaly patterns and consider their cause in light of the tectonic history of coastal California as put forward in Section 3.1 and keeping in mind any constraints imposed by other geophysical measurements. We would like to test any such hypothesis by numerical modeling of the relevant thermal and mechanical processes but that is beyond the scope of this thesis.

The velocity anomaly patterns in the mantle layers retain relatively large amplitudes and the NW linearity observed in the crustal layers. Also on a gross scale, the velocities on the SW side are higher than on the SE side; this effect is consistent with the pronounced and regular patterns of the array mislocation vectors (Figure 3.17). The velocity anomalies in layer 4 (Figure 3.27)

have rapid variations and locally very large amplitudes. These effects, observed in other inversions, are probably due to outside heterogeneity being "forced" into our model. Hence we will concentrate on interpreting Layer 3 (Figure 3.26) which is well resolved and free of the biasing effect in Layer 4.

The anomalies in Layer 3 (30-60 km) NW of Bear Valley define a linear pattern of high-low-high (H-L-H) parallel to the coastline. The regular pattern is interrupted southeast of Bear Valley where the central low is replaced by a high and the western high is replaced by a low. The abrupt change in anomaly pattern is suggestive of a strike-slip fault displacing the patterns perpendicular to the trend of the linearity. Because of the alternating nature of the anomalies, it is impossible to identify the sense of displacement on the hypothetical fault.

The easternmost line of highs in Layer 3 is not resolved in our model because there are no stations above it to provide the "cross-fire" needed for good resolution. Poor resolution, however, does not necessarily invalidate the anomalies; the effect is visible in the data as early arrivals from the east-southeast; what, in fact, is poorly resolved is the depth range of the anomalies. The inversion method will "place" the anomaly at the shallowest depth compatible with the rest of the data. In the case of Layer 3, independent evidence indicates that the unresolved high-velocity pattern may be real. It is situated beneath the

center of the Great Valley and corresponds with a broad elongate +50 mgal gravity anomaly which is located along the center of the valley. Hypotheses on the source of the Great Valley gravity high and its accompanying positive magnetic anomaly were recently reviewed and studied in detail by Cady (1977). He suggests the source of the anomalies is a tectonically emplaced fragment of oceanic crust which comes to within 2.5 km of the surface just east of the center of the Great Valley and dips steeply to the west. In an alternate model (Model A of his Figure 6), Cady demonstrates that a prominent upward bulge in the Moho beneath the valley can also produce the gravity high. The eastern line of high velocities in Layer 3 which is located at a minimum depth supports a variant of Cady's second model; that is, at least part of the Great Valley gravity high is due to a sub-Moho source.

Another feature of the Great Valley gravity anomaly relevant to our study is the major break in the linear pattern which occurs near Fresno. Cady interpreted the eastward displacement of the anomaly as due to an approximately east-trending fault in the basement rocks and further speculated that the fault was part of an ancient transform fault that was once continuous with the Mendocino fracture zone. A comparison of the location of the break in the gravity anomaly (Cady, 1977, Figure 3) with the location of the break in the velocity anomalies in Layer 3 suggest the possibility of a common cause, in particular, an

easterly-trending strike-slip fault.

The line of low velocities extending from below Clear Lake to Mt. Diablo and terminating beneath the Quien Sabe volcanic field defines another linear feature which aligns with the San Andreas-Calaveras-Hayward-Healdsburg faults. This alignment suggests that a sub-Moho throughgoing fault separating the Pacific and North American lithospheres does not coincide exactly with the San Andreas but diverges from it near Hollister to follow a straighter path to connect with the Mendocino fracture zone. Although there is no single throughgoing fault at the surface, long term seismicity patterns (Bolt, 1978) and recent microearthquake studies (Winterhalder, 1978) indicate a diffuse zone of seismicity parallel to the linear zone defined by the velocity anomalies.

The cause of the low velocities poses another problem. Their location on the edge of the Great Valley raises the question of whether the effect of thick sedimentary units in the upper crust has "leaked" down into the lower layers. There are two indicators that leakage is not a factor. First, no stations actually are situated in the valley and therefore the input to the data set of large delays due to the thickest portion of the sedimentary blanket is minimized. Secondly, the resolution matrix (Table 3.6) confirms that most of the feature is well resolved. Perhaps a clue to the source of the anomaly is the close association with Cenozoic volcanic fields at the surface. From north to south the lowest velocities occur beneath the Quarternary

Clear Lake volcanic field, the Pliocene Berkeley Hills-Santa Clara Valley volcanics, and Mt. Diablo, an igneous intrusive (?), and at the southern end, the mid-Miocene (?) Quien Sabe field (ages from Christiansen and Lipman, 1972). Considering the young ages of the volcanic fields, it is not unreasonable to assume that the low velocities define a hot zone that was associated with the source of the volcanics.

The broader question of the cause of volcanism which is obviously not the usual subduction arc magmatism is not considered in detail. However, the age progression correlates roughly with the migration of the Mendocino triple junction (Figure 3.56), thus suggesting the ultimate cause of volcanism as either the oblique or parallel subduction of the Pacific ridge (Marshak and Karig, 1977; DeLong and Fox, 1978). Further evidence for a hot zone beneath the Franciscan terrain is the very high heat flow measured in the Franciscan east of the San Andreas. Roy et al. (1972) obtain a reduced heat flow value for this area of 1.9 to 2.1 HFU, approximately 0.6 units higher than the Basin and Range (Robertson, 1972, p. 525). In fact, their calculated temperature profile across the western United States at about 38°N latitude (their Figure 19) shows an abrupt doming of the partial melt zone beneath the Diablo Range which corresponds very nicely with our results. A cautionary note, however, is that their results are based on very few heat flow measurements in the Coast Ranges and

many more measurements are required to confirm the preliminary results. Nevertheless, the volcanics and heat flow are consistent with an interpretation of the central line of low velocities as a hot zone beneath the Coast Ranges. We will return to these questions in Chapter V after an examination of Yellowstone in Chapter IV.

Figure Captions

Figure 3.1 Location map for central California. CM = Cape Mendocino; PA = Point Arena; PR = Point Reyes; MB = Monterey Bay; SF = San Francisco; SJ = San Jose; HO = Hollister.

Figure 3.2 Simplified geologic map of California. Cross ruling = Franciscan Formation; Stippling = Great Valley basal sedimentary units; Starburst = Granitic rocks.

Figure 3.3 Paleozoic tectonic evolution sequence for the western U.S. adopted from Burchfiel and Davis (1972). R.M.T. = Roberts' Mountain Thrust; G.T. = Golconda Thrust.

Figure 3.4 Mesozoic tectonic evolution sequence for western U.S. adopted from Schweichert and Cowan (1974).

Figure 3.5 a) Cenozoic plate reconstructions for the eastern Pacific from Atwater and Molnar (1973). b) Migration of the Mendocino triple junction along coastal California adopted from Snyder et al. (1976). Numbers in the ocean represent millions of years ago and mark the location of the triple junction at those times. Cross hatching represents area of andesitic volcanism.

The lines marked by numbers in millions of years represent the northward migration of the cessation of volcanism. Triangles are volcanoes or calderas: 1 = Mt. Shasta; 2 = Mt. Lassen; 3 = Mono Lake.

Figure 3.6 Simplified geologic map of the Coast Ranges, central California, adopted from Transcontinental Survey Maps (TSM).

Figure 3.7 Seismic refraction profiles, central California, adopted from TSM. Velocities in km/sec.

Figure 3.8 Bouguer gravity map of Coast Ranges, central California, adopted from TSM. Contour interval is 20 mgals.

Figure 3.9 Aeromagnetic map of Coast Ranges, central California, adopted from TSM. Contour interval is 100 gamma.

Figure 3.10 USGS Central California Seismic Array map. Stippled areas are exposed basement. Long dashed line is a gravity low that marks the deepest part of the Great Valley. Dash-dot line marks the Great Valley gravity high.

Figure 3.11 Location map of teleseismic events used in California study.

Figure 3.12 Spatial variation maps. Teleseismic delays at central California array. Displays variations with event azimuth and incidence angle (or distance).

Figure 3.13 Station Focal Sphere projection plots. Teleseismic delays at a station of the array. Displays variations with event azimuth and incidence angle. Santa Rosa region.

Figure 3.14 Same as above, except for San Jose region.

Figure 3.15 Same as above, except for Bear Valley region.

Figure 3.16 Average station residuals in hundredths of seconds with elevation correction applied. Times in parenthesis have fewer than 10 readings and are thus less reliable. Contour interval is .10 sec.

Figure 3.17 Array diagram for central California. Polar coordinates are azimuth and slowness ($dt/d\Delta$). The head of the arrow is at the USGS or "true" location and the tail represents the location determined from the array.

Figure 3.18 Comparison of crustal layers of (from left to right) plane wave inversion, Kind's Pn data, and JB inversion. Each crustal layer is 24 km thick with V_p = 6.0 km/sec. Tick marks on border are 15 km apart. Negative velocity perturbations are shaded.

Figure 3.19 Array map showing location of three subarrays. See caption for 3.10.

Figure 3.20 Results of inversion for Layer 1. Velocity perturbations in percent. Tick marks represent block size = 10 km.

Figure 3.21 Layer 2. Tick marks = 20 km. See 3.20.

Figure 3.22 Layer 3. Tick marks = 25 km. See 3.20.

Figure 3.23 Layer 4. Tick marks = 25 km. See 3.20.

Figure 3.24 Contours of percent velocity perturbations for Layer 1. Contour interval 4%.

Figure 3.25 Layer 2. Contour interval 2%. See 3.24.

Figure 3.26 Layer 3. Contour interval 2%. See 3.24.

Figure 3.27 Layer 4. Contour interval 2%. See 3.24.

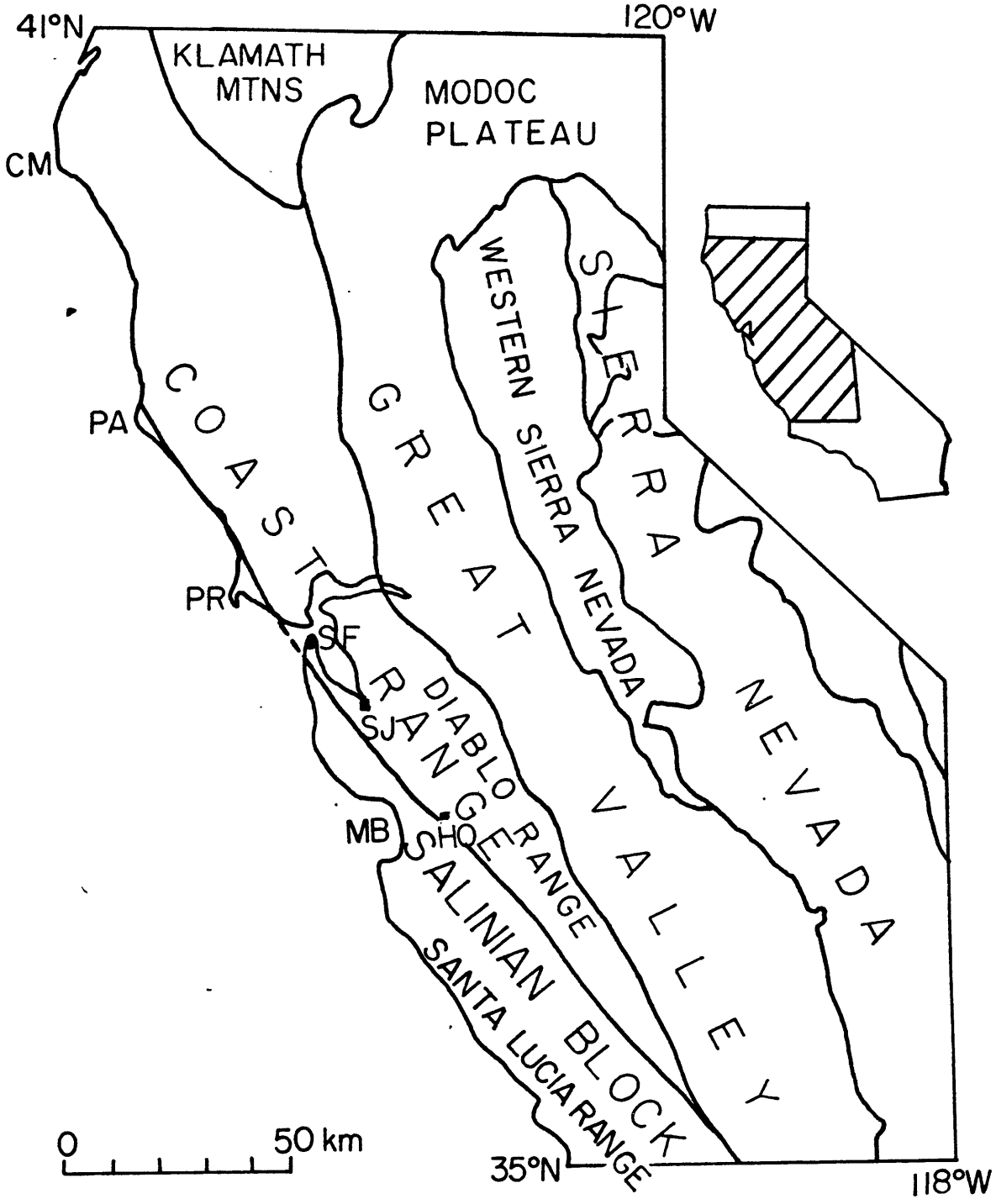
41°N
120°W
KLAMATH MTNS
MODOC PLATEAU
CM
WESTERN SIERRA NEVADA
SIERRA NEVADA
COAST
GREAT VALLEY
PA
PR
SF
SJ
DIABLO RANGE
MB
SHQ
SALINIAN BLOCK
SANTA LUCIA RANGE
0
50 km
35°N
118°W

Figure 3.1

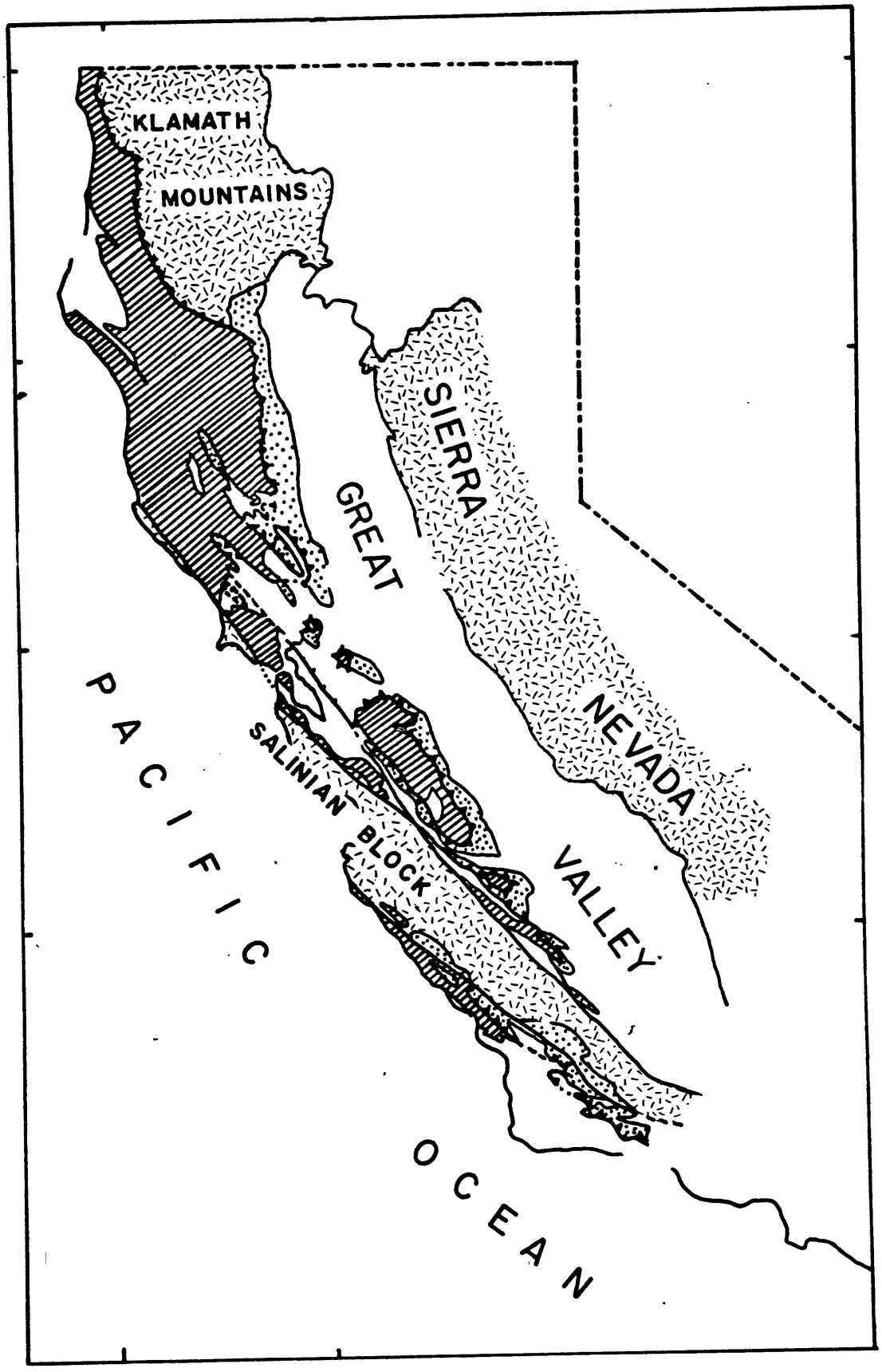
KLAMATH
MOUNTAINS
SIERRA
NEVADA
GREAT
VALLEY
SALINIAN BLOCK
PACIFIC
OCEAN

Figure 3.2

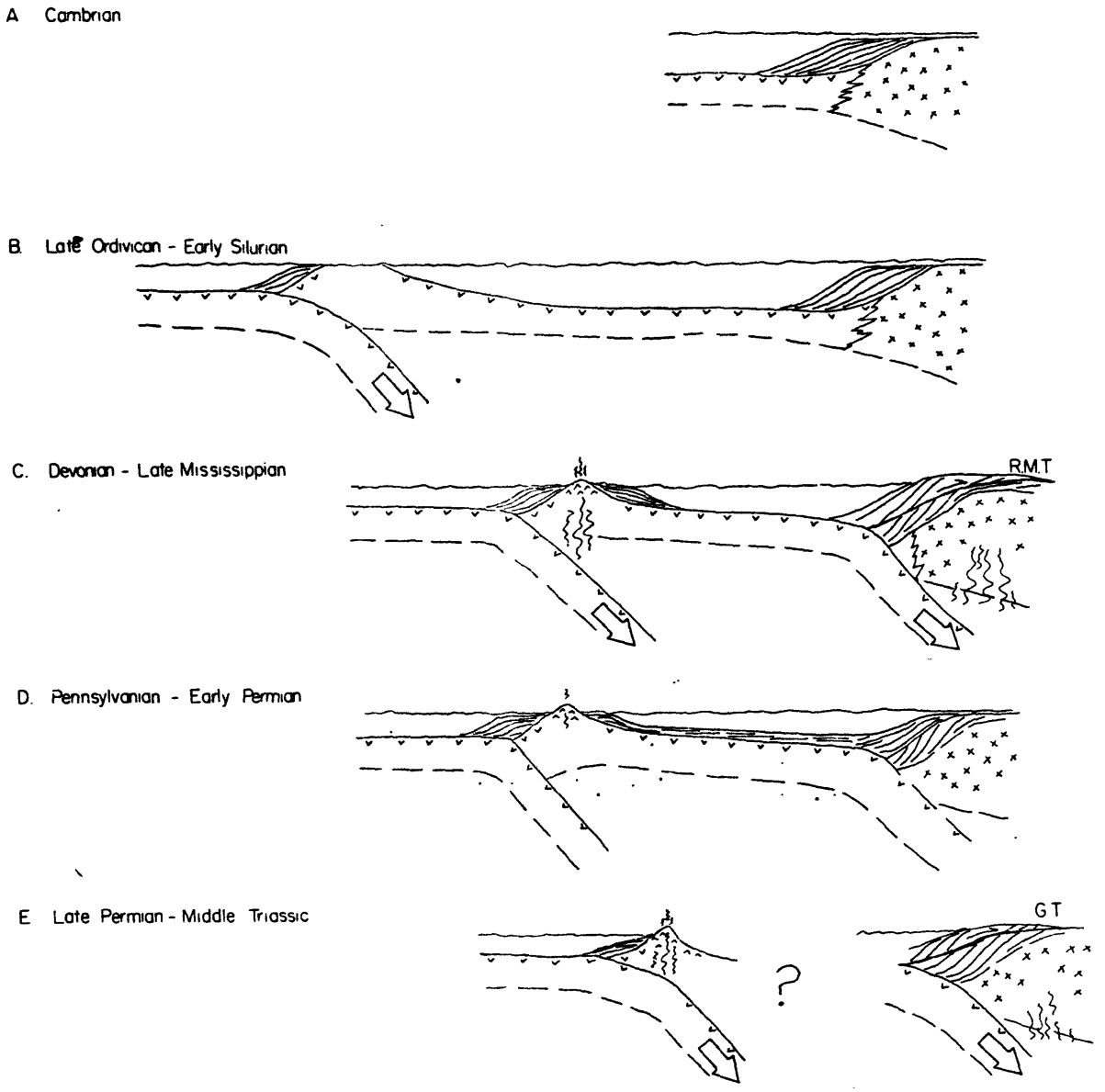
A Cambrian
B. Late Ordivican - Early Silurian
C. Devonian - Late Mississippian
R.M.T
D. Pennsylvanian - Early Permian
E Late Permian - Middle Triassic
?
G.T

Figure 3.3

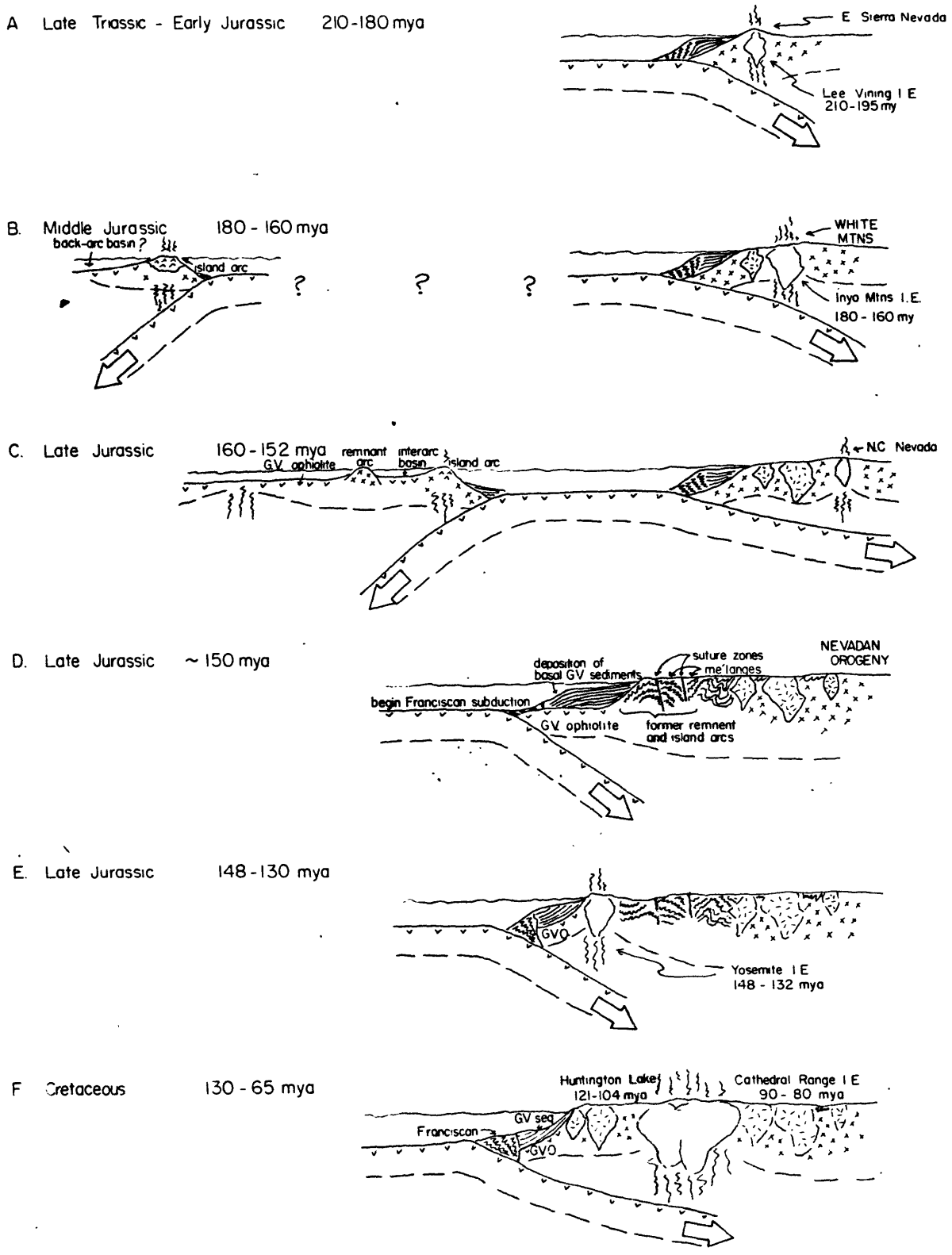
A Late Triassic - Early Jurassic 210-180 mya
E Sierra Nevada
Lee Vining I E
210-195 my
B. Middle Jurassic 180 - 160 mya
back-arc basin?
island arc
? ? ?
WHITE MTNS
Inyo Mtns I.E.
180 - 160 my
C. Late Jurassic 160 - 152 mya
G.V. ophiolite
remnant arc
interarc basin
island arc
N.C. Nevada
D. Late Jurassic ~ 150 mya
deposition of basal GV sediments
suture zones me'langes
NEVADAN OROGENY
begin Franciscan subduction
G.V. ophiolite
former remnent and island arcs
E. Late Jurassic 148 - 130 mya
GVO
Yosemite I E
148 - 132 mya
F Cretaceous 130 - 65 mya
Huntington Lake
121-104 mya
Cathedral Range I E
90 - 80 mya
Franciscan
GV seq
GVO

Figure 3.4

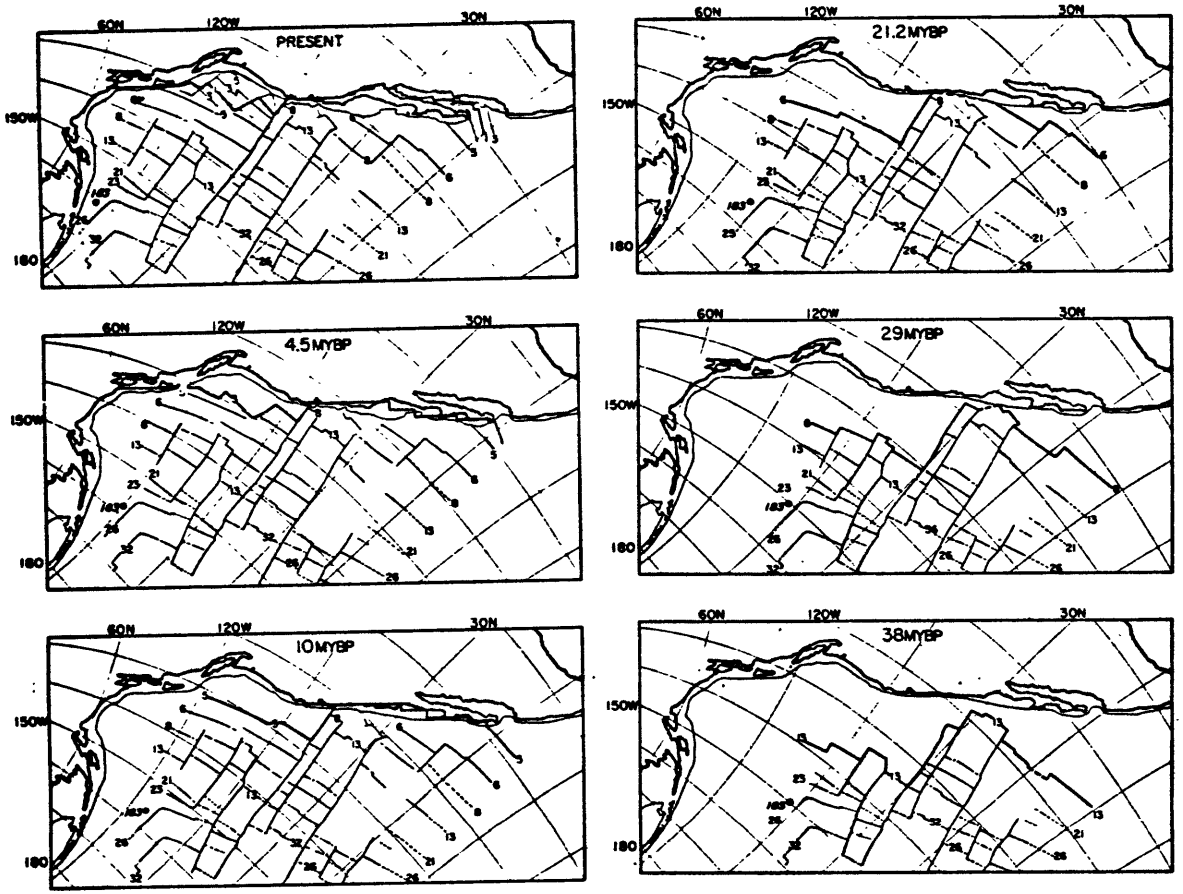
60N
120W
30N
150W
180
PRESENT
21.2MYBP
4.5MYBP
29MYBP
10MYBP
38MYBP

Figure 3.5a

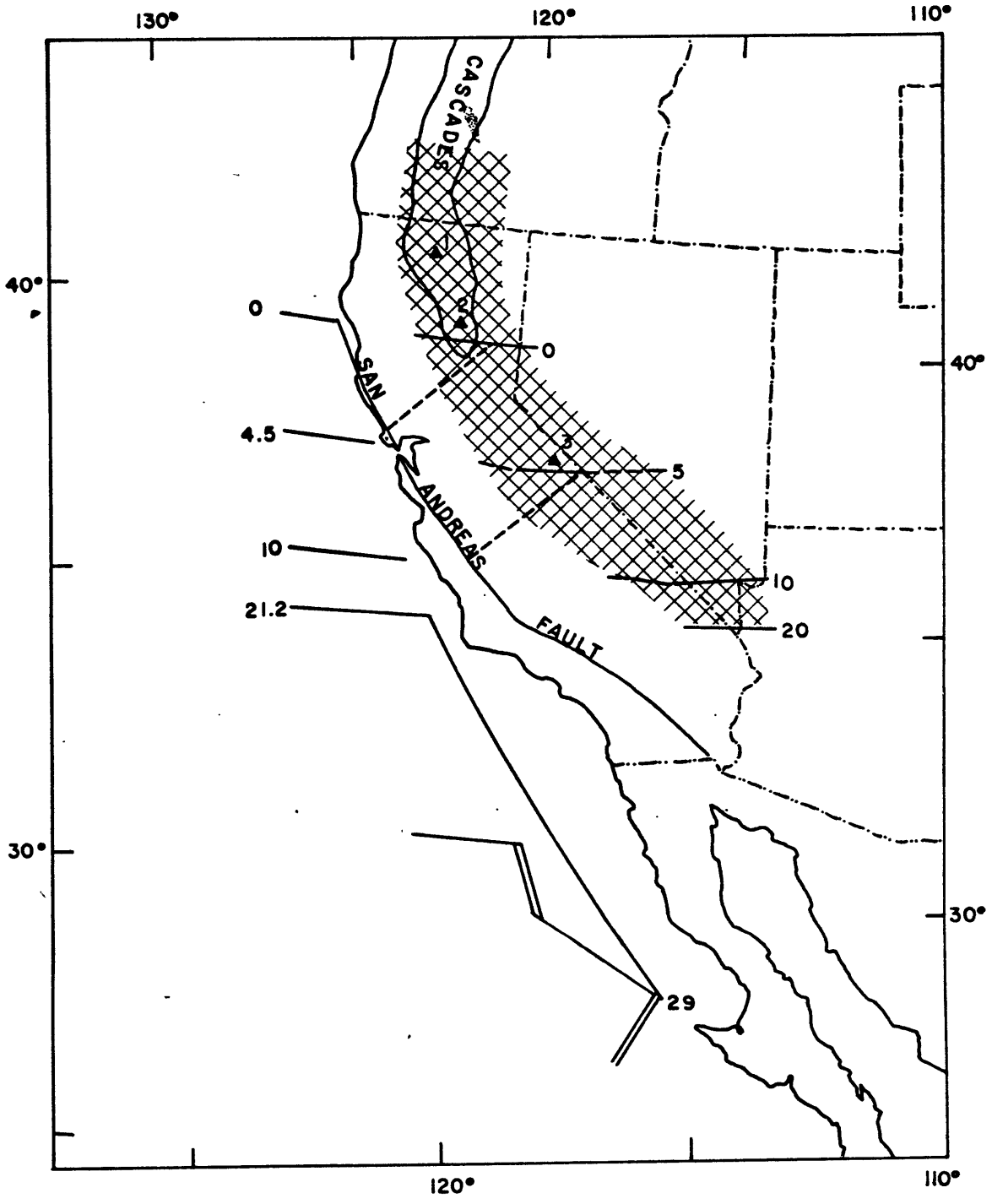
130°
120°
110°
40°
30°
CASCADES
SAN
ANDREAS
FAULT
0
0
4.5
5
10
10
21.2
20
29

Figure 3.5b

GEOLOGIC MAP OF THE COAST RANGES,
CENTRAL CALIFORNIA

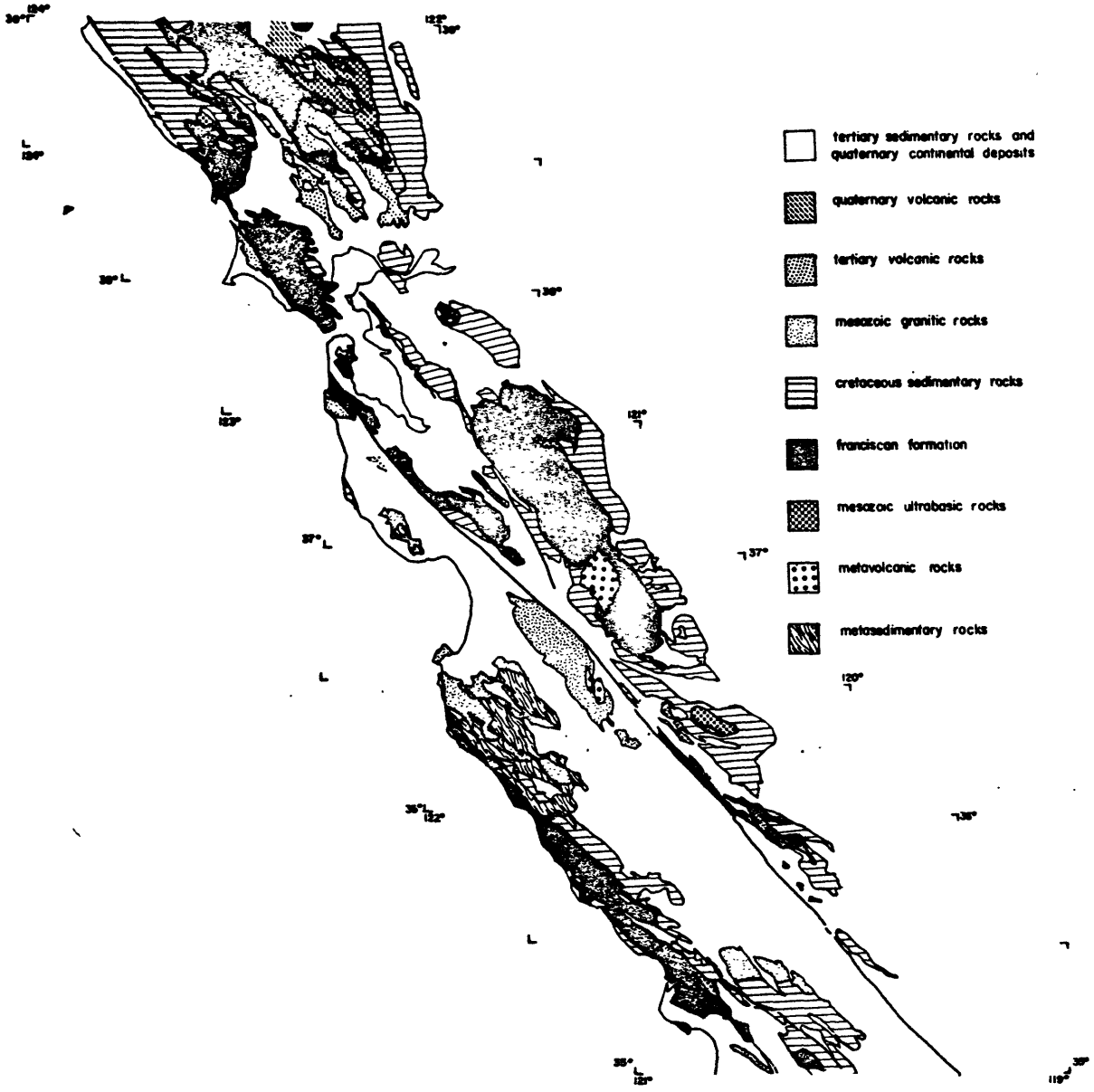

Figure 3.6

SEISMIC REFRACTION PROFILES
CENTRAL CALIFORNIA

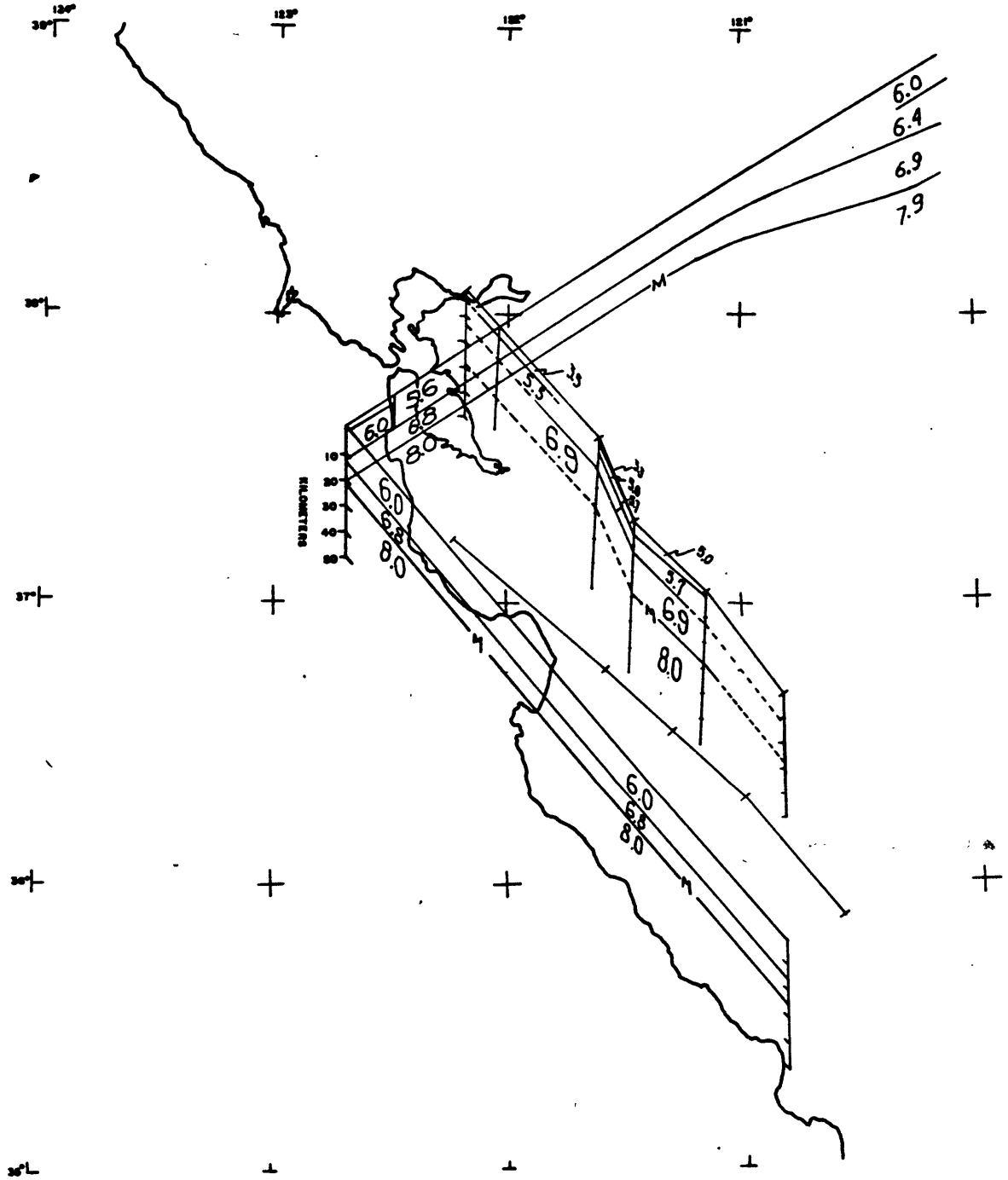

Figure 3.7

GRAVITY MAP OF COAST RANGES, CENTRAL CALIFORNIA

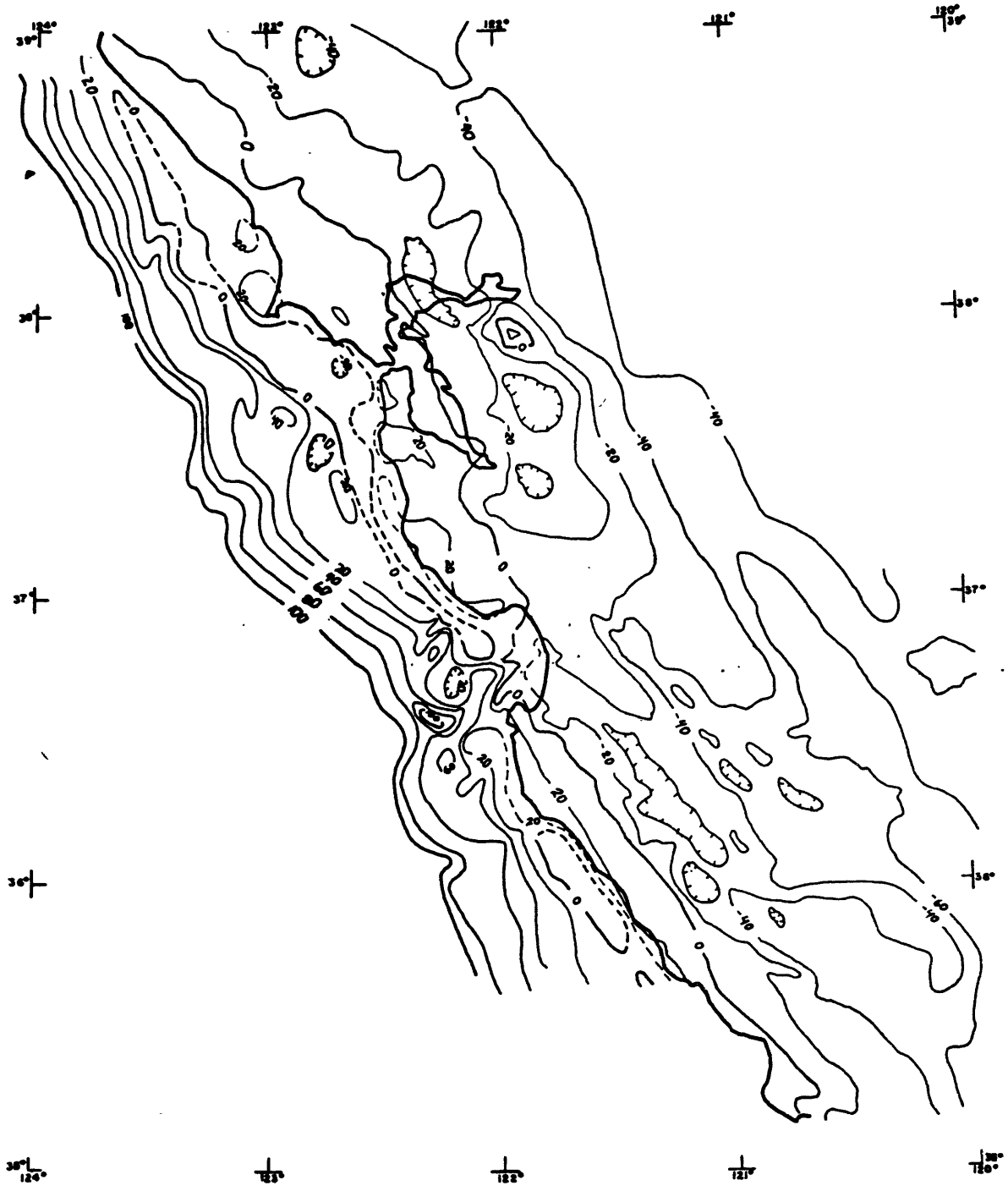

Figure 3.8

MAGNETIC MAP OF COAST RANGES,
CENTRAL CALIFORNIA

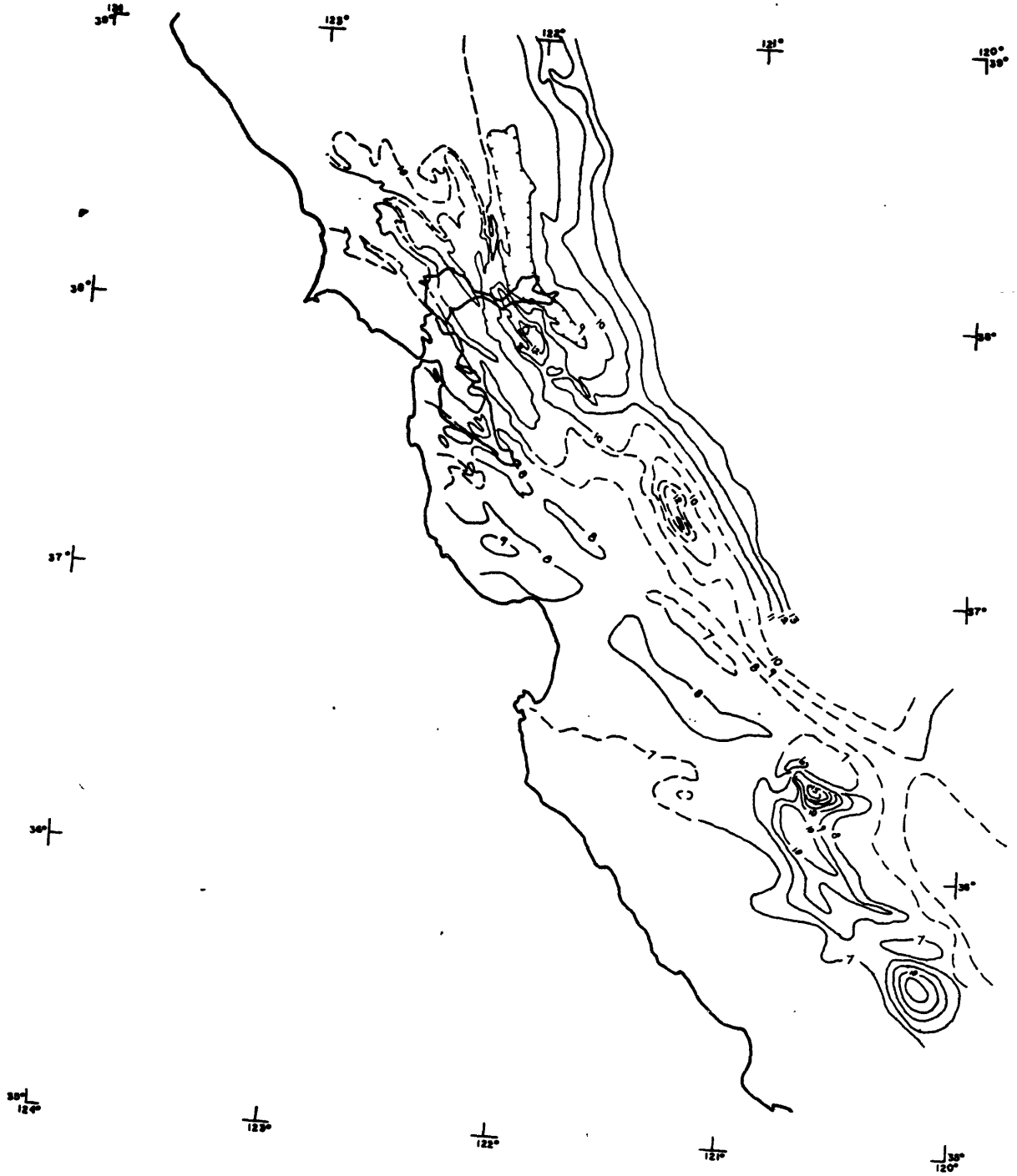

Figure 3.9

U.S.G.S. CENTRAL CALIFORNIA SEISMIC ARRAY

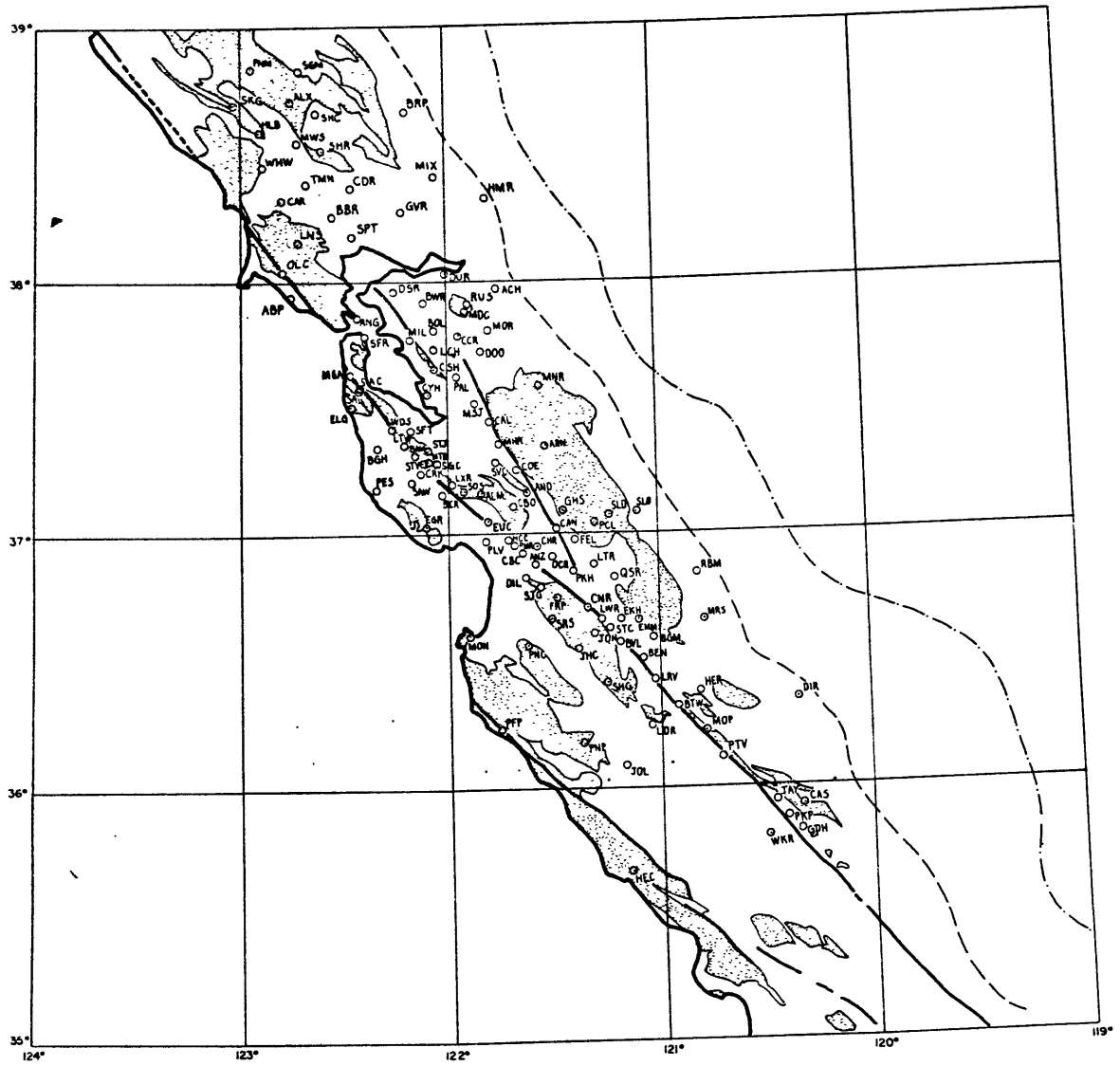

Figure 3.10

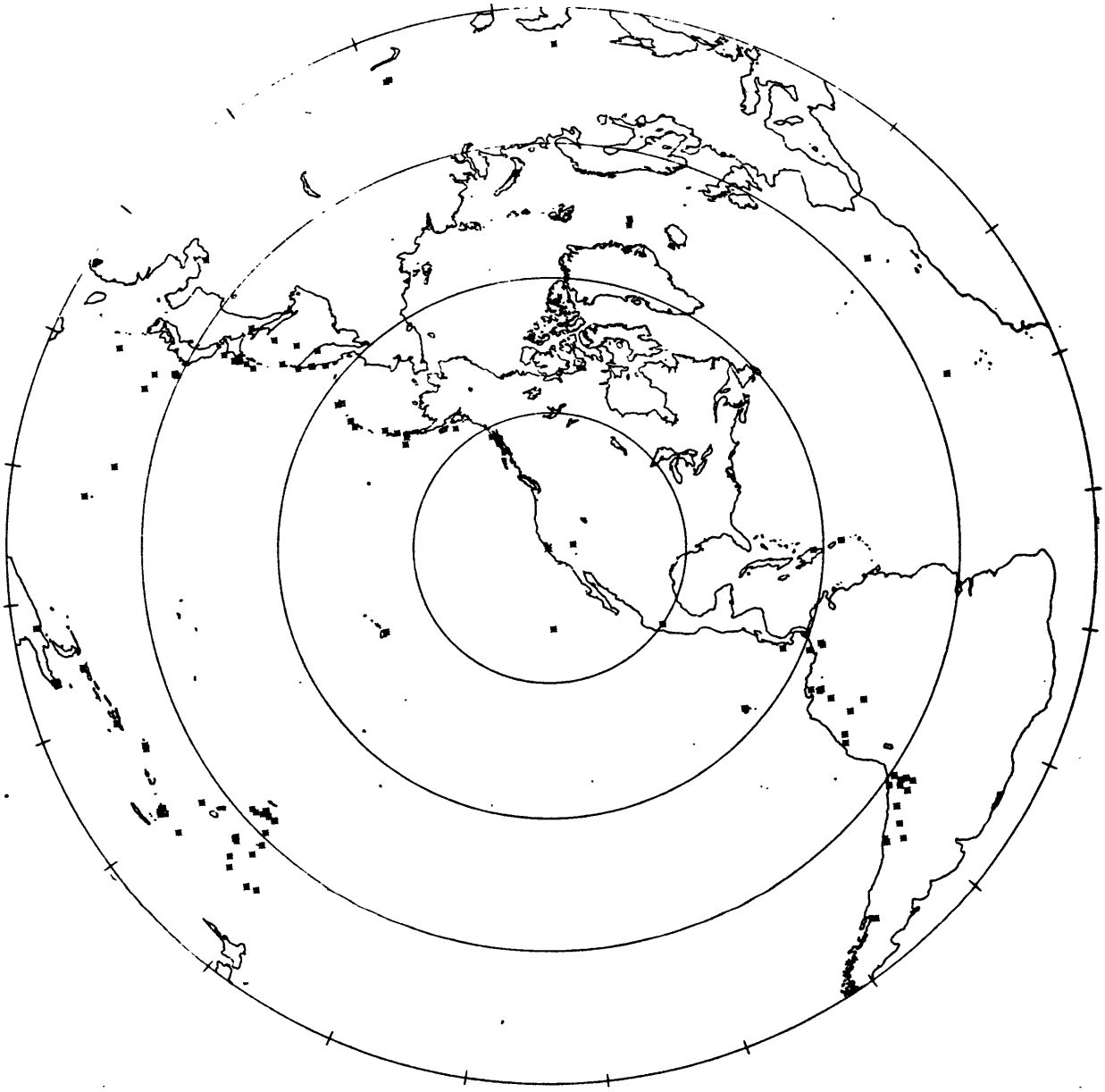

Figure 3.11

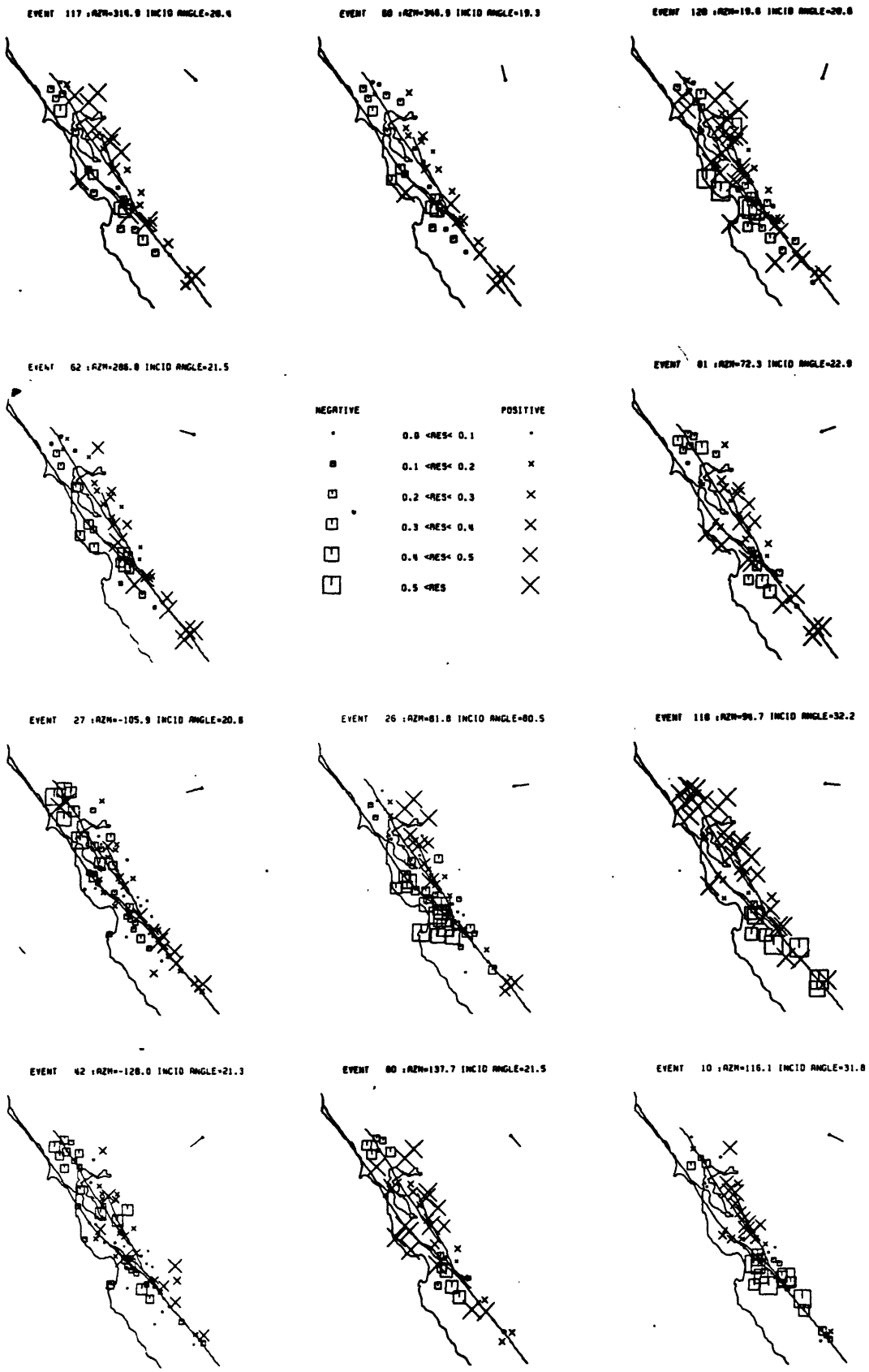
EVENT 117 :AZM=314.8 INCID ANGLE=20.4
EVENT 80 :AZM=346.9 INCID ANGLE=19.3
EVENT 120 :AZM=19.0 INCID ANGLE=20.8
EVENT 62 :AZM=286.8 INCID ANGLE=21.5
EVENT 81 :AZM=72.3 INCID ANGLE=22.9
NEGATIVE
POSITIVE
0.0 <RES< 0.1
0.1 <RES< 0.2
0.2 <RES< 0.3
0.3 <RES< 0.4
0.4 <RES< 0.5
0.5 <RES
EVENT 27 :AZM=-105.9 INCID ANGLE=20.8
EVENT 26 :AZM=81.8 INCID ANGLE=80.5
EVENT 110 :AZM=94.7 INCID ANGLE=32.2
EVENT 42 :AZM=-128.0 INCID ANGLE=21.3
EVENT 80 :AZM=137.7 INCID ANGLE=21.5
EVENT 10 :AZM=116.1 INCID ANGLE=31.8

Figure 3.12

SANTA ROSA REGION

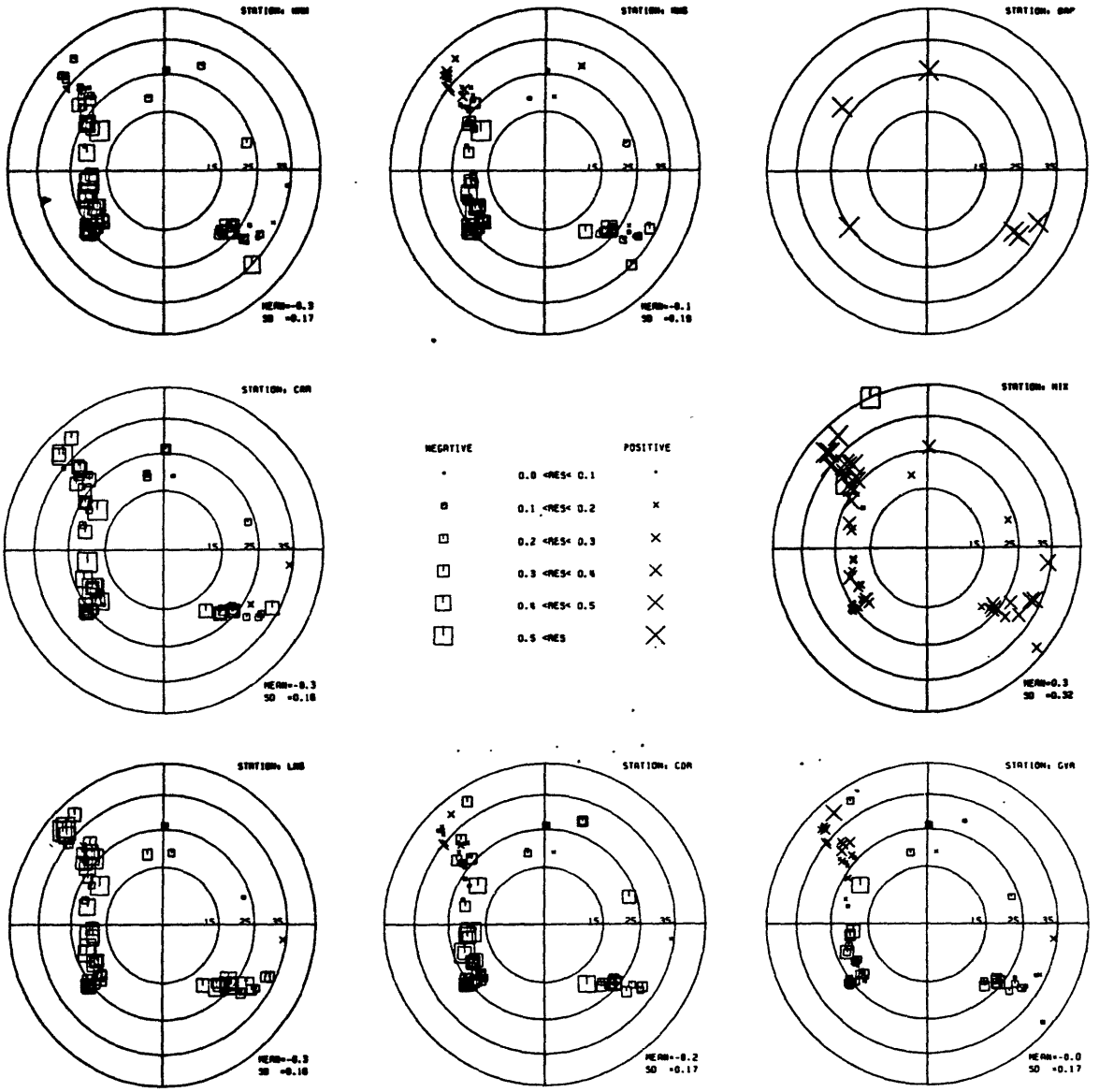

Figure 3.13

SAN JOSE REGION

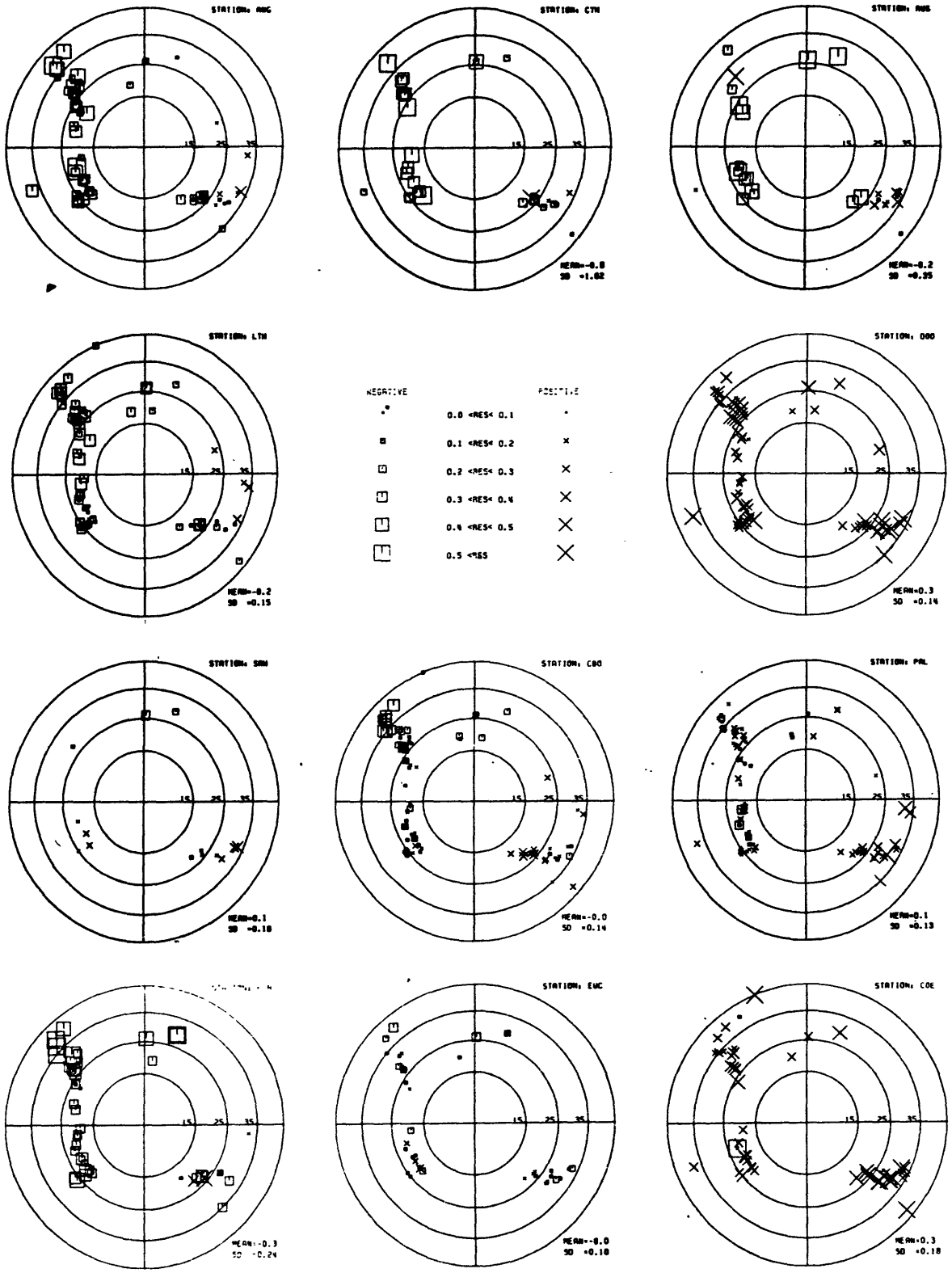

Figure 3.14

BEAR VALLEY REGION

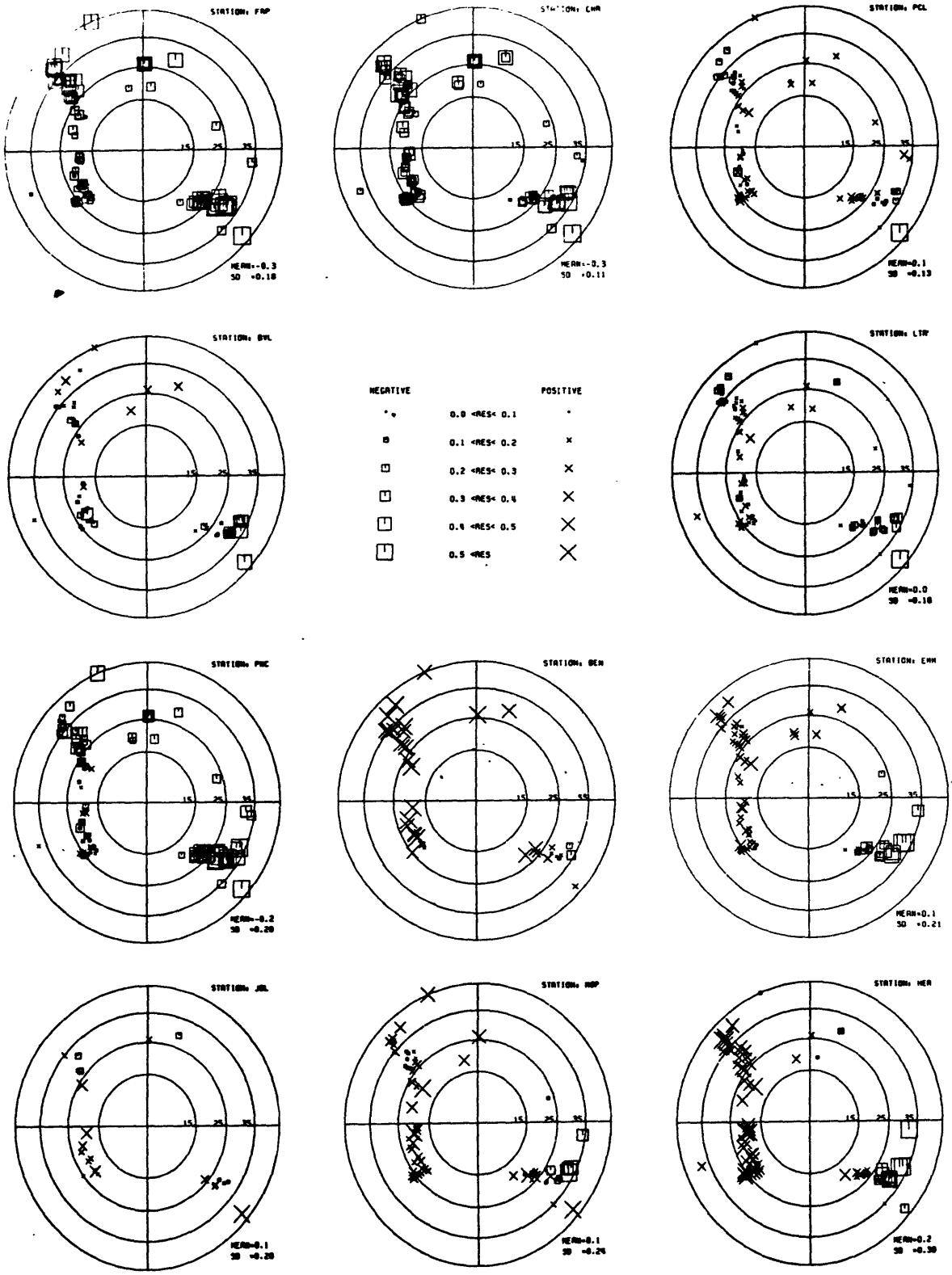

Figure 3.15

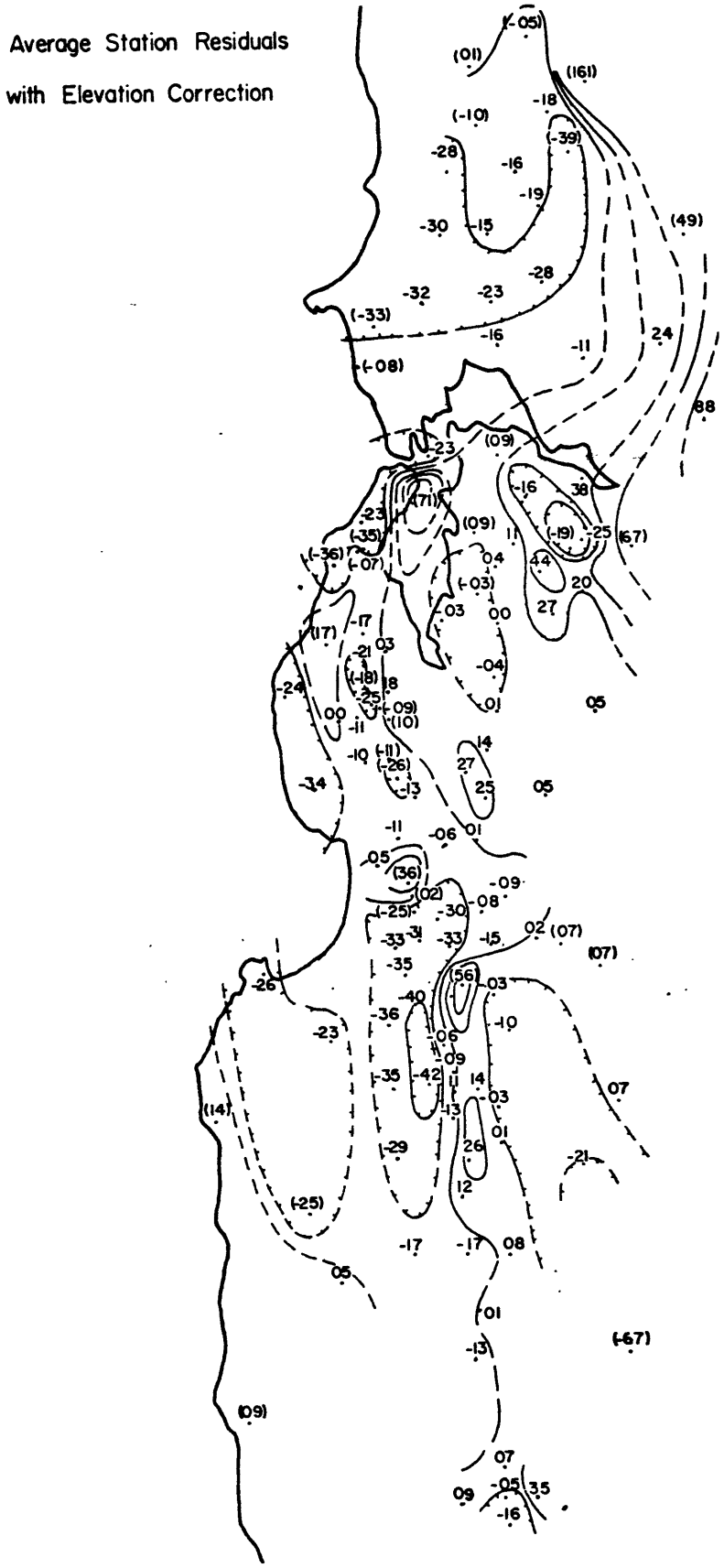

Figure 3.16

California Array Diagram
uncorrected

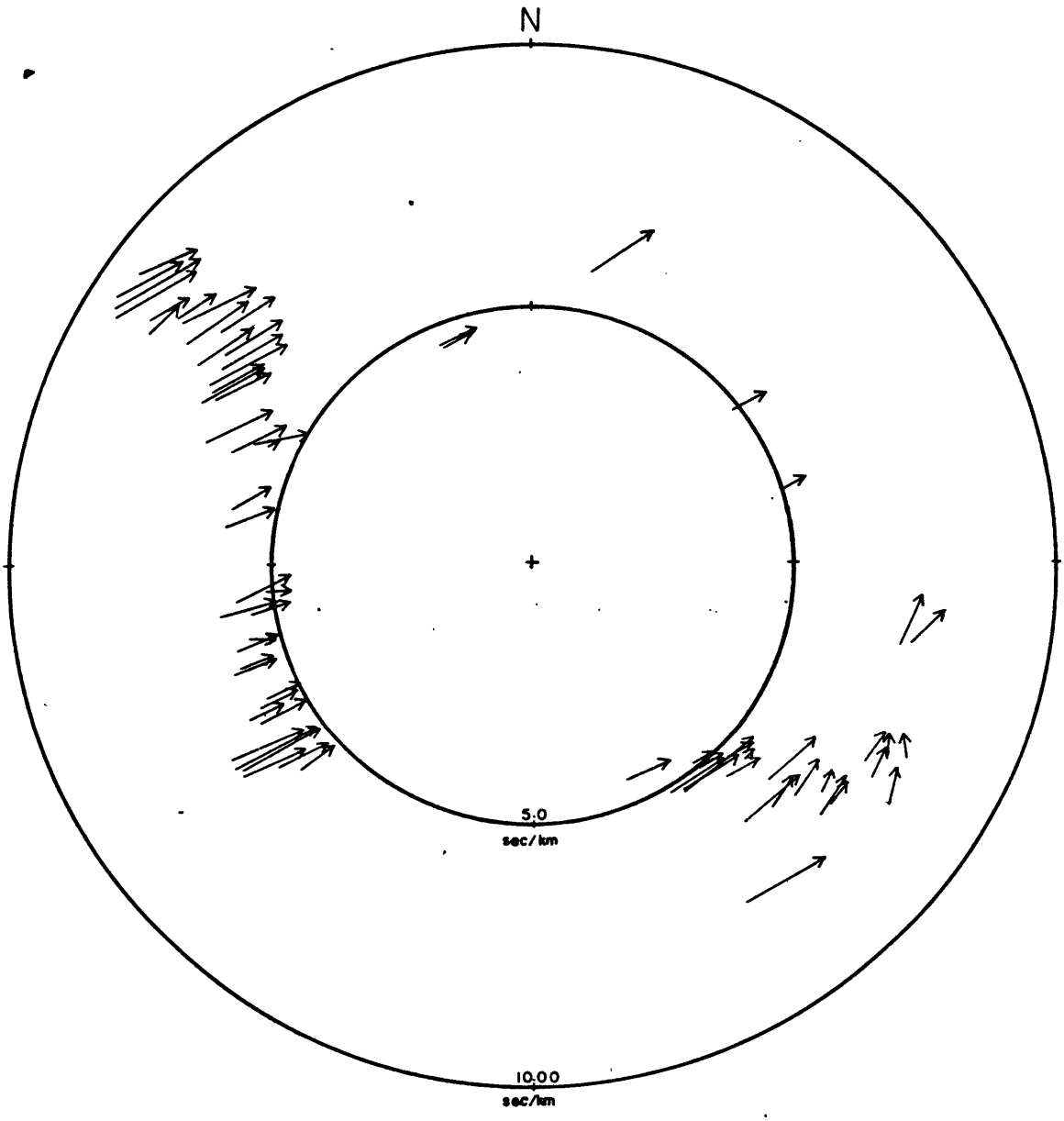

Figure 3.17

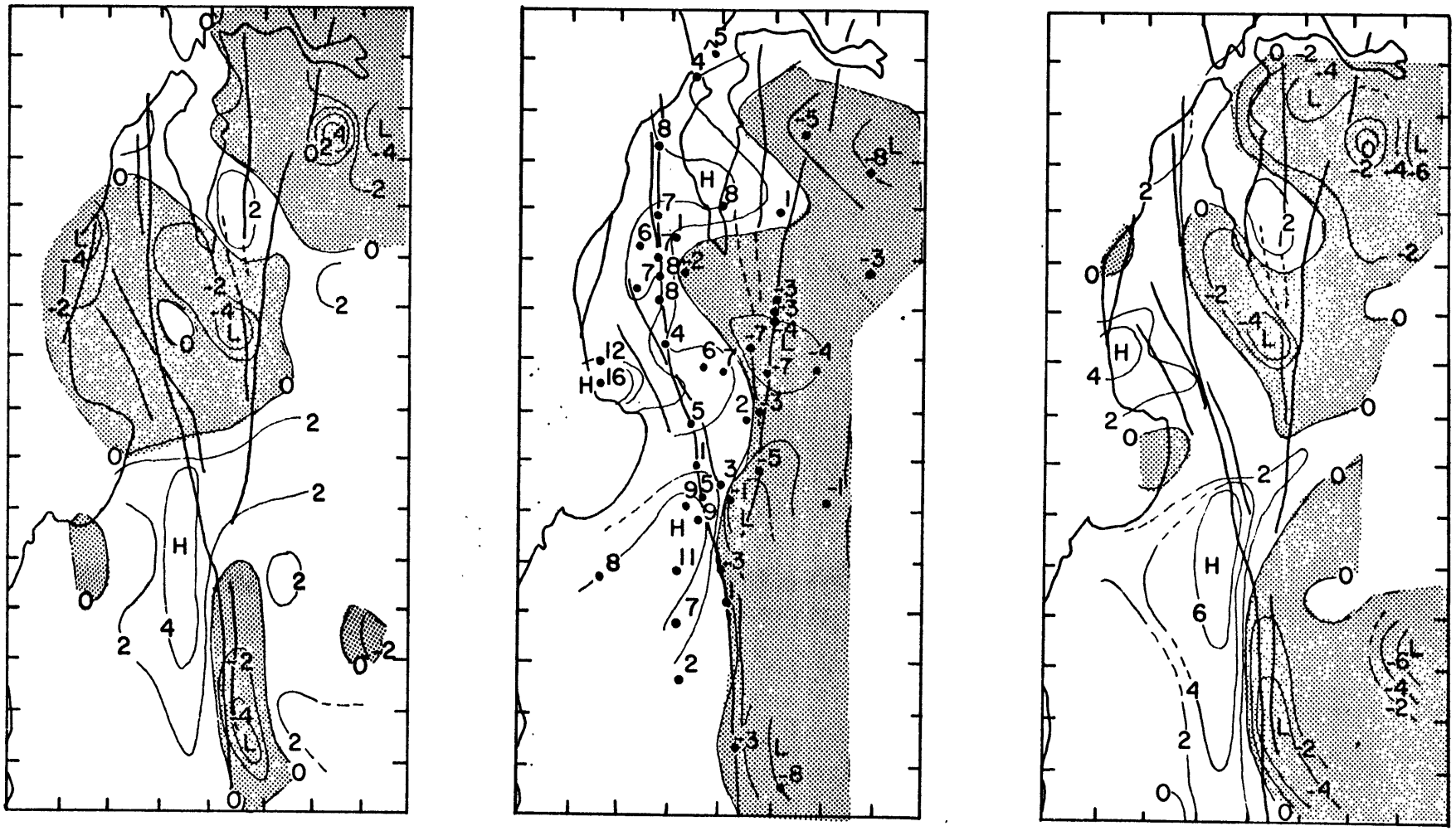

Figure 3.18

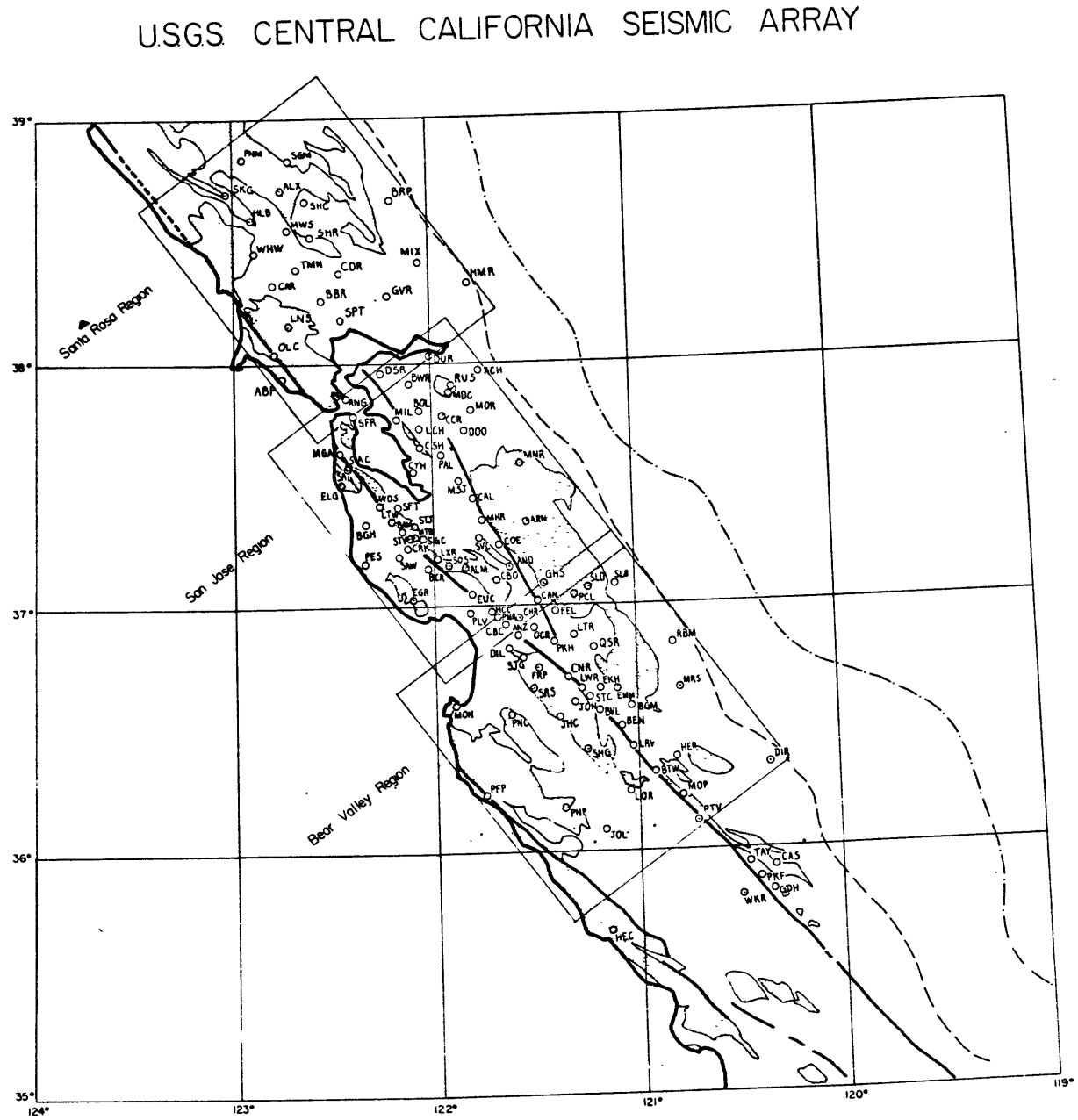
U.S.G.S. CENTRAL CALIFORNIA SEISMIC ARRAY
Santa Rosa Region
San Jose Region
Bear Valley Region
39°
38°
37°
36°
35°
124°
123°
122°
121°
120°
119°

Figure 3.19

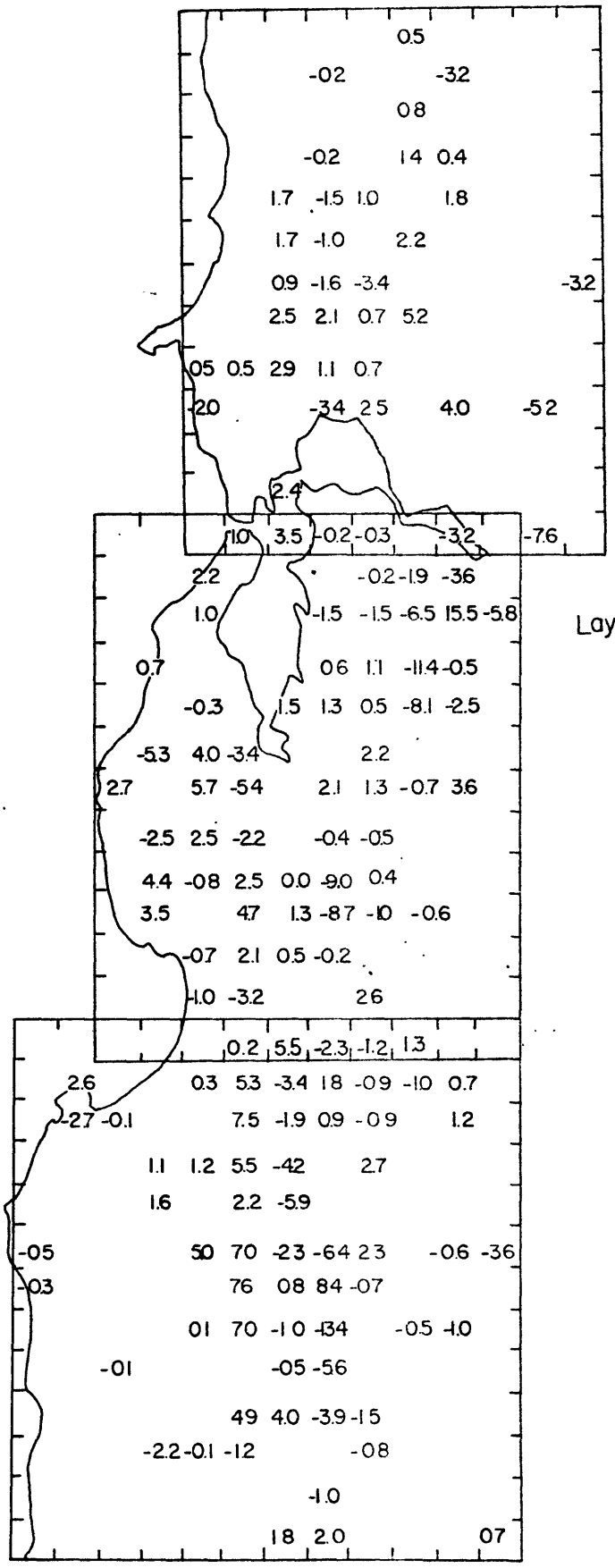
0.5
-0.2 -3.2
0.8
-0.2 1.4 0.4
1.7 -1.5 1.0 1.8
1.7 -1.0 2.2
0.9 -1.6 -3.4 -3.2
2.5 2.1 0.7 5.2
0.5 0.5 2.9 1.1 0.7
-2.0 -3.4 2.5 4.0 -5.2
2.4
1.0 3.5 -0.2 -0.3 -3.2 -7.6
2.2 -0.2 -1.9 -3.6
1.0 -1.5 -1.5 -6.5 15.5 -5.8
0.7 0.6 1.1 -11.4 -0.5
-0.3 1.5 1.3 0.5 -8.1 -2.5
-5.3 4.0 -3.4 2.2
2.7 5.7 -5.4 2.1 1.3 -0.7 3.6
-2.5 2.5 -2.2 -0.4 -0.5
4.4 -0.8 2.5 0.0 -9.0 0.4
3.5 4.7 1.3 -8.7 -1.0 -0.6
-0.7 2.1 0.5 -0.2
-1.0 -3.2 2.6
0.2 5.5 -2.3 -1.2 1.3
2.6 0.3 5.3 -3.4 1.8 -0.9 -1.0 0.7
-2.7 -0.1 7.5 -1.9 0.9 -0.9 1.2
1.1 1.2 5.5 -4.2 2.7
1.6 2.2 -5.9
-0.5 5.0 7.0 -2.3 -6.4 2.3 -0.6 -3.6
-0.3 7.6 0.8 8.4 -0.7
0.1 7.0 -1.0 -13.4 -0.5 -1.0
-0.1 -0.5 -5.6
4.9 4.0 -3.9 -1.5
-2.2 -0.1 -1.2 -0.8
-1.0
1.8 2.0 0.7
Layer 1: 0-10 km
V_o = 5.6 km/sec

Figure 3.20

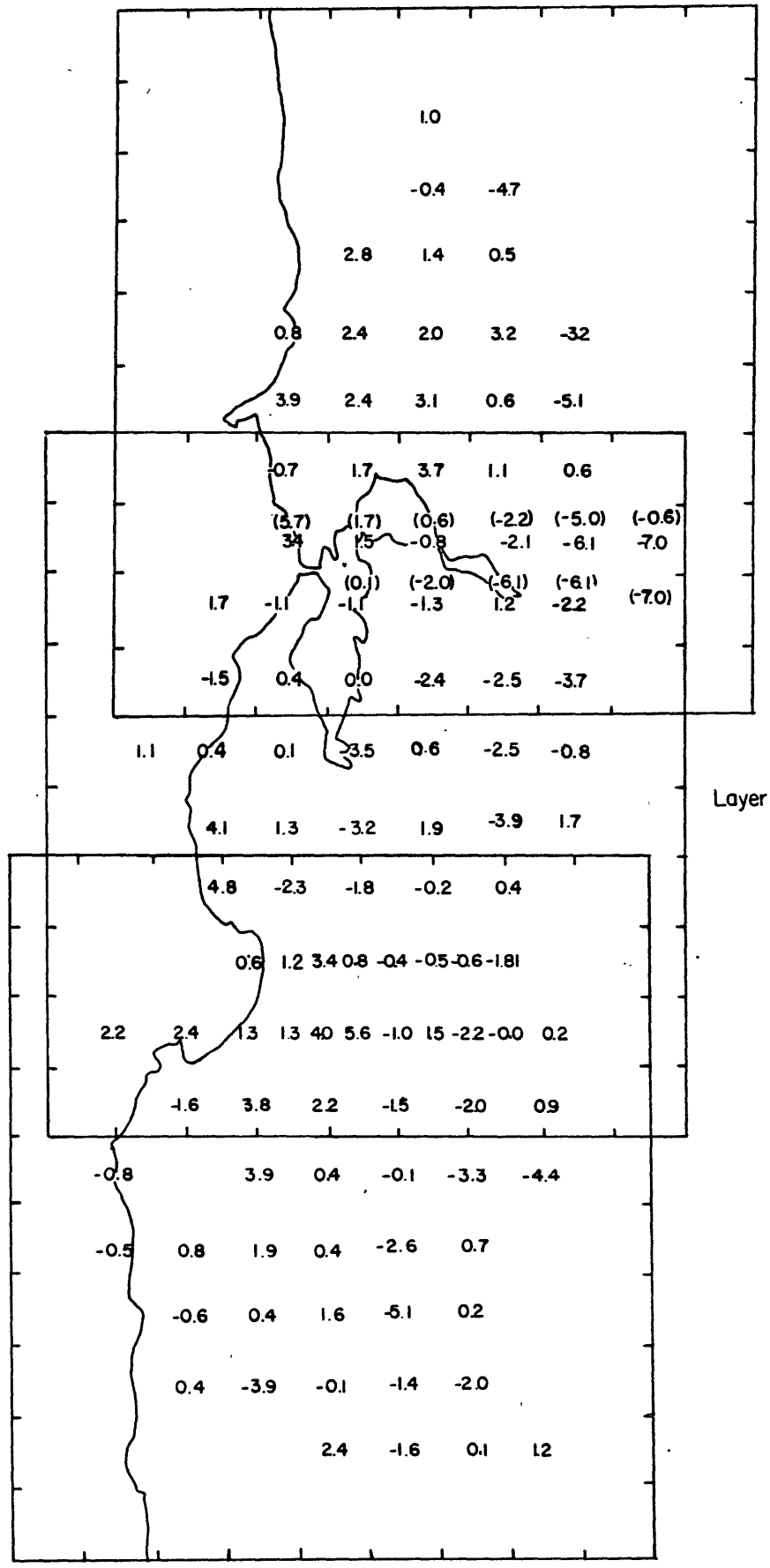
1.0
-0.4 -4.7
2.8 1.4 0.5
0.8 2.4 2.0 3.2 -3.2
3.9 2.4 3.1 0.6 -5.1
-0.7 1.7 3.7 1.1 0.6
(5.7) (1.7) (0.6) (-2.2) (-5.0) (-0.6)
3.4 1.5 -0.8 -2.1 -6.1 -7.0
(0.1) (-2.0) (-6.1) (-6.1)
1.7 -1.1 -1.1 -1.3 1.2 -2.2 (-7.0)
-1.5 0.4 0.0 -2.4 -2.5 -3.7
1.1 0.4 0.1 3.5 0.6 -2.5 -0.8
4.1 1.3 -3.2 1.9 -3.9 1.7
4.8 -2.3 -1.8 -0.2 0.4
0.6 1.2 3.4 0.8 -0.4 -0.5 -0.6 -1.81
2.2 2.4 1.3 1.3 4.0 5.6 -1.0 1.5 -2.2 -0.0 0.2
-1.6 3.8 2.2 -1.5 -2.0 0.9
-0.8 3.9 0.4 -0.1 -3.3 -4.4
-0.5 0.8 1.9 0.4 -2.6 0.7
-0.6 0.4 1.6 -5.1 0.2
0.4 -3.9 -0.1 -1.4 -2.0
2.4 -1.6 0.1 1.2
Layer 2: 10-30 km
V_o = 6.9 km/sec

Figure 3.21

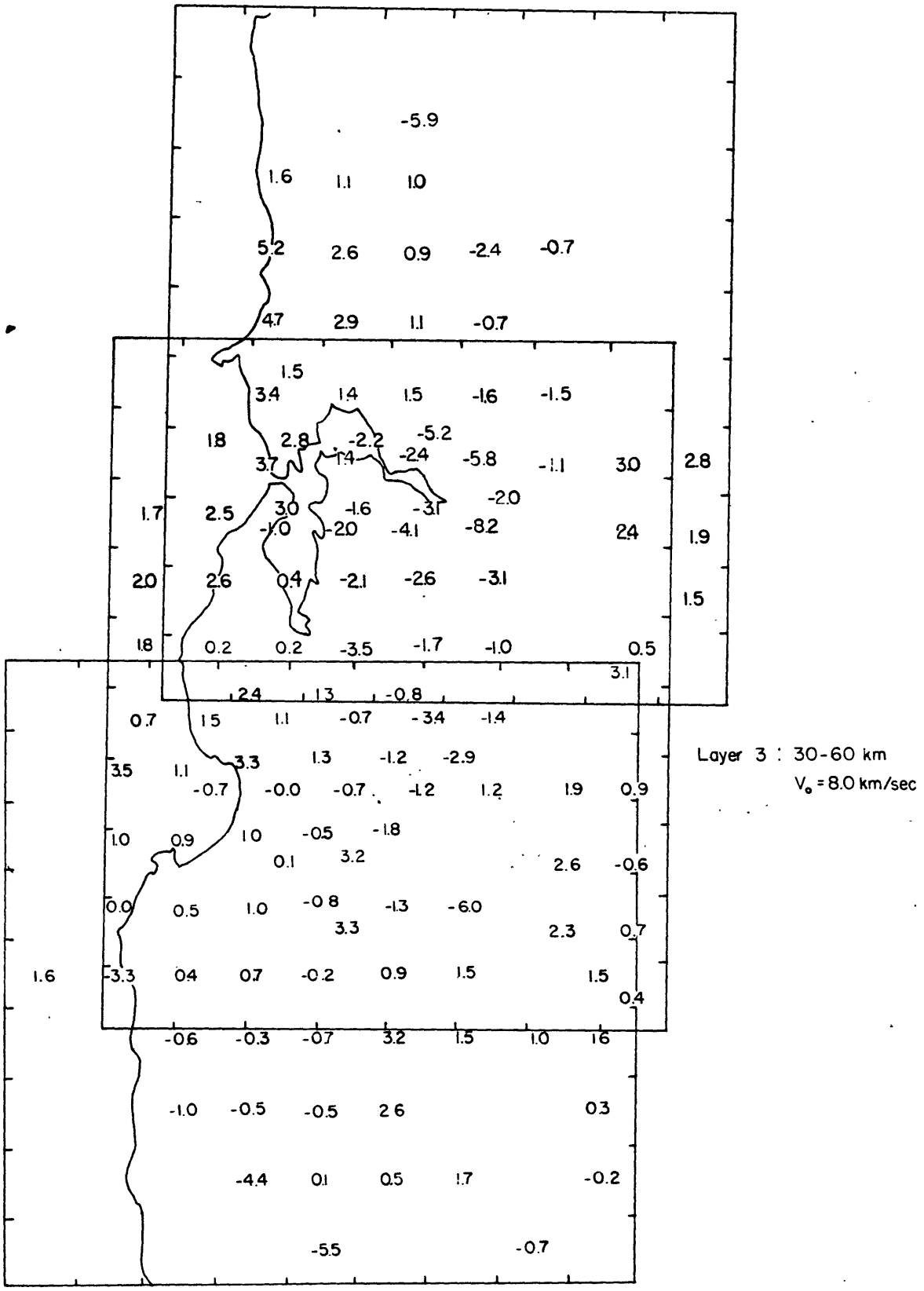

Figure 3.22

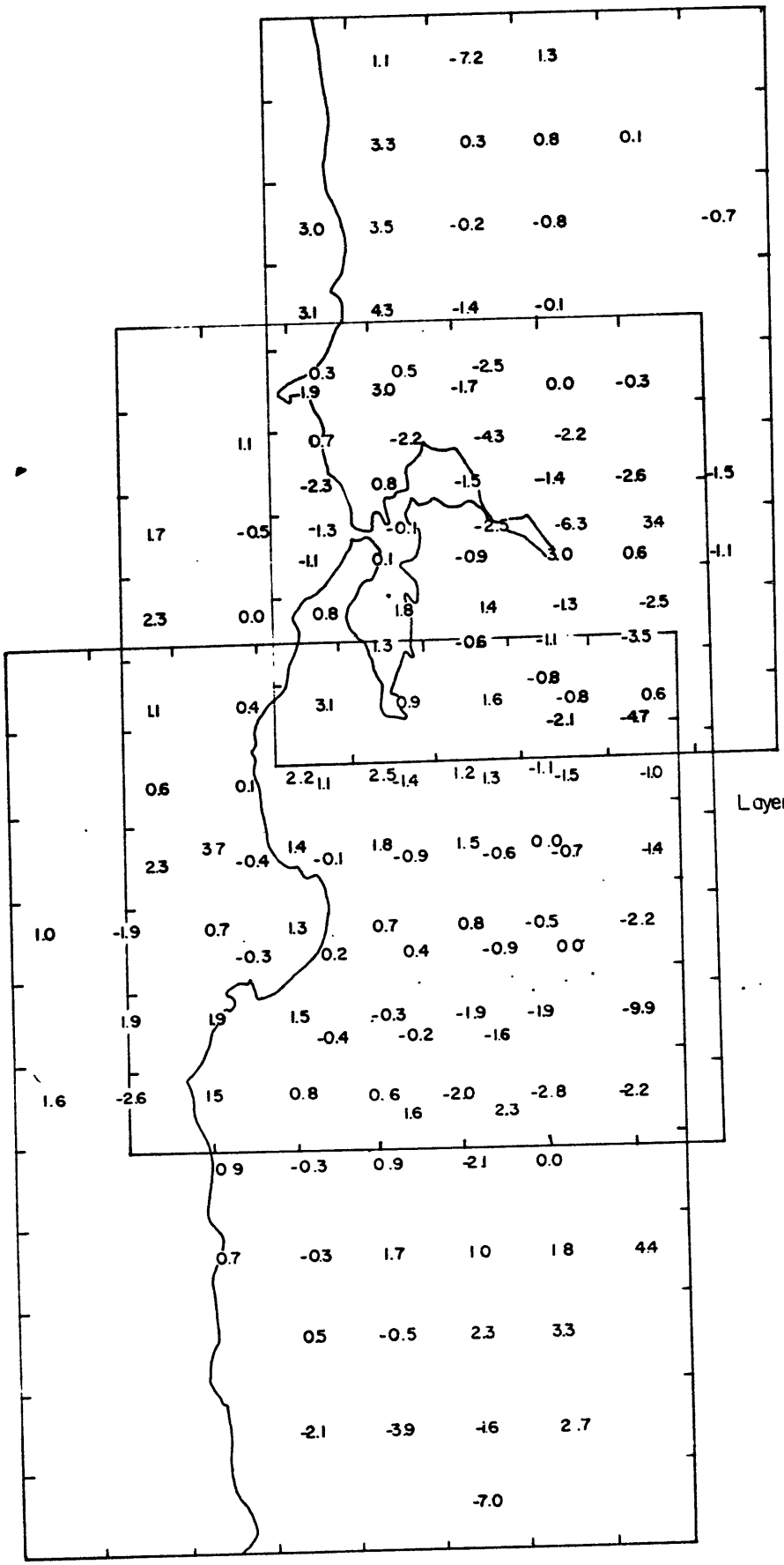

Figure 3.23

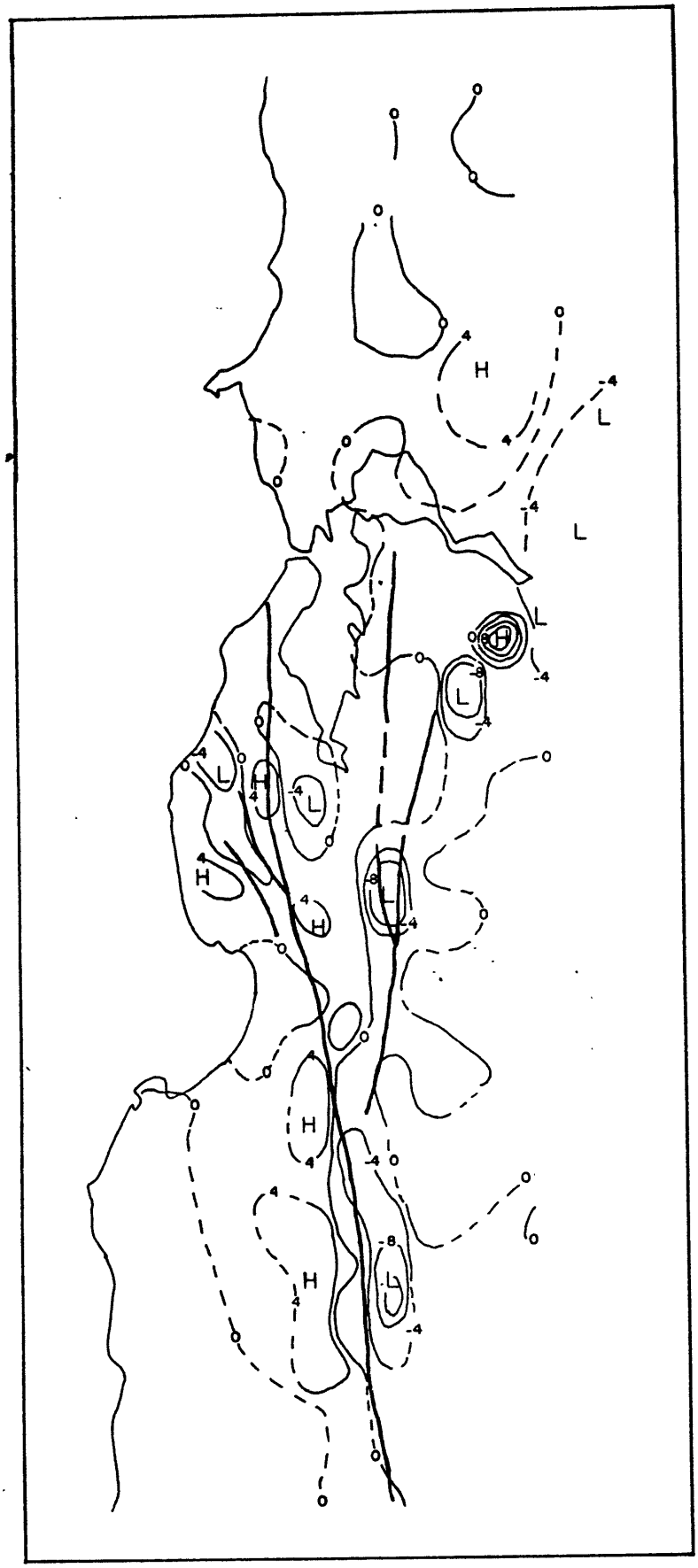

Layer 1 : 0 - 10 km
V_o = 5.6 km/sec

Contours of $\Delta V/V$
contour interval 4%

Figure 3.24

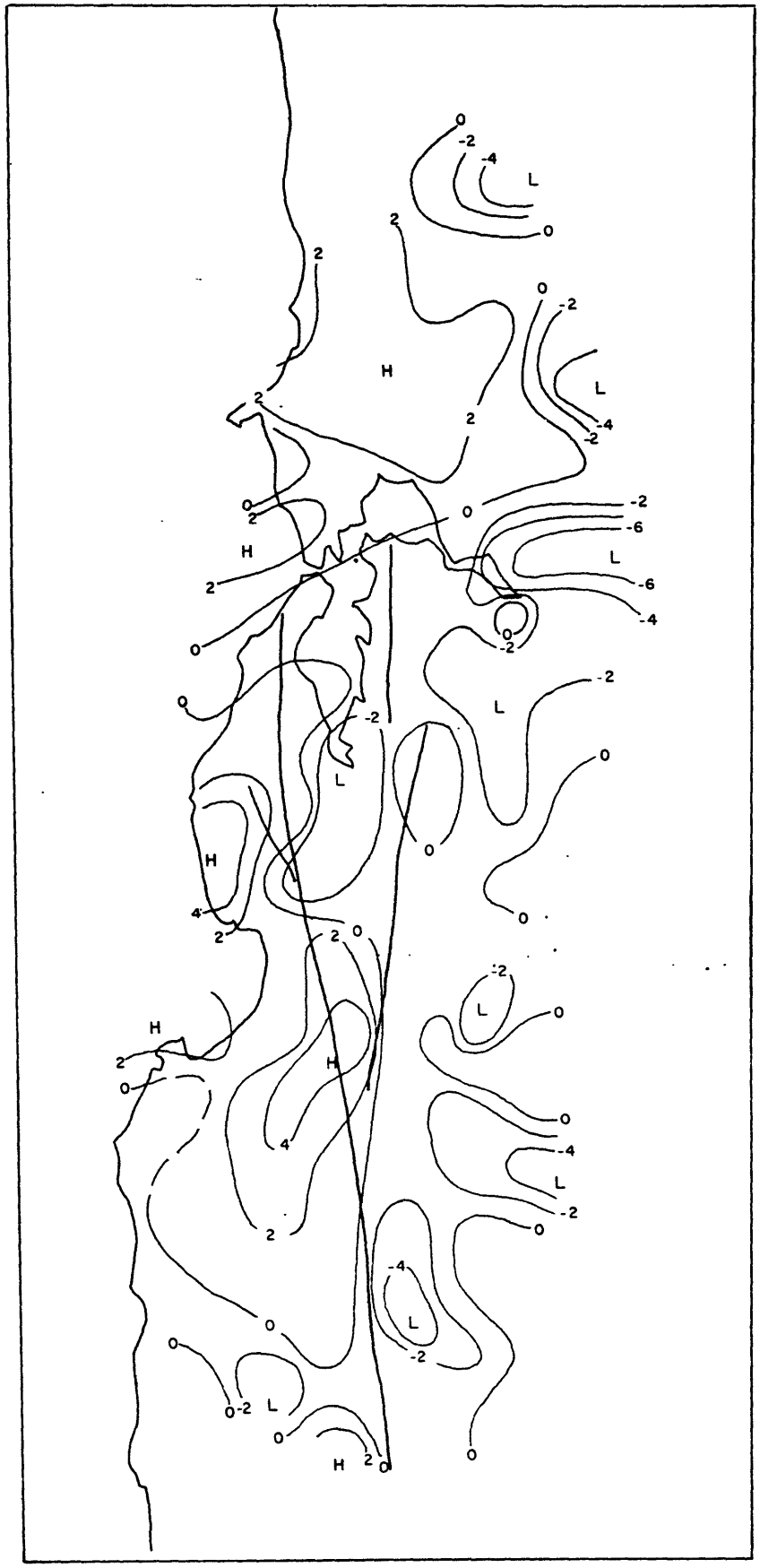
Layer 2 : 10-30 km
V_o = 6.9 km/sec
Contours of ΔV/V
contour interval 2%

Figure 3.25

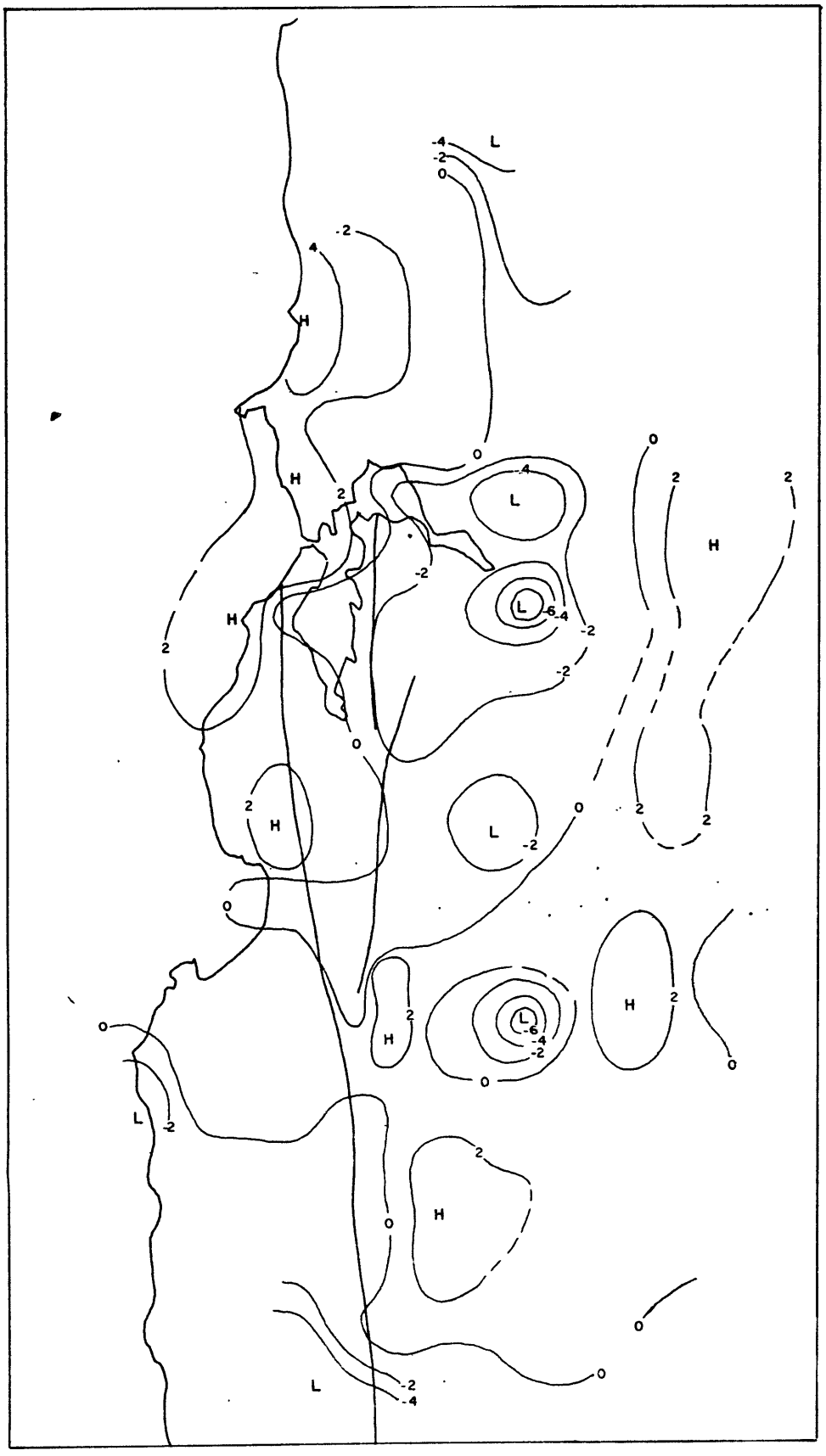
Layer 3 : 30 - 60 km
V_o = 80 km/sec
Contours of ΔV/V
contour interval 2%

Figure 3.26

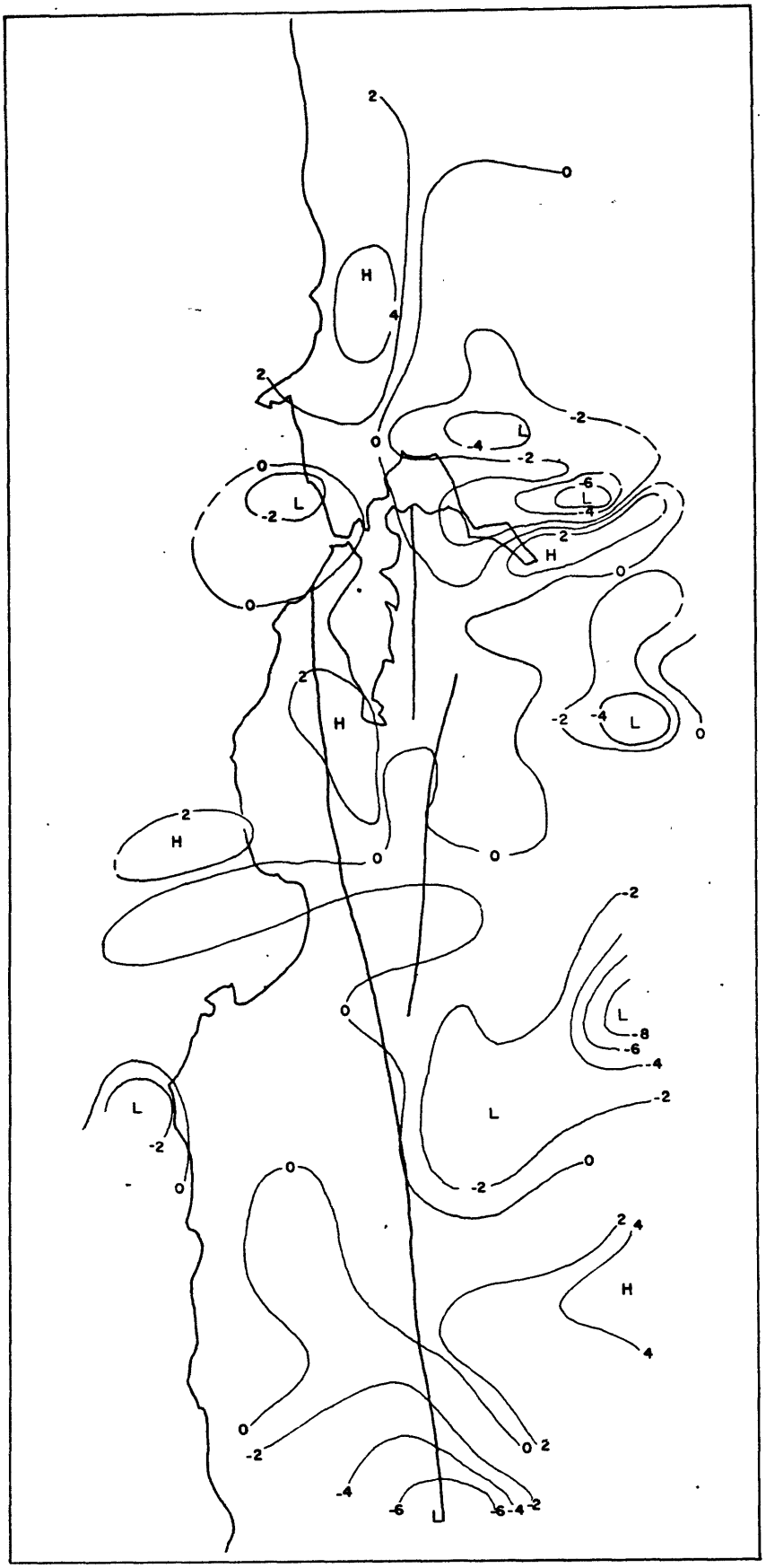
Layer 4 : 60-90 km
V_o = 8.0 km/sec
Contours of ΔV/V
contour interval 2%

Figure 3.27

CHAPTER IV. YELLOWSTONE, WYOMING: A DEEP-ROOTED HOT SPOT

Leaving California for the moment and traveling some 1400 km to the northeast brings us to Yellowstone: a large, young, silicious volcanic field. After describing the regional setting in section 4.1, we probe the structure of the thermal anomaly to ever increasing depths. In section 4.2 an upper crustal seismic refraction experiment and an attempt at inverting local earthquake data are described. In the following two sections, 4.3 and 4.4, teleseismic delays are inverted for structure down to 100 km and 300 km, respectively. Finally, in section 4.5, we come face to face with the question: plume or fracture? And delay the answer to Chapter V.

4.1 REGIONAL SETTING AND VOLCANIC EVOLUTION

From Figure 1.1 we see that Yellowstone in the northwestern corner of Wyoming is near a junction of several different physiographic provinces. This is a very complicated region where volcanics less than one million years old lie within a hundred kilometers of uplifted and exposed Precambrian basement. Let us examine the geology more closely (refer to Figure 4.1).

4.1.1 Pre-Cenozoic Tectonic History

Details of the pre-Cenozoic tectonic history of the Yellowstone area are hidden beneath the cover of Cenozoic volcanics. However, a brief description of the regional tectonic evolution is presented as a prelude to a fuller discussion of Quaternary volcanism in Yellowstone.

In late Precambrian time, the proto-North American continent was modified by one or possibly two continental rifting events (Burchfiel and Davis, 1975). The zone of rifting was generally parallel to and somewhere between the present western continental margin and the Wasatch-northern Rocky Mountain ranges. Evidence for at least one Precambrian rifting event include the preserved portions of thick sedimentary accumulations in graben-like structures (aulacogens, Burke and Dewey, 1973) transverse to the rifted margin. The Belt Trough in western Montana and another in the Uinta Range of northern Utah are two such aulocagens which bound the Yellowstone area to the north and south. The east margin of the Cordilleran geosyncline was just west of the Yellowstone area and thus the area was relatively stable throughout Paleozoic and early Mesozoic time. During early Mesozoic time the east-dipping subduction zone to the west of the magmatic arc (described in 3.1.1) existed synchronously with east-directed thrust faulting on the

east side of the arc. The frontal thrust belt progressively moved eastward culminating in Late Jurassic-Late Cretaceous time (Sevier orogeny) as a zone of deformation along a line through western Montana, eastern Idaho-western Wyoming, east-central Utah and into southern Nevada and southern California. Between 90 and 70 mya (Late Cretaceous) this eastern thrust belt ceased movement along a section from central Utah to southeastern California. North and south of this sector, low angle thrusting persisted until 50 mya, but in the central section deformation migrated further eastward and the tectonic style changed to basement uplifts bounded by high-angle faults (Laramide orogeny). Volcanism which in early Mesozoic time formed a continuous zone behind the thrust belt also migrated eastward along the central section and generally coincided with the region of basement uplift. The Yellowstone area is located in the northern transitional region where there was an overlap of the zone of low-angle thrust faulting that continued into Eocene time and the zone which underwent a transition from low-angle thrusting to basement uplifts about 80 mya. Thus, examples of both types of deformation exist within the region.

The tectonic style from post-Eocene until the present is predominantly block faulting typical of extensional regimes. Present-day mountain ranges have been uplifted along normal faults which have north-

westerly strike and often are superimposed on the older zones of thrusting.

4.1.2 Cretaceous and Cenozoic Volcanism

Late Mesozoic and Cenozoic volcanism in the western U.S. involved a two-stage history: a Cretaceous and early Cenozoic period of andesitic igneous activity coupled with plate convergence tectonics and a late Cenozoic period of fundamentally basaltic volcanism. The latter is associated with extension tectonics which dominated after cessation of subduction and the initiation of San Andreas transform movement (Lipman et al., 1972). We now consider aspects of the volcanic history of the Yellowstone and surrounding areas.

In the Yellowstone region volcanism and plutonism were widespread since Late Cretaceous time. Located northwest of Yellowstone, the Boulder Batholith is a composite mass of calc-alkaline igneous rock emplaced and cooled from 78 to 72 mya (Robinson et al., 1968). The overlying Elkhorn Mountains Volcanics are remnants of a volcanic plateau that was erupted between 76 and 80 mya. These two features constitute the only major pre-Cenozoic igneous rocks in the area.

Much more prevalent are the Cenozoic volcanic fields. In the northeast corner of Yellowstone and extending 100 km to the southeast is the 24,000 km^2 Absaroka volcanic field. The remnant of an Eocene

volcanic field which was probably twice as large as the present field, the preserved volcanics are principally calc-alkalic andesites which become progressively more alkalic to the northeast, across the strike of the field as defined by the alignment of vents (Lipman et al., 1972). Variations in K_2O content in other Eocene (40-55 mya) volcanic fields in western Montana and east-central Idaho were used by Lipman and others (1972) to reconstruct the geometry of the inferred Middle Cenozoic Benioff seismic zone using the method of Dickinson and Hatherton (1967). In the region of western Montana and northern Wyoming, the reconstructed paleosubduction zone has a northwest-southeast trend and dips to the northeast about 30° to 35°. Beneath the Yellowstone area the depth to the inferred Middle Cenozoic subduction zone is between 150 to 300 km. Andesitic volcanism terminated in the area about 40 mya to be replaced by fundamentally basaltic volcanism. Except for a small volcanic field near Helena, Montana, the post-Eocene fundamentally basaltic volcanism in the Montana-Idaho-Wyoming region is confined to the Snake River Plain (SRP) and Yellowstone Plateau (YP) areas. Because of the importance of these volcanic features to any tectonic interpretation of this region, we next describe the Snake River Plain and Yellowstone Plateau in greater detail.

Snake River Plain. The Snake River Plain extends as an 80-110 km wide arcuate topographic depression for about 560 km across southern Idaho. The lava plain is usually categorized into a western and eastern plain for structural, as well as geographical, reasons. The western SRP is a NW-SE fault-bounded depression containing a great thickness of basaltic lava and interbedded continental sediments. On its northwest end, the plain joins the great flood basalt fields of the Columbia River Plateau. Gravity studies (Hill, 1963) found three prominent northwest-trending enechelon gravity highs in the western SRP and concluded that the western plain is undercompensated with respect to the bordering highlands. A seismic refraction line across the western SRP indicates a crust with a thickness of about 45 km and composed entirely of basic rocks (Hill and Pakiser, 1966); moreover, the P_n velocity of 7.9 km/sec is a continuation of the low P_n velocity associated with the Basin and Range Province and thought to indicate anomalously high temperatures in the upper mantle. Geochronology of the western plain indicates volcanism started 13 mya and has continued until at least 0.5 mya (Armstrong et al., 1975).

The eastern Snake River Plain has a NE trend and unlike the western segment is not fault-bounded but is predominantly downwarped. Low-relief, northwest-southeast trending gravity anomalies have been interpreted as an effect of an undulating subsurface basement (Lafehr

and Pakiser, 1962). Although no seismic studies have been conducted in the eastern SRP, a combination of gravity and deep electrical sounding studies indicate that it is underlain by a more sialic crust with 3-5 km of Tertiary sediments and volcanics on a pre-Tertiary basement locally fissured by narrow deep rifts (Zody and Stanley, 1972; Thompson, 1977).

Geochronology and stratigraphic studies summarized by Armstrong et al. (1975) document an eastward transgression of three facies of volcanism and sedimentation in the Snake River Plain. In any local succession the three facies, from youngest to oldest, are: 1) the silicious volcanic sequence consisting of volcanic-clastic sediments, airfall and ash flow rhyolite tuffs, rhyolite flows, and subordinate amounts of basalt flows and pyroclastics. This sequence is typified by the Yellowstone-Island Park region where silicious volcanism is associated with large calderas. 2) The next sequence is dominated by basalt flows with some interbedded sediments and some rhyolite flows and domes. Most of the eastern Snake River Plain represents this sequence. 3) In the uppermost sequence, sediments predominate over a few basalt flows and locally abundant volcanic ash from ongoing silicious volcanism farther east.

The earliest outburst of silicious volcanism occurred in western Idaho about 15-16 mya. This phase migrated eastward at about 3.5 cm per year although the

migration may not have been smooth but may have occurred as a series of jumps of 50 to 150 km each. The basaltic flows followed and buried the silicious volcanics with about a 2 my lag and has yet to reach east of the Island Park caldera. Basaltic volcanism, unlike the silicious phase, did not completely cease and has persisted, at least in the eastern Snake River Plain, until several hundred thousand years ago.

Petrological and isotopic studies of the Snake River lavas are reviewed by Thompson (1975), Leeman and Manton (1971) and Leeman (1976). The Snake River basalts are dominantly olivine tholeites with a chemical composition consistent with a mantle origin. The lavas have strontium isotope ratios uniformly higher than that of most ridge-type oceanic basalts. Leeman and Vitaliano (1976) further concluded that the basalts were derived by partial melting of spinel peridotite at depths near 50 to 60 km. Alternatively, they suggest that if the parent magma was derived at greater depths, the magma must have re-equilibrated at a shallower depth prior to its eruption. The silicic volcanics have a high strontium isotope ratio which does not support a mantle origin for these lavas, but is consistent with remobilization of crustal rocks during formation of the Snake River depression.

Island Park and Yellowstone. The Island Park and Yellowstone areas are representative of the first phase of the

Snake River Plain volcanic cycle. The Island Park caldera is an elliptical collapse structure 29 by 37 km formed from the center of a shield volcano composed of rhyolite ash flows. The geology of the caldera and the petrogenesis of the lavas are described in detail by Hamilton (1965). He concluded that the large magma chamber into which the volcano collapsed contained liquid rhyolite overlying liquid olivine basalt.

The Yellowstone area is in a very young stage of its magmatic evolution. Boyd (1961) described the welded tuffs of the rhyolite plateau and gave a thermodynamic analysis of the eruption mechanism. The volcanic stratigraphy in Yellowstone National Park is described by Christiansen and Blank (1969) and geological and geophysical evidence for the existence of a still molten batholith beneath the Yellowstone caldera are summarized by Eaton et al. (1975). Briefly, the Quaternary volcanism involved three cycles of bimodal eruptions climaxed by explosive pyroclastic eruptions that produced enormous ash flows and formation of a large caldera. The earliest cycle climaxed about 1.9 mya and formed a caldera that extended from Island Park to perhaps as far east as the central part of Yellowstone. The second cycle was confined to the Island Park area and was responsible for the formation of the caldera there some 1.2 mya. The youngest Yellowstone caldera, a 70 by 45 km ellipse with its long axis oriented NE-SW was created

600,00 years ago during the climax of the third volcanic cycle initiated immediately after the climax of the second cycle. During a cycle rhyolite flows are erupted from a system of ring fractures around the margin of the rhyolite plateaus. The explosive pyroclastic eruptions during the climax of a cycle involves the expulsion of a hugh quantity of lava and the resulting removal of internal support results in the collapse of the roof and formation of a caldera.

After the last collapse, a resurgent dome formed in the eastern part of the Yellowstone caldera with accompanying rhyolitic tuffand lava eruptions. About 150,000 years ago another resurgent dome formed in the western part of the caldera just east of Old Faithful. The youngest flows between 150,000 and 70,000 years old are associated with this last resurgence. There is every reason to believe that magmatic activity related to this phase has not completely ceased.

4.1.3 Evidence for Molten Magma and On-Going Tectonics

Geysers, fumaroles, and hot springs in Yellowstone National Park are surface manifestations of continuing magmatic activity within deeper levels of the crust. The geothermal features are concentrated along the edges of the two resurgent domes within the Yellowstone caldera and along a north-south linear trend known as the Norris-Mammoth corridor (Eaton et al., 1975). Although the most dramatic, the geothermal features are not the only evidence

for the existence of still-fluid magma beneath Yellowstone. Eaton et al. (1975) reviewed geophysical data relating to evidence for a shallow, in part still molten, magma chamber. The Bouguer gravity map of the region has a 50 mgal closed gravity minimum centered on the Yellowstone caldera (Fig. 4.11). The -210 mgal contour enclosing the anomaly follows closely the general outline of the caldera thereby suggesting that a hot, low density body beneath the caldera or a brecciated rhyolite-fill within the caldera may be responsible for the gravity low. An important feature of the gravity map which refutes the last suggestion is the extension of the gravity low 30 km beyond the northeastern portion of the caldera rim. Also, a series of arcuate normal faults which parallel the northeastern portion of the caldera's boundary display features indicating postglacial movement. Eaton et al. interpret the youthfulness of caldera-related faults in the area as responses to movements in a shallow magma chamber. Maximum depths to the top of the low-density body calculated from the gravity gradients yield values of 5.5 to 6.0 km which is, as we will learn, consistent with other geophysical evidence on the depth to the top of the "magma chamber".

Among other evidence are Curie depth calculations from residual aeromagnetic data. The Curie isotherm, the temperature at which crustal rocks lose their magnetization, represents a minimum depth to the molten magma. The average isotherm depth for the entire Yellowstone Park area is about 10 ±3 km below sea level (Smith et al., 1974). A more

detailed analysis of the same data by Bhattacharyya and Leu (1975) yield depths of only 5-6 km over the central part of the Yellowstone caldera, but deeper (6-12 km) levels outside the caldera, especially to the northwest side. This rise of the Curie depth beneath the caldera is matched by a corresponding rise of the maximum depth of microearthquakes from 20 km to 5 km (Smith et al., 1977). The obvious cause of both observed phenomena is elevated temperatures at or near the top of the magma body; the aseismicity due to enhanced stable sliding at shallower depths.

Other seismic evidence are also consistent with the existence of a shallow magma chamber. P- and S-waves from local earthquakes with paths which cross the caldera exhibit severe attenuation and waveform changes and in some cases S-waves are completely absent from the record (Pitt, 1974). Although these effects are visible mainly for paths crossing the central caldera, not all waves show these changes and diffraction may be an important effect. These effects suggest that the anomalous material probably is not a simple shaped continuous body.

The first evidence that the anomalous body may be deep-rooted was provided by the study of teleseismic P-wave delays (Iyer, 1975). Delays as large as 1 to 2 seconds were recorded for stations in and near the Yellowstone caldera. Qualitative modeling of the delays yielded a model of a 10% lower velocity body extending down at least 100 km. Because of the near vertical incidence of teleseismic P-waves they

contain the best information on the deeper structure, if any, of the Yellowstone hot spot. Later sections of this chapter will deal with the quantitative modeling of the teleseismic data collected by Iyer and his associates.

Seismicity is also an important source of information on the on-going tectonics of the region. Although some of the microearthquakes, especially those which occur in swarms, are undoubtedly associated with geothermal features, others are due to a regional stress field. Smith et al. (1977) have recently reviewed studies on the seismicity and its relationship to the tectonics of the Yellowstone area (Fig. 4.2). The following description is based largely on their report.

Yellowstone is located at the intersection of two regional seismicity belts: the Intermountain Seismic Belt that is defined along a series of north-south trending normal faults through central Utah, along the Idaho-Wyoming border, into Yellowstone, and continues northwestward into Montana; and the Southern Idaho Belt which is a diffuse east-west zone north of the Snake River Plain (Smith and Sbar, 1974). The largest recorded earthquake in either belt was the magnitude 7.1, 1959 Hebgen Lake earthquake with an epicenter just west of the park boundary. This earthquake occurred on a south-dipping normal fault with a N80°W strike and produced a 50 km long east-west aftershock zone (Ryall, 1962; U.S. Geol. Survey , 1969). Historically, the most seismically active area has been in a 60 km long east-west

zone extending from Hebgen Lake to Norris (Figure 4.3). Focal depths range from about 5 to 20 km on the west and become shallower (less than 5 km) near the caldera boundary. Composite and single-event fault plane solutions for the Yellowstone area are shown in Figure 4.4. East-west normal faulting dominates in the Hebgen Lake-Norris zone indicating north-south extension. Three thrust fault solutions near the northwest caldera boundary suggest maximum compressive stress radial to the caldera rim. Smith et al. (1977) suggest these solutions are due either to resurgence of the inner caldera or rotation of the west Yellowstone basin.

Figure 4.5, from Smith et al. (1977), summarizes seismic and magnetic evidence on the upper crustal structure of Yellowstone and vicinity. Although the shape and dimensions of the proposed magma chamber are still unclear, the combined geophysical data are compelling evidence for a shallow body that is anomalously hot, and characterized by low density and P-wave velocity. When considered in view of the recent volcanic history, the existence of a partially crystallized (or partially molten) silicious batholith (magma chamber) beneath the Yellowstone caldera is as well established as anything can be without direct evidence. Not well established are the shape and dimensions of the anomalous body or bodies and its deep structure. These questions and their implications are pursued in the following sections.

4.2 CRUSTAL STRUCTURE

In order to delineate the deep structure of Yellowstone we first need to investigate the shallow crustal structure. This is especially important for Yellowstone where we want to define a deep low-velocity feature which may be masked by a shallow low-velocity cover. Rhyolite tuff, glacial deposits, and caldera fill compose a large proportion of the surficial deposits at Yellowstone and could conceivably contribute to the large delays observed at the Yellowstone array. Constituents of the upper crust probably include rhyolite flows with some interbedded basalt flows, with the entire section fractured by faults and dikes. Also, as described in the previous section, there is evidence of a partially-molten magma chamber emplaced high in the crust beneath Yellowstone.

The most direct means of probing the upper crust would be to perform a seismic refraction experiment. Preliminary results from a small scale refraction experiment performed in Yellowstone National Park in late summer of 1977 are summarized in the first subsection.

Yellowstone is an area of very active seismicity. These local earthquakes provide a means of investigating the upper crustal structure and this means will be pursued in the second subsection.

4.2.1 Refraction Experiment

There are a number of long range refraction lines north of Yellowstone in Montana (Figure 4.6) and to the south in Utah, but as late as 1977 no refraction lines were available which traversed any portion of the Park. In late August and early September of 1977 we performed a small-scale refraction experiment in the Park. At 12:15 a.m., MDT, Friday, September 9, 1977, we detonated 1580 pounds of explosives in two closely spaced holes. The shotpoint was about 20 km north of W. Yellowstone, at the western Park boundary where Cougar Creek flows across the boundary. More precisely, the location was 44° 45'30"N latitude and 111° 05'52"W longitude; and the shot origin time was 06h 15m 01.32s GMT. Two lines of instruments were deployed radially outward from the shotpoint (Figure 4.7); one line eastward from Gibbon Meadows to the East Entrance; the other, a 60 km long line, southeastward across the caldera from the shotpoint to the eastern edge of Shoshone Lake. The eastward line was occupied by instruments and personnel from the University of Utah under the direction of R.B. Smith and was supplemented by instruments and personnel from Purdue University. The majority of the instrumentation of the southeastern line was provided by the U.S. Geological Survey under the direction of C. Weaver. M.I.T. had five

MEQ-800's deployed in the first 11 km of the southeastern line as well as 5 portable tape-recording units between 49 and 55 km distant parallel to, but offset by about 5-10 km, from the main southeast line.

Information on the locations, distances, and travel time to the M.I.T. MEQ-800's are listed in Table 4.1. From our data we calculated a phase velocity of 4.5 km/sec from the shotpoint southward to a distance of 11 km. The geology of the shotpoint area consists of glacial and fluvial deposits of unknown thickness overlying rhyolitic volcanics. Therefore, we postulated that the 4.5 km/sec arrivals are a head wave propagating along the base of the overburden. If correct, the velocity is higher than suspected for rhyolitic volcanics which often have velocities less than 3 km/sec. However, because the line is unreversed, we cannot be confident about the validity of the velocity.

The arrivals recorded by M.I.T.'s tape-recording units were very weak and thus first arrivals could not be picked confidently. These instruments were located to the southeast of the Mallard Lake resurgent dome in an area undergoing rapid uplift (R.B. Smith, pers. comm.). It is uncertain whether the weak arrivals are due simply to the relatively weak source or to severe attenuation along the path. Comparison with the U.S.G.S. instruments at comparable distances along the main southeast line might prove useful in answering the above question but as of this time we have not yet received the data from the Survey.

Preliminary analysis of the data recorded by the U.S.G.S. has an apparent velocity of 5.3 km/sec out to 60 km and no significant variation in the velocity across either the northwest caldera boundary or the resurgent dome (Weaver and Pitt, 1978). They extended the refraction line to the southeast using seven well-located earthquakes near the shotpoint and with focal depths of 4 to 9 km as the sources. Arrival times from these sources indicate an apparent velocity of 6.0 km/sec out to 80 km and 6.9 km/sec between 80 and 210 km. A quasi-reversed profile from an earthquake south of the caldera provided similar results. Weaver and Pitt interpreted the above data as evidence for two higher velocity layers beneath the 5.3 km/sec layer and that regional velocities in the mid and upper crust are not substantially reduced within the caldera.

The eastern profile has not yet been interpreted; however, a travel time plot provided by R.B. Smith shows an apparent velocity of about 5.7 km/sec out to a distance of 89 km. This profile extends through the eastern part of the caldera and on the western side of the eastern resurgent dome.

The results of the Yellowstone refraction experiment are not conclusive by any means; however, it did provide the following information: a) apparent velocities in the uppermost crust is about 4.5 km/sec out to a distance of 11 km; b) apparent velocities at distances from 11 km to 80 or 90 km varies from 5.3 km/sec to 5.7 km/sec; c) the

difference in apparent velocities cited above may reflect the fact that a greater proportion of the southeast profile lies inside the Yellowstone caldera; if so, the 7% lower velocity along the southeast profile could be evidence of lower velocities beneath the caldera; d) there is some evidence for 6.0 and 6.9 km/sec layers deeper in the crust.

4.2.2 Inversion of Local Earthquake Travel Time Data

Recently several investigators have published reports on using local earthquake travel time data to recover information about the medium. Crosson (1976) and Aki and Lee (1976) both extended Geiger's method of locating earthquakes (Lee and Lahr, 1975) to include the effect of velocity variation along the ray paths. Crosson restricted the variations to only the z direction, that is he solved for horizontal layer velocities as well as the hypocenters. Aki and Lee (1976) used a slight variation on the ACH method of inverting teleseisms to allow variations in three-dimensions. In their method the initial model was a half space; this restriction was removed by Roecker (1977) who incorporated a layered initial model. The reader is referred to the original papers for the details of the formulation; only a brief summary is presented here.

The travel time residual of a ray from an earthquake to the j^{th} station is a three-dimensional model of K rectangular blocks is,

$$r_j = (\partial t_j/\partial x)\,\delta x + (\partial t_j/\partial y)\,\delta y + (\partial t_j/\partial z)\,\delta z$$

$$+ \delta t + \sum_{k=1}^{K} (\partial t_j/\partial v_k)\,\delta v_k$$

The first three terms on the right hand side represent the hypocenter adjustments, the fourth term the origin time adjustment, and the last K terms the velocity adjustments. If there are a total of ℓ earthquakes and m stations, then the linearized equations can be written as

$$\begin{bmatrix} [A_1] & & & \\ & [A_2] & & \\ & & \ddots & \\ & & & [A_\ell] \end{bmatrix} \begin{bmatrix} & & \\ & V & \\ & & \end{bmatrix} \begin{bmatrix} \delta x_1 \\ \delta y_1 \\ \delta z_1 \\ \delta t_1 \\ \vdots \\ \delta x_\ell \\ \delta y_\ell \\ \delta z_\ell \\ \delta t_\ell \\ \vdots \\ \delta v_R \end{bmatrix} = \begin{bmatrix} r_{11} \\ r_{21} \\ \vdots \\ r_{m1} \\ \vdots \\ r_{1\ell} \\ r_{2\ell} \\ \vdots \\ r_{m\ell} \end{bmatrix}$$

where each submatrix A_j, $j = 1, 2, \ldots, \ell$ is a matrix of m by 4 and contains the hypocenter and origin time partial

derivatives. The V submatrix is m•ℓ by k and contains the velocity partial derivatives. The vector on the right hand side contains all the travel time residuals and the vector on the left hand side contains the unknown hypocenter, origin time, and velocity adjustments. The form of the matrix equation is the same as equation (2.1) and all the techniques described to solve (2.1) in section 2.3 can be applied to the above equation.

A program which solved the inverse problem just described has been written by S. Roecker and W. Ellsworth of M.I.T. They have kindly allowed me to apply their program to a set of local earthquake data from Yellowstone. A.M. Pitt of the U.S.G.S. graciously provided a data set of 26 earthquakes located throughout Yellowstone National Park. Each event was recorded by a subset of a total of 46 stations in and around the Park. The stations include the 26 permanent stations supplemented by temporary units and are shown in Figure 4.8. A histogram of the depths of the 26 earthquakes revealed that 17 were in the upper 2 km of the crust; another 5 between 4 and 6 km, and the remaining 4 between 8 and 12 km.

Attempts at inverting for one-dimensional velocity structure were unsuccessful. This certainly is due to the very shallow depths of the majority of events. The only inversion attempt which converged was for a simple half space model. In this case the computed velocity of 5.4

km/sec is consistent with the refraction data.

The three-dimensional modeling was more successful. A number of inversion attempts were made and the following information was obtained:

1) With the given earthquake distribution, at most three layers are resolvable.
2) The models which gave the most consistent results involved a thin (1 km) layer overlying either a half-space or a layer and a half-space.
3) There were no significant differences between the results of the latter two models mentioned above.
4) Initial velocities for the layers were obtained by performing several calculations with various starting velocities and choosing the set which resulted in the most even distribution of blocks with negative and positive solutions.

The "best" model according to the criterion above is presented in Figure 4.9-4.10. Details of inversion and model parameters are provided in Table 4.2. The velocity perturbations in the thin first layer showed little correlation with the geology. This is probably because it acts as a parameter which absorbs elevation effects and very local near-surface geology. The half-space which extends from 1.5 km downward shows a very interesting pattern of lateral velocity perturbations. (Figure 4.10). First, the heterogeneity shows a definite northeastward alignment, both for the low and high

velocities. Second, the eastern half of the caldera is marked by velocities 1-4% lower than the surrounding region. This is especially interesting because it appears to extend northeastward outside the caldera boundary. Both these features are also revealed in the gravity data (Figure 4.11). The most remarkable result, however, is that the largest perturbation involves three blocks which have perturbations from -9% to -20%. Their locations outside the northwestern boundary of the caldera were completely unexpected. Unfortunately, the area is devoid of stations and thus the feature cannot be confirmed or denied on the basis of teleseismic delays.

4.3 VELOCITY STRUCTURE DOWN TO 100 KM

We are finally ready to consider the teleseismic delay data. The USGS Yellowstone Extended Array consists of 25 stations in and around the national park (the black triangles in Figure 4.8). Figure 4.12 is an array diagram of mislocation vectors for the Extended Array. The mislocations are very large and consistent. There appears to be a NE line of symmetry at which a majority of the vectors point towards. Such large, consistent mislocations must be due to a strong heterogeneity beneath the array. Also the heterogeneity must extend relatively deep (∿100 km) because crustal heterogeneity alone could not divert the rays so strongly.

The evidence from the previous section indicates that the upper crust is not strongly heterogeneous; perhaps fluctuations of no more than 7-8% (except for a specific locality which does not affect our delay data). Thus the combined evidence favors a deep origin for the large teleseismic delays observed at the Yellowstone Array. In Figure 4.13 three cartoons schematically represent different earth structures which could produce the array diagram in Figure 4.12. In the following, the results of three-dimensional inversion are presented.

4.3.1 Inversion of Extended Array Data

The 25 seismograph stations of the Yellowstone Extended Array constitute a relatively dense network which is suited for the application of three-dimensional inversion. The telemetered seismograph system is similar to the central California array instrumentation discussed briefly in section 3.3.1.

A total of 153 events recorded by at least 5 of the stations provided a total of 1382 P-wave residuals for inversion. The data set was kindly provided by H.M. Iyer and J.R. Evans of the U.S.G.S. in Menlo Park, California. They used the same technique and data reduction methods as described in section 3.3.1 for the central California data. Details of data reduction and on error analysis are available in a comprehensive open file report (Iyer et al., 1978, in preparation). the report also includes distance-azimuth (polar) plots and spatial-variation diagrams of the residuals and therefore these plots will not be presented here.

Initial model YP4-100 has four layers reaching a bottom depth of 100 km: two 20 km thick layers, each with a block size of 20 km; and two 30 km thick mantle layers, each with a 25 km block size. For this initial model configuration at least one ray penetrated 186 blocks, thus providing that many unknowns for the inversion. The data had a variance of .2094 $(sec)^2$ which was reduced to .0183 $(sec)^2$ after inver-

sion for an improvement of 91%. Since the residual variance is down to the noise level of the data, a substantial change is not expected if the inversion was iterated.

As in the California results, the detailed solution is tabulated (Table 4.3) while the contoured map of the lateral velocity perturbations (Fig. 4.15-4.18) is discussed in the following sections. A composite shelf diagram (Figure 4.14) best displays the general features of the Yellowstone low-velocity anomaly. In the upper crustal layer the anomaly exhibits the greatest velocity contrast with a maximum contrast of over 20% between neighboring "blocks". The low-velocity anomaly, as seen in a horizontal cross-section, is in the form of an irregular ellipse-shaped body with the long axis centered under, and parallel to, a NE-trending line connecting the centers of the Island Park and Yellowstone calderas. Although the velocity contrast diminishes to an average of less than 10% in the succeeding layers, continuity of the anomaly to depths of at least 100 km is observed.

4.3.2 Crustal Layers

Consider now the results in detail. Figure 4.15 depicts the first crustal layer. In the top 20 km of the crust the velocities deviate from the mean velocity (6 km/sec) as much as -12% in the center of the caldera to +9% just outside the northwestern caldera boundary. Thus over a distance of less then 50 km there is a velocity contrast

greater than 20%. The -4% contour is nearly coincident with the outline of the Yellowstone caldera except at the northeastern end where a significantly large negative anomaly exists 20 km beyond the caldera boundary. The Bouguer gravity map of Yellowstone (Figure 4.11) shows a corresponding extension of the low gravity anomaly associated with the caldera beyond the caldera boundary on the northeast end. As pointed out by Eaton et al. (1975), this departure is of critical importance in establishing that the low-velocity surficial deposits associated with the caldera cannot be responsible for the entire gravity or seismic low. We will present data later from the portable seismic net which show conclusively that the large delays have a deep origin.

Other features in this layer include a north-south extension of low velocities from Norris (NJ) to Mammoth (MH) which follows a "corridor" of numerous hot springs and geysers as well as rhyolite and basalt vents (Eaton et al., 1975). Abutting the Norris-Mammoth corridor, just west of Norris (NJ), there is an east-west zone of high velocities which include the highest velocities in layer 1. This high-velocity "ridge" does not correlate with any mapped surface geologic structure; however, there is a strong spatial correlation with a band of high microseismicity which extends from Hebgen Lake to Norris (see Figure 4.3). Low velocities continue

southwestward beneath the Island Park caldera; however, poor resolution, as indicated in Table 4.3 precludes any firm conclusions. Similarly, the high velocity blocks in the northeastern and southeastern sectors of the park are poorly resolved.

The lower crustal layer is contoured in Figure 4.16. Although the features are somewhat broadened and the amplitudes damped, the main features seen in layer 1 still persist. (Note the change in contour interval to 2% for layers 2-4; because the standard errors of these blocks may range from .4% to .9%, the 2% contours are considered to be significant.) The minimum velocity in the lower crust is defined by the -4% contour located beneath the southwestern half of the caldera. Velocities nearly as low occur under station PC located just outside the northeastern end of the caldera. These two minima are enclosed by the -2% contour which outlines a dumbbell-shaped body under the caldera. Resolution is good to about 20 km beyond the western park boundary and our results show that out to last least this distance, the anomaly persists although with a lower amplitude. The large positive values in the northeast are pooly resolved. However, the northwest area is resolved and indicates higher velocities under this corner of the park.

4.3.3 Crustal Heterogeneity and Local Seismicity

In the previous chapter we discussed the correlation between crustal heterogeneity and the mode of earthquake occurrence (section 3.5.1) in central California. The Yellowstone region is also one of very active shallow crustal (depths $\leq$ 20 km) seismicity although in a much different tectonic environment. This difference is readily discernible in a seismicity map (Figure 4.2). Unlike central California where the seismicity is concentrated on the San Andreas fault and its related branches, the seismicity in the Yellowstone region forms diffuse patterns not readily correlated with Quaternary faulting. Nevertheless the Yellowstone seismicity does tend to occur in linear spatial clusters. From Figure 4.2 three such clusters are defined: One major zone occurs along a line from about Norris extending N 80°W to about the Missouri Flats east of the Gravelly Range; another smaller cluster trending east-northeasterly is located about 20 km northeast of the Yellowstone Caldera; and the third cluster trending south-southeasterly is just outside the caldera along the western shore of Yellowstone Lake.

Consider the Norris to Missouri Flats zone first. The structural setting of this region where it is not hidden beneath the volcanic cover is marked by northwest trending mountain ranges separated by narrow valleys which result from extensional block faulting. Thus the Madison and Gravelly Ranges are typical structures justwest of West Yellow-

fault scarps produced during the earthquake may only represent secondary reactivation of older surficial faults. Returning to our velocity perturbation anomalies for layer 1 (0 - 20 km) we have already mentioned the correlation of the seismicity and an east-trending high-velocity anomaly which extends from Hebgen Lake to Norris. The anomaly is defined by the +4% contour and ends abruptly against the Norris-Mammoth low-velocity trend (Figure 4.15). Our results when considered in light of the other evidence just cited tends to confirm that the seismicity is associated with an eastward extension of Centennial type structures even though surface evidence for it is weak. The only east-trending faults in the area are parts of the Red Canyon and Hebgen faults which bend eastward as they enter the Yellowstone Park boundary. The explanation for the high velocity is not quite evident. The high-velocity anomaly is aligned with the graben-like Centennial Valley for which one might expect a low velocity associated with a thicker sedimentary sequence. One possible explanation for the high velocity is that the graben-like structure is filled with basaltic igneous rocks in a manner similar to a miniature Snake River Plain and was subsequently covered by the rhyolitic volcanics of the Yellowstone Plateau.

The second cluster of seismicity is located east of the Yellowstone Caldera and is associated with low velocities in our crustal velocity perturbation model. The northeast trending cluster occurs in a "nose" of the low-velocity

stone. A peculiar anomaly to this pattern is the Centennial Mountains which trends eastward against the predominant structural grain. The mountains are flanked to the north by the Centennial Valley along a north-dipping, high-angle normal fault which apparently terminates to the east against the Madison Range. Some geologists believe that the eastward-trending Centennial structures represent a fundamental change in a long-established structural pattern and that the Centennial structural pair are younger structures which are being extended eastward across the older northwest-trending structures (Witkind, 1975). The eastward trending seismicity appears to confirm the continuation of eastward trending structures beneath the volcanic cover of the Yellowstone plateau even though the surface faulting on the plateau is predominantly north-trending. The mechanisms of the events in the zone are predominantly east-west striking normal faults (Figure 4.5) which would be consistent with the Centennial type structures. The Hebgen Lake earthquake of 1959 was a magnitude 7.1 event in this area and, in fact, much of the current seismicity may be due to continued readjustments to the earthquake. Ryall (1962) determined the source mechanism of the Hebgen Lake earthquake from P-wave polarities and obtained a normal fault mechanism with a strike of N 80° W ± 10° and a SW dip of 54° ± 8°, again consistent with Centennial related stress field (north-south extension) even though the hypocenter was some 40 km east of the apparent termination of the Centennial structures. The north-west trending

anomaly associated with the Yellowstone Caldera. The "nose" extends outside the morphologic boundary of the caldera and was interpreted in an earlier section as a possible subsurface continuation of the magma chamber. The seismicity may be a manifestation of magma injection into this extension. The nearly radial alignment of the zone to the caldera boundary is consistent with this hypothesis.

The third linear cluster is located on the southeastern boundary of the caldera and, interestingly, is also nearly radial to the boundary. However, no known velocity anomaly is associated with this particular cluster.

4.3.4 Mantle Structure

Continuing with the description of the inversion model, we consider the two mantle layers. Notice that the transition from layer two to layer three (Figure 4.17 is quite smooth, both in the shape and magnitude of the anomaly. Recall that layers three and four are ten kilometers thicker than the top two crustal layers and have a slightly larger block size of 25 km x 25 km. The effect of these changes might be to dampen and smooth out the anomalies due to the larger averaging dimensions. Such an effect is imperceptible in our model. In fact, the -4% contour has enlarged northward to encompass the northcentral part of the park. Also significant negative anomalies extend forty kilometers west of Yellowstone under the Snake River Plain. To the east, however, higher velocities are encountered which place a

firm boundary to the anomaly at this depth to about the eastern boundary of the park. This suggests that the eastern boundary of the anomaly is nearly vertical from the upper crust to a depth of 70 km. The northwestern boundary of the anomalous body migrates with depth from the caldera boundary to the northwestern corner of the park. The lateral migration amounts to about 50 km in a depth interval of approximately 70 km implying an average slope of 36° from the vertical. The bottom layer (Figure 4.18) extends the model to a final depth of 100 km. Somewhat surprisingly the anomaly in this layer has quite irregular boundaries and locally large amplitude. The resolved portion of the model depicts an elliptical low-velocity anomaly underlying both the Island Park and Yellowstone calderas. The anomaly is shifted north-westward from a line passing through the centers of the two calderas; and the lowest velocities occur in an area centered around Norris Junction (NJ). Much of the other details in this layer are not resolved with the exception of the occurrence of high velocities northwest of Yellowstone. This appears to be a consistent feature of our model and perhaps indicates a zone of depleted mantle bordering the low-velocity anomaly.

One of the major assumptions in our method is that the earth outside the modelled region is laterally homogeneous. From the portable network data we know that significant anomalies exist much deeper than the 100 km "floor" of model YP4-100. The effects due to this deeper heterogeneity

are probably mapped into the bottom layer which may explain some of the irregularities seen in Figure 4.18.

4.3.5 Alternate Model

In order to determine the effect of the initial model on the analysis, a second inversion was performed with different initial parameters (Table 4.4). In particular we wanted to lower the bottom depth to permit a deeper expression of the Yellowstone low-velocity anomaly. The results are presented layer by layer in Fig. 4.20-4.23 and as a shalf-diagram in Figure 4.19. Recall the comments pertaining to the damping effect of larger block dimensions when comparing results with the previous model. A comparison of the crustal layer for YP4-190 (Figure 4.20 with the crustal layers one and two for YP4-100 (Fig. 4.15-4.16) illustrate this point. The details, noted in the previous discussions are smoothed out although the major anomaly remains. Even though it is 20 km thicker, layer two of YP4-190 (Figure 4.21) closely resembles layer three of YP4-100 (Figure 4.17). Thus to depths of about 70 km the two models provide consistent results. Below 70 km the models differ significantly. It appears that the features in the bottom layer of YP4-100 have been separated and projected onto the two deeper layers of YP4-190.

Comparison of layer four of model YP4-100 with layers three and four of model YP4-190 reveals the nature of the projection. The large negative values between 70 - 100 km depth in model YP4-100 are not present in the equiva-

lent depth interval of model YP4-190. In layer three, model YP4-190 has a band of low velocities with an approximate east-west strike beneath the Yellowstone Park area with the most negative values of -2% to -3% beneath the Island Park caldera. In layer four values of -3% to -4% occur beneath the northern part of the Yellowstone caldera.

The above comparison demonstrates the degree of non-uniqueness still possible in such models. The important point is that although the details of the models below 70 km are different both show the continuation of a localized low-velocity anomaly downward into the upper mantle beneath the Yellowstone volcanic terrain.

The three-dimensional inversion of the permanent Yellowstone array teleseismic P-wave delays confirmed much of what was deduced from previous analysis (Iyer, 1975). In addition, however, the following conclusions were reached:

(1) The lowest relative velocities occur in the upper crust where velocity contrasts as large as 20% occur within a lateral distance of 100 km.

(2) A strong correlation was found between anomalies in the upper crust and geologic and tectonic features such as the caldera boundary, the Bouguer gravity anomaly, the Norris-Mammoth corridor, and the location of local earthquakes.

(3) In the lower crust the maximum velocity contrast dropped to about 12% with the lowest relative

velocities located beneath the southwestern half of the caldera.

(4) In the upper mantle the maximum velocity contrast is about 6% to 10% and the minimum velocities continue to be under the Quaternary Yellowstone and Island Park calderas. This strongly suggests that the anomaly is one continuous body which extends from the upper crust to depths of at least 190 km.

(5) The area of low velocities changes from an elliptical shape with a northeasterly strike in the crust to a more east-west elongated irregular shape in the upper mantle.

(6) The cross section of the anomaly appears to increase in area gradually with depth. The wall of the anomaly is, however, near vertical at the eastern boundary and has an average slope of 36° from the vertical in the northwestern corner.

4.4 VELOCITY STRUCTURE DOWN TO 300 KM

We could "push" the model down to nearly 200 km in the last section but not much more. The information just is not there. If we had data that extended the array's periphery outward then a deeper model would make sense. This is done in the following sections.

4.4.1 Inversion of Large Aperture Array Data

Inversion of the Extended Array data produced models with a significant low velocity anomaly remaining in the bottom layer. Undoubtedly the actual structure represented by the anomaly extends deeper. In an attempt to resolve the vertical extent of the anomaly, the USGS set up portable instruments to the northwest and the southeast of the Yellowstone caldera. The location of the portable stations along with the Extended Array stations are plotted in Figure 4.24. For the inversion to be described only data from the PL (portable) stations and the Extended Array were available; a total of 44 stations (however, 5 pairs of stations shared nearly identical locations). For the inversion 44 events were available for a total of 521 residuals. The relatively small number of data forced us to use larger blocksizes and layer thicknesses in order to keep the problem overdetermined. With the additional stations we were able to model to nearly 300 km depth.

With the addition of the portable stations, the array extends over a distance greater than 300 km. Such a large aperture invalidates some of the assumptions made in the formulation of the problem; namely the plane wave assumption. Corrections for the curvature of the Earth must now be applied. These corrections are specified in Zandt (1975, unpublished manuscript). A program incorporating the corrections was used to derive the following model which we name the deep model.

4.4.2 Deep Model

Contours of significant fractional velocity perturbations for each layer of the deep model are superimposed on array maps and presented as Figure 4.20 to Figure 4.25. Starting model and inversion parameters, and the solution are tabulated in Table 4.5.

The entire crust had to be modeled with one layer, 40 km thick. As expected, a large low velocity anomaly is centered below the caldera. Comparison with layer 2 (40-90 km) demonstrates again that the strongest heterogeneity is confined to the crust. In layer 2 the lowest velocities occur beneath the southwestern half of the caldera. A relatively steep velocity gradient marks the northeastern edge of the Snake River Plain-Yellowstone trend where low velocities beneath the caldera abut against high velocities beneath the southern portion of the Beartooth Uplift. The trend of the low velocity anomaly appears to bend around the Beartooth Uplift and continue to the northeast. This pattern is also present in layer 3 (90-140 km) where the northeast trending low velocity anomaly is offset in a left-lateral sense along the NW trend of the Absaroka volcanic field. In the next two layers, down to 240 km, the alignment of the low velocity anomaly straightens out, parallel to but slightly southeast of the Snake River Plain. The pattern of low velocity anomaly aligned along a northeast trend which persists throughout the upper mantle

disappears in layer 6 (240-290 km). Low velocities persist beneath the southern portions of the Absaroka volcanic field but a high velocity anomaly is located beneath the "head" of the Snake River Plain-Yellowstone trend. The important point is that the northeast trend is no longer visible. The significance of the deep model will be discussed in the next section.

4.5 YELLOWSTONE HOT SPOT MECHANISM: PLUME OR FRACTURE?

Several hypotheses have been proposed to explain the mechanism of the Yellowstone hot spot. Basically the hypothesis fall into one of two categories: (a) mantle plumes; or (b) propagating lithospheric fractures.

Mantle plumes were proposed by Wilson (1965) to explain the long linear volcanic island chains in the Pacific Ocean. Morgan (1971, 1972a, 1972b) extended the idea to explain a number of linear volcanic features, both continental and oceanic. He also postulated that plumes were anchored at the core-mantle boundary, forming an absolute reference frame for plate motions; and further that about twenty deep mantle plumes bring heat and primordial material up to the asthenosphere. This upwelling is thought to be a driving force for continental drift.

Armstrong et al. (1975) documented the systematic age progression of the volcanic rocks in the Snake River Plain which indicated volcanism propagated northeasterly along the Snake River Plain at a rate of about 4.5 cm/yr. Christiansen's (1972) work on the volcanic stratigraphy of Yellowstone National Park provided evidence that the young rhyolitic volcanism is an initial stage of a bimodal volcanic cycle in which Snake River type basalts will eventually erupt and cover the rhyolitic volcanics.

These studies seemed at first to provide a strong argument that Yellowstone is presently underlain by an

active mantle plume and that the Snake River Plain represents a plume "track" documenting the passage of the North American plate over the plume for at least the last 17 million years. A major obstacle to this hypothesis is the discovery of a second linear volcanic progression; this one initiating near the western end of the Snake River Plain and becoming progressively younger in a northwestward direction across Oregon (Iyer et al., 1978). However, the comparison is not perfect; the northwestern trending volcanics are much less voluminous and consist of rhyolitic domes, lacking the flood basalts characterizing the Snake River Plain.

Before continuing with a discussion of the second category of hypothesis, we should mention that there exist several variants on the plume hypothesis. These include the gravitational anchor of Shaw and Jackson (1973) and the chemical plume of Anderson (1975), both of which will be discussed in a later section.

The second major class of hypothesis explaining the Snake River Plain - Yellowstone volcanics is the propagating fracture models. The basic idea of these models is that magma migrates up lithospheric fractures which propagate through a moving lithospheric plate (Green, 1971). The presence of the northwestern trending volcanic sequence and evidence that the SRP follows a Pre-Cambrian zone of weakness seem to favor this class of hypothesis.

With the models of the deep structure beneath Yellow-

stone presented earlier in this chapter, there are now available models of the lithosphere/asthenosphere structure beneath two major hot spots: Hawaii and Yellowstone. Models for both were derived with essentially the same method providing a good basis for comparison. Also, a three-dimensional velocity model is available for the lithosphere beneath LASA, Montana. Fortuitously, the LASA is situated on strike with the trend of the SRP and provides an interesting comparison with Yellowstone. In the following sections these comparisons are discussed prior to a final statement in Chapter V on the preferred tectonic model for Yellowstone based on the results of this chapter.

4.5.1 Comparison with Hawaii

Ellsworth (1977) derived three-dimensional velocity models of the lithosphere beneath Hawaii using essentially the same techniques employed in this thesis. A comparison of the two hot spots should provide some useful insights into the question of plumes or fractures.

First let us review some of the similarities. With respect to their tectonic settings:

(a) Both are young volcanic centers at the "head" of a linear zone of volcanics which become progressively older away from the "head".

(b) Both areas have high heat flow, shallow seismicity and normal faulting characteristic of regions with extensional tectonics.

In the three-dimensional models:

(1) Both areas are underlain by low-velocity anomalies which extend to great depth (>100 km).

(2) The low-velocity anomalies take on a linear trend with depth which are parallel to the regional tectonic trend: the Hawaiian Island chain and the Snake River Plain, respectively.

Now consider the differences; first in terms of the tectonic setting:

(a) The most fundamental is the oceanic setting of Hawaii and the continental setting of Yellowstone.

(b) As a result of (a) the magmatic products are quite distinct. The rhyolites of Yellowstone are probably due to crustal melting (Hamilton, 1965) and are obviously absent in Hawaii. The olivine tholeiites of Hawaii and tholeiites of the Snake River Plain are superficially similar but have distinct chemical differences characteristic of oceanic vs. continental basalts.

(c) Hawaii has deep seismicity (~60 km) which is completely absent in Yellowstone where the seismicity is confined to the upper 20 km. The deep seismicity in Hawaii is generally accepted as evidence of magmatic ascent activity. This is also evidence of brittle failure occurring deep in the Pacific lithosphere. The absence of deep seismicity can have two interpretations. Either

it is evidence for the lack of current magmatic ascent or indicates the ductile behavior of the lithosphere. Considering the active tectonics, recent volcanics, and active uplift occurring in Yellowstone today, the latter hypothesis is preferred. If it can be generalized, the observation would imply that continental lithosphere is characterized by ductile behavior at much shallower depths than oceanic lithosphere; perhaps because of the more siliceous nature of the continental lithosphere.

Comparison of the three-dimensional models indicates that:

(1) The upper crustal anomalies associated with the intrusive lava have opposite signs. The rift zones and volcanic summit regions in Hawaii are marked by positive velocity anomalies whereas the Yellowstone anomaly is negative throughout the crust. This difference can be explained by the contrast between the intrusive material and the surrounding crustal material. In Hawaii the intrusive basalt is dense and fluid thus filling and healing cracks and pores within the crust which is composed of sheets of frozen lava flows which are vesicular and highly fractured. In Yellowstone the siliceous intrusives contain a high percentage of volatiles and generally are

less dense than the compacted and metamorphosed crust that is intruded.

4.5.2 Comparison with LASA

The three-dimensional velocity model for the Montana LASA (Large Aperture Seismic Array) determined by Aki et al. (1976) provides another source of comparison with the Yellowstone results. The modelling of the LASA data revealed a linear low-velocity zone trending N 60° E through the center of the array site. The anomaly is present in the upper crust and persists to depths greater than 100 km. The authors interpreted the feature as a zone of weakness associated with a system of conjugate wrench faults present in the Rocky Mountains. One set of these faults trends N 60° E.

The Fromberg, Vanada, Weldon, and Brockton-Froid faults form a 500 km long discontinuous fracture from a position less than 100 km northeast of Yellowstone, through LASA, to nearly the Canadian border (Figure 4.1). It is interesting to note that the Brockton-Froid fault offsets Pleistocene glacial deposits (Eaton et al., 1975). These faults also delineate a major boundary which separates northeasterly trending magnetic anomalies on the northwest from northwesterly magnetic trends on the southeast. The N 60° E trend is parallel with the Colorado lineament which is interpreted to have been the southeastern margin of an old pre-Cambrian craton (Warner, 1978).

Thus there is good evidence that the Snake River

Plain is aligned along a zone of weakness that cuts deeply (>100 km?) into the lithosphere. The N 60° E trending zone appears to be a remnant of a pre-Cambrian feature; perhaps a zone of great strike-slip faults such as the ones present today sited landward of and parallel to the coastlines of the circum-Pacific.

Figure Captions

Figure 4.1 Simplified regional geology map (modified from Tectonic Map of the United States by the USGS and AAPG, 1962).

Figure 4.2 Seismicity of the Yellowstone region, from Smith et al. (1977).

Figure 4.3 Seismicity of the West Yellowstone region, from Smith et al. (1977).

Figure 4.4 Focal mechanisms from the Yellowstone region, from Smith et al. (1977).

Figure 4.5 Crustal cross sections showing velocity structure, magnetic profile, and focal depths, from Smith et al. (1977).

Figure 4.6 Seismic refraction profiles for Montana and neighboring states. Velocities in km/sec.

Figure 4.7 MIT seismic refraction experiment. Star marks shot point. Lines mark approximate recording profiles.

Figure 4.8 USGS Yellowstone Extended Array (black triangles)

and temporary stations (open triangles).

Figure 4.9 Velocity perturbations in percent obtained from local data inversion.

Figure 4.10 Contours of velocity perturbations. Contour interval 4%. Also shows locations of earthquakes used for the inversion.

Figure 4.11 Complete Bouguer gravity map of Yellowstone-Island Park region. Contour interval is 5 mgals.

Figure 4.12 Yellowstone Array diagram. Polar coordinates are azimuth and slowness ($dt/d\Delta$). Head of the arrow is at USGS or "true" location and tail is at the array location.

Figure 4.13 Three cartoons of velocity structures that could cause array mislocation diagram like 4.12. Axis of symmetry is NE-SE. Ruled area is low-velocity. The top cartoon depicts a synclinal structure on the Moho. The middle cartoon depicts a cone-shaped low-velocity structure. The bottom cartoon depicts a synclinal structure on a deep (400 km?) phase change boundary.

Figure 4.14 Three-dimensional shelf diagram illustrating continuous low-velocity anomaly under Yellowstone. Model YP4-100.

Figure 4.15 Layer 1 of model YP4-100. Yellowstone National Park boundary shown and Yellowstone and Island Park calderas shaded.

Figure 4.16 Layer 2. See 4.15.

Figure 4.17 Layer 3. See 4.15

Figure 4.18. Layer 4. See 4.15.

Figure 4.19 Three-dimensional shelf diagram for model YP4-190.

Figure 4.20 Layer 1 of model YP4-190. See 4.15.

Figure 4.21 Layer 2. See 4.20.

Figure 4.22 Layer 3. See 4.20.

Figure 4.23 Layer 4. See 4.20.

Figure 4.24 Portable station locations near Yellowstone. Also shows Extended Array.

Figure 4.25 Layer 1 of deep model. Contours of percent velocity perturbations. Contour interval 2%.

Figure 4.26 Layer 2. See 4.25.

Figure 4.27 Layer 3. See 4.25.

Figure 4.28 Layer 4. See 4.25.

Figure 4.29 Layer 5. See 4.25.

Figure 4.30 Layer 6. See 4.25.

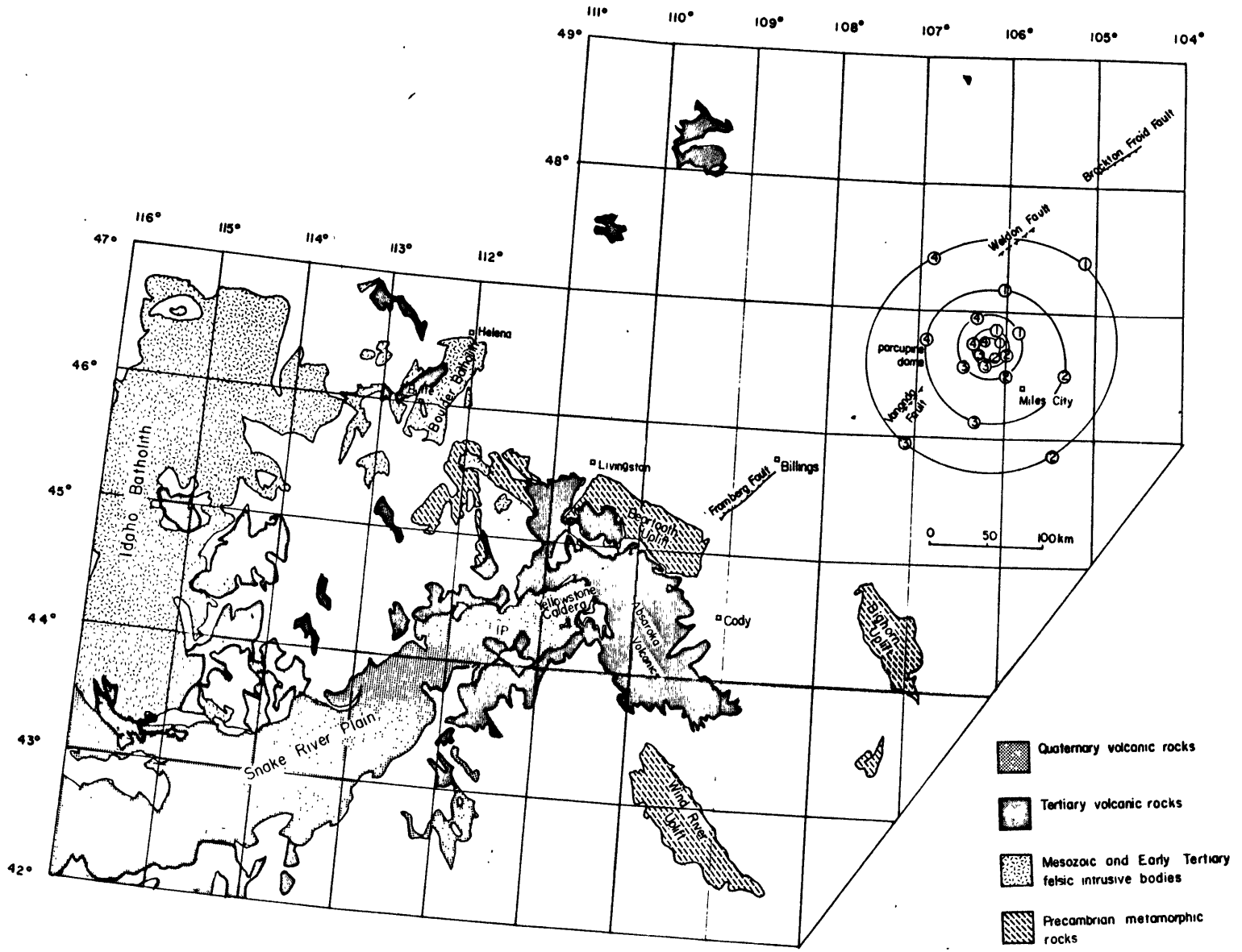
111°
110°
109°
108°
107°
106°
105°
104°
49°
48°
47°
46°
45°
44°
43°
42°
116°
115°
114°
113°
112°
Brockton Froid Fault
Weldon Fault
parcupine dome
Miles City
Yonkstp Fault
Helena
Boulder Batholith
Idaho Batholith
Livingston
Bozeman
Bridger Range
Bear Tooth Uplift
Framberg Fault
Billings
Yellowstone Caldera
IP
Absaroka Volcanics
Cody
Bighorn Uplift
Snake River Plain
Wind River Uplift
0
50
100km
Quaternary volcanic rocks
Tertiary volcanic rocks
Mesozoic and Early Tertiary felsic intrusive bodies
Precambrian metamorphic rocks

Figure 4.1

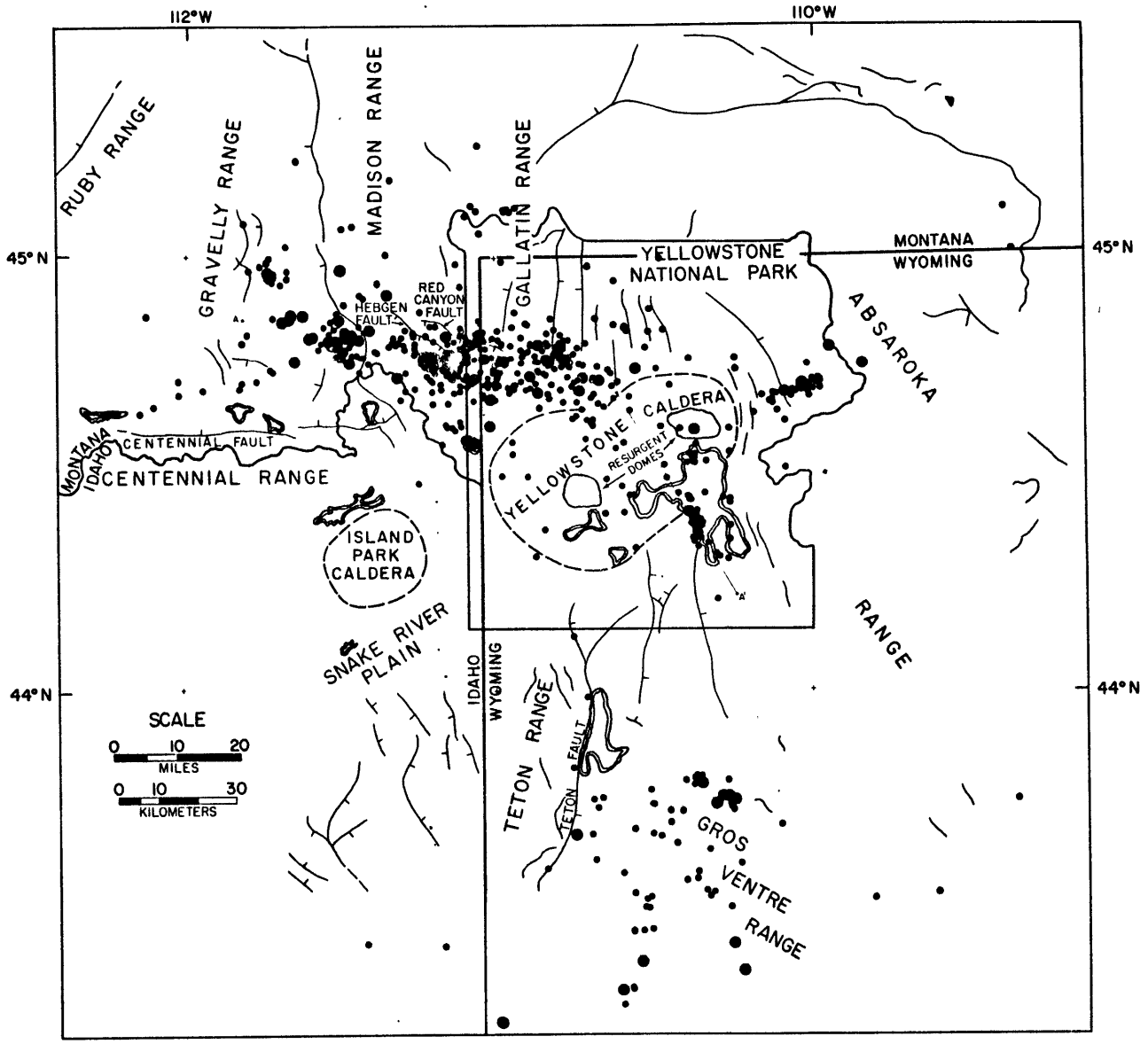
112°W
110°W
45°N
44°N
RUBY RANGE
GRAVELLY RANGE
MADISON RANGE
GALLATIN RANGE
YELLOWSTONE NATIONAL PARK
MONTANA
WYOMING
ABSAROKA
RANGE
HEBGEN FAULT
RED CANYON FAULT
YELLOWSTONE CALDERA
RESURGENT DOMES
MONTANA
IDAHO
CENTENNIAL FAULT
CENTENNIAL RANGE
ISLAND PARK CALDERA
SNAKE RIVER PLAIN
IDAHO
WYOMING
TETON RANGE
TETON FAULT
GROS VENTRE RANGE
SCALE
0 10 20
MILES
0 10 30
KILOMETERS

Figure 4.2

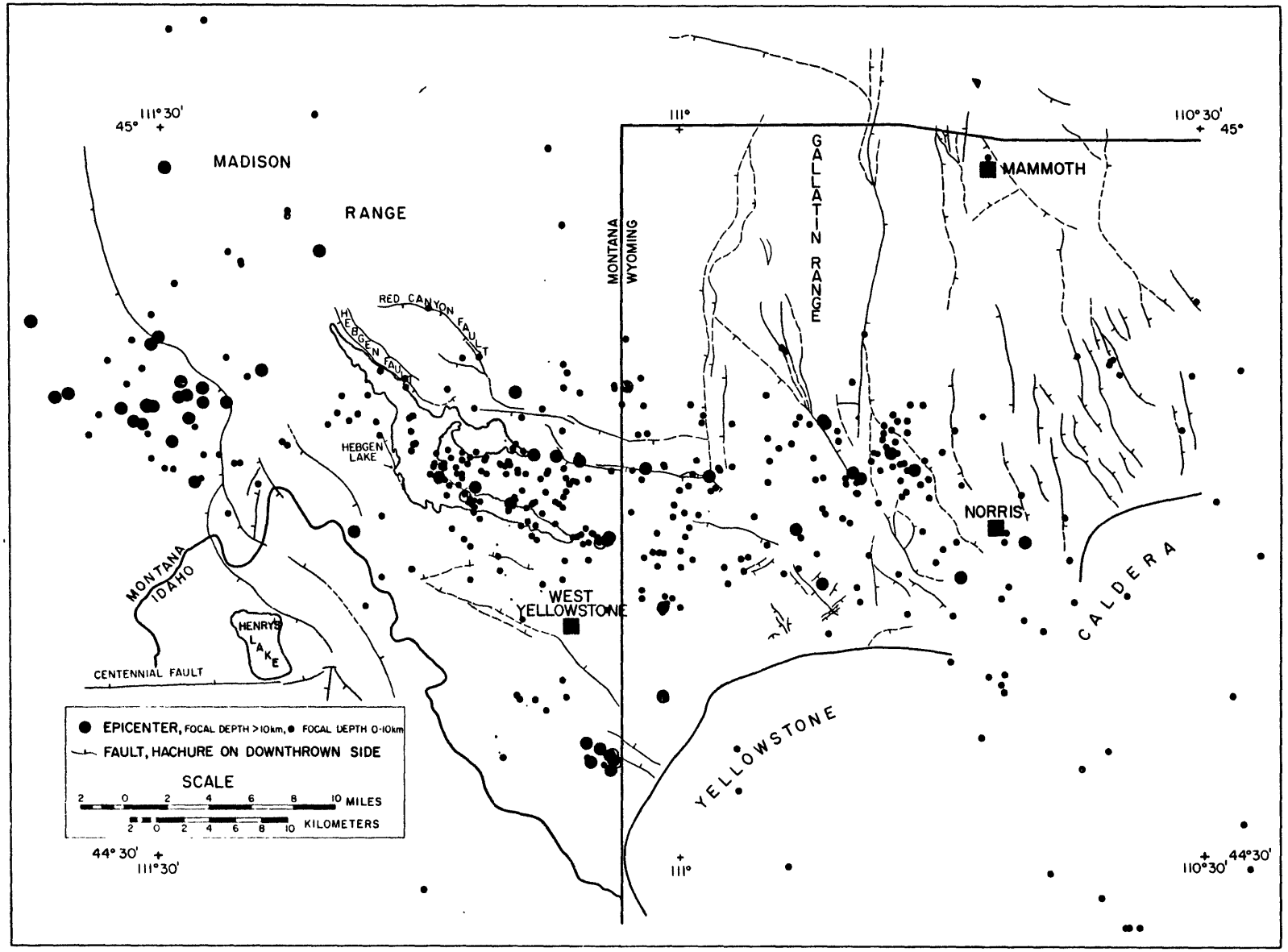
111°30'
45°
MADISON
RANGE
111°
110°30'
45°
MAMMOTH
GALLATIN RANGE
MONTANA
WYOMING
RED CANYON FAULT
HEBGEN FAULT
HEBGEN LAKE
NORRIS
MONTANA
IDAHO
WEST YELLOWSTONE
CALDERA
HENRYS LAKE
CENTENNIAL FAULT
YELLOWSTONE
EPICENTER, FOCAL DEPTH >10km, FOCAL DEPTH 0-10km
FAULT, HACHURE ON DOWNTHROWN SIDE
SCALE
2 0 2 4 6 8 10 MILES
2 0 2 4 6 8 10 KILOMETERS
44°30'
111°30'
111°
110°30'
44°30'

Figure 4.3

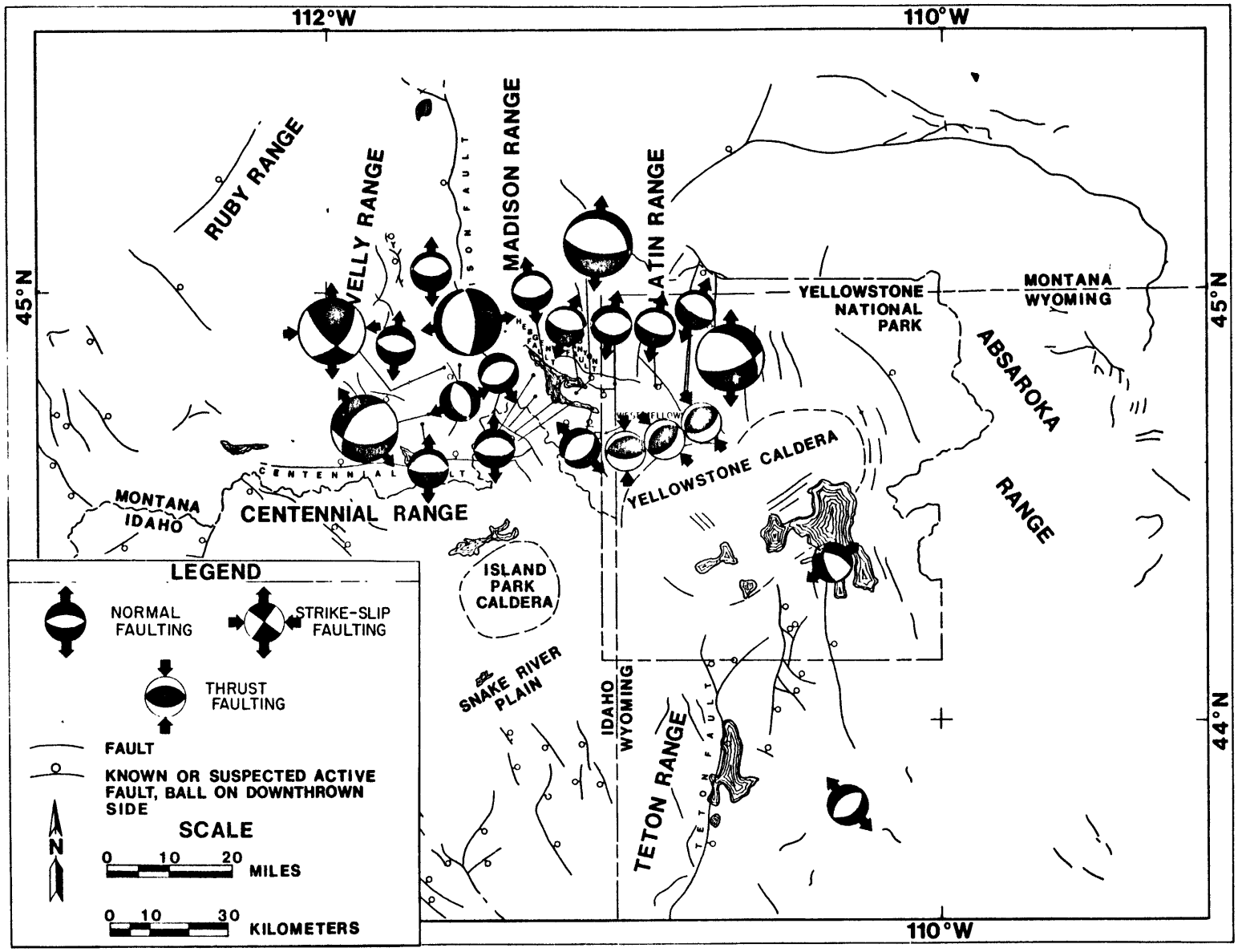
112°W
110°W
45°N
44°N
RUBY RANGE
GRAVELLY RANGE
MADISON RANGE
GALLATIN RANGE
YELLOWSTONE NATIONAL PARK
MONTANA
WYOMING
ABSAROKA RANGE
YELLOWSTONE CALDERA
CENTENNIAL RANGE
MONTANA
IDAHO
ISLAND PARK CALDERA
SNAKE RIVER PLAIN
IDAHO
WYOMING
TETON RANGE
LEGEND
NORMAL FAULTING
STRIKE-SLIP FAULTING
THRUST FAULTING
FAULT
KNOWN OR SUSPECTED ACTIVE FAULT, BALL ON DOWNTHROWN SIDE
SCALE
0 10 20 MILES
0 10 30 KILOMETERS
N

Figure 4.4

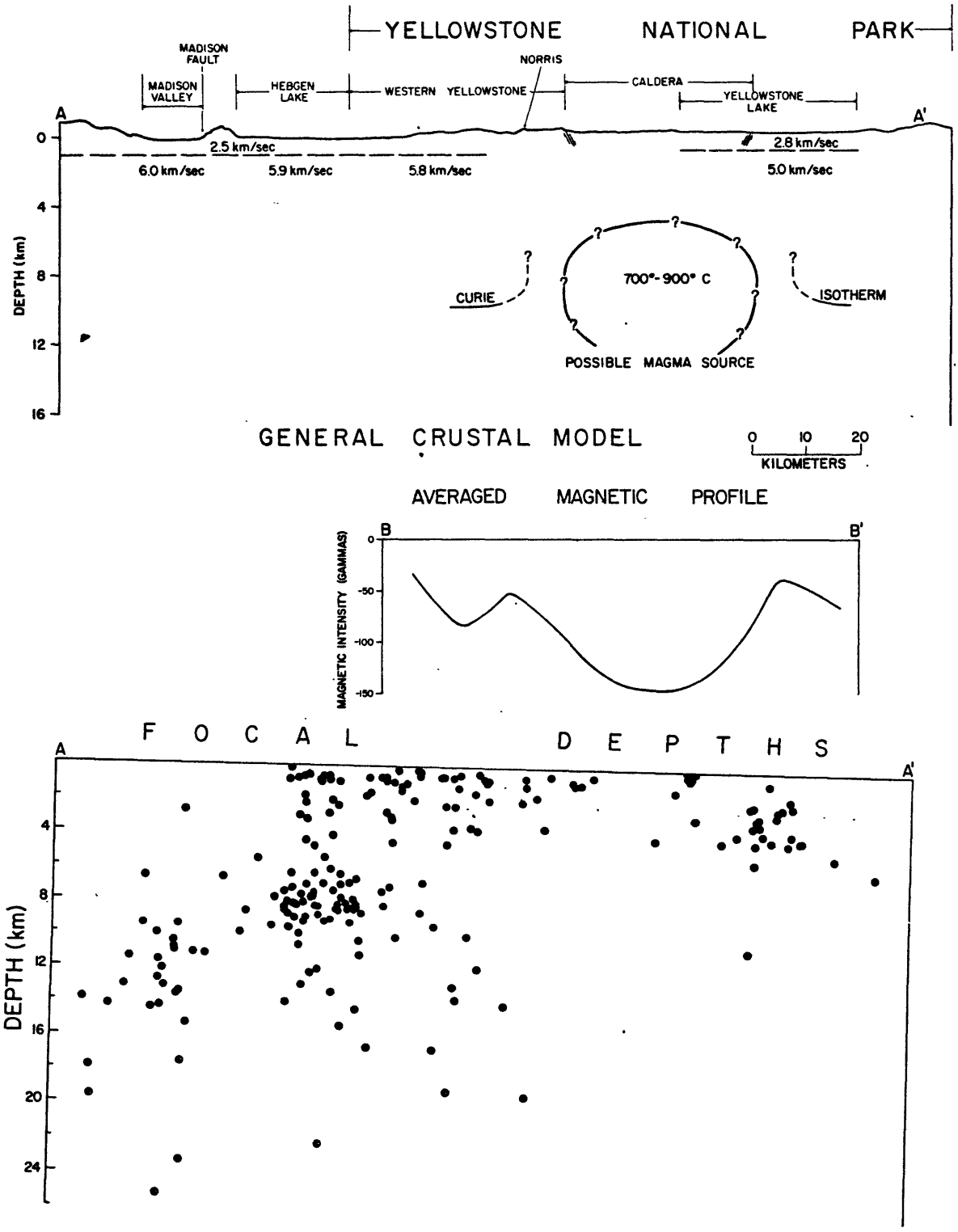
YELLOWSTONE NATIONAL PARK
MADISON FAULT
NORRIS
MADISON VALLEY
HEBGEN LAKE
WESTERN YELLOWSTONE
CALDERA
YELLOWSTONE LAKE
A
A'
2.5 km/sec
2.8 km/sec
6.0 km/sec
5.9 km/sec
5.8 km/sec
5.0 km/sec
DEPTH (km)
0
4
8
12
16
CURIE
700°-900° C
ISOTHERM
POSSIBLE MAGMA SOURCE
GENERAL CRUSTAL MODEL
0 10 20
KILOMETERS
AVERAGED MAGNETIC PROFILE
B
B'
MAGNETIC INTENSITY (GAMMAS)
0
-50
-100
-150
F O C A L D E P T H S
A
A'
DEPTH (km)
4
8
12
16
20
24

Figure 4.5

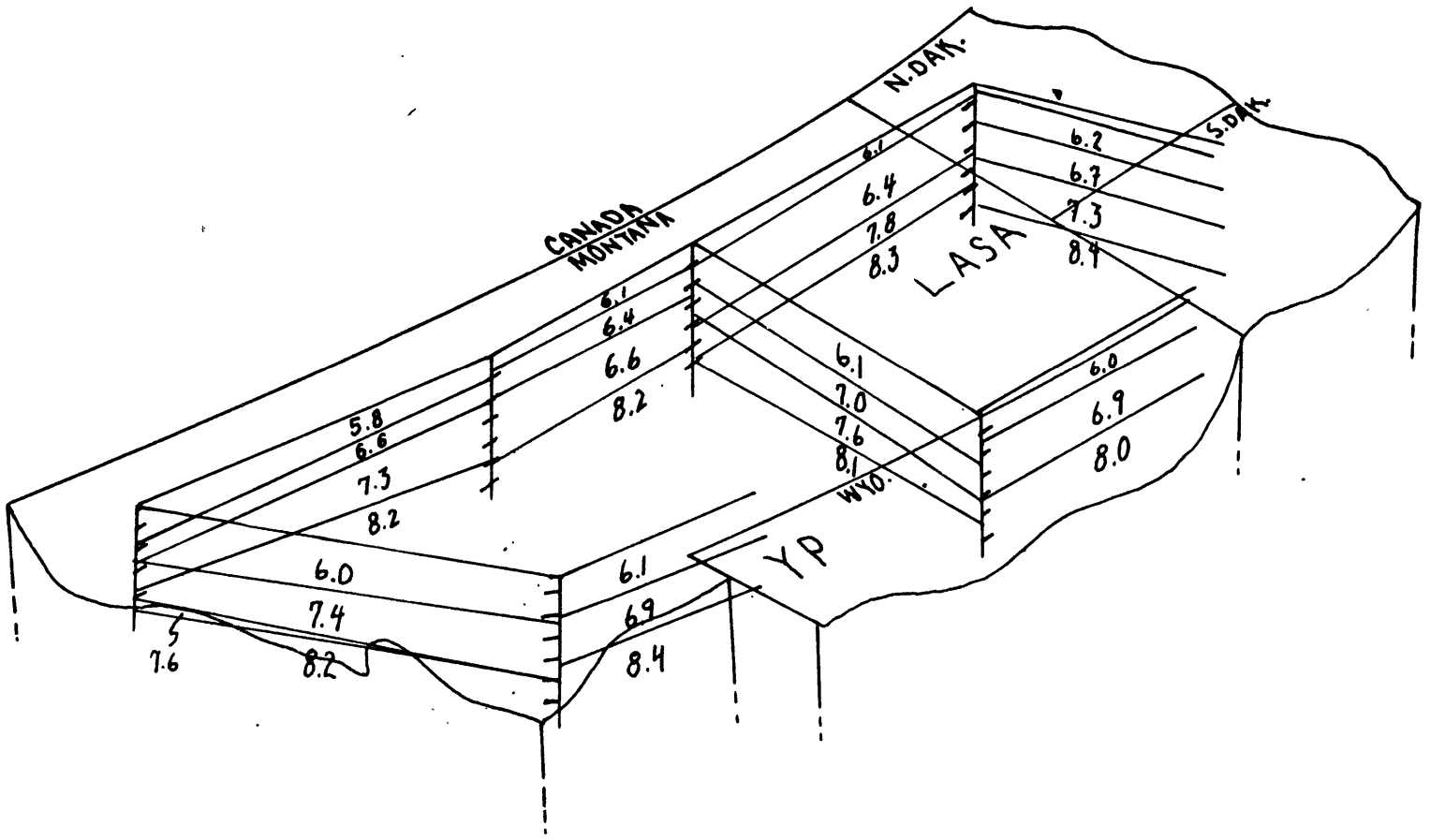
N.DAK.
S.DAK.
CANADA
MONTANA
WYO.
LASA
YP
6.1
6.4
6.6
8.2
5.8
6.6
7.3
8.2
6.0
7.4
7.6
8.2
6.1
6.9
8.4
6.2
6.7
7.3
8.4
6.4
7.8
8.3
6.1
7.0
7.6
8.1
6.0
6.9
8.0

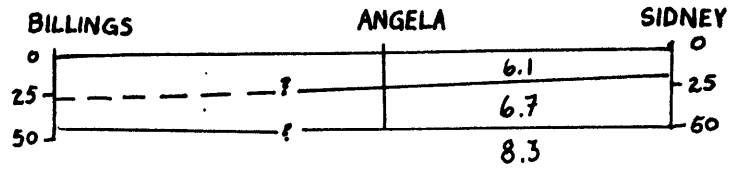
BILLINGS
ANGELA
SIDNEY
0
25
50
?
?
6.1
6.7
8.3
0
25
60

Figure 4.6

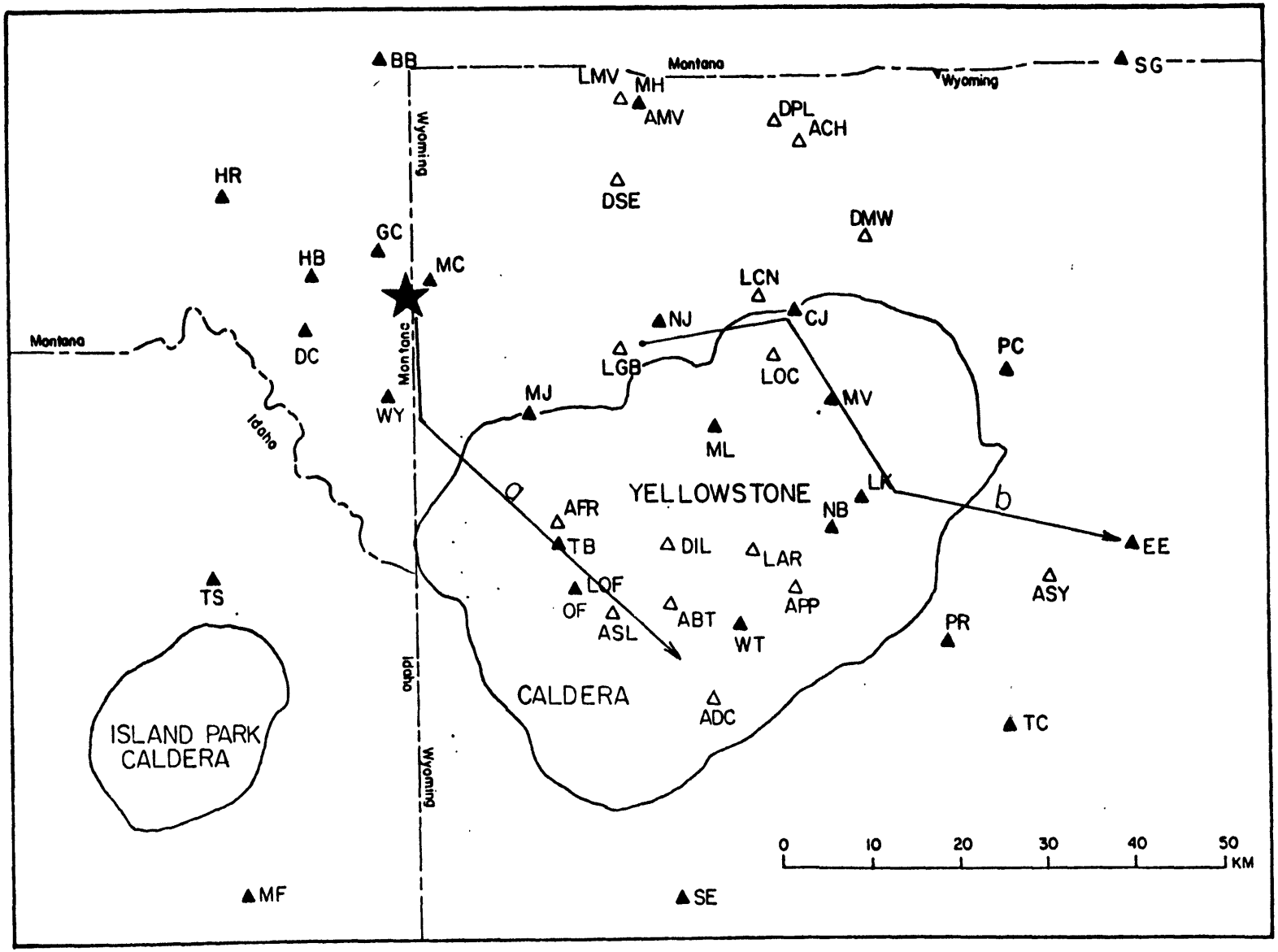
BB
SG
LMV
MH
AMV
DPL
ACH
Montana
Wyoming
HR
DSE
DMW
GC
HB
MC
LCN
NJ
CJ
PC
LGB
LOC
DC
MJ
MV
WY
ML
Idaho
YELLOWSTONE
LK
AFR
NB
TB
DIL
LAR
EE
TS
LOF
ASY
OF
ASL
ABT
APP
WT
PR
CALDERA
ADC
TC
ISLAND PARK
CALDERA
MF
SE
a
b
0
10
20
30
40
50
KM

Figure 4.7

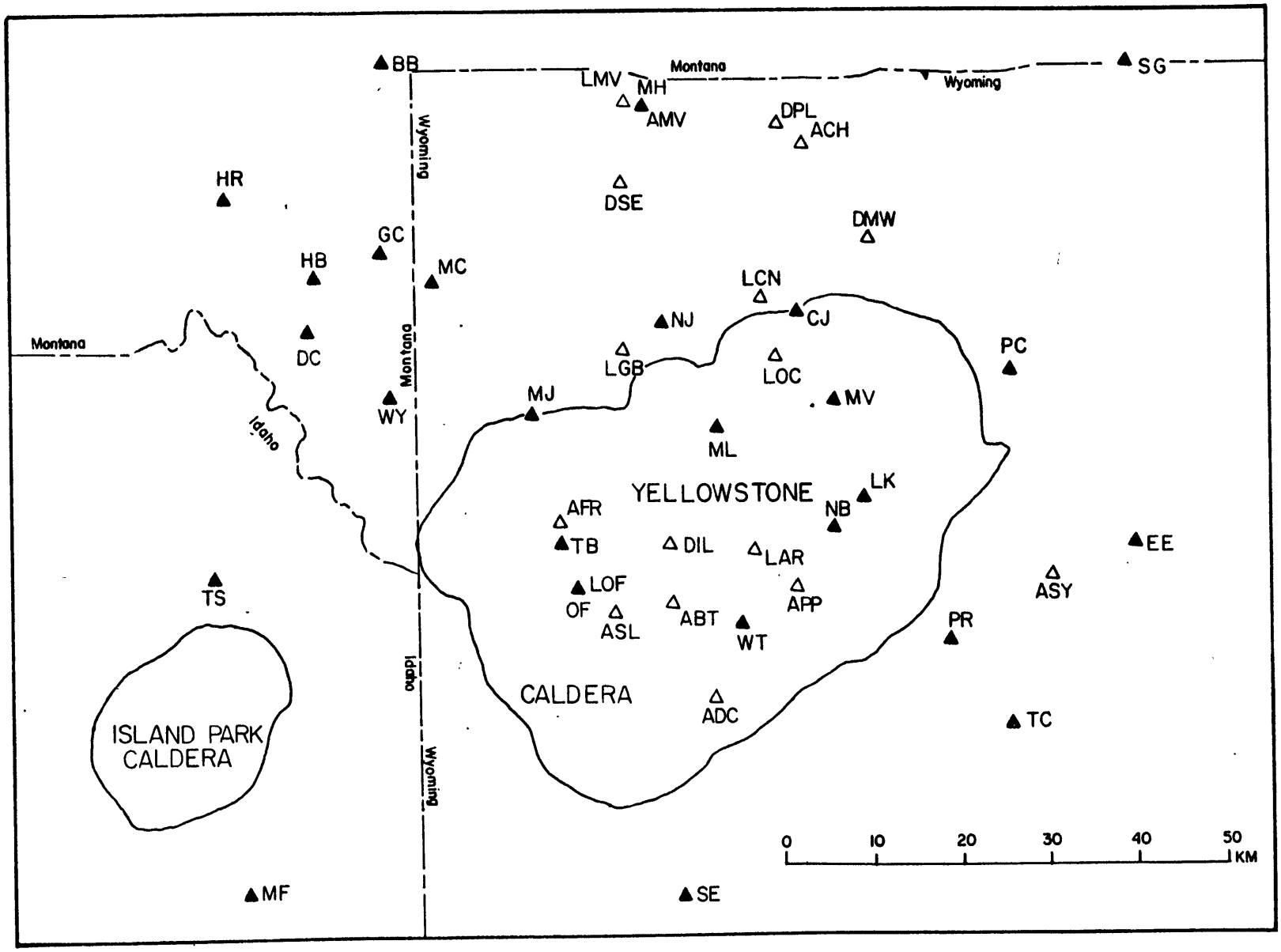
BB
Montana
LMV
MH
Wyoming
SG
AMV
DPL
ACH
Wyoming
HR
DSE
DMW
GC
HB
MC
LCN
NJ
CJ
Montana
DC
LGB
LOC
PC
Montana
MJ
MV
WY
Idaho
ML
YELLOWSTONE
LK
AFR
NB
TB
DIL
LAR
EE
LOF
APP
ASY
TS
OF
ASL
ABT
WT
PR
Idaho
CALDERA
ADC
TC
ISLAND PARK
CALDERA
Wyoming
0
10
20
30
40
50
KM
MF
SE

Figure 4.8

YELLOWSTONE LOCAL EARTHQUAKE INVERSION

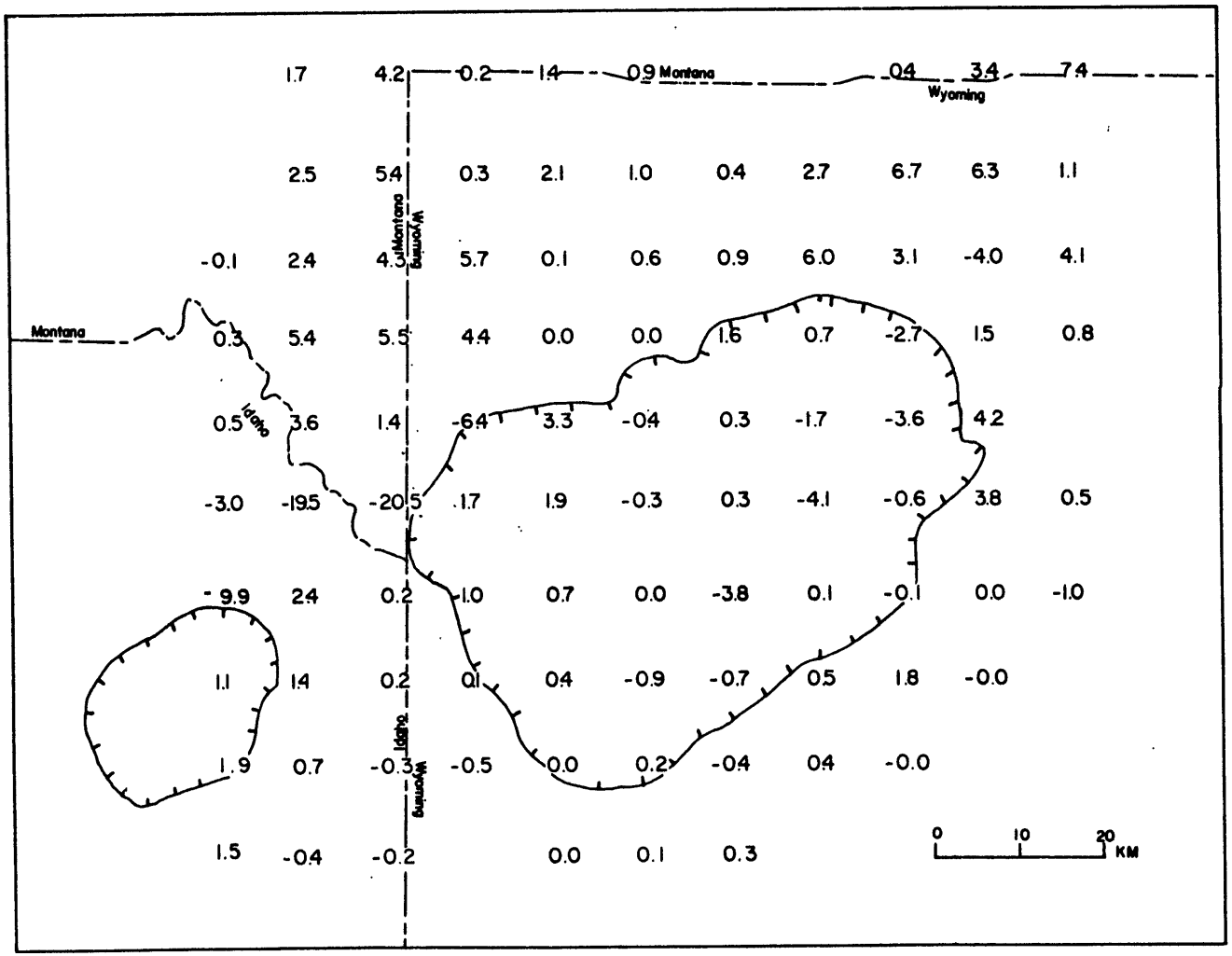

Figure 4.9

YELLOWSTONE LOCAL EARTHQUAKE INVERSION

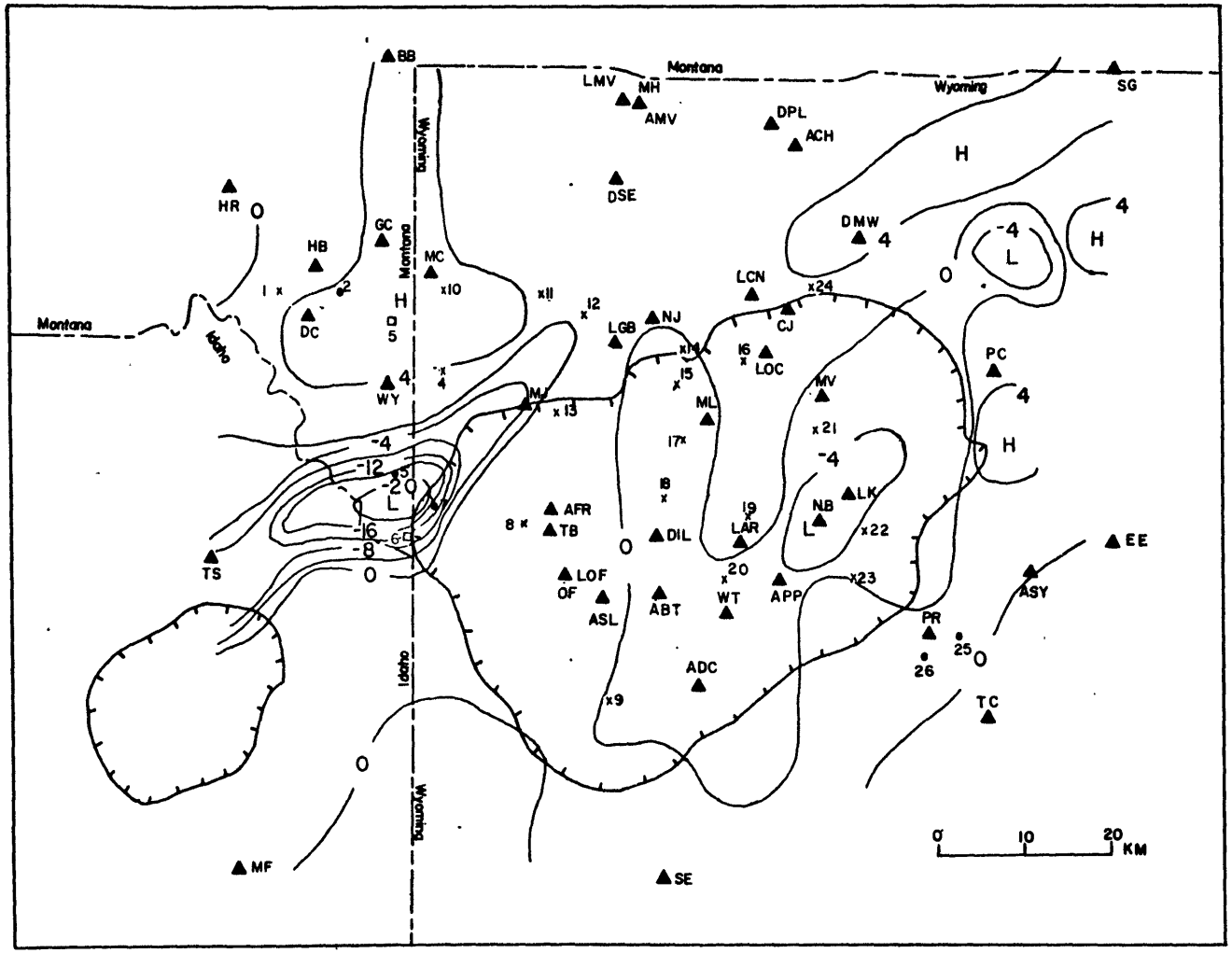

Figure 4.10

COMPLETE BOUGER GRAVITY MAP
YELLOWSTONE - ISLAND PARK REGION
CONTOUR INTERVAL 5 MGALS

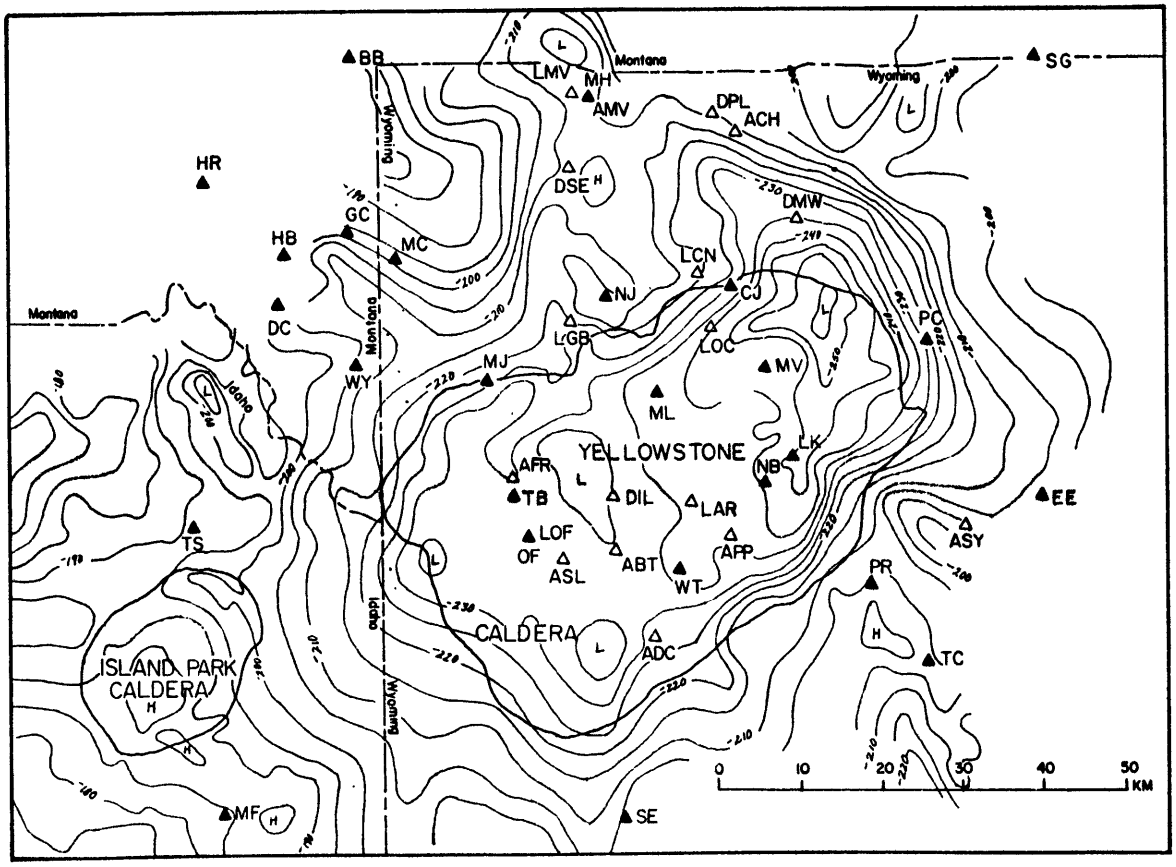

Figure 4.11

Yellowstone Array Diagram
uncorrected

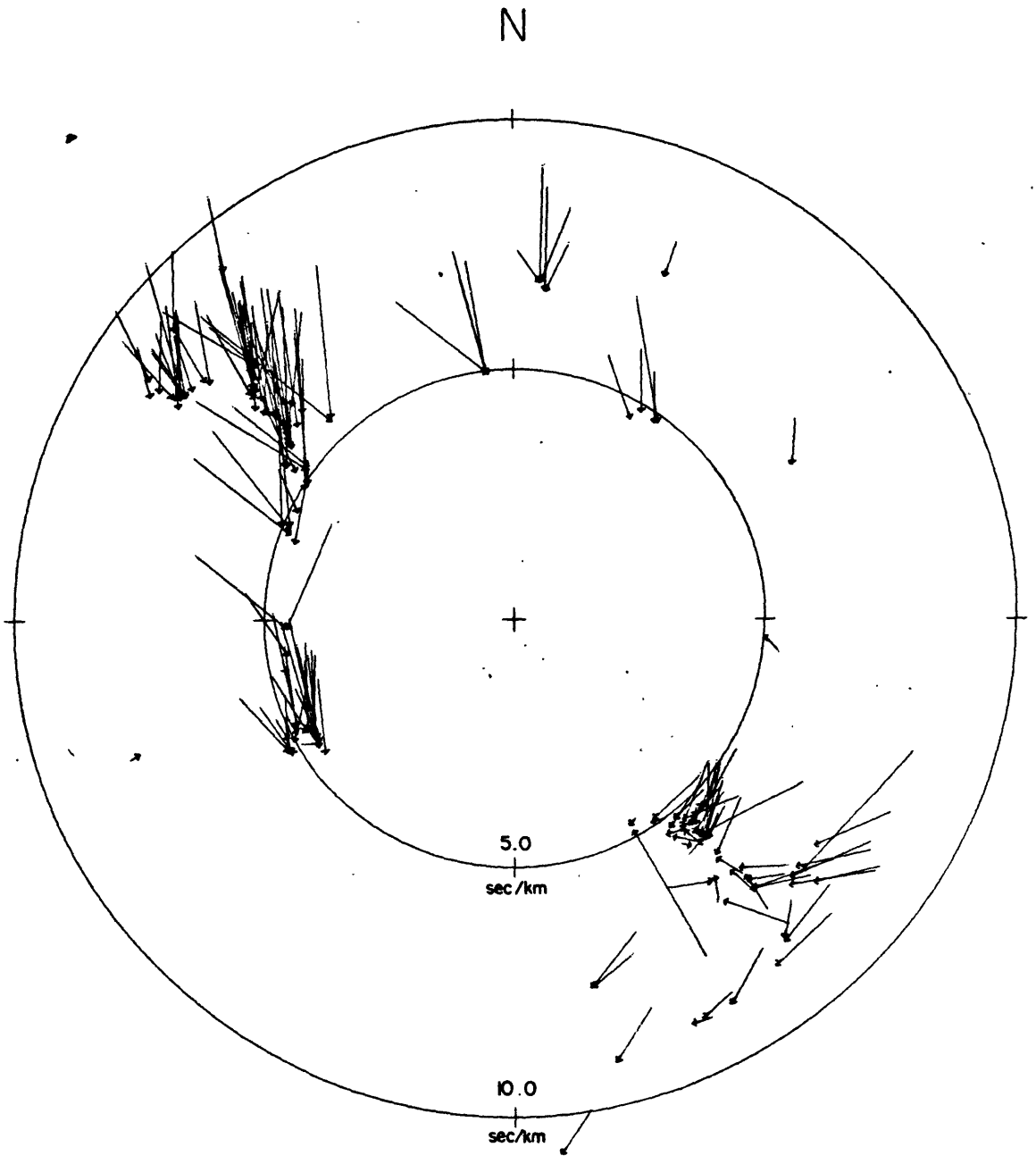

Figure 4.12

a.

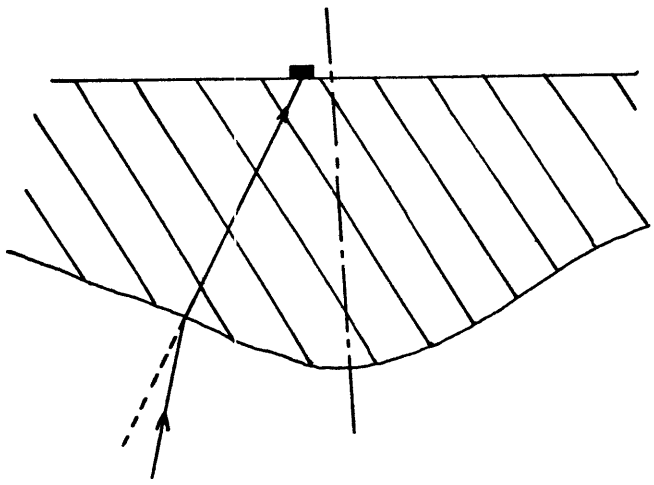

b.

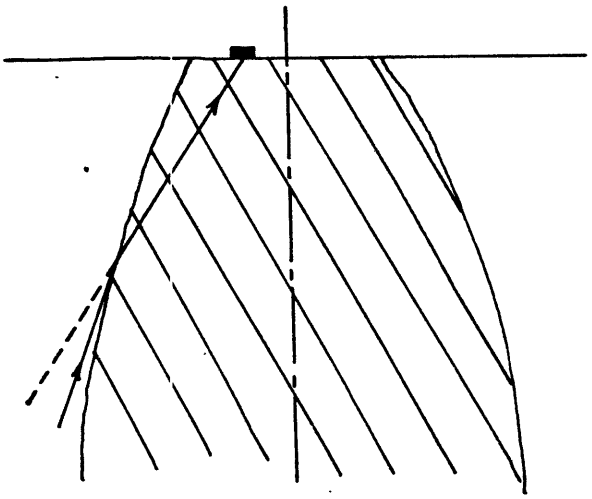

c.

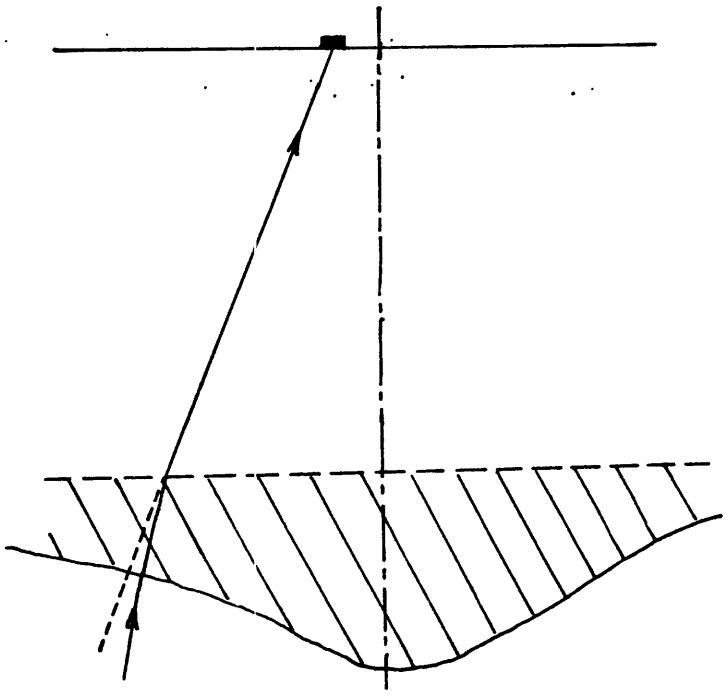

Figure 4.13

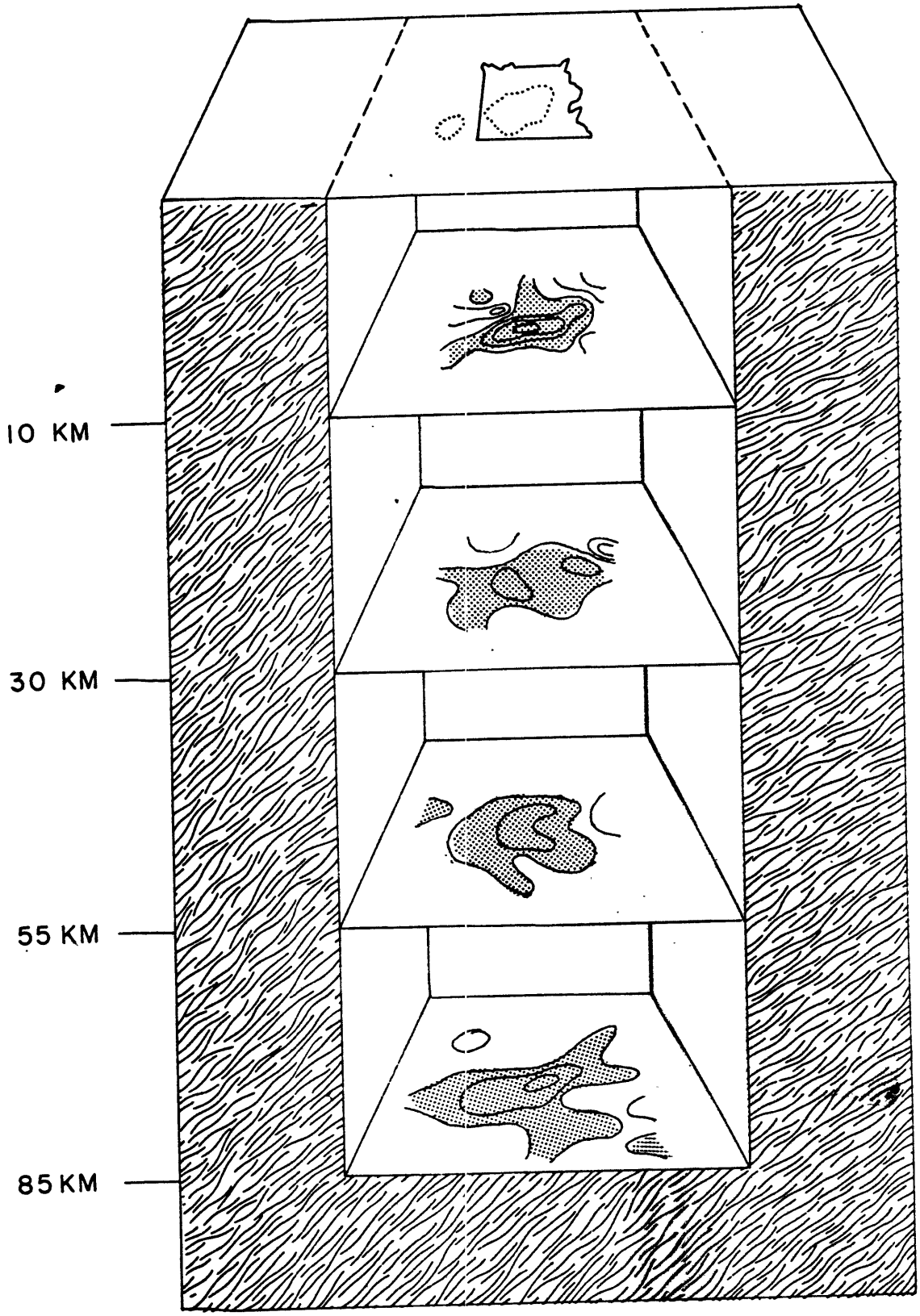

CONTOUR INTERVAL 4%

Figure 4.14

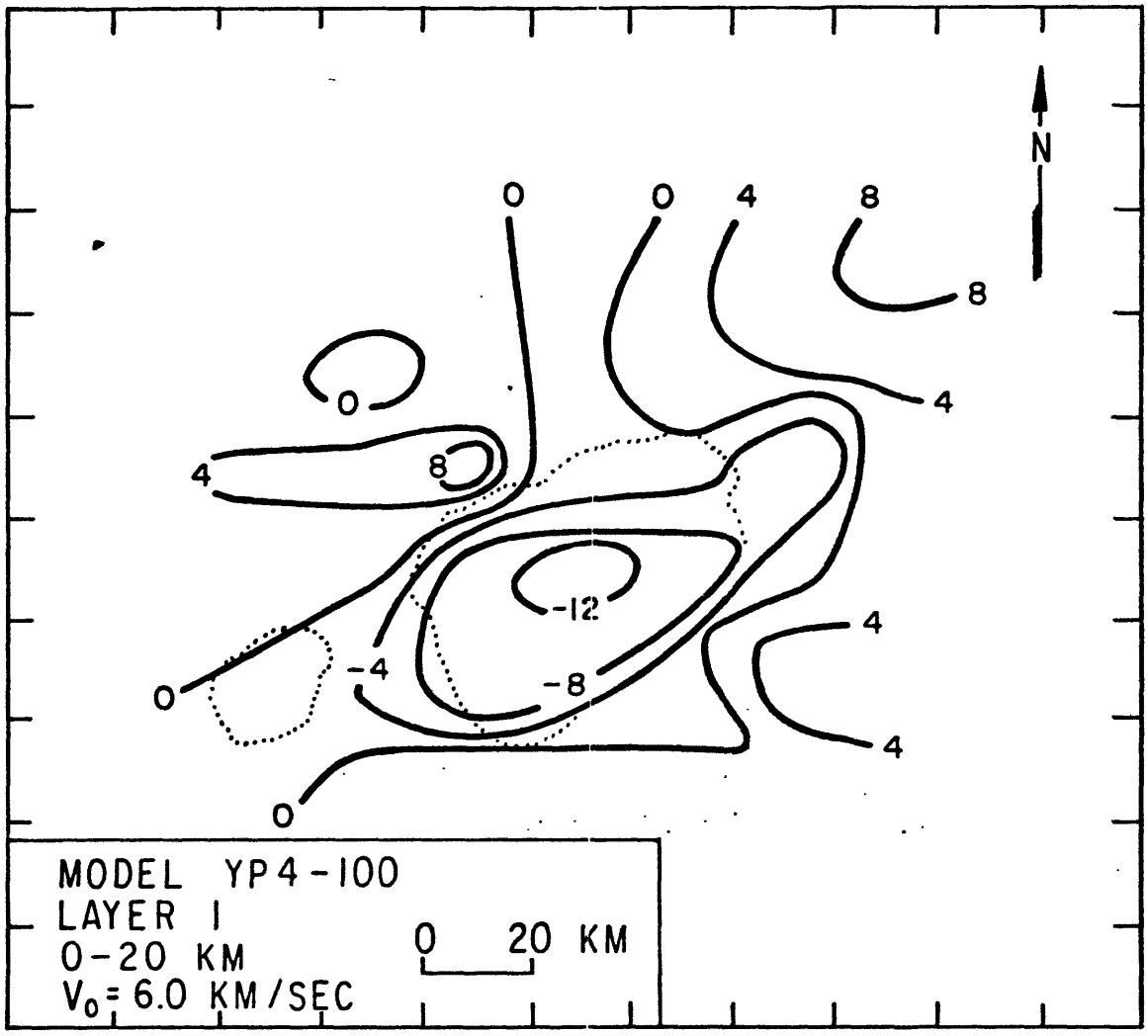
N
0
0
4
8
8
4
0
4
8
-12
4
0
-4
-8
4
0
MODEL YP4-100
LAYER 1
0-20 KM
V_0 = 6.0 KM/SEC
0 20 KM

Figure 4.15

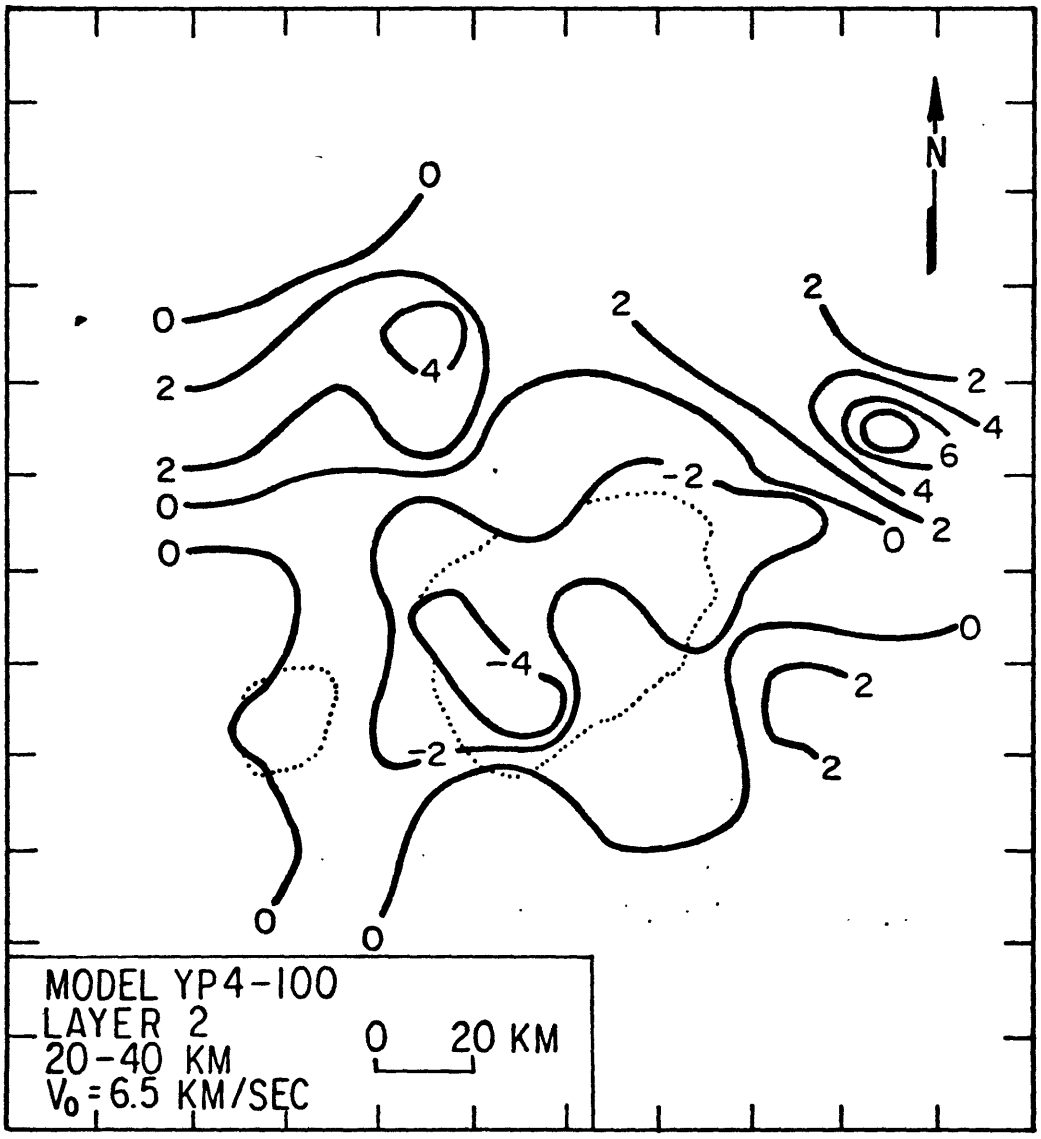
N
0
0
2
2
0
0
4
2
2
2
4
6
4
2
0
-2
0
-4
-2
2
2
0
0
0
MODEL YP4-100
LAYER 2
20-40 KM
V_0 = 6.5 KM/SEC
0 20 KM

Figure 4.16

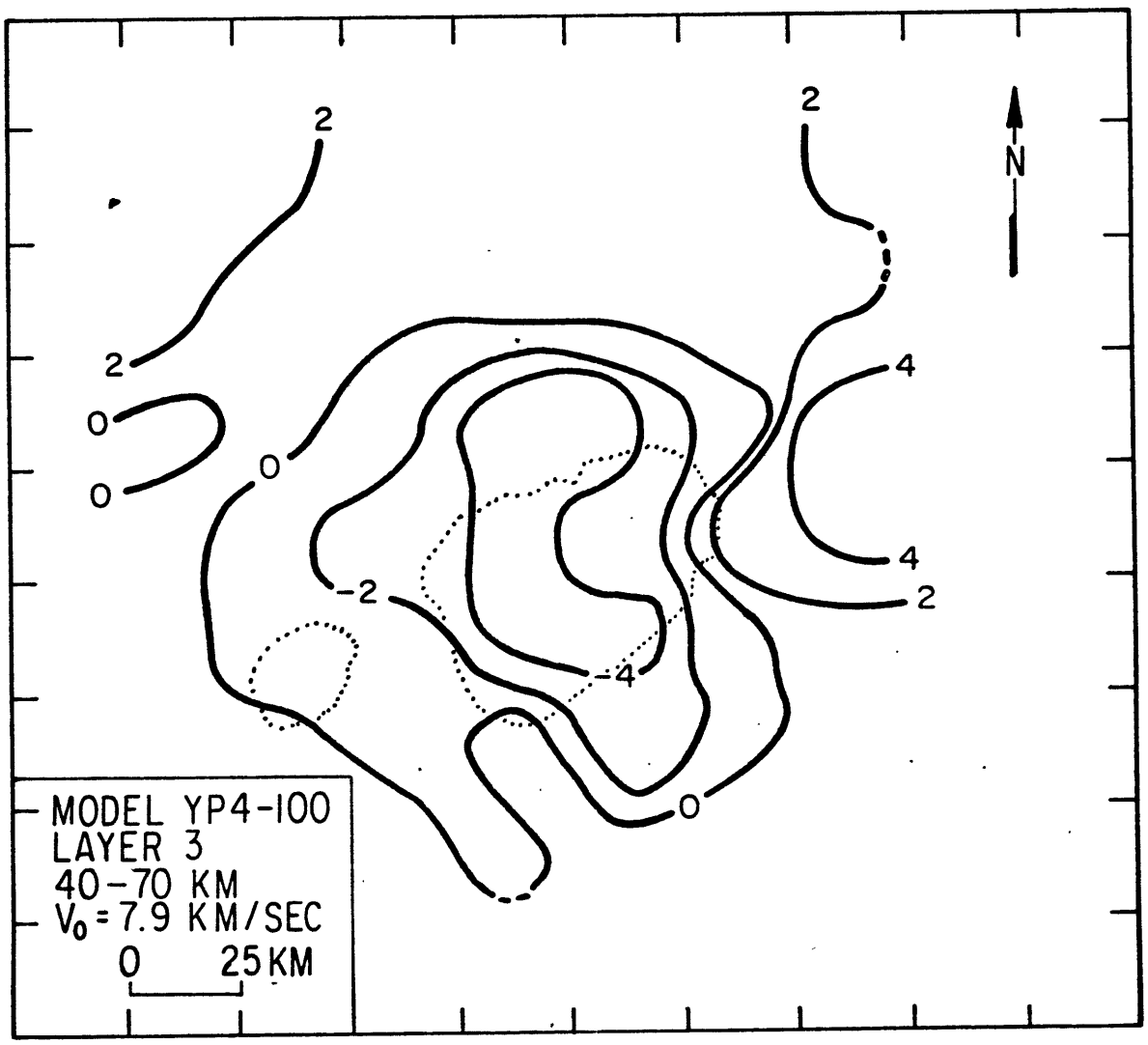
2
2
2
2
0
0
0
-2
-4
0
4
4
2
N
MODEL YP4-100
LAYER 3
40-70 KM
V_0 = 7.9 KM/SEC
0 25 KM

Figure 4.17

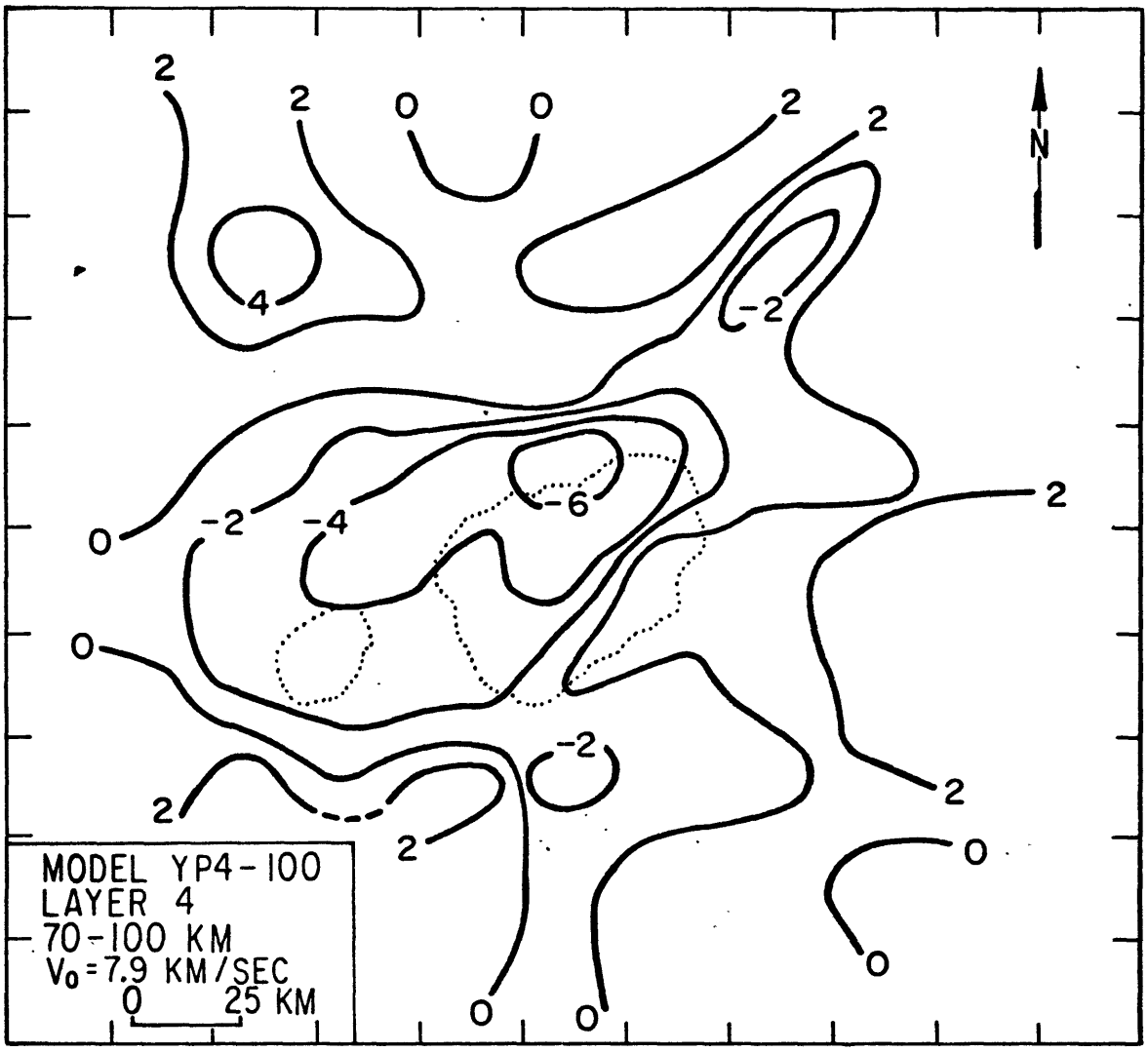
2
2
0
0
2
2
N
4
-2
-6
2
0
-2
-4
0
-2
2
2
2
0
0
0
0
MODEL YP4-100
LAYER 4
70-100 KM
V0=7.9 KM/SEC
0 25 KM

Figure 4.18

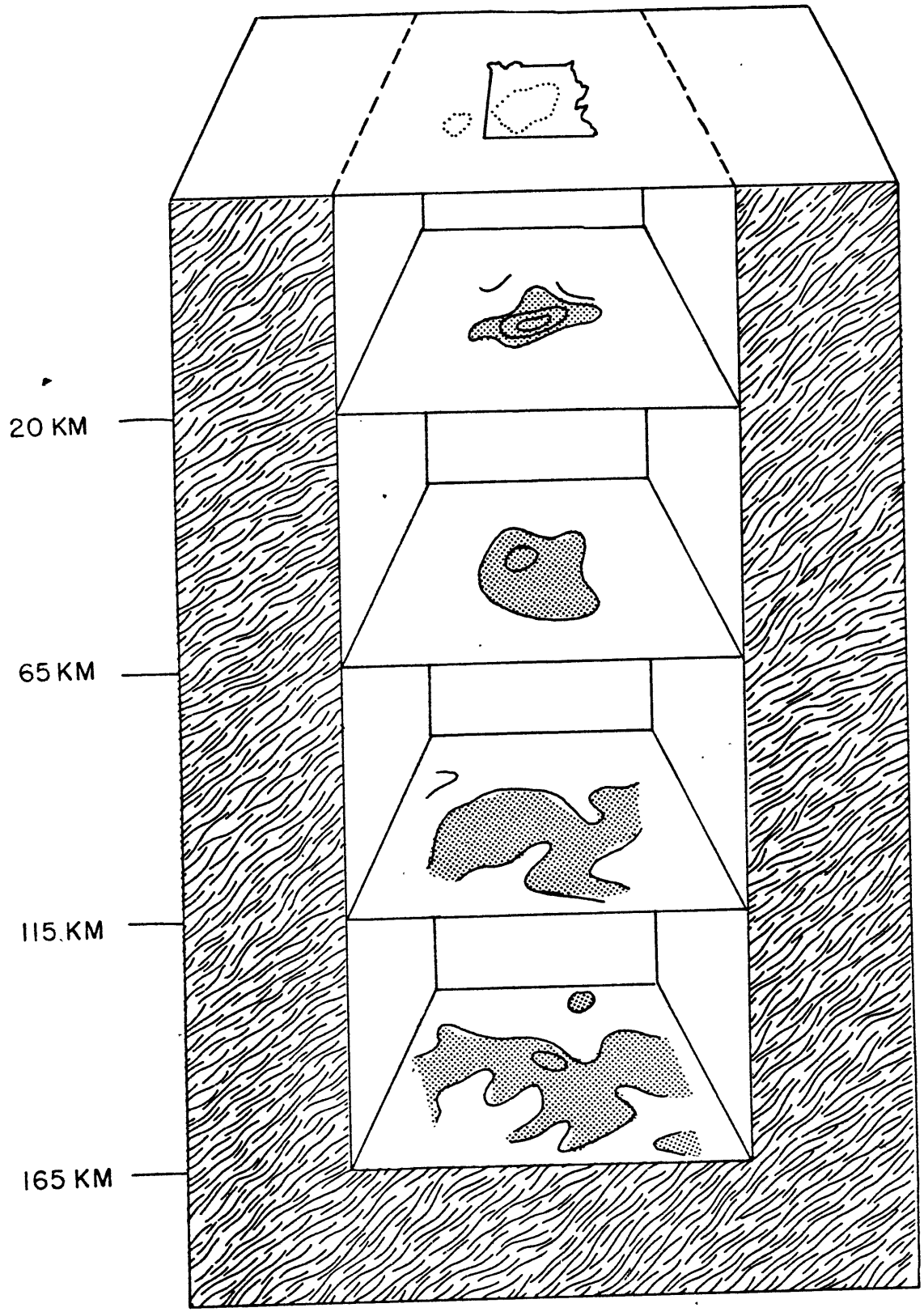

CONTOUR INTERVAL 4%

Figure 4.19

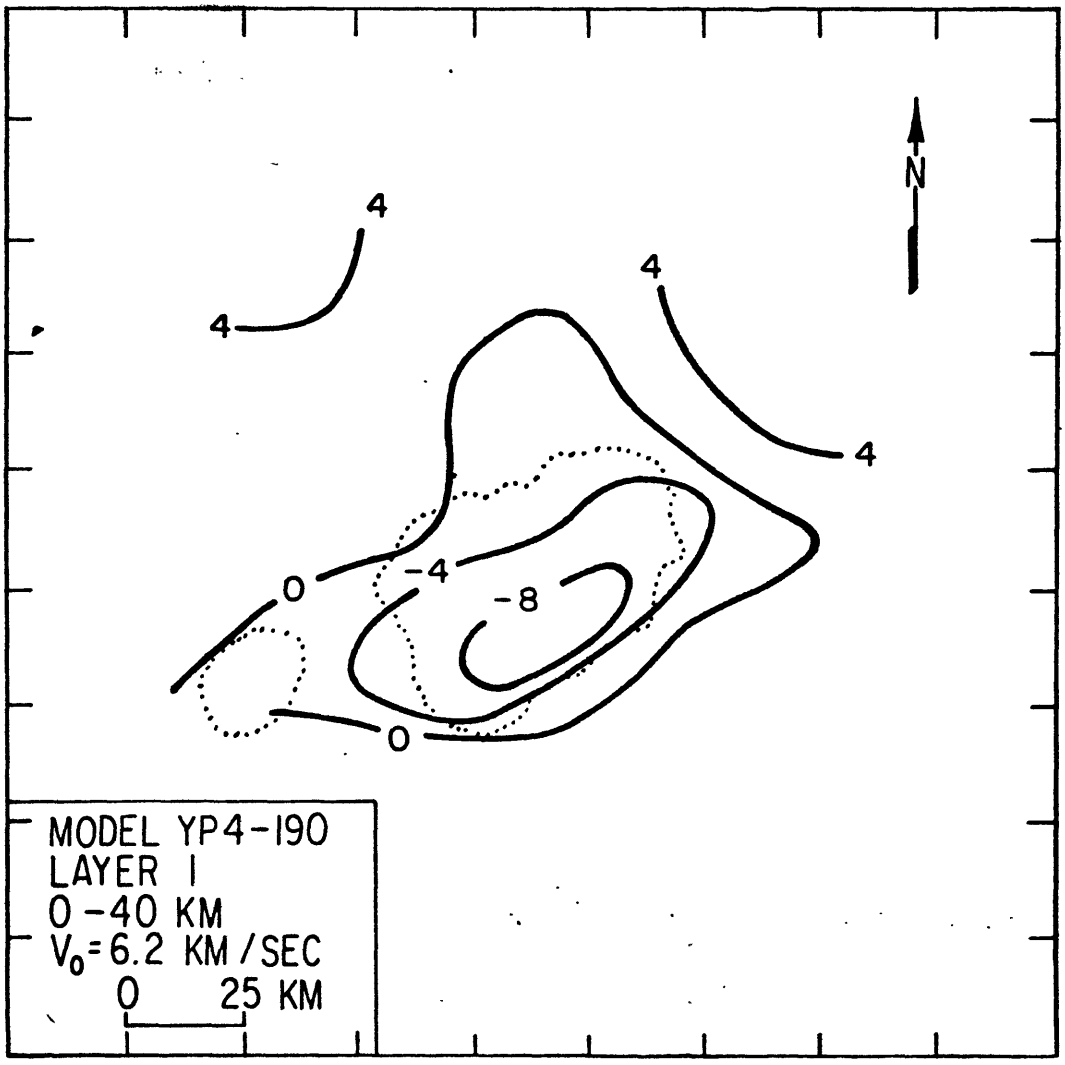

Figure 4.20

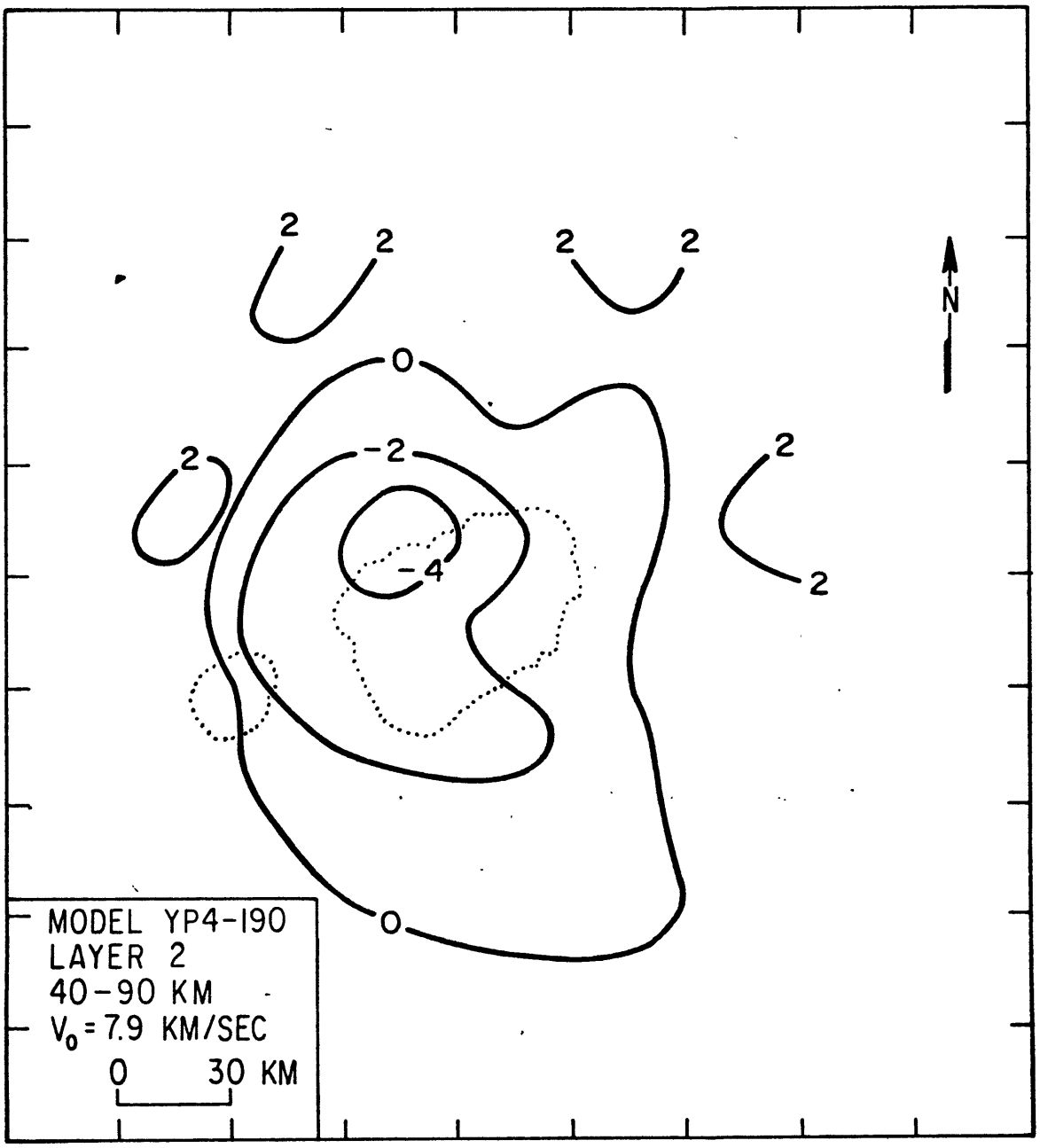

Figure 4.21

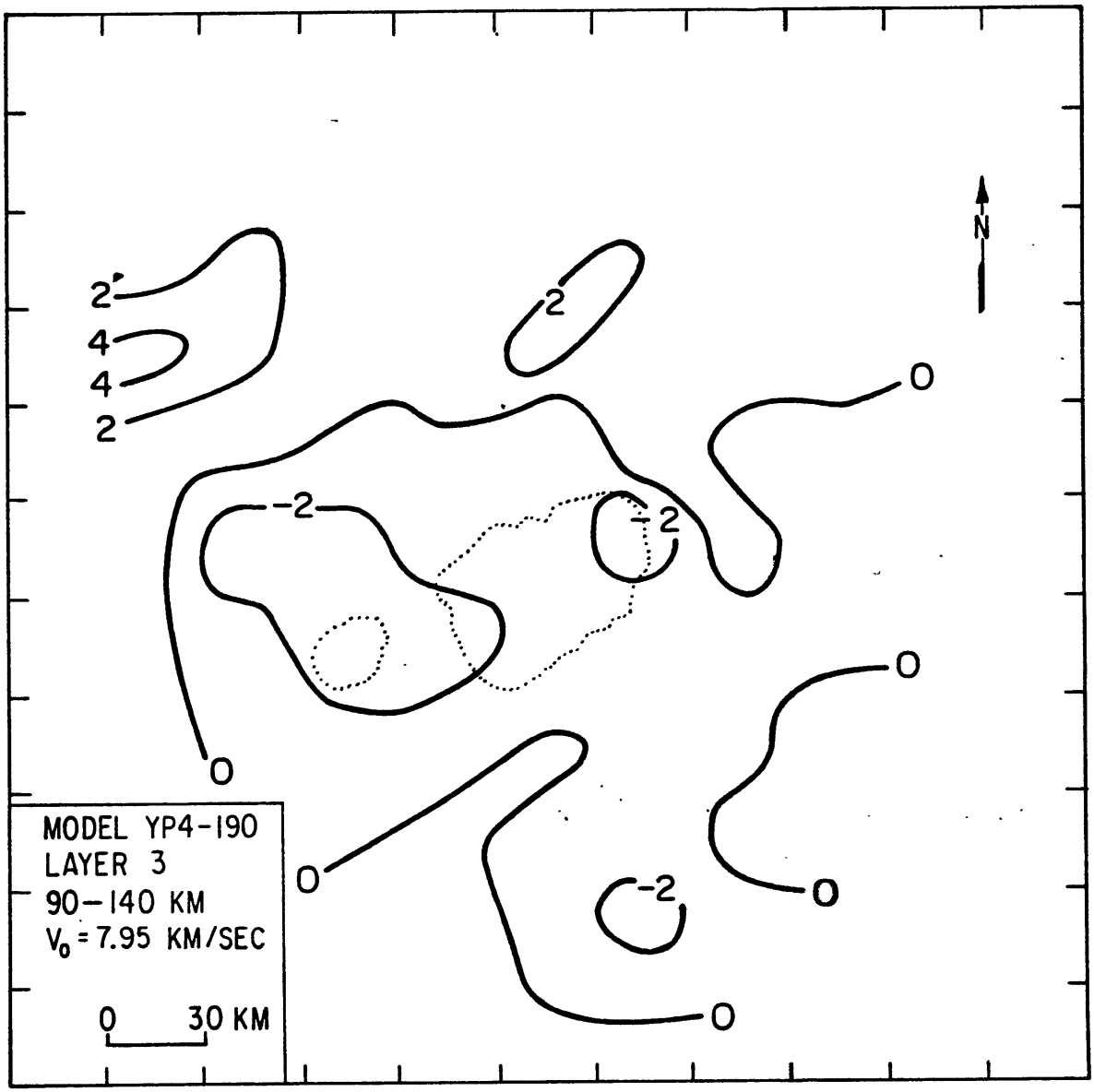
N
2
4
4
2
2
0
-2
2
0
0
0
-2
0
0
MODEL YP4-190
LAYER 3
90-140 KM
V_0 = 7.95 KM/SEC
0 30 KM

Figure 4.22

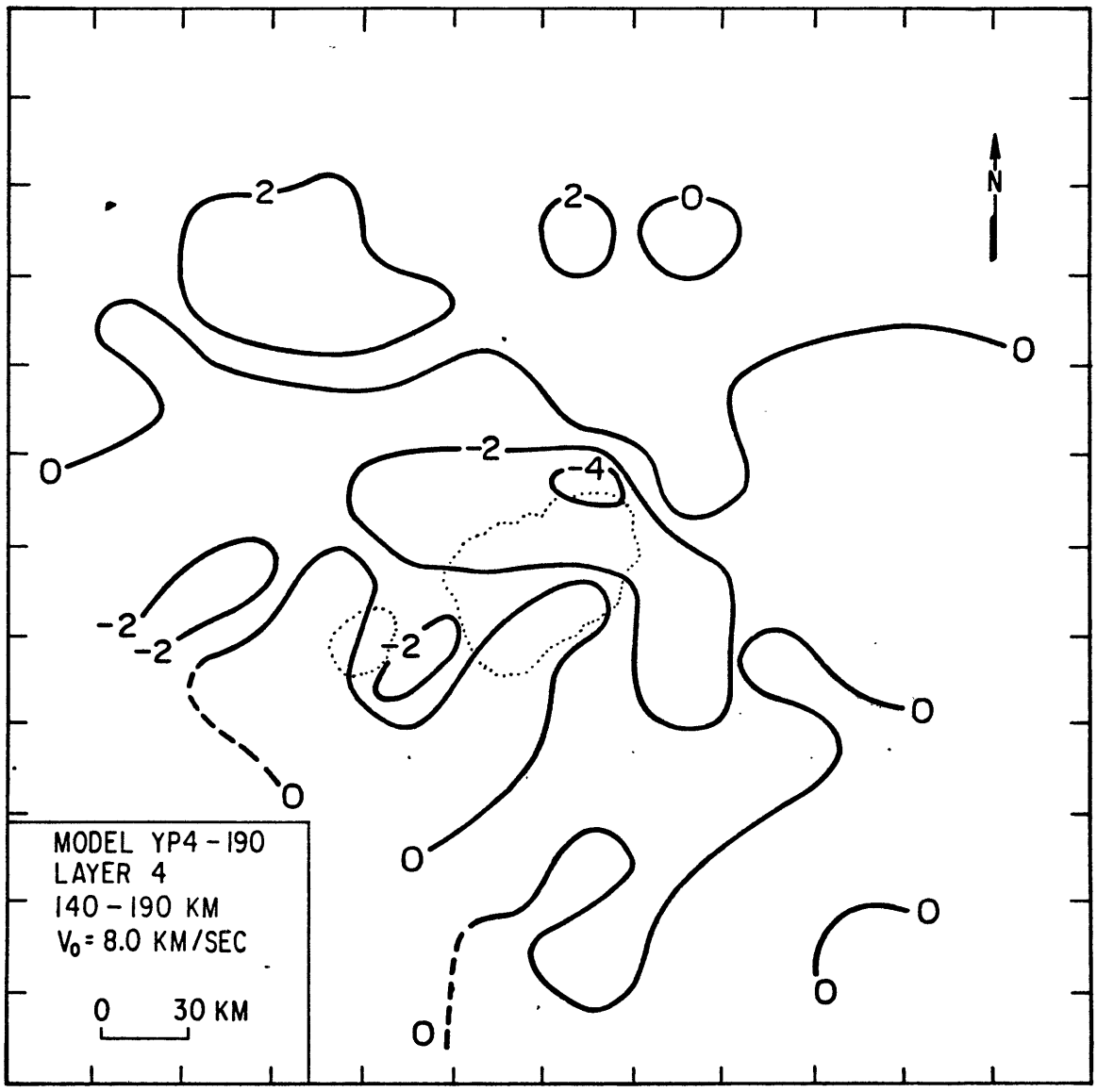
N
2
2
0
0
-2
-4
-2
-2
-2
0
0
0
0
0
0
MODEL YP4 - 190
LAYER 4
140 - 190 KM
V_0 = 8.0 KM/SEC
0 30 KM

Figure 4.23

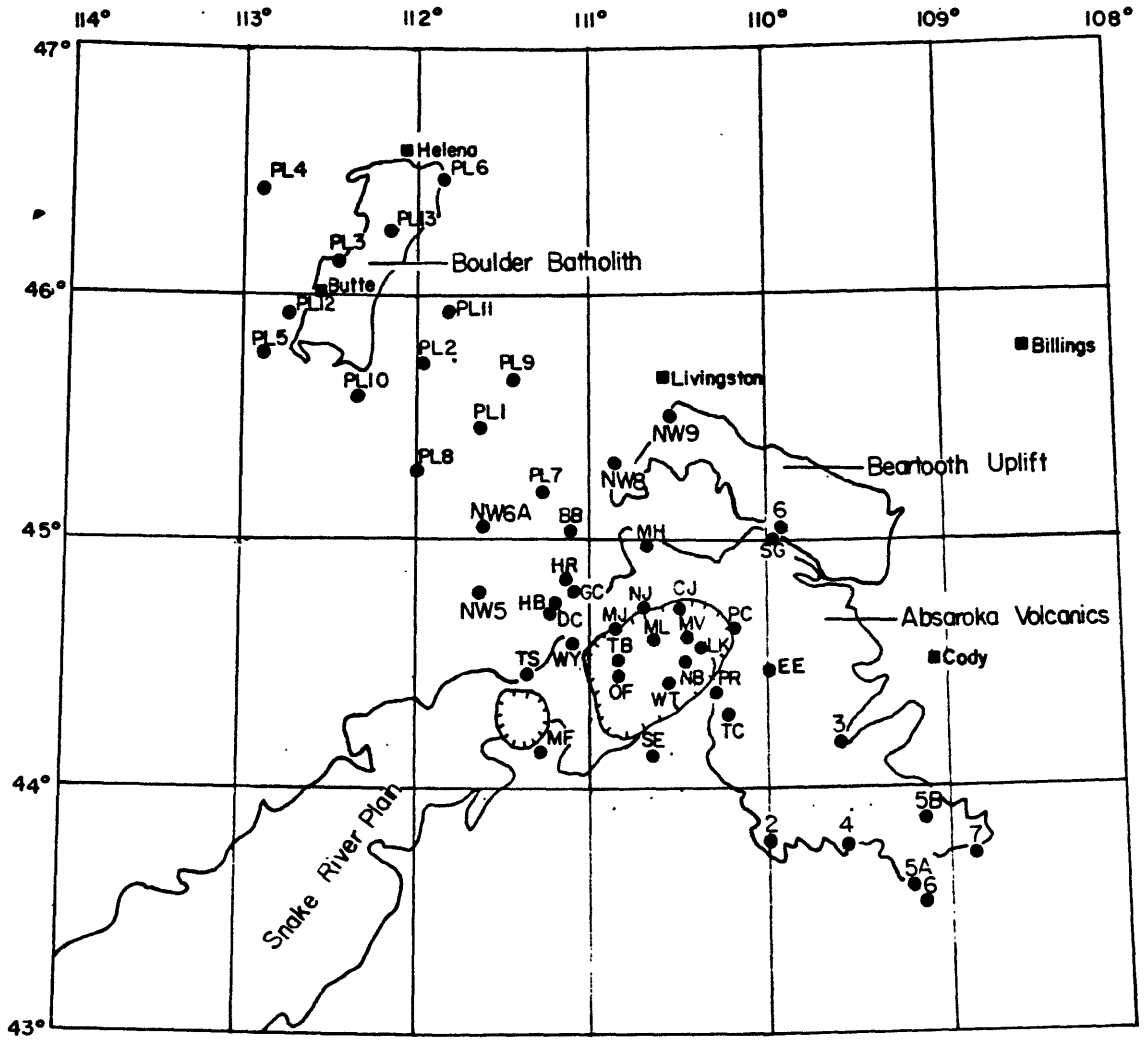
114°
113°
112°
111°
110°
109°
108°
47°
46°
45°
44°
43°
Helena
Butte
Billings
Livingston
Boulder Batholith
Beartooth Uplift
Absaroka Volcanics
Cody
Snake River Plain
PL1
PL2
PL3
PL4
PL5
PL6
PL7
PL8
PL9
PL10
PL11
PL12
PL13
NW5
NW6A
NW8
NW9
BB
HB
DC
GC
HR
MH
NJ
CJ
MJ
ML
MV
PC
LK
TB
WY
TS
OF
NB
PR
WT
EE
TC
SE
MF
SG
1
2
3
4
5A
5B
6
7

Figure 4.24

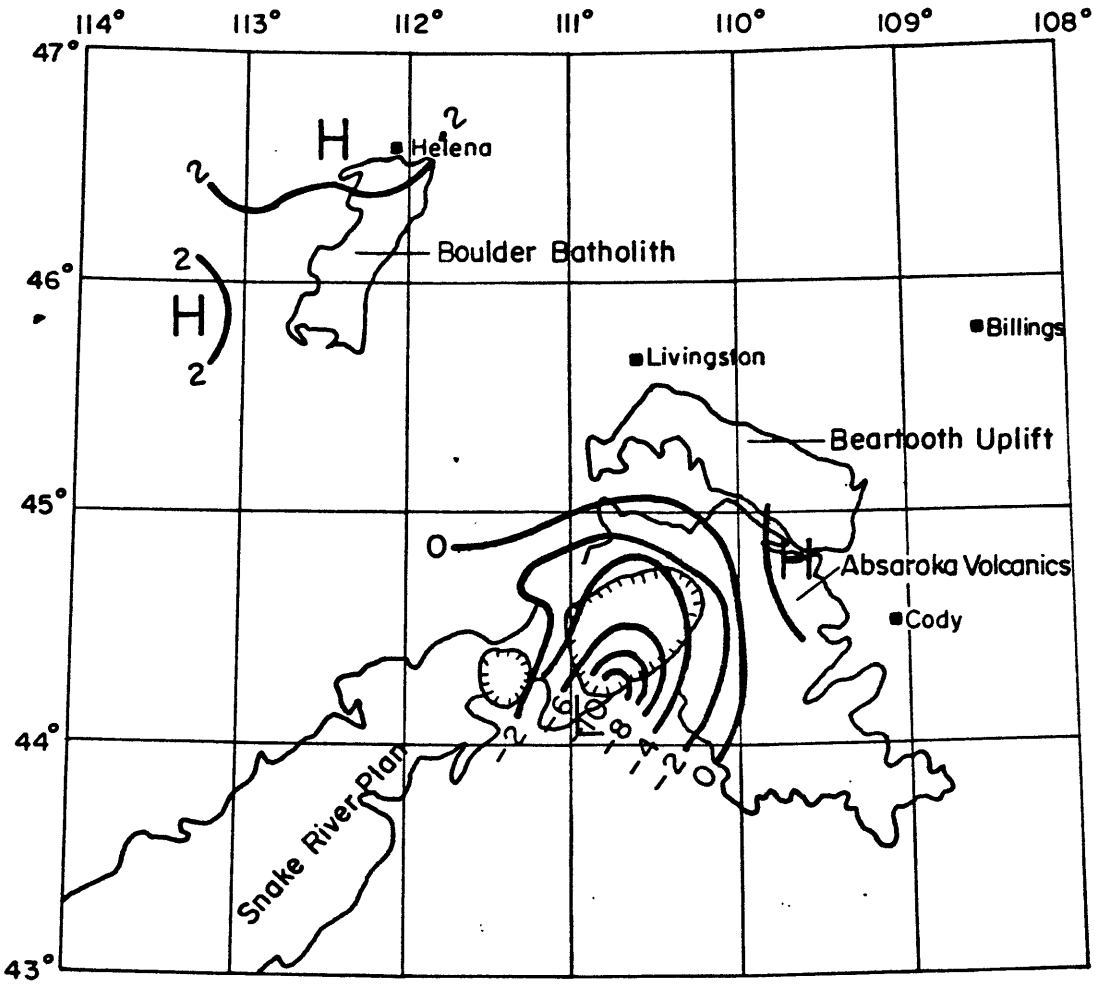

Layer 1: 0-40 km

V_o = 6.2 km/s

Figure 4.25

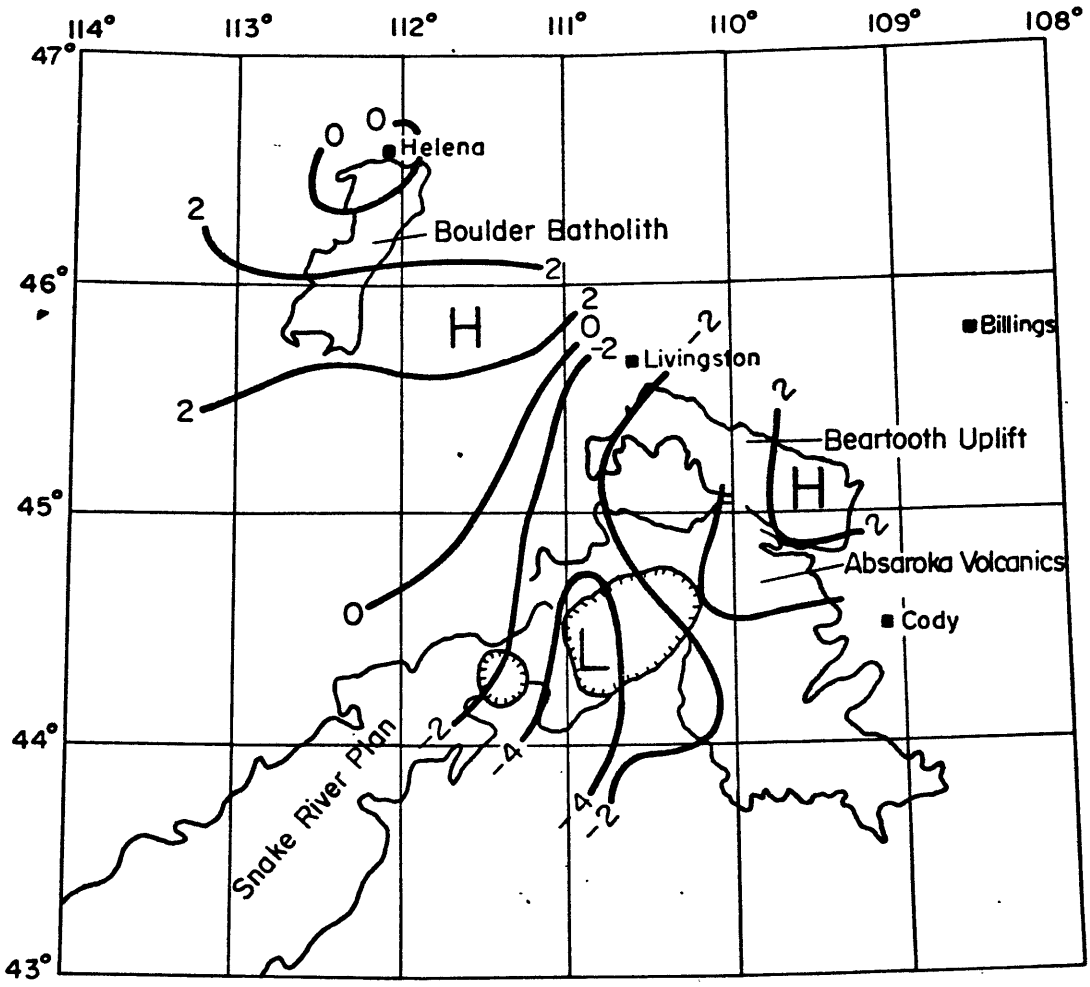

Layer 2 : 40–90 km
V_0 = 7.9 km/s

Figure 4.26

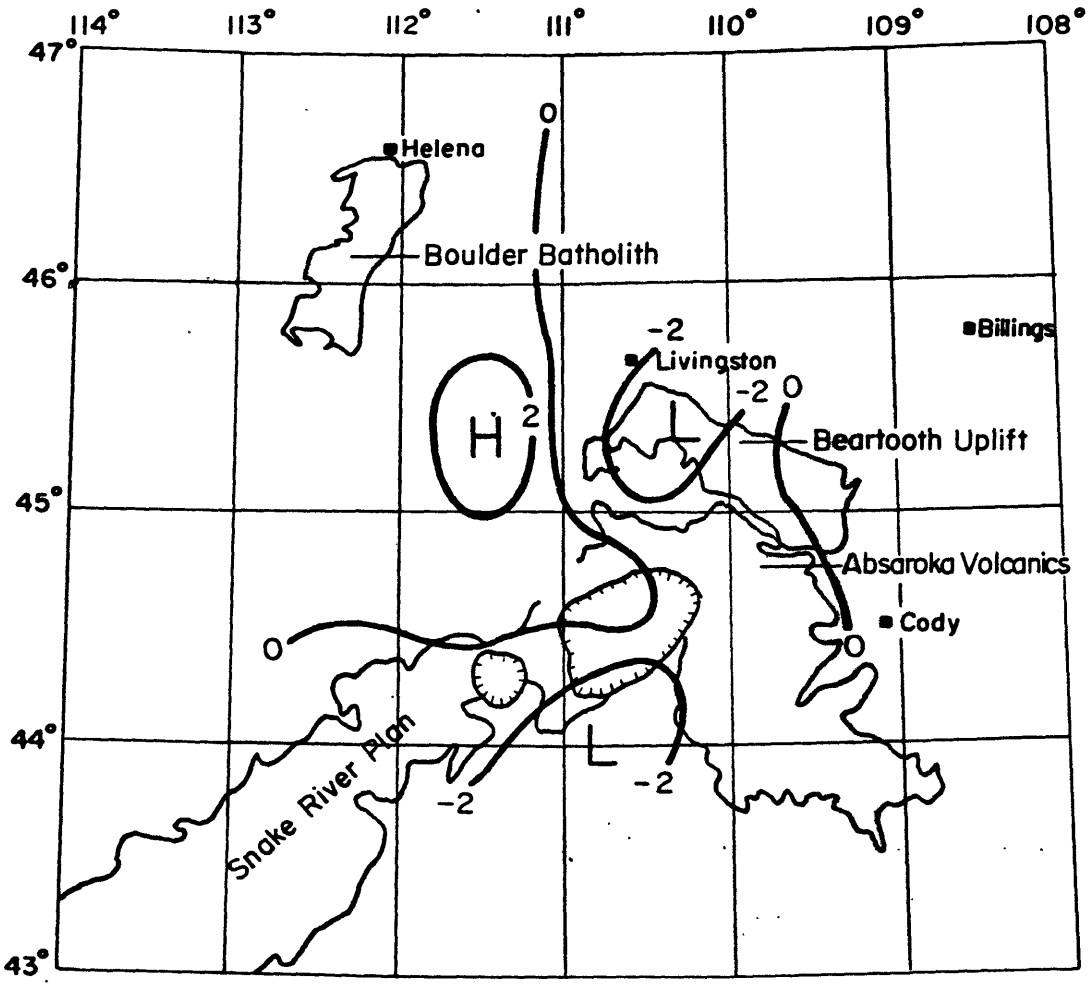

Layer 3: 90-140 km

V_o = 8.3 km/s

Figure 4.27

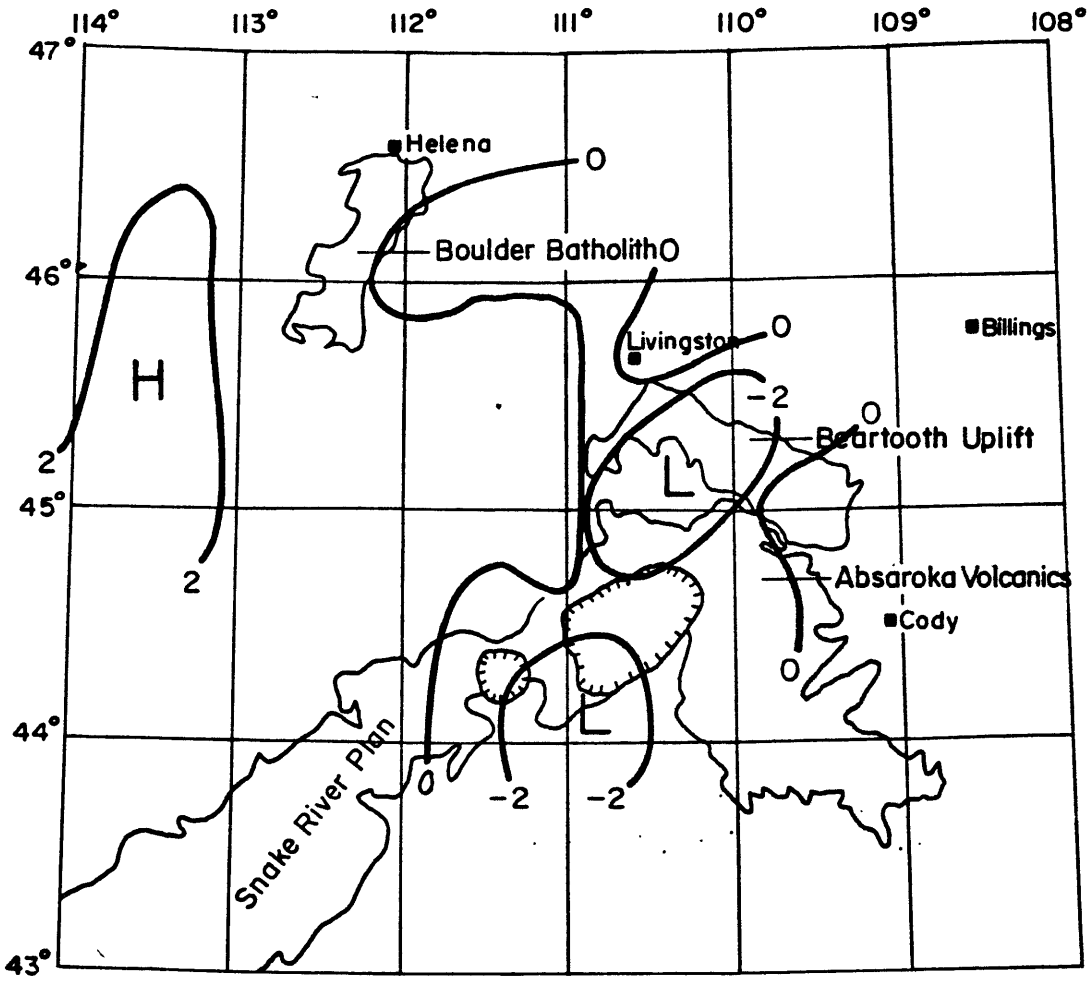

Layer 4: 140-190 km

V_0 = 8.1 km/s

Figure 4.28

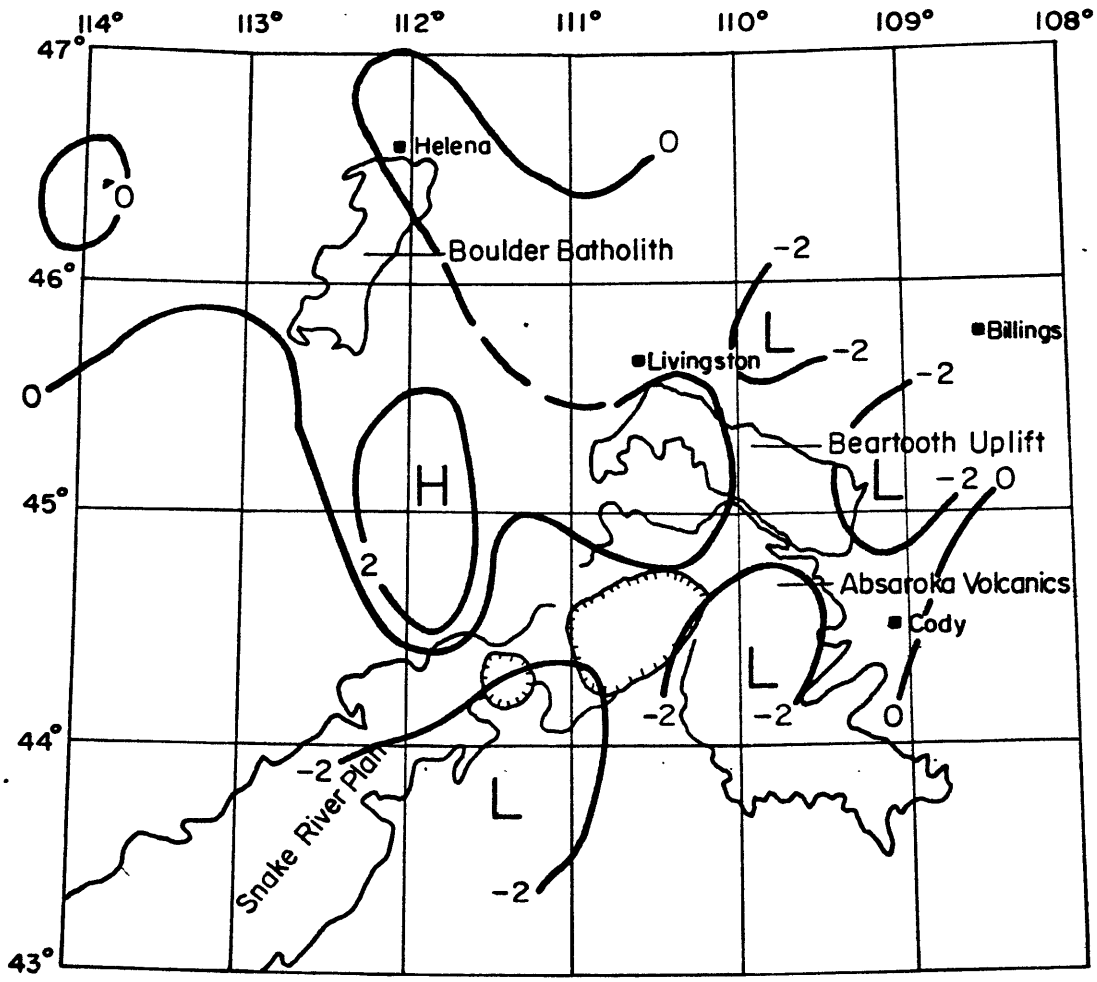

Layer 5: 190 – 240 km

V_0 = 8.4 km/s

Figure 4.29

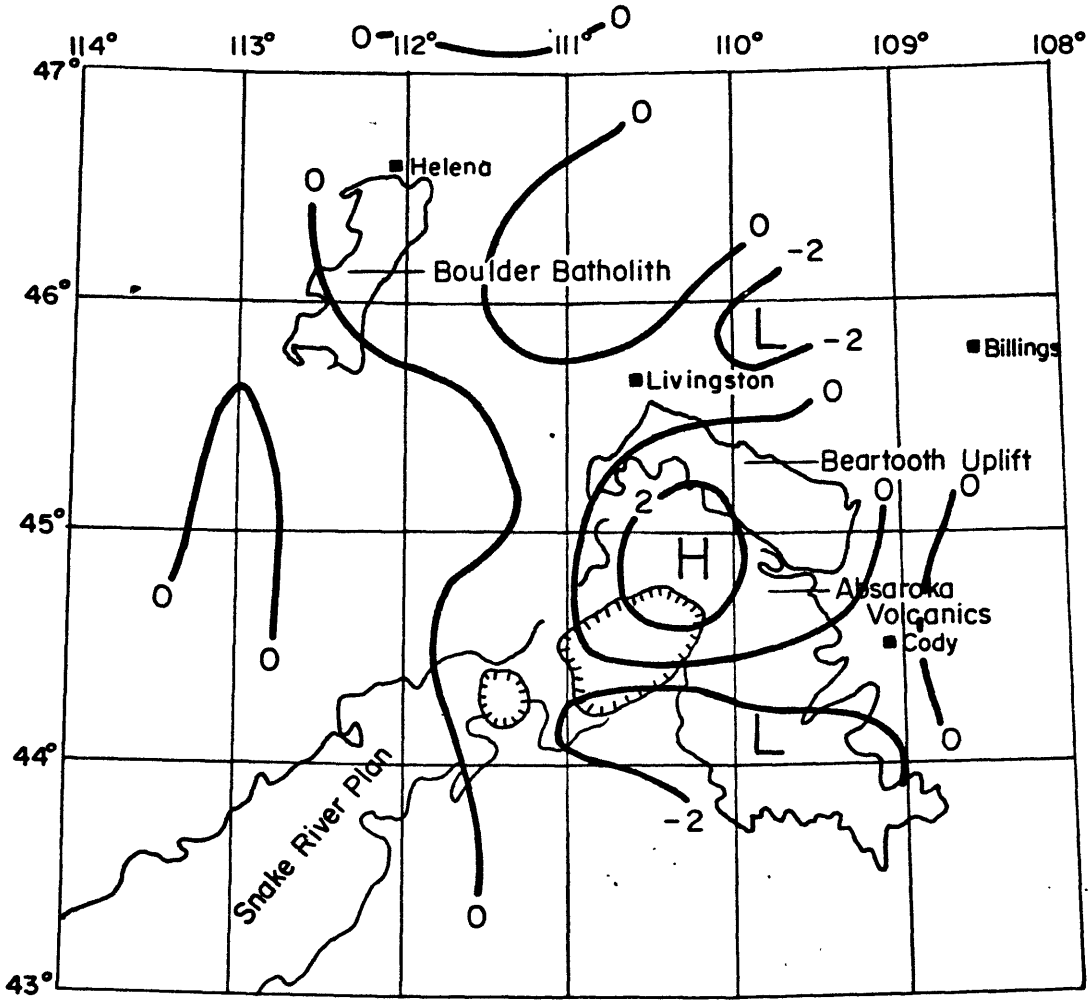

Layer 6 : 240–290 km

V_0 = 8.6 km/s

Figure 4.30

CHAPTER V. INTERPRETATIONS AND CONCLUSIONS

The pattern and magnitude of heterogeneity in the upper mantle beneath the Coast Ranges, California, and Yellowstone, Wyoming, were derived and described in the previous two chapters. In this chapter we attempt to provide interpretations of the heterogeneity which are consistent with tectonic histories and other geophysical measurements. Since crustal layers have been discussed in detail in the previous chapters, the upper mantle is the primary subject in the following sections. Yellowstone is considered first in section 5.1, followed by a discussion on California in section 5.2. A regional synthesis is attempted in section 5.3. Finally, the major conclusions of this work are iterated in section 5.4.

5.1 YELLOWSTONE SUMMARY

The Yellowstone low-velocity anomaly is deeply rooted in the upper mantle; however, the deep model indicates the anomaly dissipates near 250±50 km depth. Other important features of the deep anomaly are: 1) it is aligned with the NE trend of the Snake River Plain; and 2) it extends northeast of the surface termination of volcanism in Yellowstone. In the following the implications of the anomaly features for the various plume and fracture models are considered.

Thermal Plume. In Morgan's (1971) concept of thermal plumes,

they are manifestations of convection in the lower mantle. Morgan (1972b) envisions the plumes as cylindrical low-velocity features about 150 km in diameter rising 2 m/yr and spreading out in the asthenosphere at the base of the lithosphere. From our results it is not entirely possible to dismiss thermal plumes as the causative agent, but there are several features inconsistent with the plumes as described by Morgan (1972b). The linear form of the low-velocity anomaly was not predicted. However, this could be due to the rise of a thermal plume into a linear weak zone or due to a thermal heating track in the lithosphere. The data and inversion model place the deepest significant low-velocity anomaly no deeper than 250 km. This, again, is not consistent with the deep mantle thermal plumes which ought to be marked by a through-going low-velocity anomaly.

Plume with Gravitational Anchor. Shaw and Jackson (1973) replaced the deep mantle position of the thermal plume with their model of a sublithospheric melting spot held in place by a gravitational anchor of dense residual material that sinks down to the core-mantle boundary. This type of mantle should exhibit low velocities in the crust and uppermost mantle with a velocity reversal at some depth and a high velocity anomaly near the core-mantle boundary. Perhaps the dissipation of the low-velocity anomaly near 250 km is the anticipated velocity reversal. Evans (1977) studied PKIKP travel time residuals at the Yellowstone array and found the delays almost the same as those for the direct P-wave. He

concluded that no columnar deep mantle velocity anomaly of the lateral dimensions observed at shallower depths exists beneath Yellowstone. This evidence, if collaborated, eliminates as plausible models the deeper thermal plume and possibly also the gravitational anchor model for Yellowstone; unless the deep structure is displaced at depth from the vertical line beneath Yellowstone, thus accounting for its noneffect on the PKIKP data.

Chemical Plume. A new plume model has recently been proposed by Anderson (1975). His plume is due to chemical inhomogeneity in the lower mantle. These chemical aggregates rise due to their lower density, eventually forming mushroom-like blobs at the base of the lithosphere. The seismic features of the chemical plume are similar to that of the gravitational anchor plume with the exception that the former lack the substantial high-velocity anomaly in the deep mantle. Thus a chemical plume is marked by low velocities in the upper mantle to 200-300 km depth and slightly high velocities below that depth. Of all the plume models, Anderson's (1975) is closest to satisfying the deep model velocity structure derived in Chapter IV and the constraint imposed by the PKIKP data.

Before continuing on with a discussion of fracture propagation models, we need to consider the question of the thickness of the lithosphere in the vicinity of Yellowstone. The lithosphere-asthenosphere boundary is not well constrained for a particular location. Wiggins and Helmberger (1973)

modeling body waveforms obtained an average value for the western U.S. of 160-170 km to the top of the low-velocity zone. Other studies have placed the boundary much shallower (50-60 km) but these models usually average in the Basin and Range Province which is thought to have a much thinner lithosphere than the rest of the western U.S. There are also some important questions about the validity of equating the seismic low-velocity zone with the mechanical definition of the lithosphere-asthenosphere boundary as the zone of decoupling, but such questions are beyond the scope of this discussion.

Propagating Fracture. In this class of models, a tensional through-going fracture migrates through a moving lithosphere. Hydrostatic forces produce an upwelling of magma into the fracture resulting in the linear, age-progressive volcanics of a hot spot trace. These models were first proposed to explain linear, oceanic volcanic island chains (Green, 1971; McDougall, 1971) and later applied to the western U.S. (Smith, 1977; Christiansen and McKee, 1978).

There is considerable evidence documented in Chapter IV that the Yellowstone hot spot is at least guided by a lithospheric weak zone inherited from Precambrian tectonics. The evidence that the fracture zone is a rejuvenated Precambrian feature deflates the notion that it is a newly propagating fracture due to doming of the lithosphere above a plume. Yet the evidence that the anomaly extends down to

nearly double the lithospheric thickness implies that it is not strictly a lithospheric process; upwelling in the asthenosphere and perhaps deeper must play a part in the process.

The linearity of the low-velocity anomaly associated with the deep structure beneath Yellowstone fits well, although not uniquely, to fracture models. The fact that the anomaly at depth extends northeast of Yellowstone could be explained by a process where the fracture initiates near the bottom of the lithosphere and grows upward. This might also explain the increasing width of the anomaly with depth.

Arguments against the fracture hypothesis include the question of the depth of the anomaly and the relative motion of hot spots. If the hot spot is due to the tensional fracture of the lithosphere, is it reasonable for the velocity anomaly to extend another lithosphere thickness into the asthenosphere? One answer could be that the lithosphere is nearly 250 km thick at Yellowstone. Another is that a partial melt 'root' might grown downwards as the melt from the surrounding mantle migrates to and feeds the upwelling into the fracture.

A more troubling question is that of the relative motion of hot spots. Major plate reconstructions by Molnar and Atwater (1973) demonstrate that mantle hot spots including Yellowstone move at rates of 0.8 to 2 cm/yr with respect to one another. They concluded that hotspots do not provide a fixed reference frame and this removes a strong impetus for rooting them in the lower mantle. However, the

fact that hot spots move at such slow rates with respect to each other implies that they are not random, superficial features, but are somehow tied to some common frame of global motion in the upper mantle. The implication is that hot spots "choose" their fracture carefully; not every fracture is accompanied by a hot spot which implies that some upper mantle mechanism is involved.

From the above discussions it is obvious that the evidence presented in this thesis, or for that matter, all the accumulated evidence does not clearly define a succinct model for the mechanism of the Yellowstone hot spot.

The preferred model is one in which an old weak zone in the lithosphere is reactivated by stresses produced by major plate rearrangements. For example, the first Snake River basalts were erupted 17 m.y. ago during a period when the western U.S. was undergoing the transition from a compressional to a tensional stress regime. Once an old weak zone is ruptured and starts to rift, magma upwells to fill the gap. The initial upwelling probably first depletes the partial melt zone immediately below the fracture but if eruptions continue deeper sources must be tapped to "feed" the fracture. This could be the process by which a deep partial melt "root" grows. In this model the magmatic activity initiates as essentially a passive response to lithospheric forces but which perhaps induces convective motion in the asthenosphere. If the stress system is such that the rifting propagates through the lithosphere, it is

reasonable to assume the magmatic activity would also migrate along the rift providing the observed age progression.

An attractive feature of this model is that it can also explain the northwestern progression of increasingly younger volcanics in southern Oregon described in Section 4.5. The scissors-like rifting of the Snake River Plain could itself establish a secondary stress system responsible for a northwestward propagating deformation zone. The secondary nature (incomplete rifting?) of the southern Oregon zone of deformation may be the explanation for the presence of rhyolite domes only and the lack of flood basalts. Another feature more understandable with the fracture hypothesis is the continuous nature of volcanism along the entire Snake River Plain (Armstrong, 1975). Unlike Hawaii where the volcanism dies out progressively as the hot spot migrates onward, the Snake River has had sporadic eruptions along its entire length up to nearly the present.

Before concluding this section a brief comment is made on the significance of the 250 km bottoming depth of the Yellowstone anomaly. From section 4.1.2 recall that Eocene (40-55mya) volcanic rocks in the Yellowstone region imply that a Middle Cenozoic subducting plate existed beneath the area at a depth of 150 to 300 km. Also, Wyllie (1971) suggested that magma generation begins with diapiric uprise from the base of the asthenosphere, at depths of about 300 km; and that the uprise may be triggered by the outward migration of

water from within the deep mantle or the influx of water into the asthenosphere from a downgoing oceanic lithosphere. Solomon (1972) constructed a model for Q^{-1} in the western U.S. in which the asthenosphere is several hundred kilometers thick; therefore, the bottom of the Yellowstone anomaly does appear to extend down near the bottom of the asthenosphere. The implication is that the magma may originate at that depth as Wyllie suggested. An alternative explanation is that the bottom of the asthenosphere acts as a barrier to the further downward growth of the low-velocity root from the bottom of the lithosphere.

5.2 CALIFORNIA SUMMARY

Some of the pertinent results from the study of California presented in Chapter III are reviewed first. We found that velocity anomalies defined linear trends which correlated with major geologic features of the Coast Ranges. In layers 1 and 2 (0-30 km) the San Andreas fault between San Francisco and Parkfield approximately separated high velocities on the southwest from lower velocities on the northeast. In layer 3 (30-60 km) the trends of the anomalies appear to parallel the Calaveras-Hayward faults north of Hollister and continue parallel to the San Andreas south of Hollister. Also, a 100 km wide zone of low velocities underlies and parallels the Coast Ranges east of the San Andreas from about 26.5°N to at least 39°N. Anomalies in the bottom layer (60-90 km) no longer display the northwest-southeast linearity and are random and irregular, perhaps an indication that the asthenosphere has been reached.

The interpretation of the two crustal layers is relatively straightforward and presented in detail in Chapter III. Basically, we demonstrated a very close correlation with surface geology.

Now we return to the interpretation of the upper mantle layers. Within our knowledge of the late Cenozoic tectonic evolution of California, there are several different structures we might expect: 1) a "normal" continent-ocean transition; 2) a remnant of the subducted East Pacific Rise

"trapped" beneath the leading edge of the North American plate; 3) a wide through-going shear zone associated with the Pacific-North American transform plate boundary.

There is the possibility that the deep structure beneath coastal California simply reflects a "normal" continent-ocean transition. The velocity structure of such a transition zone is affected by both chemical and temperature variations. A thickening of both the crust and the lithosphere is expected towards the continent, whereas an increase in temperature is expected towards the ocean. For the upper mantle the chemical variations are predominant and higher velocities are expected towards the ocean. That basic pattern is present in the inversion models, however, two factors argue against such a simple interpretation. First, the region of greatest transition which occurs near the continental slope and is marked by steep gravity gradients (Figure 3.8) is 30-50 km offshore. This distance from the array should minimize the effect of the continent-ocean transition on the teleseismic arrival times. Secondly, heat flow data indicate anomalously high temperatures persist beneath the Coast Ranges. These temperature variations must also affect the seismic velocities.

Figure 3.26 illustrates the velocity anomalies of layer 3. The pattern of the linear low-velocity zone bounded on both sides by high velocities is suggestive of the lateral velocity structure of an oceanic ridge. Nevertheless, other

reasons indicate that it is not the remnants of the East Pacific Rise. For instance, one concept of the driving forces of plate tectonics views the oceanic ridges as passive features. Body forces act to pull apart the oceanic plate and magma rises into the ensuing rift. If this concept is correct, an oceanic ridge would cease to exist as it encountered a trench. Marine magnetic reconstruction of the late Cenozoic plate movements of the California coast indicate the ridge and trench collided obliquely with the Mendocino triple junction migrating northward along the coast. The magnetic lineations off central California today contain a complicated, broken geometry which indicates that the Farallon plate broke up as the ridge neared the trench. Under such circumstances, it is hard to imagine the ridge retaining until the present an identifiable signature beneath the Coast Ranges.

The third model interprets the low-velocity zone in layer 3 as a wide shear zone associated with the North American-Pacific transform boundary. The low-velocity anomaly between the depths of 30-60km is displaced to the northeast side of of the San Andreas Fault, and is more aligned with the Calaveras-Hayward fault trend. If the interpretation of the anomaly as a thermal feature associated with the shear zone is correct, the position of the anomaly suggests that perhaps someday the Calaveras-Hayward will be the major through-going fault in the area. Geometrically such a transferral of move-

ment would staighten out the fault from the central San Andreas to the Mendocino Fracture Zone. Seismicity maps of northern California display more activity along the extension of the Calaveras-Hayward trend than the off-shore course of the San Andreas. Another relevent suggestion is that extension between the diverging strike-slip faults is responsible for the young volcanics (14 to 3 mybp) located in the Coast Ranges east of the San Andreas (Pilger and Henyey, 1977). The high heat flow which characterizes the Coast Ranges (Lachenbruch and Sass, 1973) is also consistent with the thermal interpretation of the low-velocity anomaly.

5.3 REGIONAL SYNTHESIS

In the introductory chapter four current ideas on the Cenozoic tectonics of the western U.S. were presented. During the course of the thesis one idea, the persistence of the East Pacific Rise beneath the Great Basin, was rejected. The movement of the North American plate over one or more upwelling mantle plumes causing the breakup of the western U.S. is also not favored. Of the remaining two, the broad shear zone and back-arc convection, neither is definitely excluded by our results. However, the preferred models for both California and Yellowstone involve predominantly lithospheric forces with essentially passive reaction by the asthenosphere. Hence, we tentatively support the concept that the western U.S. Cenozoic tectonics are controlled by stress regimes set up by plate interactions. An important corollary is that anisotropy of the continental lithosphere due to inherited zones of weakness is an important control on the development of tectonic features.

5.4 CONCLUSIONS

The major accomplishments and conclusions of this thesis are:

1) The stochastic inverse solution is the most efficient numerical method for performing three-dimensional inversion and yields results comparable to those from singular value decomposition schemes.
2) New teleseismic P-wave residual data from the USGS Central California Seismic Network was presented and inverted for three-dimensional velocity structure.
3) California crustal anomalies show a good correlation with surface geology.
4) A linear low-velocity anomaly in the upper mantle beneath California was interpreted to be a thermal anomaly due to shearing between the Pacific and North American plates.
5) Teleseismic P-wave residuals from the USGS Yellowstone array were inverted for three-dimensional velocity structure.
6) A very large magnitude low-velocity anomaly in the upper crust coincides with the Yellowstone caldera boundary and probably marks a still molten magma chamber.
7) In the upper mantle a linear low-velocity anomaly is aligned with the trend of the Snake River Plain.

8) The Yellowstone low-velocity anomaly persists to depths of 250 ±50 km.

9) The Yellowstone hot spot is interpreted to most likely represent a propagating fracture.

In conclusion, we believe that a large amount of P-wave arrival time data processed systematically by a new seismological tool contributed to the understanding of regional tectonics in the western United States.

REFERENCES

Aki, K., A. Christoffersson, and E.S. Husebye, Three-dimensional seismic structure of the lithosphere under Montana LASA, Bull. Seis. Soc. Am., 66, 561-524, 1976.

Aki, K., and W.H.K. Lee, Determination of three-dimensional velocity anomalies under a seismic array using first P arrival times from local earthquakes. 1. A homogeneous initial model, J. Geophys. Res., 81, 4381-4399, 1976.

Aki, K., A. Christoffersson, and E.S. Husebye, Determination of the three-dimensional seismic structure of the lithosphere, J. Geophys. Res., 82, 277-296, 1977.

Anderson, D.L., The San Andreas fault, Scientific American, 225 , 51-68, 1971.

Anderson, D.L., Chemical plumes in the mantle, Geol. Soc. Am. Bull., 86, 1593-1600, 1975.

Armstrong, R.L., W.P. Leeman, and H.E. Malde, K-Ar dating, Quaternary and Neogene volcanic rocks of the Snake River Plain, Idaho., Am. Jour. Sci., 275, 225-251, 1975.

Atwater, T., Implications of plate tectonics for the Cenozoic tectonic evolution of western North America, Geol. Soc. Am. Bull., 81, 3513-3536, 1970.

Atwater, T. and P. Molnar, Relative motion of the Pacific and North American plates deduced from sea-floor spreading in the Atlantic, Indian, and South Pacific Oceans, in Proceedings of the Conference on Tectonic Problems of

the San Andreas Fault System, R.L. Kovach and A. Nur (eds.), Stanford Univ. Publ. Geol. Sci., XIII, 136-147, 1973.

Bailey, E.H., M.C. Blake, Jr., and D.L. Jones, On-land Mesozoic oceanic crust in the California Coast Ranges, U.S. Geol. Surv. Prof. Paper, 700-C, C70-C81, 1970.

Bailey, E.H. (ed.), Geology of Northern California, Calif. Div. Mines and Geol., Bull. 190, San Francisco, 507 pp., 1966.

Bailey, E.H., W.P. Irwin, and D.L. Jones, Franciscan and Related Rocks, and Their Significance in the Geology of Western California, Calif. Div. Mines and Geol., Bull. 183, San Francisco, 1964.

Bhattacharyya, B.K. and L. Leu, Analysis of magnetic anomalies over Yellowstone National Park: mapping of Curie point isothermal surface for geothermal reconnaissance, J. Geophys. Res., 80, 4461-4465, 1975.

Bolt, B.A. and O.W. Nuttli, P wave residuals as a function of azimuth. 1. Observations, J. Geophys. Res., 71, 5977-5985, 1966.

Boyd, F.R., Welded tuffs and flows in the rhyolite plateau of Yellowstone Park, Wyoming, Geol. Soc. Am. Bull., 72, 387-426, 1961.

Burchfiel, B.C. and G.A. Davis, Structural framework and evolution of the southern part of the Cordilleran orogen, western United States, Am. Jour. Sci., 272, 97-118, 1972.

Burchfiel, B.S. and G.A. Davis, Nature and controls of Cordilleran orogenesis, western United States: extensions of an earlier synthesis, Am. Jour. Sci., 275-A, 363-396, 1975.

Burke, K. and J.F. Dewey, Plume-generated triple junctions: key indicators in applying plate tectonics to old rocks, Jour. Geology, 81, 406-433, 1973.

Cady, J.W., Magnetic and gravity anomalies in the Great Valley and western Sierra Nevada metamorphic belt, California, Geol. Soc. Am., Special Paper 168, 1-56, 1977.

Chapman, R.H., Gravity field in northern California, in Geology of Northern California, E.H. Bailey (ed.), Calif. Div. Mines and Geol., Bull. 190, 1966.

Chapman, R.H., Geophysical Study of the Clear Lake Region, California, Calif. Div. Mines and Geol., Special Report 116, Sacramento, 1975.

Christensen, M.N., Quaternary of the California Coast Ranges, in Geology of Northern California, E.H. Bailey (ed.), Calif. Div. Mines and Geol., Bull. 190, 1966.

Christiansen, R.L. and H.R. Blank, Jr., Volcanic evolution of the Yellowstone rhyolite plateau and eastern Snake River Plain (abstract), in Symposium on Volcanoes and Their Roots, International Association of Volcanology and Chemistry of the Earth's Interior, Oxford, 220-221, 1969.

Christiansen, R.L. and P.W. Lipman, Cenozoic volcanism and plate tectonic evolution of the western United States. II. Late Cenozoic, Philos. Trans. Roy. Soc., London, A271, 249-284, 1972.

Christiansen, R.L. and E.H. McKee, Late Cenozoic volcanic and tectonic evolution of the Great Basin and Columbia Intermontane Region, in Cenozoic Tectonics and Regional Geophysics of the Western United States, Geol. Soc. Am., Special Paper, R.B. Smith and G.P. Eaton (eds.), in press, 1978.

Coleman, R.G., Petrological and geophysical nature of serpentinites, Geol. Soc. Am. Bull., 82, 897-918, 1971.

Coney, P.J., Cordilleran tectonic transitions and motion of the North American plate, Nature, 233, 462-465, 1971.

Coney, P.J., Cordilleran tectonics and North American plate motion, Am. Jour. Sci., 272, 603-628, 1972.

Cook, K.L. Active rift system in the Basin and Range province, Tectonophysics, 8, 469-511, 1969.

Crosson, R.S., Crustal structure modeling of earthquake data. 1. Simultaneous least squares estimation of hypocenter and velocity parameters, J. Geophys. Res., 81, 3036-3046, 1976.

Crowell, J.C., Problems concerning the San Andreas fault system in southern California, in Proceedings of the Conference on Tectonic Problems of the San Andreas Fault System, R.L. Kovach and A. Nur (eds.), Stanford Univ. Publ. Geol. Sci., Xiii, 125-135, 1973.

DeLong, S.E. and P.J. Fox, Geological consequences of ridge subduction, in Island Arcs, Deep Sea Trenches, and Back-Arc Basins, M. Talwani and W.C. Pittman III (eds.), Am. Geophys. Un., Washington, 1977.

Dickinson, W.R., Relations of andesites, granites, and derivative sandstones to arc-trench tectonics, Rev. Geophys. Space Phys., 8, 813-860, 1970.

Dickinson, W.R. and T. Hatherton, Andesitic volcanism and seismicity around the Pacific, Science, 174, 400-404, 1967.

Dott, R.H., Jr., Contrasts in tectonic history along the eastern Pacific rim, in The Geophysics of the Pacific Ocean Basin and Its Margin, Am. Geophys. Un., Monograph 19, Washington, D.C., 1976.

Draper, N.R. and H. Smith, Applied Regression Analysis, Chapter 3, John Wiley and Sons, Inc., New York, 1966.

Dziewonski, A. and F. Gilbert, The effect of small aspherical perturbations on travel times and an re-examination of the corrections for ellipticity, Geophys. J.R. Astr. Soc., 44, 7-17, 1976.

Eaton, J., Crustal structure from San Francisco, California, to Eureka, Nevada, from seismic refraction measurements, J. Geophys. Res., 68, 5798-5806, 1963.

Eaton, J.P., Crustal structure in northern and central California from seismic evidence, in Geology of Northern California, E.H. Bailey (ed.), Calif. Div. Mines and Geol., Bull. 190, 1966.

Eaton, G.P., R.L. Christiansen, H.M. Iyer, A.M. Pitt, D.R. Mabey, H.R. Blank, Jr., I. Zietz, and M.E. Gettings, Magma beneath Yellowstone National Park, Science, 188, 787-796, 1975.

Elders, W.A. and S. Biehler, Gulf of California rift system and its implications for the tectonics of western North America, Geology, 3, 85-87, 1975.

Ellsworth, W.L., Three-dimensional structure of the crust and mantle beneath the Island of Hawaii, Ph.D. Thesis, Massachusetts Institute of Technology, Cambridge, 327 pp., 1977.

Ernst, W.G., Tectonic contact between the Franciscan melange and the Great Valley sequence: crustal expression of a late Mesozoic Benioff zone, J. Geophys. Res., 75, 886-902, 1970.

Ernst, W.G., Mesozoic framework of California, in Geologic Interpretations from Global Tectonics with Applications for California Geology and Petroleum Exploration, W.R. Dickinson, (ed.), San Joaquin Geol. Soc., Bakersfield, 1974.

Evans, T.R., The very deep P velocity structure of Yellowstone from PKIKP travel time residuals (abstract), EOS, Trans. Am. Geophys. Un., 58, 1186, 1977.

Evernden, J.F. and R.W. Kistler, Chronology of emplacement of Mesozoic batholitic complexes in California and western Nevada, U.S. Geol. Surv, Prof. Pap. 623, 1-42, 1970.

Forsythe, G.E. and C.B. Moler, Computer Solution of Linear Algebraic Systems, Prentice-Hall, Englewood Cliff, 1967.

Garfunkel, Z., History of the San Andreas fault as a plate boundary, Geol. Soc. Am. Bull., 84, 2035-2042, 1973.

Golub, G.H. and P.A. Businger, Linear least squares solutions by Householder transformations, Numer. Math., 7, H.B. Series Linear Algebra, 269-276, 1965.

Golub, G.H. and W. Kahan, Calculating the singular values and pseudoinverse of a matrix, SIAM Jour. Numer. Anal., 2, 205-224, 1965.

Golub, G.H. and C. Reinsch, Singular value decomposition and least squares solutions, in Handbook for Automatic Computation, II. Linear Algebra, F.L. Bauer (ed.), F.L. Bauer, Springer-Verlag, New York, 1971.

Green, D.H., Composition of basaltic magmas as indicators on conditions of origin: application to oceanic volcanism, Phil. Trans. Roy. Soc., London, A268, 707-725, 1971.

Griscom, A., Magnetic data and regional structure in northern California, in Geology of Northern California, E.H. Bailey (ed.), Calif. Div. Mines and Geol., Bull. 190, 1966.

Hadley, D. and H. Kanamori, Seismic structure of the Transverse Ranges, California, Geol. Soc. Am. Bull., 88, 1469-1478, 1977.

Hamilton, W.H., Geology and petrogenesis of the Island Park caldera of rhyolite and basalt, eastern Idaho, U.S. Geol. Surv., Prof. Pap. 504-C, C1-C37, Washington, 1965.

Hamilton, W.H., Mesozoic California and the underflow of Pacific mantle, Geol. Soc. Am. Bull., 80, 2409-2430, 1969.

Hamilton, R.M., A. Ryall, and E. Berg, Crustal structure southwest of the San Andreas fault from quarry blasts, Bull. Seis. Soc. Am., 54, 67-77, 1964.

Handschumacher, D.W., Post-Eocene plate tectonics of the eastern Pacific, in The Geophysics of the Pacific Ocean Basin and Its Margins, Am. Geophys. Un., Monograph 19, Washington, 1976.

Hanna, W.F., R.D. Brown, D.C. Ross, and A. Griscom, Aeromagnetic reconnaissance and generalized geologic map of the San Andreas fault between San Francisco and San Bernardino, California, Geophysical Investigations Map GP-815, 1972.

Healy, J.H., Crustal structure along the coast of California from seismic refraction measurements, J. Geophys. Res., 68, 5777-5787, 1963.

Healy, J.H. and L.G. Peake, Seismic velocity structure along a section of the San Andreas fault near Bear Valley, California, Bull. Seis. Soc. Am., 65, 1177-1197, 1975.

Herrin, E., W. Tucker, J.N. Taggart, D.W. Gordon, and J.C. Lobdell, Estimation of surface focus P travel times, Bull. Seis. Soc. Am., 58, 1273-1291, 1968.

Hill, D.P., Gravity and crustal structure in the western Snake River Plain, Idaho, J. Geophys. Res., 68, 5807-5818, 1963.

Hill, D.P. and Pakiser, L.C., Crustal structure between the Nevada test site and Boise, Idaho, from seismic refraction measurements, in The Earth Beneath the Continents, J.S. Steinhart and T.J. Smith (eds.), Am. Geophys. Un. Monograph 10, 391-419, Washington, 1966.

Hill, M.L., Is the San Andreas a transform fault?, Geology, 2, 535-538, 1974.

Hsu, K.J., Franciscan melanges as a model for eugeosynclinal sedimentation and underthrusting tectonics, J. Geophys. Res., 76, 1162-1170, 1971.

Husebye, E.S., A. Christoffersson, K. Aki, and C. Powell, Preliminary results on the three-dimensional seismic structure of the lithosphere under the USGS Central California Seismic Array, Geophys. J.R. Astr. Soc., 46, 319-340, 1976.

Iyer, H.M., Anomalous delays of teleseismic P waves in Yellowstone National Park, Nature, 253, 425-427, 1975.

Iyer, H.M., J.R. Evans, G. Zandt, R.M. Stewart, and J. Coakley, A deep magma body under Yellowstone caldera: delineation using teleseismic P wave residuals and tectonic interpretation, unpublished manuscript, 1978.

Jeffreys, H. and K.E. Bullen, Seismological Tables, Brit. Assn. Gray-Milne Trust, 50 pp., 1958.

Johnson, J.D. and W.R. Normark, Neogene tectonic evolution of the Salinian block, west-central California, Geology, 2, 11-14, 1974.

Jones, D.L., W.P. Irwin, and A.T. Ovenshine, Southeastern Alaska - a displaced continental fragment?, U.S. Geol. Surv., Prof. Paper 800B, B211-B217, 1972.

Karig, D.E., Remnant arcs, Geol. Soc. Am. Bull., 83, 1057-1068, 1972.

Kind, R., Residuals and velocities of P_n waves recorded by the San Andreas seismograph network, Bull. Seis. Soc. Am., 62, 85-100, 1972.

Lachenbruch, A.H. and J.H. Sass, Thermo-mechanical aspects of the San Andreas fault system, in Proceedings of the Conference on Tectonic Problems of the San Andreas Fault System, R.L. Kovach and A. Nur (eds.), Stanford Univ. Publ. Geol. Sci., XIII, 192-205, 1973.

LaFehr, T.R. and L.C. Pakiser, Gravity, volcanism, and crustal deformation in the eastern Snake River Plain, Idaho, U.S. Geol. Surv., Prof. Paper 450D, 1962.

Lanczos, C., Linear Differential Operators, Chapter 3, Van Nostrand, New York, 1961.

Lawson, C.L. and R.J. Hanson, Solving Least Squares Problems, Prentice-Hall, Englewood Cliffs, 1974.

Leeman, W.P., Petrogenesis of McKinney (Snake River) olivine tholeiite in light rare earth and Cr/Ni distributions, Geol. Soc. Am. Bull., 87, 1582-1586, 1976.

Leeman, W.P. and W.I. Manton, Strontium isotopic composition of basaltic lavas from the Snake River Plain, southern Idaho, Earth Planet. Sci. Lett., 11, 420-434, 1971.

Leeman, W.P. and C.J. Vitaliano, Petrology of McKinney basalt, Snake River Plain, Idaho, Geol. Soc. Am. Bull., 87, 1777-1792, 1976.

Lee, W.H.K. and J.C. Lahr, HYP071 (revised): A computer program for determining hypocenter, magnitude, and first motion pattern of local earthquakes, Open File Report, 75-311, 113 pp., U.S. Geol. Surv., 1975.

Levenberg, K., A method for the solution of certain non-linear problems in least squares, Quart. Appl. Math., 2, 164-168, 1944.

Lipman, P.W., H.J. Prostka, and R.L. Christiansen, Cenozoic volcanism and plate tectonic evolution of the western United States. I. Early and Middle Cenozoic, Philos. Trans. Roy. Soc., London, 271, 217-248, 1972.

Marshak, R.S. and D.E. Karig, Triple junctions as a cause for anomalously near-trench igneous activity between the trench and volcanic arc, Geology, 5, 233-236, 1977.

Mathews, V. and C.W. Anderson, Yellowstone convection plumes and breakup of the western United States, Nature, 243, 158-159, 1973.

Mayer-Rosa, D., Travel time anomalies and distribution of earthquakes along the Calaveras fault zone, California, Bull. Seis. Soc. Am., 63, 713-729, 1973.

McDougal, I., Volcanic island chains and sea floor spreading, Nature, 231, 141-144, 1971.

Menard, H.W., Jr., The East Pacific rise, Science, 132, 1737-1746, 1960.

Moores, E., Ultramafics and orogeny with models of the U.S. Cordillera and Tethys, Nature, 228, 837-842, 1970.

Morgan, W.J., Convection plumes in the lower mantle, Nature, 230, 42-43, 1971.

Morgan, W.J., Plate motions and deep mantle convection, Geol. Soc. Am., Memoir 132, 7-22, 1972a.

Morgan, W.J., Deep mantle convection plumes and plate motions, Am. Assoc. Petr. Geol. Bull., 56, 203-213, 1972b.

Nuttli, O.W. and B.A. Bolt, P wave residuals as a function of azimuth. 2. Undulations of the mantle low-velocity layer as an explanation, J. Geophys. Res., 74, 6594-6602, 1969.

Officer, C.B., Introduction to the Theory of Sound Transmission, McGraw-Hill, New York, 1958.

Otsuka, M., Azimuth and slowness anomalies of seismic waves measured on the central California seismographic array. Part I. Observations, Bull. Seis. Soc. Am., 56, 223-240, 1966.

Otsuka, M., Azimuth and slowness anomalies of seismic waves measured on the central California seismographic array. Part II. Interpretation, Bull. Seis. Soc. Am., 56, 655-675, 1966.

Page, B., Geology of the Coast Ranges in California, in Geology of Northern California, E.H. Bailey (ed.), Calif. Div. Mines and Geol., Bull. 190, 1966.

Page, B.M., Sur-Nacimiento fault zone of California: continental margin tectonics, Geol. Soc. Am. Bull., 81, 667-690, 1970a.

Page, B.M., Time of completion of underthrusting of Franciscan beneath Great Valley rocks west of Salinian block, California, Geol. Soc. Am. Bull., 81, 2825-2834, 1970b.

Page, B.M., Oceanic crust and mantle fragment in subduction complex near San Luis Obispo, California, Geol. Soc. Am. Bull., 83, 957-972, 1972.

Pakiser, L.C., Structure of the crust and upper mantle of the western United States, Jour. Geophys. Res., 68, 5747-5756, 1963.

Pilger, R.H., Jr. and T.L. Henyey, Plate tectonic reconstructions and the Neogene tectonic and volcanic evolution of the California borderland and Coast Ranges, Geol. Soc. Am., Abstracts with Programs, 9, 482, 1977.

Pitt, A.M., Evidence from local earthquakes for the existence of a region of seismic body wave attenuation in the upper crust under the Yellowstone caldera (abstract), EOS, Trans. Am. Geophys. Un., 56, 1190, 1974.

Powell, C.A., Mantle heterogeneity: evidence from large seismic arrays, Ph.D. thesis, Princeton University, 326 pp., 1976.

Prodehl, C., Seismic refraction study of crustal structure in the western United States, Geol. Soc. Am. Bull., 81, 2629-2646, 1970.

Robbins, S., Gravity and magnetic data in the vicinity of the Calaveras-Hayward and Silver Creek faults near San Jose, California, U.S. Geol. Surv. Prof. Paper 750-B, B128-B139, 1971.

Robinson, G.D., M.R. Klepper, and J.D. Obradovich, Overlapping plutonism, volcanism, and tectonism in the Boulder batholith region, western Montana, in Studies In Volcanology, R.R. Coats, R.L. Hay, and C.A. Anderson (eds.), Geol. Soc. Am. Memoir 116, 557-576, 1968.

Roecker, S., Preliminary crustal velocity modeling under Oroville, California, unpubl. manuscript, 56 pp., 1977.

Roy, R.F., D.D. Blackwell, and E.R. Decker, Continental heat flow, in The Nature of the Solid Earth, E.C. Robertson (ed.), McGraw-Hill, 1972.

Ryall, A., The Hebgen Lake, Montana, earthquake of August 19, 1959, P-waves, Bull. Seis. Soc. Am., 52, 253-271, 1962.

Scholz, C.H., M. Barazangi, and M.L. Sbar, Late Cenozoic evolution of the Great Basin, western United States, as an ensialic interarc basin, Geol. Soc. Am. Bull., 82, 2979-2990, 1971.

Schweickert, R.A. and D.S. Cowan, Early Mesozoic tectonic evolution of the western Sierra Nevada, California, Geol. Soc. Am. Bull., 86, 1329-1336, 1975.

Schweickert, R.A., Early Mesozoic rifting and fragmentation of the Cordilleran orogen in the western U.S.A., Nature, 260, 586-591, 1976.

Sengupta, M.K., The structure of the Earth's mantle from body wave observations, Ph.D. thesis, Massachusetts Institute of Technology, Cambridge, 586 pp., 1975.

Shaw, H.R. and E.D. Jackson, Linear island chains in the Pacific: result of thermal plumes or gravitational anchors?, J. Geophys. Res., 78, 8634-8652, 1973.

Silver, E.A., Is the San Andreas a transform fault?: comments and reply, Geology, 3, 155-156, 1975.

Smith, R.B., Intraplate tectonics of the western North American plate, Tectonophysics, 37, 323-336, 1977.

Smith, R.B. and M. Sbar, Contemporary tectonics and seismicity of the western United States with emphasis on the Intermountain Seismic Belt, Geol. Soc. Am. Bull., 85, 1205-1218, 1974.

Smith, R.B., R.T. Shvey, R.O. Freidline, R.M. Otis, and L.B. Alley, Yellowstone hot spot: new magnetic and seismic evidence, Geology, 2, 451-455, 1974.

Smith, R.B., R.T. Shvey, J.R. Pelton, and J.P. Bailey, Yellowstone hot spot: contemporary tectonics and crustal properties from earthquake and aeromagnetic data, J. Geophys. Res., 82, 3665-3676, 1977.

Snyder, W.S., W.R. Dickinson, and M.L. Silberman, Tectonic implications of space-time patterns of Cenozoic magmatism in the western United States, Earth Planet. Sci. Lett., 32, 91-106, 1976.

Solomon, S.C., Seismic-wave attenuation and partial melting

in the upper mantle of North America, J. Geophys. Res., 77, 1483-1502, 1972.

Stewart, J.H., Basin and Range structure in western North America - a review, in Cenozoic Tectonics and Regional Geophysics of the Western U.S., R.B. Smith and G.P. Eaton (eds.), Geol. Soc. Am. Special Paper, in press, 1978.

Stewart, S., Preliminary comparison of seismic travel times and inferred crustal structure adjacent to the San Andreas fault in the Diablo and Gabilan Ranges of central California, in Proceedings of Conference on Geologic Problems of the San Andreas Fault System, R.L. Kovach and A. Nur (eds.), Stanford Univ. Publ. Geol. Sci., XIII, 218-230, 1968.

Suppe, J., C. Powell, and R. Berry, Regional topography, seismicity, Quaternary volcanism, and the present-day tectonics of the western United States, Am. Jour. Sci., 275-A, 397-436, 1975.

Thompson, R.N., Primary basalts and magma genesis. II. Snake River Plain, Idaho, U.S.A., Contr. Mineral. Petrol., 52, 213-232, 1975.

Thompson, R.N., Columbia/Snake River-Yellowstone magmatism in the context of western U.S.A. Cenozoic geodynamics, Tectonophysics, 39, 621-636, 1977.

U.S. Geological Survey, The Hebgen Lake, Montana, earthquake of August 17, 1959, U.S. Geol. Surv. Prof. Paper 435, 1969.

Warner, L.A., The Colorado lineament: a middle Precambrian wrench fault system, Geol. Soc. Am. Bull., 89, 161-171, 1978.

Warren, D.H., Transcontinental geophysical survey (35°-39°N). Seismic refraction profiles of the crust and upper mantle from 112°W longitude to the coast of California, U.S. Geol. Surv. Map I-532-D, 1968.

Weaver, C.S. and A.M. Pitt, Travel time curves and apparent velocities across the Yellowstone caldera (abs.), Earthquake Notes, 49, 70, 1978.

Wesson, R.L., Travel time inversion for laterally inhomogeneous crustal velocity models, Bull. Seis. Soc. Am., 61, 729-746, 1971.

Wesson, R.L., J.C. Roller, and W.H.K. Lee, Time-term analysis and geological interpretation of seismic travel time data from the Coast Ranges of central California, Bull. Seis. Soc. Am., 63, 1447-1471, 1973.

Wesson, R.L., F.W. Lester, and K.L. Meagher, Catalog of earthquakes in central California, October-December, 1972, U.S. Geol. Surv., Open File Report, 46 pp., 1974.

Wiggins, R.W., The general linear inverse problem: implication of surface waves and free oscillations for earth structure, Rev. Geophys. Space Phys., 10, 251-285, 1972.

Wiggins, R.A. and D.V. Helmberger, Upper mantle structure of the western United States, J. Geophys. Res., 78, 1870-1880, 1973.

Wilson, J.T., Evidence from oceanic islands suggesting movement in the earth, Phil. Trans. Roy. Soc. London, 258-A, 145-167, 1965.

Winterhalder, E.C. and R.C. Thompson, The Talmage fault, a newly identified active fault in Mendocina County, California (abstract), Earthquake Notes, 49, 33-34, 1978.

Witkind, I.J., The 1959 Hebgen Lake, Montana, earthquake: two geologic points of view, Earthquake Information Bull., 7, 3-7, 1975.

Wyllie, P.J., Role of water in magma generation and initiation of diapiric uprise in the mantle, J. Geophys. Res., 76, 1328-1338, 1971.

Zehdy, A.A.R. and W.D. Stanley, Profiles of deep electrical sounding on the Snake River Plain, Idaho, Geol. Soc. Am. Abstracts with Programs, 4, 423-424, 1972.

Zandt, G. and K. Aki, Lateral velocity anomalies associated with the San Andreas fault, central California, EOS, Trans. Am. Geophys. Un., 57, 283, 1976.

Zietz, I. and J.R. Kirby, Transcontinental geophysical survey (35°-39°N). Magnetic map from 112°W longitude to the coast of California, U.S. Geol. Surv. Map I-532-A, 1968.

TABLE 3.1.

Events "picked" for California study.

This is a subset of the California data set.

Table 3.1

EVCARD.DATA

1/21/73	202049.3	Tonga Islands	15.857S174.057W	129	5.5
1/31/73	205553.1	Bonin Islands	28.206N139.227E	498	6.0
2/01/73	51420.6	N. Argentina	22.655S 66.195W	229	6.1
2/20/73	74034.7	S. Alaska Coast	58.307N149.810W	12	5.5
2/23/73	42623.3	Ecuador Coast	2.088S 78.210W	67	5.7
3/04/73	175743.5	Kamchatka	54.828N161.599E	32	6.1
3/10/73	950 0.3	N. Fiji Basin	15.184S173.524W	8	5.6
3/17/73	45712.7	New Hebrides Is.	19.376S169.356E	194	6.0
3/19/73	1141 7.7	Aleutian Islands	52.835N173.773E	81	5.8
4/03/73	1354 1.8	Columbia	4.691N 75.628W	158	6.2
4/07/73	225054.5	N. Chile	20.666S 69.187W	95	5.0
4/12/73	134915.8	Kuril Islands	50.893N157.443E	52	6.1
4/15/73	61050.9	Tonga Islands	20.613S178.825W	610	5.5
4/16/73	1448 2.8	Aleutian Islands	51.123N178.829W	54	5.5
4/24/73	184231.9	Columbia	5.162N 75.810W	118	5.5
4/24/73	211645.3	Panama	7.270N 82.343W	33	5.5
4/24/73	2130 9.9	Columbia	4.066N 78.144W	50	6.3
4/25/73	142113.2	Bonin Islands	33.394N140.745E	65	5.7
4/26/73	202628.0	Hawaii Islands	19.933N155.100W	50	6.0
4/28/73	122111.7	Ecuador	1.438S 79.875W	109	5.5
5/01/73	104046.9	Papua	10.016S150.176E	27	5.9
4/14/73	219 1.6	Kuril Islands	44.062N148.223E	64	5.5
5/14/73	171113.8	Fiji Islands	16.646S175.866E	54	5.8
5/29/73	61422.3	Kamchatka	54.011N163.760W	30	6.0
5/30/73	438 1.8	Ecuador	2.260S 78.523W	111	5.7
6/06/73	13 0 0.1	NTS Nevada	37.245N116.340W	0	6.1
6/09/73	82127.3	Solomon Islands	10.294S161.360E	70	6.3
6/14/73	11 246.9	Celebes Sea	7.291S120.380E	631	5.8
6/17/73	355 2.9	N. Japan	43.233N145.780E	48	6.5
6/17/73	203757.3	N. Japan	42.706N146.040E	50	6.0
6/18/73	174543.7	N. Japan	42.498N145.980E	29	5.8
6/19/73	254 9.8	N. Japan	42.715N146.030E	43	5.6
6/20/73	12 156.7	Kermadec Islands	28.518S176.760W	41	5.6
6/24/73	24325.5	N. Japan	43.318N146.440E	50	6.3
6/24/73	3 418.6	N. Japan	43.200N146.790E	55	5.8
6/24/73	5 746.8	N. Japan	43.123N146.570E	44	5.8
7/01/73	133334.6	S.E. Alaska	57.840N137.330W	33	6.1
7/03/73	35953.7	W. Mexico Coast	19.104N101.830W	125	5.6
1/02/74	104229.9	N. Chile	22.538S 68.390W	105	6.4
1/05/74	83350.7	Columbia	12.199S 76.350W	98	6.3
3/03/74	142237.5	New Hebrides Is.	20.062S169.710E	17	6.1
3/23/74	142835.4	S. Fiji Basin	23.931S179.770E	535	6.1
6/04/74	41415.9	Tonga Islands	15.847S175.181W	276	6.0
7/13/74	11822.8	Panama-Columbia	7.747N 77.600W	12	6.4
8/20/74	95955.6	Novaya Zemlya	73.366N 55.094E	0	6.4
10/09/74	732 2.2	Kuril Islands	44.7 4N150.110E	49	6.3
12/05/74	115737.3	Peru-Brazil	7.686S 74.453W	162	6.0
2/07/75	45144.0	Solomon Sea	7.288S149.513E	33	6.3
2/20/75	53257.7	Kazakh	49.820N 78.078E	0	5.7

Table 3.1, continued

```
 3/13/75 152642.5 Chile              29.041S 71.337W   4 6.2
 3/18/75 172123.4 N. Peru             4.231S 77.015W  98 6.2
 4/16/75  12718.7 Jan Mayen Is.      71.516N 10.427W  13 6.1
READY
```

TABLE 3.2.

Average Station Residual Data for
the Central California Array.

$$\text{Mean} = \frac{1}{N} \sum_{i=1}^{N} R_{ij}$$

SD = Standard Deviation

N = Number of data for station j

Elevation in meters

Corr. = Elevation correction

Ave. Res. = Mean - Corr.

Table 3.2

Station	Mean	SD	N	Elevation	Corr.	Ave. Res.
ABP	-.05	.15	4	140	.03	-.08
ACH	.68	.11	5	74	.01	.67
ALM	-.09	.21	31	244	.04	-.13
ALX	-.11	.17	10	380	.07	-.18
AND	.05	.17	45	244	.04	.01
ANG	-.19	.17	74	223	.04	-.23
ANZ	-.29	.28	12	122	.02	-.31
ARN	.16	.14	111	628	.11	.05
BAM	-.03	.12	3	820	.15	-.18
BBR	-.21	.13	27	137	.02	-.10
BCR	.02	.31	24	660	.12	-.10
BEN	.34	.21	24	448	.08	.26
BGH	.20	.42	6	158	.03	.17
BGM	.23	.27	25	1216	.22	.01
BOL	.22	.15	98	610	.11	.11
BRP	.64	.16	6	867	.15	.49
BTW	-.10	.24	25	381	.07	-.17
BVL	-.04	.17	62	510	.09	-.13
BWR	.20	.14	73	221	.04	-.16
CAL	.06	.14	103	265	.05	.01
CAN	-.02	.21	43	332	.06	-.08
CAR	-.28	.16	60	98	.02	-.30

Table 3.2

continued

Station	Mean	SD	N	Elevation	Corr.	Ave. Res.
CAS	.56	.96	85	1189	.21	.35
CBC	-.21	.08	4	219	.04	-.25
CBO	-.03	.14	106	192	.03	-.06
CCR	.48	.14	29	207	.04	.44
CDR	-.17	.17	78	620	.11	-.28
CHR	-.26	.11	105	241	.04	-.30
CNR	-.01	.14	38	305	.05	-.06
COE	.32	.18	61	266	.07	.25
CRK	-.01	.19	12	561	.10	-.11
CSH	.00	.17	7	170	.03	-.03
DIL	-.29	.18	86	204	.04	-.33
DOO	.31	.14	87	198	.04	.27
DIR	-.58		1	496	.09	-.67
DSR	.11	.21	9	109	.02	.09
DUR	.41	.36	13	168	.03	.38
EGR	-.26	.24	56	442	.08	-.34
EKH	.20	.24	83	342	.06	.14
ELG	-.32		1	202	.04	-.36
EMM	.06	.21	90	488	.09	-.03
EUC	-.03	.10	48	438	.08	-.11
FAR	-.24		1	107	.02	-.25
FEL	-.09	.15	27	323	.06	-.15
FRP	-.27	.18	92	705	.13	-.40
GDH	-.08	.18	23	433	.08	-.16
GHS	.05	.09	30	778	.14	-.09

Table 3.2

continued

Station	Mean	SD	N	Elevation	Corr.	Ave. Res.
GVR	-.16	.16	72	257	.05	-.11
HCC	.39	.18	3	159	.03	.36
HEC	.18	.06	107	732	.13	.08
HLB	-.07		1	165	.03	-.10
HMR	.89	.18	16	65	.01	.88
JHC	-.31	.13	98	207	.04	-.35
JOL	.11	.20	24	336	.06	.05
JON	-.23	.11	10	1056	.19	-.42
LCH	.10	.22	25	312	.06	.04
LNS	-.30	.16	73	120	.02	-.32
LOR	-.11	.23	89	488	.09	.12
LTR	.00	.16	97	183	.03	-.03
LTW	-.16	.15	74	270	.05	-.21
LWR	.13	.14	14	232	.04	-.09
LXR	-.07	.22	3	244	.04	-.11
MDC	.02	.15	3	1173	.21	-.19
MGA	-.19	.16	13	201	.04	-.23
MHR	.23	.15	92	518	.9	.14
MIL	.11	.56	3	90	.02	.09
MIX	.27	.32	67	177	.03	.24
MNR	.14	.27	100	500	.09	.05
MON	-.23	.24	23	192	.03	-.26
MOP	.15	.24	83	784	.14	.01
MOR	.34	.20	93	792	.14	.20

Table 3.2

continued

Station	Mean	SD	N	Elevation	Corr.	Ave. Res.
MRS	-.07	.46	12	810	.14	-.21
MSJ	.05	.20	24	498	.09	-.04
MTB	-.03	.17	3	347	.06	-.09
MWS	-.14	.18	82	134	.02	-.16
OCR	-.11	.10	83	98	.02	-.13
OLC	-.32		1	30	.01	-.33
PAL	.08	.13	100	463	.08	0
PCL	.05	.13	100	152	.03	.02
PES	-.22	.21	56	84	.02	-.24
PFP	.20	.45	3	355	.06	.14
PKF	.03	.18	17	469	.08	-.05
PKH	.58	.49	3	122	.02	.56
PLV	.08	.11	10	158	.03	.05
PMR	.04	.40	9	94	.02	.02
PNC	-.18	.20	109	305	.05	-.23
PNM	.09	.14	2	785	.14	-.05
PNP	.03	.15	9	1591	.28	-.25
PTV	-.04	.23	28	506	.09	-.13
QSR	.00	.25	61	536	.10	-.10
RBM	.34	.82	11	372	.07	.27
RUS	-.19	.35	30	331	.06	-.25
SAC	-.31	.06	5	207	.04	-.35
SAL	-.01	.38	7	335	.06	-.07
SAW	.05	.16	14	262	.05	0

Table 3.2

continued

Station	Mean	SD	N	Elevation	Corr.	Ave. Res.
SBCC	.14	.18	11	610	.11	.03
SFR	.71	.05	2	8	0	.71
SFT	.06	.34	37	143	.03	.03
SGC	.14	.07	4	198	.04	.10
SGM	1.80		1	1075	.19	1.61
SHC	-.18	.48	7	1200	.21	-.39
SHG	-.26	.15	97	192	.03	-.29
SHR	-.13	.23	94	328	.06	-.19
SJG	-.32	.16	89	171	.03	-.35
SKG	.06	.13	2	282	.05	.01
SL8	-.10	.05	3	?		
SOS	-.09	.25	4	946	.17	-.26
SPT	-.14	.26	27	88	.02	-.16
SRS	-.29	.20	57	399	.07	-.36
STC	.16	.16	15	259	.05	.11
STJ	.20	.11	11	122	.02	.18
STV	-.19	.20	76	357	.06	-.25
SVC	.29	.22	53	128	.02	.27
TAY	.17	.25	87	552	.10	.07
TMN	-.13	.19	79	105	.02	-.15
WDS	-.12	.14	23	280	.05	-.17
WHW	-.27	.17	73	50	.01	-.28
WKR	.18	.04	2	503	.09	.09
SBSN	-.18	.04	2	259	.05	-.23

Table 3.2

continued

Station	Mean	SD	N	Elevation	Corr.	Ave. Res.
SLD	.15	.25	8	443	.08	.07
ORV	-.46	.77	7	362	.06	-.52
CYH	-.02	1.62	38	38	.01	-.03
SBLP	-.18	.24	5	134	.02	-.20
SBLC	-.06	.18	9	1190	.21	-.27
SBLG	.13	.08	2	415	.07	.06
SBCD	.10	.07	2	213	.04	.06
SBSM	-.12	.10	3	172	.03	-.15
SBSC	-.40		1	457	.08	-.48

TABLE 3.3.

Three-Dimensional Inversion of
California JB Residuals

Table 3.3a

California - Combined Data

ORIGIN OF COORDINATE SYSTEM

Latitude	Longitude	THA	VO
37N5.64	121W44.20	36.0	6.00

	Velocity	Thickness	#-North	Length	#-East	Length
1	6.00	25.00	16	15.00	8	15.00
2	8.00	30.00	11	25.00	6	25.00
3	8.00	30.00	12	25.00	7	25.00
4	8.00	30.00	13	25.00	8	25.00

THA = Rotation of coordinate system in degrees counterclockwise is positive.
VO = Elevation correction velocity.

Table 3.3b

Layer 1

*	*	*	2.21±.69	1.16±.86	1.14±.91	*	*
*	*	0.52±.84	0.76±.83	-2.69±.71	-4.14±.57	-3.27±.82	*
*	*	2.93±.83	0.08±.90	-2.68±.98	-2.28±.41	0.98±.69	-7.04±.94
*	*	1.19±.94	0.25±.95	3.84±.65	-0.65±.48	-3.65±.39	-1.05±.91
*	-0.94±.79	0.84±.52	-3.36±.58	2.22±.76	1.12±.51	-3.15±.16	*
*	0.52±.58	1.92±.50	-2.04±.52	-1.56±.67	-0.58±.41	0.15±.48	*
*	4.86±.73	0.60±.59	1.78±.68	-4.27±.44	-1.52±.52	-0.51±.74	*
*	3.39±.86	1.99±.84	1.50±.57	-0.77±.43	-0.72±.50	0.39±.78	*
*	*	-1.35±.91	1.01±.65	0.06±.48	1.95±.67	*	*
*	*	1.35±.67	6.46±.41	3.53±.36	-0.13±.44	-1.57±.80	*
2.55±.56	2.28±.86	*	7.74±.37	0.47±.50	-0.52±.48	-0.75±.76	2.92±.93
*	1.28±.77	5.04±.49	7.23±.51	-0.96±.69	0.53±.51	*	*
*	*	1.61±.67	5.96±.47	-2.74±.39	-0.46±.52	*	-6.13±.78
*	*	1.13±.66	4.48±.49	-4.03±.56	-0.59±.54	-1.66±.86	
0.55±.78	*	*	4.16±.85	-5.27±.65	*	3.80±.85	*
0.09±.66	*	-1.00±.87	2.50±.54	0.55±.66	-3.96±.48	*	*

Table 3.3c

Layer 2

*	*	2.13±.80	-0.70±.82	0.03±.89	-4.17±.60
*	1.32±.55	0.74±.74	-0.97±.54	-3.07±.65	-6.63±.85
*	-2.66±.81	0.54±.61	-2.53±.50	-2.53±.46	-4.98±.79
0.93±.52	2.62±.62	1.88±.53	-2.07±.43	-1.70±.50	-1.45±.80
*	1.09±.62	0.60±.46	-1.86±.45	-1.39±.55	-2.78±.90
*	-0.35±.81	0.50±.45	-1.98±.44	-1.39±.65	*
2.49±.55	0.03±.64	-0.66±.45	0.44±.43	0.50±.69	-2.19±.74
0.12±.75	1.21±.70	0.55±.44	0.40±.41	-0.30±.61	6.07±.40
*	0.90±.82	1.01±.47	-0.82±.46	-0.53±.67	4.45±.84
0.81±.52	0.39±.85	0.84±.57	-0.44±.49	1.73±.77	4.88±.80
*	1.85±.59	-1.44±.66	-1.54±.56	5.90±.82	*

Table 3.3d

Layer 3

*	*	*	-0.80±.82	-1.17±.76	3.45±.74	*
*	1.32±.73	1.30±.78	2.18±.68	-1.08±.59	-3.05±.80	3.26±.72
1.32±.55	3.56±.84	1.22±.71	1.35±.49	0.36±.54	-1.25±.74	-2.54±.65
2.77±.66	-0.02±.69	0.57±.63	-0.73±.45	1.14±.46	-2.72±.67	-5.86±.81
0.93±.52	0.42±.63	-0.56±.64	1.15±.46	-0.03±.50	-2.27±.62	2.15±.83
*	2.48±.81	-0.72±.50	0.24±.43	0.32±.52	-3.87±.73	-1.78±.66
0.17±.77	-0.97±.82	-0.79±.46	-1.93±.45	-1.99±.49	-1.84±.70	-2.63±.62
0.65±.78	-1.25±.67	-0.91±.47	-1.81±.44	-0.74±.57	-0.63±.80	1.62±.77
*	-1.60±.72	0.45±.54	-0.19±.43	-0.08±.50	-0.23±.72	8.06±.75
*	-1.31±.80	0.32±.55	-0.30±.47	-1.18±.54	1.74±.82	-0.23±.60
0.81±.52	-1.08±.59	-3.18±.70	-1.63±.59	-0.85±.65	3.81±.80	4.14±.61
*	0.03±.57	-0.99±.80	0.83±.78	5.03±.72	3.08±.98	*

Table 3.3e

Layer 4

*	*	*	1.92±.87	0.83±.76	-1.42±.84	-4.17±.60	*
*	2.06±.86	2.89±.82	2.65±.91	0.34±.58	-1.55±.72	-0.08±.89	-3.12±.71
1.32±.55	0.78±.92	1.66±.62	2.43±.58	0.58±.51	0.37±.66	-3.16±.78	-2.54±.65
2.77±.66	0.82±.77	1.35±.64	1.93±.45	2.35±.42	1.19±.67	1.03±.80	1.75±.78
2.76±.77	-1.84±.66	-0.16±.60	0.81±.43	1.08±.49	-1.02±.56	-2.62±.73	-2.76±.89
*	-0.37±.71	-0.00±.62	0.07±.41	-0.20±.48	-1.38±.54	-2.51±.67	-2.85±.76
1.37±.68	0.49±.84	-1.00±.50	-0.04±.41	-1.71±.45	-2.89±.51	-4.71±.61	-4.41±.73
.59±.86	-3.12±.72	-2.30±.47	-1.81±.41	-3.83±.46	-4.44±.52	-4.29±.83	-1.53±.91
1.64±.68	-1.61±.81	-2.61±.53	-2.18±.45	-2.38±.49	-5.04±.56	-3.83±.74	-8.52±.75
1.15±.67	-0.91±.77	-2.37±.55	-1.11±.49	-0.70±.45	-1.40±.53	-2.09±.74	-0.93±.91
0.81±.52	-2.46±.84	-0.89±.72	-0.64±.53	0.90±.55	1.10±.62	1.87±.85	-0.23±.68
*	0.33±.74	1.21±.75	0.69±.66	4.46±.63	6.92±.68	-0.61±.86	4.14±.6
*	*	0.03±.57	-1.54±.83	2.30±.78	2.18±.29	3.96±.87	*

Table 3.3 f

Layer 1

*	*	*	0.73	0.64	0.45	*	*
*	*	0.25	0.62	0.80	0.87	0.73	*
*	*	0.70	0.61	0.51	0.92	0.82	0.54
*	*	0.61	0.41	0.85	0.91	0.93	0.49
*	0.72	0.89	0.88	0.79	0.91	0.83	*
*	0.85	0.90	0.90	0.84	0.93	0.91	*
*	0.78	0.88	0.84	0.93	0.90	0.80	*
*	0.64	0.66	0.89	0.94	0.91	0.75	*
*	*	0.54	0.86	0.92	0.85	*	*
*	*	0.21	0.94	0.95	0.93	0.75	*
0.39	0.66	*	0.95	0.91	0.92	0.78	0.46
*	0.71	0.91	0.91	0.84	0.91	*	*
*	*	0.21	0.93	0.94	0.90	*	0.72
*	*	0.21	0.92	0.90	0.90	0.68	*
0.23	*	*	0.72	0.86	*	0.43	*
0.40	*	0.55	0.90	0.85	0.92	*	*

Table 3.3 g

Layer 2

*	*	0.56	0.67	0.38	0.18
*	0.18	0.67	0.86	0.81	0.44
*	0.60	0.84	0.89	0.90	0.72
0.29	0.80	0.88	0.92	0.89	0.68
*	0.81	0.91	0.91	0.87	0.43
*	0.63	0.91	0.92	0.82	*
0.36	0.83	0.91	0.92	0.81	0.29
0.23	0.74	0.91	0.92	0.84	0.46
*	0.66	0.90	0.90	0.81	0.42
0.15	0.40	0.85	0.89	0.74	0.39
*	0.47	0.82	0.86	0.66	*

Table 3.3h

Layer 3

*	*	*	0.59	0.73	0.29	*
*	0.22	0.62	0.81	0.84	0.65	0.27
0.18	0.59	0.75	0.89	0.87	0.74	0.32
0.21	0.76	0.84	0.91	0.90	0.80	0.51
0.29	0.80	0.84	0.91	0.90	0.83	0.47
*	0.61	0.90	0.92	0.89	0.77	0.19
0.20	0.71	0.91	0.92	0.90	0.80	0.17
0.36	0.79	0.91	0.92	0.87	0.73	0.28
*	0.73	0.89	0.92	0.89	0.78	0.34
*	0.62	0.88	0.91	0.88	0.69	0.16
0.15	0.36	0.76	0.85	0.81	0.56	0.18
*	0,25	0.68	0.74	0.75	0.46	*

Table 3.3i

Layer 4

*	*	*	0.59	0.77	0.67	0.18	*
*	0.38	0.67	0.62	0.86	0.80	0.52	0.19
0.18	0.38	0.82	0.87	0.90	0.86	0.71	0.32
0.21	0.75	0.84	0.92	0.93	0.83	0.73	0.29
0.43	0.83	0.86	0.93	0.91	0.88	0.79	0.46
*	0.79	0.87	0.93	0.91	0.89	0.82	0.33
0.22	0.70	0.91	0.94	0.93	0.90	0.83	0.30
0.55	0.79	0.91	0.93	0.92	0.90	0.73	0.50
0.22	0.66	0.89	0.92	0.91	0.89	0.79	0.29
0.21	0.66	0.89	0.91	0.92	0.89	0.79	0.36
0.15	0.60	0.78	0.89	0.88	0.85	0.25	0.16
*	0.35	0.72	0.83	0.84	0.81	0.52	0.18
*	*	0.25	0.52	0.77	0.76	0.41	*

TABLE 3.4.

Three-Dimensional Inversion of California Plane Wave Residuals

For initial model, see Table 3.3a

3.4a Solution of Layer 1

3.4b Solution for Layer 2

3.4c Solution for Layer 3

3.4d Solution for Layer 4

Table 3.4a
Layer 1

*	*	*	1.45	-1.15	-0.35	*	*
*	*	0.48	0.13	0.15	-1.45	-2.68	*
*	*	2.58	0.92	-1.48	-1.51	4.58	-5.93
*	*	-0.22	0.80	3.13	-0.74	-1.90	0.40
*	-5.22	-1.26	-3.83	2.26	0.54	-1.15	*
*	-3.41	-0.07	-3.62	-1.63	-0.07	2.20	*
*	-0.83	-1.77	0.12	-4.98	0.74	1.13	*
*	-1.07	-1.36	-0.57	-1.04	-0.16	0.52	*
*	*	-1.86	0.09	0.12	2.90	*	*
*	*	2.92	4.31	3.32	2.32	2.07	*
-1.39	-1.30	0.49	5.32	1.40	1.52	0.22	3.19
*	-2.04	0.98	4.38	-0.89	2.07	*	*
*	*	2.97	4.37	-1.48	1.66	*	-2.40
*	*	-0.23	3.64	-3.46	2.01	0.86	2.08
*	*	*	2.26	-5.93	*	3.60	*
*	*	*	0.54	-0.10	-1.10	*	*

Table 3.4b
Layer 2

*	*	0.09	-0.69	0.53	-2.21
*	-0.93	-0.94	-1.86	0.64	-2.56
*	-2.05	0.25	-1.31	-0.49	-2.74
-1.24	0.41	0.34	-0.42	0.36	1.68
*	1.17	0.68	-0.23	-0.14	-1.52
*	-2.92	-0.00	-0.80	0.95	*
1.16	-1.64	-0.35	0.68	0.16	0.97
-1.54	-0.80	0.19	-0.18	1.21	-2.36
*	0.58	0.58	-0.61	0.73	4.17
*	*	2.72	0.78	3.86	3.79
*	*	2.53	1.89	3.58	*

Table 3.4c
Layer 3

*	*	-0.75	0.54	0.32	-2.21	*
-1.08	0.15	1.07	0.33	-1.35	-1.55	-0.81
*	-0.76	0.42	0.22	1.17	-0.66	-0.53
1.48	-1.17	0.69	-0.07	1.48	1.04	-3.02
0.26	-0.90	1.58	1.36	0.18	1.46	1.21
0.87	1.07	-0.07	0.59	0.58	-3.04	-0.23
0.18	-1.15	-0.85	-0.78	-2.57	-1.30	*
0.20	-0.90	-1.72	-0.59	-0.62	-0.52	3.56
0.02	-0.73	-0.86	1.04	0.81	0.94	-7.23
*	-1.80	-0.75	0.07	0.65	2.48	1.76
*	-0.73	-1.00	-0.61	-0.49	1.92	2.03
*	*	0.48	1.45	2.16	1.28	*

Table 3.4d

Layer 4

*	*	*	0.57	1.01	-1.68	*	*
0.15	-0.53	-0.63	1.81	0.56	-1.53	*	-0.81
*	0.72	-0.99	0.64	0.33	-0.10	-0.53	-2.78
0.88	-0.33	-0.91	0.55	1.79	3.40	2.05	*
1.02	-1.60	-2.31	-0.47	0.82	0.98	-0.02	-0.32
1.02	-2.40	-0.46	0.28	0.68	0.38	-1.18	-0.56
0.92	-0.71	-0.68	-0.82	0.55	0.17	-0.62	-0.23
.72	-1.35	0.02	-1.40	-2.47	0.09	-1.02	0.97
-1.60	0.36	0.19	-1.46	-2.27	-3.17	0.18	-8.96
1.04	0.33	0.62	0.09	-0.06	-1.03	-0.14	1.73
-0.35	-0.61	-0.47	0.01	1.00	-1.24	0.63	
*	-0.33	-0.73	-0.17	2.19	2.60	1.81	2.03
*	*	*	-0.65	1.01	1.43	3.19	*

TABLE 3.5.

Three-Dimensional Inversion of California

Herrin Residuals - Santa Rosa Subarray

***** PROGRAM 3-D *****

22 NOVEMBER 1975

CALIFORNIA: SANTA ROSA REGION

LATITUDE	LONGITUDE	THA	V0	JPWT	IRES	IPUNCH	IPRINT	THETA	RESL
38N25.50	122W34.00	37.5	5.60	4	1	1	0	50.	0.100

IPARM=-1,0,1 INDICATE,RESPECTIVELY,SOLUTION IS IN TERMS OF VELOCITY PERTURBATIONS, LAYER DEPTH PERTURBATIONS, OR THAT BOTH SOLUTIONS WILL BE COMPUTED
FOR THIS RUN, IPARM= -1

	VELOCITY	THICKNESS	#-NORTH	LENGTH	#-EAST	LENGTH	COORDINATE DISPLACEMENT	
1	5.60	10.00	13	10.00	10	10.00	0.0	0.0
2	6.90	20.00	10	20.00	9	20.00	0.0	0.0
3	8.00	30.00	11	25.00	10	25.00	0.0	0.0
4	8.00	30.00	12	25.00	11	25.00	0.0	0.0

	STA	LATITUDE	LONGITUDE	ELEVATION	RELATIVE COORDINATES		INDEX
1	ABP	37 56.34N	122 45.54W	0.14	-32.45	-46.19	91
2	ALX	38 42.65N	122 45.30W	0.38	35.12	6.32	26
3	ANG	37 51.68N	122 25.77W	0.22	-56.91	-28.47	123
4	BDR	38 15.65N	122 32.99W	0.14	-15.34	-9.91	85
5	BRP	38 40.07N	122 11.60W	0.87	1.66	42.18	70
6	CAR	38 19.28N	122 47.73W	0.10	3.07	-22.84	63
7	CDR	38 22.19N	122 27.70W	0.62	-10.43	3.55	76
8	DSR	37 57.98N	122 15.17W	0.11	-57.08	-9.08	125
9	DUR	38 1.78N	122 0.05W	0.17	-64.86	12.78	127
10	GVR	38 16.84N	122 12.89W	0.26	-31.37	14.69	97
11	HLB	38 35.36N	122 54.54W	0.16	32.64	-12.51	34
12	HMR	38 9.28N	121 48.02W	0.06	-64.40	35.15	129
13	LNS	38 9.15N	122 42.75W	0.12	-16.19	-28.52	83
14	MIX	38 24.68N	122 3.44W	0.18	-28.16	34.41	99
15	MWS	38 33.03N	122 43.37W	0.13	19.33	-2.31	45
16	OLC	38 2.38N	122 47.55W	0.03	-21.82	-41.71	81
17	PNM	38 50.85N	122 56.72W	0.76	57.21	2.51	6
18	SGM	38 52.00N	122 42.60W	0.11	46.43	19.96	17
19	SHC	38 40.22N	122 38.03W	1.20	25.14	11.93	37
20	SHR	38 31.20N	122 36.43W	0.33	10.51	3.61	56
21	SKG	38 42.12N	123 0.81W	0.28	48.08	-12.05	14
22	SPT	38 10.96N	122 27.20W	0.09	-27.35	-8.48	95
23	TMN	38 23.15N	122 40.83W	0.10	2.61	-10.52	64
24	WHW	38 27.42N	122 53.26W	0.05	19.89	-20.02	43

OBSERVATION MATRIX

0	0	0	0	0	2	0	0	0	0
0	0	0	2	0	0	1	0	0	0
0	0	0	0	0	5	0	0	0	0
0	0	0	1	0	5	4	0	0	0
0	0	50	23	86	0	3	0	0	0
0	0	5	3	0	88	0	0	0	0
0	0	54	60	16	0	0	0	0	6
0	0	21	7	4	77	0	0	0	0
1	7	44	6	11	0	0	0	0	0
4	0	0	1	25	0	71	0	64	0
0	0	0	0	0	0	0	0	0	0
0	0	5	0	0	0	0	0	0	0
0	5	57	2	7	0	8	0	12	0

0	0	0	0	0	0	0	0	0
0	0	0	0	1	0	0	0	0
0	0	0	0	3	2	0	0	0
0	0	0	43	66	3	0	0	0
0	0	4	117	130	5	3	0	0
0	0	41	44	93	6	13	0	0
0	0	4	28	48	70	30	0	0
0	0	38	14	1	2	8	1	0
0	0	0	18	12	10	4	1	0
0	0	0	0	0	0	0	0	0

0	0	0	0	0	0	0	0	0	0
0	0	0	0	0	0	0	0	0	0
0	0	0	0	0	2	0	0	0	0
0	0	0	7	32	6	0	0	0	0
0	0	0	54	118	35	1	1	0	0
0	0	0	60	110	76	18	0	0	0
0	0	0	42	73	67	16	1	0	0
0	0	0	34	19	20	22	1	1	2
0	0	0	7	18	8	4	0	1	2
0	0	0	0	0	0	0	0	1	1
0	0	0	0	0	0	0	0	1	0

0	0	0	0	0	0	0	0	0	0	0
0	0	0	0	0	0	0	0	0	0	0
0	0	0	0	1	1	1	0	0	0	0
0	0	0	0	25	30	2	1	0	0	0
0	0	0	12	63	43	16	0	1	0	0
0	0	0	60	88	41	29	0	0	0	0
0	0	0	33	58	68	27	5	0	0	0
0	0	0	12	30	69	12	6	1	0	0
0	0	0	19	14	23	15	13	1	0	0
0	0	0	0	15	7	2	2	0	0	0
0	0	0	0	1	0	3	2	0	0	0
0	0	0	0	0	0	0	0	0	0	0

***** CALIFORNIA: SANTA ROSA REGION *****

NO OF STATIONS= 24
NO OF EVENTS= 95
NO OF OBSERVATIONS= 863

TOTAL BLOCKS IN MODEL= 462
NO OF BLOCKS OBSERVED= 144

DATA VARIANCE IS 0.0800
RESIDUAL VARIANCE IS 0.0203
VARIANCE IMPROVEMENT IN % IS 74.6697

VELOCITY PERTURBATIONS IN LAYER-BLOCK FORMAT

LAYER ... 1

0.0	0.0	0.0	0.0	0.0	0.45	0.0	0.0	0.0	0.0
0.0	0.0	0.0	-0.27	0.0	0.0	-3.18	0.0	0.0	0.0
0.0	0.0	0.0	0.0	0.0	0.78	0.0	0.0	0.0	0.0
0.0	0.0	0.0	-0.20	0.0	0.90	2.35	0.0	0.0	0.0
0.0	0.0	1.65	-1.54	0.62	0.0	1.74	0.0	0.0	0.0
0.0	0.0	1.72	-0.95	0.0	1.89	0.0	0.0	0.0	0.0
0.0	0.0	0.84	-1.52	-3.63	0.0	0.0	0.0	0.0	-3.19
0.0	0.0	2.76	2.19	0.70	4.82	0.0	0.0	0.0	0.0
0.49	0.37	2.84	1.07	0.71	0.0	0.0	0.0	0.0	0.0
-1.92	0.0	0.0	-3.38	2.60	0.0	3.74	0.0	-5.28	0.0
0.0	0.0	0.0	0.0	0.0	0.0	0.0	0.0	0.0	0.0
0.0	0.0	2.45	0.0	0.0	0.0	0.0	0.0	0.0	0.0
0.0	0.99	3.44	-0.24	-0.27	0.0	-3.20	0.0	-7.62	0.0

LAYER ... 2

0.0	0.0	0.0	0.0	0.0	0.0	0.0	0.0	0.0
0.0	0.0	0.0	0.0	1.00	0.0	0.0	0.0	0.0
0.0	0.0	0.0	0.0	-0.30	-4.59	0.0	0.0	0.0
0.0	0.0	0.0	2.76	1.87	0.33	0.0	0.0	0.0
0.0	0.0	0.81	2.46	1.73	3.09	-3.22	0.0	0.0
0.0	0.0	3.90	2.45	3.05	0.63	-5.19	0.0	0.0
0.0	0.0	-0.59	1.60	3.62	0.96	0.53	0.0	0.0
0.0	0.0	5.73	1.85	0.61	-2.17	-4.97	-0.58	0.0
0.0	0.0	0.0	-0.08	-2.04	-6.20	-6.17	-7.00	0.0
0.0	0.0	0.0	0.0	0.0	0.0	0.0	0.0	0.0

LAYER ... 3

0.0	0.0	0.0	0.0	0.0	0.0	0.0	0.0	0.0	0.0
0.0	0.0	0.0	0.0	0.0	0.0	0.0	0.0	0.0	0.0
0.0	0.0	0.0	0.0	0.0	-5.83	0.0	0.0	0.0	0.0
0.0	0.0	0.0	1.61	1.09	0.88	0.0	0.0	0.0	0.0
0.0	0.0	0.0	5.05	2.35	1.44	-2.35	-0.69	0.0	0.0
0.0	0.0	0.0	4.64	2.84	1.27	-0.65	0.0	0.0	0.0
0.0	0.0	0.0	3.28	1.33	1.47	-1.45	-1.50	0.0	0.0
0.0	0.0	0.0	3.53	1.36	-2.40	-5.78	-1.09	2.98	2.81
0.0	0.0	0.0	-1.28	-2.06	-4.19	-8.29	0.0	2.35	1.90
0.0	0.0	0.0	0.0	0.0	0.0	0.0	0.0	0.0	1.46
0.0	0.0	0.0	0.0	0.0	0.0	0.0	0.0	3.11	0.0

1307

LAYER ... 4

0.0	0.0	0.0	0.0	0.0	0.0	0.0	0.0	0.0	0.0	0.0
0.0	0.0	0.0	0.0	0.0	0.0	0.0	0.0	0.0	0.0	0.0
0.0	0.0	0.0	0.0	1.15	-7.17	1.34	0.0	0.0	0.0	0.0
0.0	0.0	0.0	0.0	3.37	0.07	0.71	0.19	0.0	0.0	0.0
0.0	0.0	0.0	2.96	3.59	0.40	-1.06	0.0	-0.69	0.0	0.0
0.0	0.0	0.0	2.94	4.26	-1.29	-0.05	0.0	0.0	0.0	0.0
0.0	0.0	0.0	1.75	2.97	-1.83	-0.03	-0.16	0.0	0.0	0.0
0.0	0.0	0.0	-2.29	.0.82	-1.44	-1.23	-2.59	-1.50	0.0	0.0
0.0	0.0	0.0	-1.21	0.07	-0.94	3.09	0.59	-1.09	0.0	0.0
0.0	0.0	0.0	0.0	1.45	-0.57	-1.11	-3.54	0.0	0.0	0.0
0.0	0.0	0.0	0.0	-0.49	0.0	-2.11	-4.75	0.0	0.0	0.0
0.0	0.0	0.0	0.0	0.0	0.0	0.0	0.0	0.0	0.0	0.0

DIAGONAL ELEMENTS OF RESOLUTION MATRIX IN LAYER-BLOCK FORMAT

LAYER ... 1

0.0	0.0	0.0	0.0	0.0	0.08	0.0	0.0	0.0	0.0
0.0	0.0	0.0	0.10	0.0	0.0	0.04	0.0	0.0	0.0
0.0	0.0	0.0	0.0	0.0	0.19	0.0	0.0	0.0	0.0
0.0	0.0	0.0	0.06	0.0	0.16	0.16	0.0	0.0	0.0
0.0	0.0	0.37	0.39	0.59	0.0	0.11	0.0	0.0	0.0
0.0	0.0	0.20	0.14	0.0	0.60	0.0	0.0	0.0	0.0
0.0	0.0	0.62	0.63	0.42	0.0	0.0	0.0	0.0	0.17
0.0	0.0	0.35	0.25	0.17	0.55	0.0	0.0	0.0	0.0
0.05	0.22	0.50	0.21	0.32	0.0	0.0	0.0	0.0	0.0
0.14	0.0	0.0	0.05	0.47	0.0	0.54	0.0	0.44	0.0
0.0	0.0	0.0	0.0	0.0	0.0	0.0	0.0	0.0	0.0
0.0	0.0	0.17	0.0	0.0	0.0	0.0	0.0	0.0	0.0
0.0	0.17	0.44	0.08	0.18	0.0	0.17	0.0	0.20	0.0

LAYER ... 2

0.0	0.0	0.0	0.0	0.0	0.0	0.0	0.0	0.0
0.0	0.0	0.0	0.0	0.10	0.0	0.0	0.0	0.0
0.0	0.0	0.0	0.0	0.29	0.20	0.0	0.0	0.0
0.0	0.0	0.0	0.67	0.74	0.28	0.0	0.0	0.0
0.0	0.0	0.36	0.80	0.78	0.40	0.26	0.0	0.0
0.0	0.0	0.68	0.77	0.79	0.40	0.48	0.0	0.0
0.0	0.0	0.32	0.66	0.72	0.76	0.58	0.0	0.0
0.0	0.0	0.54	0.54	0.13	0.20	0.48	0.28	0.0
0.0	0.0	0.0	0.34	0.44	0.38	0.19	0.28	0.0
0.0	0.0	0.0	0.0	0.0	0.0	0.0	0.0	0.0

LAYER ... 3

0.0	0.0	0.0	0.0	0.0	0.0	0.0	0.0	0.0	0.0
0.0	0.0	0.0	0.0	0.0	0.0	0.0	0.0	0.0	0.0
0.0	0.0	0.0	0.0	0.0	0.29	0.0	0.0	0.0	0.0
0.0	0.0	0.0	0.57	0.76	0.54	0.0	0.0	0.0	0.0
0.0	0.0	0.0	0.81	0.87	0.79	0.21	0.18	0.0	0.0
0.0	0.0	0.0	0.81	0.87	0.86	0.59	0.0	0.0	0.0
0.0	0.0	0.0	0.78	0.84	0.83	0.68	0.19	0.0	0.0
0.0	0.0	0.0	0.60	0.72	0.71	0.67	0.19	0.87	0.89
0.0	0.0	0.0	0.48	0.64	0.53	0.34	0.0	0.86	0.90
0.0	0.0	0.0	0.0	0.0	0.0	0.0	0.0	0.0	0.86
0.0	0.0	0.0	0.0	0.0	0.0	0.0	0.0	0.85	0.0

LAYER ... 4

0.0	0.0	0.0	0.0	0.0	0.0	0.0	0.0	0.0	0.0	0.0
0.0	0.0	0.0	0.0	0.0	0.0	0.0	0.0	0.0	0.0	0.0
0.0	0.0	0.0	0.0	0.26	0.18	0.18	0.0	0.0	0.0	0.0
0.0	0.0	0.0	0.0	0.76	0.74	0.29	0.19	0.0	0.0	0.0
0.0	0.0	0.0	0.69	0.84	0.83	0.69	0.0	0.18	0.0	0.0
0.0	0.0	0.0	0.80	0.87	0.84	0.73	0.0	0.0	0.0	0.0
0.0	0.0	0.0	0.71	0.86	0.87	0.83	0.49	0.0	0.0	0.0
0.0	0.0	0.0	0.61	0.80	0.87	0.72	0.55	0.19	0.0	0.0
0.0	0.0	0.0	0.61	0.70	0.73	0.61	0.54	0.19	0.0	0.0
0.0	0.0	0.0	0.0	0.53	0.52	0.31	0.28	0.0	0.0	0.0
0.0	0.0	0.0	0.0	0.20	0.0	0.38	0.29	0.0	0.0	0.0
0.0	0.0	0.0	0.0	0.0	0.0	0.0	0.0	0.0	0.0	0.0

STD ERRORS IN LAYER-BLOCK FORMAT

LAYER ... 1

0.0	0.0	0.0	0.0	0.0	0.47	0.0	0.0	0.0	0.0
0.0	0.0	0.0	0.58	0.0	0.0	0.28	0.0	0.0	0.0
0.0	0.0	0.0	0.0	0.0	0.73	0.0	0.0	0.0	0.0
0.0	0.0	0.0	0.46	0.0	0.68	0.70	0.0	0.0	0.0
0.0	0.0	0.80	0.85	0.79	0.0	0.54	0.0	0.0	0.0
0.0	0.0	0.77	0.66	0.0	0.78	0.0	0.0	0.0	0.0
0.0	0.0	0.85	0.85	0.92	0.0	0.0	0.0	0.0	0.60
0.0	0.0	0.84	0.84	0.73	0.86	0.0	0.0	0.0	0.0
0.39	0.78	0.86	0.79	0.87	0.0	0.0	0.0	0.0	0.0
0.62	0.0	0.0	0.41	0.90	0.0	0.77	0.0	0.72	0.0
0.0	0.0	0.0	0.0	0.0	0.0	0.0	0.0	0.0	0.0
0.0	0.0	0.68	0.0	0.0	0.0	0.0	0.0	0.0	0.0
0.0	0.71	0.79	0.52	0.65	0.0	0.60	0.0	0.60	0.0

LAYER ... 2

0.0	0.0	0.0	0.0	0.0	0.0	0.0	0.0	0.0
0.0	0.0	0.0	0.0	0.47	0.0	0.0	0.0	0.0
0.0	0.0	0.0	0.0	0.86	0.68	0.0	0.0	0.0
0.0	0.0	0.0	0.72	0.69	0.83	0.0	0.0	0.0
0.0	0.0	0.92	0.56	0.60	0.90	0.74	0.0	0.0
0.0	0.0	0.75	0.69	0.61	0.91	0.80	0.0	0.0
0.0	0.0	0.82	0.78	0.68	0.65	0.74	0.0	0.0
0.0	0.0	0.74	0.85	0.65	0.74	0.84	0.81	0.0
0.0	0.0	0.0	0.62	0.76	0.73	0.45	0.82	0.0
0.0	0.0	0.0	0.0	0.0	0.0	0.0	0.0	0.0

LAYER ... 3

0.0	0.0	0.0	0.0	0.0	0.0	0.0	0.0	0.0	0.0
0.0	0.0	0.0	0.0	0.0	0.0	0.0	0.0	0.0	0.0
0.0	0.0	0.0	0.0	0.0	0.72	0.0	0.0	0.0	0.0
0.0	0.0	0.0	0.89	0.69	0.85	0.0	0.0	0.0	0.0
0.0	0.0	0.0	0.60	0.47	0.67	0.75	0.63	0.0	0.0
0.0	0.0	0.0	0.61	0.49	0.52	0.78	0.0	0.0	0.0
0.0	0.0	0.0	0.66	0.55	0.58	0.76	0.65	0.0	0.0
0.0	0.0	0.0	0.69	0.74	0.73	0.69	0.66	0.62	0.52
0.0	0.0	0.0	0.83	0.72	0.79	0.61	0.0	0.62	0.51
0.0	0.0	0.0	0.0	0.0	0.0	0.0	0.0	0.0	0.62
0.0	0.0	0.0	0.0	0.0	0.0	0.0	0.0	0.62	0.0

LAYER ... 4

0.0	0.0	0.0	0.0	0.0	0.0	0.0	0.0	0.0	0.0	0.0
0.0	0.0	0.0	0.0	0.0	0.0	0.0	0.0	0.0	0.0	0.0
0.0	0.0	0.0	0.0	0.85	0.64	0.63	0.0	0.0	0.0	0.0
0.0	0.0	0.0	0.0	0.68	0.71	0.82	0.72	0.0	0.0	0.0
0.0	0.0	0.0	0.83	0.56	0.59	0.79	0.0	0.63	0.0	0.0
0.0	0.0	0.0	0.64	0.52	0.61	0.73	0.0	0.0	0.0	0.0
0.0	0.0	0.0	0.73	0.55	0.54	0.63	0.92	0.0	0.0	0.0
0.0	0.0	0.0	0.82	0.69	0.53	0.83	0.90	0.65	0.0	0.0
0.0	0.0	0.0	0.76	0.78	0.71	0.81	0.78	0.66	0.0	0.0
0.0	0.0	0.0	0.0	0.74	0.82	0.85	0.76	0.0	0.0	0.0
0.0	0.0	0.0	0.0	0.75	0.0	0.86	0.76	0.0	0.0	0.0
0.0	0.0	0.0	0.0	0.0	0.0	0.0	0.0	0.0	0.0	0.0

TABLE 3.6.

Three-Dimensional Inversion of California

Herrin Residuals - San Jose Subarray

***** PROGRAM 3-D *****

22 NOVEMBER 1975

CALIFORNIA: SAN JOSE REGION

LATITUDE	LONGITUDE	THA	VO	JPWT	IRES	IPUNCH	IPRINT	THETA	RESL
37N26.00	121W56.50	36.5	5.60	4	1	1	0	50.	0.100

IPARM=-1,0,1 INDICATE,RESPECTIVELY,SOLUTION IS IN TERMS OF VELOCITY PERTURBATIONS, LAYER DEPTH PERTURBATIONS, OR THAT BOTH SOLUTIONS WILL BE COMPUTED
FOR THIS RUN, IPARM= -1

	VELOCITY	THICKNESS	#-NORTH	LENGTH	#-EAST	LENGTH	COORDINATE	DISPLACEMENT
1	5.60	10.00	13	10.00	10	10.00	0.0	0.0
2	6.90	20.00	10	20.00	9	20.00	0.0	0.0
3	8.00	30.00	11	25.00	10	25.00	0.0	0.0
4	8.00	30.00	12	25.00	11	25.00	0.0	0.0

	STA	LATITUDE	LONGITUDE	ELEVATION	RELATIVE COORDINATES		INDEX
1	ACH	37 58.57N	121 45.62W	0.07	38.92	48.60	30
2	ALM	37 9.50N	121 50.82W	0.24	-29.50	-11.38	94
3	AND	37 9.74N	121 37.45W	0.24	-40.87	4.80	106
4	ANG	37 51.68N	122 25.77W	0.22	63.74	-6.18	5
5	ARN	37 20.96N	121 31.96W	0.63	-28.96	23.61	98
6	BAM	37 19.09N	122 9.16W	0.82	0.87	-22.60	63
7	BCR	37 9.62N	122 1.57W	0.66	-19.87	-24.03	83
8	BGH	37 20.52N	122 20.34W	0.16	12.84	-34.25	52
9	BOL	37 48.97N	122 3.72W	0.61	40.42	16.74	27
10	BWR	37 55.45N	122 6.40W	0.22	52.37	20.73	18
11	CAL	37 27.07N	121 47.95W	0.26	-5.89	11.31	77
12	CAN	37 1.52N	121 29.02W	0.33	-60.49	5.88	126
13	CEC	36 55.88N	121 39.63W	0.22	-59.59	-12.97	124
14	CBO	37 6.71N	121 41.33W	0.19	-41.98	-3.14	105
15	CCR	37 47.30N	121 57.00W	0.18	32.07	22.82	38
16	CHR	36 57.46N	121 35.01W	0.24	-61.29	-5.72	125
17	COE	37 15.46N	121 40.35W	0.37	-29.81	7.61	96
18	CRK	37 14.50N	122 7.82W	0.61	-7.12	-26.07	73
19	CRC	37 14.50N	122 7.82W	0.61	-7.12	-26.07	73
20	CSH	37 38.88N	122 2.57W	0.17	24.44	6.99	46
21	DOO	37 43.80N	121 50.12W	0.20	20.87	27.09	48
22	DSR	37 57.99N	122 15.17W	0.11	63.78	13.22	7
23	DUR	38 1.78N	122 0.05W	0.17	56.23	35.16	9
24	EGR	37 2.11N	122 6.25W	0.44	-26.88	-37.86	92
25	ELG	37 30.84N	122 27.74W	0.20	34.64	-31.57	32
26	EUC	37 3.04N	121 48.56W	0.44	-41.09	-15.78	104
27	GHS	37 5.75N	121 26.83W	0.78	-56.10	13.11	127
28	HCC	36 58.88N	121 43.35W	0.16	-51.86	-14.12	114
29	LCH	37 44.28N	122 3.83W	0.31	33.56	11.45	37
30	LTW	37 21.22N	122 12.25W	0.27	6.75	-23.91	53
31	LXR	37 12.11N	121 59.17W	0.24	-18.28	-18.44	84
32	MDC	37 52.90N	121 54.85W	1.17	38.52	31.51	29
33	MGA	37 38.22N	122 28.43W	0.20	46.17	-24.21	13
34	MHR	37 21.57N	121 45.38W	0.52	-16.32	8.33	86
35	MIL	37 46.88N	122 10.55W	0.09	43.29	6.40	26
36	MNR	37 35.68N	121 38.22W	0.50	-1.57	32.27	69
37	MOR	37 48.68N	121 48.15W	0.79	26.41	34.77	39
38	MSJ	37 31.25N	121 52.23W	0.50	4.06	10.82	67
39	MTB	37 17.44N	122 5.43W	0.35	-4.86	-20.00	64
40	PAL	37 37.89N	121 57.37W	0.46	18.41	12.03	47
41	PES	37 11.94N	122 20.90W	0.08	0.63	-44.40	61
42	PLV	36 58.62N	121 49.93W	0.16	-46.45	-22.26	113
43	PMR	36 57.19N	121 41.70W	0.09	-55.82	-14.00	124
44	RUS	37 54.75N	121 54.33W	0.33	40.81	34.15	29
45	SAC	37 34.95N	122 25.03W	0.21	38.33	-23.83	23
46	SAL	37 34.56N	122 25.40W	0.33	38.08	-24.69	23
47	SAW	37 12.74N	122 10.06W	0.26	-7.76	-30.67	72
48	SFR	37 47.28N	122 23.37W	0.01	55.12	-8.23	5
49	SFT	37 24.31N	122 10.55W	0.14	9.83	-18.49	54
50	SGC	37 16.96N	122 3.00W	0.20	-7.71	-17.65	74
51	SOS	37 10.17N	121 55.84W	0.95	-24.09	-16.61	84
52	STJ	37 20.03N	122 5.48W	0.12	-0.98	-17.21	64
53	STV	37 17.07N	122 7.42W	0.36	-3.66	-22.77	63
54	SVC	37 17.11N	121 46.35W	0.13	-22.11	2.28	86
55	WDS	37 25.08N	122 16.33W	0.28	16.06	-24.47	43
56	CYH	37 33.54N	122 5.62W	0.04	19.19	-2.49	45

OBSERVATION MATRIX

0	0	0	0	50	0	7	0	8	0
0	0	7	0	0	0	23	51	5	0
0	0	18	0	0	3	106	1	34	5
0	1	0	0	0	2	17	30	74	0
0	0	18	0	38	7	100	87	20	0
0	6	78	36	0	0	8	0	0	0
57	0	67	13	0	8	53	1	100	0
0	10	34	7	0	52	50	0	0	0
0	6	24	7	1	111	1	0	0	0
0	50	0	31	2	61	1	112	0	0
0	0	1	49	106	47	0	0	0	0
0	0	9	8	0	0	12	0	0	0
0	0	0	9	106	43	20	0	0	0

0	0	0	0	0	0	0	0	0
0	0	0	21	37	14	2	0	0
0	0	3	11	37	149	15	1	0
0	0	6	19	62	175	66	3	0
0	16	47	137	88	68	58	1	0
0	0	42	101	139	89	29	1	0
0	0	39	56	161	125	5	0	0
0	0	0	58	145	22	2	0	0
0	0	0	29	44	14	1	0	0
0	0	0	0	0	0	0	0	0

0	0	0	0	0	0	0	0	0	0
0	0	0	0	5	0	0	0	0	0
0	0	0	3	44	40	10	0	0	0
0	0	1	11	43	156	53	3	0	0
0	0	8	82	86	183	85	3	0	0
0	0	18	114	123	188	62	2	0	1
0	0	13	39	187	128	38	1	0	0
0	0	0	29	155	94	30	1	3	1
0	0	0	0	27	41	0	0	3	2
0	0	0	0	0	3	0	0	1	5
0	0	0	0	0	0	0	0	0	2

0	0	0	0	0	0	0	0	0	0	0
0	0	0	0	6	5	2	0	0	0	0
0	0	0	1	20	30	28	4	0	0	0
0	0	1	7	38	105	58	13	1	0	0
0	0	1	31	73	166	61	17	1	0	0
0	0	13	80	85	141	97	34	2	0	0
0	0	9	40	136	98	67	47	2	0	0
0	0	6	25	119	80	56	26	1	0	0
0	0	0	12	51	49	64	9	0	0	0
0	0	0	0	2	46	36	0	0	0	0
0	0	0	0	0	2	4	0	0	0	0
0	0	0	0	0	0	0	0	0	0	0

***** CALIFORNIA: SAN JOSE REGION *****

NO OF STATIONS= 56
NO OF EVENTS=121
NO OF OBSERVATIONS= 2138

TOTAL BLOCKS IN MODEL= 462
NO OF BLOCKS OBSERVED= 203

DATA VARIANCE IS 0.1086
RESIDUAL VARIANCE IS 0.0663
VARIANCE IMPROVEMENT IN % IS 38.9638

320

.VELOCITY PERTURBATIONS IN LAYER-BLOCK FORMAT

LAYER ... 1

0.0	0.0	0.0	0.0	3.06	0.0	-0.18	0.0	-3.21	0.0
0.0	0.0	2.25	0.0	0.0	0.0	-0.19	-1.94	-3.58	0.0
0.0	0.0	1.02	0.0	0.0	-1.51	-1.46	-0.48	15.53	-5.82
0.0	0.76	0.0	0.0	0.0	0.59	1.16	-11.35	-0.43	0.0
0.0	0.0	-0.25	0.0	1.77	1.25	0.50	-8.12	-2.50	0.0
0.0	-5.28	4.00	-3.41	0.0	0.0	2.19	0.0	0.0	0.0
2.66	0.0	5.67	-5.43	0.0	2.02	1.23	-0.69	3.50	0.0
0.0	-2.48	2.45	-2.22	0.0	-0.43	-0.42	0.0	0.0	0.0
0.0	4.42	-0.73	2.46	-0.01	-8.93	0.43	0.0	0.0	0.0
0.0	3.53	0.0	4.71	1.27	-8.81	-0.99	-0.69	0.0	0.0
0.0	0.0	-0.71	2.13	0.56	-0.17	0.0	0.0	0.0	0.0
0.0	0.0	-1.02	-3.19	0.0	0.0	2.54	0.0	0.0	0.0
0.0	0.0	0.0	-0.01	8.87	-1.32	-0.14	0.0	0.0	0.0

LAYER ... 2

0.0	0.0	0.0	0.0	0.0	0.0	0.0	0.0	0.0
0.0	0.0	0.0	3.41	1.48	-0.83	-2.13	0.0	0.0
0.0	0.0	1.74	-1.05	-1.11	-1.33	1.15	-2.23	0.0
0.0	0.0	-1.52	0.43	0.03	-2.43	-2.48	-3.65	0.0
0.0	1.07	0.43	0.04	-3.33	0.57	-2.46	-0.83	0.0
0.0	0.0	4.09	1.31	-3.18	1.88	-3.98	1.73	0.0
0.0	0.0	4.75	-2.32	-1.80	-0.13	0.43	0.0	0.0
0.0	0.0	0.0	1.16	0.76	-0.50	-1.76	0.0	0.0
0.0	0.0	0.0	1.33	5.61	1.46	-0.01	0.0	0.0
0.0	0.0	0.0	0.0	0.0	0.0	0.0	0.0	0.0

LAYER ... 3

0.0	0.0	0.0	0.0	0.0	0.0	0.0	0.0	0.0	0.0
0.0	0.0	0.0	0.0	1.52	0.0	0.0	0.0	0.0	0.0
0.0	0.0	0.0	1.77	2.81	-2.17	-5.16	0.0	0.0	0.0
0.0	0.0	1.71	2.49	2.94	-1.59	-3.10	-2.03	0.0	0.0
0.0	0.0	2.01	2.56	0.40	-2.12	-2.56	-3.13	0.0	0.0
0.0	0.0	1.78	0.24	0.16	-3.40	-1.72	-0.98	0.0	0.52
0.0	0.0	0.69	1.49	1.10	-0.74	-3.35	-1.36	0.0	0.0
0.0	0.0	0.0	-0.70	-0.07	-0.74	-1.28	1.23	1.88	0.87
0.0	0.0	0.0	0.0	0.05	3.20	0.0	0.0	2.55	-0.66
0.0	0.0	0.0	0.0	0.0	3.30	0.0	0.0	2.33	0.67
0.0	0.0	0.0	0.0	0.0	0.0	0.0	0.0	0.0	0.43

LAYER ... 4

0.0	0.0	0.0	0.0	0.0	0.0	0.0	0.0	0.0	0.0	0.0
0.0	0.0	0.0	0.0	0.30	0.53	-2.49	0.0	0.0	0.0	0.0
0.0	0.0	0.0	1.10	0.71	-2.18	-4.26	-2.16	0.0	0.0	0.0
0.0	0.0	1.71	-0.45	-1.29	-0.08	-2.48	-6.29	3.38	0.0	0.0
0.0	0.0	2.32	0.04	0.84	1.79	1.35	-1.32	-2.47	0.0	0.0
0.0	0.0	1.11	0.43	3.05	0.93	1.51	-0.87	0.60	0.0	0.0
0.0	0.0	0.64	0.08	1.19	-1.32	1.26	-1.52	-0.98	0.0	0.0
0.0	0.0	2.29	-0.37	-0.02	-0.84	-0.57	-0.78	-1.36	0.0	0.0
0.0	0.0	0.0	-0.23	0.23	0.36	-1.04	0.04	0.0	0.0	0.0
0.0	0.0	0.0	0.0	-0.38	-0.18	-1.64	0.0	0.0	0.0	0.0
0.0	0.0	0.0	0.0	0.0	1.55	2.30	0.0	0.0	0.0	0.0
0.0	0.0	0.0	0.0	0.0	0.0	0.0	0.0	0.0	0.0	0.0

DIAGONAL ELEMENTS OF RESOLUTION MATRIX IN LAYER-BLOCK FORMAT

324

LAYER ... 1

0.0	0.0	0.0	0.0	0.52	0.0	0.28	0.0	0.30	0.0
0.0	0.0	0.22	0.0	0.0	0.0	0.48	0.58	0.18	0.0
0.0	0.0	0.40	0.0	0.0	0.16	0.76	0.09	0.59	0.19
0.0	0.05	0.0	0.0	0.0	0.12	0.47	0.59	0.64	0.0
0.0	0.0	0.42	0.0	0.58	0.27	0.75	0.72	0.40	0.0
0.0	0.25	0.67	0.56	0.0	0.0	0.31	0.0	0.0	0.0
0.52	0.0	0.68	0.43	0.0	0.29	0.67	0.06	0.67	0.0
0.0	0.36	0.57	0.30	0.0	0.62	0.62	0.0	0.0	0.0
0.0	0.24	0.54	0.31	0.06	0.77	0.05	0.0	0.0	0.0
0.0	0.41	0.0	0.58	0.14	0.70	0.06	0.61	0.0	0.0
0.0	0.0	0.06	0.63	0.77	0.68	0.0	0.0	0.0	0.0
0.0	0.0	0.30	0.29	0.0	0.0	0.28	0.0	0.0	0.0
0.0	0.0	0.0	0.30	0.70	0.60	0.42	0.0	0.0	0.0

LAYER ... 2

0.0	0.0	0.0	0.0	0.0	0.0	0.0	0.0	0.0
0.0	0.0	0.0	0.48	0.66	0.57	0.21	0.0	0.0
0.0	0.0	0.27	0.54	0.74	0.84	0.67	0.11	0.0
0.0	0.0	0.45	0.69	0.82	0.87	0.79	0.42	0.0
0.0	0.36	0.75	0.84	0.85	0.84	0.81	0.33	0.0
0.0	0.0	0.76	0.84	0.86	0.85	0.68	0.34	0.0
0.0	0.0	0.63	0.81	0.89	0.83	0.46	0.0	0.0
0.0	0.0	0.0	0.80	0.87	0.71	0.48	0.0	0.0
0.0	0.0	0.0	0.67	0.72	0.53	0.33	0.0	0.0
0.0	0.0	0.0	0.0	0.0	0.0	0.0	0.0	0.0

LAYER ... 3

0.0	0.0	0.0	0.0	0.0	0.0	0.0	0.0	0.0	0.0
0.0	0.0	0.0	0.0	0.50	0.0	0.0	0.0	0.0	0.0
0.0	0.0	0.0	0.44	0.74	0.80	0.67	0.0	0.0	0.0
0.0	0.0	0.21	0.69	0.85	0.89	0.84	0.40	0.0	0.0
0.0	0.0	0.64	0.87	0.89	0.91	0.88	0.42	0.0	0.0
0.0	0.0	0.48	0.87	0.91	0.92	0.84	0.28	0.0	0.89
0.0	0.0	0.60	0.84	0.91	0.90	0.76	0.20	0.0	0.0
0.0	0.0	0.0	0.76	0.89	0.88	0.78	0.89	0.95	0.89
0.0	0.0	0.0	0.0	0.76	0.80	0.0	0.0	0.95	0.93
0.0	0.0	0.0	0.0	0.0	0.44	0.0	0.0	0.89	0.96
0.0	0.0	0.0	0.0	0.0	0.0	0.0	0.0	0.0	0.92

326

247

276

306

LAYER ... 4

0.0	0.0	0.0	0.0	0.0	0.0	0.0	0.0	0.0	0.0	0.0
0.0	0.0	0.0	0.0	0.54	0.60	0.41	0.0	0.0	0.0	0.0
0.0	0.0	0.0	0.24	0.72	0.82	0.83	0.51	0.0	0.0	0.0
0.0	0.0	0.21	0.64	0.85	0.89	0.88	0.73	0.21	0.0	0.0
0.0	0.0	0.26	0.83	0.89	0.93	0.90	0.76	0.21	0.0	0.0
0.0	0.0	0.53	0.86	0.91	0.93	0.91	0.84	0.38	0.0	0.0
0.0	0.0	0.60	0.85	0.91	0.92	0.90	0.83	0.28	0.0	0.0
0.0	0.0	0.50	0.78	0.91	0.91	0.87	0.74	0.20	0.0	0.0
0.0	0.0	0.0	0.69	0.85	0.86	0.85	0.66	0.0	0.0	0.0
0.0	0.0	0.0	0.0	0.34	0.83	0.81	0.0	0.0	0.0	0.0
0.0	0.0	0.0	0.0	0.0	0.40	0.53	0.0	0.0	0.0	0.0
0.0	0.0	0.0	0.0	0.0	0.0	0.0	0.0	0.0	0.0	0.0

STD ERRORS IN LAYER-BLOCK FORMAT

LAYER ... 1

0.0	0.0	0.0	0.0	1.59	0.0	1.59	0.0	1.58	0.0
0.0	0.0	1.32	0.0	0.0	0.0	1.71	1.57	1.29	0.0
0.0	0.0	1.56	0.0	0.0	1.30	1.35	1.00	1.63	1.30
0.0	0.80	0.0	0.0	0.0	1.16	1.73	1.67	1.54	0.0
0.0	0.0	1.64	0.0	1.64	1.55	1.39	1.44	1.64	0.0
0.0	1.54	1.45	1.60	0.0	0.0	1.64	0.0	0.0	0.0
1.54	0.0	1.48	1.71	0.0	1.59	1.58	0.88	1.47	0.0
0.0	1.70	1.67	1.62	0.0	1.60	1.63	0.0	0.0	0.0
0.0	1.49	1.70	1.65	0.88	1.32	0.74	0.0	0.0	0.0
0.0	1.43	0.0	1.68	1.24	1.51	0.80	1.52	0.0	0.0
0.0	0.0	0.86	1.60	1.34	1.56	0.0	0.0	0.0	0.0
0.0	0.0	1.57	1.58	0.0	0.0	1.46	0.0	0.0	0.0
0.0	0.0	0.0	1.58	1.37	1.56	1.57	0.0	0.0	0.0

LAYER ... 2

0.0	0.0	0.0	0.0	0.0	0.0	0.0	0.0	0.0
0.0	0.0	0.0	1.37	1.39	1.60	1.39	0.0	0.0
0.0	0.0	1.38	1.57	1.37	0.98	1.52	1.05	0.0
0.0	0.0	1.70	1.47	1.16	0.93	1.20	1.66	0.0
0.0	1.34	1.29	0.97	1.04	1.14	1.21	1.64	0.0
0.0	0.0	1.29	1.04	0.98	1.07	1.52	1.66	0.0
0.0	0.0	1.30	1.18	0.87	1.10	1.70	0.0	0.0
0.0	0.0	0.0	1.19	0.94	1.39	1.73	0.0	0.0
0.0	0.0	0.0	1.47	1.32	1.53	1.65	0.0	0.0
0.0	0.0	0.0	0.0	0.0	0.0	0.0	0.0	0.0

LAYER ... 3

0.0	0.0	0.0	0.0	0.0	0.0	0.0	0.0	0.0	0.0
0.0	0.0	0.0	0.0	1.54	0.0	0.0	0.0	0.0	0.0
0.0	0.0	0.0	1.60	1.18	1.18	1.50	0.0	0.0	0.0
0.0	0.0	1.17	1.50	1.09	0.86	1.09	1.55	0.0	0.0
0.0	0.0	1.60	0.95	0.90	0.81	0.93	1.64	0.0	0.0
0.0	0.0	1.13	0.99	0.78	0.74	1.09	1.24	0.0	1.09
0.0	0.0	1.47	1.13	0.78	0.82	1.29	1.23	0.0	0.0
0.0	0.0	0.0	1.30	0.84	0.89	1.24	1.08	0.72	1.09
0.0	0.0	0.0	0.0	1.30	1.18	0.0	0.0	0.72	0.85
0.0	0.0	0.0	0.0	0.0	1.59	0.0	0.0	1.08	0.63
0.0	0.0	0.0	0.0	0.0	0.0	0.0	0.0	0.0	0.88

LAYER ... 4

0.0	0.0	0.0	0.0	0.0	0.0	0.0	0.0	0.0	0.0	0.0
0.0	0.0	0.0	0.0	1.56	1.66	1.72	0.0	0.0	0.0	0.0
0.0	0.0	0.0	1.40	1.39	1.22	1.14	1.71	0.0	0.0	0.0
0.0	0.0	1.17	1.64	1.08	0.90	0.97	1.46	1.36	0.0	0.0
0.0	0.0	1.52	1.16	0.94	0.71	0.91	1.40	1.38	0.0	0.0
0.0	0.0	1.37	1.02	0.86	0.72	0.81	1.14	1.71	0.0	0.0
0.0	0.0	1.47	1.13	0.81	0.76	0.92	1.15	1.24	0.0	0.0
0.0	0.0	1.62	1.32	0.81	0.83	1.03	1.40	1.23	0.0	0.0
0.0	0.0	0.0	1.50	1.06	1.03	1.03	1.56	0.0	0.0	0.0
0.0	0.0	0.0	0.0	1.63	1.09	1.17	0.0	0.0	0.0	0.0
0.0	0.0	0.0	0.0	0.0	1.67	1.64	0.0	0.0	0.0	0.0
0.0	0.0	0.0	0.0	0.0	0.0	0.0	0.0	0.0	0.0	0.0

RESOLUTION AND STD ERROR FOR THE FOLLOWING 3 BLOCKS
247 276 306

COLUMN OF RESCLUTION MATRIX IN LAYER-BLOCK FORMAT
FOR BLOCK 247

LAYER ... 1

0.0	0.0	0.0	0.0	0.00	0.0	0.01	0.0	0.03	0.0
0.0	0.0	-0.00	0.0	0.0	0.0	0.00	0.04	0.00	0.0
0.0	0.0	-0.00	0.0	0.0	0.00	0.00	0.00	0.03	-0.00
0.0	0.00	0.0	0.0	0.0	0.00	0.01	0.01	-0.00	0.0
0.0	0.0	-0.00	0.0	-0.00	0.00	0.00	-0.01	0.00	0.0
0.0	-0.00	-0.00	0.00	0.0	0.0	-0.00	0.0	0.0	0.0
-0.01	0.0	-0.00	0.00	0.0	-0.00	-0.00	0.00	-0.00	0.0
0.0	-0.00	-0.00	-0.00	0.0	0.00	0.00	0.0	0.0	0.0
0.0	-0.00	-0.00	-0.00	-0.00	-0.00	-0.00	0.0	0.0	0.0
0.0	-0.01	0.0	-0.00	0.00	-0.00	-0.00	-0.00	0.0	0.0
0.0	0.0	-0.00	-0.00	-0.00	-0.00	0.0	0.0	0.0	0.0
0.0	0.0	-0.00	-0.00	0.0	0.0	-0.00	0.0	0.0	0.0
0.0	0.0	0.0	-0.00	-0.01	-0.01	-0.00	0.0	0.0	0.0

LAYER ... 2

0.0	0.0	0.0	0.0	0.0	0.0	0.0	0.0	0.0
0.0	0.0	0.0	-0.00	-0.02	0.00	0.08	0.0	0.0
0.0	0.0	-0.00	-0.01	0.02	0.03	0.04	-0.01	0.0
0.0	0.0	-0.00	-0.00	0.00	0.01	0.01	-0.00	0.0
0.0	-0.01	-0.01	-0.01	0.00	0.00	0.00	0.00	0.0
0.0	0.0	-0.01	-0.01	-0.01	-0.00	0.00	0.00	0.0
0.0	0.0	-0.01	-0.01	-0.01	-0.00	-0.00	0.0	0.0
0.0	0.0	0.0	-0.01	-0.01	-0.01	0.00	0.0	0.0
0.0	0.0	0.0	-0.01	-0.01	-0.01	0.00	0.0	0.0
0.0	0.0	0.0	0.0	0.0	0.0	0.0	0.0	0.0

LAYER ... 3

0.0	0.0	0.0	0.0	0.0	0.0	0.0	0.0	0.0	0.0
0.0	0.0	0.0	0.0	-0.01	0.0	0.0	0.0	0.0	0.0
0.0	0.0	0.0	-0.01	-0.01	-0.07	0.67	0.0	0.0	0.0
0.0	0.0	-0.00	-0.01	-0.03	-0.05	-0.07	-0.02	0.0	0.0
0.0	0.0	-0.01	-0.01	-0.02	-0.03	-0.03	-0.01	0.0	0.0
0.0	0.0	-0.01	-0.01	-0.01	-0.02	-0.02	-0.01	0.0	-0.00
0.0	0.0	-0.01	-0.01	-0.01	-0.01	-0.02	-0.00	0.0	0.0
0.0	0.0	0.0	-0.01	-0.01	-0.01	-0.01	0.00	0.00	0.00
0.0	0.0	0.0	0.0	-0.01	-0.01	0.0	0.0	0.00	0.00
0.0	0.0	0.0	0.0	0.0	-0.01	0.0	0.0	0.00	0.00
0.0	0.0	0.0	0.0	0.0	0.0	0.0	0.0	0.0	0.00

LAYER ... 4

0.0	0.0	0.0	0.0	0.0	0.0	0.0	0.0	0.0	0.0	0.0
0.0	0.0	0.0	0.0	-0.00	0.01	0.01	0.0	0.0	0.0	0.0
0.0	0.0	0.0	-0.00	-0.00	0.02	0.06	0.11	0.0	0.0	0.0
0.0	0.0	-0.00	-0.01	-0.00	0.01	0.03	0.02	-0.01	0.0	0.0
0.0	0.0	-0.00	-0.01	-0.01	-0.00	-0.00	0.00	-0.00	0.0	0.0
0.0	0.0	-0.01	-0.00	-0.01	-0.00	-0.01	-0.01	-0.00	0.0	0.0
0.0	0.0	-0.00	-0.00	-0.00	-0.01	-0.01	-0.01	-0.01	0.0	0.0
0.0	0.0	-0.00	-0.00	-0.00	-0.00	-0.01	-0.00	-0.00	0.0	0.0
0.0	0.0	0.0	-0.00	-0.00	-0.00	-0.00	-0.00	0.0	0.0	0.0
0.0	0.0	0.0	0.0	-0.00	-0.00	-0.00	0.0	0.0	0.0	0.0
0.0	0.0	0.0	0.0	0.0	-0.00	-0.00	0.0	0.0	0.0	0.0

STANDARD ERROR IN % IS 1.50

COLUMN OF COVARIANCE MATRIX IN LAYER-BLOCK FORMAT
FOR BLOCK 247

333

LAYER ... 1

0.0	0.0	0.0	0.0	0.31	0.0	0.45	0.0	-0.70	0.0
0.0	0.0	0.07	0.0	0.0	0.0	0.44	-1.43	0.39	0.0
0.0	0.0	0.19	0.0	0.0	0.18	0.89	-0.05	-0.37	0.12
0.0	0.01	0.0	0.0	0.0	0.04	0.31	-0.22	0.25	0.0
0.0	0.0	-0.12	0.0	-0.02	-0.00	-0.04	0.44	0.14	0.0
0.0	0.09	-0.06	0.22	0.0	0.0	0.14	0.0	0.0	0.0
0.18	0.0	0.07	0.12	0.0	-0.35	0.28	-0.02	0.05	0.0
0.0	-0.06	0.00	-0.05	0.0	0.22	0.03	0.0	0.0	0.0
0.0	-0.01	-0.05	0.00	-0.04	0.09	-0.02	0.0	0.0	0.0
0.0	0.28	0.0	-0.04	-0.01	0.15	-0.17	0.27	0.0	0.0
0.0	0.0	-0.06	0.19	0.09	0.02	0.0	0.0	0.0	0.0
0.0	0.0	-0.08	-0.09	0.0	0.0	0.06	0.0	0.0	0.0
0.0	0.0	0.0	-0.11	0.37	0.22	0.10	0.0	0.0	0.0

LAYER ... 2

0.0	0.0	0.0	0.0	0.0	0.0	0.0	0.0	0.0
0.0	0.0	0.0	0.05	0.76	0.70	0.99	0.0	0.0
0.0	0.0	-0.10	0.13	-0.22	-1.44	-1.14	-0.39	0.0
0.0	0.0	-0.13	0.17	0.22	-0.04	0.56	-0.05	0.0
0.0	0.02	0.35	0.27	0.26	0.21	0.51	0.28	0.0
0.0	0.0	0.29	0.25	0.33	0.29	0.29	0.33	0.0
0.0	0.0	0.22	0.48	0.45	0.29	-0.01	0.0	0.0
0.0	0.0	0.0	0.24	0.36	0.28	0.19	0.0	0.0
0.0	0.0	0.0	0.04	0.09	-0.04	0.35	0.0	0.0
0.0	0.0	0.0	0.0	0.0	0.0	0.0	0.0	0.0

LAYER ... 3

0.0	0.0	0.0	0.0	0.0	0.0	0.0	0.0	0.0	0.0
0.0	0.0	0.0	0.0	-0.66	0.0	0.0	0.0	0.0	0.0
0.0	0.0	0.0	-0.63	-0.72	0.95	22.41	0.0	0.0	0.0
0.0	0.0	-0.25	-0.50	-0.86	-0.01	0.39	-1.03	0.0	0.0
0.0	0.0	-0.46	-0.32	-0.59	-0.68	-0.52	-0.84	0.0	0.0
0.0	0.0	-0.09	-0.25	-0.47	-0.54	-0.61	-0.56	0.0	0.28
0.0	0.0	-0.23	-0.40	-0.35	-0.37	-0.20	-0.41	0.0	0.0
0.0	0.0	0.0	-0.34	-0.20	-0.20	-0.36	0.02	-0.02	0.01
0.0	0.0	0.0	0.0	-0.28	-0.27	0.0	0.0	-0.02	0.03
0.0	0.0	0.0	0.0	0.0	-0.34	0.0	0.0	0.02	-0.01
0.0	0.0	0.0	0.0	0.0	0.0	0.0	0.0	0.0	0.06

LAYER ... 4

0.0	0.0	0.0	0.0	0.0	0.0	0.0	0.0	0.0	0.0	0.0
0.0	0.0	0.0	0.0	0.44	0.54	1.08	0.0	0.0	0.0	0.0
0.0	0.0	0.0	-0.11	0.68	0.73	-2.55	-1.92	0.0	0.0	0.0
0.0	0.0	-0.25	0.37	0.74	0.99	0.05	0.88	-0.54	0.0	0.0
0.0	0.0	-0.00	0.55	0.72	0.91	1.00	0.67	0.01	0.0	0.0
0.0	0.0	-0.02	0.31	0.58	0.71	0.92	0.67	-0.13	0.0	0.0
0.0	0.0	-0.04	0.21	0.37	0.53	0.46	0.22	-0.56	0.0	0.0
0.0	0.0	-0.11	0.14	0.16	0.25	0.18	-0.06	-0.41	0.0	0.0
0.0	0.0	0.0	0.12	0.11	-0.08	-0.05	-0.08	0.0	0.0	0.0
0.0	0.0	0.0	0.0	-0.06	0.03	0.04	0.0	0.0	0.0	0.0
0.0	0.0	0.0	0.0	0.0	-0.12	-0.07	0.0	0.0	0.0	0.0

COLUMN OF RESOLUTION MATRIX IN LAYER-BLOCK FORMAT
FOR BLOCK 276

334

LAYER ... 1

0.0	0.0	0.0	0.0	-0.01	0.0	-0.01	0.0	0.00	0.0
0.0	0.0	-0.00	0.0	0.0	0.0	0.00	-0.01	-0.00	0.0
0.0	0.0	0.00	0.0	0.0	-0.00	-0.01	0.00	-0.00	-0.01
0.0	-0.00	0.0	0.0	0.0	0.00	0.01	0.00	0.00	0.0
0.0	0.0	-0.00	0.0	0.02	0.01	0.01	-0.00	0.01	0.0
0.0	0.00	-0.00	0.01	0.0	0.0	-0.00	0.0	0.0	0.0
-0.01	0.0	-0.00	0.00	0.0	0.00	0.00	0.01	0.02	0.0
0.0	-0.00	0.00	-0.00	0.0	0.02	-0.01	0.0	0.0	0.0
0.0	-0.00	-0.00	0.00	-0.00	-0.00	0.00	0.0	0.0	0.0
0.0	-0.00	0.0	-0.00	-0.00	0.02	0.00	0.01	0.0	0.0
0.0	0.0	-0.00	0.00	-0.00	-0.00	0.0	0.0	0.0	0.0
0.0	0.0	-0.00	-0.00	0.0	0.0	0.00	0.0	0.0	0.0
0.0	0.0	0.0	-0.00	-0.00	-0.00	-0.00	0.0	0.0	0.0

LAYER ... 2

0.0	0.0	0.0	0.0	0.0	0.0	0.0	0.0	0.0
0.0	0.0	0.0	-0.00	-0.01	-0.00	-0.00	0.0	0.0
0.0	0.0	-0.00	-0.00	-0.00	-0.00	-0.00	-0.00	0.0
0.0	0.0	-0.00	-0.00	-0.00	0.00	0.00	-0.00	0.0
0.0	-0.00	0.00	0.00	0.01	0.02	0.00	-0.00	0.0
0.0	0.0	-0.00	0.00	0.02	0.03	0.00	-0.00	0.0
0.0	0.0	-0.01	0.01	0.01	0.01	0.00	0.0	0.0
0.0	0.0	0.0	-0.00	0.00	0.00	-0.00	0.0	0.0
0.0	0.0	0.0	0.00	-0.00	-0.00	0.00	0.0	0.0
0.0	0.0	0.0	0.0	0.0	0.0	0.0	0.0	0.0

LAYER ... 3

0.0	0.0	0.0	0.0	0.0	0.0	0.0	0.0	0.0	0.0
0.0	0.0	0.0	0.0	-0.01	0.0	0.0	0.0	0.0	0.0
0.0	0.0	0.0	-0.01	-0.01	-0.02	-0.02	0.0	0.0	0.0
0.0	0.0	-0.01	-0.02	-0.03	-0.03	-0.03	-0.01	0.0	0.0
0.0	0.0	-0.02	-0.03	-0.04	-0.04	-0.04	-0.02	0.0	0.0
0.0	0.0	-0.01	-0.02	-0.05	0.92	-0.05	-0.01	0.0	0.00
0.0	0.0	-0.01	-0.03	-0.04	-0.05	-0.04	-0.01	0.0	0.0
0.0	0.0	0.0	-0.02	-0.03	-0.03	-0.03	0.00	-0.00	-0.01
0.0	0.0	0.0	0.0	-0.02	-0.02	0.0	0.0	-0.00	-0.00
0.0	0.0	0.0	0.0	0.0	-0.01	0.0	0.0	0.00	0.00
0.0	0.0	0.0	0.0	0.0	0.0	0.0	0.0	0.0	0.00

LAYER ... 4

0.0	0.0	0.0	0.0	0.0	0.0	0.0	0.0	0.0	0.0	0.0
0.0	0.0	0.0	0.0	-0.01	-0.00	-0.00	0.0	0.0	0.0	0.0
0.0	0.0	0.0	-0.00	-0.01	0.00	-0.00	-0.00	0.0	0.0	0.0
0.0	0.0	-0.01	-0.00	0.00	0.00	0.00	0.00	-0.00	0.0	0.0
0.0	0.0	-0.00	0.00	0.01	0.01	0.01	0.01	-0.00	0.0	0.0
0.0	0.0	-0.01	0.00	0.01	0.03	0.03	0.01	0.01	0.0	0.0
0.0	0.0	-0.00	0.00	0.01	0.02	0.02	0.01	-0.01	0.0	0.0
0.0	0.0	-0.00	-0.00	0.00	0.01	0.00	0.00	-0.01	0.0	0.0
0.0	0.0	0.0	0.00	0.00	-0.00	-0.01	-0.01	0.0	0.0	0.0
0.0	0.0	0.0	0.0	-0.00	-0.01	-0.01	0.0	0.0	0.0	0.0
0.0	0.0	0.0	0.0	0.0	-0.01	-0.01	0.0	0.0	0.0	0.0
0.0	0.0	0.0	0.0	0.0	0.0	0.0	0.0	0.0	0.0	0.0

STANDARD ERROR IN % IS 0.74

COLUMN OF COVARIANCE MATRIX IN LAYER-BLOCK FORMAT
FOR BLOCK 276

LAYER ... 1

0.0	0.0	0.0	0.0	0.34	0.0	-0.25	0.0	0.06	0.0
0.0	0.0	0.12	0.0	0.0	0.0	-0.13	0.60	-0.06	0.0
0.0	0.0	0.20	0.0	0.0	0.05	0.60	-0.02	0.22	-0.06
0.0	-0.02	0.0	0.0	0.0	0.02	-0.12	0.27	0.11	0.0
0.0	0.0	0.18	0.0	-0.93	0.03	-0.74	0.89	0.04	0.0
0.0	0.10	0.07	-0.11	0.0	0.0	0.18	0.0	0.0	0.0
0.33	0.0	0.37	0.01	0.0	0.12	0.09	0.11	-0.74	0.0
0.0	0.01	-0.05	0.06	0.0	-1.29	0.78	0.0	0.0	0.0
0.0	0.11	0.19	-0.08	-0.06	0.31	0.06	0.0	0.0	0.0
0.0	0.47	0.0	0.08	-0.01	-1.04	0.13	-0.40	0.0	0.0
0.0	0.0	-0.06	0.02	0.38	0.30	0.0	0.0	0.0	0.0
0.0	0.0	0.07	0.04	0.0	0.0	0.37	0.0	0.0	0.0
0.0	0.0	0.0	0.02	0.47	0.50	0.31	0.0	0.0	0.0

LAYER ... 2

0.0	0.0	0.0	0.0	0.0	0.0	0.0	0.0	0.0
0.0	0.0	0.0	0.11	0.66	0.60	0.06	0.0	0.0
0.0	0.0	0.05	0.23	0.74	0.74	0.38	-0.08	0.0
0.0	0.0	0.11	0.27	0.44	0.30	0.34	0.20	0.0
0.0	0.35	0.43	0.25	-0.91	-1.58	0.16	0.00	0.0
0.0	0.0	0.55	0.29	-1.24	-2.34	0.42	-0.01	0.0
0.0	0.0	0.67	0.13	-0.11	-0.24	0.28	0.0	0.0
0.0	0.0	0.0	0.77	0.68	0.49	0.16	0.0	0.0
0.0	0.0	0.0	0.42	0.68	0.50	0.08	0.0	0.0
0.0	0.0	0.0	0.0	0.0	0.0	0.0	0.0	0.0

LAYER ... 3

0.0	0.0	0.0	0.0	0.0	0.0	0.0	0.0	0.0	0.0
0.0	0.0	0.0	0.0	-0.19	0.0	0.0	0.0	0.0	0.0
0.0	0.0	0.0	-0.27	-0.11	-0.34	-0.54	0.0	0.0	0.0
0.0	0.0	-0.11	-0.47	0.12	0.10	-0.07	-0.40	0.0	0.0
0.0	0.0	-0.58	0.09	0.78	1.54	0.91	-0.77	0.0	0.0
0.0	0.0	0.04	-0.11	1.74	5.51	1.12	-0.34	0.0	-0.13
0.0	0.0	-0.38	-0.01	0.96	1.71	0.28	-0.40	0.0	0.0
0.0	0.0	0.0	-0.47	0.05	0.09	0.04	-0.05	0.29	0.32
0.0	0.0	0.0	0.0	-0.38	-0.41	0.0	0.0	0.23	0.01
0.0	0.0	0.0	0.0	0.0	-0.43	0.0	0.0	-0.11	-0.08
0.0	0.0	0.0	0.0	0.0	0.0	0.0	0.0	0.0	-0.11

LAYER ... 4

0.0	0.0	0.0	0.0	0.0	0.0	0.0	0.0	0.0	0.0	0.0
0.0	0.0	0.0	0.0	0.33	0.37	0.36	0.0	0.0	0.0	0.0
0.0	0.0	0.0	0.08	0.59	0.49	0.76	0.37	0.0	0.0	0.0
0.0	0.0	-0.11	0.59	0.69	0.46	0.54	0.47	-0.11	0.0	0.0
0.0	0.0	0.13	0.75	0.41	-0.38	0.15	0.02	-0.19	0.0	0.0
0.0	0.0	0.18	0.65	0.41	-1.79	-1.95	0.13	0.32	0.0	0.0
0.0	0.0	0.18	0.61	0.12	-1.01	-1.54	0.06	-0.34	0.0	0.0
0.0	0.0	0.16	0.61	0.17	-0.27	0.29	0.68	-0.40	0.0	0.0
0.0	0.0	0.0	0.45	0.32	0.47	0.93	0.67	0.0	0.0	0.0
0.0	0.0	0.0	0.0	0.06	0.55	0.60	0.0	0.0	0.0	0.0
0.0	0.0	0.0	0.0	0.0	-0.00	0.21	0.0	0.0	0.0	0.0

COLUMN OF RESOLUTION MATRIX IN LAYER-BLOCK FORMAT
FOR BLOCK 306

336

LAYER ... 1

0.0	0.0	0.0	0.0	-0.01	0.0	-0.00	0.0	-0.00	0.0
0.0	0.0	-0.01	0.0	0.0	0.0	-0.00	-0.00	-0.00	0.0
0.0	0.0	-0.01	0.0	0.0	-0.00	-0.00	0.00	-0.00	-0.00
0.0	-0.00	0.0	0.0	0.0	-0.00	-0.00	-0.00	-0.00	0.0
0.0	0.0	-0.00	0.0	-0.01	-0.00	-0.00	-0.00	-0.00	0.0
0.0	-0.00	-0.00	-0.00	0.0	0.0	-0.00	0.0	0.0	0.0
-0.01	0.0	-0.00	-0.00	0.0	0.00	-0.00	0.00	-0.00	0.0
0.0	-0.00	-0.00	0.00	0.0	-0.00	-0.00	0.0	0.0	0.0
0.0	0.00	-0.00	-0.00	0.00	0.00	0.00	0.0	0.0	0.0
0.0	-0.00	0.0	-0.00	0.00	0.00	0.00	0.00	0.0	0.0
0.0	0.0	-0.00	-0.01	0.03	-0.00	0.0	0.0	0.0	0.0
0.0	0.0	0.01	0.00	0.0	0.0	0.01	0.0	0.0	0.0
0.0	0.0	0.0	-0.00	0.03	0.03	0.03	0.0	0.0	0.0

LAYER ... 2

0.0	0.0	0.0	0.0	0.0	0.0	0.0	0.0	0.0
0.0	0.0	0.0	-0.01	-0.01	-0.01	-0.00	0.0	0.0
0.0	0.0	-0.00	-0.01	-0.01	-0.01	-0.00	-0.00	0.0
0.0	0.0	-0.01	-0.01	-0.01	-0.01	-0.00	-0.00	0.0
0.0	-0.01	-0.01	-0.01	-0.00	-0.00	-0.00	0.00	0.0
0.0	0.0	-0.01	-0.01	0.00	-0.00	-0.01	-0.00	0.0
0.0	0.0	-0.00	0.01	0.00	0.00	0.00	0.0	0.0
0.0	0.0	0.0	0.01	0.02	0.01	0.00	0.0	0.0
0.0	0.0	0.0	0.02	0.06	0.06	-0.01	0.0	0.0
0.0	0.0	0.0	0.0	0.0	0.0	0.0	0.0	0.0

LAYER ... 3

0.0	0.0	0.0	0.0	0.0	0.0	0.0	0.0	0.0	0.0
0.0	0.0	0.0	0.0	-0.01	0.0	0.0	0.0	0.0	0.0
0.0	0.0	0.0	-0.00	-0.01	-0.01	-0.01	0.0	0.0	0.0
0.0	0.0	-0.00	-0.01	-0.01	-0.01	-0.01	-0.01	0.0	0.0
0.0	0.0	-0.01	-0.01	-0.01	-0.01	-0.02	-0.01	0.0	0.0
0.0	0.0	-0.01	-0.01	-0.02	-0.02	-0.01	-0.01	0.0	0.00
0.0	0.0	-0.01	-0.02	-0.03	-0.03	-0.02	-0.01	0.0	0.0
0.0	0.0	0.0	-0.02	-0.05	-0.07	-0.05	0.00	-0.00	0.00
0.0	0.0	0.0	0.0	-0.10	0.80	0.0	0.0	-0.00	-0.00
0.0	0.0	0.0	0.0	0.0	-0.05	0.0	0.0	-0.01	-0.00
0.0	0.0	0.0	0.0	0.0	0.0	0.0	0.0	0.0	-0.02

LAYER ... 4

0.0	0.0	0.0	0.0	0.0	0.0	0.0	0.0	0.0	0.0	0.0
0.0	0.0	0.0	0.0	-0.00	-0.00	-0.00	0.0	0.0	0.0	0.0
0.0	0.0	0.0	-0.00	-0.00	-0.00	-0.00	-0.00	0.0	0.0	0.0
0.0	0.0	-0.00	-0.00	-0.00	-0.00	-0.00	-0.01	-0.00	0.0	0.0
0.0	0.0	-0.00	-0.00	-0.00	-0.00	-0.00	-0.01	-0.00	0.0	0.0
0.0	0.0	-0.01	-0.00	-0.00	-0.00	-0.01	-0.01	-0.00	0.0	0.0
0.0	0.0	-0.01	-0.00	-0.00	-0.00	-0.01	-0.01	-0.01	0.0	0.0
0.0	0.0	-0.00	-0.00	0.00	0.00	0.00	-0.01	-0.01	0.0	0.0
0.0	0.0	0.0	-0.00	-0.00	0.02	0.02	0.01	0.0	0.0	0.0
0.0	0.0	0.0	0.0	0.03	0.05	0.08	0.0	0.0	0.0	0.0
0.0	0.0	0.0	0.0	0.0	-0.00	0.02	0.0	0.0	0.0	0.0
0.0	0.0	0.0	0.0	0.0	0.0	0.0	0.0	0.0	0.0	0.0

STANDARD ERROR IN % IS 1.18

COLUMN OF COVARIANCE MATRIX IN LAYER-BLOCK FORMAT
FOR BLOCK 306

337

LAYER ... 1

0.0	0.0	0.0	0.0	0.35	0.0	-0.07	0.0	-0.08	0.0
0.0	0.0	-0.12	0.0	0.0	0.0	-0.07	0.35	0.09	0.0
0.0	0.0	0.14	0.0	0.0	-0.09	0.16	0.02	0.08	-0.06
0.0	-0.07	0.0	0.0	0.0	-0.09	-0.04	-0.06	0.00	0.0
0.0	0.0	0.00	0.0	0.21	-0.02	0.10	-0.06	0.22	0.0
0.0	-0.02	0.19	0.11	0.0	0.0	-0.07	0.0	0.0	0.0
0.36	0.0	0.10	0.03	0.0	0.40	0.09	0.07	0.14	0.0
0.0	0.02	0.24	0.12	0.0	0.12	0.39	0.0	0.0	0.0
0.0	0.13	0.14	-0.15	0.05	0.23	0.04	0.0	0.0	0.0
0.0	0.38	0.0	0.15	0.09	0.15	0.29	0.46	0.0	0.0
0.0	0.0	-0.06	0.41	-1.16	0.84	0.0	0.0	0.0	0.0
0.0	0.0	0.22	0.38	0.0	0.0	0.52	0.0	0.0	0.0
0.0	0.0	0.0	0.43	-1.16	-0.63	-1.15	0.0	0.0	0.0

LAYER ... 2

0.0	0.0	0.0	0.0	0.0	0.0	0.0	0.0	0.0
0.0	0.0	0.0	-0.14	0.15	0.02	-0.07	0.0	0.0
0.0	0.0	-0.16	0.05	0.40	0.40	0.26	-0.02	0.0
0.0	0.0	0.04	0.36	0.39	0.51	0.40	0.05	0.0
0.0	0.17	0.45	0.64	0.45	0.51	0.37	0.03	0.0
0.0	0.0	0.60	0.78	0.38	0.55	0.55	-0.02	0.0
0.0	0.0	0.69	0.49	0.41	0.47	0.33	0.0	0.0
0.0	0.0	0.0	0.74	-0.47	0.42	0.14	0.0	0.0
0.0	0.0	0.0	0.54	-3.34	-2.33	-0.25	0.0	0.0
0.0	0.0	0.0	0.0	0.0	0.0	0.0	0.0	0.0

LAYER ... 3

0.0	0.0	0.0	0.0	0.0	0.0	0.0	0.0	0.0	0.0
0.0	0.0	0.0	0.0	-0.13	0.0	0.0	0.0	0.0	0.0
0.0	0.0	0.0	-0.15	0.09	-0.12	-0.27	0.0	0.0	0.0
0.0	0.0	-0.15	-0.21	-0.17	-0.07	-0.04	-0.35	0.0	0.0
0.0	0.0	-0.53	-0.39	-0.29	-0.20	0.09	-0.35	0.0	0.0
0.0	0.0	-0.00	-0.52	-0.39	-0.41	-0.35	-0.12	0.0	-0.06
0.0	0.0	-0.48	-0.49	-0.33	-0.41	-0.76	-0.26	0.0	0.0
0.0	0.0	0.0	-0.63	0.52	1.18	0.03	-0.16	-0.07	-0.07
0.0	0.0	0.0	0.0	2.43	13.90	0.0	0.0	-0.07	-0.08
0.0	0.0	0.0	0.0	0.0	-1.49	0.0	0.0	0.03	-0.07
0.0	0.0	0.0	0.0	0.0	0.0	0.0	0.0	0.0	0.58

LAYER ... 4

0.0	0.0	0.0	0.0	0.0	0.0	0.0	0.0	0.0	0.0	0.0
0.0	0.0	0.0	0.0	0.08	0.10	0.08	0.0	0.0	0.0	0.0
0.0	0.0	0.0	-0.07	0.21	0.16	0.26	0.01	0.0	0.0	0.0
0.0	0.0	-0.15	0.21	0.27	0.25	0.17	0.13	-0.14	0.0	0.0
0.0	0.0	-0.05	0.41	0.31	0.33	0.18	0.18	-0.18	0.0	0.0
0.0	0.0	0.01	0.43	0.47	0.46	0.49	0.66	-0.05	0.0	0.0
0.0	0.0	0.02	0.35	0.58	0.63	0.82	1.09	-0.12	0.0	0.0
0.0	0.0	0.00	0.33	0.59	0.59	0.76	1.30	-0.26	0.0	0.0
0.0	0.0	0.0	0.14	0.59	0.27	0.17	1.12	0.0	0.0	0.0
0.0	0.0	0.0	0.0	1.16	-2.44	-5.90	0.0	0.0	0.0	0.0
0.0	0.0	0.0	0.0	0.0	1.29	-0.08	0.0	0.0	0.0	0.0

TABLE 3.7.

Three-Dimensional Inversion of California

Herrin Residuals - San Jose Subarray: 5 Layer Model

3.5a Initial Model and Stations

3.5b Observation Matrix - Number of "Hits" Per Block

3.5c Inversion Solution - Layer 1

3.5d Inversion Solution - Layer 2

3.5e Inversion Solution - Layer 3

3.5f Inversion Solution - Layer 4

3.5g Inversion Solution - Layer 5

***** PROGRAM 3-D ***** 22 NOVEMBER 1975.

CALIFORNIA: SAN JOSE REGION

ATITUDE	LONGITUDE	THA	VO	JPWT	IRES	IPUNCH	IPRINT	THETA	RESL
37N26.00	121W56.50	36.5	5.60	40	0	0	0	50.	0.100

ARM=-1,0,1 INDICATE,RESPECTIVELY,SOLUTION IS IN TERMS OF VELOCITY PERTURBATIONS,
YER DEPTH PERTURBATIONS, OR THAT BOTH SOLUTIONS WILL BE COMPUTED
R THIS RUN, IPARM= -1

VELOCITY	THICKNESS	#-NORTH	LENGTH	#-EAST	LENGTH	COORDINATE	DISPLACEMENT
5.60	10.00	13	10.00	10	10.00	0.0	0.0
6.90	20.00	10	20.00	9	20.00	0.0	0.0
8.00	30.00	11	25.00	10	25.00	0.0	0.0
8.00	30.00	12	25.00	11	25.00	0.0	0.0
8.10	30.00	13	25.00	12	25.00	0.0	0.0

	STA	LATITUDE	LONGITUDE	ELEVATION	RELATIVE COCRDINATES		INDEX
1	ACH	37 58.57N	121 45.62W	0.07	38.92	48.60	30
2	ALM	37 9.50N	121 50.82W	0.24	-29.50	-11.38	94
3	AND	37 9.74N	121 37.45W	0.24	-40.87	4.80	106
4	ANG	37 51.68N	122 25.77W	0.22	63.74	-6.18	5
5	ARN	37 20.96N	121 31.96W	0.63	-28.96	23.61	98
6	BAM	37 19.09N	122 9.16W	0.82	0.87	-22.60	63
7	BCP	37 9.62N	122 1.57W	0.66	-19.87	-24.03	83
8	BGH	37 20.52N	122 20.34W	0.16	12.84	-34.25	52
9	BOL	37 48.97N	122 3.72W	0.61	40.42	16.74	27
0	BWS	37 55.45N	122 6.40W	0.22	52.37	20.73	18
1	CAL	37 27.07N	121 47.95W	0.26	-5.89	11.31	77
2	CAN	37 1.52N	121 29.02W	0.33	-60.49	5.88	126
3	CBC	36 55.88N	121 39.63W	0.22	-59.59	-12.97	124
4	CBO	37 6.71N	121 41.33W	0.19	-41.98	-3.14	105
5	CCR	37 47.30N	121 57.00W	0.18	32.07	22.82	38
6	CHR	36 57.46N	121 35.01W	0.24	-61.29	-5.72	125
7	COE	37 15.46N	121 40.35W	0.37	-29.81	7.61	96
8	CRK	37 14.50N	122 7.82W	0.61	-7.12	-26.07	73
9	CRC	37 14.50N	122 7.82W	0.61	-7.12	-26.07	73
0	CSH	37 38.88N	122 2.57W	0.17	24.44	6.99	46
1	DOO	37 43.80N	121 50.12W	0.20	20.87	27.09	48
2	DSR	37 57.98N	122 15.17W	0.11	63.78	13.22	7
3	DUR	38 1.78N	122 0.05W	0.17	56.23	35.16	9
4	EGR	37 2.11N	122 6.25W	0.44	-26.88	-37.86	92
5	ELG	37 30.84N	122 27.74W	0.20	34.64	-31.57	32
6	EUC	37 3.04N	121 48.56W	0.44	-41.09	-15.78	104
7	GHS	37 5.75N	121 26.83W	0.78	-56.10	13.11	127
8	HCC	36 58.88N	121 43.35W	0.16	-51.86	-14.12	114
9	LCH	37 44.28N	122 3.83W	0.31	33.56	11.45	37
0	LTW	37 21.22N	122 12.25W	0.27	6.75	-23.91	53
1	LXR	37 12.11N	121 59.17W	0.24	-18.28	-18.44	84
2	MDC	37 52.90N	121 54.85W	1.17	38.52	31.51	29
3	MGA	37 38.22N	122 28.43W	0.20	46.17	-24.21	13
4	MHR	37 21.57N	121 45.38W	0.52	-16.32	8.33	86
5	MIL	37 46.88N	122 10.55W	0.09	43.29	6.40	26
6	MNR	37 35.68N	121 38.22W	0.50	-1.57	32.27	69
7	MOR	37 48.68N	121 48.15W	0.79	26.41	34.77	39
8	MSJ	37 31.25N	121 52.23W	0.50	4.06	10.82	67
9	MTB	37 17.44N	122 5.43W	0.35	-4.86	-20.00	64
0	PAL	37 37.88N	121 57.37W	0.46	18.41	12.03	47
1	PFS	37 11.94N	122 20.90W	0.08	0.63	-44.40	61
2	PLV	36 58.62N	121 49.93W	0.16	-46.45	-22.26	113
3	PMR	36 57.19N	121 41.70W	0.09	-55.82	-14.00	124
4	RUS	37 54.75N	121 54.33W	0.33	40.81	34.15	29
5	SAC	37 34.95N	122 25.03W	0.21	38.33	-23.83	23
6	SAL	37 34.56N	122 25.40W	0.33	38.08	-24.69	23
7	SAW	37 12.74N	122 10.06W	0.26	-7.76	-30.67	72
8	SFR	37 47.28N	122 23.37W	0.01	55.12	-8.23	5
9	SPT	37 24.31N	122 10.55W	0.14	9.83	-18.49	54
0	SGC	37 16.96N	122 3.00W	0.20	-7.71	-17.65	74
1	SOS	37 10.17N	121 55.84W	0.95	-24.09	-16.61	84
2	STJ	37 20.03N	122 5.48W	0.12	-0.98	-17.21	64
3	STV	37 17.07N	122 7.42W	0.36	-3.66	-22.77	63
4	SVC	37 17.11N	121 46.35W	0.13	-22.11	2.28	86
5	WDS	37 25.08N	122 16.33W	0.28	16.06	-24.47	43
6	CYH	37 33.54N	122 5.62W	0.04	19.19	-2.49	45

OBSERVATION MATRIX

0	0	0	0	50	0	7	0	8	0
0	0	7	0	0	0	23	51	5	0
0	0	18	0	0	3	106	1	34	5
0	1	0	0	0	2	17	30	74	0
0	0	18	0	37	7	100	87	20	0
0	6	78	36	0	0	8	0	0	0
57	0	67	13	0	8	53	1	98	0
0	10	34	7	0	50	50	0	0	0
0	6	24	7	1	110	1	0	0	0
0	50	0	31	2	59	1	110	0	0
0	0	1	49	104	47	0	0	0	0
0	0	9	8	0	0	12	0	0	0
0	0	0	9	106	43	20	0	0	0

0	0	0	0	0	0	0	0	0
0	0	0	21	37	14	2	0	0
0	0	3	11	37	149	15	1	0
0	0	6	19	62	175	66	3	0
0	16	47	137	87	68	58	1	0
0	0	42	101	135	87	28	1	0
0	0	39	56	159	124	5	0	0
0	0	0	58	144	22	2	0	0
0	0	0	29	44	14	1	0	0
0	0	0	0	0	0	0	0	0

0	0	0	0	0	0	0	0	0	0
0	0	0	0	5	0	0	0	0	0
0	0	0	3	44	40	10	0	0	0
0	0	1	11	43	156	53	3	0	0
0	0	8	82	86	183	85	3	0	0
0	0	18	114	122	183	62	2	0	1
0	0	13	39	185	128	37	1	0	0
0	0	0	29	154	93	29	1	3	1
0	0	0	0	27	41	0	0	3	2
0	0	0	0	0	3	0	0	1	5
0	0	0	0	0	0	0	0	0	2

0	0	0	0	0	0	0	0	0	0	0
0	0	0	0	6	5	2	0	0	0	0
0	0	0	1	20	30	28	4	0	0	0
0	0	1	7	38	105	58	13	1	0	0
0	0	1	31	73	165	61	17	1	0	0
0	0	13	80	84	138	97	34	2	0	0
0	0	9	40	134	97	67	47	2	0	0
0	0	6	25	118	80	56	25	1	0	0
0	0	0	12	51	49	62	9	0	0	0
0	0	0	0	2	46	36	0	0	0	0
0	0	0	0	0	2	4	0	0	0	0
0	0	0	0	0	0	0	0	0	0	0

0	0	0	0	0	2	0	0	0	0	0	0
0	0	0	0	0	15	11	4	0	0	0	0
0	0	0	0	7	15	54	4	4	0	0	0
0	0	2	5	38	51	60	18	11	1	0	0
0	0	1	26	65	116	65	19	12	1	0	0
0	0	3	38	62	158	60	25	11	2	0	0
0	0	18	71	68	116	36	58	21	0	0	0
0	0	7	15	70	59	39	58	29	2	0	0
0	0	1	24	66	49	39	32	16	1	0	0
0	0	0	4	12	17	50	45	8	0	0	0
0	0	0	0	1	14	45	17	1	0	0	0
0	0	0	0	0	0	13	5	0	0	0	0
0	0	0	0	0	0	1	2	0	0	0	0

***** CALIFORNIA: SAN JOSE REGION *****

NO OF STATIONS= 56
NO OF EVENTS=118
NO OF OBSERVATIONS= 2126

TOTAL BLOCKS IN MODEL= 618
NO OF BLOCKS OBSERVED= 274

DATA VARIANCE IS 0.1089
RESIDUAL VARIANCE IS 0.0649
VARIANCE IMPROVEMENT IN % IS 40.4003

VELOCITY PERTURBATIONS IN LAYER-BLOCK FORMAT

LAYER ... 1

0.0	0.0	0.0	0.0	2.59	0.0	-0.62	0.0	-3.51	0.0
0.0	0.0	2.07	0.0	0.0	0.0	-0.19	-1.64	-3.17	0.0
0.0	0.0	0.32	0.0	0.0	-1.22	-1.11	-0.54	15.80	-5.56
0.0	0.73	0.0	0.0	0.0	0.65	0.75	-11.28	-0.81	0.0
0.0	0.0	-0.04	0.0	2.16	1.52	1.20	-8.10	-1.86	0.0
0.0	-5.30	4.71	-2.53	0.0	0.0	1.92	0.0	0.0	0.0
2.02	0.0	5.84	-4.81	0.0	2.19	1.24	-0.69	2.09	0.0
0.0	-2.34	2.50	-2.27	0.0	-0.07	-0.34	0.0	0.0	0.0
0.0	3.72	-0.99	1.99	0.08	-8.57	0.39	0.0	0.0	0.0
0.0	2.67	0.0	4.22	1.23	-8.23	-1.01	-0.92	0.0	0.0
0.0	0.0	-0.70	1.73	0.59	-0.19	0.0	0.0	0.0	0.0
0.0	0.0	-1.28	-2.25	0.0	0.0	1.92	0.0	0.0	0.0
0.0	0.0	0.0	0.81	8.02	-1.22	0.08	0.0	0.0	0.0

LAYER ... 2

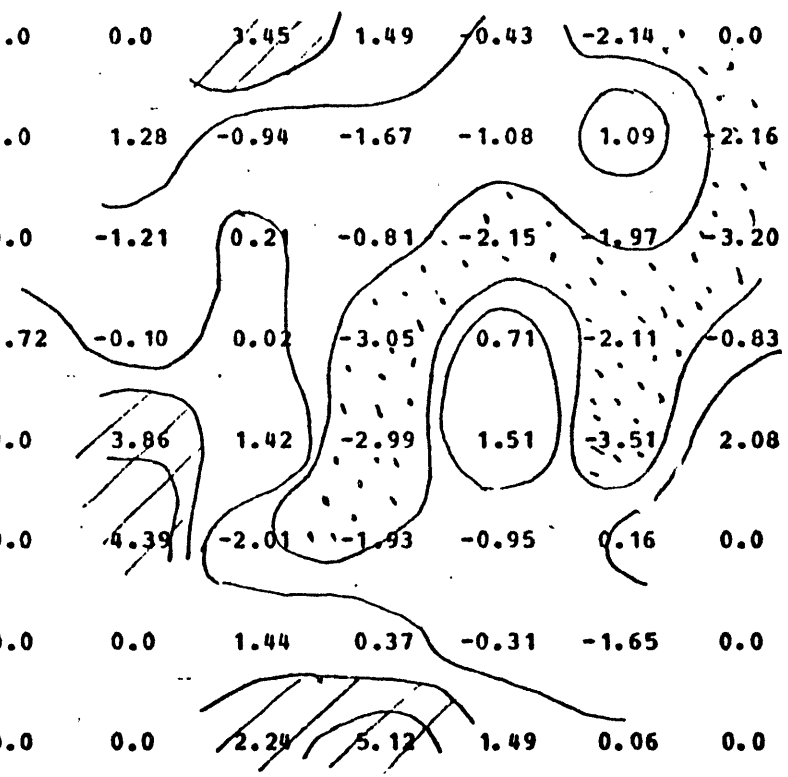
0.0 0.0 0.0 0.0 0.0 0.0 0.0 0.0 0.0
0.0 0.0 0.0 3.45 1.49 -0.43 -2.14 0.0 0.0
0.0 0.0 1.28 -0.94 -1.67 -1.08 1.09 -2.16 0.0
0.0 0.0 -1.21 0.21 -0.81 -2.15 -1.97 -3.20 0.0
0.0 0.72 -0.10 0.02 -3.05 0.71 -2.11 -0.83 0.0
0.0 0.0 3.86 1.42 -2.99 1.51 -3.51 2.08 0.0
0.0 0.0 -4.39 -2.01 -1.93 -0.95 0.16 0.0 0.0
0.0 0.0 0.0 1.44 0.37 -0.31 -1.65 0.0 0.0
0.0 0.0 0.0 2.24 5.12 1.49 0.06 0.0 0.0
0.0 0.0 0.0 0.0 0.0 0.0 0.0 0.0 0.0

LAYER ... 3

0.0	0.0	0.0	0.0	0.0	0.0	0.0	0.0	0.0	0.0
0.0	0.0	0.0	0.0	0.93	0.0	0.0	0.0	0.0	0.0
0.0	0.0	0.0	1.00	2.97	-1.93	-4.26	0.0	0.0	0.0
0.0	0.0	1.34	1.90	3.17	-1.63	-3.01	-2.26	0.0	0.0
0.0	0.0	2.07	2.51	0.01	-2.01	-1.84	-2.96	0.0	0.0
0.0	0.0	1.02	0.61	-0.13	-3.34	-1.76	-1.03	0.0	0.58
0.0	0.0	1.00	1.70	1.05	-1.26	-2.70	-1.24	0.0	0.0
0.0	0.0	0.0	-0.29	0.13	-0.94	-0.89	1.33	1.82	0.88
0.0	0.0	0.0	0.0	0.92	2.55	0.0	0.0	2.62	-0.48
0.0	0.0	0.0	0.0	0.0	2.79	0.0	0.0	2.38	0.74
0.0	0.0	0.0	0.0	0.0	0.0	0.0	0.0	0.0	0.52

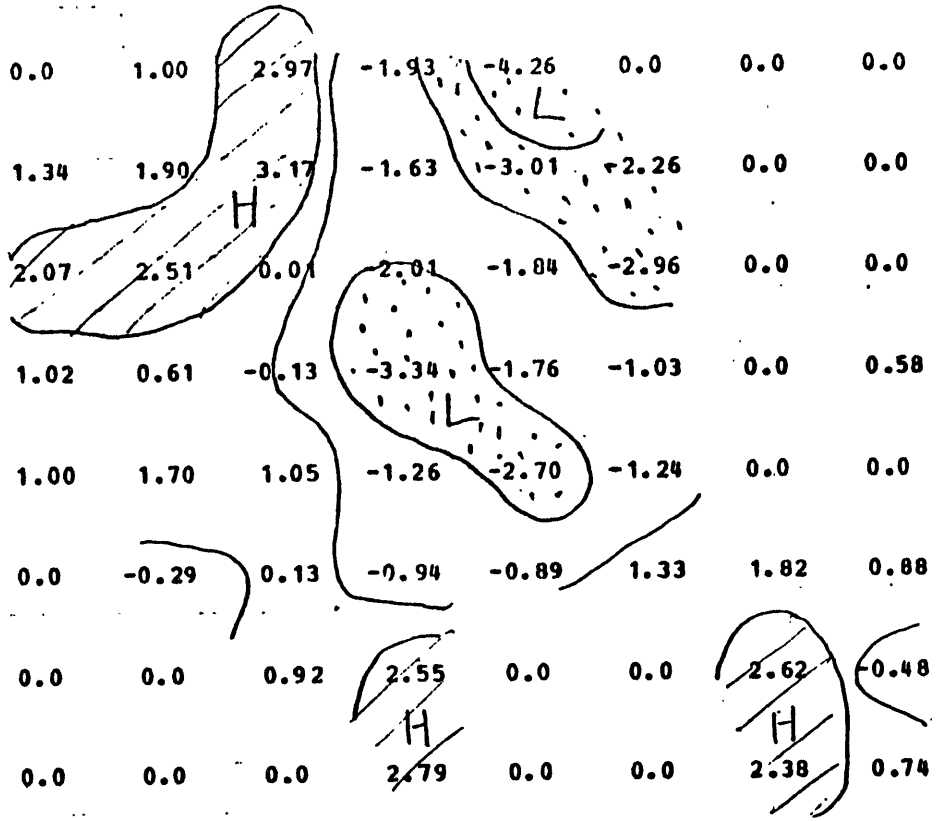

LAYER ... 4

0.0	0.0	0.0	0.0	0.0	0.0	0.0	0.0	0.0	0.0	0.0
0.0	0.0	0.0	0.0	0.41	0.40	-2.34	0.0	0.0	0.0	0.0
0.0	0.0	0.0	0.78	0.74	-1.67	-3.83	-0.71	0.0	0.0	0.0
0.0	0.0	1.34	-0.51	-0.78	-0.55	-2.08	-6.08	2.62	0.0	0.0
0.0	0.0	1.84	0.09	2.55	1.08	1.10	-1.80	-2.04	0.0	0.0
0.0	0.0	0.81	0.68	2.21	0.10	0.98	-0.59	0.42	0.0	0.0
0.0	0.0	0.53	0.98	0.25	-2.12	2.11	0.02	-1.03	0.0	0.0
0.0	0.0	1.62	-0.23	-0.32	-1.50	0.83	0.15	-1.24	0.0	0.0
0.0	0.0	0.0	-0.12	0.23	-0.29	-1.45	0.05	0.0	0.0	0.0
0.0	0.0	0.0	0.0	0.69	-0.79	-2.41	0.0	0.0	0.0	0.0
0.0	0.0	0.0	0.0	0.0	1.12	1.96	0.0	0.0	0.0	0.0
0.0	0.0	0.0	0.0	0.0	0.0	0.0	0.0	0.0	0.0	0.0

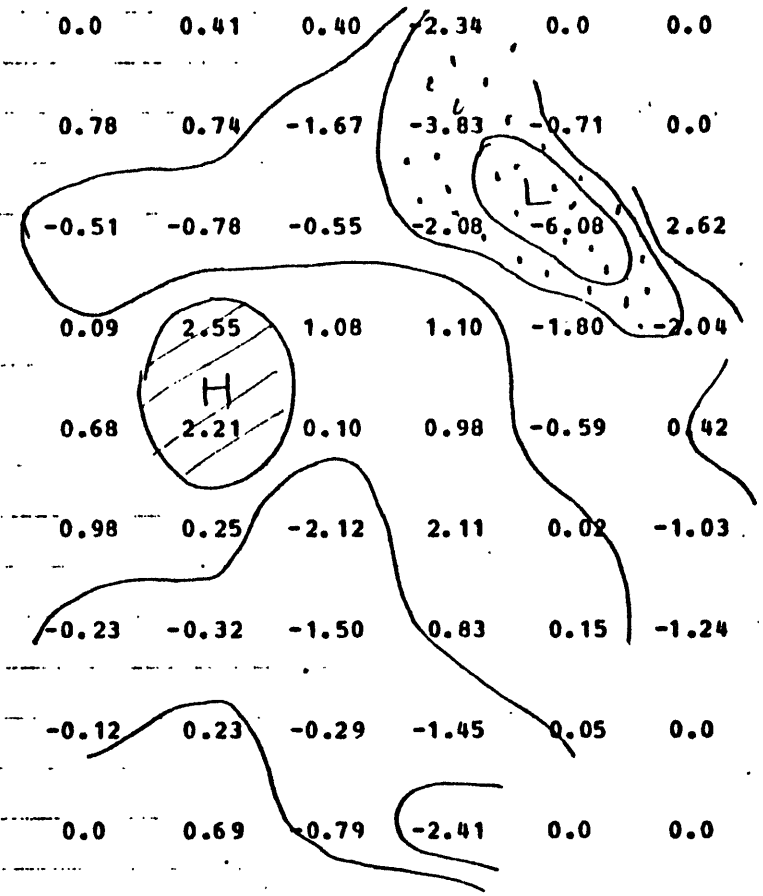

LAYER ... 5

0.0	0.0	0.0	0.0	0.0	1.79	0.0	0.0	0.0	0.0	0.0	0.0
0.0	0.0	0.0	0.0	0.0	-0.07	-1.30	-1.55	0.0	0.0	0.0	0.0
0.0	0.0	0.0	0.0	1.52	-0.45	-0.97	-1.79	-4.60	0.0	0.0	0.0
0.0	0.0	2.10	-0.47	-0.53	1.37	-0.34	-1.44	-0.41	2.69	0.0	0.0
0.0	0.0	0.28	1.27	-2.46	0.64	0.15	-0.99	-1.27	-2.03	0.0	0.0
0.0	0.0	1.88	0.32	0.82	0.47	1.50	0.14	0.43	0.42	0.0	0.0
0.0	0.0	1.51	-1.63	0.63	1.87	1.53	-0.62	-2.38	0.0	0.0	0.0
0.0	0.0	1.12	-0.12	0.54	2.29	-1.86	-1.23	-3.02	-1.02	0.0	0.0
0.0	0.0	0.49	-1.30	-0.35	0.14	-0.47	-1.57	-1.69	-1.23	0.0	0.0
0.0	0.0	0.0	-0.41	-0.59	1.31	0.27	0.85	-0.57	0.0	0.0	0.0
0.0	0.0	0.0	0.0	1.64	-3.86	2.07	1.19	0.28	0.0	0.0	0.0
0.0	0.0	0.0	0.0	0.0	0.0	1.47	-0.93	0.0	0.0	0.0	0.0
0.0	0.0	0.0	0.0	0.0	0.0	1.65	1.13	0.0	0.0	0.0	0.0

TABLE 3.8.

Three-Dimensional Inversion of California

Herrin Residuals - Bear Valley Subarray

3.8a Initial Model and Stations

3.8b Observation Matrix - Number of "Hits" Per Block

3.8c Inversion Parameters

3.8d Inversion Solution - Layer 1

3.8e Inversion Solution - Layer 2

3.8f Inversion Solution - Layer 3

3.8g Inversion Solution - Layer 4

3.8h Diagonal Elements of Resolution - Layer 1

3.8i Diagonal Elements of Resolution - Layer 2

3.8j Diagonal Elements of Resolution - Layer 3

3.8k Diagonal Elements of Resolution - Layer 4

3.8l Standard Error of Solution - Layer 1

3.8m Standard Error of Solution - Layer 2

3.8n Standard Error of Solution - Layer 3

3.8o Standard Error of Solution - Layer 4

CALIFORNIA: BEAR VALLEY REGION

LATITUDE	LONGITUDE	THA	V0	JPWT	IRES	IPUNCH	IPRINT	THETA	RESL
36N30.00	121W13.50	36.3	5.85	4	1	1	0	50.	0.100

IPARM=-1,0,1 INDICATE,RESPECTIVELY,SOLUTION IS IN TERMS OF VELOCITY PERTURBATIONS
LAYER DEPTH PERTURBATIONS, OR THAT BOTH SOLUTIONS WILL BE COMPUTED
FOR THIS RUN, IPARM= -1

	VELOCITY	THICKNESS	#-NORTH	LENGTH	#-EAST	LENGTH	COORDINATE	DISPLACEMENT
1	5.85	10.00	13	10.00	12	10.00	0.0	0.0
2	6.85	20.00	10	20.00	9	20.00	0.0	0.0
3	8.00	30.00	11	25.00	10	25.00	0.0	0.0
4	8.00	30.00	12	25.00	11	25.00	0.0	0.0

	STA	LATITUDE	LONGITUDE	ELEVATION	RELATIVE COORDINATES		INDEX
1	ANZ	36 53.08N	121 35.45W	0.12	53.70	-0.98	18
2	BEN	36 30.60N	121 4.53W	0.45	-7.02	11.45	92
3	BGM	36 35.48N	121 1.52W	1.22	-2.39	20.39	81
4	BTW	36 18.90N	120 55.75W	0.38	-32.21	9.27	115
5	BVL	36 34.51N	121 11.34W	0.51	4.81	7.53	79
6	CAN	37 1.52N	121 29.02W	0.33	60.57	15.96	8
7	CBC	36 55.88N	121 39.63W	0.22	61.55	-2.88	6
8	CHR	36 57.46N	121 35.01W	0.24	59.82	4.36	7
9	CNR	36 42.55N	121 20.60W	0.30	24.94	5.22	55
10	DIL	36 50.12N	121 38.64W	0.20	52.13	-8.04	18
11	DIR	36 20.16N	120 22.56W	0.50	-59.46	50.80	156
12	EKH	36 39.88N	121 10.45W	0.34	12.02	14.47	68
13	EMM	36 39.68N	121 5.76W	0.49	7.60	19.88	68
14	FEL	36 59.00N	121 24.09W	0.32	52.48	19.08	20
15	FRP	36 45.22N	121 29.43W	0.70	36.71	-2.42	30
16	GHS	37 5.75N	121 26.83W	0.78	64.93	23.21	9
17	HER	36 22.38N	120 49.13W	0.75	-32.84	21.05	117
18	JHC	36 32.82N	121 23.53W	0.21	13.06	-8.96	66
19	JOL	36 5.02N	121 10.15W	0.34	-40.16	-23.27	124
20	JON	36 36.65N	121 18.81W	1.05	14.59	0.90	67
21	LOR	36 14.79N	121 2.55W	0.31	-32.33	-3.42	114
22	LRV	36 25.46N	121 1.08W	0.55	-17.72	9.99	103
23	LTR	36 53.07N	121 18.49W	0.18	38.74	19.26	32
24	LWR	36 39.96N	121 16.36W	0.23	17.35	7.46	55
25	MON	36 36.03N	121 55.06W	0.19	45.81	-43.17	14
26	MOP	36 12.91N	120 47.69W	0.78	-48.25	12.50	140
27	MRS	36 39.48N	120 47.62W	0.77	-8.62	41.47	95
28	OCR	36 55.03N	121 30.46W	0.10	52.19	7.12	19
29	PCL	37 3.13N	121 17.40W	0.15	52.75	31.58	22
30	PFP	36 13.80N	121 46.30W	0.35	5.06	-57.20	61
31	PKH	36 51.38N	121 24.37W	0.12	41.40	10.39	32
32	PNC	36 33.73N	121 38.18W	0.30	27.39	-25.52	40
33	PNP	36 10.12N	121 22.68W	1.59	-21.45	-32.82	99
34	PTV	36 6.50N	120 43.27W	0.51	-61.72	10.89	152
35	QSR	36 50.02N	121 12.76W	0.54	29.16	22.78	45
36	RBM	36 50.70N	120 49.42W	0.37	9.71	51.50	72
37	SHG	36 24.83N	121 15.22W	0.19	-6.18	-7.72	90
38	SJG	36 47.88N	121 34.43W	0.17	45.08	-5.47	18
39	SLB	37 4.81N	121 5.65W	0.12	44.96	47.44	35
40	SRS	36 40.11N	121 31.13W	0.40	30.62	-10.07	41
41	STC	36 38.10N	121 14.00W	0.26	12.50	8.26	67
42	TWN	36 3.16N	121 30.45W	1.48	-24.88	-49.82	98
43	SLD	37 4.48N	121 13.23W	0.44	51.10	38.03	22

OBSERVATION MATRIX

0	0	0	0	0	6	107	44	16	4	0	0
0	16	0	0	1	158	84	22	15	95	1	0
0	7	1	0	0	110	1	84	15	0	2	0
0	0	0	108	34	33	21	0	61	0	0	0
0	0	0	2	0	12	34	0	0	0	0	0
2	0	0	0	32	59	52	146	31	0	1	10
1	0	0	0	0	33	28	24	10	0	0	0
0	0	0	0	1	64	1	43	0	1	11	0
0	0	9	0	0	0	8	10	0	0	0	0
0	0	0	0	0	88	22	40	68	0	0	0
0	0	0	24	1	1	0	0	3	0	0	0
0	0	0	0	0	0	0	83	0	0	0	0
0	0	0	0	0	0	10	19	0	0	0	1

0	0	0	0	0	0	0	0	0
0	0	0	5	81	65	9	0	0
0	2	14	84	216	151	50	1	0
0	0	44	109	130	124	3	1	0
0	2	0	63	166	164	8	6	0
0	1	3	42	63	55	17	0	0
0	0	3	24	86	115	1	0	0
0	0	1	10	58	52	1	0	0
0	0	0	0	7	7	2	1	0
0	0	0	0	0	0	0	0	0

0	0	0	0	0	0	0	0	0	0
0	0	0	0	4	5	2	0	0	0
0	0	0	3	79	110	43	1	0	0
0	0	8	50	207	185	28	0	0	0
0	0	1	58	165	223	71	5	0	0
0	1	2	18	155	150	35	5	0	4
0	0	0	11	81	134	22	2	1	4
0	0	0	8	48	50	18	0	0	4
0	0	0	0	2	24	2	1	0	1
0	0	0	0	0	1	0	0	1	0
0	0	0	0	0	0	0	0	0	0

0	0	0	0	0	0	0	1	0	0	0
0	0	0	0	4	18	10	1	0	0	0
0	0	0	2	42	86	57	11	0	0	0
0	1	3	19	164	131	46	16	2	0	0
0	0	5	50	129	142	50	17	2	0	0
0	1	1	16	104	151	98	41	3	0	0
0	0	0	14	69	104	84	16	0	0	0
0	0	0	10	53	67	51	9	3	0	0
0	0	0	0	14	23	36	4	0	0	0
0	0	0	0	2	6	22	2	0	0	0
0	0	0	0	0	0	4	0	0	0	0
0	0	0	0	0	0	0	0	0	0	0

***** CALIFORNIA: BEAR VALLEY REGION *****

NO OF STATIONS= 43
NO OF EVENTS=119
NO OF OBSERVATIONS= 2047

TOTAL BLOCKS IN MODEL= 488
NO OF BLOCKS OBSERVED= 204

DATA VARIANCE IS 0.0634
RESIDUAL VARIANCE IS 0.0201
VARIANCE IMPROVEMENT IN % IS 68.2354

VELOCITY PERTURBATIONS IN LAYER-BLOCK FORMAT

LAYER ... 1

0.0	0.0	0.0	0.0	0.0	0.68	2.72	-3.31	-2.34	0.99	0.0	0.0
0.0	2.38	0.0	0.0	0.30	5.49	-2.95	1.79	-0.96	-1.01	0.71	0.0
0.0	-2.68	-0.10	0.0	0.0	7.67	-1.83	0.86	-1.13	0.0	1.15	0.0
0.0	0.0	0.0	1.04	1.30	5.45	-4.18	0.0	2.67	0.0	0.0	0.0
0.0	0.0	0.0	1.55	0.0	2.39	-5.92	0.0	0.0	0.0	0.0	0.0
-0.47	0.0	0.0	0.0	4.88	6.99	-2.25	-6.31	2.38	0.0	-0.55	-3.54
-0.28	0.0	0.0	0.0	0.0	7.65	0.82	-8.23	-0.70	0.0	0.0	0.0
0.0	0.0	0.0	0.0	0.08	7.03	-1.03	-13.30	0.0	-0.46	-0.94	0.0
0.0	0.0	0.09	0.0	0.0	0.0	-0.41	-5.93	0.0	0.0	0.0	0.0
0.0	0.0	0.0	0.0	0.0	4.83	4.07	-4.05	-1.47	0.0	0.0	0.0
0.0	0.0	0.0	-2.40	-0.07	-1.19	0.0	0.0	-0.78	0.0	0.0	0.0
0.0	0.0	0.0	0.0	0.0	0.0	0.0	-1.04	0.0	0.0	0.0	0.0
0.0	0.0	0.0	0.0	0.0	0.0	1.76	1.99	0.0	0.0	0.0	0.71

LAYER ... 2

0.0	0.0	0.0	0.0	0.0	0.0	0.0	0.0	0.0
0.0	0.0	0.0	0.81	2.62	0.39	-0.19	0.0	0.0
0.0	2.15	2.07	1.11	3.67	-0.83	-2.00	0.27	0.0
0.0	0.0	-1.58	3.69	2.19	-1.46	-1.89	0.87	0.0
0.0	-0.80	0.0	3.88	0.46	-0.04	-3.22	-4.42	0.0
0.0	-0.49	0.81	1.96	0.39	-2.73	0.69	0.0	0.0
0.0	0.0	-1.41	0.82	1.71	-5.05	0.26	0.0	0.0
0.0	0.0	0.41	-3.84	-0.03	-1.36	-2.02	0.0	0.0
0.0	0.0	0.0	0.0	2.31	-1.05	0.11	1.24	0.0
0.0	0.0	0.0	0.0	0.0	0.0	0.0	0.0	0.0

LAYER ... 3

0.0	0.0	0.0	0.0	0.0	0.0	0.0	0.0	0.0	0.0
0.0	0.0	0.0	0.0	2.63	1.80	-1.67	0.0	0.0	0.0
0.0	0.0	0.0	3.48	3.57	1.22	-1.35	-2.88	0.0	0.0
0.0	0.0	1.19	1.04	1.23	-0.41	-1.91	0.0	0.0	0.0
0.0	0.0	0.02	0.55	1.08	-0.74	-1.35	-5.97	0.0	0.0
0.0	1.58	-3.24	0.45	0.73	-0.19	0.98	1.50	0.0	1.46
0.0	0.0	0.0	-0.65	-0.34	-0.58	3.27	1.54	0.95	1.62
0.0	0.0	0.0	-0.77	-0.47	-0.52	2.57	0.0	0.0	0.27
0.0	0.0	0.0	0.0	-4.39	0.11	0.53	1.65	0.0	-0.22
0.0	0.0	0.0	0.0	0.0	-5.53	0.0	0.0	-0.68	0.0
0.0	0.0	0.0	0.0	0.0	0.0	0.0	0.0	0.0	0.0

LAYER ...

0.0	0.0	0.0	0.0	0.0	0.0	0.0	-0.61	0.0	0.0	0.0
0.0	0.0	0.0	0.0	1.54	2.50	1.53	-1.07	0.0	0.0	0.0
0.0	0.0	0.0	3.45	1.31	1.85	1.39	-0.17	0.0	0.0	0.0
0.0	0.98	-1.75	0.72	1.27	0.71	0.80	-0.34	-2.18	0.0	0.0
0.0	0.0	1.99	1.99	1.43	-0.25	-1.95	-1.87	-9.88	0.0	0.0
0.0	1.58	-2.60	1.55	0.81	0.65	-2.05	-2.78	-2.22	0.0	0.0
0.0	0.0	0.0	0.91	-0.29	0.94	-2.16	-0.05	0.0	0.0	0.0
0.0	0.0	0.0	0.55	-0.31	1.74	1.03	1.84	4.34	0.0	0.0
0.0	0.0	0.0	0.0	0.62	-0.54	2.24	3.30	0.0	0.0	0.0
0.0	0.0	0.0	0.0	-2.10	-3.87	-1.59	2.72	0.0	0.0	0.0
0.0	0.0	0.0	0.0	0.0	0.0	-7.00	0.0	0.0	0.0	0.0
0.0	0.0	0.0	0.0	0.0	0.0	0.0	0.0	0.0	0.0	0.0

DIAGONAL ELEMENTS OF RESOLUTION MATRIX IN LAYER-BLOCK FORMAT

LAYER ... 1

0.0	0.0	0.0	0.0	0.0	0.24	0.70	0.61	0.42	0.17	0.0	0.0
0.0	0.17	0.0	0.0	0.06	0.72	0.72	0.52	0.43	0.66	0.05	0.0
0.0	0.20	0.01	0.0	0.0	0.74	0.06	0.72	0.41	0.0	0.09	0.0
0.0	0.0	0.0	0.63	0.54	0.54	0.49	0.0	0.62	0.0	0.0	0.0
0.0	0.0	0.0	0.07	0.0	0.39	0.61	0.0	0.0	0.0	0.0	0.0
0.06	0.0	0.0	0.0	0.42	0.69	0.67	0.76	0.57	0.0	0.05	0.22
0.04	0.0	0.0	0.0	0.0	0.56	0.55	0.53	0.36	0.0	0.0	0.0
0.0	0.0	0.0	0.0	0.05	0.53	0.06	0.63	0.0	0.05	0.25	0.0
0.0	0.0	0.26	0.0	0.0	0.0	0.27	0.36	0.0	0.0	0.0	0.0
0.0	0.0	0.0	0.0	0.0	0.55	0.45	0.44	0.56	0.0	0.0	0.0
0.0	0.0	0.0	0.27	0.01	0.05	0.0	0.0	0.14	0.0	0.0	0.0
0.0	0.0	0.0	0.0	0.0	0.0	0.0	0.59	0.0	0.0	0.0	0.0
0.0	0.0	0.0	0.0	0.0	0.0	0.20	0.39	0.0	0.0	0.0	0.03

LAYER ... 2

0.0	0.0	0.0	0.0	0.0	0.0	0.0	0.0	0.0
0.0	0.0	0.0	0.40	0.81	0.80	0.54	0.0	0.0
0.0	0.20	0.50	0.81	0.88	0.88	0.79	0.33	0.0
0.0	0.0	0.60	0.84	0.86	0.86	0.51	0.13	0.0
0.0	0.17	0.0	0.82	0.89	0.88	0.62	0.32	0.0
0.0	0.11	0.30	0.70	0.83	0.79	0.74	0.0	0.0
0.0	0.0	0.26	0.66	0.79	0.80	0.33	0.0	0.0
0.0	0.0	0.14	0.46	0.76	0.74	0.32	0.0	0.0
0.0	0.0	0.0	0.0	0.36	0.38	0.47	0.10	0.0
0.0	0.0	0.0	0.0	0.0	0.0	0.0	0.0	0.0

LAYER ... 3

0.0	0.0	0.0	0.0	0.0	0.0	0.0	0.0	0.0	0.0
0.0	0.0	0.0	0.0	0.54	0.59	0.42	0.0	0.0	0.0
0.0	0.0	0.0	0.40	0.87	0.89	0.82	0.22	0.0	0.0
0.0	0.0	0.50	0.83	0.90	0.91	0.81	0.0	0.0	0.0
0.0	0.0	0.24	0.78	0.92	0.92	0.87	0.51	0.0	0.0
0.0	0.17	0.30	0.71	0.91	0.91	0.86	0.52	0.0	0.96
0.0	0.0	0.0	0.65	0.86	0.89	0.76	0.89	0.89	0.96
0.0	0.0	0.0	0.55	0.82	0.83	0.68	0.0	0.0	0.96
0.0	0.0	0.0	0.0	0.39	0.68	0.39	0.18	0.0	0.89
0.0	0.0	0.0	0.0	0.0	0.27	0.0	0.0	0.88	0.0
0.0	0.0	0.0	0.0	0.0	0.0	0.0	0.0	0.0	0.0

LAYER ... 4

0.0	0.0	0.0	0.0	0.0	0.0	0.0	0.27	0.0	0.0	0.0
0.0	0.0	0.0	0.0	0.53	0.78	0.70	0.30	0.0	0.0	0.0
0.0	0.0	0.0	0.31	0.85	0.89	0.87	0.68	0.0	0.0	0.0
0.0	0.23	0.36	0.75	0.91	0.92	0.88	0.74	0.35	0.0	0.0
0.0	0.0	0.49	0.81	0.91	0.93	0.89	0.79	0.30	0.0	0.0
0.0	0.17	0.17	0.73	0.91	0.93	0.92	0.84	0.46	0.0	0.0
0.0	0.0	0.0	0.70	0.89	0.91	0.90	0.77	0.0	0.0	0.0
0.0	0.0	0.0	0.61	0.84	0.88	0.85	0.62	0.43	0.0	0.0
0.0	0.0	0.0	0.0	0.68	0.77	0.79	0.48	0.0	0.0	0.0
0.0	0.0	0.0	0.0	0.35	0.60	0.68	0.33	0.0	0.0	0.0
0.0	0.0	0.0	0.0	0.0	0.0	0.44	0.0	0.0	0.0	0.0
0.0	0.0	0.0	0.0	0.0	0.0	0.0	0.0	0.0	0.0	0.0

STD ERRORS IN LAYER-BLOCK FORMAT

LAYER ... 1

0.0	0.0	0.0	0.0	0.0	0.84	0.78	0.92	0.93	0.70	0.0	0.0
0.0	0.46	0.0	0.0	0.48	0.75	0.79	0.96	0.95	0.83	0.44	0.0
0.0	0.72	0.12	0.0	0.0	0.76	0.46	0.81	0.93	0.0	0.52	0.0
0.0	0.0	0.0	0.81	0.92	0.92	0.94	0.0	0.89	0.0	0.0	0.0
0.0	0.0	0.0	0.48	0.0	0.94	0.93	0.0	0.0	0.0	0.0	0.0
0.33	0.0	0.0	0.0	0.91	0.86	0.87	0.75	0.94	0.0	0.44	0.68
0.32	0.0	0.0	0.0	0.0	0.93	0.95	0.95	0.93	0.0	0.0	0.0
0.0	0.0	0.0	0.0	0.44	0.85	0.46	0.90	0.0	0.45	0.76	0.0
0.0	0.0	0.77	0.0	0.0	0.0	0.86	0.91	0.0	0.0	0.0	0.0
0.0	0.0	0.0	0.0	0.0	0.82	0.89	0.88	0.84	0.0	0.0	0.0
0.0	0.0	0.0	0.65	0.06	0.39	0.0	0.0	0.59	0.0	0.0	0.0
0.0	0.0	0.0	0.0	0.0	0.0	0.0	0.82	0.0	0.0	0.0	0.0
0.0	0.0	0.0	0.0	0.0	0.0	0.67	0.84	0.0	0.0	0.0	0.27

LAYER ... 2

0.0	0.0	0.0	0.0	0.0	0.0	0.0	0.0	0.0
0.0	0.0	0.0	0.88	0.63	0.66	0.93	0.0	0.0
0.0	0.68	0.74	0.64	0.45	0.49	0.68	0.91	0.0
0.0	0.0	0.82	0.55	0.52	0.52	0.96	0.62	0.0
0.0	0.58	0.0	0.62	0.46	0.51	0.90	0.69	0.0
0.0	0.55	0.85	0.74	0.61	0.68	0.75	0.0	0.0
0.0	0.0	0.76	0.80	0.61	0.58	0.90	0.0	0.0
0.0	0.0	0.67	0.82	0.69	0.70	0.88	0.0	0.0
0.0	0.0	0.0	0.0	0.82	0.80	0.94	0.48	0.0
0.0	0.0	0.0	0.0	0.0	0.0	0.0	0.0	0.0

LAYER ... 3

0.0	0.0	0.0	0.0	0.0	0.0	0.0	0.0	0.0	0.0
0.0	0.0	0.0	0.0	0.95	0.91	0.89	0.0	0.0	0.0
0.0	0.0	0.0	0.79	0.54	0.47	0.61	0.76	0.0	0.0
0.0	0.0	0.72	0.61	0.44	0.41	0.67	0.0	0.0	0.0
0.0	0.0	0.77	0.67	0.41	0.38	0.53	0.83	0.0	0.0
0.0	0.61	0.78	0.79	0.43	0.41	0.59	0.87	0.0	0.36
0.0	0.0	0.0	0.81	0.56	0.47	0.72	0.58	0.59	0.36
0.0	0.0	0.0	0.81	0.61	0.58	0.77	0.0	0.0	0.36
0.0	0.0	0.0	0.0	0.93	0.72	0.90	0.64	0.0	0.60
0.0	0.0	0.0	0.0	0.0	0.83	0.0	0.0	0.59	0.0
0.0	0.0	0.0	0.0	0.0	0.0	0.0	0.0	0.0	0.0

LAYER ... 4

0.0	0.0	0.0	0.0	0.0	0.0	0.0	0.80	0.0	0.0	0.0
0.0	0.0	0.0	0.0	0.87	0.72	0.80	0.87	0.0	0.0	0.0
0.0	0.0	0.0	0.80	0.59	0.48	0.53	0.86	0.0	0.0	0.0
0.0	0.74	0.83	0.78	0.44	0.40	0.56	0.79	0.89	0.0	0.0
0.0	0.0	0.83	0.66	0.44	0.41	0.52	0.74	0.81	0.0	0.0
0.0	0.61	0.64	0.78	0.45	0.37	0.42	0.63	0.93	0.0	0.0
0.0	0.0	0.0	0.81	0.51	0.43	0.49	0.76	0.0	0.0	0.0
0.0	0.0	0.0	0.84	0.62	0.52	0.61	0.87	0.91	0.0	0.0
0.0	0.0	0.0	0.0	0.79	0.72	0.66	0.93	0.0	0.0	0.0
0.0	0.0	0.0	0.0	0.90	0.87	0.75	0.80	0.0	0.0	0.0
0.0	0.0	0.0	0.0	0.0	0.0	0.81	0.0	0.0	0.0	0.0
0.0	0.0	0.0	0.0	0.0	0.0	0.0	0.0	0.0	0.0	0.0

Table 4.1

Yellowstone Seismic Refraction Experiment

Shotpoint (Cougar Creek): 44°45.40N, 111°05.82W

Origin Time: 06h 15m 01.32s GMT on 9/9/77

MEQ-800 Sites Along Madison River Valley:

MR-1	44° 43' 12" N 111° 05' 48" W
MR-2	44° 42' 00" N 111° 05' 08" W
MR-3	44° 41' 00" N 111° 04' 45" W
MR-4	44" 39' 37" N 111° 04' 22" W

Arrival Times of First Motion:

MR-1	12:15:2.925s
MR-2	12:15:3.300s
MR-3	noisy
MR-4	12:15:4.200s

TABLE 4.2.

Inversion of Local Yellowstone Earthquakes

4.2a Initial Model and Station data

4.2b Earthquake Summary

4.2c Observation Matrix, Number of "Hits" Per Block

4.2d Solution for Hypocenters: from left to right δt_i, δx_i, δy_i, δz_i where i = 1,...,26 are the earthquakes listed in 4.2b.

4.2e Solution for Velocity for Layer 1. Each percent perturbation is for the area immediately beneath a station. From left to right each number is associated with the alphabetical sequences of station names in 4.2a.

4.2f Solution for Velocity in Layer 2. In this layer each perturbation is associated with the block it is in. The block configuration is given in 4.2a.

4.2g Resolution for Parameters

origin of cartesian coordinates: 44-34.90n 110-40.70w

depth: 0.00

rotation: 0.00

zmin	ittmax	delmin	veladj	swtfac	vthet	ipunch	zadj	thet	tthet	zthet
-1.50	6	0.01	0.50	0.00	50.00	703	5.00	0.01	0.20	0.02

ray segments divided into 0.100 second intervals

nl	neqs	nshot	ires	nkr	nmin	kfirst
2	26	0	1	0	1	1

layer	depth	pvel	svel	west	length	north	length	cordinate displacement	
1	-1.50	3.50		13	10.00	12	10.00	0.000	0.000
2	1.00	5.70		13	10.00	12	10.00	0.000	0.000

	stn	latitude	longitude	elev	pdelay					
1	YPBB	45* 1.73	111* 7.01	2193	0.00	0.00	3.50	34.56	49.79	-2.20
2	YPCJ	44*44.63	110*29.85	2426	0.00	0.00	3.50	-14.32	18.04	-2.43
3	YPDC	44*42.57	111*14.38	2025	0.00	0.00	3.50	44.48	14.36	-2.03
4	YPEE	44*29.43	110* 0.06	2134	0.00	0.00	3.50	-53.88	-9.91	-2.13
5	YPGC	44*47.77	111* 6.39	2075	0.00	0.00	3.50	33.88	23.93	-2.07
6	YPHB	44*45.06	111*11.72	2157	0.00	0.00	3.50	40.94	18.95	-2.16
7	YPHR	44*51.14	111*18.96	2060	0.00	0.00	3.50	50.41	30.28	-2.06
8	YPLK	44*34.18	110*23.18	2391	0.00	0.00	3.50	-23.20	-1.29	-2.39
9	YPMC	44*45.56	111* 0.36	2073	0.00	0.00	3.50	25.95	19.80	-2.07
10	YPMF	44* 8.60	111*17.29	1788	0.00	0.00	3.50	48.80	-48.53	-1.79
11	YPMH	44*58.62	110*41.12	1781	0.00	0.00	3.50	0.55	43.93	-1.78
12	YPMJ	44*38.90	110*51.52	2111	0.00	0.00	3.50	14.31	7.42	-2.11
13	YPML	44*36.17	110*38.38	2518	0.00	0.00	3.50	-3.07	2.35	-2.52
14	YPMV	44*37.63	110*26.75	2400	0.00	0.00	3.50	-18.45	5.08	-2.40
15	YPNB	44*31.48	110*27.55	2405	0.00	0.00	3.50	-17.42	-6.31	-2.41
16	YPNJ	44*43.82	110*41.58	2290	0.00	0.00	3.50	1.16	16.52	-2.29
17	YPOF	44*27.15	110*50.48	2260	0.00	0.00	3.50	12.97	-14.34	-2.26
18	YPPC	44*38.90	110*11.58	2932	0.00	0.00	3.50	-38.50	7.52	-2.93
19	YPPR	44*23.55	110*17.19	2390	0.00	0.00	3.50	-31.22	-20.95	-2.39
20	YPSE	44* 8.18	110*40.00	2073	0.00	0.00	3.50	-0.93	-49.49	-2.07
21	YPSG	45* 0.18	109*59.25	2270	0.00	0.00	3.50	-54.47	47.05	-2.27
22	YPTB	44*31.50	110*50.76	2224	0.00	0.00	3.50	13.33	-6.28	-2.22
23	YPTC	44*17.79	110*13.92	2360	0.00	0.00	3.50	-35.62	-31.59	-2.36
24	YPTS	44*27.74	111*21.15	1923	0.00	0.00	3.50	53.65	-13.04	-1.92
25	YPWT	44*24.87	110*34.27	2365	0.00	0.00	3.50	-8.54	-18.57	-2.37
26	YPWY	44*36.36	111* 5.81	2294	0.00	0.00	3.50	33.22	2.79	-2.29
27	YLGB	44*42.31	110*44.56	2200	0.00	0.00	3.50	5.10	13.73	-2.20
28	YLAR	44*28.72	110*32.53	2590	0.00	0.00	3.50	-10.83	-11.44	-2.59
29	YLOC	44*42.14	110*30.38	2426	0.00	0.00	3.50	-13.63	13.42	-2.43
30	YLOF	44*27.44	110*50.42	2260	0.00	0.00	3.50	12.89	-13.80	-2.26
31	YLMV	44*58.48	110*41.38	1829	0.00	0.00	3.50	0.89	43.67	-1.83
32	YAFR	44*35.52	110*49.72	2184	0.00	0.00	3.50	11.94	1.16	-2.18
33	YASL	44*25.88	110*44.98	2440	0.00	0.00	3.50	5.68	-16.70	-2.44
34	YABT	44*25.90	110*39.35	2589	0.00	0.00	3.50	-1.79	-16.67	-2.59
35	YADC	44*19.79	110*36.56	2387	0.00	0.00	3.50	-5.50	-27.98	-2.39
36	YAPP	44*27.89	110*30.56	2393	0.00	0.00	3.50	-13.45	-12.97	-2.39
37	YACH	44*55.69	110*28.56	2294	0.00	0.00	3.50	-15.97	38.53	-2.29
38	YAMV	44*58.40	110*41.28	1829	0.00	0.00	3.50	0.76	43.53	-1.83
39	YASY	44*28.55	110* 9.33	2574	0.00	0.00	3.50	-41.60	-11.63	-2.57
40	YDIL	44*43.10	110*38.25	2417	0.00	0.00	3.50	-3.24	15.19	-2.42
41	YDCN	44*42.83	110*32.56	2426	0.00	0.00	3.50	-10.75	14.70	-2.43
42	YDSE	44*53.51	110*43.75	2240	0.00	0.00	3.50	4.02	34.47	-2.24

```
 45 YDYR  45*21.80 110*45.40  1539  0.00  0.00  3.50  6.14 86.87 -1.54
 46 YDMB  45*31.55 110*13.40  1632  0.00  0.00  3.50-35.55105.03 -1.63

  nags=  26              0        26       416      86736
 1 750715 1935 55.0344n40.53 110w34.18   1.09     -8.62      10.43      1.09
        direct is stuck; using dif ratio=   0.000015979
        direct is stuck; using dif ratio=   0.000010241
 2 751205 11 6 35.0144n45.31 111w10.58   5.91     39.43      19.40      5.91
 3 751229  357 52.7844n43.64 111w 6.64  11.64     34.25      16.28     11.64
 4 760408  947  3.0044n45.65 111w15.28   1.07     45.63      20.07      1.07
        direct is stuck; using dif ratio=   0.000015724
 5 770304 1419 49.3744n45.66 111w 1.52   4.04     27.48      19.99      4.04
 6 770525 1058 32.2344n32.13 111w 1.10   8.37     27.03      -5.07      8.37
 7 770524  9 5 24.8544n32.18 110w40.71   0.64      0.01      -5.04      0.64
 8 750215 2240 58.9744n27.94 110w24.08   0.94    -22.04     -12.85      0.94
 9 751125  920 52.8644n30.61 110w22.20   0.07    -24.52      -7.90      0.07
10 750318  231 18.4944n36.30 110w26.42   0.35    -18.90       2.62      0.35
11 761011 12 5 37.0644n36.27 110w38.68   1.70     -2.67       2.54      1.70
12 750130   50 39.0044n37.92 110w49.02   1.21     11.00       5.60      1.21
13 761019  618 35.1544n44.47 110w48.95   0.73     10.89      17.73      0.73
14 750401  1 2 54.3844n23.44 110w14.89   8.21    -34.28     -21.13      8.21
15 770411  651 10.3244n23.06 110w18.86   1.78    -29.01     -21.86      1.78
16 750908 1156 39.7544n33.80 111w 4.42   4.10     31.41      -1.96      4.10
17 760711 1622 28.4044n29.71 111w 4.63   9.17     31.72      -9.54      9.17
18 750905  536 40.1644n31.18 110w54.37   1.31     18.11      -6.86      1.31
19 751125 18 9 29.6944n20.18 110w44.35   0.40      4.85     -27.26      0.40
20 750509 1238 57.6344n27.33 110w35.39   0.83     -7.04     -14.02      0.83
21 760314  336 15.9544n31.10 110w33.60   0.76     -9.41      -7.03      0.76
22 750217 2045 53.5144n46.60 110w27.94   5.00    -16.83      21.69      5.00
23 750711  129 47.5844n40.53 111w 1.66   4.06     27.70      10.49      4.06
24 750713  854 38.4844n45.41 110w52.50   0.74     15.57      19.48      0.74
25 750711   53 52.5744n42.27 110w39.55   0.85     -1.52      13.65      0.85
26 750713 10 1  6.6944n40.05 110w40.04   0.78     -0.87       9.54      0.78

data variance=  0.17251     nobs=  503

average residuals      -0.65 -0.59 -0.63 -0.61 -0.69 -0.76 -0.52 -0.59 -0.44 -0.47
                       -0.64 -0.25 -0.60 -0.77 -0.82 -0.64 -0.67 -0.70 -0.51 -0.58
                       -0.56 -0.64 -0.64 -0.59 -0.62 -0.62

rms values              0.20  0.18  0.14  0.19  0.29  0.39  0.10  0.41  0.22  0.28
                        0.18  1.71  0.18  0.32  0.42  0.23  0.25  0.15  0.36  0.16
                        0.13  0.11  0.21  0.15  0.21  0.21
```

observation matrix

22	19	24	6	21	9	20	14	22	13	0	25	25
20	21	25	24	11	6	11	25	16	17	11	21	15
2	2	2	2	1	0	5	3	4	5	4	5	1
5	0	5	4	5	5	0	0	0	0	0	0	0
0	0	0	0	0	0	0	0	0	0	0	0	0
0	0	0	0	0	0	0	0	0	0	0	0	0
0	0	0	0	0	0	0	0	0	0	0	0	0
0	0	0	0	0	0	0	0	0	0	0	0	0
0	0	0	0	0	0	0	0	0	0	0	0	0
0	0	0	0	0	0	0	0	0	0	0	0	0
0	0	0	0	0	0	0	0	0	0	0	0	0
0	0	0	0	0	0	0	0	0	0	0	0	0

0	0	0	0	0	1	4	0	0	0	0	0	0
0	0	2	21	5	1	10	0	0	4	14	25	0
0	0	2	14	13	12	21	14	8	17	17	10	0
0	26	26	39	26	28	29	24	27	13	7	4	0
0	10	69	109	105	92	106	72	16	8	4	1	0
0	2	19	66	72	103	131	79	58	13	13	0	0
0	9	10	64	67	69	91	96	72	15	7	3	0
0	12	8	13	23	47	43	67	53	30	5	3	0
0	2	7	3	6	16	18	10	16	42	2	0	0
									3	0	0	0

solution for hypocenters

-0.581	0.071	-0.002	-0.008	-0.545	0.331	-0.384	0.918	-0.530	-0.200	-0.752	0.420
-0.499	0.116	0.039	-0.011	-0.513	-0.965	-0.121	0.582	-0.742	-0.518	0.557	0.469
-0.306	-0.376	0.489	0.689	-0.379	0.133	0.244	0.854	-0.347	0.896	0.086	0.174
-0.364	0.723	-0.838	-0.013	-0.599	-0.083	-0.038	0.267	-0.216	-1.886	3.426	-0.896
-0.341	-0.378	-0.157	0.770	-0.677	-0.027	0.981	0.414	-0.682	-0.876	1.597	0.212
-0.745	-0.481	-0.835	0.367	-0.815	-0.434	1.223	0.508	-0.707	0.287	-0.698	-0.023
-0.360	2.013	0.175	0.812	-0.404	-0.706	-0.159	0.912	-0.354	-0.613	0.407	0.798
-0.464	0.491	-0.730	0.023	-0.513	-0.920	-0.476	-0.114	-0.324	-0.634	-0.034	0.731
-0.542	-0.326	-0.136	0.147	-0.377	-0.383	-0.006	0.850				

solution for velocity model

layer 1

1.483	-3.337	0.077	1.047	-1.798	1.694	0.185	-1.102	-0.246	-1.790	0.000	-1.893	1.621
-0.965	2.227	1.767	1.287	-0.618	2.423	0.185	-0.215	0.006	-0.124	-3.995	3.057	-1.503
-0.819	0.314	-0.532	-0.011	-0.324	0.000	1.998	-0.247	-1.048	1.040	-2.352	0.398	0.989
0.042	0.000	-1.302	-3.887	0.504	2.093	0.000	0.000	0.000	0.000	0.000	0.000	0.000
0.000	0.000	0.000	0.000	0.000	0.000	0.000	0.000	0.000	0.000	0.000	0.000	0.000
0.000	0.000	0.000	0.000	0.000	0.000	0.000	0.000	0.000	0.000	0.000	0.000	0.000
0.000	0.000	0.000	0.000	0.000	0.000	0.000	0.000	0.000	0.000	0.000	0.000	0.000
0.000	0.000	0.000	0.000	0.000	0.000	0.000	0.000	0.000	0.000	0.000	0.000	0.000
0.000	0.000	0.000	0.000	0.000	0.000	0.000	0.000	0.000	0.000	0.000	0.000	0.000
0.000	0.000	0.000	0.000	0.000	0.000	0.000	0.000	0.000	0.000	0.000	0.000	0.000
0.000	0.000	0.000	0.000	0.000	0.000	0.000	0.000	0.000	0.000	0.000	0.000	0.000
0.000	0.000	0.000	0.000	0.000	0.000	0.000	0.000	0.000	0.000	0.000	0.000	0.000

layer 2

370	0.000	0.000	0.000	0.000	0.000	1.407	0.797	0.000	0.000	0.000	0.000	0.000	0.000
	0.000	0.000	1.725	4.213	0.170	1.407	0.895	0.000	0.000	0.430	3.433	7.398	0.000
	0.000	0.000	2.508	5.376	0.278	2.053	1.029	0.408	2.707	6.689	6.267	1.130	0.000
	0.000	-0.111	2.409	4.268	3.672	0.127	0.550	0.945	5.979	3.112	-3.979	4.088	0.000
	0.000	0.268	5.385	5.473	4.348	-0.022	0.043	1.623	0.656	-2.658	1.489	0.764	0.000
	0.000	0.521	3.619	1.379	-6.431	3.281	-0.379	0.305	-1.684	-3.597	4.200	0.000	0.000
	0.000	-3.045	-19.477	-20.493	1.740	1.852	-0.311	0.296	-4.141	-0.603	3.838	0.537	0.000
	0.000	-9.906	2.374	0.183	0.953	0.741	-0.037	-3.837	0.125	-0.069	0.033	-1.008	0.000
	0.000	1.123	1.350	0.205	0.096	0.414	-0.901	-0.676	0.514	1.769	-0.021	0.000	0.000
	0.000	1.889	0.774	-0.295	-0.459	0.013	0.171	-0.382	0.448	-0.015	0.000	0.000	0.000
	0.000	1.535	-0.384	-0.155	0.000	0.011	0.096	0.261	0.000	0.000	0.000	0.000	0.000
	0.000	0.000	0.000	0.000	0.000	0.000	0.000	0.000	0.000	0.000	0.000	0.000	0.000

resolution control

1	r= 0.988
2	r= 0.964
3	r= 0.971
4	r= 0.001
5	r= 0.963
6	r= 0.939
7	r= 0.944
8	r= 0.618
9	r= 0.939
10	r= 0.919
11	r= 0.925
12	r= 0.506
13	r= 0.958
14	r= 0.878
15	r= 0.933
16	r= 0.002
17	r= 0.975
18	r= 0.950
19	r= 0.914
20	r= 0.539
21	r= 0.909
22	r= 0.905
23	r= 0.836
24	r= 0.324
25	r= 0.654
26	r= 0.951
27	r= 0.947
28	r= 0.333
29	r= 0.651
30	r= 0.929
31	r= 0.947
32	r= 0.331
33	r= 0.931
34	r= 0.947
35	r= 0.947
36	r= 0.901
37	r= 0.973
38	r= 0.933
39	r= 0.943
40	r= 0.921
41	r= 0.985
42	r= 0.966
43	r= 0.947
44	r= 0.612
45	r= 0.987
46	r= 0.967
47	r= 0.953
48	r= 0.033
49	r= 0.655
50	r= 0.957
51	r= 0.940
52	r= 0.333
53	r= 0.934
54	r= 0.895
55	r= 0.895
56	r= 0.204
57	r= 0.966
58	r= 0.915
59	r= 0.912
60	r= 0.004
61	r= 0.968
62	r= 0.932
63	r= 0.936
64	r= 0.042
65	r= 0.956
66	r= 0.943
67	r= 0.931
68	r= 0.326
69	r= 0.959
70	r= 0.935
71	r= 0.880
72	r= 0.000
73	r= 0.648
74	r= 0.901
75	r= 0.927
76	r= 0.329
77	r= 0.655
78	r= 0.953
79	r= 0.956
80	r= 0.333
81	r= 0.655
82	r= 0.960
83	r= 0.943
84	r= 0.333
85	r= 0.954
86	r= 0.913
87	r= 0.875
88	r= 0.421
89	r= 0.977
90	r= 0.955
91	r= 0.958
92	r= 0.227
93	r= 0.657
94	r= 0.961
95	r= 0.964
96	r= 0.334
97	r= 0.974
98	r= 0.963
99	r= 0.969
100	r= 0.950
101	r= 0.658
102	r= 0.963
103	r= 0.976
104	r= 0.335
105	r= 0.806
106	r= 0.418
107	r= 0.900
108	r= 0.881
109	r= 0.898
110	r= 0.844
111	r= 0.909
112	r= 0.665
113	r= 0.877
114	r= 0.739
116	r= 0.783
117	r= 0.406
118	r= 0.753
119	r= 0.737
120	r= 0.402
121	r= 0.747
122	r= 0.875
123	r= 0.518
124	r= 0.072
125	r= 0.925
126	r= 0.742
127	r= 0.836
128	r= 0.505
129	r= 0.460
130	r= 0.780
131	r= 0.126
132	r= 0.084
133	r= 0.133
134	r= 0.254
135	r= 0.026
137	r= 0.318
138	r= 0.076
139	r= 0.072
140	r= 0.367
141	r= 0.433
142	r= 0.121
143	r= 0.662
144	r= 0.095
146	r= 0.216
147	r= 0.521
148	r= 0.373
149	r= 0.240
266	r= 0.054
267	r= 0.131

TABLE 4.3.

Three-Dimensional Inversion
of Yellowstone Residuals - Model YP4-100

***** PROGRAM 3-D ***** 22 NOVEMBER 1975

YE_LOWSTONE - YP DATA C(A,B,C)

LATITUDE	LONGITUDE	THA	V0	JPWT	IRES	IPUNCH	IPRINT	THETA	RESL
44N36.17	110W38.38	0.0	6.00	0	1	1	0	50.	0.100

	VELOCITY	THICKNESS	#-NORTH	LENGTH	#-EAST	LENGTH	COORDINATE DISPLACEMENT	
1	6.00	20.00	10	20.00	11	20.00	0.0	0.0
2	6.50	20.00	12	20.00	12	20.00	0.0	0.0
3	7.90	30.00	9	25.00	10	25.00	0.0	0.0
4	7.90	30.00	10	25.00	11	25.00	0.0	0.0

STA	LATITUDE	LONGITUDE	ELEVATION	RELATIVE COORDINATES	
1YPAA	45N 1.73	111W 7.01	2199.	47.45	-37.61
2YPCJ	44N34.63	110W29.85	2426.	15.68	11.26
3YPDC	44N42.57	111W14.38	2025.	12.03	-47.55
4YPEE	44N29.43	110W 0.06	2134.	-12.29	50.80
5YPGC	44N47.77	111W 6.39	2075.	21.59	-36.94
6YPHA	44N45.06	111W11.72	2157.	16.61	-44.00
7YPHR	44N51.14	111W18.96	2060.	27.95	-53.47
8YPLK	44N34.18	110W23.18	2391.	-3.65	20.12
9YPMC	44N45.56	111W 0.76	2073.	17.46	-29.01
10YPMF	44N 8.60	111W17.29	1788.	-50.96	-51.89
11YPMH	44N58.62	110W41.12	1781.	41.58	-3.60
12YPMJ	44N38.90	110W51.52	2111.	5.08	-17.37
13YPML	44N36.17	110W38.38	2518.	0.0	0.0
14YPMV	44N37.63	110W26.75	2400.	2.72	15.38
15YPNB	44N31.48	110W27.56	2405.	-8.67	14.35
16YPNJ	44N43.92	110W41.58	2250.	14.17	-4.23
17YPOF	44N27.15	110W50.48	2260.	-16.69	-16.05
18YPPC	44N38.90	110W11.58	2932.	5.15	35.44
19YPPR	44N23.55	110W17.19	2390.	-23.31	28.14
20YPSE	44N 8.18	110W40.00	2073.	-51.84	-2.16
21YPSG	45N 0.18	109W59.25	2270.	44.69	51.42
22YPTB	44N31.50	110W50.76	2224.	-8.63	-16.40
23YPTC	44N17.79	110W13.92	2360.	-33.96	32.54
24YPTS	44N27.74	111W21.15	1923.	-15.37	-56.73
25YPWT	44N24.87	110W34.27	2365.	-20.93	5.46
26YPWY	44N36.36	111W 5.81	2294.	0.45	-36.29

	ONLY 3 READINGS FOR *TONG	Z1(11/22/73)	17:53	57	239.41	5.21				
1	*BONIN	Z1(01/15/73)	9: 2	477	302.08	4.93			7	3.18
2	*TONGA	Z1(01/17/73)	9:44	251	241.15	5.04			6	3.48
3	*BONIN	Z2(01/31/73)	20:55	498	303.44	4.94			8	3.22
	ONLY 4 READINGS FOR *ARGEN	Z1(02/01/73)	5:14	229	138.70	5.45				
4	*TONGA	Z2(02/16/73)	4:51	60	239.70	5.21			7	4.40
5	*ECUAD	Z2(02/23/73)	4:26	67	138.94	7.20			6	5.09
6	*KURIL	Z1(03/12/73)	19:39	84	311.76	6.97			7	3.59
7	*ALEU	Z2(03/19/73)	11:41	81	307.94	7.68			7	2.98
8	*COLUM	Z1(04/03/73)	13:54	158	131.78	7.49			7	3.43
9	*CHILE	Z2(04/07/73)	22:50	95	140.05	5.73			6	4.18
10	*FIJI	Z2(04/06/73)	20:43	122	236.86	4.66			7	3.63
11	*KURIL	Z1(04/12/73)	13:49	52	311.78	6.99			9	3.99
12	*ALEU	Z2(04/16/73)	14:48	54	303.47	7.97			7	3.60
13	*PANAM	Z4(04/24/73)	21:30	50	134.45	7.65			6	4.92
	ONLY 3 READINGS FOR *HAWAI	Z2(04/26/73)	20:26	50	250.58	7.99				
14	*FIJI	Z1(05/03/73)	13:26	600	241.66	4.70			6	3.59
15	*ECUDR	Z1(05/30/73)	4:38	111	139.30	7.18			7	3.57
16	*SOLOM	Z2(06/09/73)	8:21	70	261.07	4.58			5	4.88
17	*JAPAN	Z3(06/17/73)	3:55	48	310.38	6.25			7	4.39
18	*CHILE	Z2(07/18/73)	15:21	151	138.82	5.85			7	3.31
19	*FIJI	Z1(07/19/73)	5:44	571	241.57	4.70			8	3.88
20	*JAPAN	Z1(07/20/73)	8:12	46	307.91	5.68			5	3.16
21	*FIJI	Z1(07/21/73)	4:19	411	237.66	4.59			7	3.05
22	*EKSSR	Z2(07/23/73)	1:22	1	353.71	4.95			7	3.35
23	*NICAR	Z2(07/28/73)	20:48	79	140.22	8.39			6	4.27
24	*TONGA	Z1(08/05/73)	15:47	33	238.86	5.17			7	3.72
	ONLY 4 READINGS FOR *CHILE	Z1(08/07/73)	3:41	25	144.22	5.37				
25	*CHILE	Z2(08/07/73)	10: 4	34	144.34	5.38			5	4.25
26	*ALEU	Z2(08/16/73)	14:25	62	303.12	8.07			5	3.36
27	*ALASK	Z2(08/22/73)	18:14	38	310.33	8.90			5	3.85
28	*MEXCO	Z1(08/28/73)	9:50	84	151.05	8.90			7	4.24
29	*JAPAN	Z1(09/05/73)	0:30	191	311.79	5.80			7	3.08
30	*ALASK	Z3(09/06/73)	10:59	29	320.33	9.05			7	4.23
	ONLY 4 READINGS FOR *PERU	Z2(09/08/73)	7:46	168	138.17	6.65				
31	*CHINA	Z1(09/10/73)	7:43	532	318.05	5.44			7	2.56
32	*NZSSR	FB(09/12/73)	6:59	1	4.53	6.75			8	2.99
	ONLY 4 READINGS FOR *EASTR	FB(09/21/73)	7:13	33	168.38	7.59				
33	*EASTR	Z2(09/21/73)	7:31	33	168.28	7.59			6	3.90
34	*NZSSR	Z1(09/27/73)	6:59	1	5.52	6.59			6	3.65
35	*KOREA	Z1(09/29/73)	0:44	575	317.60	5.39			7	2.76
36	*JAPAN	Z2(09/30/73)	6:17	62	307.73	5.61			7	3.47
37	*MEXCO	Z1(10/17/73)	10:49	45	167.28	9.15			6	4.48
38	*ARGEN	FB(10/25/73)	14: 8	529	136.18	5.29			8	1.94
39	*NZSSR	FB(10/27/73)	6:59	1	5.48	6.58			9	3.16
40	*ARGEN	Z1(11/03/73)	14:17	36	141.63	5.34			5	3.01
41	*ALEU	Z1(11/06/73)	9:36	34	303.18	8.13			7	2.88
42	*KURIL	Z1(11/08/73)	8:59	33	311.45	6.91			8	4.35
43	*ARGEN	Z1(11/19/73)	11:19	40	138.48	5.32			5	3.29
44	*JAPAN	Z1(11/19/73)	13: 1	56	309.25	5.84			6	2.88
45	*CHILE	Z1(11/19/73)	18:40	58	146.31	5.27			6	3.03
46	*KAMCH	Z2(11/27/73)	13:52	60	313.35	7.21			8	3.42
47	*CHILE	Z2(12/01/73)	17: 0	35	151.05	4.85			5	2.88
48	*EKSSR	Z1(12/14/73)	7:46	1	353.65	4.95			6	2.71
	ONLY 4 READINGS FOR *FIGI	Z1(12/19/73)	12:55	246	238.68	4.72				
	ONLY 3 READINGS FOR *CHILE	FB(01/02/74)	10:42	105	140.31	5.58				
49	*PERU	Z1(01/05/74)	8:33	98	142.40	6.52			7	4.33
50	*ARGEN	Z1(01/07/74)	16:35	33	140.51	5.22			5	3.57
51	*MARAI	Z1(01/25/74)	20:28	141	292.82	4.86			6	3.47
52	*KURIL	Z2(02/25/74)	5:46	12	309.94	6.37			6	3.36
53	*KURIL	FB(03/11/74)	11:37	169	311.14	6.69			6	2.73
54	*SAMOA	Z2(03/13/74)	10:56	27	239.56	5.26			8	3.85
55	*FIJI	FB(03/23/74)	14:28	535	237.02	4.58			5	2.13
56	*MARIA	Z2(03/24/74)	4:21	79	299.26	4.65			7	5.14
		Z1(03/27/74)	16:28	37	302.41	7.92			7	2.11
									6	3.28

	ONLY 4 READINGS FOR	*JAPAN	Z1(05/08/74)	23:33	2	307.95	5.49			
60	*EASTR	T1(05/10/74)	8:12	33	168.50	7.60			6	3.19
61	*MARIA	Z2(05/11/74)	6:14	6	292.15	5.01			10	4.40
62	*CHILE	Z2(05/12/74)	10: 5	112	139.26	5.80			6	3.14
63	*KURIL	P3(05/15/74)	18:59	56	311.47	6.89			5	3.67
64	*FIJI	Z1(05/26/74)	5:47	565	239.92	4.64			6	2.74
65	*KURIL	Z1(05/27/74)	4:41	47	311.73	6.98			7	3.67
66	*USSR	Z2(05/31/74)	3:28	1	353.71	4.95			6	3.44
67	*PERU	Z2(06/09/74)	14:16	50	143.75	7.05			5	4.63
68	*JAPAN	Z2(07/08/74)	5:45	35	307.87	5.69			6	3.76
69	*COLMB	Z3(07/13/74)	1:18	12	131.70	7.65			6	5.23
70	*COLMB	Z2(07/14/74)	2:13	15	131.68	7.97			7	4.53
71	*TONGA	Z3(07/18/74)	11: 4	33	239.85	5.22			5	5.31
72	*MEXCO	Z2(07/18/74)	19:21	48	155.08	8.90			6	5.24
73	*KURIL	Z1(07/29/74)	7:16	33	309.17	6.65			9	4.25
74	*PERU	T1(12/05/74)	11:57	162	138.26	6.71			12	3.66
75	*CHILE	P1(12/13/74)	13:23	118	139.46	5.85			12	3.27
76	*GREECE	T1(12/14/74)	2:36	33	36.16	4.87			8	4.27
77	*FIGI	P1(12/20/74)	2:40	374	242.44	4.90			12	3.45
78	*KURIL	P1(12/20/74)	16:38	416	314.00	6.54			9	3.05
79	*SAMOA	P1(12/23/74)	1: 4	33	242.05	5.12			11	3.67
80	*ALEU	Z1(12/31/74)	4:37	228	305.62	7.88			12	1.47
81	*HAWAI	P1(12/31/74)	22:40	5	250.30	7.96			14	3.34
82	*MRANA	P1(01/02/75)	14:16	313	296.50	4.83			13	3.19
83	*TONGA	P1(01/02/75)	17:14	33	239.80	5.21			9	3.50
84	*CHILE	P1(01/02/75)	21:35	108	146.61	4.90			13	2.50
85	*FIGI	T1(01/03/75)	0:30	572	240.37	4.66			6	2.33
86	*ALEU	T1(02/09/75)	11: 1	14	307.80	7.79			8	3.22
87	*BOLIV	Z1(02/11/75)	21:56	562	135.09	5.34			6	2.44
88	*FKSSR	Z1(02/20/75)	5:32	1	354.25	4.93			8	3.05
89	*ALEU	Z1(02/22/75)	8:36	48	304.24	7.95			19	3.78
90	*FIGI	Z5(02/22/75)	22: 4	375	237.64	4.59			17	4.95
91	*ALEU	Z2(02/23/75)	1:16	55	304.00	7.95			11	3.65
92	*CHILE	Z1(02/23/75)	3:53	33	142.42	5.77			13	3.82
93	*CHILE	Z1(02/26/75)	20:14	82	139.71	5.81			13	3.35
94	*FIGI	Z1(02/27/75)	18:42	586	241.99	4.70			19	2.86
95	*PERU	Z2(03/18/75)	17:21	98	138.70	7.00			10	4.58
96	*ALEU	Z1(03/20/75)	7:30	57	304.16	7.92			11	3.04
97	*CH-BL	P1(03/25/75)	2:21	60	140.08	5.66			8	4.15
98	*TURKY	P2(03/27/75)	5:15	5	31.54	4.85			9	4.07
99	*GREECE	Z1(04/04/75)	5:16	53	35.54	4.82			7	3.57
100	*JAPAN	Z1(04/08/75)	6:27	46	308.56	5.77			10	3.45
101	*ALEU	Z1(04/08/75)	20:32	33	301.57	8.51			9	2.92
102	*FIJI	Z1(04/11/75)	11:42	571	242.26	4.71			14	2.72
103	*PERU	Z1(04/12/75)	15:33	81	140.05	6.27			12	3.33
104	*MAYEN	Z1(04/16/75)	1:27	13	23.66	7.47			15	3.84
105	*KURIL	Z1(04/16/75)	21:33	32	310.49	6.80			15	4.22
106	*MEXCO	Z1(04/23/75)	11:14	11	156.76	8.89			15	4.72
107	*TURKY	Z1(04/30/75)	4:28	66	30.23	4.63			15	3.24
108	*ALEU	Z1(04/30/75)	7: 8	48	304.48	7.91			15	2.77
109	*ARGEN	Z1(05/01/75)	6: 7	168	141.74	5.13			17	2.86
110	*CHILE	P1(05/10/75)	14:27	6	151.36	4.73			14	3.24
111	*KURIL	Z1(05/19/75)	22:42	57	310.65	6.92			10	3.73
112	*N ATL	Z1(05/26/75)	20:19	33	60.95	6.34			16	3.13
113	*FIJI	Z1(5/29/75)	6:42	616	240.25	4.59			7	3.00
114	*FIGI	Z4(08/10/74)	9:47	595	242.14	4.67			6	3.20
115	*CH-BOL	Z2(08/10/74)	9:49	116	139.53	5.70			6	4.31
116	*FIGI	P1(08/10/74)	11:22	602	240.01	4.62			6	2.48
117	*FIGI	Z1(08/12/74)	2:52	70	243.78	4.84			5	6.77
118	*ALEU	Z1(08/13/74)	3:46	52	303.88	8.01			8	2.96
119	*FIGI	P3(08/13/74)	12:52	55	243.96	4.85			5	6.50
120	*ALEU	Z2(08/14/74)	5:34	56	304.01	8.01			9	4.21
121	*JAPAN	Z1(08/14/74)	6:49	41	310.31	6.01			5	3.01
122	*ARG	Z2(08/14/74)	17:56	132	145.72	4.88			7	3.35
123	*MARIAN	P1(08/15/74)	0:26	51	291.07	4.78			5	4.23
	ONLY 4 READINGS FOR	*CHILE	Z2(08/15/74)	18:27	96	148.30	4.79			
124	*ALEU	Z1(08/16/74)	9:41	46	303.85	8.02			7	3.26
125	*CHILE	P1(08/20/74)	21:37	93	143.69	5.21			6	3.34
126	*CHILE	Z1(08/23/74)	12: 0	102	142.31	5.40			7	3.17
127	*COLUM	Z2(08/24/74)	2:47	84	133.50	7.55			7	4.73
128	*CHILE	P1(08/24/74)	4:16	109	140.62	5.58			7	3.48
129	*ALEU	T1(08/24/74)	10:41	41	302.78	8.42			8	3.05
130	*JAPAN	Z2(08/25/74)	1:18	33	303.97	8.50			8	3.66
131	*JAPAN	Z1(08/25/74)	9:55	81	303.37	5.47			6	3.41
132	*MEXCO	Z2(08/26/74)	6:27	33	143.47	8.72			7	4.09
133	*ARGEN	Z2(08/27/74)	15:20	147	141.66	5.13			5	2.94
						6.75			10	3.51

	ONLY 4 READINGS FOR *CHILE	F1(09/06/74)	14: 5	106	140.36	5.51				
	ONLY 4 READINGS FOR *CARIB	F1(09/07/74)	19:40	58	108.30	7.44				
139	*CHILE	Z1(09/11/74)	1:21	113	139.47	5.84			5	3.66
140	*KAMCH	Z1(09/13/74)	7:53	55	314.72	7.31			6	3.76
141	*ARGEN	Z1(09/16/74)	0:38	280	138.65	5.32			5	2.61
142	*KURIL	Z1(09/16/74)	21:55	48	311.08	6.89			5	3.50
143	*HOKK	T2(09/20/74)	0:53	51	310.44	6.19			5	3.90
144	*KAMCH	Z1(09/21/74)	15:54	118	313.03	7.02			5	3.77
	ONLY 4 READINGS FOR *PERU	T1(10/02/74)	2:54	5	144.09	7.07				
145	*JAPAN	Z1(10/07/74)	9:53	325	313.98	6.17			6	2.80
146	*KURIL	Z1(10/09/74)	7:32	49	309.48	6.46			7	3.66
147	*KAMCH	Z1(10/21/74)	12:49	33	313.76	7.21			6	3.39
	ONLY 4 READINGS FOR *JAPAN	Z1(10/27/74)	2:29	223	311.96	6.25				
148	*SOLMN	Z2(07/20/75)	14:37	49	268.03	4.56			5	3.28
149	*SOLOM	T1(07/21/75)	2:39	95	267.71	4.56			5	3.36
150	*FIJI	Z1(07/24/75)	19: 1	579	239.06	4.59			7	2.59
	ONLY 4 READINGS FOR *ALASK	Z2(07/25/75)	10:40	17	306.38	8.73				
151	*MRIAN	P1(08/01/75)	14:41	193	292.32	4.83			5	3.51
152	*ALASK	Z1(08/02/75)	10:18	33	303.41	8.70			17	3.69
153	*GUL*	Z1(08/02/75)	17:15	33	175.17	10.77			10	4.13
154	*JAPAN	Z1(8/ 6/75)	21:37	230	314.49	5.92			9	2.89
155	*ARGEN	Z1(08/10/75)	10:25	166	138.80	5.50			15	3.55
156	*PERU	Z1(8/11/75)	10:39	74	143.22	6.60			9	4.05
157	*JAPAN	P2(08/12/75)	14:21	391	306.95	5.14			9	3.63
158	*PERU	T1(08/16/75)	0:53	123	138.31	6.90			11	3.63
159	*FIJI	Z1(08/16/75)	7:24	631	240.03	4.62			6	2.97
160	*JAPAN	Z2(08/22/75)	19:36	399	306.16	5.13			7	3.58
161	*N/SSR	Z1(08/23/75)	8:59	1	4.67	6.75			14	3.68
162	*KAMCH	T1(08/23/75)	13:51	141	314.72	7.19			6	2.90
163	*CHILE	T1(09/25/75)	21:42	119	139.22	5.83			9	3.11
164	*CHILE	Z2(08/26/75)	0:34	79	139.81	5.70			5	3.63
	ONLY 4 READINGS FOR *FIJI	Z1(08/26/75)	12:19	114	237.00	4.65				
165	*JAPAN	Z2(9/ 2/75)	10:23	26	304.27	5.26			6	4.29
	ONLY 4 READINGS FOR *ARGEN	T1(9/ 5/75)	19:10	193	139.57	5.38				
	ONLY 4 READINGS FOR *FIJI	Z2(9/13/75)	11:14	619	240.12	4.63				
166	*KAMCH	Z2(09/24/75)	17:54	94	314.67	7.20			5	3.27
167	*PERU	Z1(9/30/75)	3:50	135	139.58	6.64			10	3.37
168	*M ATL	Z1(10/ 7/75)	8:28	33	93.80	4.98			12	4.50
169	*CHILE	Z1(10/10/75)	13:13	96	141.52	5.42			11	3.20
170	*SOLOM	Z2(11/ 8/75)	11: 0	77	257.33	4.62			15	3.67
171	*KURIL	Z1(11/11/75)	4:25	355	313.42	6.27			18	2.76

OBSERVATION MATRIX

0	0	0	0	0	0	0	0	0	0	0
0	0	0	0	0	0	0	0	0	0	0
0	0	0	147	0	25	0	78	58	0	0
0	0	66	107	3	17	0	0	4	0	0
0	0	54	195	132	64	3	9	0	0	0
0	0	24	9	127	35	54	6	11	0	0
0	0	1	0	10	0	33	40	0	0	0
0	0	26	8	0	35	0	1	0	0	0
0	0	0	0	0	0	0	0	0	0	0
0	0	0	0	0	0	0	0	0	0	0

0	0	0	0	0	0	0	0	0	0	0
0	0	0	0	0	0	0	0	0	0	0
0	0	0	1	0	0	0	0	0	0	0
0	0	1	87	25	18	0	14	75	2	0
0	0	39	126	73	37	17	1	41	7	0
0	0	1	131	163	37	21	3	3	0	0
0	0	11	12	67	64	49	26	11	1	0
0	0	1	12	23	41	7	38	7	0	0
0	0	8	23	0	18	11	20	3	0	0
0	0	0	1	0	0	5	0	0	0	0
0	0	0	0	0	0	0	0	0	0	0

0	0	0	0	0	0	0	0	0	
0	0	34	10	1	2	5	5	0	
0	11	102	22	20	3	50	6	0	
0	3	123	107	87	27	22	47	0	
0	5	47	168	118	21	14	5	0	
0	3	12	58	48	72	22	11	0	
0	1	10	5	14	11	21	3	0	
0	0	0	9	1	13	3	0	0	
0	0	0	0	0	0	0	0	0	

0	0	0	0	0	0	0	0	0	0	0
0	1	27	4	6	4	3	4	1	0	0
0	11	56	24	23	21	37	3	5	0	0
0	14	106	81	51	15	24	1	2	0	0
0	4	37	82	69	37	25	2	43	1	0
0	3	31	49	104	92	14	8	6	0	0
0	1	11	26	24	48	31	17	8	0	0
0	1	5	3	13	4	9	18	2	0	0
0	0	0	0	7	4	12	3	1	0	0
0	0	0	0	0	1	1	1	0	0	0

***** YELLOWSTONE - YP DATA O(A,B,C) *****

NO OF STATIONS= 26
NO OF EVENTS=~~171~~ 153
NO OF OBSERVATIONS= 1382

TOTAL BLOCKS IN MODEL= 454
NO OF BLOCKS OBSERVED= 186

Table 4.3d

Layer 1

*	3.94	*	-0.28	*	8.34	*
1.07	-0.98	1.49	-1.30	*	*	4.44
4.61	5.27	9.16	-1.74	-0.31	-6.22	*
0.85	0.18	-11.26	-12.27	-11.03	0.72	2.96
0.13	*	-8.54	*	-1.34	4.18	*
-1.67	1.50	*	1.34	*	0.70	*

Table 4.3e
Layer 2

*	-0.22	*	*	*	*	*	*
0.79	3.75	4.32	0.56	*	3.18	2.60	1.65
3.31	0.54	2.95	-0.40	-1.54	-0.27	2.04	8.52
-0.96	-1.04	-3.54	-1.63	-2.96	-3.76	-3.49	
2.66	-0.85	-4.33	-2.47	-1.64	-3.01	-0.12	-0.29
0.07	-0.65	-3.31	-5.16	0.28	-0.38	3.68	*
1.20	-0.99	*	1.25	-1.14	-0.71	0.91	*

Table 4.3f
Layer 3

*	2.12	1.06	0.18	1.54	0.53	2.33
3.26	0.80	0.50	1.22	0.74	1.90	1.94
-0.06	1.44	-1.52	-4.79	-4.00	-0.58	5.67
0.15	-1.94	-2.46	-4.71	-2.52	2.79	4.06
0.46	-1.52	-0.88	-5.14	-5.01	-0.69	1.24
0.64	0.48	-0.58	0.81	-3.29	-0.33	1.18
*	*	1.28	-0.40	1.31	0.72	*

Table 4.3g

Layer 4

1.08	2.58	1.46	-0.40	1.52	0.70	2.32	0.02	*
1.66	4.96	2.22	0.82	2.86	3.05	-2.21	0.99	*
1.27	1.89	0.82	1.12	0.69	-0.76	0.03	0.78	*
1.42	-1.55	-3.64	-4.50	-7.82	-4.53	-0.61	-1.07	2.05
-0.90	-2.60	-5.40	-3.92	-4.21	1.97	1.76	2.80	*
0.09	-2.52	-3.75	-2.20	0.12	-0.22	0.18	3.81	*
0.64	2.69	-0.03	2.52	-3.30	-1.22	-0.47	1.94	*
*	*	*	0.93	-0.12	1.34	0.23	-0.76	*
*	*	*	*	-0.40	0.73	1.01	*	*

Table 4.3h

Layer 1

*	0.76	0.00	0.59	0.00	0.53	0.55
0.79	0.84	0.37	0.41	0.00	0.00	0.27
0.79	0.87	0.86	0.80	0.35	0.53	0.00
0.64	0.55	0.81	0.78	0.77	0.44	0.42
0.15	0.00	0.43	0.00	0.68	0.67	0.00
0.59	0.38	0.00	0.59	0.00	0.12	0.00

Table 4.3i

Layer 2

*	0.17	*	*	*	*	*	*
0.12	0.68	0.60	0.42	*	0.36	0.55	0.20
0.66	0.82	0.80	0.71	0.42	0.15	0.51	0.40
0.12	0.83	0.84	0.72	0.68	0.26	0.27	*
0.42	0.62	0.75	0.81	0.73	0.63	0.50	0.12
0.11	0.51	0.48	0.65	0.49	0.65	0.39	*
0.36	0.50	*	0.46	0.45	0.39	0.17	*
*	0.14	*	*	0.33	*	*	*

Table 4.3j

Layer 3

*	0.62	0.47	0.19	0.30	0.44	0.37
0.50	0.83	0.75	0.64	0.45	0.66	0.37
0.43	0.85	0.87	0.84	0.71	0.51	0.57
0.41	0.76	0.89	0.88	0.77	0.65	0.51
0.38	0.61	0.81	0.80	0.83	0.58	0.47
0.20	0.47	0.57	0.64	0.69	0.54	0.30
*	*	0.49	0.24	0.45	0.38	*

Table 4.3k

Layer 4

0.22	0.64	0.38	0.43	0.46	0.35	0.35	0.22	*
0.51	0.82	0.78	0.72	0.67	0.61	0.32	0.36	*
0.71	0.87	0.84	0.84	0.73	0.57	0.18	0.32	*
0.34	0.84	0.87	0.88	0.84	0.75	0.35	0.64	0.21
0.39	0.77	0.84	0.89	0.89	0.72	0.57	0.57	*
0.19	0.63	0.66	0.82	0.82	0.78	0.71	0.40	*
0.20	0.42	0.50	0.70	0.41	0.62	0.44	0.27	*
*	*	*	0.49	0.55	0.57	0.43	0.22	*
*	*	*	*	0.24	0.25	0.25	*	*

Table 4.31

Layer 1

*	0.55	*	0.74	*	0.54	0.56
0.57	0.50	0.89	0.67	*	*	0.64
0.61	0.42	0.49	0.60	0.86	0.78	*
0.70	0.85	0.54	0.68	0.61	0.82	0.71
0.64	*	0.74	*	0.73	0.69	*
0.65	0.74	*	0.57	*	0.45	*

Table 4.3m

Layer 2

*	0.69	*	*	*	*	*	*
0.49	0.70	0.78	0.73	*	0.57	0.57	0.67
0.73	0.55	0.60	0.72	0.70	0.63	0.62	0.72
0.51	0.54	0.53	0.72	0.75	0.71	0.71	*
0.76	0.83	0.67	0.61	0.68	0.77	0.79	0.56
0.47	0.80	0.77	0.72	0.85	0.72	0.80	*
0.71	0.69	*	0.68	0.76	0.64	0.44	*
*	0.63	*	*	0.73	*	*	*

Table 4.3n

Layer 3

*	0.72	0.63	0.69	0.71	0.73	0.61
0.67	0.53	0.70	0.71	0.84	0.60	0.59
0.87	0.51	0.48	0.53	0.70	0.68	0.62
0.67	0.67	0.44	0.47	0.69	0.73	0.75
0.71	0.75	0.58	0.62	0.54	0.72	0.68
0.62	0.72	0.82	0.72	0.74	0.72	0.58
*	*	0.73	0.62	0.64	0.66	*

Table 4.3o
Layer 4

0.67	0.74	0.75	0.70	0.77	0.80	0.69	0.72	*
0.69	0.56	0.66	0.72	0.65	0.62	0.74	0.67	*
0.76	0.48	0.49	0.59	0.75	0.72	0.66	0.78	*
0.65	0.61	0.50	0.50	0.59	0.72	0.86	0.70	0.75
0.75	0.68	0.58	0.47	0.48	0.76	0.82	0.80	*
0.62	0.77	0.76	0.64	0.61	0.65	0.71	0.70	*
0.62	0.80	0.89	0.75	0.80	0.80	0.62	0.70	*
*	*	*	0.76	0.85	0.76	0.81	0.70	*
*	*	*	*	0.62	0.75	0.65	*	*

TABLE 4.4.

Three-Dimensional Inversion

of Yellowstone Residuals - Model YP4-190

4.4a	Initial Model and Station Data
4.4b	Observation Matrix - Number of "Hits" Per Block
4.4c	Inversion Parameters - Solution for Layer 1
4.4d	Inversion Parameters - Solution for Layer 2
4.4e	Inversion Parameters - Solution for Layer 3
4.4f	Inversion Parameters - Solution for Layer 4
4.4g	Diagonal of Resolution Matrix for Layer 1
4.4h	Diagonal of Resolution Matrix for Layer 2
4.4i	Diagonal of Resolution Matrix for Layer 3
4.4j	Diagonal of Resolution Matrix for Layer 4
4.4k	Standard Errors of Solution - Layer 1
4.4l	Standard Errors of Solution - Layer 2
4.4m	Standard Errors of Solution - Layer 3
4.4n	Standard Errors of Solution - Layer 4

***** PROGRAM 3-C *****

22 NOVEMBER 1975

YELLOWSTONE - YP DATA 0(A,B,C)

LATITUDE	LONGITUDE	THA	V0	JPWT	IRES	IFUNCH	IFRINT	THETA	RESL
44N36.17	110W38.38	0.0	6.00	0	1	1	0	100.	0.100

	VELOCITY	THICKNESS	#-NORTH	LENGTH	#-EAST	LENGTH	COORDINATE	DISPLACEMENT
1	6.20	40.00	9	25.00	9	25.00	0.0	0.0
2	7.90	50.00	10	30.00	10	30.00	0.0	0.0
3	7.95	50.00	11	30.00	11	30.00	0.0	0.0
4	8.00	50.00	12	30.00	12	30.00	0.0	0.0

STA	LATITUDE	LONGITUDE	ELEVATION	RELATIVE COORDINATES	
1YPBR	45N 1.73	111W 7.01	2199.	47.45	-37.61
2YPCJ	44N44.63	110W29.65	2426.	15.68	11.26
3YPFC	44N42.57	111W14.38	2025.	12.03	-47.55
4YPFE	44N29.43	110W 0.06	2134.	-12.29	50.80
5YPGC	44N47.77	111W 6.39	2075.	21.59	-36.54
6YPHB	44N45.06	111W11.72	2157.	16.61	-44.00
7YPHR	44N51.14	111W18.96	2060.	27.95	-53.47
8YPLK	44N34.18	110W23.18	2391.	-3.65	20.12
9YPMC	44N45.56	111W 0.36	2073.	17.46	-29.01
10YPMF	44N 8.60	111W17.29	1788.	-50.86	-51.89
11YPMH	44N58.62	110W41.12	1781.	41.58	-3.60
12YPMJ	44N38.90	110W51.52	2111.	5.08	-17.37
13YPPL	44N36.17	110W38.38	2518.	0.0	0.0
14YPRV	44N37.63	110W26.75	2400.	2.72	15.39
15YPND	44N31.48	110W27.55	2405.	-8.67	14.35
16YPNJ	44N43.82	110W41.58	2290.	14.17	-4.23
17YPOF	44N27.15	110W50.48	2260.	-16.69	-16.05
18YPPC	44N36.90	110W11.56	2932.	5.15	35.44
19YPPR	44N23.55	110W17.19	2390.	-23.31	28.14
20YPSE	44N 8.18	110W40.00	2073.	-51.84	-2.16
21YPSG	45N 0.18	109W59.25	2270.	44.68	51.42
22YPTB	44N31.50	110W50.76	2224.	-8.63	-16.40
23YPTC	44N17.79	110W13.92	2360.	-33.56	32.54
24YPTS	44N27.74	111W21.15	1923.	-15.37	-56.73
25YPWT	44N24.87	110W34.27	2365.	-20.93	5.46
26YPWY	44N36.36	111W 6.81	2294.	0.45	-36.29

OBSERVATION MATRIX

0	0	0	0	0	0	0	0	0			
0	0	0	0	0	0	0	0	0			
0	0	89	54	25	0	132	0	0			
0	1	246	108	50	0	8	0	0			
0	4	94	173	89	22	12	0	0			
0	1	16	45	46	62	14	0	0			
0	0	34	0	35	20	3	0	0			
0	0	0	0	0	0	0	0	0			
0	0	0	0	0	0	0	0	0			
0	0	0	0	0	0	0	0	0	0		
0	0	0	0	0	0	0	0	0	0		
0	0	31	32	11	31	20	5	0	0		
0	0	98	119	56	4	33	2	0	0		
0	1	73	146	127	33	9	47	0	0		
0	1	9	109	114	80	23	3	0	0		
0	0	12	21	27	29	27	7	0	0		
0	0	5	10	8	13	4	0	0	0		
0	0	0	0	0	1	1	0	0	0		
0	0	0	0	0	0	0	0	0	0		
0	0	0	0	0	0	0	0	0	0	0	
0	0	1	0	0	2	0	0	0	0	0	
0	2	38	23	21	43	3	11	1	0	0	
0	24	97	62	32	22	9	0	2	0	0	
0	2	42	94	49	26	28	4	2	0	0	
0	3	50	77	38	80	19	8	40	0	0	
0	1	12	36	53	94	42	16	6	0	0	
0	1	5	0	23	34	22	27	6	0	0	
0	0	0	1	10	4	19	2	3	0	0	
0	0	0	0	2	2	2	2	0	0	0	
0	0	0	0	0	1	1	0	0	0	0	
0	0	0	0	0	0	0	0	0	0	0	0
0	3	1	0	5	2	2	4	0	1	0	0
1	19	27	10	31	36	8	4	4	0	0	0
0	44	113	29	19	30	14	2	1	0	1	0
1	3	44	62	23	11	11	7	3	2	0	0
0	3	24	45	34	18	18	3	1	4	0	0
0	3	45	59	15	23	44	19	14	28	4	0
1	0	7	23	9	34	83	31	11	2	2	0
1	0	6	1	7	16	32	29	32	8	0	0
0	0	0	0	0	9	14	18	2	2	0	0
0	0	0	0	0	2	1	3	4	1	0	0
0	0	0	0	1	3	1	1	0	0	0	0

***** YELLOWSTONE - YP DATA Q(A,B,C) *****

NO OF STATIONS= 26
NO OF EVENTS=171
NO OF OBSERVATIONS= 1382

Table 4.4c

Layer 1

*	4.16	2.35	-0.72	*	5.56
0.35	1.15	0.56	-2.62	*	5.70
1.36	1.26	0.09	-3.05	-7.73	-1.39
0.23	-1.13	-7.45	-9.01	-0.01	3.76
*	1.13	*	3.72	1.23	0.46

Table 4.4d

Layer 2

*	1.83	2.23	1.73	1.73	2.07	0.58
*	1.61	0.04	-0.53	0.14	-0.38	0.90
1.18	2.73	-2.06	-4.75	-2.04	-0.16	3.32
0.24	1.28	-2.79	-2.87	-0.97	-0.04	0.04
*	0.87	-0.92	-2.24	-2.47	-0.14	1.66
*	0.13	0.15	-1.17	-0.49	-0.86	*
*	*	*	*	0.19	0.17	*

Table 4.4e

Layer 3

*	0.11	*	*	0.17	*	*	*
1.40	2.21	1.33	0.93	1.61	2.02	0.73	0.26
4.47	2.45	0.76	0.86	2.21	1.67	*	0.55
1.19	0.88	-0.93	-0.17	-1.79	0.77	-0.42	-1.00
0.20	-2.44	-2.70	-0.74	-1.40	-2.31	0.45	-1.22
0.24	-1.57	-2.62	-2.91	-0.60	-0.58	-0.55	-0.64
0.18	-0.23	*	-0.79	0.13	-0.12	-0.41	1.17
*	*	-0.12	0.49	-1.07	-1.73	0.56	0.46
*	*	*	1.19	-0.25	-2.22	-0.60	*
*	*	*	*	0.22	0.17	*	*

Table 4.4f

Layer 4

1.07	0.31	*	0.96	*	0.38	1.75	*	0.26	*
0.72	2.71	3.20	085	0.75	2.25	-0.92	0.31	*	*
-0.26	2.36	3.80	2.71	0.98	1.38	0.93	0.39	*	0.16
0.29	-1.89	-1.02	-0.71	-1.39	0.81	1.64	-0.35	-1.00	*
-1.11	-1.25	-1.57	-3.38	-3.33	-4.21	0.63	-0.06	-0.54	*
-1.65	-3.15	1.02	-0.29	-1.77	0.19	-2.77	-1.46	-1.14	3.56
*	0.43	0.40	-2.29	1.70	-1.17	-3.25	0.86	-0.74	0.61
*	-0.35	1.80	1.00	0.49	-1.72	-0.94	-1.72	0.22	*
*	*	*	*	-0.82	0.23	-0.32	1.84	1.03	*
*	*	*	*	0.35	-1.10	0.69	0.91	-0.57	*
*	*	*	-0.57	1.40	0.28	0.19	*	*	*

Table 4.4g
Layer 1

*	0.84	0.84	0.78	*	0.76
0.22	0.90	0.91	0.87	*	0.55
0.36	0.89	0.91	0.89	0.82	0.71
0.15	0.66	0.83	0.82	0.86	0.67
*	0.76	*	0.80	0.71	0.26

Table 4.4h
Layer 2

*	0.69	0.76	0.68	0.70	0.69	0.38
*	0.83	0.88	0.86	0.57	0.66	0.32
0.21	0.82	0.90	0.89	0.82	0.66	0.68
0.17	0.65	0.87	0.88	0.85	0.79	0.39
*	0.63	0.79	0.82	0.78	0.62	0.41
*	0.42	0.53	0.56	0.58	0.41	*
*	*	*	*	0.22	0.27	*

Table 4.4i

Layer 3

*	0.29	*	*	0.41	*	*	*
0.45	0.73	0.78	0.79	0.77	0.45	0.51	0.21
0.77	0.84	0.85	0.83	0.79	0.64	*	0.34
0.35	0.82	0.87	0.85	0.82	0.74	0.42	0.28
0.48	0.77	0.83	0.85	0.85	0.70	0.60	0.62
0.17	0.62	0.72	0.82	0.85	0.78	0.64	0.50
0.21	0.34	*	0.74	0.80	0.76	0.61	0.31
*	*	0.23	0.62	0.51	0.60	0.41	0.30
*	*	*	0.43	0.48	0.43	0.33	*
*	*	*	*	0.34	0.27	*	*

Table 4.4j

Layer 4

0.44	0.32	*	0.60	0.39	0.38	0.43	*	0.20	*
0.74	0.76	0.68	0.82	0.81	0.66	0.48	0.32	*	*
0.79	0.87	0.83	0.76	0.84	0.74	0.42	0.23	*	0.20
0.37	0.84	0.87	0.82	0.75	0.68	0.65	0.38	0.28	*
0.48	0.80	0.86	0.86	0.78	0.75	0.46	0.23	0.49	*
0.48	0.79	0.80	0.72	0.81	0.83	0.77	0.70	0.68	0.51
*	0.56	0.67	0.64	0.78	0.85	0.83	0.57	0.34	0.36
*	0.43	0.29	0.44	0.72	0.81	0.82	0.74	0.50	*
*	*	*	*	0.57	0.74	0.72	0.43	0.28	*
*	*	*	*	0.51	0.26	0.46	0.48	0.22	*
*	*	*	0.34	0.54	0.33	0.22	*	*	*

Table 4.4k

Layer 1

*	0.48	0.50	0.63	*	0.43
0.59	0.34	0.33	0.48	*	0.68
0.55	0.39	0.33	0.41	0.58	0.69
0.40	0.71	0.54	0.56	0.46	0.66
*	0.55	*	0.54	0.68	0.43

Table 4.41
Layer 2

*	0.64	0.59	0.72	0.69	0.59	0.55
*	0.52	0.42	0.50	0.83	0.63	0.68
0.52	0.54	0.37	0.42	0.57	0.72	0.58
0.42	0.74	0.45	0.42	0.49	0.60	0.74
*	0.71	0.61	0.56	0.60	0.68	0.63
*	0.67	0.68	0.67	0.69	0.60	*
*	*	*	*	0.55	0.57	*

Table 4.4m
Layer 3

*	0.76	*	*	0.80	*	*	*
0.83	0.64	0.63	0.61	0.61	0.84	0.61	0.54
0.63	0.50	0.51	0.57	0.62	0.74	*	0.66
0.73	0.58	0.48	0.53	0.58	0.64	0.63	0.58
0.77	0.62	0.51	0.52	0.51	0.71	0.74	0.59
0.42	0.70	0.66	0.55	0.49	0.60	0.65	0.67
0.56	0.57	*	0.61	0.59	0.62	0.67	0.54
*	*	0.62	0.71	0.79	0.63	0.78	0.46
*	*	*	0.75	0.77	0.71	0.69	*
*	*	*	*	0.73	0.57	*	*

Table 4.4n

Layer 4

0.78	0.81	*	0.79	0.83	0.80	0.73	*	0.54	*
0.64	0.63	0.77	0.56	0.57	0.77	0.78	0.56	*	*
0.60	0.44	0.58	0.70	0.55	0.69	0.85	0.64	*	0.58
0.65	0.55	0.50	0.61	0.72	0.76	0.78	0.67	0.58	*
0.80	0.60	0.51	0.54	0.67	0.71	0.84	0.68	0.78	*
0.82	0.60	0.57	0.71	0.62	0.57	0.67	0.68	0.64	0.77
*	0.77	0.72	0.77	0.64	0.49	0.56	0.74	0.79	0.75
*	0.58	0.78	0.71	0.69	0.59	0.58	0.65	0.66	*
*	*	*	*	0.75	0.67	0.66	0.84	0.59	*
*	*	*	*	0.83	0.70	0.79	0.66	0.59	*
*	*	*	0.74	0.76	0.73	0.55	*	*	*

TABLE 4.5.

Three-Dimensional Inversion of

Yellowstone Residuals - Deep Model

***** PROGRAM 3-D *****

22 NOVEMBER 1975

YELLOWSTONE - PL DATA Q(A,B,C) - REGIONAL

LATITUDE	LONGITUDE	THA	V0	JPWT	IRES	IPUNCH	IPRINT	THETA	RESL
45N25.88	111W20.10	42.0	6.00	0	1	1	0	75.	0.100

	VELOCITY	THICKNESS	#-NORTH	LENGTH	#-EAST	LENGTH	COORDINATE	DISPLACEMENT
1	6.20	40.00	9	40.00	5	40.00	0.000	0.000
2	7.90	50.00	8	50.00	4	50.00	0.000	0.000
3	8.30	50.00	9	50.00	5	50.00	0.000	0.000
4	8.10	50.00	10	50.00	6	50.00	0.000	0.000
5	8.40	50.00	11	50.00	6	50.00	0.000	0.000
6	8.60	50.00	11	50.00	6	50.00	0.000	0.000

STA	LATITUDE	LONGITUDE	ELEVATION	RELATIVE COORDINATES	
1YPBB	45N 1.73	111W 7.01	2199.	-44.68	-17.12
2YPCJ	44N44.63	110W29.85	2426.	-100.80	-1.60
3YPDC	44N42.57	111W14.38	2025.	-64.60	-48.01
4YPEE	44N29.43	110W 0.06	2134.	-147.89	9.47
5YPGC	44N47.77	111W 6.39	2075.	-64.47	-33.74
6YPHB	44N45.06	111W11.72	2157.	-63.51	-42.32
7YPHR	44N51.14	111W18.96	2060.	-48.77	-41.89
8YPLK	44N34.18	110W23.18	2391.	-121.13	-7.77
9YPMC	44N45.56	111W 0.36	2073.	-72.81	-30.54
10YPMF	44N 9.60	111W17.29	1788.	-108.75	-92.89
11YPMH	44N58.62	110W41.12	1781.	-71.58	4.43
12YPMJ	44N38.90	110W51.52	2111.	-89.77	-30.04
13YPML	44N35.17	110W38.38	2518.	-105.07	-20.40
14YPMV	44N37.63	110W26.75	2400.	-113.22	-7.09
15YPNB	44N31.48	110W27.55	2405.	-121.05	-15.41
16YPNJ	44N43.82	110W41.58	2290.	-91.67	-14.18
17YPQF	44N27.15	110W50.48	2260.	-106.92	-43.46
18YPRC	44N39.90	110W11.58	2932.	-124.67	9.52
19YPPR	44N23.55	110W17.19	2390.	-141.14	-14.79
20YPSE	44N 8.18	110W40.00	2073.	-142.41	-56.34
21YPSG	45N 0.18	109W59.25	2270.	-105.69	47.64
22YPTB	44N31.50	110W50.76	2224.	-100.66	-38.39
23YPTC	44N17.79	110W13.92	2360.	-152.01	-18.55
24YPTS	44N27.74	111W21.15	1923.	-79.01	-73.01
25YPWT	44N24.87	110W34.27	2365.	-124.33	-30.18
26YPWY	44N30.36	111W 5.81	2294.	-80.70	-47.25
27 PL1	45N27.01	111W38.94	1625.	18.01	-16.80
28OPL2	45N41.82	111W59.51	1728.	59.00	-15.60
29 PL2	45N43.54	111W59.31	1811.	58.44	-15.76
30OPL3	46N 7.58	112W27.11	2048.	115.48	-12.05
31 PL3	46N 7.57	112W27.21	2073.	115.56	-12.15
32OPL4	46N26.55	112W53.10	1747.	163.90	-12.53
33 PL4	46N26.12	112W54.31	1868.	164.38	-14.21
34OPL5	45N45.59	112W52.28	1847.	107.84	-63.56
35 PL5	45N46.34	112W52.29	1817.	108.86	-62.62
36 PL6	46N29.35	111W51.02	1609.	113.82	49.30
37 PL7	45N11.63	111W15.63	2146.	-23.50	-13.29
38 PL8	45N18.32	111W59.75	1743.	24.40	-47.69
39 PL9	45N40.12	111W26.17	1500.	24.85	11.78
40PL10	45N36.22	112W21.82	1527.	68.24	-46.43
41PL11	45N56.90	111W49.64	1494.	68.26	10.15
42OL12	45N56.34	112W43.51	1926.	114.63	-41.69
43PL12	45N55.62	112W43.79	2012.	113.91	-42.86
44PL13	46N16.03	112W 9.83	1820.	111.92	14.88

OBSERVATION MATRIX

0	12	30	0	0	
16	24	40	28	0	
0	9	5	0	0	
0	24	27	0	0	
0	17	20	0	0	
0	41	40	0	0	
0	97	4	1	0	
0	29	0	36	0	
1	11	9	0	0	

0	21	19	0	
18	43	28	16	
6	28	15	0	
5	34	19	0	
9	31	16	0	
43	61	20	0	
11	28	19	17	
1	5	8	0	

0	3	0	1	0	
3	22	14	9	1	
19	31	28	10	15	
11	28	16	7	0	
8	21	16	6	0	
36	20	30	15	0	
17	24	56	5	14	
5	10	8	7	3	
0	0	0	1	0	

0	2	0	0	0	0
6	17	1	0	2	0
15	20	11	17	6	2
11	18	16	14	7	10
12	22	4	16	5	0
14	26	5	20	9	0
32	19	12	41	0	0
10	12	12	18	9	13
1	5	0	9	2	0
0	0	0	0	0	0

0	2	0	0	0	0
10	3	1	0	1	0
14	13	1	1	16	2
17	13	7	13	16	13
27	13	4	2	14	3
17	8	5	0	17	4
34	5	4	3	27	6
17	13	13	26	8	5
8	7	5	12	3	16
0	0	0	0	6	2
0	0	0	0	0	0

2	0	1	0	0	0

9	0	0	0	0	1
16	5	0	0	13	3
16	1	7	10	15	12
26	3	4	2	10	4
15	1	5	0	16	5
23	2	4	0	12	8
13	9	6	4	37	8
3	5	6	2	9	12

Table 4.5c

Layer 1

*	0.01	3.48	*	*
3.36	0.81	0.65	2.40	*
*	1.10	0.76	*	*
*	1.09	1.83	*	*
*	1.23	0.89	*	*
*	-1.98	0.11	*	*
*	-1.50	-4.69	1.30	*
*	-10.06	*	3.10	*
-1.00	-3.06	0.07	*	*

Table 4.5 d
Layer 2

*	1.87	0.13	*
2.64	1.63	-0.34	1.69
0.68	3.16	2.09	*
1.37	-0.03	2.72	*
-0.59	0.72	-2.12	*
-1.79	-3.66	-1.40	*
-4.73	-2.78	0.30	2.89
-1.61	-1.90	-1.23	*

Table 4.5e continued

Layer 3

*	1.22	*	0.99	*
1.14	1.75	1.37	1.30	1.84
1.04	0.29	0.96	1.31	0.12
0.59	0.18	0.30	-0.02	*
-0.20	*	2.78	-0.88	*
-0.12	0.85	-0.57	-3.14	*
-1.67	-0.97	0.20	-1.08	1.98
-3.85	-3.77	-0.62	-1.11	0.94
*	*	*	-0.83	*

Table 4.5f

Layer 4

*	0.90	*	*	*	*
-0.14	1.98	1.85	*	0.51	*
2.00	1.83	0.14	-0.00	1.70	1.20
3.02	1.11	0.02	-0.78	-0.49	0.53
-0.33	0.57	0.43	0.99	-1.93	*
1.03	1.27	0.23	-0.28	0.20	*
0.46	-1.19	0.10	-2.25	-2.21	*
-1.22	-2.29	-1.65	-0.85	1.49	-0.65
-1.62	-2.08	*	-1.61	0.03	*

Table 4.5g continued

Layer 5

*	0.80	*	*	*	*
0.58	-0.60	1.82	*	1.00	*
0.01	0.19	0.80	0.34	-0.17	0.80
-0.13	-0.77	1.51	0.02	-0.06	0.89
-0.35	0.90	1.69	*	-0.28	1.00
-0.56	2.13	1.75	*	-0.92	-1.76
-0.31	2.15	-1.08	1.53	0.16	-3.26
02.61	-2.48	-0.70	0.28	-0.85	-1.06
-2.89	1.90	-1.88	-2.96	-1.18	-3.77
*	*	*	*	0.28	0.04

Table 4.5h

Layer 6

-0.16	*	1.80	*	*	*
0.17	*	*	*	*	0.99
0.59	0.58	*	*	-0.58	0.20
0.58	-0.01	1.50	-0.57	-0.31	-0.63
-0.47	1.54	1.66	-1.07	1.63	0.26
0.01	0.42	1.71	*	-0.89	0.49
1.07	-0.74	-1.06	*	0.44	-2.38
0.27	-2.00	-0.17	2.96	0.58	0.06
-0.43	-0.01	-2.42	0.13	-0.03	-0.15
*	-0.18	*	-2.33	-0.04	0.86

Table 4.5i

Layer 1

0.0	0.51	0.62	0.0	0.0
0.59	0.63	0.66	0.55	0.0
0.0	0.57	0.52	0.0	0.0
0.0	0.64	0.68	0.0	0.0
0.0	0.60	0.57	0.0	0.0
0.0	0.70	0.69	0.0	0.0
0.0	0.74	0.54	0.18	0.0
0.0	0.67	0.0	0.57	0.0
0.25	0.49	0.27	0.0	0.0

Table 4.5j

Layer 2

0.0	0.49	0.48	0.0
0.55	0.72	0.58	0.37
0.48	0.76	0.51	0.0
0.42	0.72	0.51	0.0
0.61	0.69	0.63	0.0
0.72	0.77	0.71	0.0
0.56	0.69	0.64	0.39
0.23	0.53	0.42	0.0

Table 4.5k

Layer 3

0.0	0.38	0.0	0.16	0.0
0.44	0.66	0.62	0.54	0.21
0.69	0.75	0.74	0.58	0.39
0.57	0.72	0.50	0.55	0.0
0.64	0.71	0.49	0.53	0.0
0.76	0.74	0.68	0.64	0.0
0.70	0.74	0.75	0.51	0.39
0.49	0.45	0.36	0.57	0.43
0.0	0.0	0.0	0.26	0.0

Table 4.51

Layer 4

0.0	0.22	0.0	0.0	0.0	0.0
0.54	0.52	0.18	0.0	0.33	0.0
0.71	0.55	0.54	0.59	0.55	0.40
0.62	0.59	0.45	0.58	0.63	0.55
0.64	0.63	0.26	0.55	0.42	0.0
0.72	0.69	0.35	0.63	0.61	0.0
0.78	0.72	0.55	0.66	0.66	0.0
0.65	0.70	0.60	0.67	0.63	0.57
0.23	0.29	0.0	0.43	0.23	0.0
0.0	0.0	0.0	0.0	0.0	0.0

Table 4.5m

Layer 5

0.0	0.22	0.0	0.0	0.0	0.0
0.63	0.42	0.17	0.0	0.16	0.0
0.72	0.70	0.28	0.27	0.54	0.38
0.80	0.71	0.36	0.41	0.53	0.61
0.78	0.67	0.24	0.38	0.51	0.45
0.79	0.63	0.28	0.0	0.60	0.48
0.85	0.59	0.22	0.43	0.70	0.63
0.78	0.69	0.59	0.65	0.61	0.59
0.45	0.47	0.41	0.56	0.48	0.63
0.0	0.0	0.0	0.0	0.34	0.22
0.0	0.0	0.0	0.0	0.0	0.0

Table 4.5n

Layer 6

0.43	0.0	0.17	0.0	0.0	0.0
0.68	0.0	0.0	0.0	0.0	0.15
0.73	0.58	0.0	0.0	0.46	0.45
0.78	0.28	0.35	0.44	0.55	0.68
0.80	0.44	0.23	0.33	0.55	0.53
0.75	0.27	0.27	0.0	0.58	0.52
0.80	0.41	0.21	0.0	0.54	0.67
0.72	0.52	0.51	0.51	0.69	0.62
0.45	0.44	0.40	0.35	0.60	0.72
0.0	0.27	0.0	0.22	0.21	0.22
0.0	0.0	0.0	0.0	0.0	0.0

Table 4.5o

Layer 1

0.0	0.40	0.34	0.0	0.0
0.41	0.40	0.35	0.35	0.0
0.0	0.44	0.46	0.0	0.0
0.0	0.38	0.39	0.0	0.0
0.0	0.42	0.42	0.0	0.0
0.0	0.32	0.36	0.0	0.0
0.0	0.31	0.49	0.33	0.0
0.0	0.37	0.0	0.33	0.0
0.42	0.41	0.26	0.0	0.0

Table 4.5p

Layer 2

0.0	0.32	0.39	0.0
0.40	0.37	0.32	0.28
0.43	0.35	0.41	0.0
0.43	0.37	0.36	0.0
0.42	0.37	0.44	0.0
0.37	0.31	0.38	0.0
0.42	0.37	0.39	0.28
0.34	0.45	0.42	0.0

Table 4.5q

Layer 3

0.0	0.46	0.0	0.28	0.0
0.49	0.43	0.42	0.43	0.36
0.46	0.40	0.37	0.47	0.34
0.45	0.41	0.43	0.44	0.0
0.46	0.41	0.44	0.46	0.0
0.37	0.41	0.38	0.44	0.0
0.43	0.40	0.35	0.45	0.37
0.42	0.38	0.40	0.43	0.40
0.0	0.0	0.0	0.41	0.0

Table 4.5r

Layer 4

0.0	0.31	0.0	0.0	0.0	0.0
0.44	0.40	0.29	0.0	0.42	0.0
0.46	0.42	0.45	0.43	0.45	0.51
0.44	0.40	0.32	0.44	0.46	0.51
0.40	0.41	0.32	0.45	0.40	0.0
0.42	0.42	0.34	0.40	0.46	0.0
0.36	0.41	0.40	0.40	0.46	0.0
0.45	0.42	0.42	0.43	0.46	0.51
0.34	0.32	0.0	0.45	0.26	0.0
0.0	0.0	0.0	0.0	0.0	0.0

Table 4.5s

Layer 5

0.0	0.31	0.0	0.0	0.0	0.0
0.46	0.49	0.29	0.0	0.28	0.0
0.43	0.44	0.50	0.46	0.45	0.45
0.42	0.45	0.31	0.41	0.45	0.47
0.40	0.45	0.28	0.48	0.43	0.47
0.42	0.52	0.26	0.0	0.44	0.47
0.38	0.54	0.26	0.51	0.41	0.49
0.44	0.44	0.44	0.43	0.46	0.50
0.41	0.48	0.47	0.43	0.49	0.46
0.0	0.0	0.0	0.0	0.43	0.26
0.0	0.0	0.0	0.0	0.0	0.0

Table 4.5t

Layer 6

0.55	0.0	0.29	0.0	0.0	0.0
0.51	0.0	0.0	0.0	0.0	0.27
0.45	0.51	0.0	0.0	0.43	0.48
0.43	0.52	0.31	0.41	0.43	0.49
0.41	0.53	0.27	0.46	0.47	0.49
0.47	0.51	0.26	0.0	0.43	0.47
0.43	0.52	0.25	0.0	0.44	0.50
0.46	0.45	0.49	0.52	0.41	0.48
0.54	0.49	0.44	0.50	0.48	0.49
0.0	0.37	0.0	0.28	0.26	0.39
0.0	0.0	0.0	0.0	0.0	0.0

APPENDIX A. FORMULATION OF THREE-DIMENSIONAL INVERSION SCHEME AND SOME PROPERTIES OF THE SOLUTION

Although we have presented the major concepts of the inversion scheme in Chapter II, the following derivation is more detailed and is presented as a whole for better continuity. Because the notation is slightly different than that used in the main text, we start with some definitions.

Definitions:

t_{ij}^{obs} = observed P-wave arrival time at station i from event j.

O_j = true origin time of event j.

O_j^{JB} = origin time from ISC bulletin.

Δ_j^0 = $O_j - O_j^{JB}$, error in ISC origin time.

T_{ij}^{obs} = $t_{ij}^{obs} - O_j$, observed travel time.

T_{ij}^{JB} = theoretical travel time from ISC.

R_{ij} = $T_{ij}^{obs} - T_{ij}^{JB}$, residual travel time.

$\bar{R}_j = \frac{1}{n} \sum_{i=1}^{n} R_{ij}$, average residual over n stations for event j.

L_k = straight ray path distance in block k.

V_k = P-wave velocity in block k.

$T_k = \frac{L_k}{V_k}$, travel time in block k.

δV_k = perturbation of velocity from initial velocity in block k.

$D_k = \frac{-\delta V_k}{V_k}$, % perturbation in slowness $\left(\frac{1}{V_k}\right)$

The arrival time of a P-wave at station i from event j is expressed as

$$t_{ij}^{obs} = O_j + \int_s \frac{ds}{V(s)}$$

s = ray path. According to Fermat's principle, the ray path s is such as to make the travel time integral stationary (i.e., a small change in s causes only a second order change in the integral). Here, we know the position of the station exactly and we must assume we know the location of the event from the ISC bulletin. Then the travel time is a function of only the ray path and the velocity along the ray path, V(s). We write this as,

$$T_{ij}[V(s)] = \int_s \frac{ds}{V(s)} \quad .$$

In the previously defined notation:

$$t_{ij}^{obs} = O_j + T_{ij}$$

$$t_{ij}^{obs} - O_j^{JB} = O_j - O_j^{JB} + T_{ij}$$

or

$$T_{ij}^{obs} = \Delta_j^0 + T_{ij} \quad . \qquad \text{(A-1)}$$

T_{ij} is a nonlinear functional which we linearize by expanding in a Taylor's series about a starting model. We simplify the expansion by ignoring the path dependence of the velocity for small changes in the velocity. From Fermat's principle we argue that the effect on the travel time due to the change in the ray path is of second order compared to that due to the change in velocity. Thus we consider only the effect on travel time due to the change in velocity along the original ray path. Then the expansion is

$$T_{ij}(V) \cong T_{ij}^{JB} + \frac{\partial}{\partial V} T_{ij} \delta V \qquad \text{(A-2)}$$

Substituting equation (2) into equation (1),

$$T_{ij} = \Delta_j^0 + T_{ij}^{JB} + \frac{\partial T_{ij}}{\partial V} \delta V$$

or

$$R_{ij} = \Delta_j^0 + \frac{\partial T_{ij}}{\partial V} \delta V \qquad \text{(A-3)}$$

The partial derivative is

$$\frac{\partial T}{\partial V} = \int_s \frac{-ds}{V^2}$$

so,

$$R_{ij} = \Delta_j^\circ + \left(\int_s \frac{-ds}{v^2} \delta v \right)_{ij} \qquad \text{(A-4)}$$

Now, assume that the earth is composed of layers divided into blocks (see Fig. 2) of varying velocities. Then the integral can be converted to a sum,

$$\int_s \frac{-ds}{v^2} = \sum_{k=1}^{\ell} \frac{-L_k}{v_k^2}$$

where the k = 1, ℓ blocks are the ones penetrated by the ray path. Equation (4) now becomes,

$$R_{ij} = \Delta_j^\circ + \left[\sum_{k=1}^{\ell} \left(\frac{L_k}{v_k} \right) \left(\frac{-\delta v_k}{v_k} \right) \right]_{ij}$$

$$= \Delta_j^\circ + \left(\sum_{k=1}^{\ell} T_k D_k \right)_{ij} \quad . \qquad \text{(A-5)}$$

We have completed the linearization of the problem, but it involves an unknown quantity Δ_j°. However, we argued intuitively that we can eliminate this term and also the far-from-receiver component of the residual by subtracting out the average residual for each event. Note that from equation (5),

$$\frac{1}{n} \sum_{i=1}^{n} R_{ij} = \frac{1}{n} \sum_{i=1}^{n} \Delta_j^\circ + \frac{1}{n} \sum_{i=1}^{n} \left(\sum_{k=1}^{\ell} T_{ijk} D_{ijk} \right)$$

or

$$\bar{R}_j = \Delta_j^c + \frac{1}{n} \sum_{i=1}^{n} \left(\sum_{k=1}^{\ell} T_{ijk} D_{ijk} \right) \qquad (A-6)$$

Subtracting equation (6) from equation (5),

$$R_{ij} - \bar{R}_{ij} = \sum_{k=1}^{\ell} T_{ijk} D_{ijk} - \frac{1}{n} \sum_{i=1}^{n} \left(\sum_{k=1}^{\ell} T_{ijk} D_{ijk} \right) \qquad (A-7)$$

Now divide the ray path into two parts: The near-receiver path (blocks 1-a) which is within the area we are modeling, and the far-from-receiver path (blocks a-ℓ) which is common to all the stations for a particular event. Then the right hand side of equation (7) becomes,

$$RHS = \sum_{k=1}^{a} T_{ijk} D_{ijk} + \sum_{k=a}^{\ell} T_{jk} D_{jk} - \frac{1}{n} \sum_{i=1}^{n} \left(\sum_{k=1}^{a} T_{ijk} D_{ijk} + \sum_{k=a}^{\ell} T_{jk} D_{jk} \right)$$

$$= \sum_{k=1}^{a} T_{ijk} D_{ijk} + \sum_{k=a}^{\ell} T_{jk} D_{jk} - \frac{1}{n} \left(\sum_{k=1}^{a} \sum_{i=1}^{n} T_{ijk} D_{ijk} + n \sum_{k=a}^{\ell} T_{jk} D_{jk} \right)$$

$$= \sum_{k=1}^{a} T_{ijk} D_{ijk} - \sum_{k=1}^{a} \frac{1}{n} \sum_{i=1}^{n} T_{ijk} D_{ijk}$$

$$= \sum_{k=1}^{a} \left(T_{ijk} - \frac{1}{n} \sum_{i=1}^{n} T_{ijk} \right) D_{ijk}$$

Let

$$r_{ij} = R_{ij} - \bar{R}_j$$

and

$$T'_{ijk} = T_{ijk} - \frac{1}{n} \sum_{i=1}^{n} T_{ijk} \quad .$$

Equation (7) now is

$$r_{ij} = \sum_{k=1}^{a} T'_{ijk} D_{ijk} . \qquad \text{(A-8)}$$

Notice that by this procedure any error which affects all the stations alike, such as mislocation, errors in the J-B tables, or heterogeneities near the source, are cancelled out. Our new reduced residuals, r_{ij}, contain only the effects of heterogeneities along the near-receiver path as defined earlier and reading errors at the stations. Finally, to write equation (8) as a matrix equation, let ij = p, the ray path between station i and event j. Then,

$$r_p = \sum_{k=1}^{a} T'_{pk} D_{pk}$$

which is a set of linear simultaneous equations. In vector notation,

$$d = Am \qquad \text{(A-9)}$$

where the vector d contains the reduced residuals r_p, the vector m contains the unknowns, D_{pk}, and A is the matrix of the reduced travel times, T'_{pk}. Equation (9) is the equation we must invert.

The damped least squares solution is derived along with its resolution and covariance matrices. The derivation of the formula used in the calculation of the variance improvement is also included. For the "damped" least squares solution instead of minimizing only $|d - Am|^2$, we introduce a damping term in the minimization function,

$$M = (d - Am)^T(d - Am) + \varepsilon^2(m^Tm)$$
$$= d^Td - 2m^TA^Td + m^TA^TAm + \varepsilon^2m^Tm$$

where ε^2 is a weighting factor. Differentiate M with respect to m, and setting equal to zero,

$$-2A^Td + 2A^TA\hat{m} + 2\varepsilon^2\hat{m} = 0$$
$$(A^TA + \varepsilon^2I)\,\hat{m} = A^Td$$
$$\hat{m} = (A^TA + \varepsilon^2I)^{-1}\,A^Td \qquad (B\text{-}1)$$

Substitute for d using the original equation d = Am, then,

$$\hat{m} = (A^TA + \varepsilon^2I)^{-1}\,A^TAm \quad .$$

The resolution matrix, R, is

$$R = (A^TA + \varepsilon^2 I)^{-1} A^TA \quad . \tag{B-2}$$

If the data contains errors, Δd, the influence in the solution is

$$\Delta \hat{m} = (A^TA + \varepsilon^2 I)^{-1} A^T \Delta d \quad .$$

Then,

$$\langle \Delta m \Delta m^T \rangle = (A^TA + \varepsilon^2 I)^{-1} A^T \langle \Delta d \Delta d^T \rangle A \ (A^TA + \varepsilon^2 I)^{-1}$$

is the covariance matrix, C. If the errors are uncorrelated and have constant variance σ^2, i.e., if

$$\langle \Delta d \Delta d^T \rangle = \sigma^2 I$$

the covariance matrix reduces to

$$\begin{aligned} C &= (A^TA + \varepsilon^2 I)^{-1} A^TA (A^TA + \varepsilon^2 I)^{-1} s^2 I \\ &= (A^TA + \varepsilon^2 I)^{-1} Rs^2 I \end{aligned} \tag{B-3}$$

where R is the resolution matrix and s^2 is the estimate of the variance, σ^2 .

The variance improvement is expressed by,

$$\frac{\langle |d|^2 \rangle - \langle |e|^2 \rangle}{\langle |d|^2 \rangle}$$

where $e = d - A\hat{m}$. Then,

$$e^T e = d^T d - 2\hat{m}^T A^T d + \hat{m}^T A^T A \hat{m} .$$

Using $A^T A\hat{m} = A^T d - \varepsilon^2 \hat{m}$,

$$e^T e = d^T d - \hat{m}^T A^T d - \varepsilon^2 \hat{m}^T \hat{m}$$

$$|e|^2 = |d|^2 - \hat{m}^T A^T d - \varepsilon^2 |\hat{m}|^2$$

and

$$\langle |e|^2 \rangle = \langle |d|^2 \rangle - \langle \hat{m}^T A^T d \rangle - \varepsilon^2 \langle |\hat{m}|^2 \rangle .$$

Thus, the variance improvement is calculated with,

$$\frac{\langle \hat{m}^T A^T d \rangle + \varepsilon^2 \langle |\hat{m}|^2 \rangle}{\langle |d|^2 \rangle} . \qquad \text{(B-4)}$$

We prove two important properties: 1) that our resolution matrix is symmetric, and 2) that our estimates of the standard errors are upper limits.

For the first proof, we require the following property of matrices,

$$(A^{-1})^T = A^{-1} \quad \text{if } A = A^T \qquad \text{(C-1)}$$

The proof is simple:

$$AA^{-1} = I$$
$$(A^{-1})^T A^T = I$$
$$(A^{-1})^T = (A^T)^{-1}$$

and if $A = A^T$

$$(A^{-1})^T = A^{-1} \quad .$$

Then the proof that our resolution matrix is symmetric is straightforward:

$$R = (A^TA + \varepsilon^2 I)^{-1} A^TA$$
$$R^T = A^TA(A^TA + \varepsilon^2 I)^{-1} \quad \text{using C-1} \; .$$

We want to know if $R^T = R$,

$$(A^TA + \varepsilon^2 I)^{-1} A^TA \stackrel{?}{=} A^TA(A^TA + \varepsilon^2 I)^{-1} \quad .$$

Pre- and post-multiply by $(A^TA + \varepsilon^2 I)$,

$$A^TA(A^TA + \varepsilon^2 I) \stackrel{?}{=} (A^TA + \varepsilon^2 I)\ A^TA$$
$$A^TAA^TA + \varepsilon^2 A^TA = A^TAA^TA + \varepsilon^2 A^TA$$
$$R = R^T \quad .$$

For the second proof, recall that the standard errors are given by the square root of the diagonal elements of the covariance matrix,

$$C = (A^TA + \varepsilon^2 I)^{-1}\ R\ s^2 I \quad .$$

Thus they are directly proportional to s^2, our estimate of the variance of the error in the data, σ^2. Including the error explicitly, our original equation can be written as,

$$d = Am + e \qquad \text{(C-2)}$$

where d is n x 1, A is n x k, m is k x 1 and e is n x 1 and $\langle e \rangle = 0$, $\langle e^Te \rangle = \sigma^2$.

Assume both the least squares solution,

$$m_1 = (A^TA)^{-1}\ A^Td$$

and the damped least squares solution,

$$m = (A^TA + \varepsilon^2 I)^{-1}\ A^Td$$

exist. The corresponding residuals and estimates of the variance are,

$$r_1 = d - Am_1$$
$$s_1^2 = \frac{|r_1|^2}{n - k}$$

$$r_2 = d - Am_2$$

$$s_2^2 = \frac{|r_2|^2}{n - k}$$

We have shown previously that m_1 minimizes $|d - Am|^2$ and m_2 minimizes $|d - Am|^2 + \varepsilon^2|m|^2$, thus

$$|d - Am_1|^2 \leq |d - Am_2|^2$$

where the equality holds only when $\varepsilon^2 = 0$. Therefore,

$$|r_1|^2 < |r_2|^2$$

and

$$s_1^2 < s_2^2 .$$

Johnston (1963) showed that for the least squares solution,

$$\langle |r_1|^2 \rangle = \sigma^2(n - k)$$

so that,

$$\langle s_1^2 \rangle = \sigma^2$$

and so s_1^2 is an unbiased estimate of σ^2. We have just shown, however, that

$$s_2^2 > s_1^2$$

so

$$\langle s_2^2 \rangle > \langle s_1^2 \rangle$$

or

$$\langle s_2^2 \rangle > \sigma^2$$

Thus, the estimate s_2^2 corresponding to the damped least squares is biased and, in fact, overestimates the variance.

APPENDIX B. COMPARISON OF DAMPED LEAST SQUARES AND SINGULAR VALUE DECOMPOSITION

In this appendix a series of computer runs are documented. First, a synthetic data problem is solved using three different programs:

1) DLS - uses damped least squares on A^TA.
2) SVD1 - uses singular value decomposition on A^TA.
3) SVD2 - uses singluar value decomposition on A.

For a comparison with real data, an inversion of the Yellowstone data with SVD1 is included. Initial model YP4-190 is used so comparison can be made with Table 4.4. In the run, several solutions are generated by cutting out different numbers of eigenvalues. Corresponding resolution and covariance matrices are shown for each solution.

TABLE B.1.

Synthetic Data Generation

The synthetic structure used is:

Layer 1:

-2.0	+2.0
+2.0	-2.0

Layer 2:

+2.0	+1.0	-2.0
+3.0	-10.0	0.0
+1.0	-1.0	1.0

Also shown are the synthetic events with azimuth and slowness.

```
U.H5171.12038.SYN.DATA

SYNTHETIC DATA CALCULATION                                                    00000010
0000NC0.CCCCCCECC.CC                                                          00000020
  6.0                                                                         00000030
      6.0      30.0     2      20.C     2      20.0                          00000040
      8.0      30.0     3      20.C     3      20.0                          00000050
                                                                            00000060
     -2.0      +2.C       2.C      -2.0                                     00000070
      2.0       1.0      -2.0       3.0     -10.0      0.0       1.0       00000080
     -1.0       1.0                                                         00000090
AAA  ON  0.0   OE  0.0                                                       00000100
BBB  ON  5.5   CE  5.5                                                       00000110
CCC  OS  5.5   OE  5.5                                                       00000120
DDD  OS  5.5   OW  5.5                                                       00000130
EEE  ON  5.5   OW  5.5                                                       00000140
                                                                            00000150
EVENT 1                          1.0      8.90                              00000160
EVENT 2                          1.0      6.95                              00000170
EVENT 3                          1.0      4.60                              00000180
EVENT 4                         31.0      8.90                              00000190
EVENT 5                         31.0      6.95                              00000200
EVENT 6                         31.0      4.60                              00000210
EVENT 7                         61.0      8.90                              00000220
EVENT 8                         61.0      6.95                              00000230
EVENT 9                         61.0      4.60                              00000240
EVENT 10                        91.0      8.90                              00000250
EVENT 11                        91.0      6.95                              00000260
EVENT 12                        91.0      4.60                              00000270
EVENT 13                       121.0      8.90                              00000280
EVENT 14                       121.0      6.95                              00000290
EVENT 15                       121.0      4.60                              00000300
EVENT 16                       151.0      8.90                              00000310
EVENT 17                       151.0      6.95                              00000320
EVENT 18                       151.0      4.60                              00000330
EVENT 19                       181.0      8.90                              00000340
EVENT 20                       181.0      6.95                              00000350
EVENT 21                       181.0      4.60                              00000360
EVENT 22                       211.0      8.90                              00000370
EVENT 23                       211.0      6.95                              00000380
EVENT 24                       211.0      4.60                              00000390
EVENT 25                       241.0      8.90                              00000400
EVENT 26                       241.0      6.95                              00000410
EVENT 27                       241.0      4.60                              00000420
EVENT 28                       271.0      8.90                              00000430
EVENT 29                       271.0      6.95                              00000440
EVENT 30                       271.0      4.60                              00000450
EVENT 31                       301.0      8.90                              00000460
EVENT 32                       301.0      6.95                              00000470
EVENT 33                       301.0      4.60                              00000480
EVENT 34                       331.0      8.90                              00000490
EVENT 35                       331.0      6.95                              00000500
EVENT 36                       331.0      4.60                              00000510
****                                                                        00000511
```

Information Processing Center

Information Processing Center

TABLE B.2.

Solution Using DLS

note: $\theta^2 = .001(\text{sec}/\%)^2$

***** PROGRAM 3-D ***** 22 NOVEMBER 1975

SYNTHETIC DATA CALCULATION 00000010

LATITUDE	LONGITUDE	THA	VO	JPWT	IRES	IPUNCH	IPRINT	THETA	RESL
ON 0.0	OF 0.0	0.0	6.00	0	0	0	0	10.	0.0

	VELOCITY	THICKNESS	#-NORTH	LENGTH	#-EAST	LENGTH	COORDINATE DISPLACEMENT	
1	6.00	30.00	2	20.00	2	20.00	0.0	0.0
2	8.00	30.00	3	20.00	3	20.00	0.0	0.0

STA LATITUDE LONGITUDE ELEVATION RELATIVE COORDINATES

1	AAA	ON 0.0	OF 0.0	0.	0.0	0.0
2	BBB	ON 5.50	OE 5.50	0.	10.12	10.19
3	CCC	OS 5.50	OF 5.50	0.	-10.12	10.19
4	DDD	OS 5.50	OW 5.50	0.	-10.12	-10.19
5	EEE	ON 5.50	OW 5.50	0.	10.12	-10.19

OBSERVATION MATRIX

45 45
45 45

13 19 13
19 20 19
13 19 13

***** SYNTHETIC DATA CALCULATION 00C00010

NO OF STATIONS= 5
NO OF EVENTS= 36
NO OF OBSERVATIONS= 180

TOTAL BLOCKS IN MODEL= 13
NO OF BLOCKS OBSERVED= 13

DATA VARIANCE IS 0.0368
RESIDUAL VARIANCE IS 0.0000
VARIANCE IMPROVEMENT IN % IS 99.8910

VELOCITY PERTURBATIONS IN LAYER-BLOCK FORMAT

LAYER ... 1
-1.97 1.97

1.99 -1.99

LAYER ... 2
1.99 1.14 -1.77

2.98 -9.51 0.19

1.04 -0.84 1.08

TABLE B.3.

Solution Using SVD1

***** PROGRAM 3-D ***** 22 NOVEMBER 1975

SYNTHETIC DATA CALCULATION 00000010

LATITUDE	LONGITUDE	THA	VO	JPWT	IRES	IPUNCH	IPRINT	THETA	RESL
ON 0.0	OE 0.0	0.0	6.00	0	0	0	0	10.	0.0

	VELOCITY	THICKNESS	#-NORTH	LENGTH	#-EAST	LENGTH	COORDINATE	DISPLACEMENT
1	6.00	30.00	2	20.00	2	20.00	0.0	0.0
2	8.00	30.00	3	20.00	3	20.00	0.0	0.0

	STA	LATITUDE	LONGITUDE	ELEVATION	RELATIVE COORDINATES	
1	AAA	ON 0.0	OE 0.0	0.	0.0	0.0
2	BBB	ON 5.50	OE 5.50	0.	10.12	10.19
3	CCC	OS 5.50	OE 5.50	0.	-10.12	10.19
4	DDD	OS 5.50	OW 5.50	0.	-10.12	-10.19
5	EEE	ON 5.50	OW 5.50	0.	10.12	-10.19

OBSERVATION MATRIX

45	45	
45	45	
13	19	13
19	20	19
13	19	13

**** SYNTHETIC DATA CALCULATION 00000010 *****

NO OF STATIONS= 5
NO OF EVENTS= 36
NO OF OBSERVATIONS= 180

TOTAL BLOCKS IN MODEL= 13
NO OF BLOCKS OBSERVED= 13

DATA RMS = 0.367554E-01

VALUE ANALYSIS OF THE LEAST SQUARES NORMAL EQUATIONS , (A**T)*A*X=(A**T)*B.

3, N = 13, NDATA = 144

FROM MINFIT = 0

SING. VALUE	P COEF	RECIP. S.V.	G COEF	G**2	C.S.S.	N.S.R.C.S.S
					3.4163E+03	8.9707E+00
0.1299E+04	2.3849E-03	7.6961E-04	3.0989E+00	9.6031E+00	3.4067E+03	8.8095E+00
0.1299E+04	-4.1436E-03	7.6962E-04	-5.3839E+00	2.8987E+01	3.3777E+03	8.8771E+00
0.1282E+04	3.7657E-02	7.8028E-04	4.8261E+01	2.3292E+03	1.0485E+03	2.7269E+00
0.3280E+03	-8.8292E-02	3.0484E-03	-2.8964E+01	8.3890E+02	2.0961E+02	1.2236E+00
0.2919E+03	-1.4311E-02	3.4255E-03	-4.1779E+00	1.7455E+01	1.9216E+02	1.1758E+00
0.2840E+03	-1.2150E-02	3.5206E-03	-3.4510E+00	1.1910E+01	1.8025E+02	1.1429E+00
0.2840E+03	1.6224E-02	3.5207E-03	4.6083E+00	2.1236E+01	1.5901E+02	1.0773E+00
0.2618E+03	-4.3903E-02	3.8195E-03	-1.1495E+01	1.3212E+02	2.6886E+01	8.4463E-01
0.1680E+03	-2.4956E-02	5.9526E-03	-4.1925E+00	1.7577E+01	9.3093E+00	2.6260E-01
0.1052E+03	1.4898E-02	9.5037E-03	1.5665E+00	2.4539E+00	6.8554E+00	2.2619E-01
0.1052E+03	-2.2749E-02	9.5037E-03	-2.3937E+00	5.7299E+00	1.1255E+00	9.1991E-02
47.0076	2.2568E-02	2.1273E-02	1.0609E+00	1.1255E+00	7.1265E-10	2.3235E-06
0.0012	2.1764E-02	8.1527E+02	2.6695E-05	7.1265E-10	0.0	0.0

YNORM	RNORM	LOG10(YNORM)	LOG10(RNORM)
0.0	0.58449E+02	-1000.00000	1.76678
0.23849E-02	0.58367E+02	-2.62252	1.76616
0.47909E-02	0.58118E+02	-2.32049	1.76431
0.37960E-01	0.32381E+02	-1.42068	1.51029
0.96106E-01	0.14478E+02	-1.01725	1.16071
0.97166E-01	0.13862E+02	-1.01249	1.14183
0.97923E-01	0.13426E+02	-1.00912	1.12793
0.99258E-01	0.12610E+02	-1.00328	1.10071
0.10853E+00	0.51952E+01	-0.96444	0.71476
0.11137E+00	0.30511E+01	-0.95325	0.48446
0.11236E+00	0.26183E+01	-0.94940	0.41802
0.11464E+00	0.10609E+01	-0.94068	0.02567
0.11684E+00	0.26695E-04	-0.93242	-4.57356
0.11885E+00	0.0	-0.92501	-1000.00000

P SOLUTION AND RESIDUAL VECTORS FOR A RANGE OF VALUES OF THE LEVENBERG-MARQUARDT PARAMETER, LAMBDA.

LAMBDA	YNORM	RNORM	LOG10(LAMBDA)	LOG10(YNORM)	LOG10(RNORM)
0.12994E+05	0.37084E-03	0.58048E+02	4.11373	-3.43081	1.76379
0.51579E+04	0.22410E-02	0.56045E+02	3.71248	-2.64956	1.74854
0.20475E+04	0.10950E-01	0.47145E+02	3.31122	-1.96059	1.67344
0.81278E+03	0.30197E-01	0.31043E+02	2.90997	-1.52004	1.49753
0.32264E+03	0.61217E-01	0.17138E+02	2.50872	-1.21313	1.23395
0.12808E+03	0.96650E-01	0.52346E+01	2.10747	-1.01490	0.71899
0.50841E+02	0.11116E+00	0.11971E+01	1.70622	-0.95406	0.07812
0.20182E+02	0.11553E+00	0.24298E+00	1.30497	-0.93730	-0.61443
0.80115E+01	0.11661E+00	0.41318E-01	0.90371	-0.93327	-1.38385
0.31803E+01	0.11688E+00	0.66014E-02	0.50246	-0.93256	-2.18037
0.12624E+01	0.11693E+00	0.10429E-02	0.10121	-0.93244	-2.98176
0.50114E+00	0.11684E+00	0.16649E-03	-0.30004	-0.93242	-3.77860
0.19893E+00	0.11684E+00	0.37193E-04	-0.70129	-0.93242	-4.42954
0.78969E-01	0.11684E+00	0.26999E-04	-1.10254	-0.93242	-4.56865
0.31348E-01	0.11684E+00	0.28662E-04	-1.50379	-0.93242	-4.57410
0.12444E-01	0.11684E+00	0.26439E-04	-1.90504	-0.93242	-4.57776
0.49398E-02	0.11684E+00	0.25145E-04	-2.30629	-0.93239	-4.59955
0.19609E-02	0.11700E+00	0.19188E-04	-2.70755	-0.93182	-4.71698
0.77846E-03	0.11786E+00	0.76643E-05	-3.10880	-0.92862	-5.11553
0.30900E-03	0.11962E+00	0.15930E-05	-3.51005	-0.92586	-5.79778
0.12266E-03	0.11881E+00	0.26432E-06	-3.91130	-0.92516	-6.57788

EIGENVECTORS IN LAYER-BLOCK FORMAT
(ELEMENTS ARE SCALED UP BY FACTOR OF 10**4)

EIGENVECTOR OF EIGENVALUE NO. 1

LAYER ... 1

803.	6938.
-6938.	-803.

LAYER ... 2

427.	423.	836.
-401.	0.	402.
-836.	-423.	-427.

EIGENVECTOR OF EIGENVALUE NO. 13

LAYER ... 1

-5000.	-5000.
-5000.	-5000.

LAYER ... 2

-0.	-0.	-0.
0.	-0.	-0.
0.	-0.	-0.

SOLUTION, RESOLUTION , AND COVARIANCE WITH VARIOUS EIGENVALUE CUTOFFS
THIS PROBLEM HAS 0 ZERO EIGENVALUES

SOLUTION NO. 1 THIS SOLUTION HAS 2 EIGENVALUES REMOVED IN ADDITION TO THE ZERO EIGENVALUES

LAYER ... 1

-2.01	2.01
2.00	-1.99

LAYER ... 2

2.77	1.78	-1.30
3.77	-9.06	0.77
1.73	-0.26	1.71

RESOLUTION MATRIX DIAGONAL ELEMENTS

LAYER ... 1

0.750E+00	0.750E+00
0.750E+00	0.750E+00

LAYER ... 2

0.897E+00	0.892E+00	0.897E+00
0.892E+00	0.845E+00	0.892E+00
0.897E+00	0.892E+00	0.897E+00

COVARIANCE MATRIX DIAGONAL ELEMENTS

LAYER ... 1

0.153E-05	0.153E-05
0.153E-05	0.153E-05

LAYER ... 2

0.447E-04	0.211E-04	0.447E-04
0.211E-04	0.887E-05	0.211E-04
0.447E-04	0.211E-04	0.447E-04

SOLUTION NO. 2 THIS SOLUTION HAS 1 EIGENVALUES REMOVED IN ADDITION TO THE ZERO EIGENVALUES

LAYER ... 1

-2.01	2.01
2.00	-1.99

LAYER ... 2

2.05	1.04	-2.03
3.03	-9.95	0.03
1.00	-1.00	0.99

RESOLUTION MATRIX DIAGONAL ELEMENTS

LAYER ... 1

0.750E+00	0.750E+00
0.750E+00	0.750E+00

LAYER ... 2

0.100E+01	0.100E+01	0.100E+01
0.100E+01	0.100E+01	0.100E+01
0.100E+01	0.100E+01	0.100E+01

COVARIANCE MATRIX DIAGONAL ELEMENTS

LAYER ... 1

0.153E-05	0.153E-05
0.153E-05	0.153E-05

LAYER ... 2

0.912E-04	0.702E-04	0.912E-04
0.702E-04	0.792E-04	0.702E-04
0.912E-04	0.702E-04	0.912E-04

TABLE B.4.

Solution Using SVD2

***** PROGRAM 3-D ***** 22 NOVEMBER 1975

SYNTHETIC DATA CALCULATION 00000010

LATITUDE	LONGITUDE	THA	VO	JPWT	IRES	IPUNCH	IPRINT	THETA	RESL
ON 0.0	OE 0.0	0.0	6.00	0	0	0	0	10.	0.0

	VELOCITY	THICKNESS	#-NORTH	LENGTH	#-EAST	LENGTH	COORDINATE DISPLACEMENT	
1	6.00	30.00	2	20.00	2	20.00	0.0	0.0
2	8.00	30.00	3	20.00	3	20.00	0.0	0.0

	STA	LATITUDE	LONGITUDE	ELEVATION	RELATIVE COORDINATES	
1	AAA	ON 0.0	OE 0.0	0.	0.0	0.0
2	BBB	ON 5.50	OE 5.50	0.	10.12	10.19
3	CCC	OS 5.50	OE 5.50	0.	-10.12	10.19
4	DDD	OS 5.50	OW 5.50	0.	-10.12	-10.19
5	EEE	ON 5.50	OW 5.50	0.	10.12	-10.19

Information Processing Center

OBSERVATION MATRIX

45 45
45 45

13 19 13
19 20 19
13 19 13

**** SYNTHETIC DATA CALCULATION 00000010 *****

NO OF STATIONS= 5
NO OF EVENTS= 36
NO OF OBSERVATIONS= 180

TOTAL BLOCKS IN MODEL= 13
NO OF BLOCKS OBSERVED= 13

DATA RMS = 0.367554E-01
SOLN RMS=-0.101218E-03

AR VALUE ANALYSIS OF THE LEAST SQUARES PROBLEM , A*X=B.

13, N = 13, MDATA = 144

RE FROM MINFIT = 0

SING. VALUE	P COEF	RECIP. S.V.	G COEF	G**2	C.S.S.	N.S.R.C.S
					5.2918E+00	1.9170E-0
36.0462	3.2585E-03	2.7742E-02	1.1746E-01	1.3796E-02	5.2780E+00	1.9212E-0
36.0461	3.4711E-03	2.7742E-02	1.2512E-01	1.5655E-02	5.2624E+00	1.9251E-0
35.7989	3.7661E-02	2.7934E-02	1.3482E+00	1.8177E+00	3.4447E+00	1.5630E-0
18.1119	8.8293E-02	5.5212E-02	1.5992E+00	2.5573E+00	8.8741E-01	7.9616E-0
17.0858	-1.4314E-02	5.8528E-02	-2.4456E-01	5.9809E-02	8.2760E-01	7.7162E-0
16.8533	1.3544E-02	5.9335E-02	2.2826E-01	5.2102E-02	7.7550E-01	7.4964E-0
16.8531	1.5072E-02	5.9336E-02	2.5402E-01	6.4524E-02	7.1098E-01	7.2039E-0
16.1805	-4.3903E-02	6.1803E-02	-7.1037E-01	5.0462E-01	2.0636E-01	3.8953E-0
12.9611	-2.4956E-02	7.7154E-02	-3.2346E-01	1.0463E-01	1.0173E-01	2.7451E-0
10.2577	1.2497E-02	9.7488E-02	1.2819E-01	1.6433E-02	8.5295E-02	2.5230E-0
10.2576	-2.4145E-02	9.7489E-02	-2.4767E-01	6.1340E-02	2.3954E-02	1.3420E-
6.8561	-2.2569E-02	1.4586E-01	-1.5473E-01	2.3942E-02	1.2512E-05	3.0788E-0
0.2447E-03	-1.4456E+01	4.0869E+03	-3.5372E-03	1.2512E-05	0.0	0.0

YNORM	RNORM	LOG10(YNORM)	LOG10(RNORM)
0.0	0.23004E+01	-1000.00000	0.36180
0.32585E-02	0.22974E+01	-2.48698	0.36124
0.47609E-02	0.22940E+01	-2.32231	0.36059
0.37960E-01	0.18560E+01	-1.42067	0.26858
0.96107E-01	0.94202E+00	-1.01724	-0.02594
0.97167E-01	0.90973E+00	-1.01248	-0.04109
0.98107E-01	0.88062E+00	-1.00830	-0.05521
0.99258E-01	0.84319E+00	-1.00323	-0.07407
0.10853E+00	0.45426E+00	-0.96444	-0.34269
0.11137E+00	0.31895E+00	-0.95325	-0.49628
0.11206E+00	0.29205E+00	-0.95053	-0.53454
0.11464E+00	0.15477E+00	-0.94068	-0.81031
0.11684E+00	0.35372E-02	-0.93242	-2.45134
0.14457E+02	0.0	1.16038	-1000.00000

OF SOLUTION AND RESIDUAL VECTORS FOR A RANGE OF VALUES OF THE LEVENBERG-MARQUARDT PARAMETER, LAMBDA.

LAMBDA	YNORM	RNORM	LOG10(LAMBDA)	LOG10(YNORM)	LOG10(RNORM)
0.36046E+03	0.44646E-03	0.22891E+01	2.55686	-3.35021	0.35966
0.15792E+03	0.22556E-02	0.22435E+01	2.19844	-2.64673	0.35092
0.69188E+02	0.10228E-01	0.20483E+01	1.84003	-1.99022	0.31138
0.30312E+02	0.34380E-01	0.15093E+01	1.48162	-1.46370	0.17877
0.13280E+02	0.74892E-01	0.72104E+00	1.12320	-1.12557	-0.14204
0.58182E+01	0.10394E+00	0.20962E+00	0.76479	-0.98322	-0.67856
0.25490E+01	0.11390E+00	0.46563E-01	0.40638	-0.94350	-1.33196
0.11168E+01	0.11625E+00	0.98968E-02	0.04796	-0.93462	-2.00451
0.48927E+00	0.11672E+00	0.39633E-02	-0.31045	-0.93285	-2.40195
0.21436E+00	0.11681E+00	0.35539E-02	-0.66886	-0.93250	-2.44930
0.93913E-01	0.11683E+00	0.35378E-02	-1.02727	-0.93244	-2.45126
0.41145E-01	0.11684E+00	0.35371E-02	-1.38569	-0.93242	-2.45135
0.18024E-01	0.11687E+00	0.35365E-02	-1.74410	-0.93231	-2.45142
0.78975E-02	0.11766E+00	0.35338E-02	-2.10251	-0.92938	-2.45175
0.34600E-02	0.13721E+00	0.35196E-02	-2.46092	-0.86263	-2.45350
0.15159E-02	0.39523E+00	0.34474E-02	-2.81934	-0.41428	-2.46251
0.66413E-03	0.17317E+01	0.31145E-02	-3.17775	0.23847	-2.50661
0.29096E-03	0.59895E+01	0.20720E-02	-3.53616	0.77739	-2.68361
0.12748E-03	0.11371E+02	0.75513E-03	-3.89458	1.05579	-3.12198
0.55849E-04	0.13741E+02	0.17516E-03	-4.25299	1.13802	-3.75657
0.24468E-04	0.14314E+02	0.35022E-04	-4.61140	1.15576	-4.45566

EIGENVECTORS IN LAYER-BLOCK FORMAT
(ELEMENTS ARE SCALED UP BY FACTOR OF 10**4)

EIGENVECTOR OF SINGULAR VALUE NO. 1

LAYER ... 1

-822.	6938.
-6934.	817.

LAYER ... 2

223.	320.	912.
-489.	-0.	488.
-912.	-319.	-223.

EIGENVECTOR OF SINGULAR VALUE NO. 13

LAYER ... 1

5000.	5000.
5000.	5000.

LAYER ... 2

0.	-0.	0.
0.	-0.	-0.
-0.	-0.	-0.

SOLUTION WITH DIAGONAL ELEMENTS OF CORRESPONDING RESOLUTION AND COVARIANCE MATRICES FOR VARIOUS SING. VALUE CUTOFFS
THIS PROBLEM HAS 0 ZERO SINGULAR VALUES

SOLUTION *** NO. 1 *** THIS SOLUTION HAS 2 SINGULAR VALUES REMOVED IN ADDITION TO ANY ZERO SING. VALUES

LAYER ... 1

-2.01	2.01
2.00	-1.99

LAYER ... 2

2.77	1.78	-1.30
3.77	-9.06	0.77
1.73	-0.26	1.71

RESOLUTION MATRIX DIAGONAL ELEMENTS

LAYER ... 1

0.750E+00	0.750E+00
0.750E+00	0.750E+00

LAYER ... 2

0.897E+00	0.892E+00	0.897E+00
0.892E+00	0.845E+00	0.892E+00
0.897E+00	0.892E+00	0.897E+00

COVARIANCE MATRIX DIAGONAL ELEMENTS

LAYER ... 1

0.691E-03	0.691E-03
0.691E-03	0.691E-03

LAYER ... 2

0.590E-02	0.389E-02	0.590E-02
0.389E-02	0.272E-02	0.389E-02
0.590E-02	0.389E-02	0.590E-02

SOLUTION *** NO. 2 *** THIS SOLUTION HAS 1 SINGULAR VALUES REMOVED IN ADDITION TO ANY ZERO SING. VALUES

LAYER ... 1

-2.01	2.01
2.00	-1.99

LAYER ... 2

2.05	1.04	-2.03
3.03	-9.95	0.03
1.00	-1.00	0.99

RESOLUTION MATRIX DIAGONAL ELEMENTS

LAYER ... 1

0.750E+00	0.750E+00
0.750E+00	0.750E+00

LAYER ... 2

0.100E+01	0.100E+01	0.100E+01
0.100E+01	0.100E+01	0.100E+01
0.100E+01	0.100E+01	0.100E+01

COVARIANCE MATRIX DIAGONAL ELEMENTS

LAYER ... 1

0.691E-03	0.691E-03
0.691E-03	0.691E-03

LAYER ... 2

0.808E-02	0.619E-02	0.808E-02
0.619E-02	0.603E-02	0.619E-02
0.808E-02	0.619E-02	0.808E-02

TABLE B.5.

Solution Using SVD1 of Yellowstone Data

With Initial Model YP4-190

***** PROGRAM 3-D *****

22 NOVEMBER 1975

YELLOWSTONE - YP DATA Q(A,B,C)

LATITUDE	LONGITUDE	TRA	VO	JPWT	IRES	IPUNCH	IPRINT	THETA	RESL
44N36.17	110W38.38	0.0	6.00	0	1	0	0	50.	0.100.

	VELOCITY	THICKNESS	#-NORTH	LENGTH	#-EAST	LENGTH	COORDINATE DISPLACEMENT	
1	6.20	40.00	9	25.00	9	25.00	0.0	0.0
2	7.90	50.00	10	30.00	10	30.00	0.0	0.0
3	7.95	50.00	11	30.00	11	30.00	0.0	0.0
4	8.00	50.00	12	30.00	12	30.00	0.0	0.0

STA	LATITUDE	LONGITUDE	ELEVATION	RELATIVE COORDINATES	
1YPBB	45N 1.73	111W 7.01	2199.	47.45	-37.61
2YPCJ	44N44.63	110W29.85	2426.	15.68	11.26
3YPDC	44N42.57	111W14.38	2025.	12.03	-47.55
4YPEE	44N29.43	110W 0.06	2134.	-12.29	50.80
5YPGC	44N47.77	111W 6.39	2075.	21.59	-36.94
6YPHR	44N45.06	111W11.72	2157.	16.61	-44.00
7YPHR	44N51.14	111W13.96	2060.	27.95	-53.47
8YPLK	44N34.18	110W23.18	2391.	-3.65	20.12
9YPMC	44N45.56	111W 0.36	2073.	17.46	-29.01
10YPMF	44N 8.80	111W17.29	1789.	-50.86	-81.89
11YPMH	44N53.62	110W41.12	1781.	41.58	-3.60
12YPMJ	44N38.90	110W51.52	2111.	5.08	-17.37
13YPML	44N36.17	110W38.38	2518.	0.0	0.0
14YPMV	44N37.63	110W26.75	2400.	2.72	15.38
15YPNB	44N31.48	110W27.55	2405.	-8.67	14.35
16YPNJ	44N43.82	110W41.58	2290.	14.17	-4.23
17YPQF	44N27.15	110W50.48	2260.	-16.69	-16.05
18YPPC	44N38.90	110W11.58	2932.	5.15	35.44
19YPPR	44N23.55	110W17.19	2390.	-23.31	28.14
20YPSE	44N 8.18	110W40.00	2073.	-51.84	-2.16
21YPSG	45N 0.1M	109W59.25	2270.	44.68	51.42
22YPTB	44N31.50	110W50.76	2224.	-8.63	-16.40
23YPTC	44N17.79	110W13.92	2360.	-33.96	32.54
24YPTS	44N27.74	111W21.15	1923.	-15.37	-56.73
25YPWT	44N24.87	110W14.27	2365.	-20.93	5.46
26YPWY	44N36.36	111W 5.81	2294.	0.45	-36.29

OBSERVATION MATRIX

0	0	0	0	0	0	0	0	0			
0	0	0	0	0	0	0	0	0			
0	0	89	54	25	0	131	0	0			
0	1	246	108	50	0	8	0	0			
0	4	93	173	89	22	12	0	0			
0	1	16	45	46	61	14	0	0			
0	0	34	0	35	20	3	0	0			
0	0	0	0	0	0	0	0	0			
0	0	0	0	0	0	0	0	0			
0	0	0	0	0	0	0	0	0	0		
0	0	0	0	0	0	0	0	0	0		
0	0	31	32	11	31	19	5	0	0		
0	0	98	119	56	4	23	2	0	0		
0	1	72	146	127	33	9	47	0	0		
0	1	9	109	114	79	23	3	0	0		
0	0	12	21	27	29	27	7	0	0		
0	0	5	10	8	13	4	0	0	0		
0	0	0	0	0	1	1	0	0	0		
0	0	0	0	0	0	0	0	0	0	0	
0	0	1	0	0	2	0	0	0	0	0	
0	2	38	23	21	42	3	11	1	0	0	
0	24	97	62	32	22	9	0	2	0	0	
0	2	41	94	49	26	28	4	2	0	0	
0	3	50	77	38	79	19	8	40	0	0	
0	1	12	36	53	94	42	16	6	0	0	
0	1	5	0	23	34	22	27	6	0	0	
0	0	0	1	10	4	19	2	3	0	0	
0	0	0	0	2	2	2	2	0	0	0	
0	0	0	0	0	1	1	0	0	0	0	
0	0	0	0	0	0	0	0	0	0	0	0
0	3	1	0	5	2	2	4	0	1	0	0
1	19	27	10	31	35	8	4	4	0	0	0
0	44	113	29	19	30	14	2	1	0	0	0
1	3	43	62	23	11	11	7	3	2	0	0
0	3	24	45	34	17	18	3	1	4	1	0
0	3	45	59	15	23	44	19	14	28	0	0
1	0	7	23	9	34	83	31	11	2	4	2
1	0	6	1	7	16	32	29	32	8	2	0
1	0	0	0	0	9	14	18	2	2	0	0
0	0	0	0	0	2	1	3	4	1	0	0
0	0	0	0	1	3	1	1	0	0	0	0

**** YELLOWSTONE - YP DATA G(A,B,C) *****

NO OF STATIONS= 26
NO OF EVENTS=171
NO OF OBSERVATIONS= 1375

TOTAL BLOCKS IN MODEL= 446
NO OF BLOCKS OBSERVED= 211

DATA RMS = 0.209483E+00

460

SINGULAR VALUE ANALYSIS OF THE LEAST SQUARES NORMAL EQUATIONS , (A**T)*A*X=(A**T)*B.

M = 211, N = 211, MDATA = 1208

*** IERR FROM MINFIT = 0

INDEX	SING. VALUE	P COEF	RECIP. S.V.	G COEF	G**2	C.S.S.	N.S.R.C.S.S.
0						1.4345E+06	3.4461E+01
1	0.1162E+05	-3.5364E-02	8.6058E-05	-4.1094E+02	1.6887E+05	1.2657E+06	3.2382E+01
2	0.9758E+04	-5.1467E-02	1.0248E-04	-5.0223E+02	2.5223E+05	1.0134E+06	2.8988E+01
3	0.7706E+04	-6.0645E-02	1.2977E-04	-4.6734E+02	2.1840E+05	7.9504E+05	2.5686E+01
4	0.7117E+04	-2.3409E-02	1.4051E-04	-1.6659E+02	2.7754E+04	7.6728E+05	2.5244E+01
5	0.6093E+04	5.4123E-02	1.4941E-04	3.6229E+02	1.3125E+05	6.3603E+05	2.2994E+01
6	0.5490E+04	3.9479E-02	1.5409E-04	2.4972E+02	6.2358E+04	5.7367E+05	2.1846E+01
7	0.6009E+04	-1.6876E-02	1.6643E-04	-1.0140E+02	1.0282E+04	5.6339E+05	2.1659E+01
8	0.5516E+04	-7.4225E-03	1.8129E-04	-4.0942E+01	1.6762E+03	5.6171E+05	2.1636E+01
9	0.5349E+04	8.3660E-02	1.8695E-04	4.4749E+02	2.0025E+05	3.6146E+05	1.7361E+01
10	0.5224E+04	3.4640E-03	1.9141E-04	1.8097E+01	3.2751E+02	3.6114E+05	1.7362E+01
11	0.4979E+04	-8.4519E-03	2.0086E-04	-4.2078E+01	1.7706E+03	3.5937E+05	1.7327E+01
12	0.4667E+04	1.3316E-02	2.1427E-04	6.2145E+01	3.8620E+03	3.5550E+05	1.7241E+01
13	0.4433E+04	9.1475E-03	2.2556E-04	4.0554E+01	1.6446E+03	3.5386E+05	1.7208E+01
14	0.4181E+04	-5.3273E-02	2.3916E-04	-2.2277E+02	4.9628E+04	3.0423E+05	1.5962E+01
15	0.3931E+04	4.0325E-02	2.5440E-04	1.5851E+02	2.5126E+04	2.7910E+05	1.5295E+01
16	0.3567E+04	-3.6960E-02	2.7879E-04	-1.3257E+02	1.7575E+04	2.6153E+05	1.4812E+01
17	0.3541E+04	1.9506E-02	2.8239E-04	5.4909E+01	3.0150E+03	2.5851E+05	1.4733E+01
18	0.3453E+04	3.7133E-02	2.8961E-04	1.2829E+02	1.6458E+04	2.4206E+05	1.4262E+01
19	0.3319E+04	3.2660E-02	3.0129E-04	1.0840E+02	1.1750E+04	2.3031E+05	1.3918E+01
20	0.3283E+04	1.9719E-03	3.0464E-04	6.4729E+00	4.1898E+01	2.3026E+05	1.3922E+01
21	0.3190E+04	-3.7970E-02	3.1345E-04	-1.2114E+02	1.4674E+04	2.1559E+05	1.3477E+01
22	0.3012E+04	-7.0781E-02	3.3197E-04	-2.1322E+02	4.5462E+04	1.7013E+05	1.1977E+01
23	0.2951E+04	2.7219E-02	3.5073E-04	7.7606E+01	6.0227E+03	1.6411E+05	1.1768E+01
24	0.2784E+04	-2.4912E-02	3.5924E-04	-6.9347E+01	4.8090E+03	1.5930E+05	1.1599E+01
25	0.2714E+04	-2.7303E-02	3.6848E-04	-7.4096E+01	5.4902E+03	1.5381E+05	1.1402E+01
26	0.2699E+04	-1.1767E-02	3.7169E-04	-3.1659E+01	1.0023E+03	1.5281E+05	1.1370E+01
27	0.2513E+04	-1.6027E-02	3.9798E-04	-4.0271E+01	1.6217E+03	1.5118E+05	1.1314E+01
28	0.2421E+04	5.3286E-02	4.1310E-04	1.4352E+02	2.0597E+04	1.3059E+05	1.0520E+01
29	0.2400E+04	-2.2146E-02	4.1662E-04	-5.3157E+01	2.8257E+03	1.2776E+05	1.0410E+01
30	0.2375E+04	8.6717E-03	4.2103E-04	2.0597E+01	4.2422E+02	1.2734E+05	1.0397E+01
31	0.2284E+04	-1.9780E-02	4.3782E-04	-4.5179E+01	2.0411E+03	1.2530E+05	1.0318E+01
32	0.2234E+04	2.6997E-02	4.4761E-04	6.0315E+01	3.6379E+03	1.2166E+05	1.0171E+01
33	0.2219E+04	-2.1356E-02	4.5055E-04	-4.7400E+01	2.2468E+03	1.1941E+05	1.0081E+01
34	0.2143E+04	-7.4700E-03	4.6658E-04	-1.6010E+01	2.5633E+02	1.1915E+05	1.0074E+01
35	0.2129E+04	-1.9575E-02	4.6963E-04	-4.1682E+01	1.7374E+03	1.1742E+05	1.0005E+01
36	0.2076E+04	1.8168E-03	4.8180E-04	3.7709E+00	1.4220E+01	1.1740E+05	1.0009E+01
37	0.2029E+04	-9.6276E-03	4.9276E-04	-1.9538E+01	3.8174E+02	1.1702E+05	9.9966E+00
38	0.1999E+04	-3.6947E-02	5.0061E-04	-7.3804E+01	5.4471E+03	1.1157E+05	9.7654E+00
39	0.1975E+04	2.5899E-02	5.0622E-04	5.1162E+01	2.6175E+03	1.0896E+05	9.6543E+00
40	0.1931E+04	7.6982E-02	5.1797E-04	1.4862E+02	2.2089E+04	8.6868E+04	8.6240E+00
41	0.1896E+04	-3.3602E-02	5.2735E-04	-6.3871E+01	4.0795E+03	8.2788E+04	8.4227E+00
42	0.1885E+04	3.3270E-02	5.3044E-04	6.2739E+01	3.9361E+03	7.8852E+04	8.2235E+00
43	0.1807E+04	-3.5748E-02	5.5335E-04	-6.4603E+01	4.1735E+03	7.4679E+04	8.0064E+00
44	0.1719E+04	7.7547E-03	5.8163E-04	1.3333E+01	1.7776E+02	7.4501E+04	8.0003E+00
45	0.1685E+04	-4.1786E-02	5.9351E-04	-7.0405E+01	4.9568E+03	6.9544E+04	7.7329E+00

46	0.1680E+04	5.7884E-03	5.9532E-04	9.7232E+00	9.4541E+01	6.9450E+04	7.7309E+00
47	0.1641E+04	-2.9471E-02	6.0948E-04	-4.8355E+01	2.3382E+03	6.7111E+04	7.6029E+00
48	0.1599E+04	-2.4655E-02	6.2522E-04	-3.9434E+01	1.5551E+03	6.5556E+04	7.5176E+00
49	0.1553E+04	-4.6932E-02	6.4390E-04	-7.2840E+01	5.3057E+03	6.0251E+04	7.2101E+00
50	0.1509E+04	4.5095E-02	6.6247E-04	6.8071E+01	4.6337E+03	5.5617E+04	6.9303E+00
51	0.1476E+04	2.8508E-03	6.7756E-04	4.2074E+00	1.7702E+01	5.5599E+04	6.9321E+00
52	0.1471E+04	1.2960E-02	6.7958E-04	1.9070E+01	3.6367E+02	5.5236E+04	6.9124E+00
53	0.1415E+04	2.8931E-02	7.0691E-04	4.0926E+01	1.6749E+03	5.3561E+04	6.8098E+00
54	0.1392E+04	9.0420E-03	7.1855E-04	1.2584E+01	1.5835E+02	5.3402E+04	6.8026E+00
55	0.1374E+04	-2.0389E-02	7.2799E-04	-2.8008E+01	7.8442E+02	5.2618E+04	6.7554E+00
56	0.1359E+04	-2.1438E-02	7.3602E-04	-2.9127E+01	8.4837E+02	5.1769E+04	6.7036E+00
57	0.1347E+04	6.8298E-03	7.4223E-04	9.2018E+00	8.4673E+01	5.1685E+04	6.7011E+00
58	0.1332E+04	6.7854E-03	7.5095E-04	9.0357E+00	8.1644E+01	5.1603E+04	6.6987E+00
59	0.1309E+04	1.0928E-02	7.6389E-04	1.4306E+01	2.0465E+02	5.1399E+04	6.6883E+00
60	0.1304E+04	-3.3285E-02	7.6708E-04	-4.3391E+01	1.8828E+03	4.9516E+04	6.5675E+00
61	0.1252E+04	-3.2944E-03	7.9848E-04	-4.1258E+00	1.7022E+01	4.9499E+04	6.5692E+00
62	0.1222E+04	-5.0726E-02	8.1801E-04	-6.2012E+01	3.8454E+03	4.5653E+04	6.3117E+00
63	0.1205E+04	-2.2710E-02	8.2958E-04	-2.7375E+01	7.4940E+02	4.4904E+04	6.2624E+00
64	0.1178E+04	1.5149E-02	8.4925E-04	1.7837E+01	3.1816E+02	4.4586E+04	6.2429E+00
65	0.1166E+04	-4.7141E-02	8.5749E-04	-5.4975E+01	3.0223E+03	4.1563E+04	6.0302E+00
66	0.1155E+04	3.6278E-03	8.6604E-04	4.1889E+00	1.7547E+01	4.1546E+04	6.0316E+00
67	0.1144E+04	3.9649E-02	8.7441E-04	4.5342E+01	2.0559E+03	3.9490E+04	5.8830E+00
68	0.1136E+04	2.8541E-02	8.8046E-04	3.2416E+01	1.0508E+03	3.8439E+04	5.8068E+00
69	0.1105E+04	-1.8259E-02	9.0477E-04	-2.0180E+01	4.0724E+02	3.8032E+04	5.7785E+00
70	0.1097E+04	-3.0231E-02	9.1154E-04	-3.3150E+01	1.0989E+03	3.6933E+04	5.6969E+00
71	0.1087E+04	-1.0479E-02	9.1968E-04	-1.1394E+01	1.2983E+02	3.6803E+04	5.6893E+00
72	0.1066E+04	-1.5360E-02	9.3803E-04	-1.6375E+01	2.6813E+02	3.6535E+04	5.6711E+00
73	0.1061E+04	1.9314E-03	9.4223E-04	2.0503E+00	4.2035E+00	3.6531E+04	5.6732E+00
74	0.1024E+04	1.7873E-02	9.7625E-04	1.8329E+01	3.3594E+02	3.6195E+04	5.6496E+00
75	0.1023E+04	-2.7100E-02	9.8030E-04	-2.7645E+01	7.6423E+02	3.5431E+04	5.5921E+00
76	0.1005E+04	-1.2501E-03	9.9523E-04	-1.2561E+00	1.5778E+00	3.5429E+04	5.5944E+00
77	0.9719E+03	-1.1684E-02	1.0290E-03	-1.1355E+01	1.2894E+02	3.5300E+04	5.5867E+00
78	0.9549E+03	-7.0911E-02	1.0472E-03	-6.7716E+01	4.5854E+03	3.0715E+04	5.2136E+00
79	0.9462E+03	4.5440E-02	1.0569E-03	4.2994E+01	1.8485E+03	2.8866E+04	5.0565E+00
80	0.9326E+03	2.6410E-02	1.0722E-03	2.4632E+01	6.0672E+02	2.8260E+04	5.0053E+00
81	0.9178E+03	2.3861E-03	1.0895E-03	2.1901E+00	4.7965E+00	2.8255E+04	5.0071E+00
82	0.8962E+03	2.9819E-02	1.1159E-03	2.6723E+01	7.1411E+02	2.7541E+04	4.9456E+00
83	0.8837E+03	-4.7484E-02	1.1316E-03	-4.1961E+01	1.7607E+03	2.5780E+04	4.7870E+00
84	0.8725E+03	-5.8058E-02	1.1461E-03	-5.0658E+01	2.5663E+03	2.3214E+04	4.5445E+00
85	0.8627E+03	1.5075E-02	1.1591E-03	1.3005E+01	1.6913E+02	2.3044E+04	4.5300E+00
86	0.8384E+03	3.6479E-03	1.1925E-03	3.0590E+00	9.3575E+00	2.3035E+04	4.5310E+00
87	0.8276E+03	-5.3379E-02	1.2084E-03	-4.4175E+01	1.9514E+03	2.1084E+04	4.3369E+00
88	0.8230E+03	3.3489E-02	1.2151E-03	2.7560E+01	7.5955E+02	2.0324E+04	4.2599E+00
89	0.8123E+03	3.2775E-02	1.2311E-03	2.6623E+01	7.0878E+02	1.9615E+04	4.1868E+00
90	0.8005E+03	-9.4019E-03	1.2493E-03	-7.5260E+00	5.6641E+01	1.9559E+04	4.1826E+00
91	0.7915E+03	2.3474E-02	1.2634E-03	1.8583E+01	3.4533E+02	1.9213E+04	4.1474E+00
92	0.7700E+03	-2.9211E-02	1.2987E-03	-2.2493E+01	5.0596E+02	1.8707E+04	4.0943E+00
93	0.7502E+03	4.3369E-02	1.3330E-03	3.2534E+01	1.0585E+03	1.7649E+04	3.9785E+00
94	0.7194E+03	4.2624E-02	1.3901E-03	3.0663E+01	9.4021E+02	1.6709E+04	3.8728E+00
95	0.6990E+03	3.9219E-02	1.4306E-03	2.7413E+01	7.5150E+02	1.5957E+04	3.7864E+00
96	0.6947E+03	-8.1715E-03	1.4395E-03	-5.6767E+00	3.2225E+01	1.5925E+04	3.7843E+00
97	0.6722E+03	2.4934E-02	1.4877E-03	1.6760E+01	2.8089E+02	1.5644E+04	3.7525E+00
98	0.6640E+03	-4.0796E-03	1.5059E-03	-2.7091E+00	7.3390E+00	1.5637E+04	3.7533E+00
99	0.6448E+03	-3.4691E-02	1.5432E-03	-2.2480E+01	5.0537E+02	1.5131E+04	3.6938E+00
100	0.6284E+03	1.9881E-02	1.5913E-03	1.2494E+01	1.5609E+02	1.4975E+04	3.6764E+00
101	0.6196E+03	2.5948E-02	1.6141E-03	1.6076E+01	2.5843E+02	1.4717E+04	3.6461E+00
102	0.6169E+03	1.0313E-02	1.6211E-03	6.3519E+00	4.0473E+01	1.4676E+04	3.6428E+00
			1.6705E-03	2.1815E+01	4.7588E+02	1.4201E+04	3.5845E+00
							3.4445E+00

106	0.5820E+03	-1.5369E-02	1.7183E-03	-8.944CE+00	7.9995E+01	1.2318E+04	3.3433E+00
107	0.5641E+03	-2.4690E-02	1.7728E-03	-1.3927E+01	1.9396E+02	1.2124E+04	3.3184E+00
108	0.5545E+03	4.8053E-02	1.8033E-03	2.6648E+01	7.1009E+02	1.1414E+04	3.2212E+00
109	0.5514E+03	5.6262E-02	1.8136E-03	3.1023E+01	9.6243E+02	1.0452E+04	3.0839E+00
110	0.5407E+03	-1.2416E-02	1.8494E-03	-6.7136E+00	4.5072E+01	1.0407E+04	3.0786E+00
111	0.5212E+03	-1.2396E-02	1.9185E-03	-6.4612E+00	4.1747E+01	1.0365E+04	3.0738E+00
112	0.5098E+03	7.5623E-02	1.9614E-03	3.8555E+01	1.4865E+03	8.8783E+03	2.8462E+00
113	0.4792E+03	-2.5726E-02	2.0867E-03	-1.2328E+01	1.5199E+02	8.7264E+03	2.8230E+00
114	0.4682E+03	3.5813E-02	2.1357E-03	1.8642E+01	3.4752E+02	8.3788E+03	2.7675E+00
115	0.4592E+03	-4.2016E-03	2.1775E-03	-1.9296E+00	3.7233E+00	8.3751E+03	2.7681E+00
116	0.4506E+03	1.6053E-02	2.2193E-03	7.2334E+00	5.2322E+01	8.3228E+03	2.7607E+00
117	0.4284E+03	4.9602E-02	2.3341E-03	2.1251E+01	4.5160E+02	7.8712E+03	2.6860E+00
118	0.4242E+03	-3.3985E-02	2.3572E-03	-1.4417E+01	2.0786E+02	7.6633E+03	2.6515E+00
119	0.4153E+03	7.0875E-03	2.4078E-03	2.9436E+00	8.6649E+00	7.6547E+03	2.6512E+00
120	0.3962E+03	2.4460E-03	2.5239E-03	9.6912E-01	9.3920E-01	7.6537E+03	2.6523E+00
121	0.3679E+03	-1.4605E-02	2.5781E-03	-5.6656E+00	3.2099E+01	7.6216E+03	2.6479E+00
122	0.3794E+03	-3.0024E-02	2.6332E-03	-1.1402E+01	1.3000E+02	7.4916E+03	2.6265E+00
123	0.3677E+03	-6.6809E-02	2.7196E-03	-2.4566E+01	6.0350E+02	6.8881E+03	2.5196E+00
124	0.3629E+03	4.9624E-02	2.7555E-03	1.8009E+01	3.2433E+02	6.5638E+03	2.4607E+00
125	0.3544E+03	-7.4621E-02	2.8213E-03	-2.6095E+01	6.8095E+02	5.8929E+03	2.3307E+00
126	0.3539E+03	-5.8333E-03	2.8257E-03	-2.0644E+00	4.2616E+00	5.8786E+03	2.3309E+00
127	0.3483E+03	3.1226E-03	2.8708E-03	1.0877E+00	1.1832E+00	5.8774E+03	2.3317E+00
128	0.3225E+03	8.6651E-03	3.1005E-03	2.7947E+00	7.8105E+00	5.8696E+03	2.3313E+00
129	0.3171E+03	1.1864E-02	3.1540E-03	3.7616E+00	1.4150E+01	5.8554E+03	2.3295E+00
130	0.3095E+03	2.9690E-02	3.2312E-03	9.1887E+00	8.4432E+01	5.7710E+03	2.3138E+00
131	0.3077E+03	-4.2858E-02	3.2504E-03	-1.3185E+01	1.7385E+02	5.5972E+03	2.2797E+00
132	0.2980E+03	-3.6791E-02	3.3562E-03	-1.0962E+01	1.2017E+02	5.4770E+03	2.2561E+00
133	0.2933E+03	-9.9394E-03	3.4091E-03	-2.9156E+00	8.5007E+00	5.4685E+03	2.2554E+00
134	0.2880E+03	-1.0504E-01	3.4725E-03	-3.0250E+01	9.1506E+02	4.5534E+03	2.0591E+00
135	0.2806E+03	-1.7407E-02	3.5634E-03	-4.8849E+00	2.3862E+01	4.5296E+03	2.0546E+00
136	0.2747E+03	-1.9967E-03	3.6404E-03	-5.4849E-01	3.0084E-01	4.5293E+03	2.0555E+00
137	0.2719E+03	3.4130E-02	3.6789E-03	9.2771E+00	8.6065E+01	4.4432E+03	2.0368E+00
138	0.2582E+03	-9.9448E-03	3.8727E-03	-2.5680E+00	6.5944E+00	4.4366E+03	2.0363E+00
139	0.2510E+03	-6.8106E-02	3.9834E-03	-1.7098E+01	2.9233E+02	4.1443E+03	1.9690E+00
140	0.2451E+03	9.4104E-03	4.0802E-03	2.3063E+00	5.3192E+00	4.1390E+03	1.9686E+00
141	0.2345E+03	-7.2657E-02	4.2663E-03	-1.7043E+01	2.9045E+02	3.8485E+03	1.8992E+00
142	0.2302E+03	8.0211E-02	4.3441E-03	1.8482E+01	3.4160E+02	3.5069E+03	1.8138E+00
143	0.2284E+03	-2.4903E-02	4.3706E-03	-5.6978E+00	3.2465E+01	3.4745E+03	1.8062E+00
144	0.2183E+03	-1.2359E-02	4.5814E-03	-2.6976E+00	7.2768E+00	3.4672E+03	1.8052E+00
145	0.2144E+03	-4.6166E-03	4.6641E-03	-9.9981E-01	9.7972E-01	3.4662E+03	1.8058E+00
146	0.2124E+03	3.6556E-02	4.7065E-03	7.7637E+00	6.0276E+01	3.4059E+03	1.7908E+00
147	0.2101E+03	3.6923E-02	4.7602E-03	7.7566E+00	6.0165E+01	3.3458E+03	1.7758E+00
148	0.2081E+03	-3.7100E-02	4.8043E-03	-7.7222E+00	5.9633E+01	3.2861E+03	1.7607E+00
149	0.1976E+03	5.0404E-02	5.0611E-03	9.9591E+00	9.9184E+01	3.1869E+03	1.7348E+00
150	0.1933E+03	-6.4125E-02	5.1723E-03	-1.2398E+01	1.5370E+02	3.0332E+03	1.6932E+00
151	0.1847E+03	-9.3491E-02	5.4450E-03	-1.7170E+01	2.9481E+02	2.7384E+03	1.6096E+00
152	0.1825E+03	-2.2481E-03	5.4793E-03	-4.1030E-01	1.6835E-01	2.7383E+03	1.6103E+00
153	0.1773E+03	8.2783E-02	5.6408E-03	1.4676E+01	2.1538E+02	2.5229E+03	1.5464E+00
154	0.1728E+03	-1.1253E-02	5.7878E-03	-1.9443E+00	3.7803E+00	2.5191E+03	1.5460E+00
155	0.1711E+03	-8.7616E-02	5.8458E-03	-1.4988E+01	2.2464E+02	2.2945E+03	1.4761E+00
156	0.1653E+03	-2.5449E-02	6.0485E-03	-4.2066E+00	1.7691E+01	2.2768E+03	1.4711E+00
157	0.1608E+03	-8.1833E-02	6.2202E-03	-1.3156E+01	1.7308E+02	2.1037E+03	1.4148E+00
158	0.1591E+03	1.4365E-02	6.2849E-03	2.2856E+00	5.2240E+00	2.0945E+03	1.4137E+00
159	0.1578E+03	1.2948E-02	6.3381E-03	1.9955E+00	3.9821E+00	2.0945E+03	1.4130E+00
160	0.1554E+03	1.2794E-01	6.4338E-03	1.9885E+01	3.9543E+02	1.6991E+03	1.2733E+00
161	0.1514E+03	-6.1847E-03	6.6070E-03	-1.2388E+00	1.5346E+00	1.6975E+03	1.2733E+00
162	0.1481E+03	1.6837E-02	6.7518E-03	2.4937E+00	6.2186E+00	1.6913E+03	1.2716E+00
163	0.1466E+03	3.9395E-02	6.8100E-03	5.7848E+00	3.3464E+01	1.6578E+03	1.2595E+00
164	0.1417E+03	-7.9324E-03	7.0572E-03	-1.1240E+00	1.2634E+00	1.6566E+03	1.2597E+00
165	0.1399E+03	6.8868E-02	7.1484E-03	9.6340E+00	9.2814E+01	1.5638E+03	1.2245E+00

166	0.1383E+03	-3.8109E-02	7.2303E-03	-5.2707E+00	2.7780E+01	1.5360E+03	1.2141E+00
167	0.1364E+03	1.4518E-01	7.3312E-03	1.9802E+01	3.9213E+02	1.1438E+03	1.0482E+00
168	0.1337E+03	-2.0610E-02	7.4785E-03	-2.6757E+00	7.1593E+00	1.1367E+03	1.0455E+00
169	0.1329E+03	5.0759E-02	7.5269E-03	6.7436E+00	4.5476E+01	1.0912E+03	1.0248E+00
170	0.1286E+03	1.0379E-01	7.7748E-03	1.3349E+01	1.7821E+02	9.1301E+02	9.3786E-01
171	0.1273E+03	6.0476E-02	7.8575E-03	7.6967E+00	5.9239E+01	8.5377E+02	9.0736E-01
172	0.1224E+03	-7.8702E-03	8.1715E-03	-9.6313E-01	9.2762E-01	8.5284E+02	9.0731E-01
173	0.1186E+03	-5.9780E-02	8.4348E-03	-7.0872E+00	5.0229E+01	8.0261E+02	8.8061E-01
174	0.1159E+03	-7.4742E-02	8.6261E-03	-9.1284E+00	8.3327E+01	7.1928E+02	8.3405E-01
175	0.1129E+03	-1.7483E-02	8.8637E-03	-1.9724E+00	3.8905E+00	7.1530E+02	8.3219E-01
176	0.1085E+03	-2.6608E-02	9.1913E-03	-2.8949E+00	8.3806E+00	7.0701E+02	8.2770E-01
177	0.1059E+03	8.0513E-03	9.4450E-03	8.5234E-01	7.2648E-01	7.0629E+02	8.2768E-01
178	98.0128	-2.2397E-02	1.0203E-02	-2.1952E+00	4.8191E+00	7.0147E+02	8.2525E-01
179	92.2363	8.1645E-02	1.0842E-02	7.5306E+00	5.6710E+01	6.4476E+02	7.9157E-01
180	89.5340	3.0253E-02	1.1169E-02	2.7087E+00	7.3368E+00	6.3742E+02	7.8744E-01
181	88.1679	1.5049E-02	1.1342E-02	1.3268E+00	1.7604E+00	6.3566E+02	7.8673E-01
182	82.4185	1.0925E-02	1.2133E-02	1.6422E+00	2.6969E+00	6.3296E+02	7.8544E-01
183	81.2142	5.4784E-02	1.2313E-02	4.4493E+00	1.9796E+01	6.1317E+02	7.7344E-01
184	79.8715	-8.3253E-02	1.2520E-02	-6.6495E+00	4.4216E+01	5.6895E+02	7.4540E-01
185	77.5190	8.2771E-02	1.2900E-02	6.4163E+00	4.1169E+01	5.2778E+02	7.1827E-01
186	75.8618	-1.0719E-01	1.3182E-02	-8.1320E+00	6.6129E+01	4.6165E+02	6.7210E-01
187	72.0107	-4.3297E-03	1.3987E-02	-3.1179E-01	9.7210E-02	4.6155E+02	6.7236E-01
188	68.2831	-2.2102E-02	1.4645E-02	-1.5229E+00	2.3191E+00	4.5924E+02	6.7099E-01
189	66.0917	3.7179E-02	1.5130E-02	2.4572E+00	6.0378E+00	4.5320E+02	6.6689E-01
190	64.8022	-1.1104E-01	1.5432E-02	-7.1958E+00	5.1779E+01	4.0142E+02	6.2795E-01
191	62.7393	2.6366E-02	1.5939E-02	1.6542E+00	2.7363E+00	3.9868E+02	6.2611E-01
192	60.2139	2.4176E-02	1.6607E-02	1.4558E+00	2.1192E+00	3.9656E+02	6.2475E-01
193	58.0717	4.7592E-02	1.7220E-02	2.7638E+00	7.6385E+00	3.8892E+02	6.1901E-01
194	55.9048	-3.4897E-02	1.7868E-02	-1.9530E+00	3.8141E+00	3.8511E+02	6.1627E-01
195	54.1287	1.2835E-02	1.8474E-02	6.9582E-01	4.8417E-01	3.8463E+02	6.1619E-01
196	52.5642	1.4974E-01	1.9024E-02	7.8707E+00	6.1949E+01	3.2268E+02	5.6467E-01
197	50.9716	-3.0489E-02	1.9619E-02	-1.5541E+00	2.4152E+00	3.2026E+02	5.6283E-01
198	47.7509	1.8202E-02	2.0939E-02	8.6929E-01	7.5566E-01	3.1951E+02	5.6244E-01
199	45.5673	-2.0144E-02	2.1947E-02	-9.1781E-01	8.4238E-01	3.1866E+02	5.6198E-01
200	42.3723	1.7800E-01	2.3600E-02	7.5423E+00	5.6887E+01	2.6178E+02	5.0961E-01
201	41.5129	1.1315E-01	2.4089E-02	4.6973E+00	2.2064E+01	2.3971E+02	4.8790E-01
202	39.8991	2.1344E-01	2.5063E-02	8.5160E+00	7.2523E+01	1.6719E+02	4.0767E-01
203	36.5637	2.3978E-01	2.7350E-02	8.7673E+00	7.6866E+01	9.0325E+01	2.9579E-01
204	35.6154	-1.7175E-02	2.8077E-02	-6.1171E-01	3.7419E-01	8.9951E+01	2.9532E-01
205	33.1158	-2.8975E-02	3.0197E-02	-9.5953E-01	9.2069E-01	8.9030E+01	2.9793E-01
206	29.6677	-5.4120E-02	3.3707E-02	-1.6056E+00	2.5780E+00	8.6452E+01	2.9373E-01
207	26.3306	-6.6642E-02	3.7979E-02	-1.7547E+00	3.0791E+00	8.3373E+01	2.8860E-01
208	23.1220	-2.3010E-01	4.3249E-02	-5.3204E+00	2.8307E+01	5.5066E+01	2.3466E-01
209	19.7103	3.2938E-01	5.0735E-02	6.4922E+00	4.2148E+01	1.2918E+01	1.1372E-01
210	15.8098	-4.3364E-02	6.3252E-02	-6.8558E-01	4.7002E-01	1.2448E+01	1.1168E-01
211	14.0714	-2.5074E-01	7.1066E-02	-3.5282E+00	1.2448E+01	0.0	0.0

INDEX	YNORM	RNORM	LOG10(YNORM)	LOG10(RNORM)
0	0.0	0.11977E+04	-1000.00000	3.07836
1	0.35364E-01	0.11250E+04	-1.45144	3.05116
2	0.62446E-01	0.10067E+04	-1.20449	3.00290
3	0.87048E-01	0.89165E+03	-1.06024	2.95019
4	0.90141E-01	0.87555E+03	-1.04508	2.94248
5	0.10514E+00	0.79152E+03	-0.97822	2.90174
6	0.11196E+00	0.75741E+03	-0.95092	2.87933
7	0.11323E+00	0.75059E+03	-0.94605	2.87540
8	0.11347E+00	0.74948E+03	-0.94511	2.87476
9	0.14098E+00	0.60122E+03	-0.85085	2.77903
10	0.14102E+00	0.60095E+03	-0.85072	2.77884

11	0.14127E+00	0.59547E+03	-0.84994	2.77777
12	0.14190E+00	0.59624E+03	-0.84802	2.77542
13	0.14210E+00	0.59486E+03	-0.84712	2.77442
14	0.15185E+00	0.55157E+03	-0.81859	2.74160
15	0.15711E+00	0.52830E+03	-0.80379	2.72288
16	0.16140E+00	0.51140E+03	-0.79210	2.70876
17	0.15214E+00	0.50844E+03	-0.79010	2.70624
18	0.16634E+00	0.49199E+03	-0.77899	2.69196
19	0.16952E+00	0.47990E+03	-0.77078	2.68115
20	0.16953E+00	0.47986E+03	-0.77075	2.68111
21	0.17373E+00	0.46432E+03	-0.76012	2.66681
22	0.18760E+00	0.41247E+03	-0.72677	2.61539
23	0.18955E+00	0.40510E+03	-0.72225	2.60756
24	0.19110E+00	0.39912E+03	-0.71853	2.60110
25	0.19313E+00	0.39213E+03	-0.71415	2.59349
26	0.19340E+00	0.39090E+03	-0.71334	2.59207
27	0.19415E+00	0.38802E+03	-0.71186	2.58975
28	0.20300E+00	0.36137E+03	-0.69250	2.55795
29	0.20421E+00	0.35744E+03	-0.68993	2.55320
30	0.20439E+00	0.35684E+03	-0.68954	2.55248
31	0.20535E+00	0.35397E+03	-0.68752	2.54897
32	0.20711E+00	0.34879E+03	-0.68379	2.54257
33	0.20821E+00	0.34556E+03	-0.68150	2.53852
34	0.20934E+00	0.34519E+03	-0.68122	2.53806
35	0.20926E+00	0.34266E+03	-0.67931	2.53487
36	0.20927E+00	0.34264E+03	-0.67929	2.53484
37	0.20949E+00	0.34208E+03	-0.67883	2.53413
38	0.21272E+00	0.33403E+03	-0.67218	2.52378
39	0.21430E+00	0.33009E+03	-0.66899	2.51863
40	0.22770E+00	0.29473E+03	-0.64263	2.46943
41	0.23018E+00	0.28773E+03	-0.63703	2.45898
42	0.23257E+00	0.28091E+03	-0.63344	2.44841
43	0.23531E+00	0.27327E+03	-0.62837	2.43660
44	0.23543E+00	0.27295E+03	-0.62813	2.43608
45	0.23911E+00	0.26371E+03	-0.62140	2.42113
46	0.23918E+00	0.26353E+03	-0.62127	2.42083
47	0.24099E+00	0.25906E+03	-0.61800	2.41340
48	0.24225E+00	0.25604E+03	-0.61574	2.40831
49	0.24675E+00	0.24546E+03	-0.60775	2.38998
50	0.25083E+00	0.23583E+03	-0.60061	2.37260
51	0.25085E+00	0.23579E+03	-0.60058	2.37253
52	0.25119E+00	0.23502E+03	-0.60001	2.37111
53	0.25285E+00	0.23143E+03	-0.59714	2.36442
54	0.25301E+00	0.23109E+03	-0.59687	2.36378
55	0.25383E+00	0.22939E+03	-0.59546	2.36057
56	0.25473E+00	0.22753E+03	-0.59392	2.35704
57	0.25482E+00	0.22734E+03	-0.59376	2.35668
58	0.25491E+00	0.22716E+03	-0.59361	2.35634
59	0.25515E+00	0.22671E+03	-0.59321	2.35548
60	0.25731E+00	0.22252E+03	-0.58955	2.34737
61	0.25733E+00	0.22248E+03	-0.58951	2.34730
62	0.26228E+00	0.21367E+03	-0.58123	2.32974
63	0.26326E+00	0.21191E+03	-0.57961	2.32614
64	0.26170E+00	0.21115E+03	-0.57889	2.32460
65	0.26788E+00	0.20307E+03	-0.57206	2.30936
66	0.26790E+00	0.20383E+03	-0.57202	2.30926
67	0.27082E+00	0.19872E+03	-0.56732	2.29824
68	0.27232E+00	0.19606E+03	-0.56492	2.29239
69	0.27291E+00	0.19562E+03	-0.56395	2.29007
70	0.27460E+00	0.19219E+03	-0.56130	2.28371

71	0.27480E+00	0.19184E+03	-0.56098	2.28294
72	0.27523E+00	0.19114E+03	-0.56030	2.28135
73	0.27524E+00	0.19113E+03	-0.56029	2.28133
74	0.27582E+00	0.19025E+03	-0.55938	2.27932
75	0.27715E+00	0.18823E+03	-0.55729	2.27469
76	0.27715E+00	0.18823E+03	-0.55729	2.27468
77	0.27739E+00	0.18788E+03	-0.55690	2.27389
78	0.28631E+00	0.17526E+03	-0.54316	2.24367
79	0.28990E+00	0.16990E+03	-0.53775	2.23020
80	0.29110E+00	0.16811E+03	-0.53596	2.22558
81	0.29111E+00	0.16809E+03	-0.53595	2.22554
82	0.29263E+00	0.16585E+03	-0.53368	2.21999
83	0.29646E+00	0.16056E+03	-0.52804	2.20564
84	0.30209E+00	0.15236E+03	-0.51986	2.18287
85	0.30247E+00	0.15180E+03	-0.51932	2.18128
86	0.30249E+00	0.15177E+03	-0.51929	2.18120
87	0.30716E+00	0.14520E+03	-0.51263	2.16197
88	0.30898E+00	0.14256E+03	-0.51007	2.15401
89	0.31072E+00	0.14005E+03	-0.50764	2.14630
90	0.31086E+00	0.13985E+03	-0.50744	2.14567
91	0.31174E+00	0.13861E+03	-0.50620	2.14180
92	0.31311E+00	0.13678E+03	-0.50430	2.13601
93	0.31610E+00	0.13285E+03	-0.50018	2.12336
94	0.31896E+00	0.12926E+03	-0.49627	2.11147
95	0.32136E+00	0.12632E+03	-0.49301	2.10148
96	0.32146E+00	0.12619E+03	-0.49287	2.10104
97	0.32243E+00	0.12508E+03	-0.49156	2.09718
98	0.32246E+00	0.12505E+03	-0.49153	2.09707
99	0.32432E+00	0.12301E+03	-0.48903	2.08994
100	0.32493E+00	0.12247E+03	-0.48822	2.08769
101	0.32596E+00	0.12131E+03	-0.48684	2.08391
102	0.32612E+00	0.12115E+03	-0.48662	2.08331
103	0.32815E+00	0.11917E+03	-0.48392	2.07615
104	0.33298E+00	0.11445E+03	-0.47771	2.05861
105	0.33589E+00	0.11135E+03	-0.47380	2.04668
106	0.33624E+00	0.11099E+03	-0.47335	2.04527
107	0.33715E+00	0.11011E+03	-0.47218	2.04183
108	0.34055E+00	0.10684E+03	-0.46781	2.02872
109	0.34517E+00	0.10223E+03	-0.46197	2.00959
110	0.34539E+00	0.10201E+03	-0.46169	2.00865
111	0.34561E+00	0.10181E+03	-0.46141	2.00778
112	0.35379E+00	0.94225E+02	-0.45125	1.97417
113	0.35473E+00	0.93415E+02	-0.45011	1.97042
114	0.35695E+00	0.91516E+02	-0.44739	1.96159
115	0.35698E+00	0.91516E+02	-0.44736	1.96150
116	0.35734E+00	0.91229E+02	-0.44692	1.96013
117	0.36076E+00	0.88720E+02	-0.44278	1.94802
118	0.36236E+00	0.87540E+02	-0.44086	1.94221
119	0.36243E+00	0.87491E+02	-0.44077	1.94196
120	0.36244E+00	0.87486E+02	-0.44076	1.94194
121	0.36273E+00	0.87302E+02	-0.44041	1.94102
122	0.36397E+00	0.86554E+02	-0.43893	1.93729
123	0.37005E+00	0.82555E+02	-0.43173	1.91905
124	0.37337E+00	0.81017E+02	-0.42786	1.90858
125	0.38056E+00	0.76700E+02	-0.41958	1.88479
126	0.38060E+00	0.76672E+02	-0.41953	1.88464
127	0.38061E+00	0.76664E+02	-0.41952	1.88459
128	0.38071E+00	0.76613E+02	-0.41940	1.88430
129	0.38090E+00	0.76521E+02	-0.41919	1.88378
130	0.38205E+00	0.75567E+02	-0.41788	1.88063

131	0.38445E+00	0.74814E+02	-0.41516	1.87398
132	0.38620E+00	0.74007E+02	-0.41318	1.86927
133	0.38631E+00	0.73949E+02	-0.41304	1.86893
134	0.40036E+00	0.67479E+02	-0.39755	1.82917
135	0.40074E+00	0.67302E+02	-0.39714	1.82803
136	0.40074E+00	0.67300E+02	-0.39714	1.82801
137	0.40219E+00	0.66657E+02	-0.39557	1.82385
138	0.40232E+00	0.66609E+02	-0.39543	1.82353
139	0.40804E+00	0.64376E+02	-0.38930	1.80872
140	0.40815E+00	0.64335E+02	-0.38918	1.80845
141	0.41456E+00	0.62036E+02	-0.38241	1.79265
142	0.42227E+00	0.59219E+02	-0.37441	1.77246
143	0.42300E+00	0.58944E+02	-0.37366	1.77044
144	0.42313E+00	0.58883E+02	-0.37347	1.76999
145	0.42321E+00	0.58874E+02	-0.37345	1.76993
146	0.42478E+00	0.58360E+02	-0.37183	1.76612
147	0.42638E+00	0.57842E+02	-0.37020	1.76225
148	0.42900E+00	0.57325E+02	-0.36856	1.75834
149	0.43095E+00	0.56953E+02	-0.36557	1.75169
150	0.43570E+00	0.55075E+02	-0.36081	1.74095
151	0.44562E+00	0.52330E+02	-0.35104	1.71875
152	0.44562E+00	0.52329E+02	-0.35103	1.71874
153	0.45324E+00	0.50228E+02	-0.34367	1.70095
154	0.45338E+00	0.50191E+02	-0.34353	1.70062
155	0.46177E+00	0.47901E+02	-0.33557	1.68034
156	0.46247E+00	0.47716E+02	-0.33491	1.67866
157	0.46966E+00	0.45866E+02	-0.32822	1.66149
158	0.46988E+00	0.45809E+02	-0.32802	1.66095
159	0.47005E+00	0.45766E+02	-0.32786	1.66054
160	0.48715E+00	0.41220E+02	-0.31234	1.61510
161	0.48722E+00	0.41201E+02	-0.31228	1.61491
162	0.48751E+00	0.41125E+02	-0.31202	1.61411
163	0.48910E+00	0.40717E+02	-0.31061	1.60977
164	0.48916E+00	0.40701E+02	-0.31055	1.60960
165	0.49398E+00	0.39544E+02	-0.30629	1.59708
166	0.49945E+00	0.39192E+02	-0.30500	1.59319
167	0.51628E+00	0.33821E+02	-0.28711	1.52918
168	0.51667E+00	0.33715E+02	-0.28679	1.52782
169	0.51916E+00	0.33034E+02	-0.28470	1.51895
170	0.52941E+00	0.30216E+02	-0.27619	1.48024
171	0.53297E+00	0.29219E+02	-0.27338	1.46567
172	0.53293E+00	0.29203E+02	-0.27333	1.46543
173	0.53627E+00	0.28330E+02	-0.27061	1.45225
174	0.54202E+00	0.26819E+02	-0.26598	1.42845
175	0.54231E+00	0.26747E+02	-0.26576	1.42727
176	0.54296E+00	0.26590E+02	-0.26523	1.42471
177	0.54302E+00	0.26576E+02	-0.26519	1.42449
178	0.54348E+00	0.26495E+02	-0.26482	1.42300
179	0.54958E+00	0.25392E+02	-0.25997	1.40470
180	0.55041E+00	0.25247E+02	-0.25931	1.40221
181	0.55062E+00	0.25212E+02	-0.25915	1.40161
182	0.55098E+00	0.25159E+02	-0.25887	1.40069
183	0.55369E+00	0.24762E+02	-0.25673	1.39379
184	0.55992E+00	0.23853E+02	-0.25188	1.37754
185	0.56600E+00	0.22973E+02	-0.24718	1.36123
186	0.57606E+00	0.21486E+02	-0.23953	1.33216
187	0.57604E+00	0.21484E+02	-0.23952	1.33211
188	0.57651E+00	0.21430E+02	-0.23919	1.33102
189	0.57771E+00	0.21288E+02	-0.23829	1.32814
190	0.58828E+00	0.20035E+02	-0.23041	1.30180

191	0.56887E+00	0.19967E+02	-0.22998	1.30031
192	0.58937E+00	0.19914E+02	-0.22961	1.29916
193	0.59129E+00	0.19721E+02	-0.22920	1.29493
194	0.59232E+00	0.19624E+02	-0.22745	1.29279
195	0.59246E+00	0.19612E+02	-0.22734	1.29252
196	0.61109E+00	0.17963E+02	-0.21390	1.25438
197	0.61185E+00	0.17896E+02	-0.21336	1.25275
198	0.61212E+00	0.17875E+02	-0.21317	1.25224
199	0.61246E+00	0.17851E+02	-0.21293	1.25167
200	0.63779E+00	0.16180E+02	-0.19532	1.20897
201	0.64775E+00	0.15483E+02	-0.18859	1.18985
202	0.68201E+00	0.12930E+02	-0.16621	1.11161
203	0.72293E+00	0.95039E+01	-0.14090	0.97790
204	0.72314E+00	0.94842E+01	-0.14078	0.97700
205	0.72372E+00	0.94356E+01	-0.14043	0.97477
206	0.72574E+00	0.92980E+01	-0.13922	0.96839
207	0.72879E+00	0.91309E+01	-0.13740	0.96051
208	0.76425E+00	0.74207E+01	-0.11676	0.87044
209	0.83221E+00	0.35942E+01	-0.07977	0.55560
210	0.83334E+00	0.35282E+01	-0.07918	0.54755
211	0.87024E+00	0.0	-0.06036	-1000.00000

NORMS OF SOLUTION AND RESIDUAL VECTORS FOR A RANGE OF VALUES OF THE LEVENBERG-MARQUARDT PARAMETER, LAMBDA.

LAMBDA	YNORM	RNORM	LOG10(LAMBDA)	LOG10(YNORM)	LOG10(RNORM)
0.11620E+06	0.65417E-03	0.11928E+04	5.06521	-3.18431	3.07658
0.65573E+05	0.20330E-02	0.11829E+04	4.81937	-2.69832	3.07294
0.37456E+05	0.59759E-02	0.11538E+04	4.57352	-2.22359	3.06213
0.21266E+05	0.16646E-01	0.10778E+04	4.32768	-1.77868	3.03252
0.12073E+05	0.40141E-01	0.92109E+03	4.08183	-1.39642	2.96430
0.68547E+04	0.78554E-01	0.69731E+03	3.83599	-1.10483	2.84343
0.38919E+04	0.12576E+00	0.47559E+03	3.59015	-0.90046	2.67996
0.22095E+04	0.17552E+00	0.31216E+03	3.34430	-0.75566	2.49465
0.12545E+04	0.22612E+00	0.19909E+03	3.09846	-0.64566	2.29902
0.71222E+03	0.27719E+00	0.12604E+03	2.85261	-0.55722	2.10050
0.40436E+03	0.32867E+00	0.81120E+02	2.60677	-0.48324	1.90913
0.22958E+03	0.38430E+00	0.52965E+02	2.36093	-0.41533	1.72399
0.13034E+03	0.44981E+00	0.33613E+02	2.11508	-0.34697	1.52651
0.74001E+02	0.52090E+00	0.20993E+02	1.86924	-0.28333	1.32207
0.42014E+02	0.59710E+00	0.12555E+02	1.62339	-0.22396	1.11249
0.23853E+02	0.68312E+00	0.73335E+01	1.37755	-0.16550	0.86531
0.13543E+02	0.76564E+00	0.35720E+01	1.13171	-0.11586	0.55291
0.76889E+01	0.82427E+00	0.14571E+01	0.88586	-0.08393	0.16350
0.43654E+01	0.85326E+00	0.52069E+00	0.64002	-0.06892	-0.28342
0.24784E+01	0.86449E+00	0.17430E+00	0.39418	-0.06324	-0.75870
0.14071E+01	0.86836E+00	0.56906E-01	0.14833	-0.06130	-1.24484

EIGENVECTORS IN LAYER-BLOCK FORMAT
(ELEMENTS ARE SCALED UP BY FACTOR OF 10**4)

EIGENVECTOR OF EIGENVALUE NO. 1

LAYER ... 1

1.	1.	1.	1.	1.	1.	1.	1.	1.
1.	1.	1.	1.	1.	1.	1.	1.	1.
1.	1.	-301.	-151.	-220.	1.	-1256.	1.	1.
1.	6.	6405.	-365.	-243.	1.	12.	1.	1.
1.	-24.	-2.	-2758.	-597.	-116.	-24.	1.	1.
1.	-4.	3.	-140.	-58.	-510.	3.	1.	1.
1.	1.	-148.	1.	-164.	18.	-5.	1.	1.
1.	1.	1.	1.	1.	1.	1.	1.	1.
1.	1.	1.	1.	1.	1.	1.	1.	1.

LAYER ... 2

1.	1.	1.	1.	1.	1.	1.	1.	1.	1.
1.	1.	1.	1.	1.	1.	1.	1.	1.	1.
1.	1.	-386.	-449.	-80.	-644.	-301.	-54.	1.	1.
1.	1.	3872.	532.	-470.	-35.	-330.	-11.	1.	1.
1.	-9.	1230.	-1105.	-733.	-102.	-24.	-206.	1.	1.
1.	-4.	-35.	-535.	-582.	-434.	-3.	6.	1.	1.
1.	1.	-100.	-42.	-41.	-25.	19.	6.	1.	1.
1.	1.	-20.	13.	-16.	22.	8.	1.	1.	1.
1.	1.	1.	1.	1.	0.	3.	1.	1.	1.
1.	1.	1.	1.	1.	1.	1.	1.	1.	1.

LAYER ... 3

1.	1.	1.	1.	1.	1.	1.	1.	1.	1.	1.
1.	1.	-28.	1.	1.	-36.	1.	1.	1.	1.	1.
1.	5.	-434.	-79.	-110.	-780.	-45.	-150.	-14.	1.	1.
1.	948.	3485.	257.	333.	-217.	-88.	1.	-15.	1.	1.
1.	-12.	245.	-935.	-442.	-257.	-211.	-17.	-5.	1.	1.
1.	-21.	502.	62.	69.	-303.	-17.	-21.	-182.	1.	1.
1.	-4.	-60.	-186.	-16.	-143.	-129.	27.	4.	1.	1.
1.	-5.	-20.	1.	38.	1.	-35.	28.	10.	1.	1.
1.	1.	1.	-5.	6.	9.	19.	-4.	-5.	1.	1.
1.	1.	1.	1.	7.	-8.	3.	6.	1.	1.	1.
1.	1.	1.	1.	1.	2.	3.	1.	1.	1.	1.

LAYER ... 4

1.	1.	1.	1.	1.	1.	1.	1.	1.	1.	1.	1.
1.	-34.	38.	1.	-82.	-20.	-16.	-61.	1.	-14.	1.	1.
7.	-212.	-362.	-122.	37.	-421.	-84.	-56.	-40.	1.	1.	1.
1.	1972.	2559.	8.	136.	-170.	-106.	-11.	-8.	1.	-7.	1.
-9.	-17.	310.	-802.	-227.	-39.	-91.	-38.	-16.	-5.	1.	1.
1.	-14.	92.	-399.	-272.	-111.	-152.	-4.	-1.	-3.	1.	1.
1.	74.	425.	63.	-103.	198.	-109.	-39.	-41.	-130.	-29.	1.
-4.	1.	-44.	-105.	-43.	100.	-36.	-91.	20.	4.	3.	1.
-5.	1.	-24.	-5.	-26.	52.	56.	-51.	9.	6.	1.	1.

1.	1.	1.	1.	1.	11.	-30.	-16.	-6.	-6.	1.	1.
1.	1.	1.	1.	1.	1.	3.	3.	9.	2.	1.	1.
1.	1.	1.	1.	5.	-21.	3.	0.	1.	1.	1.	1.

EIGENVECTOR OF EIGENVALUE NO. 2

LAYER ... 1

1.	1.	1.	1.	1.	1.	1.	1.	1.
1.	1.	1.	1.	1.	1.	1.	1.	1.
1.	1.	522.	314.	118.	1.	2491.	1.	1.
1.	16.	-1963.	95.	524.	1.	86.	1.	1.
1.	65.	357.	-5316.	394.	153.	85.	1.	1.
1.	4.	107.	401.	168.	764.	58.	1.	1.
1.	1.	289.	1.	277.	88.	10.	1.	1.
1.	1.	1.	1.	1.	1.	1.	1.	1.
1.	1.	1.	1.	1.	1.	1.	1.	1.

LAYER ... 2

1.	1.	1.	1.	1.	1.	1.	1.	1.	1.
1.	1.	1.	1.	1.	1.	1.	1.	1.	1.
1.	1.	719.	534.	133.	951.	456.	98.	1.	1.
1.	1.	172.	273.	317.	31.	655.	21.	1.	1.
1.	10.	335.	-6095.	267.	143.	69.	705.	1.	1.
1.	4.	92.	-321.	-1378.	857.	151.	0.	1.	1.
1.	1.	172.	169.	6.	180.	114.	47.	1.	1.
1.	1.	40.	56.	73.	91.	47.	1.	1.	1.
1.	1.	1.	1.	1.	12.	12.	1.	1.	1.
1.	1.	1.	1.	1.	1.	1.	1.	1.	1.

LAYER ... 3

1.	1.	1.	1.	1.	1.	1.	1.	1.	1.	1.
1.	1.	23.	1.	1.	33.	1.	1.	1.	1.	1.
1.	30.	874.	302.	228.	1178.	76.	200.	14.	1.	1.
1.	113.	-394.	89.	-14.	213.	142.	1.	15.	1.	1.
1.	16.	-719.	-891.	275.	-122.	437.	10.	9.	1.	1.
1.	39.	322.	-1075.	1.	576.	29.	67.	608.	1.	1.
1.	4.	76.	14.	36.	-1440.	276.	140.	38.	1.	1.
1.	4.	45.	1.	113.	-104.	76.	142.	41.	1.	1.
1.	1.	1.	4.	3.	55.	148.	20.	11.	1.	1.
1.	1.	1.	1.	24.	-32.	26.	31.	1.	1.	1.
1.	1.	1.	1.	1.	11.	12.	1.	1.	1.	1.

LAYER ... 4

1.	1.	1.	1.	1.	1.	1.	1.	1.	1.	1.	1.
1.	51.	-1.	1.	81.	13.	10.	66.	1.	14.	1.	1.
18.	427.	590.	226.	461.	816.	60.	52.	83.	1.	1.	1.
1.	104.	-749.	26.	20.	-6.	143.	6.	4.	1.	11.	1.
19.	50.	-731.	-1044.	186.	-74.	-121.	21.	10.	9.	1.	1.
1.	44.	117.	-154.	501.	282.	227.	0.	-0.	2.	1.	1.

1.	-12.	204.	-1168.	101.	-142.	298.	70.	128.	482.	63.	1.
4.	1.	-1.	116.	43.	-12.	-1428.	59.	109.	-4.	10.	1.
4.	1.	49.	5.	64.	41.	-51.	130.	177.	69.	1.	1.
1.	1.	1.	1.	1.	-0.	-67.	66.	21.	7.	1.	1.
1.	1.	1.	1.	1.	16.	8.	43.	56.	4.	1.	1.
1.	1.	1.	1.	12.	-78.	12.	12.	1.	1.	1.	1.

EIGENVECTOR OF EIGENVALUE NO. 61

LAYER ... 1

1.	1.	1.	1.	1.	1.	1.	1.	1.
1.	1.	1.	1.	1.	1.	1.	1.	1.
1.	1.	-274.	93.	-340.	1.	-55.	1.	1.
1.	-59.	163.	-104.	-473.	1.	-394.	1.	1.
1.	489.	-202.	-105.	-174.	-47.	24.	1.	1.
1.	11.	136.	-549.	-1458.	161.	248.	1.	1.
1.	1.	-291.	1.	-678.	135.	17.	1.	1.
1.	1.	1.	1.	1.	1.	1.	1.	1.
1.	1.	1.	1.	1.	1.	1.	1.	1.

LAYER ... 2

1.	1.	1.	1.	1.	1.	1.	1.	1.	1.
1.	1.	1.	1.	1.	1.	1.	1.	1.	1.
1.	1.	575.	61.	58.	185.	0.	2.	1.	1.
1.	1.	120.	306.	-336.	78.	-89.	-12.	1.	1.
1.	21.	-35.	141.	55.	11.	-18.	-1385.	1.	1.
1.	-17.	-171.	76.	-94.	-77.	-288.	96.	1.	1.
1.	1.	-66.	-322.	580.	472.	19.	82.	1.	1.
1.	1.	11.	-78.	36.	-203.	15.	1.	1.	1.
1.	1.	1.	1.	1.	-50.	11.	1.	1.	1.
1.	1.	1.	1.	1.	1.	1.	1.	1.	1.

LAYER ... 3

1.	1.	1.	1.	1.	1.	1.	1.	1.	1.	1.
1.	1.	31.	1.	1.	36.	1.	1.	1.	1.	1.
1.	68.	-288.	20.	-178.	291.	-71.	116.	13.	1.	1.
1.	-767.	300.	-319.	-894.	468.	72.	1.	-35.	1.	1.
1.	48.	4788.	317.	-627.	376.	-1071.	36.	-11.	1.	1.
1.	-16.	-696.	462.	-1060.	-334.	80.	-125.	259.	1.	1.
1.	-13.	50.	-550.	384.	2.	-393.	-164.	-308.	1.	1.
1.	-22.	26.	1.	136.	536.	484.	-252.	129.	1.	1.
1.	1.	1.	-62.	41.	128.	340.	15.	17.	1.	1.
1.	1.	1.	1.	-88.	85.	-44.	-7.	1.	1.	1.
1.	1.	1.	1.	1.	-29.	24.	1.	1.	1.	1.

LAYER ... 4

1.	1.	1.	1.	1.	1.	1.	1.	1.	1.	1.	1.
1.	24.	-14.	1.	-6.	36.	17.	53.	1.	13.	1.	1.
-61.	-71.	-276.	-114.	-423.	-363.	-2.	82.	-12.	1.	1.	1.

1.	13.	-579.	1954.	-664.	1119.	185.	13.	-34.	1.	7.	1.
22.	526.	-6817.	-203.	-495.	-144.	27.	-221.	31.	-16.	1.	1.
1.	321.	248.	-730.	1461.	-282.	-583.	-60.	4.	108.	1.	1.
1.	-160.	755.	-1056.	-245.	-936.	66.	56.	-190.	952.	-21.	1.
-13.	1.	-28.	10.	113.	-509.	-122.	664.	-143.	-7.	-146.	1.
-37.	1.	-41.	23.	-151.	98.	-312.	-667.	-53.	-112.	1.	1.
1.	1.	1.	1.	1.	4.	223.	519.	27.	-3.	1.	1.
1.	1.	1.	1.	1.	-21.	45.	26.	-32.	12.	1.	1.
1.	1.	1.	1.	-40.	81.	20.	-55.	1.	1.	1.	1.

EIGENVECTOR OF EIGENVALUE NO. 136

LAYER ... 1

1.	1.	1.	1.	1.	1.	1.	1.	1.
1.	1.	1.	1.	1.	1.	1.	1.	1.
1.	1.	14.	86.	-34.	1.	22.	1.	1.
1.	-12.	9.	3.	80.	1.	852.	1.	1.
1.	635.	27.	-73.	77.	-100.	-193.	1.	1.
1.	284.	271.	15.	72.	10.	-55.	1.	1.
1.	1.	-496.	1.	-592.	278.	-202.	1.	1.
1.	1.	1.	1.	1.	1.	1.	1.	1.
1.	1.	1.	1.	1.	1.	1.	1.	1.

LAYER ... 2

1.	1.	1.	1.	1.	1.	1.	1.	1.	1.
1.	1.	1.	1.	1.	1.	1.	1.	1.	1.
1.	1.	-38.	160.	-30.	96.	-70.	-12.	1.	1.
1.	1.	-2.	-45.	38.	499.	109.	-303.	1.	1.
1.	270.	-31.	-10.	-48.	-41.	-239.	-49.	1.	1.
1.	114.	501.	79.	-37.	11.	257.	-276.	1.	1.
1.	1.	-46.	-164.	-306.	-22.	-129.	-227.	1.	1.
1.	1.	-299.	792.	-1344.	114.	1.	1.	1.	1.
1.	1.	1.	1.	1.	-57.	-490.	1.	1.	1.
1.	1.	1.	1.	1.	1.	1.	1.	1.	1.

LAYER ... 3

1.	1.	1.	1.	1.	1.	1.	1.	1.	1.	1.
1.	1.	186.	1.	1.	-1163.	1.	1.	1.	1.	1.
1.	-18.	-22.	-35.	343.	265.	278.	-285.	122.	1.	1.
1.	-19.	48.	23.	-37.	253.	-485.	1.	-108.	1.	1.
1.	537.	11.	-13.	-57.	-239.	-0.	440.	-65.	1.	1.
1.	-142.	316.	169.	-60.	-12.	-61.	467.	-95.	1.	1.
1.	147.	4090.	136.	53.	10.	7.	393.	-827.	1.	1.
1.	237.	74.	1.	-243.	-14.	-17.	29.	-251.	1.	1.
1.	1.	1.	194.	-1002.	-184.	105.	57.	-29.	1.	1.
1.	1.	1.	1.	432.	970.	-240.	-27.	1.	1.	1.
1.	1.	1.	1.	1.	-609.	-482.	1.	1.	1.	1.

LAYER ... 4

1.	1.	1.	1.	1.	1.	1.	1.	1.	1.	1.	1.
1.	550.	-442.	1.	-2653.	18.	-378.	128.	1.	186.	1.	1.
-26.	-111.	-54.	-116.	-258.	-64.	-1193.	316.	68.	1.	1.	1.
1.	-58.	-19.	28.	74.	-19.	-122.	-176.	24.	1.	-139.	1.
124.	565.	59.	142.	96.	382.	749.	-438.	568.	-74.	1.	1.
1.	-309.	-48.	172.	80.	-81.	-67.	-327.	61.	881.	1.	1.
1.	1632.	-634.	-96.	-43.	58.	-13.	89.	-136.	-54.	586.	1.
69.	1.	-6125.	-42.	-70.	-48.	-31.	-21.	-722.	-239.	-384.	1.
156.	1.	104.	135.	2432.	-229.	-1.	-8.	-121.	414.	1.	1.
1.	1.	1.	1.	1.	1101.	58.	193.	-8.	295.	1.	1.
1.	1.	1.	1.	1.	-198.	-563.	66.	-188.	154.	1.	1.
1.	1.	1.	1.	-48.	2919.	-188.	-158.	1.	1.	1.	1.

EIGENVECTOR OF EIGENVALUE NO. 205

LAYER ... 1

1.	1.	1.	1.	1.	1.	1.	1.	1.
1.	1.	1.	1.	1.	1.	1.	1.	1.
1.	1.	9.	-32.	111.	1.	25.	1.	1.
1.	-128.	24.	20.	-2.	1.	198.	1.	1.
1.	-551.	25.	-7.	-29.	16.	212.	1.	1.
1.	927.	-33.	14.	14.	-117.	-84.	1.	1.
1.	1.	31.	1.	-35.	-69.	-410.	1.	1.
1.	1.	1.	1.	1.	1.	1.	1.	1.
1.	1.	1.	1.	1.	1.	1.	1.	1.

LAYER ... 2

1.	1.	1.	1.	1.	1.	1.	1.	1.	1.
1.	1.	1.	1.	1.	1.	1.	1.	1.	1.
1.	1.	-59.	-9.	-488.	-42.	-198.	-787.	1.	1.
1.	1.	21.	1.	32.	44.	111.	-1942.	1.	1.
1.	-180.	-29.	-18.	-1.	27.	-603.	-14.	1.	1.
1.	551.	2.	9.	-5.	63.	49.	677.	1.	1.
1.	1.	-12.	10.	-34.	-34.	6.	216.	1.	1.
1.	1.	130.	-148.	216.	27.	-574.	1.	1.	1.
1.	1.	1.	1.	1.	-998.	2000.	1.	1.	1.
1.	1.	1.	1.	1.	1.	1.	1.	1.	1.

LAYER ... 3

1.	1.	1.	1.	1.	1.	1.	1.	1.	1.	1.
1.	1.	757.	1.	1.	-217.	1.	1.	1.	1.	1.
1.	-113.	118.	-14.	7.	-2.	778.	144.	-1713.	1.	1.
1.	-92.	-13.	-18.	-0.	-172.	12.	1.	-1367.	1.	1.
1.	-553.	-55.	5.	-9.	80.	-140.	314.	75.	1.	1.
1.	-165.	-12.	10.	-8.	3.	-21.	-42.	27.	1.	1.
1.	401.	-82.	15.	-16.	-3.	-25.	-69.	-1125.	1.	1.
1.	-1984.	324.	1.	-113.	-5.	42.	7.	-120.	1.	1.
1.	1.	1.	1499.	86.	-21.	9.	873.	-313.	1.	1.
1.	1.	1.	1.	312.	410.	337.	183.	1.	1.	1.
1.	1.	1.	1.	1.	-231.	-544.	1.	1.	1.	1.

LAYER ... 4

1.	1.	1.	1.	1.	1.	1.	1.	1.	1.	1.
1.	-837.	-3519.	1.	-29.	-44.	466.	302.	1.	1354.	1.	1.
1346.	-90.	-46.	-91.	26.	-24.	17.	-270.	189.	1.	1.	1.
1.	17.	-45.	-20.	-64.	-21.	-2.	3945.	337.	1.	3575.	1.
-35.	1405.	18.	11.	14.	15.	-167.	84.	-388.	750.	1.	1.
1.	306.	15.	6.	29.	7.	4.	57.	23.	-272.	1.	1.
1.	619.	21.	-4.	62.	25.	-18.	-31.	17.	-32.	8.	1.
-1034.	1.	242.	22.	112.	-29.	-17.	18.	-64.	893.	2064.	1.
2013.	1.	-210.	2585.	-29.	-37.	-26.	12.	1.	184.	1.	1.
1.	1.	1.	1.	1.	62.	-121.	-11.	-1052.	116.	1.	1.
1.	1.	1.	1.	1.	-8.	-311.	-56.	-11.	1984.	1.	1.
1.	1.	1.	1.	98.	-238.	-166.	124.	1.	1.	1.	1.

EIGENVECTOR OF EIGENVALUE NO. 211

LAYER ... 1

1.	1.	1.	1.	1.	1.	1.	1.	1.
1.	1.	1.	1.	1.	1.	1.	1.	1.
1.	1.	8.	7.	-2.	1.	4.	1.	1.
1.	6567.	17.	-3.	-3.	1.	11.	1.	1.
1.	118.	-9.	1.	12.	-3.	-75.	1.	1.
1.	597.	-38.	-8.	-0.	20.	22.	1.	1.
1.	1.	18.	1.	23.	26.	94.	1.	1.
1.	1.	1.	1.	1.	1.	1.	1.	1.
1.	1.	1.	1.	1.	1.	1.	1.	1.

LAYER ... 2

1.	1.	1.	1.	1.	1.	1.	1.	1.	1.
1.	1.	1.	1.	1.	1.	1.	1.	1.	1.
1.	1.	3.	-2.	-68.	14.	-10.	-17.	1.	1.
1.	1.	-31.	-2.	3.	31.	7.	-8.	1.	1.
1.	4238.	10.	2.	1.	24	6.	-11.	1.	1.
1.	-1686.	33.	0.	3.	-9.	12.	55.	1.	1.
1.	1.	2.	-3.	-2.	-18.	-11.	-63.	1.	1.
1.	1.	135.	-142.	-138.	7.	16.	1.	1.	1.
1.	1.	1.	1.	1.	-1833.	-91.	1.	1.	1.
1.	1.	1.	1.	1.	1.	1.	1.	1.	1.

LAYER ... 3

1.	1.	1.	1.	1.	1.	1.	1.	1.	1.	1.
1.	1.	-216.	1.	1.	-184.	1.	1.	1.	1.	1.
1.	65.	-9.	6.	41.	-12.	-47.	-1.	629.	1.	1.
1.	-154.	-23.	-8.	5.	-14.	-2.	1.	-942.	1.	1.
1.	-1088.	-10.	4.	1.	10.	7.	-198.	2.	1.	1.
1.	-57.	-3.	-2.	-3.	-4.	-3.	-5.	-2.	1.	1.
1.	2279.	-14.	1.	3.	-4.	-6.	2.	-25.	1.	1.
1.	-360.	48.	1.	51.	1.	-2.	-7.	-5.	1.	1.
1.	1.	1.	641.	77.	180.	-1.	-61.	111.	1.	1.
1.	1.	1.	1.	-38.	236.	-122.	-84.	1.	1.	1.

1.	1.	1.	1.	1.	770.	24.	1.	1.	1.	1.	

LAYER ... 4

1.	1.	1.	1.	1.	1.	1.	1.	1.	1.	1.	1.
1.	55.	28.	1.	44.	-190.	383.	54.	1.	-227.	1.	1.
-2784.	1.	-4.	-10.	7.	11.	43.	34.	-55.	1.	1.	1.
1.	95.	14.	14.	-5.	1.	7.	5.	1431.	1.	-72.	1.
-3276.	260.	0.	3.	-3.	16.	-34.	-24.	132.	73.	1.	1.
1.	37.	-6.	-5.	-9.	-4.	-18.	18.	370.	-21.	1.	1.
1.	59.	-0.	4.	1.	-4.	-12.	-2.	-4.	-6.	42.	1.
-981.	1.	33.	6.	2.	-5.	-5.	-4.	15.	-108.	-40.	1.
116.	1.	-99.	17.	-7.	4.	-11.	1.	-2.	29.	1.	1.
1.	1.	1.	1.	1.	-1.	-51.	-41.	-27.	35.	1.	1.
1.	1.	1.	1.	1.	-7.	-330.	-8.	59.	-428.	1.	1.
1.	1.	1.	1.	314.	-134.	19.	834.	1.	1.	1.	1.

SOLUTION, RESOLUTION , AND COVARIANCE WITH VARIOUS EIGENVALUE CUTOFFS
THIS PROBLEM HAS 0 ZERO EIGENVALUES

SOLUTION NO. 1 THIS SOLUTION HAS 150 EIGENVALUES REMOVED IN ADDITION TO THE ZERO EIGENVALUES

LAYER ... 1

99.99	99.99	99.99	99.99	99.99	99.99	99.99	99.99	99.99
99.99	99.99	99.99	99.99	99.99	99.99	99.99	99.99	99.99
99.99	99.99	0.19	0.51	0.29	99.99	0.90	99.99	99.99
99.99	0.04	-0.09	-0.46	1.09	99.99	0.49	99.99	99.99
99.99	0.03	0.45	-0.64	-4.77	-1.89	-0.08	99.99	99.99
99.99	0.04	0.58	-4.72	-5.54	-5.19	0.70	99.99	99.99
99.99	99.99	0.09	99.99	-0.61	1.06	0.21	99.99	99.99
99.99	99.99	99.99	99.99	99.99	99.99	99.99	99.99	99.99
99.99	99.99	99.99	99.99	99.99	99.99	99.99	99.99	99.99

LAYER ... 2

99.99	99.99	99.99	99.99	99.99	99.99	99.99	99.99	99.99	99.99
99.99	99.99	99.99	99.99	99.99	99.99	99.99	99.99	99.99	99.99
99.99	99.99	1.41	5.84	0.36	-0.69	0.59	0.07	99.99	99.99
99.99	99.99	1.38	0.45	0.57	-0.23	3.45	0.08	99.99	99.99
99.99	-0.04	2.94	-1.85	-1.73	-5.06	0.20	2.18	99.99	99.99
99.99	0.05	0.07	-1.22	-0.78	0.33	0.18	0.32	99.99	99.99
99.99	99.99	-0.17	-0.61	-2.11	-3.55	0.91	0.32	99.99	99.99
99.99	99.99	0.21	0.44	0.07	0.88	0.22	99.99	99.99	99.99
99.99	99.99	99.99	99.99	99.99	0.04	0.09	99.99	99.99	99.99
99.99	99.99	99.99	99.99	99.99	99.99	99.99	99.99	99.99	99.99

LAYER ... 3

99.99	99.99	99.99	99.99	99.99	99.99	99.99	99.99	99.99	99.99	99.99
99.99	99.99	-0.05	99.99	99.99	-0.13	99.99	99.99	99.99	99.99	99.99
99.99	-0.05	5.91	1.92	1.93	3.73	0.08	-0.16	-0.02	99.99	99.99
99.99	1.96	1.65	1.40	1.11	0.24	0.56	99.99	-0.00	99.99	99.99
99.99	-0.01	-1.21	0.48	-3.94	-3.30	3.56	-0.27	0.06	99.99	99.99
99.99	-0.00	0.62	-2.50	-2.19	-1.85	-2.35	-0.00	6.83	99.99	99.99
99.99	0.04	0.32	-4.64	-1.51	-0.67	-1.32	0.50	0.36	99.99	99.99
99.99	0.06	0.16	99.99	1.46	-2.66	-2.36	0.58	0.25	99.99	99.99
99.99	99.99	99.99	0.04	0.43	-0.13	-0.01	0.12	0.24	99.99	99.99
99.99	99.99	99.99	99.99	-0.12	-0.17	0.08	0.15	99.99	99.99	99.99
99.99	99.99	99.99	99.99	99.99	-0.11	0.10	99.99	99.99	99.99	99.99

LAYER ... 4

99.99	99.99	99.99	99.99	99.99	99.99	99.99	99.99	99.99	99.99	99.99	99.99
99.99	-0.04	0.12	99.99	0.44	0.19	0.12	-0.04	99.99	-0.01	99.99	99.99
0.05	1.56	5.52	0.50	2.68	4.49	0.22	-0.11	0.07	99.99	99.99	99.99
99.99	3.25	4.13	0.67	0.47	1.23	-0.32	0.10	-0.03	99.99	0.03	99.99
-0.04	0.07	-0.28	-1.04	-1.73	-0.84	-1.02	-0.24	-0.25	0.06	99.99	99.99
99.99	0.03	0.08	-1.58	-1.50	0.54	2.78	-0.47	-0.01	0.48	99.99	99.99
99.99	0.17	0.80	-0.38	-0.90	-0.04	-0.36	-1.89	0.30	6.54	0.94	99.99
0.05	99.99	-0.02	-4.64	-0.49	-1.06	-1.90	-0.83	0.22	0.06	0.17	99.99
0.06	99.99	0.22	0.01	0.23	0.71	-4.11	-2.38	0.78	0.31	99.99	99.99

RESOLUTION MATRIX DIAGONAL ELEMENTS

LAYER ... 1

0.0	0.0	0.0	0.0	0.0	0.0	0.0	0.0	0.0
0.0	0.0	0.0	0.0	0.0	0.0	0.0	0.0	0.0
0.0	0.0	0.946E+00	0.910E+00	0.102E+00	0.0	0.944E+00	0.0	0.0
0.0	0.402E-03	0.993E+00	0.969E+00	0.940E+00	0.0	0.312E-01	0.0	0.0
0.0	0.682E-02	0.977E+00	0.993E+00	0.954E+00	0.202E+00	0.362E-01	0.0	0.0
0.0	0.114E-03	0.221E+00	0.934E+00	0.805E+00	0.967E+00	0.224E-01	0.0	0.0
0.0	0.0	0.659E+00	0.0	0.658E+00	0.103E+00	0.153E-02	0.0	0.0
0.0	0.0	0.0	0.0	0.0	0.0	0.0	0.0	0.0
0.0	0.0	0.0	0.0	0.0	0.0	0.0	0.0	0.0

LAYER ... 2

0.0	0.0	0.0	0.0	0.0	0.0	0.0	0.0	0.0	0.0
0.0	0.0	0.0	0.0	0.0	0.0	0.0	0.0	0.0	0.0
0.0	0.0	0.311E+00	0.638E+00	0.183E-01	0.374E+00	0.132E+00	0.344E-02	0.0	0.0
0.0	0.0	0.978E+00	0.995E+00	0.884E+00	0.444E-02	0.346E+00	0.762E-03	0.0	0.0
0.0	0.238E-03	0.977E+00	0.990E+00	0.981E+00	0.513E+00	0.100E-01	0.878E+00	0.0	0.0
0.0	0.129E-03	0.141E-01	0.974E+00	0.970E+00	0.958E+00	0.572E+00	0.179E-02	0.0	0.0
0.0	0.0	0.118E+00	0.366E+00	0.206E+00	0.405E+00	0.324E+00	0.996E-02	0.0	0.0
0.0	0.0	0.158E-01	0.852E-01	0.200E-01	0.225E+00	0.360E-02	0.0	0.0	0.0
0.0	0.0	0.0	0.0	0.0	0.408E-03	0.522E-03	0.0	0.0	0.0
0.0	0.0	0.0	0.0	0.0	0.0	0.0	0.0	0.0	0.0

LAYER ... 3

0.0	0.0	0.0	0.0	0.0	0.0	0.0	0.0	0.0	0.0	0.0
0.0	0.0	0.554E-03	0.0	0.0	0.201E-02	0.0	0.0	0.0	0.0	0.0
0.0	0.177E-02	0.570E+00	0.17CE+00	0.177E+00	0.604E+00	0.406E-02	0.165E-01	0.207E-03	0.0	0.0
0.0	0.332E+00	0.956E+00	0.860E+00	0.668E+00	0.226E+00	0.186E-01	0.0	0.837E-03	0.0	0.0
0.0	0.116E-02	0.957E+00	0.981E+00	0.830E+00	0.22CE+00	0.446E+00	0.190E-02	0.475E-03	0.0	0.0
0.0	0.447E-02	0.981E+00	0.972E+00	0.813E+00	0.982E+00	0.191E+00	0.928E-02	0.489E+00	0.0	0.0
0.0	0.142E-03	0.594E-01	0.534E+00	0.626E+00	0.964E+00	0.587E+00	0.808E-01	0.188E-01	0.0	0.0
0.0	0.809E-03	0.153E-01	0.0	0.232E+00	0.401E+00	0.392E+00	0.482E+00	0.101E-01	0.0	0.0
0.0	0.0	0.0	0.50CE-03	0.814E-01	0.111E-01	0.143E+00	0.116E-02	0.169E-02	0.0	0.0
0.0	0.0	0.0	0.0	0.411E-02	0.222E-02	0.171E-02	0.132E-02	0.0	0.0	0.0
0.0	0.0	0.0	0.0	0.0	0.139E-02	0.532E-03	0.0	0.0	0.0	0.0

LAYER ... 4

0.0	0.0	0.0	0.0	0.0	0.0	0.0	0.0	0.0	0.0	0.0	0.0
0.0	0.355E-02	0.503E-03	0.0	0.123E-01	0.346E-02	0.796E-03	0.429E-02	0.0	0.208E-03	0.0	0.0
0.478E-03	0.195E+00	0.326E+00	0.355E-01	0.530E+00	0.718E+00	0.376E-01	0.310E-02	0.222E-02	0.0	0.0	0.0
0.0	0.684E+00	0.979E+00	0.295E+00	0.174E+00	0.476E+00	0.259E-01	0.127E-02	0.733E-03	0.0	0.175E-03	0.0
0.242E-03	0.735E-02	0.929E+00	0.954E+00	0.163E+00	0.191E-01	0.355E-01	0.123E-01	0.134E-02	0.493E-03	0.0	0.0
0.0	0.549E-02	0.170E+00	0.928E+00	0.833E+00	0.402E-01	0.189E+00	0.446E-02	0.174E-03	0.504E-02	0.0	0.0

0.0	0.252E-02	0.892E+00	0.925E+00	0.766E-01	0.175E+00	0.889E+00	0.165E+00	0.254E-01	0.518E+00	0.825E-02	0.0
0.133E-03	0.0	0.648E-02	0.454E+00	0.353E-01	0.409E+00	0.942E+00	0.489E+00	0.918E-01	0.666E-03	0.400E-02	0.0
0.833E-03	0.0	0.167E-01	0.141E-02	0.432E-01	0.155E+00	0.516E+00	0.305E+00	0.172E+00	0.105E-01	0.0	0.0
0.0	0.0	0.0	0.0	0.0	0.914E-02	0.382E-01	0.184E+00	0.103E-02	0.864E-03	0.0	0.0
0.0	0.0	0.0	0.0	0.0	0.435E-02	0.135E-02	0.130E-01	0.459E-02	0.265E-03	0.0	0.0
0.0	0.0	0.0	0.0	0.110E-02	0.351E-02	0.185E-02	0.405E-03	0.0	0.0	0.0	0.0

COVARIANCE MATRIX DIAGONAL ELEMENTS

LAYER ... 1

0.0	0.0	0.0	0.0	0.0	0.0	0.0	0.0	0.0
0.0	0.0	0.0	0.0	0.0	0.0	0.0	0.0	0.0
0.0	0.0	0.136E-06	0.228E-06	0.392E-07	0.0	0.858E-07	0.0	0.0
0.0	0.101E-09	0.383E-07	0.556E-07	0.206E-06	0.0	0.119E-07	0.0	0.0
0.0	0.281E-08	0.111E-06	0.402E-07	0.929E-07	0.841E-07	0.142E-07	0.0	0.0
0.0	0.416E-10	0.757E-07	0.381E-06	0.284E-06	0.143E-06	0.862E-08	0.0	0.0
0.0	0.0	0.195E-06	0.0	0.163E-06	0.169E-07	0.392E-09	0.0	0.0
0.0	0.0	0.0	0.0	0.0	0.0	0.0	0.0	0.0
0.0	0.0	0.0	0.0	0.0	0.0	0.0	0.0	0.0

LAYER ... 2

0.0	0.0	0.0	0.0	0.0	0.0	0.0	0.0	0.0	0.0
0.0	0.0	0.0	0.0	0.0	0.0	0.0	0.0	0.0	0.0
0.0	0.0	0.826E-07	0.182E-06	0.540E-08	0.119E-06	0.451E-07	0.813E-09	0.0	0.0
0.0	0.0	0.120E-06	0.942E-07	0.180E-06	0.160E-08	0.974E-07	0.239E-09	0.0	0.0
0.0	0.566E-10	0.245E-06	0.488E-07	0.785E-07	0.160E-06	0.374E-08	0.325E-06	0.0	0.0
0.0	0.477E-10	0.527E-08	0.115E-06	0.766E-07	0.142E-06	0.259E-06	0.761E-09	0.0	0.0
0.0	0.0	0.324E-07	0.133E-06	0.630E-07	0.813E-07	0.497E-07	0.365E-08	0.0	0.0
0.0	0.0	0.523E-09	0.282E-07	0.783E-08	0.587E-07	0.101E-08	0.0	0.0	0.0
0.0	0.0	0.0	0.0	0.0	0.120E-09	0.192E-09	0.0	0.0	0.0
0.0	0.0	0.0	0.0	0.0	0.0	0.0	0.0	0.0	0.0

LAYER ... 3

0.0	0.0	0.0	0.0	0.0	0.0	0.0	0.0	0.0	0.0	0.0	
0.0	0.0	0.176E-09	0.0	0.0	0.704E-09	0.0	0.0	0.0	0.0	0.0	
0.0	0.564E-09	0.891E-07	0.552E-07	0.759E-07	0.105E-06	0.152E-08	0.396E-08	0.466E-10	0.0	0.0	
0.0	0.746E-07	0.930E-07	0.153E-06	0.283E-06	0.968E-07	0.585E-08	0.0	0.321E-09	0.0	0.0	
0.0	0.366E-09	0.285E-06	0.132E-06	0.184E-06	0.857E-07	0.140E-06	0.546E-09	0.188E-09	0.0	0.0	
0.0	0.135E-08	0.300E-06	0.216E-06	0.259E-06	0.187E-06	0.496E-07	0.377E-08	0.757E-07	0.0	0.0	
0.0	0.533E-10	0.257E-07	0.175E-06	0.989E-07	0.137E-06	0.126E-06	0.332E-07	0.721E-08	0.0	0.0	
0.0	0.273E-09	0.502E-08	0.0	0.769E-07	0.830E-07	0.129E-06	0.815E-07	0.404E-08	0.0	0.0	
0.0	0.0	0.0	0.166E-09	0.273E-07	0.427E-08	0.429E-07	0.351E-09	0.426E-09	0.0	0.0	
0.0	0.0	0.0	0.0	0.144E-08	0.597E-09	0.442E-09	0.370E-09	0.0	0.0	0.0	
0.0	0.0	0.0	0.0	0.0	0.581E-09	0.198E-09	0.0	0.0	0.0	0.0	

LAYER ... 4

0.0	0.0	0.0	0.0	0.0	0.0	0.0	0.0	0.0	0.0	0.0	0.0
0.0	0.104E-08	0.150E-09	0.0	0.364E-08	0.993E-09	0.216E-09	0.128E-08	0.0	0.470E-10	0.0	0.0
0.121E-09	0.330E-07	0.945E-07	0.135E-07	0.185E-06	0.217E-06	0.134E-07	0.104E-08	0.581E-09	0.0	0.0	0.0

0.0	0.154E-06	0.641E-07	0.942E-07	0.781E-07	0.234E-06	0.109E-07	0.376E-09	0.277E-09	0.0	0.441E-10	0.0
0.687E-10	0.314E-08	0.408E-06	0.169E-06	0.450E-07	0.648E-08	0.147E-07	0.482E-08	0.352E-09	0.196E-09	0.0	0.0
0.0	0.209E-08	0.807E-07	0.285E-06	0.374E-06	0.115E-07	0.532E-07	0.162E-08	0.638E-10	0.191E-08	0.0	0.0
0.0	0.766E-09	0.290E-06	0.263E-06	0.197E-07	0.696E-07	0.317E-06	0.470E-07	0.621E-08	0.149E-06	0.156E-08	0.0
0.496E-10	0.0	0.248E-08	0.162E-06	0.696E-08	0.688E-07	0.128E-06	0.147E-06	0.405E-07	0.225E-09	0.150E-08	0.0
0.283E-09	0.0	0.550E-08	0.482E-09	0.137E-07	0.520E-07	0.109E-06	0.109E-06	0.284E-07	0.388E-08	0.0	0.0
0.0	0.0	0.0	0.0	0.0	0.242E-08	0.917E-08	0.516E-07	0.274E-09	0.234E-09	0.0	0.0
0.0	0.0	0.0	0.0	0.0	0.134E-08	0.557E-09	0.374E-08	0.126E-08	0.730E-10	0.0	0.0
0.0	0.0	0.0	0.0	0.314E-09	0.114E-08	0.406E-09	0.127E-09	0.0	0.0	0.0	0.0

SOLUTION NO. 2 THIS SOLUTION HAS 75 EIGENVALUES REMOVED IN ADDITION TO THE ZERO EIGENVALUES

LAYER ... 1

99.99	99.99	99.99	99.99	99.99	99.99	99.99	99.99	99.99
99.99	99.99	99.99	99.99	99.99	99.99	99.99	99.99	99.99
99.99	99.99	0.14	0.66	-1.90	99.99	0.70	99.99	99.99
99.99	-0.02	0.25	-0.41	-0.84	99.99	10.03	99.99	99.99
99.99	2.89	-0.15	-0.42	-3.65	-7.67	-1.19	99.99	99.99
99.99	0.37	-0.15	-3.62	-4.15	-4.55	5.51	99.99	99.99
99.99	99.99	-1.52	99.99	0.25	0.19	1.21	99.99	99.99
99.99	99.99	99.99	99.99	99.99	99.99	99.99	99.99	99.99
99.99	99.99	99.99	99.99	99.99	99.99	99.99	99.99	99.99

LAYER ... 2

99.99	99.99	99.99	99.99	99.99	99.99	99.99	99.99	99.99	99.99
99.99	99.99	99.99	99.99	99.99	99.99	99.99	99.99	99.99	99.99
99.99	99.99	1.80	5.70	0.97	0.82	5.53	5.46	99.99	99.99
99.99	99.99	0.82	0.78	1.50	-1.13	-0.21	-0.48	99.99	99.99
99.99	1.34	1.89	-1.45	-0.70	-0.40	1.78	0.58	99.99	99.99
99.99	-0.60	2.53	-1.09	-0.06	0.65	-0.42	3.15	99.99	99.99
99.99	99.99	-2.14	0.37	-1.98	-3.51	0.60	2.57	99.99	99.99
99.99	99.99	2.15	0.92	-0.23	2.66	1.69	99.99	99.99	99.99
99.99	99.99	99.99	99.99	99.99	-0.26	-0.09	99.99	99.99	99.99
99.99	99.99	99.99	99.99	99.99	99.99	99.99	99.99	99.99	99.99

LAYER ... 3

99.99	99.99	99.99	99.99	99.99	99.99	99.99	99.99	99.99	99.99	99.99
99.99	99.99	-0.18	99.99	99.99	0.46	99.99	99.99	99.99	99.99	99.99
99.99	0.13	2.88	1.18	3.99	2.49	3.56	1.84	1.44	99.99	99.99
99.99	4.32	1.96	0.29	-0.12	2.49	4.10	99.99	-0.72	99.99	99.99
99.99	2.52	-0.58	0.69	-2.72	-5.17	4.48	-1.81	-0.11	99.99	99.99
99.99	-0.36	1.16	-2.03	-1.08	-1.54	-1.63	1.79	2.11	99.99	99.99
99.99	-0.49	-0.01	-1.83	-1.27	0.48	0.25	1.04	5.10	99.99	99.99
99.99	0.95	1.93	99.99	0.76	-0.78	-3.86	2.21	4.49	99.99	99.99
99.99	99.99	99.99	0.31	3.92	-1.28	-2.12	0.22	2.65	99.99	99.99
99.99	99.99	99.99	99.99	-0.61	-0.44	-0.65	0.59	99.99	99.99	99.99
99.99	99.99	99.99	99.99	99.99	-0.36	-0.16	99.99	99.99	99.99	99.99

LAYER ... 4

99.99	99.99	99.99	99.99	99.99	99.99	99.99	99.99	99.99	99.99	99.99	99.99
99.99	-1.03	-0.15	99.99	1.92	-0.02	0.11	0.93	99.99	1.56	99.99	99.99
-0.05	6.05	8.25	1.51	4.80	3.57	-1.00	0.58	6.33	99.99	99.99	99.99
99.99	3.21	4.99	4.14	4.67	2.45	3.66	0.49	-0.71	99.99	-0.24	99.99
1.32	3.54	-0.26	-1.57	-3.02	-4.00	-5.63	-0.87	-1.19	-0.22	99.99	99.99
99.99	-0.35	1.16	-2.40	-2.42	3.38	2.22	-1.39	-0.67	1.87	99.99	99.99
99.99	0.57	0.76	-1.49	-4.42	-0.28	0.40	-4.85	8.13	10.16	1.67	99.99
-0.09	99.99	-0.09	-8.73	-8.23	1.05	-1.88	-2.92	3.44	0.62	2.52	99.99
0.13	99.99	1.71	-0.34	3.22	0.41	-8.60	-0.29	-1.08	-0.04	99.99	99.99
99.99	99.99	99.99	99.99	99.99	-0.34	2.07	-0.08	-0.48	1.75	99.99	99.99
99.99	99.99	99.99	99.99	99.99	-0.31	-1.01	-0.87	3.64	0.87	99.99	99.99

RESOLUTION MATRIX DIAGONAL ELEMENTS

LAYER ... 1

0.0	0.0	0.0	0.0	0.0	0.0	0.0	0.0	0.0
0.0	0.0	0.0	0.0	0.0	0.0	0.0	0.0	0.0
0.0	0.0	0.999E+00	0.999E+00	0.996E+00	0.0	0.999E+00	0.0	0.0
0.0	0.320E-02	0.100E+01	0.999E+00	0.997E+00	0.0	0.772E+00	0.0	0.0
0.0	0.244E+00	0.999E+00	0.100E+01	0.999E+00	0.979E+00	0.920E+00	0.0	0.0
0.0	0.869E-02	0.987E+00	0.999E+00	0.997E+00	0.996E+00	0.787E+00	0.0	0.0
0.0	0.0	0.980E+00	0.0	0.973E+00	0.962E+00	0.977E-01	0.0	0.0
0.0	0.0	0.0	0.0	0.0	0.0	0.0	0.0	0.0
0.0	0.0	0.0	0.0	0.0	0.0	0.0	0.0	0.0

LAYER ... 2

0.0	0.0	0.0	0.0	0.0	0.0	0.0	0.0	0.0	0.0
0.0	0.0	0.0	0.0	0.0	0.0	0.0	0.0	0.0	0.0
0.0	0.0	0.982E+00	0.997E+00	0.925E+00	0.995E+00	0.946E+00	0.354E+00	0.0	0.0
0.0	0.0	0.999E+00	0.100E+01	0.998E+00	0.147E+00	0.992E+00	0.128E-01	0.0	0.0
0.0	0.612E-01	0.996E+00	0.100E+01	0.100E+01	0.995E+00	0.911E+00	0.993E+00	0.0	0.0
0.0	0.122E-01	0.891E+00	0.999E+00	0.100E+01	0.999E+00	0.972E+00	0.193E+00	0.0	0.0
0.0	0.0	0.895E+00	0.999E+00	0.972E+00	0.986E+00	0.992E+00	0.506E+00	0.0	0.0
0.0	0.0	0.146E+00	0.904E+00	0.629E+00	0.944E+00	0.336E+00	0.0	0.0	0.0
0.0	0.0	0.0	0.0	0.0	0.839E-02	0.197E-01	0.0	0.0	0.0
0.0	0.0	0.0	0.0	0.0	0.0	0.0	0.0	0.0	0.0

LAYER ... 3

0.0	0.0	0.0	0.0	0.0	0.0	0.0	0.0	0.0	0.0	0.0
0.0	0.0	0.947E-02	0.0	0.0	0.868E-01	0.0	0.0	0.0	0.0	0.0
0.0	0.569E-01	0.997E+00	0.998E+00	0.980E+00	0.993E+00	0.149E+00	0.717E+00	0.310E-01	0.0	0.0
0.0	0.995E+00	0.100E+01	0.100E+01	0.998E+00	0.986E+00	0.897E+00	0.0	0.239E-01	0.0	0.0
0.0	0.192E+00	0.997E+00	0.100E+01	0.999E+00	0.991E+00	0.992E+00	0.196E+00	0.133E-01	0.0	0.0
0.0	0.154E+00	0.995E+00	0.999E+00	0.999E+00	0.100E+01	0.971E+00	0.850E+00	0.982E+00	0.0	0.0
0.0	0.683E-02	0.836E+00	0.998E+00	0.999E+00	0.100E+01	0.999E+00	0.981E+00	0.513E+00	0.0	0.0
0.0	0.150E-01	0.277E+00	0.0	0.982E+00	0.997E+00	0.995E+00	0.996E+00	0.463E+00	0.0	0.0
0.0	0.0	0.0	0.264E-01	0.939E+00	0.132E+00	0.949E+00	0.993E-02	0.373E+00	0.0	0.0
0.0	0.0	0.0	0.0	0.654E-01	0.532E-01	0.465E-01	0.120E+00	0.0	0.0	0.0
0.0	0.0	0.0	0.0	0.0	0.424E-01	0.189E-01	0.0	0.0	0.0	0.0

LAYER ... 4

0.0	0.0	0.0	0.0	0.0	0.0	0.0	0.0	0.0	0.0	0.0	0.0
0.0	0.513E-01	0.172E-01	0.0	0.418E+00	0.189E-01	0.565E-01	0.184E+00	0.0	0.357E-01	0.0	0.0
0.407E-02	0.993E+00	0.999E+00	0.987E+00	0.992E+00	0.997E+00	0.878E+00	0.132E+00	0.427E+00	0.0	0.0	0.0
0.0	0.998E+00	0.999E+00	0.999E+00	0.992E+00	0.996E+00	0.969E+00	0.258E-01	0.184E-01	0.0	0.393E-02	0.0
0.628E-01	0.331E+00	0.998E+00	0.999E+00	0.998E+00	0.980E+00	0.918E+00	0.761E+00	0.159E+00	0.150E-01	0.0	0.0
0.0	0.871E-01	0.987E+00	0.998E+00	0.998E+00	0.997E+00	0.996E+00	0.401E-01	0.269E-01	0.116E+00	0.0	0.0
0.0	0.244E-01	0.998E+00	0.998E+00	0.997E+00	0.999E+00	0.998E+00	0.996E+00	0.988E+00	0.999E+00	0.673E-01	0.0

COVARIANCE MATRIX DIAGONAL ELEMENTS

LAYER ... 1

0.0	0.0	0.0	0.0	0.0	0.0	0.0	0.0	0.0
0.0	0.0	0.0	0.0	0.0	0.0	0.0	0.0	0.0
0.0	0.0	0.192E-06	0.402E-06	0.162E-05	0.0	0.169E-06	0.0	0.0
0.0	0.517E-08	0.514E-07	0.778E-07	0.418E-06	0.0	0.570E-05	0.0	0.0
0.0	0.243E-05	0.163E-06	0.514E-07	0.190E-06	0.128E-05	0.311E-05	0.0	0.0
0.0	0.857E-07	0.271E-05	0.455E-06	0.456E-06	0.207E-06	0.232E-05	0.0	0.0
0.0	0.0	0.140E-05	0.0	0.870E-06	0.239E-05	0.960E-06	0.0	0.0
0.0	0.0	0.0	0.0	0.0	0.0	0.0	0.0	0.0
0.0	0.0	0.0	0.0	0.0	0.0	0.0	0.0	0.0

LAYER ... 2

0.0	0.0	0.0	0.0	0.0	0.0	0.0	0.0	0.0	0.0
0.0	0.0	0.0	0.0	0.0	0.0	0.0	0.0	0.0	0.0
0.0	0.0	0.653E-06	0.632E-06	0.386E-05	0.723E-06	0.210E-05	0.286E-05	0.0	0.0
0.0	0.0	0.142E-06	0.113E-06	0.365E-06	0.106E-05	0.136E-05	0.114E-06	0.0	0.0
0.0	0.631E-06	0.317E-06	0.658E-07	0.106E-06	0.894E-06	0.605E-05	0.601E-06	0.0	0.0
0.0	0.119E-06	0.580E-05	0.155E-06	0.125E-06	0.193E-06	0.104E-05	0.140E-05	0.0	0.0
0.0	0.0	0.256E-05	0.136E-05	0.874E-06	0.877E-06	0.160E-05	0.245E-05	0.0	0.0
0.0	0.0	0.710E-06	0.532E-05	0.308E-05	0.226E-05	0.246E-05	0.0	0.0	0.0
0.0	0.0	0.0	0.0	0.0	0.363E-07	0.110E-06	0.0	0.0	0.0
0.0	0.0	0.0	0.0	0.0	0.0	0.0	0.0	0.0	0.0

LAYER ... 3

0.0	0.0	0.0	0.0	0.0	0.0	0.0	0.0	0.0	0.0	0.0
0.0	0.0	0.808E-07	0.0	0.0	0.798E-06	0.0	0.0	0.0	0.0	0.0
0.0	0.365E-06	0.711E-06	0.174E-05	0.141E-05	0.800E-06	0.145E-05	0.308E-05	0.346E-06	0.0	0.0
0.0	0.734E-06	0.136E-06	0.277E-06	0.113E-05	0.181E-05	0.614E-05	0.0	0.171E-06	0.0	0.0
0.0	0.194E-05	0.350E-06	0.159E-06	0.452E-06	0.149E-05	0.172E-05	0.176E-05	0.520E-07	0.0	0.0
0.0	0.990E-06	0.518E-06	0.269E-06	0.618E-06	0.219E-06	0.227E-05	0.863E-05	0.746E-06	0.0	0.0
0.0	0.604E-07	0.421E-05	0.105E-05	0.672E-06	0.181E-06	0.556E-06	0.381E-05	0.257E-05	0.0	0.0
0.0	0.101E-06	0.139E-05	0.0	0.177E-05	0.873E-06	0.104E-05	0.832E-06	0.180E-05	0.0	0.0
0.0	0.0	0.0	0.186E-06	0.331E-05	0.568E-06	0.173E-05	0.366E-07	0.372E-05	0.0	0.0
0.0	0.0	0.0	0.0	0.336E-06	0.387E-06	0.208E-06	0.762E-06	0.0	0.0	0.0
0.0	0.0	0.0	0.0	0.0	0.241E-06	0.103E-06	0.0	0.0	0.0	0.0

LAYER ... 4

0.0	0.0	0.0	0.0	0.0	0.0	0.0	0.0	0.0	0.0	0.0	0.0
0.0	0.429E-06	0.144E-06	0.0	0.442E-05	0.491E-07	0.309E-06	0.929E-06	0.0	0.401E-06	0.0	0.0
0.848E-08	0.110E-05	0.948E-06	0.472E-05	0.638E-06	0.629E-06	0.673E-05	0.687E-06	0.361E-05	0.0	0.0	0.0
0.0	0.472E-06	0.102E-06	0.804E-06	0.260E-05	0.920E-06	0.330E-05	0.136E-06	0.119E-06	0.0	0.314E-07	0.0
0.646E-06	0.333E-05	0.489E-06	0.281E-06	0.118E-05	0.498E-05	0.564E-05	0.717E-05	0.155E-05	0.673E-07	0.0	0.0

0.0	0.432E-06	0.139E-05	0.410E-06	0.621E-06	0.232E-05	0.209E-05	0.179E-06	0.199E-06	0.970E-06	0.0	0.0
0.0	0.524E-06	0.549E-06	0.449E-06	0.289E-05	0.154E-05	0.511E-06	0.163E-05	0.333E-05	0.802E-06	0.391E-06	0.0
0.256E-07	0.0	0.609E-05	0.130E-05	0.669E-05	0.601E-06	0.264E-06	0.668E-06	0.446E-05	0.298E-06	0.386E-06	0.0
0.726E-07	0.0	0.320E-05	0.613E-07	0.272E-05	0.240E-05	0.602E-06	0.920E-06	0.101E-05	0.406E-05	0.0	0.0
0.0	0.0	0.0	0.0	0.0	0.769E-05	0.247E-05	0.170E-05	0.112E-06	0.290E-05	0.0	0.0
0.0	0.0	0.0	0.0	0.0	0.232E-06	0.332E-06	0.225E-06	0.486E-05	0.624E-06	0.0	0.0
0.0	0.0	0.0	0.0	0.887E-07	0.163E-05	0.738E-07	0.506E-07	0.0	0.0	0.0	0.0

SOLUTION NO. 3 THIS SOLUTION HAS 6 EIGENVALUES REMOVED IN ADDITION TO THE ZERO EIGENVALUES

LAYER ••• 1

99.99	99.99	99.99	99.99	99.99	99.99	99.99	99.99	99.99
99.99	99.99	99.99	99.99	99.99	99.99	99.99	99.99	99.99
99.99	99.99	0.29	0.78	-2.02	99.99	0.65	99.99	99.99
99.99	1.08	0.30	-0.50	-0.78	99.99	4.98	99.99	99.99
99.99	-3.84	-0.23	-0.68	-3.49	-8.36	-1.45	99.99	99.99
99.99	0.37	0.19	-3.56	-3.94	-4.40	2.81	99.99	99.99
99.99	99.99	-0.76	99.99	-1.01	1.50	7.85	99.99	99.99
99.99	99.99	99.99	99.99	99.99	99.99	99.99	99.99	99.99
99.99	99.99	99.99	99.99	99.99	99.99	99.99	99.99	99.99

LAYER ••• 2

99.99	99.99	99.99	99.99	99.99	99.99	99.99	99.99	99.99	99.99
99.99	99.99	99.99	99.99	99.99	99.99	99.99	99.99	99.99	99.99
99.99	99.99	1.37	5.42	0.34	0.72	4.40	2.84	99.99	99.99
99.99	99.99	0.60	0.75	1.37	-1.52	-0.09	7.49	99.99	99.99
99.99	7.54	2.18	-1.38	-0.69	-0.03	2.62	0.31	99.99	99.99
99.99	0.97	1.52	-1.05	0.05	0.50	-0.27	6.78	99.99	99.99
99.99	99.99	-3.94	0.44	-1.87	-2.05	-0.04	-6.28	99.99	99.99
99.99	99.99	-5.55	1.33	0.18	2.51	-2.50	99.99	99.99	99.99
99.99	99.99	99.99	99.99	99.99	-3.01	-4.56	99.99	99.99	99.99
99.99	99.99	99.99	99.99	99.99	99.99	99.99	99.99	99.99	99.99

LAYER ••• 3

99.99	99.99	99.99	99.99	99.99	99.99	99.99	99.99	99.99	99.99	99.99
99.99	99.99	5.82	99.99	99.99	3.99	99.99	99.99	99.99	99.99	99.99
99.99	3.24	2.34	1.44	3.38	2.36	7.64	-1.84	-3.70	99.99	99.99
99.99	3.99	1.81	0.49	-0.05	3.27	4.56	99.99	-4.98	99.99	99.99
99.99	2.21	-0.07	0.84	-2.66	-5.63	4.30	-4.30	11.26	99.99	99.99
99.99	4.33	1.46	-1.91	-1.03	-1.34	-2.71	1.26	-0.05	99.99	99.99
99.99	1.14	0.23	-1.78	-1.12	0.75	-0.13	1.28	2.86	99.99	99.99
99.99	6.78	5.86	99.99	0.85	-0.47	-3.63	1.75	9.68	99.99	99.99
99.99	99.99	99.99	13.19	2.82	-3.22	-0.18	0.80	-0.83	99.99	99.99
99.99	99.99	99.99	99.99	-0.71	3.24	7.70	-5.46	99.99	99.99	99.99
99.99	99.99	99.99	99.99	99.99	1.28	4.36	99.99	99.99	99.99	99.99

LAYER ••• 4

99.99	99.99	99.99	99.99	99.99	99.99	99.99	99.99	99.99	99.99	99.99	99.99
99.99	3.84	17.57	99.99	4.58	3.66	2.83	8.64	99.99	-8.18	99.99	99.99
10.69	6.75	8.30	2.93	5.57	3.97	-1.03	2.59	10.25	99.99	99.99	99.99
99.99	3.73	5.19	4.33	4.71	2.75	3.82	-7.52	4.49	99.99	18.69	99.99
7.79	3.45	-0.52	-1.44	-3.06	-4.11	-2.34	1.49	-4.24	-3.17	99.99	99.99
99.99	0.90	1.38	-1.99	-2.32	3.66	2.43	0.57	7.92	2.47	99.99	99.99
99.99	-2.51	1.01	-1.14	-4.61	-0.48	0.27	-3.57	9.06	10.23	21.91	99.99
9.43	99.99	2.02	-8.40	-7.80	0.83	-1.78	-2.05	4.31	2.22	12.59	99.99
8.05	99.99	1.04	-3.61	7.68	-2.12	-5.95	-0.04	-1.01	4.29	99.99	99.99
99.99	99.99	99.99	99.99	99.99	-1.44	1.48	0.31	3.60	7.78	99.99	99.99
99.99	99.99	99.99	99.99	99.99	2.59	-12.11	-7.91	10.26	9.79	99.99	99.99

99.99	99.99	99.99	99.99	3.22	2.08	-9.74	-0.39	99.99	99.99	99.99	99.99

RESOLUTION MATRIX DIAGONAL ELEMENTS

LAYER ... 1

0.0	0.0	0.0	0.0	0.0	0.0	0.0	0.0	0.0
0.0	0.0	0.0	0.0	0.0	0.0	0.0	0.0	0.0
0.0	0.0	0.100E+01	0.100E+01	0.100E+01	0.0	0.100E+01	0.0	0.0
0.0	0.244E+00	0.100E+01	0.100E+01	0.100E+01	0.0	0.100E+01	0.0	0.0
0.0	0.860E+00	0.100E+01	0.100E+01	0.100E+01	0.100E+01	0.999E+00	0.0	0.0
0.0	0.577E+00	0.100E+01	0.100E+01	0.100E+01	0.100E+01	0.100E+01	0.0	0.0
0.0	0.0	0.100E+01	0.0	0.999E+00	0.100E+01	0.999E+00	0.0	0.0
0.0	0.0	0.0	0.0	0.0	0.0	0.0	0.0	0.0
0.0	0.0	0.0	0.0	0.0	0.0	0.0	0.0	0.0

LAYER ... 2

0.0	0.0	0.0	0.0	0.0	0.0	0.0	0.0	0.0	0.0
0.0	0.0	0.0	0.0	0.0	0.0	0.0	0.0	0.0	0.0
0.0	0.0	0.100E+01	0.100E+01	0.999E+00	0.100E+01	0.999E+00	0.994E+00	0.0	0.0
0.0	0.0	0.100E+01	0.100E+01	0.100E+01	0.998E+00	0.100E+01	0.100E+01	0.0	0.0
0.0	0.525E+00	0.100E+01	0.100E+01	0.100E+01	0.100E+01	0.999E+00	0.100E+01	0.0	0.0
0.0	0.806E+00	0.999E+00	0.100E+01	0.100E+01	0.100E+01	0.100E+01	0.996E+00	0.0	0.0
0.0	0.0	0.100E+01	0.100E+01	0.100E+01	0.100E+01	0.100E+01	0.100E+01	0.0	0.0
0.0	0.0	0.991E+00	0.997E+00	0.999E+00	0.999E+00	0.990E+00	0.0	0.0	0.0
0.0	0.0	0.0	0.0	0.0	0.650E+00	0.982E+00	0.0	0.0	0.0
0.0	0.0	0.0	0.0	0.0	0.0	0.0	0.0	0.0	0.0

LAYER ... 3

0.0	0.0	0.0	0.0	0.0	0.0	0.0	0.0	0.0	0.0	0.0
0.0	0.0	0.969E+00	0.0	0.0	0.995E+00	0.0	0.0	0.0	0.0	0.0
0.0	0.997E+00	0.100E+01	0.100E+01	0.100E+01	0.100E+01	0.996E+00	0.999E+00	0.396E+00	0.0	0.0
0.0	0.999E+00	0.100E+01	0.100E+01	0.100E+01	0.100E+01	0.100E+01	0.0	0.933E+00	0.0	0.0
0.0	0.707E+00	0.100E+01	0.100E+01	0.100E+01	0.100E+01	0.100E+01	0.992E+00	0.951E+00	0.0	0.0
0.0	0.100E+01	0.100E+01	0.100E+01	0.100E+01	0.100E+01	0.100E+01	0.100E+01	0.100E+01	0.0	0.0
0.0	0.851E+00	0.100E+01	0.100E+01	0.100E+01	0.100E+01	0.100E+01	0.999E+00	0.0	0.0	0.0
0.0	0.628E+00	0.997E+00	0.0	0.100E+01	0.100E+01	0.100E+01	0.100E+01	0.998E+00	0.0	0.0
0.0	0.0	0.0	0.913E+00	0.999E+00	0.997E+00	0.100E+01	0.995E+00	0.987E+00	0.0	0.0
0.0	0.0	0.0	0.0	0.994E+00	0.993E+00	0.990E+00	0.998E+00	0.0	0.0	0.0
0.0	0.0	0.0	0.0	0.0	0.986E+00	0.995E+00	0.0	0.0	0.0	0.0

LAYER ... 4

0.0	0.0	0.0	0.0	0.0	0.0	0.0	0.0	0.0	0.0	0.0	0.0
0.0	0.993E+00	0.991E+00	0.0	0.100E+01	0.995E+00	0.989E+00	0.999E+00	0.0	0.780E+00	0.0	0.0
0.594E+00	0.100E+01	0.100E+01	0.100E+01	0.100E+01	0.100E+01	0.100E+01	0.999E+00	0.998E+00	0.0	0.0	0.0
0.0	0.999E+00	0.100E+01	0.100E+01	0.100E+01	0.100E+01	0.100E+01	0.988E+00	0.809E+00	0.0	0.999E+00	0.0
0.693E+00	0.863E+00	0.100E+01	0.100E+01	0.100E+01	0.100E+01	0.999E+00	0.100E+01	0.998E+00	0.974E+00	0.0	0.0
0.0	0.999E+00	0.100E+01	0.100E+01	0.100E+01	0.100E+01	0.100E+01	0.998E+00	0.913E+00	0.995E+00	0.0	0.0
0.0	0.995E+00	0.100E+01	0.100E+01	0.100E+01	0.100E+01	0.100E+01	0.100E+01	0.100E+01	0.100E+01	0.100E+01	0.0
0.956E+00	0.0	0.998E+00	0.100E+01	0.100E+01	0.100E+01	0.100E+01	0.100E+01	0.100E+01	0.990E+00	0.999E+00	0.0

COVARIANCE MATRIX DIAGONAL ELEMENTS

LAYER ... 1

0.0	0.0	0.0	0.0	0.0	0.0	0.0	0.0	0.0
0.0	0.0	0.0	0.0	0.0	0.0	0.0	0.0	0.0
0.0	0.0	0.257E-05	0.604E-06	0.199E-05	0.0	0.243E-06	0.0	0.0
0.0	0.347E-04	0.482E-07	0.129E-06	0.543E-06	0.0	0.153E-04	0.0	0.0
0.0	0.751E-04	0.230E-06	0.688E-07	0.264E-06	0.441E-05	0.997E-05	0.0	0.0
0.0	0.732E-04	0.359E-05	0.858E-06	0.700E-06	0.823E-06	0.120E-04	0.0	0.0
0.0	0.0	0.223E-05	0.0	0.279E-05	0.574E-05	0.101E-03	0.0	0.0
0.0	0.0	0.0	0.0	0.0	0.0	0.0	0.0	0.0
0.0	0.0	0.0	0.0	0.0	0.0	0.0	0.0	0.0

LAYER ... 2

0.0	0.0	0.0	0.0	0.0	0.0	0.0	0.0	0.0	0.0
0.0	0.0	0.0	0.0	0.0	0.0	0.0	0.0	0.0	0.0
0.0	0.0	0.141E-05	0.922E-06	0.119E-04	0.111E-05	0.762E-05	0.610E-04	0.0	0.0
0.0	0.0	0.208E-06	0.128E-06	0.445E-06	0.358E-04	0.181E-05	0.186E-03	0.0	0.0
0.0	0.887E-04	0.567E-06	0.866E-07	0.126E-06	0.113E-05	0.179E-04	0.100E-05	0.0	0.0
0.0	0.287E-03	0.106E-04	0.191E-06	0.142E-06	0.361E-06	0.241E-05	0.134E-03	0.0	0.0
0.0	0.0	0.540E-05	0.251E-05	0.242E-05	0.150E-05	0.246E-05	0.229E-04	0.0	0.0
0.0	0.0	0.520E-04	0.144E-04	0.240E-04	0.913E-05	0.460E-04	0.0	0.0	0.0
0.0	0.0	0.0	0.0	0.0	0.879E-04	0.320E-03	0.0	0.0	0.0
0.0	0.0	0.0	0.0	0.0	0.0	0.0	0.0	0.0	0.0

LAYER ... 3

0.0	0.0	0.0	0.0	0.0	0.0	0.0	0.0	0.0	0.0	0.0
0.0	0.0	0.308E-03	0.0	0.0	0.143E-03	0.0	0.0	0.0	0.0	0.0
0.0	0.719E-04	0.113E-05	0.187E-05	0.298E-05	0.101E-05	0.104E-03	0.194E-04	0.113E-03	0.0	0.0
0.0	0.113E-05	0.149E-05	0.295E-06	0.123E-05	0.282E-05	0.929E-05	0.0	0.198E-03	0.0	0.0
0.0	0.872E-04	0.641E-06	0.172E-06	0.491E-06	0.227E-05	0.243E-05	0.142E-03	0.257E-03	0.0	0.0
0.0	0.420E-04	0.705E-06	0.292E-06	0.670E-06	0.238E-06	0.444E-05	0.131E-04	0.143E-05	0.0	0.0
0.0	0.107E-03	0.769E-05	0.113E-05	0.731E-06	0.209E-06	0.680E-06	0.503E-05	0.649E-04	0.0	0.0
0.0	0.125E-03	0.533E-04	0.0	0.461E-05	0.109E-05	0.152E-05	0.110E-05	0.158E-04	0.0	0.0
0.0	0.0	0.0	0.340E-03	0.823E-05	0.410E-04	0.367E-05	0.111E-03	0.115E-03	0.0	0.0
0.0	0.0	0.0	0.0	0.111E-03	0.897E-04	0.251E-03	0.923E-04	0.0	0.0	0.0
0.0	0.0	0.0	0.0	0.0	0.217E-03	0.141E-03	0.0	0.0	0.0	0.0

LAYER ... 4

0.0	0.0	0.0	0.0	0.0	0.0	0.0	0.0	0.0	0.0	0.0	0.0
0.0	0.746E-04	0.318E-03	0.0	0.292E-04	0.133E-03	0.103E-03	0.361E-04	0.0	0.178E-03	0.0	0.0
0.982E-04	0.166E-05	0.105E-05	0.577E-05	0.126E-05	0.851E-06	0.106E-04	0.382E-04	0.403E-04	0.0	0.0	0.0
0.0	0.055E-06	0.184E-06	0.886E-06	0.302E-05	0.119E-05	0.423E-05	0.352E-03	0.861E-04	0.0	0.410E-03	0.0
0.743E-04	0.651E-04	0.626E-06	0.285E-06	0.128E-05	0.609E-05	0.103E-04	0.146E-04	0.995E-04	0.167E-03	0.0	0.0

0.0	0.591E-04	0.182E-05	0.491E-06	0.719E-06	0.250E-05	0.223E-05	0.889E-04	0.417E-03	0.537E-04	0.0	0.0
0.0	0.710E-04	0.678E-06	0.531E-06	0.306E-05	0.161E-05	0.684E-06	0.184E-05	0.402E-05	0.102E-05	0.299E-04	0.0
0.210E-03	0.0	0.171E-04	0.147E-05	0.790E-05	0.670E-06	0.369E-06	0.801E-06	0.762E-05	0.212E-03	0.195E-03	0.0
0.233E-03	0.0	0.266E-04	0.488E-03	0.128E-04	0.389E-05	0.754E-06	0.114E-05	0.193E-05	0.221E-04	0.0	0.0
0.0	0.0	0.0	0.0	0.0	0.123E-04	0.515E-05	0.327E-05	0.941E-04	0.109E-03	0.0	0.0
0.0	0.0	0.0	0.0	0.0	0.612E-04	0.224E-03	0.347E-04	0.263E-04	0.341E-03	0.0	0.0
0.0	0.0	0.0	0.0	0.188E-03	0.469E-04	0.127E-03	0.412E-03	0.0	0.0	0.0	0.0

SOLUTION NO. 4 THIS SOLUTION HAS 4 EIGENVALUES REMOVED IN ADDITION TO THE ZERO EIGENVALUES

LAYER ••• 1

99.99	99.99	99.99	99.99	99.99	99.99	99.99	99.99	99.99
99.99	99.99	99.99	99.99	99.99	99.99	99.99	99.99	99.99
99.99	99.99	0.28	0.78	-1.99	99.99	0.64	99.99	99.99
99.99	1.70	0.30	-0.50	-0.77	99.99	5.05	99.99	99.99
99.99	-3.15	-0.24	-0.68	-3.47	-8.27	-1.24	99.99	99.99
99.99	-0.57	0.17	-3.57	-3.90	-4.41	2.78	99.99	99.99
99.99	99.99	-0.71	99.99	-1.00	1.62	7.96	99.99	99.99
99.99	99.99	99.99	99.99	99.99	99.99	99.99	99.99	99.99
99.99	99.99	99.99	99.99	99.99	99.99	99.99	99.99	99.99

LAYER ••• 2

99.99	99.99	99.99	99.99	99.99	99.99	99.99	99.99	99.99	99.99
99.99	99.99	99.99	99.99	99.99	99.99	99.99	99.99	99.99	99.99
99.99	99.99	1.37	5.42	0.07	0.71	4.22	2.31	99.99	99.99
99.99	99.99	0.57	0.75	1.38	-1.28	-0.05	7.41	99.99	99.99
99.99	7.96	2.21	-1.39	-0.68	-0.03	2.60	0.29	99.99	99.99
99.99	1.94	1.43	-1.05	0.05	0.52	-0.25	6.51	99.99	99.99
99.99	99.99	-4.00	0.38	-1.88	-2.07	-0.05	-6.36	99.99	99.99
99.99	99.99	-5.95	1.22	0.01	2.61	-2.94	99.99	99.99	99.99
99.99	99.99	99.99	99.99	99.99	-5.10	-4.28	99.99	99.99	99.99
99.99	99.99	99.99	99.99	99.99	99.99	99.99	99.99	99.99	99.99

LAYER ••• 3

99.99	99.99	99.99	99.99	99.99	99.99	99.99	99.99	99.99	99.99	99.99
99.99	99.99	6.55	99.99	99.99	3.77	99.99	99.99	99.99	99.99	99.99
99.99	3.51	2.41	1.44	3.48	2.36	8.03	-1.60	1.08	99.99	99.99
99.99	3.90	1.80	0.49	-0.05	3.19	4.54	99.99	-4.36	99.99	99.99
99.99	3.72	0.00	0.65	-2.65	-5.65	4.28	-4.17	10.08	99.99	99.99
99.99	4.40	1.46	-1.90	-1.03	-1.35	-2.65	1.32	-0.02	99.99	99.99
99.99	1.00	0.22	-1.77	-1.12	0.73	-0.14	1.24	2.98	99.99	99.99
99.99	9.49	5.96	99.99	0.83	-0.51	-3.62	1.77	9.94	99.99	99.99
99.99	99.99	99.99	13.80	2.82	-3.36	-0.19	1.21	-1.41	99.99	99.99
99.99	99.99	99.99	99.99	-0.24	3.68	7.37	-5.80	99.99	99.99	99.99
99.99	99.99	99.99	99.99	99.99	1.84	3.98	99.99	99.99	99.99	99.99

LAYER ••• 4

99.99	99.99	99.99	99.99	99.99	99.99	99.99	99.99	99.99	99.99	99.99	99.99
99.99	3.31	16.86	99.99	5.03	3.38	3.46	8.86	99.99	-10.73	99.99	99.99
12.59	6.74	8.29	2.92	5.59	3.99	-0.95	2.39	9.93	99.99	99.99	99.99
99.99	3.83	5.10	4.35	4.68	2.75	3.81	-6.60	3.31	99.99	18.83	99.99
7.55	1.70	-0.57	-1.44	-3.09	-4.17	-2.44	1.44	-4.35	-2.33	99.99	99.99
99.99	0.96	1.36	-1.99	-2.33	3.67	2.39	0.24	6.46	1.92	99.99	99.99
99.99	-2.29	1.00	-1.16	-4.62	-0.47	0.26	-3.60	9.02	10.23	21.05	99.99
9.28	99.99	2.15	-8.39	-7.75	0.81	-1.80	-2.07	4.17	2.77	12.46	99.99
6.92	99.99	1.00	-2.20	7.66	-2.08	-5.97	-0.05	-1.06	4.09	99.99	99.99
99.99	99.99	99.99	99.99	99.99	-1.33	1.42	0.23	3.05	7.81	99.99	99.99
99.99	99.99	99.99	99.99	99.99	2.69	-11.62	-8.03	10.32	11.45	99.99	99.99

99.99	99.99	99.99	99.99	3.29	1.95	-10.00	0.43	99.99	99.99	99.99	99.99

485 RESOLUTION MATRIX DIAGONAL ELEMENTS

LAYER ... 1

0.0	0.0	0.0	0.0	0.0	0.0	0.0	0.0	0.0
0.0	0.0	0.0	0.0	0.0	0.0	0.0	0.0	0.0
0.0	0.0	0.100E+01	0.100E+01	0.100E+01	0.0	0.100E+01	0.0	0.0
0.0	0.249E+00	0.100E+01	0.100E+01	0.100E+01	0.0	0.100E+01	0.0	0.0
0.0	0.913E+00	0.100E+01	0.100E+01	0.100E+01	0.100E+01	0.100E+01	0.0	0.0
0.0	0.747E+00	0.100E+01	0.100E+01	0.100E+01	0.100E+01	0.100E+01	0.0	0.0
0.0	0.0	0.100E+01	0.0	0.100E+01	0.100E+01	0.999E+00	0.0	0.0
0.0	0.0	0.0	0.0	0.0	0.0	0.0	0.0	0.0
0.0	0.0	0.0	0.0	0.0	0.0	0.0	0.0	0.0

LAYER ... 2

0.0	0.0	0.0	0.0	0.0	0.0	0.0	0.0	0.0	0.0
0.0	0.0	0.0	0.0	0.0	0.0	0.0	0.0	0.0	0.0
0.0	0.0	0.100E+01	0.100E+01	0.100E+01	0.100E+01	0.100E+01	0.999E+00	0.0	0.0
0.0	0.0	0.100E+01	0.100E+01	0.100E+01	0.999E+00	0.100E+01	0.100E+01	0.0	0.0
0.0	0.530E+00	0.100E+01	0.100E+01	0.100E+01	0.100E+01	0.100E+01	0.100E+01	0.0	0.0
0.0	0.300E+00	0.100E+01	0.100E+01	0.100E+01	0.100E+01	0.100E+01	0.999E+00	0.0	0.0
0.0	0.0	0.100E+01	0.100E+01	0.100E+01	0.100E+01	0.100E+01	0.100E+01	0.0	0.0
0.0	0.0	0.994E+00	0.995E+00	0.995E+00	0.999E+00	0.997E+00	0.0	0.0	0.0
0.0	0.0	0.0	0.0	0.0	0.834E+00	0.983E+00	0.0	0.0	0.0
0.0	0.0	0.0	0.0	0.0	0.0	0.0	0.0	0.0	0.0

LAYER ... 3

0.0	0.0	0.0	0.0	0.0	0.0	0.0	0.0	0.0	0.0	0.0
0.0	0.0	0.979E+00	0.0	0.0	0.997E+00	0.0	0.0	0.0	0.0	0.0
0.0	0.999E+00	0.100E+01	0.100E+01	0.100E+01	0.100E+01	0.999E+00	0.100E+01	0.716E+00	0.0	0.0
0.0	0.999E+00	0.100E+01	0.100E+01	0.100E+01	0.100E+01	0.100E+01	0.0	0.961E+00	0.0	0.0
0.0	0.822E+00	0.100E+01	0.100E+01	0.100E+01	0.100E+01	0.100E+01	0.992E+00	0.975E+00	0.0	0.0
0.0	0.100E+01	0.100E+01	0.100E+01	0.100E+01	0.100E+01	0.100E+01	0.100E+01	0.100E+01	0.0	0.0
0.0	0.851E+00	0.100E+01	0.100E+01	0.100E+01	0.100E+01	0.100E+01	0.100E+01	0.100E+01	0.0	0.0
0.0	0.731E+00	0.999E+00	0.0	0.100E+01	0.100E+01	0.100E+01	0.100E+01	0.999E+00	0.0	0.0
0.0	0.0	0.0	0.995E+00	0.999E+00	0.998E+00	0.100E+01	0.999E+00	0.995E+00	0.0	0.0
0.0	0.0	0.0	0.0	0.998E+00	0.995E+00	0.992E+00	0.999E+00	0.0	0.0	0.0
0.0	0.0	0.0	0.0	0.0	0.991E+00	0.997E+00	0.0	0.0	0.0	0.0

LAYER ... 4

0.0	0.0	0.0	0.0	0.0	0.0	0.0	0.0	0.0	0.0	0.0	0.0
0.0	0.999E+00	0.999E+00	0.0	0.100E+01	0.998E+00	0.996E+00	0.100E+01	0.0	0.876E+00	0.0	0.0
0.913E+00	0.100E+01	0.100E+01	0.100E+01	0.100E+01	0.100E+01	0.100E+01	0.999E+00	0.999E+00	0.0	0.0	0.0
0.0	0.999E+00	0.100E+01	0.100E+01	0.100E+01	0.100E+01	0.100E+01	0.100E+01	0.939E+00	0.0	0.100E+01	0.0
0.694E+00	0.902E+00	0.100E+01	0.100E+01	0.100E+01	0.100E+01	0.100E+01	0.100E+01	0.998E+00	0.984E+00	0.0	0.0
0.0	0.999E+00	0.100E+01	0.100E+01	0.100E+01	0.100E+01	0.100E+01	0.100E+01	0.945E+00	0.100E+01	0.0	0.0
0.0	0.996E+00	0.100E+01	0.100E+01	0.100E+01	0.100E+01	0.100E+01	0.100E+01	0.100E+01	0.100E+01	0.100E+01	0.0
0.957E+00	0.0	0.999E+00	0.100E+01	0.100E+01	0.100E+01	0.100E+01	0.100E+01	0.100E+01	0.997E+00	0.100E+01	0.0

0.947E+00	0.0	0.999E+00	0.995E+00	0.100E+01	0.100E+01	0.100E+01	0.100E+01	0.100E+01	0.100E+01	0.0	0.0
0.0	0.0	0.0	0.0	0.0	0.999E+00	0.100E+01	0.100E+01	0.999E+00	0.100E+01	0.0	0.0
0.0	0.0	0.0	0.0	0.0	0.998E+00	0.977E+00	0.100E+01	0.999E+00	0.945E+00	0.0	0.0
0.0	0.0	0.0	0.0	0.991E+00	0.999E+00	0.999E+00	0.978E+00	0.0	0.0	0.0	0.0

COVARIANCE MATRIX DIAGONAL ELEMENTS

LAYER ... 1

0.0	0.0	0.0	0.0	0.0	0.0	0.0	0.0	0.0
0.0	0.0	0.0	0.0	0.0	0.0	0.0	0.0	0.0
0.0	0.0	0.238E-06	0.607E-06	0.202E-05	0.0	0.253E-06	0.0	0.0
0.0	0.419E-04	0.100E-06	0.130E-06	0.545E-06	0.0	0.154E-04	0.0	0.0
0.0	0.148E-03	0.239E-06	0.688E-07	0.277E-06	0.457E-05	0.109E-04	0.0	0.0
0.0	0.275E-03	0.361E-05	0.862E-06	0.738E-06	0.815E-06	0.123E-04	0.0	0.0
0.0	0.0	0.229E-05	0.0	0.300E-05	0.598E-05	0.101E-03	0.0	0.0
0.0	0.0	0.0	0.0	0.0	0.0	0.0	0.0	0.0
0.0	0.0	0.0	0.0	0.0	0.0	0.0	0.0	0.0

LAYER ... 2

0.0	0.0	0.0	0.0	0.0	0.0	0.0	0.0	0.0	0.0
0.0	0.0	0.0	0.0	0.0	0.0	0.0	0.0	0.0	0.0
0.0	0.0	0.141E-05	0.923E-06	0.132E-04	0.112E-05	0.829E-05	0.677E-04	0.0	0.0
0.0	0.0	0.243E-06	0.130E-06	0.449E-06	0.369E-04	0.185E-05	0.186E-03	0.0	0.0
0.0	0.939E-04	0.588E-06	0.874E-07	0.128E-06	0.113E-05	0.183E-04	0.101E-05	0.0	0.0
0.0	0.395E-03	0.108E-04	0.191E-06	0.142E-06	0.365E-06	0.243E-05	0.138E-03	0.0	0.0
0.0	0.0	0.547E-05	0.260E-05	0.243E-05	0.151E-05	0.248E-05	0.230E-04	0.0	0.0
0.0	0.0	0.552E-04	0.157E-04	0.245E-04	0.934E-05	0.531E-04	0.0	0.0	0.0
0.0	0.0	0.0	0.0	0.0	0.349E-03	0.322E-03	0.0	0.0	0.0
0.0	0.0	0.0	0.0	0.0	0.0	0.0	0.0	0.0	0.0

LAYER ... 3

0.0	0.0	0.0	0.0	0.0	0.0	0.0	0.0	0.0	0.0	0.0
0.0	0.0	0.322E-03	0.0	0.0	0.146E-03	0.0	0.0	0.0	0.0	0.0
0.0	0.747E-04	0.116E-05	0.188E-05	0.308E-05	0.101E-05	0.109E-03	0.205E-04	0.517E-03	0.0	0.0
0.0	0.199E-05	0.168E-06	0.302E-06	0.123E-05	0.294E-05	0.930E-05	0.0	0.236E-03	0.0	0.0
0.0	0.218E-03	0.312E-06	0.174E-06	0.492E-06	0.229E-05	0.244E-05	0.142E-03	0.286E-03	0.0	0.0
0.0	0.421E-04	0.706E-06	0.296E-06	0.672E-06	0.241E-06	0.450E-05	0.132E-04	0.145E-05	0.0	0.0
0.0	0.107E-03	0.774E-05	0.113E-05	0.732E-06	0.213E-06	0.688E-06	0.511E-05	0.652E-04	0.0	0.0
0.0	0.267E-03	0.549E-04	0.0	0.461E-05	0.112E-05	0.153E-05	0.110E-05	0.172E-04	0.0	0.0
0.0	0.0	0.0	0.394E-03	0.831E-05	0.425E-04	0.368E-05	0.115E-03	0.125E-03	0.0	0.0
0.0	0.0	0.0	0.0	0.116E-03	0.931E-04	0.253E-03	0.948E-04	0.0	0.0	0.0
0.0	0.0	0.0	0.0	0.0	0.224E-03	0.144E-03	0.0	0.0	0.0	0.0

LAYER ... 4

0.0	0.0	0.0	0.0	0.0	0.0	0.0	0.0	0.0	0.0	0.0	0.0
0.0	0.821E-04	0.327E-03	0.0	0.294E-04	0.137E-03	0.114E-03	0.370E-04	0.0	0.296E-03	0.0	0.0
0.404E-03	0.168E-05	0.106E-05	0.578E-05	0.127E-05	0.859E-06	0.107E-04	0.390E-04	0.424E-04	0.0	0.0	0.0
0.0	0.105E-05	0.195E-06	0.894E-06	0.305E-05	0.119E-05	0.424E-05	0.367E-03	0.265E-03	0.0	0.410E-03	0.0
0.760E-04	0.121E-03	0.695E-06	0.286E-06	0.130E-05	0.614E-05	0.106E-04	0.148E-04	0.997E-04	0.181E-03	0.0	0.0

0.0	0.592E-04	0.183E-05	0.503E-06	0.725E-06	0.250E-05	0.226E-05	0.909E-04	0.455E-03	0.592E-04	0.0	0.0
0.0	0.719E-04	0.682E-06	0.536E-06	0.306E-05	0.161E-05	0.689E-06	0.186E-05	0.406E-05	0.103E-05	0.299E-04	0.0
0.211E-03	0.0	0.175E-04	0.147E-05	0.794E-05	0.683E-06	0.371E-06	0.809E-06	0.796E-05	0.222E-03	0.196E-03	0.0
0.259E-03	0.0	0.282E-04	0.527E-03	0.128E-04	0.398E-05	0.773E-06	0.115E-05	0.203E-05	0.228E-04	0.0	0.0
0.0	0.0	0.0	0.0	0.0	0.130E-04	0.556E-05	0.346E-05	0.994E-04	0.110E-03	0.0	0.0
0.0	0.0	0.0	0.0	0.0	0.815E-04	0.253E-03	0.351E-04	0.265E-04	0.416E-03	0.0	0.0
0.0	0.0	0.0	0.0	0.189E-03	0.473E-04	0.129E-03	0.459E-03	0.0	0.0	0.0	0.0

SOLUTION NO. 5 THIS SOLUTION HAS 0 EIGENVALUES REMOVED IN ADDITION TO THE ZERO EIGENVALUES

LAYER ••• 1

99.99	99.99	99.99	99.99	99.99	99.99	99.99	99.99	99.99
99.99	99.99	99.99	99.99	99.99	99.99	99.99	99.99	99.99
99.99	99.99	0.26	0.79	-1.94	99.99	0.67	99.99	99.99
99.99	11.21	0.28	-0.49	-0.89	99.99	5.31	99.99	99.99
99.99	5.69	-0.29	-0.66	-3.82	-8.65	-1.56	99.99	99.99
99.99	20.39	-0.10	-3.67	-3.90	-4.29	2.60	99.99	99.99
99.99	99.99	-0.42	99.99	-1.42	1.92	9.02	99.99	99.99
99.99	99.99	99.99	99.99	99.99	99.99	99.99	99.99	99.99
99.99	99.99	99.99	99.99	99.99	99.99	99.99	99.99	99.99

LAYER ••• 2

99.99	99.99	99.99	99.99	99.99	99.99	99.99	99.99	99.99	99.99
99.99	99.99	99.99	99.99	99.99	99.99	99.99	99.99	99.99	99.99
99.99	99.99	1.37	5.43	-0.01	0.57	4.04	1.27	99.99	99.99
99.99	99.99	0.75	0.75	1.38	-0.40	0.05	7.22	99.99	99.99
99.99	15.20	2.11	-1.40	-0.70	0.01	1.97	0.26	99.99	99.99
99.99	-11.85	1.36	-1.07	0.04	0.58	0.02	6.17	99.99	99.99
99.99	99.99	-4.11	0.16	-1.66	-1.98	-0.06	-6.58	99.99	99.99
99.99	99.99	-5.63	0.29	-0.80	3.42	-4.82	99.99	99.99	99.99
99.99	99.99	99.99	99.99	99.99	2.21	-3.54	99.99	99.99	99.99
99.99	99.99	99.99	99.99	99.99	99.99	99.99	99.99	99.99	99.99

LAYER ••• 3

99.99	99.99	99.99	99.99	99.99	99.99	99.99	99.99	99.99	99.99	99.99
99.99	99.99	7.01	99.99	99.99	5.05	99.99	99.99	99.99	99.99	99.99
99.99	3.30	2.43	1.43	3.47	2.34	7.79	-0.99	16.55	99.99	99.99
99.99	4.14	1.84	0.46	-0.05	3.05	4.51	99.99	-11.68	99.99	99.99
99.99	-14.72	-0.50	0.80	-2.63	-5.53	4.23	-3.92	15.57	99.99	99.99
99.99	4.28	1.54	-1.85	-1.11	-1.37	-2.45	1.31	0.02	99.99	99.99
99.99	7.48	0.21	-1.73	-1.13	0.73	-0.08	1.30	3.39	99.99	99.99
99.99	9.36	6.72	99.99	1.23	-0.63	-3.55	1.78	10.66	99.99	99.99
99.99	99.99	99.99	20.08	3.15	-4.46	-0.25	2.27	-3.84	99.99	99.99
99.99	99.99	99.99	99.99	0.86	4.80	3.75	-6.80	99.99	99.99	99.99
99.99	99.99	99.99	99.99	99.99	3.84	2.60	99.99	99.99	99.99	99.99

LAYER ••• 4

99.99	99.99	99.99	99.99	99.99	99.99	99.99	99.99	99.99	99.99	99.99	99.99
99.99	3.36	17.12	99.99	4.67	3.74	2.75	8.88	99.99	-18.84	99.99	99.99
-4.96	6.59	8.33	2.90	5.54	4.11	-0.68	2.75	9.22	99.99	99.99	99.99
99.99	3.45	5.16	4.32	4.72	2.71	3.74	-6.13	10.91	99.99	19.01	99.99
2.59	3.02	-0.27	-1.47	-3.01	-3.99	-2.61	1.54	-5.52	-7.04	99.99	99.99
99.99	1.18	1.50	-1.90	-2.33	3.54	2.39	-0.23	8.37	1.71	99.99	99.99
99.99	-0.94	0.98	-1.15	-4.59	-0.44	0.35	-3.55	9.07	10.32	21.87	99.99
7.34	99.99	3.01	-8.28	-7.47	0.91	-1.72	-2.02	4.35	3.25	12.40	99.99
7.89	99.99	0.27	-1.06	7.63	-1.80	-5.87	-0.08	-1.18	3.71	99.99	99.99
99.99	99.99	99.99	99.99	99.99	-0.82	1.68	0.13	3.48	8.07	99.99	99.99
99.99	99.99	99.99	99.99	99.99	3.40	-6.54	-8.29	10.99	18.44	99.99	99.99

99.99	99.99	99.99	99.99	6.20	1.50	-10.64	-1.04	99.99	99.99	99.99	99.99

RESOLUTION MATRIX DIAGONAL ELEMENTS

LAYER ... 1

0.0	0.0	0.0	0.0	0.0	0.0	0.0	0.0	0.0
0.0	0.0	0.0	0.0	0.0	0.0	0.0	0.0	0.0
0.0	0.0	0.100E+01	0.10CE+01	0.100E+01	0.0	0.100E+01	0.0	0.0
0.0	0.100E+01	0.100E+01	0.100E+01	0.100E+01	0.0	0.100E+01	0.0	0.0
0.0	0.100E+01	0.100E+01	0.100E+01	0.100E+01	0.100E+01	0.100E+01	0.0	0.0
0.0	0.100E+01	0.100E+01	0.100E+01	0.100E+01	0.100E+01	0.100E+01	0.0	0.0
0.0	0.0	0.100E+01	0.0	0.100E+01	0.100E+01	0.100E+01	0.0	0.0
0.0	0.0	0.0	0.0	0.0	0.0	0.0	0.0	0.0
0.0	0.0	0.0	0.0	0.0	0.0	0.0	0.0	0.0

LAYER ... 2

0.0	0.0	0.0	0.0	0.0	0.0	0.0	0.0	0.0	0.0
0.0	0.0	0.0	0.0	0.0	0.0	0.0	0.0	0.0	0.0
0.0	0.0	0.100E+01	0.10CE+01	0.100E+01	0.100E+01	0.100E+01	0.100E+01	0.0	0.0
0.0	0.0	0.100E+01	0.100E+01	0.100E+01	0.100E+01	0.100E+01	0.100E+01	0.0	0.0
0.0	0.100E+01	0.100E+01	0.10CE+01	0.100E+01	0.100E+01	0.100E+01	0.100E+01	0.0	0.0
0.0	0.100E+01	0.100E+01	0.10CE+01	0.100E+01	0.100E+01	0.100E+01	0.100E+01	0.0	0.0
0.0	0.0	0.100E+01	0.10CE+01	0.100E+01	0.10CE+01	0.100E+01	0.100E+01	0.0	0.0
0.0	0.0	0.10CE+01	0.10CE+01	0.100E+01	0.10CE+01	0.100E+01	0.0	0.0	0.0
0.0	0.0	0.0	0.0	0.0	0.100E+01	0.100E+01	0.0	0.0	0.0
0.0	0.0	0.0	0.0	0.0	0.0	0.0	0.0	0.0	0.0

LAYER ... 3

0.0	0.0	0.0	0.0	0.0	0.0	0.0	0.0	0.0	0.0	0.0
0.0	0.0	0.100E+01	0.0	0.0	0.100E+01	0.0	0.0	0.0	0.0	0.0
0.0	0.100E+01	0.100E+01	0.100E+01	0.100E+01	0.100E+01	0.100E+01	0.100E+01	0.100E+01	0.0	0.0
0.0	0.100E+01	0.100E+01	0.100E+01	0.10CE+01	0.100E+01	0.100E+01	0.0	0.100E+01	0.0	0.0
0.0	0.100E+01	0.100E+01	0.10CE+01	0.100E+01	0.100E+01	0.100E+01	0.100E+01	0.100E+01	0.0	0.0
0.0	0.100E+01	0.100E+01	0.10CE+01	0.100E+01	0.100E+01	0.100E+01	0.100E+01	0.100E+01	0.0	0.0
0.0	0.100E+01	0.100E+01	0.10CE+01	0.100E+01	0.100E+01	0.100E+01	0.100E+01	0.100E+01	0.0	0.0
0.0	0.100E+01	0.100E+01	0.0	0.100E+01	0.10CE+01	0.100E+01	0.100E+01	0.100E+01	0.0	0.0
0.0	0.0	0.0	0.100E+01	0.100E+01	0.100E+01	0.100E+01	0.100E+01	0.100E+01	0.0	0.0
0.0	0.0	0.0	0.0	0.100E+01	0.100E+01	0.100E+01	0.100E+01	0.0	0.0	0.0
0.0	0.0	0.0	0.0	0.0	0.10CE+01	0.100E+01	0.0	0.0	0.0	0.0

LAYER ... 4

0.0	0.0	0.0	0.0	0.0	0.0	0.0	0.0	0.0	0.0	0.0	0.0
0.0	0.100E+01	0.100E+01	0.0	0.100E+01	0.100E+01	0.100E+01	0.100E+01	0.0	0.100E+01	0.0	0.0
0.100E+01	0.100E+01	0.100E+01	0.100E+01	0.100E+01	0.100E+01	0.100E+01	0.100E+01	0.100E+01	0.0	0.0	0.0
0.0	0.100E+01	0.100E+01	0.10CE+01	0.100E+01	0.100E+01	0.100E+01	0.100E+01	0.100E+01	0.0	0.100E+01	0.0
0.100E+01	0.100E+01	0.100E+01	0.100E+01	0.100E+01	0.100E+01	0.100E+01	0.100E+01	0.100E+01	0.100E+01	0.0	0.0
0.0	0.100E+01	0.100E+01	0.10CE+01	0.100E+01	0.10CE+01	0.100E+01	0.100E+01	0.100E+01	0.100E+01	0.0	0.0
0.0	0.100E+01	0.100E+01	0.100E+01	0.100E+01	0.100E+01	0.100E+01	0.100E+01	0.100E+01	0.100E+01	0.100E+01	0.0
0.0	0.100E+01	0.100E+01	0.100E+01	0.100E+01	0.100E+01	0.100E+01	0.100E+01	0.100E+01	0.100E+01	0.100E+01	0.0
0.100E+01	0.0	0.100E+01	0.100E+01	0.100E+01	0.100E+01	0.100E+01	0.100E+01	0.100E+01	0.100E+01	0.100E+01	0.0

COVARIANCE MATRIX DIAGONAL ELEMENTS

LAYER ... 1

0.0	0.0	0.0	0.0	0.0	0.0	0.0	0.0	0.0
0.0	0.0	0.0	0.0	0.0	0.0	0.0	0.0	0.0
0.0	0.0	0.259E-06	0.610E-06	0.203E-05	0.0	0.258E-06	0.0	0.0
0.0	0.348E-02	0.142E-06	0.133E-06	0.589E-06	0.0	0.157E-04	0.0	0.0
0.0	0.314E-03	0.246E-06	0.655E-07	0.299E-06	0.491E-05	0.117E-04	0.0	0.0
0.0	0.847E-03	0.380E-05	0.889E-06	0.755E-06	0.861E-06	0.125E-04	0.0	0.0
0.0	0.0	0.253E-05	0.0	0.346E-05	0.614E-05	0.103E-03	0.0	0.0
0.0	0.0	0.0	0.0	0.0	0.0	0.0	0.0	0.0
0.0	0.0	0.0	0.0	0.0	0.0	0.0	0.0	0.0

LAYER ... 2

0.0	0.0	0.0	0.0	0.0	0.0	0.0	0.0	0.0	0.0
0.0	0.0	0.0	0.0	0.0	0.0	0.0	0.0	0.0	0.0
0.0	0.0	0.141E-05	0.923E-06	0.135E-04	0.117E-05	0.834E-05	0.699E-04	0.0	0.0
0.0	0.0	0.427E-06	0.131E-06	0.450E-06	0.392E-04	0.186E-05	0.187E-03	0.0	0.0
0.0	0.213E-02	0.648E-06	0.905E-07	0.129E-06	0.116E-05	0.190E-04	0.103E-05	0.0	0.0
0.0	0.706E-03	0.116E-04	0.193E-06	0.145E-06	0.380E-06	0.255E-05	0.140E-03	0.0	0.0
0.0	0.0	0.558E-05	0.270E-05	0.258E-05	0.155E-05	0.250E-05	0.233E-04	0.0	0.0
0.0	0.0	0.690E-04	0.196E-04	0.271E-04	0.103E-04	0.598E-04	0.0	0.0	0.0
0.0	0.0	0.0	0.0	0.0	0.663E-03	0.358E-03	0.0	0.0	0.0
0.0	0.0	0.0	0.0	0.0	0.0	0.0	0.0	0.0	0.0

LAYER ... 3

0.0	0.0	0.0	0.0	0.0	0.0	0.0	0.0	0.0	0.0	0.0
0.0	0.0	0.365E-03	0.0	0.0	0.153E-03	0.0	0.0	0.0	0.0	0.0
0.0	0.783E-04	0.117E-05	0.189E-05	0.329E-05	0.102E-05	0.110E-03	0.212E-04	0.125E-02	0.0	0.0
0.0	0.472E-05	0.232E-06	0.313E-06	0.125E-05	0.297E-05	0.936E-05	0.0	0.338E-03	0.0	0.0
0.0	0.699E-03	0.130E-05	0.183E-06	0.493E-06	0.231E-05	0.246E-05	0.158E-03	0.350E-03	0.0	0.0
0.0	0.424E-04	0.725E-06	0.302E-06	0.683E-06	0.243E-06	0.456E-05	0.132E-04	0.145E-05	0.0	0.0
0.0	0.747E-03	0.775E-05	0.114E-05	0.735E-06	0.215E-06	0.699E-06	0.513E-05	0.656E-04	0.0	0.0
0.0	0.829E-03	0.569E-04	0.0	0.518E-05	0.115E-05	0.154E-05	0.112E-05	0.182E-04	0.0	0.0
0.0	0.0	0.0	0.484E-03	0.101E-04	0.479E-04	0.370E-05	0.117E-03	0.137E-03	0.0	0.0
0.0	0.0	0.0	0.0	0.122E-03	0.105E-03	0.274E-03	0.963E-04	0.0	0.0	0.0
0.0	0.0	0.0	0.0	0.0	0.267E-03	0.150E-03	0.0	0.0	0.0	0.0

LAYER ... 4

0.0	0.0	0.0	0.0	0.0	0.0	0.0	0.0	0.0	0.0	0.0	0.0
0.0	0.860E-04	0.329E-03	0.0	0.298E-04	0.143E-03	0.129E-03	0.372E-04	0.0	0.607E-03	0.0	0.0
0.108E-02	0.172E-05	0.106E-05	0.580E-05	0.128E-05	0.888E-06	0.110E-04	0.401E-04	0.440E-04	0.0	0.0	0.0
0.0	0.243E-05	0.220E-06	0.929E-06	0.306E-05	0.121E-05	0.426E-05	0.368E-03	0.469E-03	0.0	0.411E-03	0.0
0.139E-02	0.333E-03	0.870E-06	0.293E-06	0.131E-05	0.621E-05	0.109E-04	0.148E-04	0.104E-03	0.217E-03	0.0	0.0

0.0	0.605E-04	0.187E-05	0.824E-06	0.734E-06	0.253E-05	0.228E-05	0.916E-04	0.580E-03	0.595E-04	0.0	0.0
0.0	0.756E-04	0.607E-06	0.540E-06	0.307E-05	0.162E-05	0.735E-06	0.187E-05	0.407E-05	0.106E-05	0.300E-04	0.0
0.390E-03	0.0	0.201E-04	0.150E-06	0.813E-05	0.713E-06	0.394E-06	0.822E-06	0.800E-05	0.229E-03	0.196E-03	0.0
0.373E-03	0.0	0.294E-04	0.544E-03	0.128E-04	0.410E-05	0.826E-06	0.117E-05	0.206E-05	0.231E-04	0.0	0.0
0.0	0.0	0.0	0.0	0.0	0.137E-04	0.610E-05	0.377E-05	0.101E-03	0.111E-03	0.0	0.0
0.0	0.0	0.0	0.0	0.0	0.844E-04	0.312E-03	0.352E-04	0.279E-04	0.537E-03	0.0	0.0
0.0	0.0	0.0	0.0	0.208E-03	0.519E-04	0.130E-03	0.540E-03	0.0	0.0	0.0	0.0

BIOGRAPHY *

George Zandt was born on Christmas day, 1950 in Hino, a suburb of Tokyo, Japan. When he was seven, his family moved back to the United States and settled down in Milwaukee, Wisconsin where he attended the University of Wisconsin at Milwaukee and graduated with a bachelor's degree in geology in 1973. While at UWM, he met Heidi Zorn, one of the few persons with a last name that comes after his alphabetically. George and Heidi were married on July 3, 1975. Their union produced Roo, a rabbit used for earthquake prediction by the M.I.T. seismology group where George pursued his graduate studies. While at M.I.T., the author gained notoriety as the first recipient of the M. Nafi Toksöz Award given by the Institute of Applied Theoretical Geophysics for spending the most time away from M.I.T. without a formal leave of absence in an academic year. He was also quoted as the "famous M.I.T. scientist" by Tech Talk, the official M.I.T. newspaper. His hobbies include photography, softball, hiking and looking for blocks under Japan. The Zandts make their home now in Salt Lake City, Utah where George is employed as a research geophysicist at the University of Utah.

* by Arthur C.H. Cheng